

Shin Horiuchi · Nao Terasaki ·
Takayuki Miyamae *Editors*

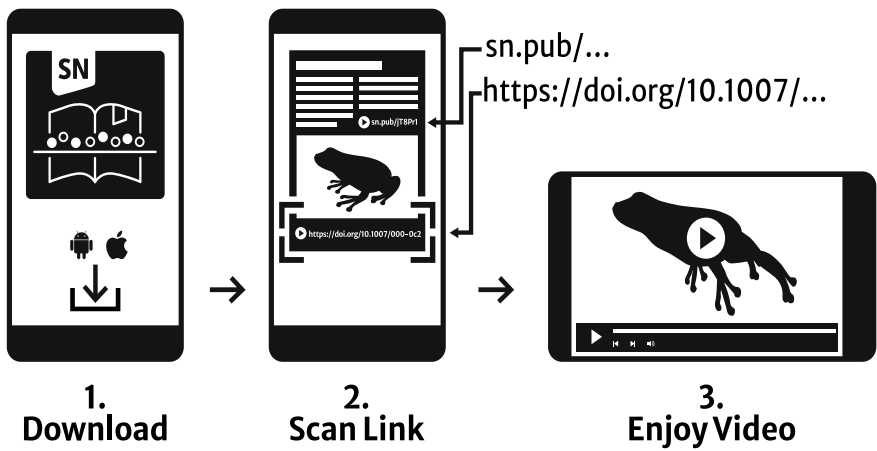
Interfacial Phenomena in Adhesion and Adhesive Bonding

OPEN ACCESS

 Springer

Interfacial Phenomena in Adhesion and Adhesive Bonding

Springer Nature More Media App



Support: customerservice@springernature.com

Shin Horiuchi · Nao Terasaki · Takayuki Miyamae
Editors

Interfacial Phenomena in Adhesion and Adhesive Bonding

 Springer

Editors

Shin Horiuchi
Nanomaterials Research Institute
National Institute of Advanced Industrial
Science and Technology
Tsukuba, Japan

Nao Terasaki
Sensing System Research Center
National Institute of Advanced Industrial
Science and Technology
Tosu, Japan

Takayuki Miyamae
Graduate School of Engineering
Chiba University
Chiba, Japan



This work contains media enhancements, which are displayed with a “play” icon. Material in the print book can be viewed on a mobile device by downloading the Springer Nature “More Media” app available in the major app stores. The media enhancements in the online version of the work can be accessed directly by authorized users.

ISBN 978-981-99-4455-2 ISBN 978-981-99-4456-9 (eBook)
<https://doi.org/10.1007/978-981-99-4456-9>

© The Editor(s) (if applicable) and The Author(s) 2024. This book is an open access publication.

Open Access This book is licensed under the terms of the Creative Commons Attribution 4.0 International License (<http://creativecommons.org/licenses/by/4.0/>), which permits use, sharing, adaptation, distribution and reproduction in any medium or format, as long as you give appropriate credit to the original author(s) and the source, provide a link to the Creative Commons license and indicate if changes were made.

The images or other third party material in this book are included in the book’s Creative Commons license, unless indicated otherwise in a credit line to the material. If material is not included in the book’s Creative Commons license and your intended use is not permitted by statutory regulation or exceeds the permitted use, you will need to obtain permission directly from the copyright holder.

The use of general descriptive names, registered names, trademarks, service marks, etc. in this publication does not imply, even in the absence of a specific statement, that such names are exempt from the relevant protective laws and regulations and therefore free for general use.

The publisher, the authors, and the editors are safe to assume that the advice and information in this book are believed to be true and accurate at the date of publication. Neither the publisher nor the authors or the editors give a warranty, expressed or implied, with respect to the material contained herein or for any errors or omissions that may have been made. The publisher remains neutral with regard to jurisdictional claims in published maps and institutional affiliations.

This Springer imprint is published by the registered company Springer Nature Singapore Pte Ltd. The registered company address is: 152 Beach Road, #21-01/04 Gateway East, Singapore 189721, Singapore

Preface

Studies of interfaces are essential in the science and technology of adhesion and adhesive bonding. Interfaces are also involved in many polymer materials in various forms, such as polymer blends, composites, laminates, coatings, and paintings. The physical and mechanical properties of these materials are significantly affected by the structure and strength of the interfaces. To understand this, one must know how the interface is formed, its physical and chemical structures, and how the interface creates the stress field and fracture process. The problem is thus quite complicated, requiring an interdisciplinary approach combining chemistry, interfacial physics, polymer science, and fracture mechanics.

As stated in chapter “[Introduction—Interfaces in Adhesion and Adhesive Bonding](#)”, adhesive bonding is a promising manufacturing technology for lightweight mobility that will help solve global warming and reduce CO₂ emissions. Our research on interfaces originally started from a purely scientific interest, but recently, due to social concerns and demands, a strong interest has been provoked in adhesion mechanisms.

Adhesion is a term that people may have different meanings depending on their field of interest. Adhesion is crucial in any materials, paints, coatings, and thin films in electrical devices. Friction and wear are also issues where adhesion is involved. Cell and protein adhesion on surfaces in biocompatible materials is complex in biology. The adhesion we study in this book is the phenomenon in the joints of different materials that can resist mechanical loading. The interface is formed when one material in a liquid state (adhesive) is brought into contact with the other solid (adherend) and then solidified.

Fundamental adhesion forces anchor the adhesive molecules to the adherend/adhesive interface and strongly influence the chemical and morphological structures and molecular dynamics in a wide area adjacent to the interface. Therefore, it is called *interphase*. The interphase includes a three-dimensional structure, with additional time factors such as the resistance to external stresses and durability to environmental conditions. Therefore, we need to elucidate the hierarchical structures of the interphases in time and space. As summarized in chapter “[Introduction—Interfaces in Adhesion and Adhesive Bonding](#)”, the interphase

contains various forms and phenomena with scales ranging from the molecular level to large structural products. To understand the adhesion mechanism, it is necessary to clarify the structures contained in the interphase and the interplay between the structures.

This book presents our recent research results for elucidating interfacial phenomena of multi-scale and hierarchical structures in interphases, mainly introducing three cutting-edge analysis methods. Sum frequency generation (SFG) vibrational spectroscopy is a new spectroscopic technique that can obtain information from embedded interfacial monolayers. Various electron microscopy techniques can provide direct views of the interphases on a sub-10 nm to micrometer scale. Mechanoluminescence (ML) can directly visualize the mechanical behavior in the failure process of adhesive bonding.

Chapter “[Electron Microscopy for Visualization of Interfaces in Adhesion and Adhesive Bonding](#)” provides an overview of electron microscopy techniques helpful in investigating the interphases in polymers and polymer/metal hybrid systems, and chapter “[Interfacial Phenomena in Adhesion and Adhesive Bonding Investigated by Electron Microscopy](#)” describes the interfacial phenomenon in adhesion and adhesive bonding revealed by these analytical techniques. In chapter “[Direct Visualization of Mechanical Behavior During Adhesive Bonding Failure Using Mechanoluminescence \(ML\)](#)”, ML is used to visualize the failure processes and the invisible mechanical behavior of adhesive joints in test specimens and even in much larger products found in mobility structures (e.g., automobiles, aircraft) and civil engineering structures (e.g., bridges, buildings). Chapter “[Analysis of Molecular Surface/Interfacial Layer by Sum-Frequency Generation \(SFG\) Spectroscopy](#)” introduces recent progress in molecular analysis at various interfaces using SFG vibrational spectroscopy. SFG can be used to investigate chemical reactions and molecular orientations at buried interfaces.

We hope that readers in the scientific community and those in the industry related to adhesives and adhesive bonding will benefit from the results of our research. The book will also be helpful for students of polymer physics, chemistry, and mechanical engineering and those interested in the micro- and nanoscopic world of polymers and hybrid materials.

Finally, the editors would like to express their sincere thanks to our colleagues at *Research Laboratory for Adhesion and Interfacial Phenomena (AIRL), National Institute of Advanced Industrial Science and Technology (AIST), Japan*, and Professor Chiaki Sato (Tokyo Institute of Technology), Leader of AIRL, for their support to our R&D activities.

Tsukuba, Japan
March 2023

Shin Horiuchi

Contents

Introduction—Interfaces in Adhesion and Adhesive Bonding	1
Shin Horiuchi, Nao Terasaki, and Takayuki Miyamae	
Electron Microscopy for Visualization of Interfaces in Adhesion and Adhesive Bonding	17
Shin Horiuchi	
Interfacial Phenomena in Adhesion and Adhesive Bonding Investigated by Electron Microscopy	113
Shin Horiuchi	
Direct Visualization of Mechanical Behavior During Adhesive Bonding Failure Using Mechanoluminescence (ML)	209
Nao Terasaki	
Analysis of Molecular Surface/Interfacial Layer by Sum-Frequency Generation (SFG) Spectroscopy	291
Takayuki Miyamae and Kouki Akaike	

Abbreviations

AB	Alkylborane
ABS	Acrylonitrile-butadiene-styrene
ADCB	Asymmetric double cantilever beam
ADF	Annular dark field
ATR-IR	Attenuated total reflection infrared spectroscopy
BG	Background
BSEs	Backscattered electrons
CBM	Conditioning based monitoring
CF	Cohesive failure
CFRP	Carbon fiber reinforced plastic
CFRTP	Carbon fiber reinforced thermoplastic
CMOD	Crack mouth opening displacement
COD	Crack opening distance
CTS	Cross tension Strength
DCB	Double cantilever beam
DGEBA	Diglycidyl ether Bisphenol A
DIC	Digital image correlation
EDX	Energy dispersive X-ray spectrometry
EELS	Electron energy loss spectroscopy
EFTEM	Energy-filtering transmission electron microscopy
ELNES	Electron energy-loss near-edge structure
ENF	End notch flexure
ESI	Electron spectroscopic imaging
FFT	Fast Fourier transforms
FSW	Friction stir welding
G _c	Critical energy release rate
HAADF	High angle annular dark field
ILF	Inter-laminar failure
iPP	Isotactic polypropylene
IR	Polyisoprene rubber
KP	Kelvin probe method

LCST	Lower critical solution temperature
MDI	Diphenylmethane diisocyanate
ML	Mechanoluminescence
MLLS	Multiple linear least-square fitting
NanoTA	Nano thermal analysis
NIR	Near infrared
OPG/OPA	Optical parametric generators/amplifiers
PA6	Polyamide6
PC	Polycarbonate
PE	Polyethylene
Pes	Primary electrons
PEVODC	Poly(ethylene- <i>co</i> -vinyl- <i>n</i> -octadecyl carbamate)
PFO	Poly(9,9-dioctylfluorene)
PLA	Poly(lactic acid)
PMMA	Polymethyl methacrylate
PNIPAM	Poly(<i>N</i> -isopropylacrylamide)
PP	Polypropylene
PPgMA	Polypropylene- <i>grafted</i> -maleic anhydride
PPS	Polyphenylene sulfide
PS	Polystyrene
PSA	Pressure-sensitive adhesive
PVDC	Poly(vinyl <i>N</i> -octadecyl carbamate- <i>co</i> -vinyl acetate)
ROI	Region-of-interest
SAN	Styrene-acrylonitrile random copolymer
SBR	Styrene-butadiene rubber
SEM	Scanning electron microscopy
SEs	Secondary electrons
SFG	Sum frequency generation
SHM	Structural health monitoring
SI	Spectral imaging
STEM	Scanning transmission electron microscopy
TETA	Triethylenetetramine
TL	Thermoluminescence
TSS	Tensile shear strength
XPS	X-ray photoelectron spectroscopy
ZLP	Zero-loss peak

Introduction—Interfaces in Adhesion and Adhesive Bonding



Shin Horiuchi, Nao Terasaki, and Takayuki Miyamae

Abstract The social background of research on adhesion and adhesive bonding is reviewed. Next, the interphase in the adhesive bond is defined, and the multi-scale and hierarchical structures contained in the interface are arranged based on their sizes. Finally, the analytical methodologies this book introduces to elucidate interfacial phenomena in adhesion and adhesive bonding are overviewed.

Keywords Adhesion · Bonding · Interphase · Multi-material · Hierarchical structure · Testing of adhesive bonding

S. Horiuchi (✉)

Research Laboratory for Adhesion and Interfacial Phenomena (AIRL), National Institute of Advanced Industrial Science and Technology (AIST), 1-1-1 Higashi, Tsukuba 305-8565, Ibaraki, Japan

e-mail: s.horiuchi@aist.go.jp

N. Terasaki

Sensing System Research Center (SSRC), National Institute of Advanced Industrial Science and Technology (AIST), 807-1 Shuku-machi, Tosu 841-0052, Saga, Japan

T. Miyamae

Graduate School of Engineering, Chiba University, 1-33 Yayoi-cho, Inage-ku, Chiba 263-8522, Japan

Molecular Chirality Research Center, Chiba University, 1-33 Yayoi-cho, Inage-ku, Chiba 263-8522, Japan

Soft Molecular Activation Research Center, Chiba University, 1-33 Yayoi-cho, Inage-ku, Chiba 263-8522, Japan

© The Author(s) 2024

S. Horiuchi et al. (eds.), *Interfacial Phenomena in Adhesion and Adhesive Bonding*, https://doi.org/10.1007/978-981-99-4456-9_1

1 Social Background of Research on Adhesion and Adhesive Bonding

To realize an energy-saving and carbon-neutral society, the weight reduction of transportation structures such as automobiles and airplanes has become an issue to be addressed. In modern automobiles and aircraft, reducing weight, fuel consumption, and CO₂ emissions is crucial, and one way to achieve this is through the use of lightweight hybrid designs. To meet the rising demand for energy-efficient vehicles, manufacturers are turning to lightweight materials like high-strength steel, magnesium alloys, aluminum alloys, and polymer-based composites to make automotive body components. The utilization of lightweight materials has led to changes in the structural design of lightweight constructions.

Furthermore, researchers and engineers are developing and investigating new joining technologies that can be applied to both similar and dissimilar material combinations. A prevalent approach is to enhance the strength, weight, and durability of hybrid structures by combining traditional metals with polymeric composites. While composites are more structurally efficient than metals and are not prone to galvanic corrosion, metals have better damage tolerance and failure predictability than composites and are resistant to solvents and high temperatures that tend to degrade polymers. As a result, dissimilar joints between metals and composite materials are being developed to optimize the advantages of both materials.

In engineering applications, adhesive bonding is becoming an increasingly popular alternative to mechanical joints due to its numerous advantages over conventional mechanical fasteners. Adhesive bonding offers benefits such as lower structural weight, reduced fabrication cost, improved damage tolerance, design flexibility, and the ability to bond a wide range of materials, both similar and dissimilar. Additionally, adhesive bonding minimizes the thermal effects on the bonding substrates. The automotive industry has seen a significant increase in the application of adhesive bonding in recent years. This is primarily due to the potential for weight reduction, fuel savings, and reduced emissions in vehicles. A new manufacturing concept for car bodies that utilizes lightweight and high-strength materials placed in the appropriate locations is under research and development, as shown in Fig. 1 [1]. Adhesive bonding is considered a promising joining method for constructing multi-material car bodies because conventional welding joints are challenging to implement. However, there are still significant issues that need to be addressed before this technique can be fully trusted. A critical limitation of adhesive bonding is that the heat distortion temperatures of adhesives are often closer to the operating temperatures of the products than those of mechanical joints, which raises concerns about the adhesive bonding's mechanical resistance and durability. To ensure safety, adhesively bonded structures may need to include mechanical fasteners as an additional safety precaution. These practices result in heavier and more costly components, sacrificing the advantages of adhesive bonding. More efficient use of lightweight materials and adhesives could be realized by developing reliable joint design and predictive methodologies for the strength and durability of adhesive bonding. To introduce adhesive bonding to

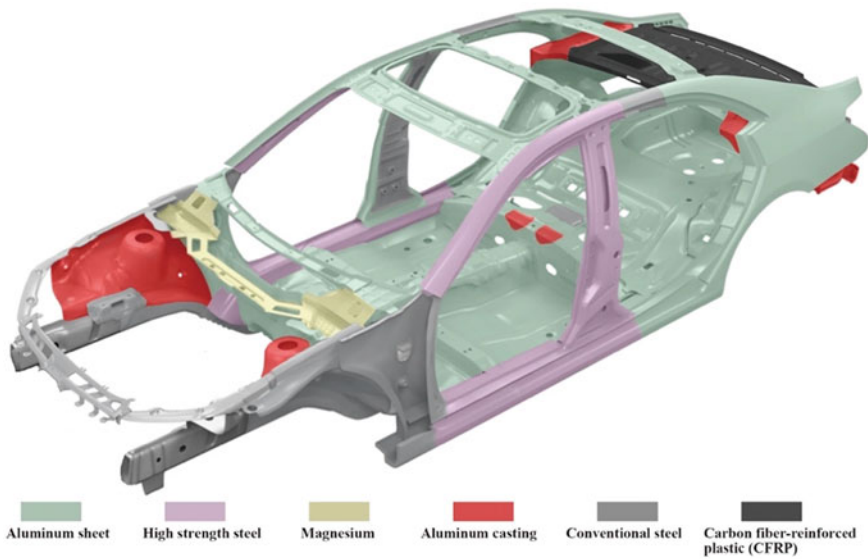


Fig. 1 An example of the multi-material car body structure

such engineering applications that concern safety and reliability strongly, a deeper understanding of the adhesion and bonding mechanisms is necessary. Research on adhesion and its mechanisms is not only crucial as basic science, but it is also essential to connect it to social implementation. The fundamentals and applications of adhesive bonding are described in many books [2–6]. This book features comprehensive studies of interfacial phenomena in adhesion and adhesive bonding, focusing on a wide range of length-scale structures from the atomic level to a large-scale product fabricated using adhesive bonding with cutting-edge analytical techniques and evaluation test methods developed for the strength and durability of interfaces.

2 Interphase in Adhesive Bonding

Before discussing the mechanism of adhesion and adhesive bonding, it is necessary to clarify what an “interface” is in adhesion and adhesive bonding. “Interface” is an important issue not only in material science but also in various fields such as electronic devices, catalysts, colloid chemistry, and biological tissues, and interfacial interactions at the molecular and atomic levels are being studied in these fields. The interfaces that should be dealt with when discussing the adhesion mechanism refer to regions with structures and properties different from the bulk part of the adherend or adhesive. These are formed during the surface pretreatment of adherend or the bonding process in the adhesive layer. It is not simply a two-dimensional interface where dissimilar materials come into contact. It can be called an “interphase” because

it is a three-dimensional area [7]. In metal/polymer joints, three terms have been frequently used: interface, interfacial region, and interphase. In material science, the interface refers to the boundary between two phases, namely the metal or oxide metal and the polymer. The interfacial region refers to the volume of material slightly below the metal's surface and extending into the polymer. In contrast, the interphase refers to the volume of the polymer that is adjacent to the substrate.

The bonding performance is determined by the two-dimensional interface between the adherend and adhesive and a three-dimensional region with different properties and structural characteristics that extend into the bulk materials. Therefore, the interphase or interfacial region, the area below the interface, plays a crucial role in adhesion phenomena and requires analysis. Researchers have studied the thickness of this region extensively, but it is still unknown. To understand the bonding mechanism, it is essential to identify the interfacial region, how it is formed during the bonding process, and how it can be damaged and degraded.

3 Testing of Adhesion and Adhesive Bonding

It is necessary to perform appropriate mechanical measurements and clarify the interfacial properties to elucidate the adhesion and adhesive bonding mechanism. Many ASTM and ISO standards have been written to evaluate the mechanical behavior of adhesive joints. New joining technologies have been developed especially for joining dissimilar materials, and their new applications are being investigated. Since these bonding technologies can achieve extremely high bonding strength, existing test methods do not cause the failure of the joint part and cannot correctly evaluate bonding characteristics. Therefore, several new test methods have been established as ISO standards in the last decade.

The test method for measuring the lap shear joint strength has been standardized as ISO4587 [8]. When a metal-plastic lap joint having high joint strength is tested by this standard, the relatively weak plastic part breaks due to the large bond area of the specimen. ISO 19095 specifies the test specimen geometries, as shown in Fig. 2 to quantify the metal-plastic joint performances regarding lap-shear strength, tensile strength, and peeling resistivity [9]. This standard also specifies the test method for sealing properties and environmental conditions for durability tests. Sealing property evaluation of metal/resin joints requires a test method different from that for joint strength. To evaluate the sealing performance of a metal-plastic joint, the detection of the leakage (leak rate) of helium gas is employed using the specimen shown in Fig. 2c, where a vacuum line is sealed with the specimen and the leaked helium is monitored by a mass spectrometer [10]. Using the test specimens and the test methods specified in the standard, the aluminum-PPS (polyphenylene sulfide) direct joints prepared by injection molding can be evaluated as described in Sect. 7 in chapter "Interfacial Phenomena in Adhesion and Adhesive Bonding Investigated by Electron Microscopy". For the dissimilar adhesive bonding of carbon fiber-reinforced plastic and metal, the test method to determine the cross-tension

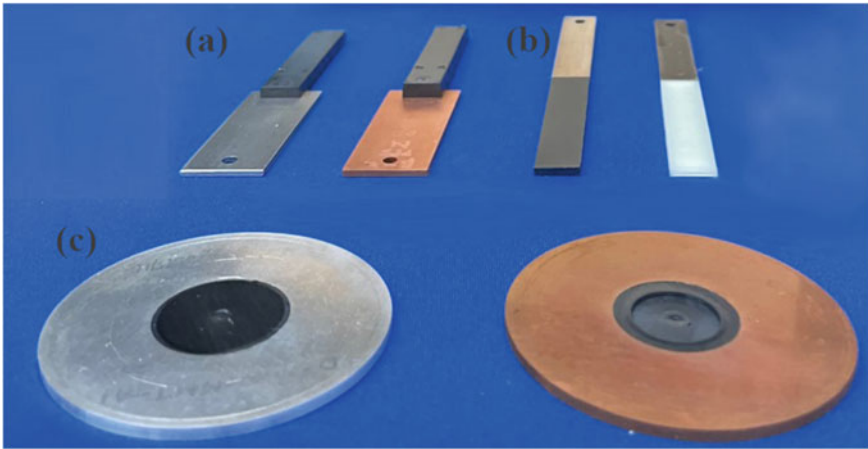


Fig. 2 Test specimens of metal-plastic assemblies specified by ISO 19095: **a** lap joints of steel/PPS (*left*) and copper/PPS (*right*); **b** butt joints of aluminum/PPS (*left*) and steel/PP (*right*); **c** sealing test specimens of aluminum/PPS (*left*) and copper/PPS (*right*)

strength, a standard test method for spot welding as defined by ISO 14272 [11], has been defined as ISO 24360 [12]. The detail of this test is described in Sect. 4 in chapter “Direct Visualization of Mechanical Behavior During Adhesive Bonding Failure Using Mechanoluminescence (ML)”.

Commonly employed test methods are developed for the tensile, shear, bending, and peeling strength measurements of the specimens having a joint part. Even if there is an interfacial failure, it is difficult to determine the intrinsic adhesion forces acting across the interface using standard test methods. It is important to note that the strength measured for traditional joint designs and test methods depends on the intrinsic adhesion and the mechanical properties of the adhesive, substrates, and joint geometry. For instance, the stiffness, strength, and resistance to creep of a single-lap joint can vary depending on the substrates’ modulus, thickness, and overlap length. This is due to the complex stress distributions in the joint’s geometry.

As described in chapter “Direct Visualization of Mechanical Behavior During Adhesive Bonding Failure Using Mechanoluminescence (ML)”, the mechanoluminescence (ML) successfully visualizes the strain distribution in lap joints, depending enormously on Young’s modulus of the adhesive and the adherend to be used (Figs. 33 and 45 in chapter “Direct Visualization of Mechanical Behavior During Adhesive Bonding Failure Using Mechanoluminescence (ML)”). Conventional adhesion tests, such as lap shear and peel adhesion tests, are often affected by inelastic deformations that occur in the adherend away from the interface, making them unsuitable for providing accurate interfacial characteristics. To characterize the adhesion properties of interfaces, the fracture resistance of the interfaces is estimated under tensile opening force in the appropriate double cantilever beam (DCB) geometry, as shown in Fig. 3 [13]. During the DCB test, a specimen is pulled apart at a constant velocity,

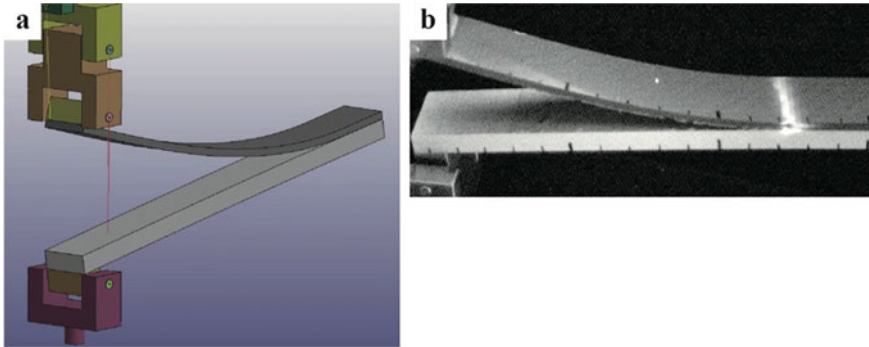


Fig. 3 DCB test of a dissimilar adhesive joint of CFRTP and aluminum: **a** FEM analysis; **b** visualization of the crack propagation by ML

and the locus of failure is examined to deepen the understanding of the bonding mechanism of surface treatments. Sections 8 in chapter “Interfacial Phenomena in Adhesion and Adhesive Bonding Investigated by Electron Microscopy” and 4 in chapter “Direct Visualization of Mechanical Behavior During Adhesive Bonding Failure Using Mechanoluminescence (ML)” provide details of the DCB test performed on dissimilar joints of carbon fiber-reinforced thermoplastic and aluminum.

4 Multiscale and Hierarchical Structures in the Interphase and Interfacial Region in Adhesive Bonding

Adhesion and adhesive bonding mechanisms refer to the questions of how bond strength is achieved and how initial bond strength degrades under different environmental conditions. There are various ways in which bonding can occur. Mechanical interlocking into rough surface structures is one possibility to explain the bonding. Another potential factor is chemical bonding, which may enhance joint strength and occasionally even exceed the role of mechanical interlocking. The bonding mechanism has long been considered simply by mechanical adhesion (anchor effect), chemical bonding, or intermolecular forces based on surface energy. However, it is challenging to fully understand the adhesion mechanism based on such a simple concept. Gaining the trust of those considering the use of adhesive bonding in manufacturing their products requires deep insight into the phenomena that occur in the interphase of adhesive bonding.

The “interphase” involves several characteristics with different size features from atomic to macro scales, as shown in Fig. 4, where typical structures involved in the interphase are arranged in the order of their scales:

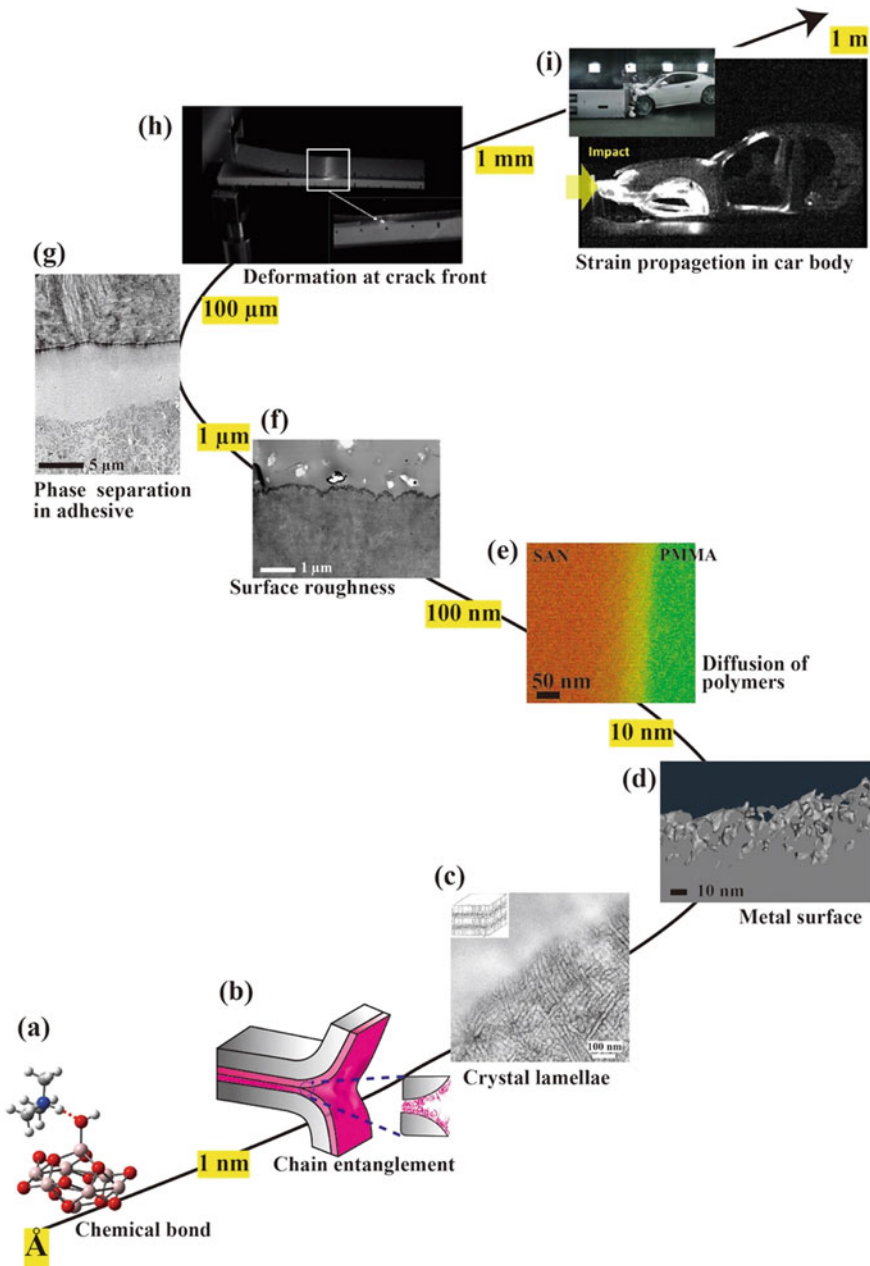


Fig. 4 Overview of multi-scale structures involved in the interphase in adhesive bonding: **a** chemical bond; **b** polymer chain entanglement; **c** lamellar morphology of a semicrystalline polymer; **d** porous structure in the oxide layer of metal adherent; **e** interfacial layer formed vis interdiffusion of polymers; **f** surface roughness created by surface treatment; **g** segregation or absence of a component in adhesive; **h** local deformation at a crack tip; **i** strain propagation and stress distribution in a structural body

(a) Chemical bonding

Van der Waals forces, ionic interaction, hydrogen bonding, and covalent bonding are the primal sources for adhesion, the smallest structure in the interphase. One practical approach to enhancing adhesion is incorporating chemically reactive moieties into the adherend. The formation of chemical bonds at interfaces is widely considered the primary factor in improving adhesion. Detecting these chemical bonds at adhesion interfaces has long been a significant objective of researchers studying the bonding mechanism and assessing bonding reliability. However, directly observing covalent bonding at interfaces is challenging. The chemical bonding at interfaces is investigated by sum-frequency generation spectroscopy (SFG) in chapter “[Analysis of Molecular Surface/Interfacial Layer by Sum-Frequency Generation \(SFG\) Spectroscopy](#)” and by electron energy loss spectroscopy (EELS) in Sect. 6 in chapter “[Interfacial Phenomena in Adhesion and Adhesive Bonding Investigated by Electron Microscopy](#)”.

(b) Interfacial segmental entanglement

Intermolecular chain entanglements across the interface control the adhesion between polymers. The chain coupling across an interface can provide physical links. The length of the entanglements that determines the adhesion strength is around 10 nm. The correlation between the entanglement of polymer chains at an interface and its resistance to crack propagation is investigated in Sect. 3 in chapter “[Interfacial Phenomena in Adhesion and Adhesive Bonding Investigated by Electron Microscopy](#)” by fractography studies with scanning electron microscopy (SEM).

(c) Lamellar structures of semicrystalline polymers

Semicrystalline polymers such as polyethylene (PE), polypropylene (PP), and polyamide (PA) form lamellar structures by folding polymer chains. The lamellae’s orientation and the interfacial region’s crystallinity influence the adhesion properties. The thicknesses of the lamellae are 10–20 nm and the lamellar structures below the surface with a depth of about 100 nm are affected by surface pretreatment. The effect of the lamellar structures on adhesion properties is described in Sect. 4 in chapter “[Interfacial Phenomena in Adhesion and Adhesive Bonding Investigated by Electron Microscopy](#)”.

(d) Metal oxide porous structure

Natural aluminum surfaces are covered with a thin oxide and/or hydroxide open porous layer with pore sizes of about 10 nm. Chemical or laser treatments can also artificially create porous surfaces on aluminum surfaces. Adhesive molecules infiltrate these narrow pores to enhance bond strength. Sections 6–8 in chapter “[Interfacial Phenomena in Adhesion and Adhesive Bonding Investigated by Electron Microscopy](#)” describe the effect of the aluminum oxide surface structures on bonding.

(e) *The interfacial layer formed via the interdiffusion of polymers*

When similar or dissimilar polymers are welded at high temperatures, interdiffusion occurs, creating a coexistent interfacial layer with a concentration gradient between the two polymers. Layer thicknesses range from a few to 10 nm for immiscible polymer pairs determined according to the interaction parameter (χ parameter). In contrast, thermodynamically miscible pairs exhibit quite a fast diffusion, forming the layer with a few hundred nm thicknesses. The interfacial layers are visualized and characterized by energy-filtering transmission electron microscopy (EFTEM), as described in Sects. 1 and 2 in chapter “Interfacial Phenomena in Adhesion and Adhesive Bonding Investigated by Electron Microscopy”.

(f) *Surface roughness created by surface pretreatments*

Atmospheric plasma treatment of the polymer surface creates a rough surface in the order of several hundred nm together with polar functional groups. The topological features of the surface roughness of isotactic PP (*i*PP) are described in Sect. 4 in chapter “Interfacial Phenomena in Adhesion and Adhesive Bonding Investigated by Electron Microscopy”.

(g) *Interfacial segregation of the components in the adhesive*

Commercial adhesives intentionally contain several organic and inorganic components to meet the specifications of a particular application. These components may be unevenly distributed in the adhesive, with different distributions of components between the interfacial region and the bulk well-separated from the adherend surface. The regions that form at these interfaces can be several microns in size and affect bonding properties. The segregation of a component in an adhesive is investigated in the bonding of aluminum to *i*PP in Sect. 5 in chapter “Interfacial Phenomena in Adhesion and Adhesive Bonding Investigated by Electron Microscopy”.

(h) *Plastic deformation ahead of the crack*

When a crack opening load is applied to a laminated specimen, plastic deformation occurs before the crack tip during crack propagation along the interface. This region absorbs the energy that causes an interfacial fracture, and the plastic deformation region’s expansion enhances interfacial toughness. Mechanoluminescence (ML) visualization of plastic deformation at the crack tip under specific test conditions in various specimen geometries is useful for stress–strain analysis of joint structures, as presented in Sect. 4 in chapter “Direct Visualization of Mechanical Behavior During Adhesive Bonding Failure Using Mechanoluminescence (ML)”.

(i) *Strain distribution in adhesive joints in structural bodies*

It is possible to visualize the strain propagation of the structure due to adhesion when impact strength is applied to the car body by combining ML and high-speed video recording. This technique helps predict possible points of failure in large-scale adhesive-bonded structures, as described in Sect. 3 in chapter “Direct Visualization of Mechanical Behavior During Adhesive Bonding Failure Using Mechanoluminescence (ML)”.

5 Visualization and Analysis of Interphases in Adhesion and Adhesive Bonding

The structures mentioned above with variable length scales are investigated mainly by following three analytical techniques:

1. Multi-dimensional visualization of interphases by electron microscopy (EFTEM, STEM, EELS, tomography, and in-situ tensile TEM, etc.);
2. Mechanoluminescence (ML) visualization of strain and crack propagation at interfaces;
3. Atomic characterization of buried interfaces by sum-frequency generation spectroscopy (SFG).

Transmission electron microscopy (TEM) conventionally presents two-dimensional (2D) projections of the internal structures of samples with a high spatial resolution. Here, we introduce additional 2D structural information using scanning transmission electron microscopy (STEM). As shown in Fig. 5, in STEM, the electron beam is focused on a spot on a specimen surface and is scanned across the specimen area to be investigated. In contrast, the transmitted electrons are collected in the annular detectors aligned “on-axis” below the specimen. A unique specimen holder performing in-situ tensile joint specimen testing allows real-time failure observation. As a result, it is possible to add dynamic (t) information to 2D structural information (x, y). The STEM instrument also can perform tomography for 3D visualization of interfaces. The combination of energy-dispersive X-ray spectrometry (EDX) and the tomography function allows us to construct 3D elemental distributions, which add elemental information (E) to 3D structural information (x, y, z). Electron energy loss spectroscopy (EELS) provides information on the electronic and bonding environment of the excited atom. Therefore, it can add chemical information (C) of an element of interest (E) to the 2D structural information.

Chapter “[Electron Microscopy for Visualization of Interfaces in Adhesion and Adhesive Bonding](#)” provides an overview of electron microscopy techniques used to investigate interphases in polymers and polymer/metal hybrid systems. First, how the instruments of energy-filtering transmission electron microscopy (EFTEM), STEM, and SEM work and are operated is briefly described. The principles of EELS and EDX are described. Next, the specimen preparation techniques such as ultramicrotomy, heavy metal staining, focused ion beam (FIB) fabrications, and replica method, which are essential for these electron microscopy tasks, are introduced. This chapter also reviews advanced electron microscopy techniques, such as STEM-EDX-tomography, and chemical phase mapping using electron energy-loss near-edge structure (ELNES) and in-situ tensile TEM. Numerous examples of the application of these techniques to various surfaces and interfaces present in polymer alloys and composites, crystalline polymers, adhesive bonds, and metal substrate surfaces are presented.

Interfacial phenomena in adhesion and adhesive bonding are investigated in chapter “[Interfacial Phenomena in Adhesion and Adhesive Bonding Investigated by Electron Microscopy](#)”. Polymer–polymer interfaces formed via interdiffusion are

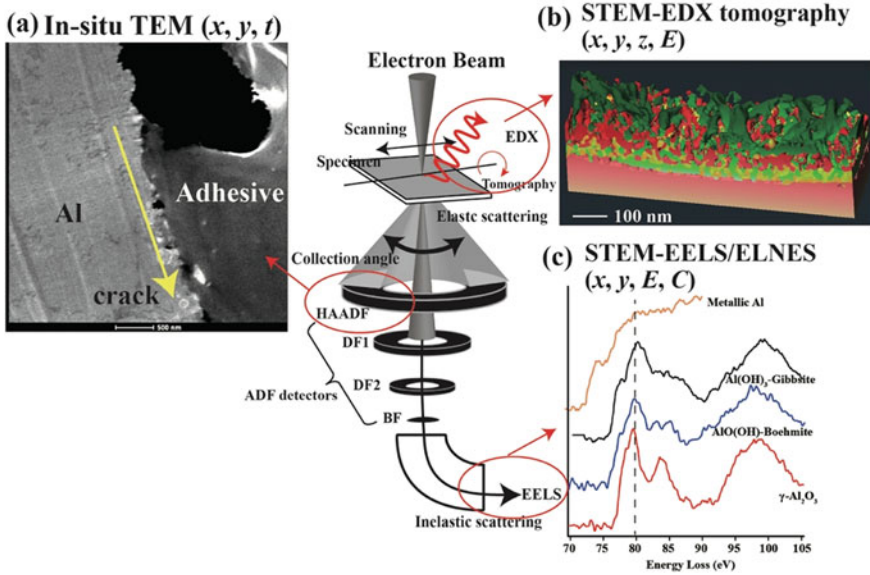


Fig. 5 Multi-dimensional interface analyses by STEM: **a** STEM-HAADF images of in-situ observation of the crack propagation of Al5052/epoxy adhesive interface under tensile loading; **b** 3D elemental maps of the laser-irradiated Zn-coated steel surface created by STEM-EDX tomography; Fe (red), Zn (green) and Fe/Zn co-existing (yellow) region; **c** EELS spectra of aluminum compounds metallic Al, Al(OH)₃ (gibbsite), AlO(OH) (boehmite) and γ -alumina

visualized and characterized by EFTEM. Fractographic studies using high-resolution SEM investigate entanglements at the polymer–polymer interfaces, and the adhesion mechanism is discussed about the interfacial entanglements. The effect of surface treatments of polymers for adhesion improvement is studied in terms of the surface roughness and the chemical functionality of the adherend. We then describe the role of chemical interactions between polymers and metals on bonding by the analysis of fracture surfaces by the STEM-replica technique. Bonding mechanisms of adhesive bonding and recently developed direct bonding of metal and plastic are also investigated by STEM-EELS/ELNES and STEM-tomography. Finally, special attention is made to the toughness and durability of adhesive joints between metal and carbon fiber-reinforced plastics (CFRP) and discuss the durability of the adhesive bonding.

In chapter “[Direct Visualization of Mechanical Behavior During Adhesive Bonding Failure Using Mechanoluminescence \(ML\)](#)”, we introduce recent progress in direct visualization of mechanical behavior in the failure process of adhesive bonding by mechanoluminescence (ML). In bonding and joining, obtaining the necessary “force” in the required period is extremely important. However, we cannot see mechanical behavior. We need to predict the information appropriately based on our accumulated experience and knowledge of experts, reflecting it in the design and simulation. Do we have full confidence in our past knowledge, simulations, and designs to be correct? Are there any assumptions included in the knowledge? Is

there any information that we need to be made aware of? Questions always remain. To address this issue, we have utilized ML sensing technology as our originally developed (Fig. 6), which can visualize dynamic strain distribution generated at the adhesive bonding area and its interface. ML is a fascinating and promising visual sensing technology. However, many readers should not be familiar with ML sensing.

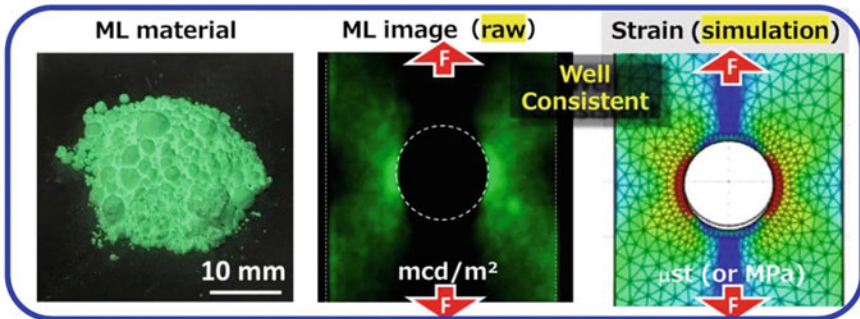
Therefore, firstly basic ML technologies are introduced in terms of materials, sensors, and sensing technologies in Sects. 1 and 2 in chapter “Direct Visualization of Mechanical Behavior During Adhesive Bonding Failure Using Mechanoluminescence (ML)”. Then, for considering the effective application of ML sensing that take advantage of technological features, (Sect. 3 in chapter “Direct Visualization of Mechanical Behavior During Adhesive Bonding Failure Using Mechanoluminescence (ML)”) structural health monitoring (SHM)/conditioning-based monitoring (CBM) and (Sect. 4 in chapter “Direct Visualization of Mechanical Behavior During Adhesive Bonding Failure Using Mechanoluminescence (ML)”) innovation in design and prediction are discussed from the viewpoint of visualizing mechanical behavior, deterioration, and failure process as the killer application of ML sensing. Furthermore, using internationally standardized adhesion strength tests, visualizing the mechanical behavior of adhesive joints, fracture initiation points, and fracture processes will be introduced based on time-series information of ML images.

The purpose of this chapter “[Direct Visualization of Mechanical Behavior During Adhesive Bonding Failure Using Mechanoluminescence \(ML\)](#)” is to show the invisible mechanical behavior of adhesive joints, which are becoming increasingly crucial in multi-material lightweight design, and to provide an opportunity to gain confidence in conventional experience and inspiration for completely different designs and predictions.

In chapter “[Analysis of Molecular Surface/Interfacial Layer by Sum-Frequency Generation \(SFG\) Spectroscopy](#)”, we introduce recent progress in analyses of the various kinds of interfaces using sum-frequency generation (SFG) vibrational spectroscopy. Surfaces of materials are important sites for a wide variety of physical properties, such as hydrophilicity, hydrophobicity, friction, adhesion, biocompatibility, and catalysis, and sometimes exhibit properties “different” from those of the bulk and are very complicated. Wolfgang Pauli, the Nobel Prize winner in physics, was annoyed by the complexity of surfaces and said, “*God made solids, but surfaces were made by the Devil*”. The orientation of molecules at the surface is also important in considering the probability of the chemical reaction occurring. For example, the SN-2 reaction, a significant chemical reaction, proceeds when negatively charged functional groups attack positively charged sites, such as the carbon atoms of the carbonyl groups. Therefore, one can easily imagine that if the carbonyl carbon sites are not facing a direction favorable to the reaction on the surface, the reaction will not proceed easily.

SFG spectroscopy is a novel spectroscopic technique that uses laser light at two different wavelengths to “specifically” obtain the information from molecules at surfaces and interfaces. Since this spectroscopic technique uses lights, it can obtain information not only from the surfaces, but also from the molecules at the interfaces, as far as the lights can penetrate and reach the interface. This makes it possible, for

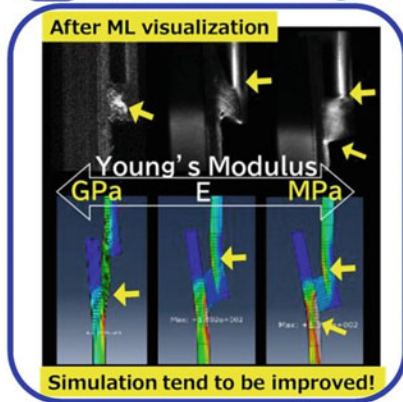
4.1 & 4.2 Mechanoluminescence (ML) visualizes strain distribution



4.3 SHM & CMB



4.4 Simulation & Design



4.5 ML studies mechanical behavior during IS adhesive

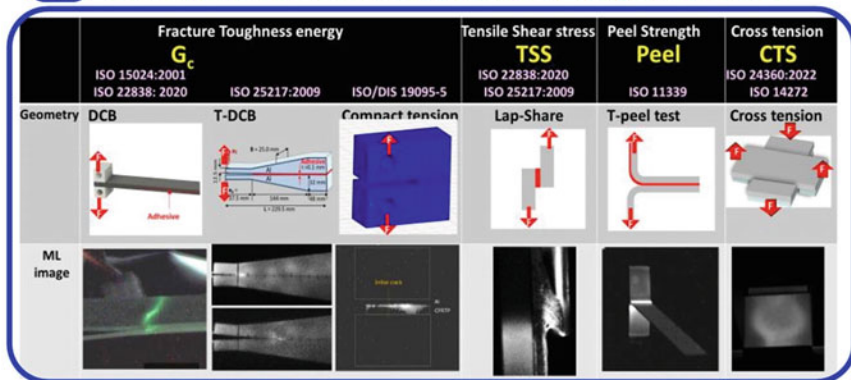


Fig. 6 Brief introduction of chapter “Direct Visualization of Mechanical Behavior During Adhesive Bonding Failure Using Mechanoluminescence (ML)”; direct visualization of mechanical behavior in failure process of adhesive bonding by mechanoluminescence (ML)

example, to study the chemical reactions of molecules at the interface of electrodes in liquids or the orientation of molecules at the interface of adhesives and the curing process, which have been difficult to investigate directly.

Figure 7 presents the example of the SFG spectra obtained at the aluminum oxide interface with an adhesive containing a small amount of aminopropyltrimethoxysilane. Immediately after the application (black line), an SFG peak can be observed at 2840 cm^{-1} . This peak originates from the methoxy group of the silane coupling agents, indicating that the coupling agents are concentrated at the interface immediately after the application. As time proceeds, the intensity of this peak gradually decreases, and instead, new peaks appear at 2850 and 2880 cm^{-1} . These peaks can be attributed to the methylene (CH_2) and methyl (CH_3) groups in the polymer components of the adhesive. The peaks derived from the adhesive components are not visible immediately after the application, which is thought to be due to the molecules of the adhesive polymer being in random orientation at the interface immediately after the application. The methoxy groups of the silane coupling agent readily react with a small amount of water present at the interface and are decomposed. As the adhesive cures, its main component, the macromolecule, is thought to become ordered at the interface. Thus, SFG spectroscopy allows us to understand the static chemical structures and molecular orientations at the “buried interfaces” and the dynamics of the molecular behaviors at the interfaces.

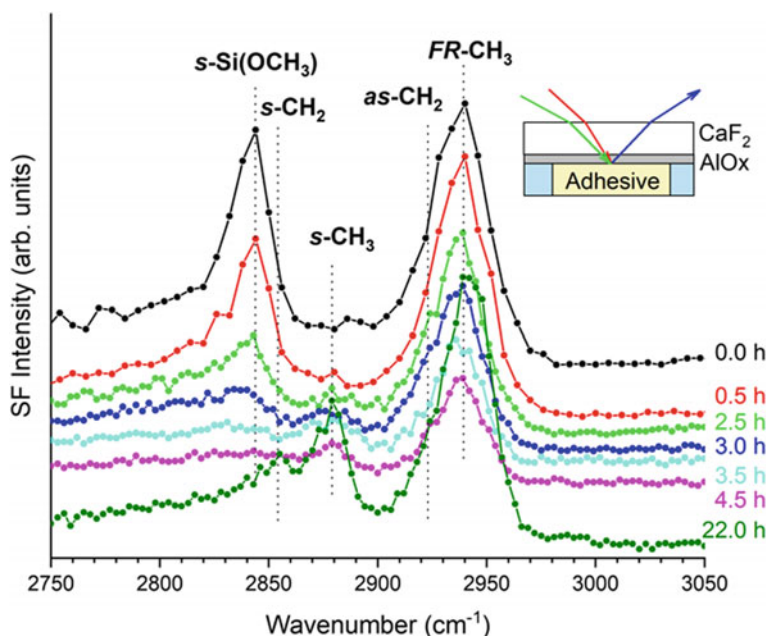


Fig. 7 SSP polarized SFG spectra following the time evolution of the silyl-terminated polyether adhesives and aluminum oxide interface after application

References

1. M.D. Banea, M. Rosioara, R.J.C. Carbas, L.F.M. da Silva, *Comp. Part B* **151**, 71–77 (2018)
2. S. Wu, *Polymer Interface and Adhesion* (Marcel Dekker, New York and Basel, 1982)
3. R.D. Adams (ed.), *Adhesive Bonding, Science, Technology and Applications* (Elsevier, Amsterdam, 2021)
4. S.T. Amencio-Filho, L.-A. Blaga, *Joining of Polymer-Metal Hybrid Structures: Principles and Applications* (Wiley, Hoboken, 2018)
5. A.J. Kinloch, *Adhesion and Adhesives: Science and Technology* (Springer, Berlin, 1987)
6. W. Possart (ed.), *Adhesion: Current Research and Applications* (Wiley-VCH, Weinheim, 2005)
7. H. Leidheiser, P.D. Deck, *Science* **241**, 1176–1181 (1988)
8. International Standardization Organization, *ISO4587: 2003: Adhesive Lap-Shear Strength of Rigid-to-Rigid Bonded Assemblies* (2003)
9. International Standardization Organization, *ISO19095: 2015: Plastics-Evaluation of the Adhesion Interface Performance in Plastic-Metal Assemblies* (2015)
10. S. Horiuchi, *J. Soc. Instrum. Control Eng.* **54**, 743–747 (2015)
11. International Standardization Organization, *ISO14272: 2016: Resistance Welding—Destructive Testing of Welds—Specimen Dimensions and Procedure for Cross Tension Testing of Resistance Spot and Embossed Projection Welds* (2016)
12. International Standardization Organization, *ISO24360: 2022: Composites and Reinforcements Fibres—Carbon Fibre Reinforced Plastics (CFRPs) and Metal Assemblies—Determination of the Cross Tension Strength* (2022)
13. International Standardization Organization, *ISO22838: 2021: Composites and Reinforcements Fibres—Determination of the Fracture Energy of Bonded Plates of Carbon Fibre Reinforced Plastics (CFRPs) and Metal Using Double Cantilever Beam Specimens* (2020)

Open Access This chapter is licensed under the terms of the Creative Commons Attribution 4.0 International License (<http://creativecommons.org/licenses/by/4.0/>), which permits use, sharing, adaptation, distribution and reproduction in any medium or format, as long as you give appropriate credit to the original author(s) and the source, provide a link to the Creative Commons license and indicate if changes were made.

The images or other third party material in this chapter are included in the chapter's Creative Commons license, unless indicated otherwise in a credit line to the material. If material is not included in the chapter's Creative Commons license and your intended use is not permitted by statutory regulation or exceeds the permitted use, you will need to obtain permission directly from the copyright holder.



Electron Microscopy for Visualization of Interfaces in Adhesion and Adhesive Bonding



Shin Horiuchi

Abstract This chapter provides an overview of electron microscopy techniques to investigate interfaces in polymeric materials and adhesive bonds. First, how the instruments of energy-filtering transmission electron microscopy (EFTEM), scanning transmission electron microscopy (STEM), and scanning electron microscopy (SEM) work and are operated is briefly described. The principles of electron energy-loss spectroscopy (EELS) and energy-dispersive X-ray spectrometry (EDX), which are spectroscopic techniques associated with these instruments, are described. Next, the specimen preparation techniques, such as ultramicrotomy, heavy metal staining, focused ion beam (FIB) fabrications, and replica method, which are essential for these electron microscopy tasks, are introduced. This chapter also reviews advanced electron microscopy techniques, such as STEM-EDX-tomography, chemical phase mapping using electron energy-loss near-edge structure (ELNES), and in situ tensile TEM. Numerous examples of the application of these techniques to various surfaces and interfaces present in polymer alloys and composites, crystalline polymers, adhesive bonds, and metal substrate surfaces are presented.

Keywords EFTEM · STEM · SEM · EELS · ELNES · EDX · Tomography · Polymer blend · Composite · Interface

Supplementary Information The online version contains supplementary material available at https://doi.org/10.1007/978-981-99-4456-9_2. The videos can be accessed individually by clicking the DOI link in the accompanying figure caption or by scanning this link with the SN More Media App.

S. Horiuchi (✉)

Research Laboratory for Adhesion and Interfacial Phenomena (AIRL), National Institute of Advanced Industrial Science and Technology (AIST), 1-1-1, Higashi, Tsukuba 305-8565, Ibaraki, Japan

e-mail: s.horiuchi@aist.go.jp

© The Author(s) 2024

S. Horiuchi et al. (eds.), *Interfacial Phenomena in Adhesion and Adhesive Bonding*, https://doi.org/10.1007/978-981-99-4456-9_2

1 Instrumentation of Electron Microscopy

Studying interfaces in polymer and polymer/metal hybrid materials is crucial for developing adhesives, polymer blends and composites, and optoelectrical materials. These interfaces exist in various situations, such as laminates, between a matrix polymer and dispersed domains in the case of polymer blends and composites, and between hard substrates such as glass or silicon wafers in optoelectrical devices. However, accessing interfaces localized in various situations can be challenging. Identifying chemical interactions in buried interfaces is challenging as most surface analytical techniques have limited applicability. X-ray photoelectron spectroscopy (XPS) [1–4] and time of flight secondary ion mass spectrometry (ToF-SIMS) [3–5], combined with etching techniques, have been employed for the investigation of adhesive interfaces. XPS, which can detect signals from a depth of only a few nm and is sensitive to the chemical states of elements, has been frequently used to analyze thin surface structures [6–9]. However, XPS's lateral resolution is insufficient to resolve heterogeneous structures in the surface thin layer. To analyze buried interfaces non-destructively, sum frequency generation (SFG) spectroscopy [10, 11], infrared spectroscopy (IR) [12, 13], and scanning Kelvin probe (SKP) [14] have been used. Most studies have been performed with model samples that mimic the bonded interfaces, such as ultrathin polymer layers cast on metal, representative functional molecules adsorbed on metal, or metal thin films deposited on polymer substrate to serve as flat interfaces covered with a thin counter layer. Many experimental techniques, such as Rutherford backscattering spectrometry (BRS) [15, 16], forward recoil spectrometry (FRES) [17–23], neutron reflection (NR) [24–28], nuclear reaction analysis (NRA) [26, 29–31], rheometry [32, 33], X-ray reflectometry (XR) [34, 35], fluorescence spectroscopy (FS) [36, 37], dynamic light scattering (LS) [38], positron annihilation lifetime spectroscopy (PALS) [39], and nuclear magnetic resonance spectroscopy (NMR) [17, 40, 41], have been employed to study polymer/polymer interfaces. However, BRS, FRES, NR, and NRA cannot measure the concentration profile directly. Deuterated samples (or special preprocessing) are necessary, although these techniques have high resolution with a scale of angstrom. On the other hand, assumptions must be made for rheometry, FS, ellipsometry, XR, LS, and PALS to obtain corresponding interfacial concentration profiles. While IR and Raman spectroscopies provide helpful information at large interdiffusion depth in interfaces, they are limited by a depth resolution of ~ 0.1 – $1 \mu\text{m}$.

The structures of materials used in industry are often complex, containing multiple phases or additives to achieve specific properties. As a result, industrial material interfaces can exist in various scenarios, making applying conventional techniques for their characterization challenging. Therefore, there is a need for a technique that can analyze interfaces without requiring special sample preparations. Electron microscopy, with its high spatial resolution, is a valuable tool for studying small structures. Recent advances in instrumental and analytical techniques have made it possible to observe and analyze small features of materials at atomic resolution. Electron microscopy is also a promising technique for understanding interfacial

phenomena in adhesion and adhesive bonding. Although current advanced electron microscopes are capable of atomic-scale imaging and analysis, the interfaces are difficult to be analyzed because they are buried inside materials in various situations. As mentioned in “[Introduction—Interfaces in Adhesion and Adhesive Bonding](#)” chapter, the interfaces in adhesion and adhesive bonding have multiple structures on a wide range of length scales from molecules to micrometer levels, such as chemical bonds, polymer chain entanglement, distributions of molecular weight and functional groups of polymers, crystallinity, and so on. The high spatial resolution capability of electron microscopy alone is insufficient to analyze such various structures. This chapter provides an overview of the instrumental and analytical techniques that electron microscopy can provide for analyzing metal/polymer and polymer/polymer interfaces.

An electron microscope irradiates a sample with electrons as an incident probe and detects various signals generated by interactions with the sample, thereby extracting information on the surface and internal structure of the sample. One of the characteristics of the electron is that it interacts with a specimen with high probability. The scattering probability (scattered electrons/incident electrons) is approximately 10,000 times that of X-rays, making it possible to obtain a large amount of structural information from a small region. Figure 1 shows various signal information generated by the specimen and electron beam interaction. By detecting and analyzing the signals from the target region, it is possible to know the atomic arrangement, composition, electronic state, etc. When high-energy primary electrons are incident on solid, various processes occur. In a thin specimen, the electron beam traverses the specimen, and the electron–solid interaction creates the signals. The elastic scattering involves no change in the energy of the primary electron, although there may be significant changes in direction. In transmission electron microscopy (TEM), elastic scattering is the major mechanism by which electrons are deflected and is the main contribution to diffraction patterns and images. Inelastic scattering involves a loss in the energy of the incident electrons. The energy analysis of the inelastically scattered electrons is the bases of electron energy-loss spectroscopy (EELS).

The signals created by the electron–solid interaction are divided into two groups. One is primary or direct processes and the other is secondary processes. The elastic and inelastic scattering are categorized to be the primary processes. Secondary processes occur due to electron–electron scattering and the subsequent de-excitation of atoms in the solid, which produce X-rays, Auger electrons, photons, etc. Secondary electrons (SEs) are the electrons that escape from the specimen surface with energies below about 50 eV. There are likely to be electrons bound initially to atoms in the specimen to which a small amount of energy has been transferred within a short distance of the surface. SEs are commonly used for imaging signals in scanning electron microscopy (SEM), providing topographic contrast from the specimen surface. Backscattered electrons (BSEs) are the primary electrons that undergo large deflections and leave the specimen surface with the remainder of their energy intact. Backscattered electrons are used for imaging and chemical phase identification in the SEM since their yield is sensitive to the atomic number of the specimen.

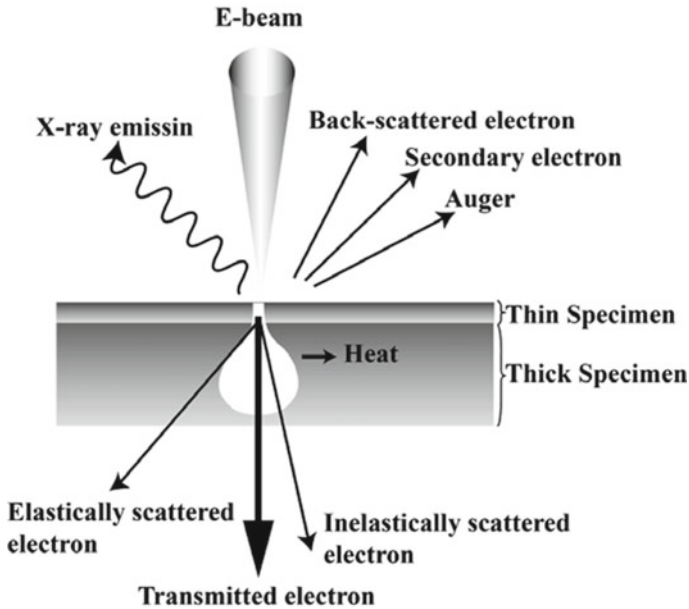


Fig. 1 Schematic diagram of the signals created during irradiation of a high-energy electron beam on a solid or transmission through a thin specimen

If an atomic electron has been ionized or excited to an empty higher energy level, the atom is in an excited, high-energy state. Subsequently, the empty electron state or hole will be filled by an electron dropping down from a higher occupied energy level and the atom will relax. The excess energy will be released via a secondary effect involving the emission of another particle or a photon of radiation. There are three ways in which this relaxation can happen: cathodoluminescence (photon), X-ray emission, and Auger emission (ejection of outer electrons). The distinct energy levels of atoms suggest that the energies of the X-rays released will have unique values for each atomic species within a sample. As a result, it is feasible to identify the specific elements located at the electron probe's position, which is the basis of energy-dispersive X-ray analysis (EDX).

Figure 2 illustrates the instrumental configurations of the three types of electron microscopes used in our studies.

- (a) Energy-filtering transmission electron microscope (EFTEM).
- (b) Scanning transmission electron microscope (STEM).
- (c) Scanning electron microscope (SEM).

The applications of these electron microscopes will be shown in the following sections and “[Interfacial Phenomena in Adhesion and Adhesive Bonding Investigated by Electron Microscopy](#)” chapter. Here the imaging and analysis principles of

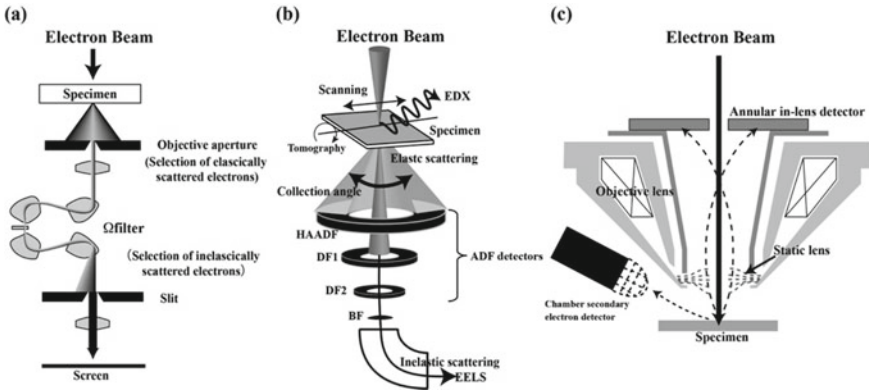


Fig. 2 Schematic diagrams of the configurations of the electron microscopes used in our works: **a** EFTEM, **b** STEM, and **c** SEM with two SE detectors

these instruments are briefly described. An electron lens in a conventional transmission electron microscope (CTEM) magnifies and creates images of elastically and inelastically scattered electrons produced when high-speed electrons pass through a thin film specimen. Image contrast and structural information can be obtained by selecting elastically scattered electrons according to the scattering angle using an objective aperture below a specimen. A viewer can see the image on the fluorescent screen below the projector lens, which converts the electron to visible light. In CTEM, the scattered electrons used for imaging are selected only via the objective aperture according to their scattering angles. Therefore, only electrons with large scattering angles contribute to contrast generation and enough contrast cannot be expected for imaging polymer specimens composed of light elements. Despite the significant impact on contrast and resolution caused by the chromatic aberration of the objective lens, the energy differences of the electrons and their variations are still not accounted for.

In EFTEM, the transmitted electrons are not only selected according to their angle but also to their energy [42, 43]. An energy filter (Ω filter) disperses the inelastically scattered electrons according to their energy. As a result, an EELS spectrum is imaged below the filter and can be seen on the screen. By insertion of a slit of variable width at the point where the EELS spectrum is formed, they are then selected for imaging with an energy loss and a defined energy width. Dual electron selection results in considerably enhanced contrast. By imaging energy-selected electrons, new information can be obtained with contrasts such as the structure-, thickness- and element-specific contrast. In addition, elemental mapping with rapid acquisition and high lateral resolution is capable of electron spectroscopic imaging (ESI). As the filter is integrated into the middle of the TEM column between the objective and projector lenses, this is called an in-column-type EFTEM. Another type of EFTEM is a post-column type, in which the filter is attached to a CTEM at the bottom below the fluorescent screen. An advantage of the in-column type over the post-column is

the possibility of seeing the energy-filtered image directly on the screen, making it easier for the viewer to find objects of interest in a specimen.

In STEM, the electron beam is focused on a spot and is scanned across the specimen area to be investigated while the transmitted electrons are collected [44]. The elastically scattered electrons are collected in the three annular dark-field (ADF) detectors which can collect the elastically scattered electrons according to the scattering angles. The bright-field (BF) detector, which is located at the lowest position in the array of detectors, collects the unscattered electrons and the scattered electrons with low scattering angles. Those four imaging detectors allow us to acquire images with different contrast simultaneously and obtain the desired contrast. Two types of spectrometers are equipped: EELS and EDX. An EDX spectrometer is located above the specimen. A post-column-type EELS spectrometer is attached to the bottom of the column, enabling the simultaneous recording of EDX and EELS spectra at a point of interest. It also can perform tomography for 3D visualization of the internal structures of a thin section. A series of tilted images with tilt angles ranging from -60° to $+60^\circ$ can be acquired and reconstruction generates a 3D volume within a specimen.

In SEM, the focused electron beam scans line by line over the surface of the specimen and forms signals based on the interactions between the beam and the specimen. The electrons interact with atoms in the specimen, producing various signals that contain information about the specimen's surface topography and composition. As stated above, SEM imaging uses SEs and BSEs emitted from the surface of the specimen. The contrast formation in the BSE mode is mainly determined by the atomic number (material contrast). In contrast, the contrast in the SE mode is primarily determined by the local inclination of the specimen surface with respect to the incident beam (topographic contrast). This effect of the SE on SEM imaging is called as "edge effect". In polymeric materials, the BSE mode cannot be expected; thus, the SE mode is mainly used for imaging the topographic features of surfaces. As described in Fig. 2c, the column of the SEM instrument used in our study integrates two detector systems for the collection of the SE signals: One is a conventional scintillator-type detector located outside the objective lens with a positively biased grid, and the other is an annular type positioned above the objective lens "on-axis". Those two detectors are called the "chamber detector" and the "in-lens" detector. The electrostatic lens formed at the entrance of the objective lens accelerates the SE electrons backward and directs them into the in-lens detector. The SE signals can be separated from BSE, which may not reach the detector because the higher kinetic energy causes different trajectories. Combining the chamber and the in-lens detectors is advantageous for low-voltage SEM imaging. As mentioned in Sect. 6, SE imaging with the two-detector system allows us to perform energy-filtered surface imaging, which offers the opportunity for high-resolution surface imaging of polymer specimens.

2 Analytical Electron Microscopy—EDX and EELS

Electron microscopes offer high-resolution imaging and elemental microanalysis, owing to element-specific electron scattering. Both energy-dispersive X-ray analysis (EDX) and electron energy-loss spectroscopy (EELS) are based on the fact that each element has a unique atomic electronic structure, and the primary electron can excite electrons on a particular shell of atoms. As illustrated in Fig. 3a, when high-energy electrons hit an atom's inner shell, an electron may be ejected, creating an electron hole. The energy difference between the outer and inner shells is then released as an X-ray. The energy of these X-rays is characteristic of the energy difference between the two shells and the atomic structure of the emitting element. An energy-dispersive spectrometer can measure the number and energy of X-rays emitted from a specimen. Thus, EDX allows for the determination of the specimen's elemental composition. Figure 3b depicts a typical EDX spectrum obtained from an STEM mode image of an aluminum 6061 alloy, providing an overview of the sample's elemental composition. The spectrum contains characteristic peaks for the excited atoms and a background continuum with low background contribution compared to EELS spectra.

In STEM-EDX, signals can be collected over a specimen area by sequential data collection, enabling the intensity of characteristic signals to represent the sample's local composition variation, as displayed in an elemental map.

The energy that primary electrons lose due to inelastic scattering is measured in EELS. Figure 4 shows a typical EELS spectrum, which presents the intensity of electrons as a function of energy loss. When a sample is thinner than the mean free path for inelastic scattering, the most noticeable aspect of the EELS spectrum is the zero-loss peak (ZLP) at 0 eV. This peak contains all elastically scattered electrons. The low-loss region of the EELS spectrum, which extends up to around 50 eV,

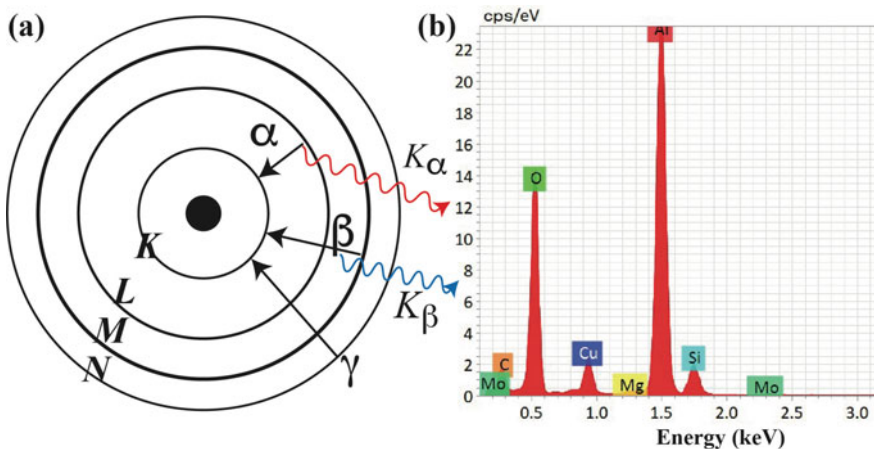


Fig. 3 De-excitation mechanisms for an atom that causes the characteristic X-ray emission from electron irradiation (a) and STEM-EDX spectra taken from aluminum 6061 alloy (b)

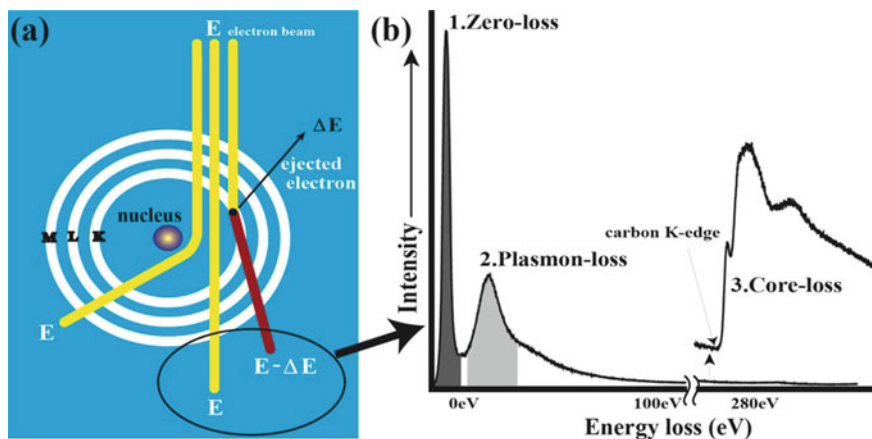


Fig. 4 Schematic diagram showing the process of the inelastic scattering and ionization of inner shell (a) and a typical EELS spectrum presenting zero-loss, plasmon-loss, and core-loss peaks (b)

corresponds to the excitation of weakly bound outermost atomic orbital electrons. This region is primarily characterized by plasmons caused by the valence electrons' resonant oscillations. It is mainly utilized to determine the thickness of the sample and correct for multiple inelastic scattering when performing quantitative microanalysis on thicker specimens.

In contrast, the high-loss region, extending from 50 eV to several thousand eV, corresponds to the excitation of electrons from well-localized orbitals on a single atomic site to unoccupied energy levels. This region reflects the atomic character of the specimen, with edges indicating the ionization of inner shell electrons and peaks known as core-loss peaks. The intensity of this region decreases monotonically, and gain changes are typically inserted in the linear intensity scale. EELS is beneficial for analyzing light elements such as those found in polymer samples, as the energy of an edge is determined by the binding energy of a particular electron shell, allowing for the identification of the atomic type [45]. Generally, the K-shell ionization edge of carbon (C K-edge) appears at around 285 eV as shown in Fig. 4b. The nitrogen and oxygen K-shell ionization edges appear at about 410 and 535 eV, respectively. The intensity under an edge is proportional to the number of atoms present, allowing for quantitative analysis.

The electron energy-loss spectroscopy (EELS) technique enables the identification of a compound's chemical state and nature by analyzing the fine modulations in the higher energy-loss region beyond the ionization edge, which typically spans an energy width of 50–100 eV. These modulations are referred to as electron energy-loss near-edge structures (ELNES), and they provide information about the electronic and bonding environment of the excited atom [46–48]. Figure 5 depicts typical examples of ELNES obtained from aluminum compounds. The EELS spectra of oxygen-containing aluminum compounds are presented in three energy-loss regions: (a) the plasmon loss, (b) Al L_{23-} , and (c) O K-edges. The powder samples of metallic Al,

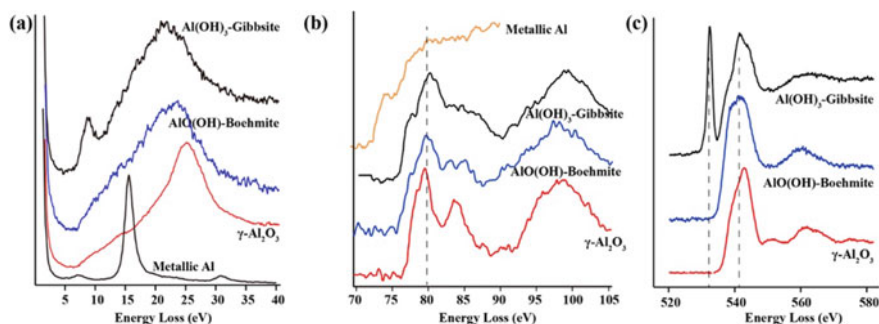


Fig. 5 EELS spectra of aluminum compounds obtained from the powder samples of metallic Al, $\text{Al}(\text{OH})_3$ (gibbsite), $\text{AlO}(\text{OH})$ (boehmite), and γ -alumina: **a** plasmon-loss region; **b** Al L_{23} -edge; **c** O K-edge. All the spectra except the plasmon-loss spectra are presented after the background subtraction by fitting the pre-edge regions with the power law function

γ -alumina (Al_2O_3), boehmite ($\text{AlO}(\text{OH})$), and aluminum hydroxide ($\text{Al}(\text{OH})_3$) were used to obtain these spectra, which were collected from multiple points (10×10 points) in the STEM mode, energy-drift-corrected, and summed into a single spectrum. The O K-edge ELNES features of the three oxygen-containing compounds show distinct differences. γ -alumina has two maxima at 550 and 563 eV energy losses, followed by a major peak at 542 eV. Boehmite has a broadened first peak, followed by only one maximum at an energy loss of 560 eV, and $\text{Al}(\text{OH})_3$ exhibits an intense peak at 532.6 eV, followed by two maxima at energy losses of 540 and 560 eV. Thus, the O K-edge ELNES features can be used as unique identifiers to determine the chemical compositions of aluminum compounds. However, the ELNES features in these compounds are not yet fully understood [49].

The intensity of the core-loss ionization edge in an EELS spectrum relative to the background is highly dependent on the thickness of the analyzed region, making the edge less detectable as the sample thickness increases. Therefore, the specimen must be thin to obtain chemical information by ELNES. EDX; on the other hand, tolerates thicker specimens and the background signals in the EDX spectrum are much lower than those in EELS, even though EDX background signals increase with increasing specimen thickness. The energy resolution of EDX detectors is typically 100–150 eV, which gives rise to peak overlap at low X-ray energies and precludes any chemical state information. EDX suffers from severe spectral resolution issues when dealing with compounds that have overlapping X-ray lines. This issue is not present in EELS, which is generated by the primary event of energy loss, providing an advantage over EDX. In EDX, signal intensity is linked to the secondary fluorescence process resulting from de-excitation via X-ray emission, which is not the case with EELS. Therefore, the spectral energy resolution of EELS is significantly higher than that of EDX. We generally perform EDX analysis for the quick survey of the elemental composition in a region of interest (ROI) in a specimen. In contrast, EELS is performed for the detailed chemical analysis of an element of interest involved in the ROI.

3 Specimen Preparation

3.1 Preparation of Thin Sections by Ultramicrotomy

For the electron microscopic investigations by TEM and STEM, specimens must be thin enough for the electron beam to transmit to obtain fine images and reliable microanalysis. In TEM and STEM, preparing thin sections of uniform thickness and free from artifacts is a key issue for achieving reliable results. Thin sections from polymeric bulk samples are commonly prepared by ultramicrotomy. Ultramicrotomy is a standard method for preparing ultrathin sections (<100 nm) and flat surfaces for polymeric materials. This method allows high-throughput sample preparation and is also sample-friendly compared to other techniques, such as focused ion beam (FIB) fabrication. The traditional application of ultramicrotomy involves the sectioning of soft materials. Even metallic materials, however, like aluminum, copper, magnesium, titanium, and steel, have been successfully sectioned by ultramicrotomy. The key to achieving artifact-free successful sectioning lies in the experience of the experimentalist rather than the instrumentation used. It is crucial to master the optimal specimen preparation and sectioning technique while understanding the materials to be cut. The general procedure for specimen preparation by ultramicrotomy has been described in detail in the literature [50, 51]. Here, the technical topics for the sectioning of surfaces and interfaces in metallic and polymeric samples are reviewed.

Figure 6a shows the appearance of an ultramicrotome apparatus and Fig. 6b shows the inside of the ultramicrotome where a sample holder (left part) and the diamond knife (right part) are fixed. The diamond knife is supplied with a trough to be filled with water. The sample holder approaches the knife at a given distance while repeating vertical movement. During the downward motion of the sample holder, a section is produced and simultaneously floats on the water filled in the knife's trough. After sectioning the sample, the sample holder moves backward and then rises to the position where the next sectioning starts. Before the sectioning with an ultramicrotome, the sample must be trimmed to serve a cutting surface with an appropriate area and shape. Before the sectioning with an ultramicrotome, the specimen is trimmed to create a square plane of 0.3 mm or less on the tip of the pyramidal specimen, as shown in Fig. 6c. Figure 7 is a video demonstrating the sectioning procedure. The section is connected to the one cut during the previous cutting cycle, and several sections are connected and lined up. The sections can be picked up easily onto a copper grid on the water surface in the trough. The surface must be trimmed smoothly on all sides with a fresh glass knife on an ultramicrotome to obtain serially thin sections in a desired thickness, as shown in the video. The size and shape of the trimmed surface should be optimized by watching the cutting behavior.

Sections cut in a uniform thickness exhibit interference color reflecting the thickness of the sections as shown in Fig. 8. The thickness can be estimated from the interference color of the section floating on the water surface as shown in the table (right panel in Fig. 8). Suitable sections for TEM/STEM are silver- or gray-colored sections.

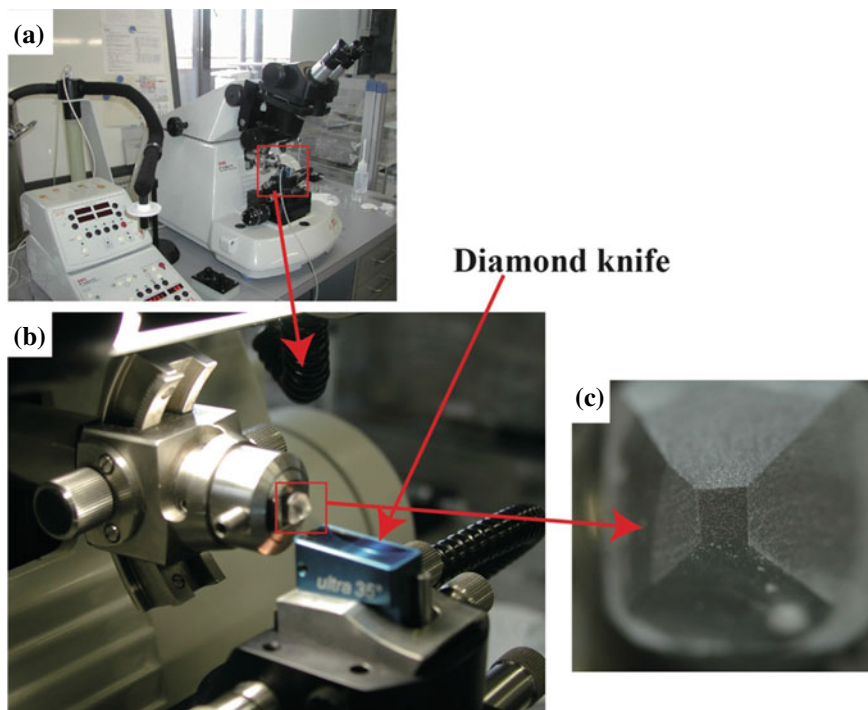


Fig. 6 Appearance of the ultramicrotome apparatus (a) used in this work, the specimen holder, and the diamond knife fixed in the ultramicrotome (b). c A cutting face created in a square plane of 0.3 mm on the tip of the pyramidal specimen

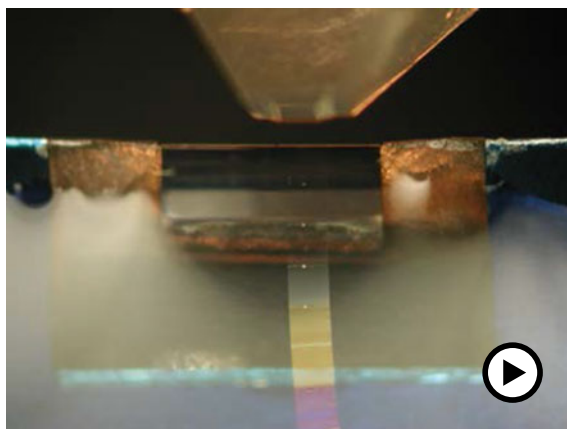


Fig. 7 Video demonstrating the sectioning procedure by ultramicrotomy. The width of the diamond knife is 1.5 mm (► <https://doi.org/10.1007/000-aye>)

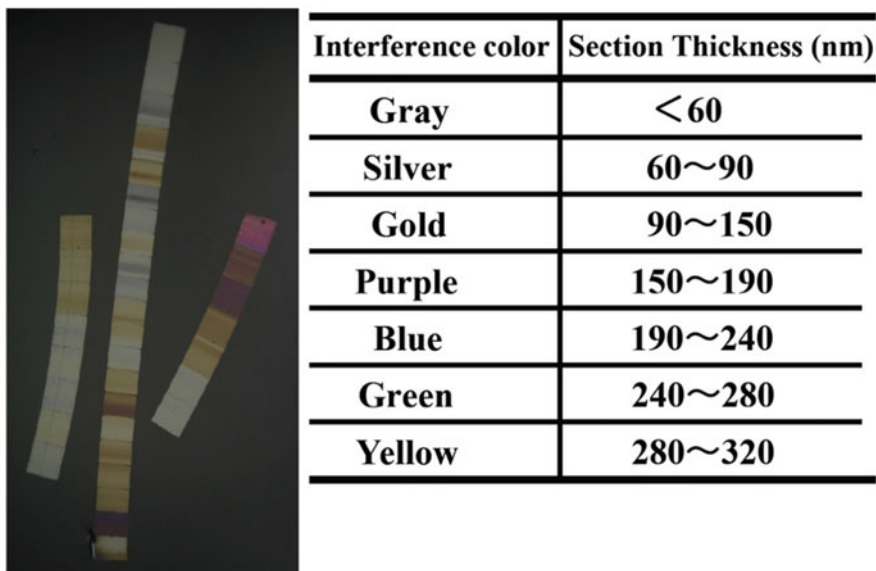


Fig. 8 Serial thin sections floating on water with different thicknesses prepared by ultramicrotomy (*left*) and the relationship between section thickness and interference color (*right*)

To observe a cross section of a substrate's surface thin skin layer or the interfacial region in a laminate, the samples are commonly cut where the angle between a cutting face and a surface/interface plane is adjusted at 90° . When specimens are cut like this, the two-dimensional (2D) image projection cannot observe the interface detail due to the overlapping of three-dimensional (3D) structures within the regions. To resolve this problem, specimens are prepared by oblique cutting of the surface/interface plane, resulting in the regions' oblique projections. Figure 9 shows a typical example of the sample setup and the preparation of a cutting surface for the oblique sectioning of the aluminum surface oxide layer with a defined angle. An aluminum plate is a preliminary cut into a roof-like shape. It is fixed on a cylindrical plastic base that has been obliquely cut at an angle of 60° or more, with the aluminum surface facing up. The cutting face is then created by trimming the tip of the roof horizontally. Figure 10 is a video demonstrating the oblique sectioning of aluminum 6061 alloy surface where thin serial sections are floating on the water filled in diamond knife's trough. Figure 11 shows STEM-HAADF (high angle annular dark field) images, indicating the comparison between the cross section and the oblique section of the interface between aluminum and adhesive [48]. As depicted in the insets, the projection of the interface in the oblique section shows a thinner aluminum surface region, allowing us to see the structural details regarding the roughness and porous nature of the aluminum skin layer.

Cryoultramicrotomy is required when the sample is too soft, like a rubber material, or when the sectioning at room temperature causes severe deformation of structural

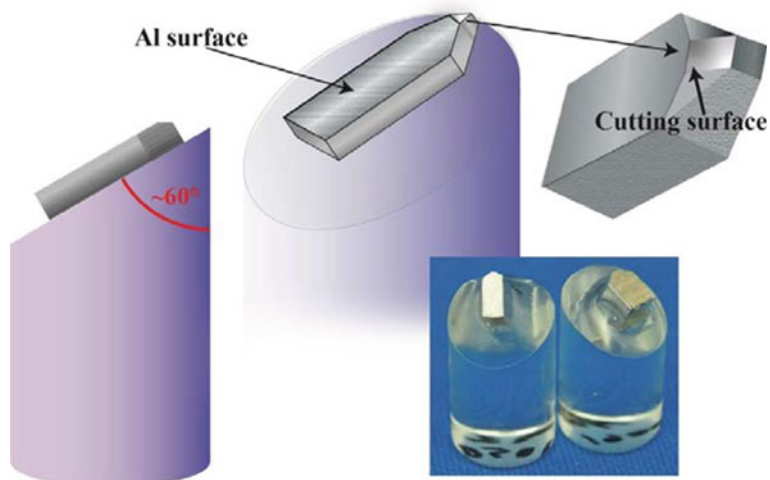
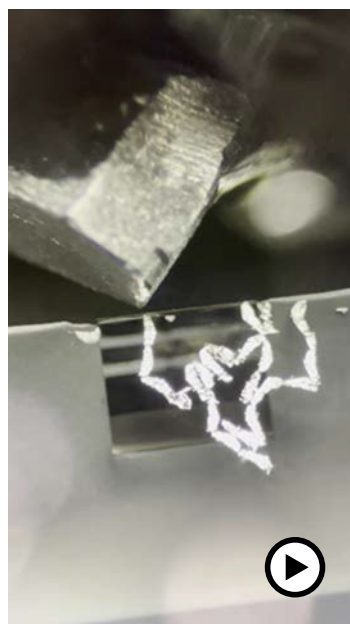


Fig. 9 Schematic illustration and the actual samples showing the process for the oblique sectioning of an aluminum surface by ultramicrotomy

Fig. 10 Video presenting the oblique sectioning of aluminum 6061 alloy surface where thin sections float on the water filled in diamond knife's trough

(► <https://doi.org/10.1007/000-ayc>)



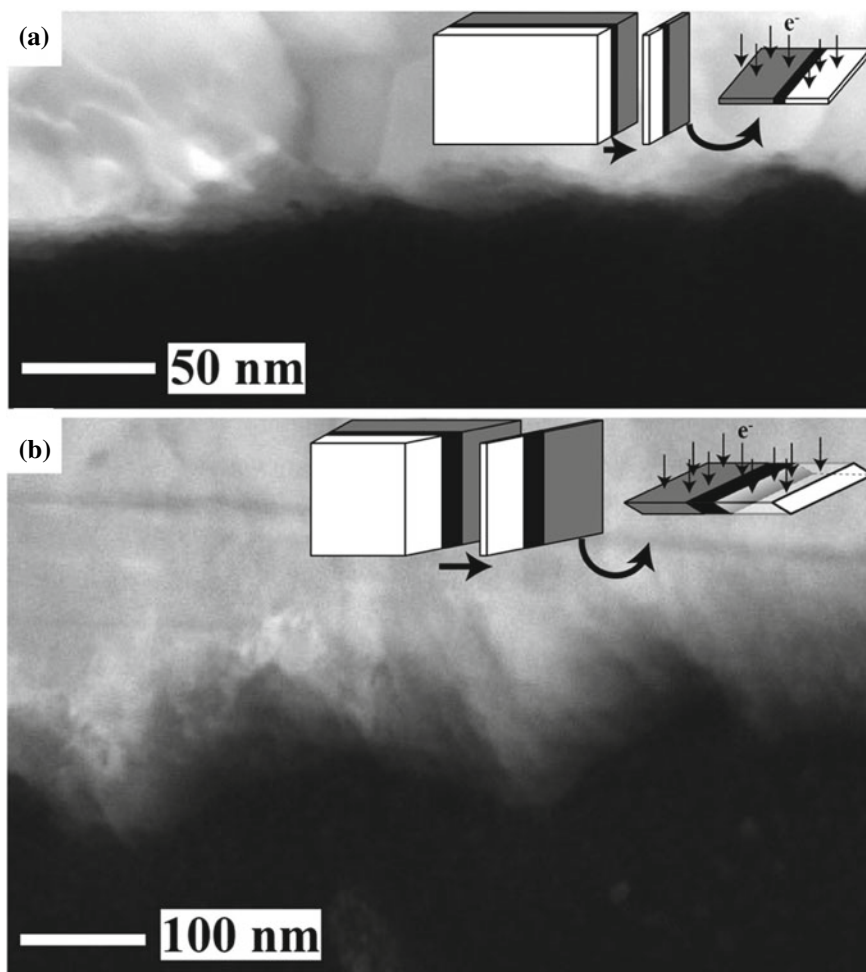


Fig. 11 STEM-HAADF images of a cross (a) and an oblique (b) sections of aluminum adhesive interface. The insets depict the planes of sections obtained by cross and oblique sectioning. Reprinted with permission from Ref. [48]. Copyright 2022, Elsevier. All Rights Reserved

details. The cryo-chamber is attached to the ultramicrotome as shown in Fig. 12, which is cooled by liquid nitrogen at a controlled temperature down to $-185\text{ }^{\circ}\text{C}$. The sectioning under a cryogenic temperature is carried out with a diamond knife, and the collection of sections is performed either in the presence of a floating liquid (wet sectioning) or on the surface of the knife (dry sectioning). For wet sectioning, ethanol can be used down to $-100\text{ }^{\circ}\text{C}$, while in the dry sectioning, the sections are transferred directly onto a grid.

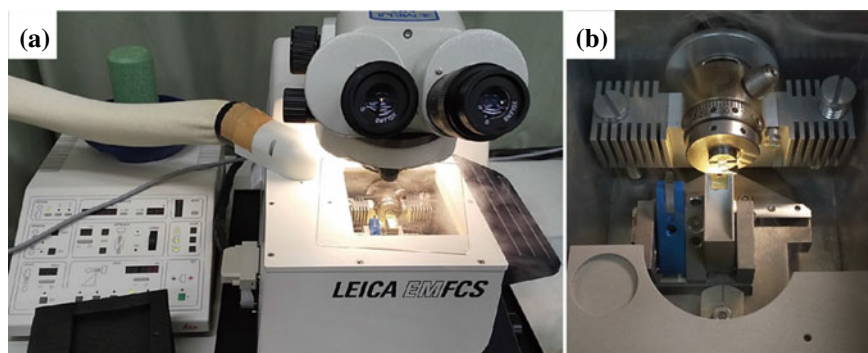


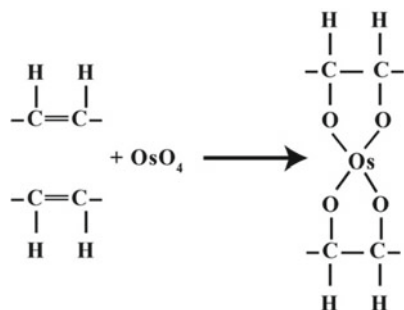
Fig. 12 The appearance of the cryo-ultramicrotome equipment (a) and the interior of the cryo-compartment (b) with two diamond knives for trimming (*left*) and wet sectioning (*right*)

3.2 Staining

Image contrast acquired in the conventional TEM (CTEM) results from variations in electron density in the structures present. Most polymers are composed of low atomic number elements, and thus they exhibit slight variations in electron density. The morphological observation of polymeric samples by CTEM requires appropriate staining to introduce a heavy atom into specific structures in a specimen. In addition to enhancing contrast with staining, staining serves the important function of fixing and hardening polymeric materials. This effect of staining enables the sectioning of soft materials by ultramicrotomy with the preservation of structural details. Staining can also increase specimen stability against electron beam irradiation to maintain the structural dimensions of the specimens. Two staining agents have been widely used for polymer staining: osmium tetroxide (OsO_4) and ruthenium tetroxide (RuO_4) [52]. Different procedures have been known for selective staining, either on the bulk materials before sectioning, called “block staining” or on the thin sections after cutting, called “section staining”. Several TEM and STEM images taken with different sectioning and staining procedures are presented as examples. We can see in these images the interfacial regions in heterogeneous polymer systems such as polymer blends, block copolymers, and semicrystalline polymers.

OsO_4 reacts to the carbon–carbon double bonds in unsaturated rubber phases, which cross-links the polymer chains as indicated in Scheme 1. OsO_4 can enhance the contrast in TEM by the increased electron scattering of the heavy atom in the rubber phase compared with the unstained matrix. It also enhances the hardness and stiffness of the rubber phase. It thus allows the sectioning of the samples at room temperature by ultramicrotomy without the loss of the rubber phase.

Scheme 1 The chemical reaction between OsO_4 and unsaturated rubber polymers



3.2.1 Observation of an Interface Between ABS and Copper-Plated Film by OsO_4 Staining

For the fixation and staining of a polymer sample containing a rubber phase, the sample is stained with OsO_4 by the block staining. The sample is preliminarily trimmed to create the cutting face for ultramicrotomy, as shown in Fig. 6c. The trimmed blocks are placed in a glass container with a small amount of OsO_4 , sealed well, and stained with the OsO_4 vapor for a specific time and temperature. The vaporized OsO_4 penetrated the sample surface and the region below the surface with a depth of several microns to several tens of microns can be stained. Therefore, one must carefully approach the diamond knife to the cutting face to avoid cutting off the stained part before collecting the thin sections in ultramicrotomy. Figure 13 is a STEM bright-field (BF) image showing a cross section of acrylonitrile–butadiene–styrene (ABS) with a copper foil deposited by electroless plating. ABS is a multi-component polymer containing the polybutadiene (PB) domains distributed in the acrylonitrile–styrene (AS) random copolymer matrix. The sample was stained with OsO_4 after trimming at 60 °C overnight and was cut into a thin section with about 70 nm thickness by ultramicrotomy at room temperature. The sectioning direction is horizontal in the image, which the shallow knife marks on the copper side can identify. The knife marks are produced in the section due to the diamond knife’s edge damage. When this is the case, ridges on the surface of the section are created along the sectioning direction. In the ABS part (top in the micrograph), the stained PB domains with the occluded unstained AS particulates are distributed in the AS matrix. The sectioning seems to be carried out successfully because no deformation of the PB domains along the cutting direction was recognized. For electroless plating on the ABS plate, the PB domains on the surface were etched with chromic acid to create holes on the surface filled with copper. As shown in the inset, it can be confirmed that Pd nanoparticles, which act as a catalyst for electroless plating, are adsorbed on the entire ABS surface at high density. As a result, copper plating starts evenly from the ABS surface, which fills the holes on the ABS surface, and excellent adhesion was achieved due to an anchoring effect.

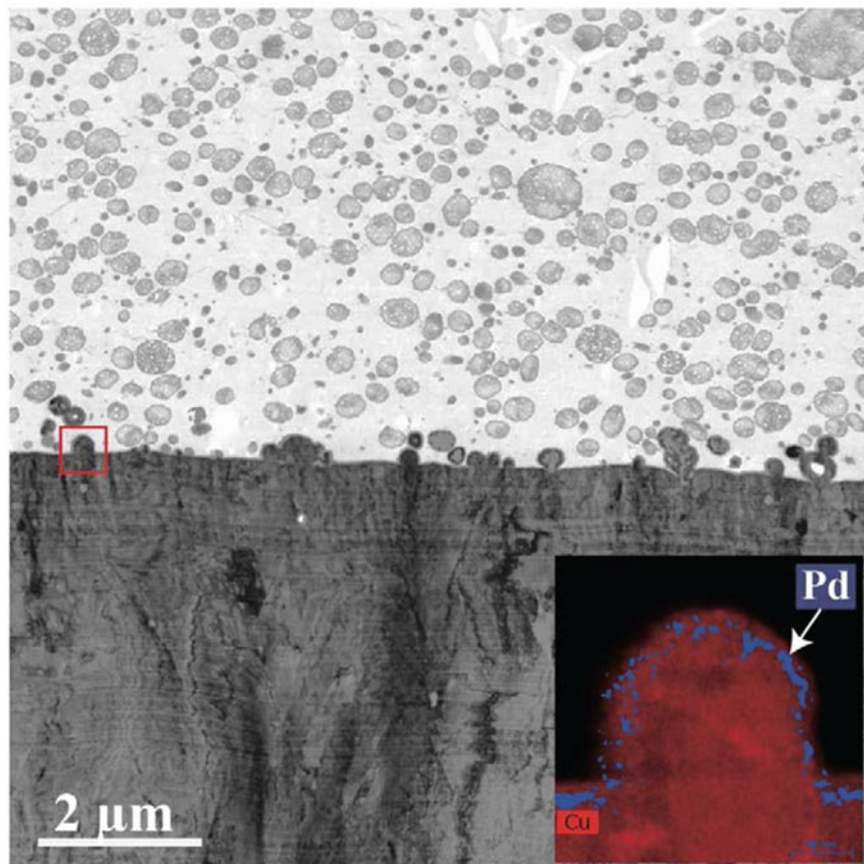


Fig. 13 STEM-BF image showing the OsO_4 -stained polybutadiene domains dispersed in ABS polymer (*upper part*) and the copper foil deposited by electroless plating on a chromate-etched ABS plate (*lower part*). The inset shows the STEM-EDX elemental map showing the distribution of copper (red) and palladium (blue) in the interfacial region indicated as a red box

3.2.2 Observation of Lamellar Structures in Semicrystalline Polymers by RuO_4 Block Staining

RuO_4 is a stronger oxidizing agent than OsO_4 [53]. The staining mechanism of RuO_4 is different from that of OsO_4 . RuO_4 does not react directly to polymers as OsO_4 can crosslink the $\text{C}=\text{C}$ double bonds in unsaturated polymers, while it forms ruthenium-containing clusters instead. RuO_4 can stain both saturated and unsaturated polymers that contain in their unit structure ether, alcohol, aromatic, or amide moieties. Most polymers, therefore, can be stained with RuO_4 , except poly(methyl methacrylate) (PMMA), poly(vinyl chloride) (PVC), poly(vinylidene fluoride) (PCDF), and polyacrylonitrile (PAN). As shown in the following three examples, RuO_4 can stain most polymers, but the degree of the staining varies depending on the structures of the

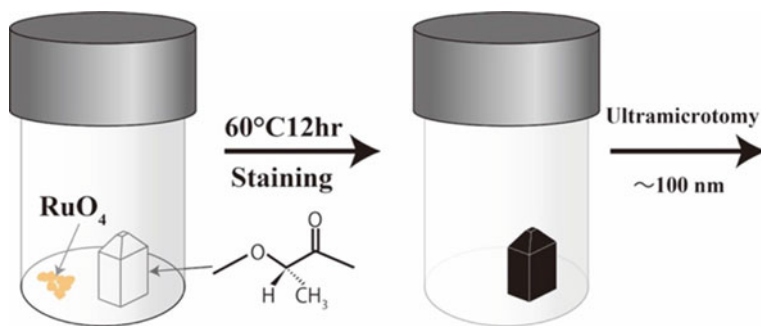


Fig. 14 Schematic illustration for the block staining of a trimmed polymer sample (L-PLA)

polymers investigated. Polyolefin with no functional groups such as polyethylene (PE) and polypropylene (PP) can be stained, where RuO_4 diffuses preferentially into the amorphous regions and stains them in semicrystalline structures, whereas the crystalline regions remain unstained. Therefore, the lamellae in semicrystalline polymers can be visualized by the RuO_4 staining.

The samples were stained by RuO_4 vapor at 60 °C overnight before ultramicrotomy and were then cut into about 70 nm thick sections, as illustrated in Fig. 14. The RuO_4 vapor may diffuse into the amorphous part preferentially, allowing the sectioning at room temperature without losing structural details. Figures 15 and 16 show TEM micrographs showing typical lamellar structures of semicrystalline polymers observed in interfacial regions by the selective RuO_4 staining. Figure 15a, b shows the spherulitic texture and the lamellae in a spherulite of L-poly(lactic acid) (L-PLA), respectively. PLA is inherently slow to crystallize. If the annealing time inside the mold in injection molding is limited, the growth of spherulites terminates in the middle of the crystallization from the melt. As a result, the amorphous phase remains between nearby spherulites. As a result, the sample exhibits a morphology in which spherulites with several tens of microns diameters are dispersed in the amorphous phase, as shown in Fig. 15a. Spherulite is a typical crystal form of semicrystalline polymers, which is usually formed under the quiescent condition as organized lamellae growing in the radial direction from the spherulite's center. When the lamellae grow outward from the center, they twist around the radius with helical configurations. The texture of the spherulites shown in the TEM micrograph may represent such a lamellar arrangement in a spherulite. Figure 15b is a high-magnification image showing the border between a spherulite and the amorphous phase. The selective staining of the L-PLA allows the lamellae to be visible as loosely packed thin filaments, which represent the transformation of the polymer chains from random coils to crystalline lamellae at the forefront of the growing spherulite toward the amorphous region.

Fig. 15 TEM micrographs of L-PLA: **a** spherulites formed in the crystallization from the melt; **b** lamellae grown at the forefront of the spherulite's growth

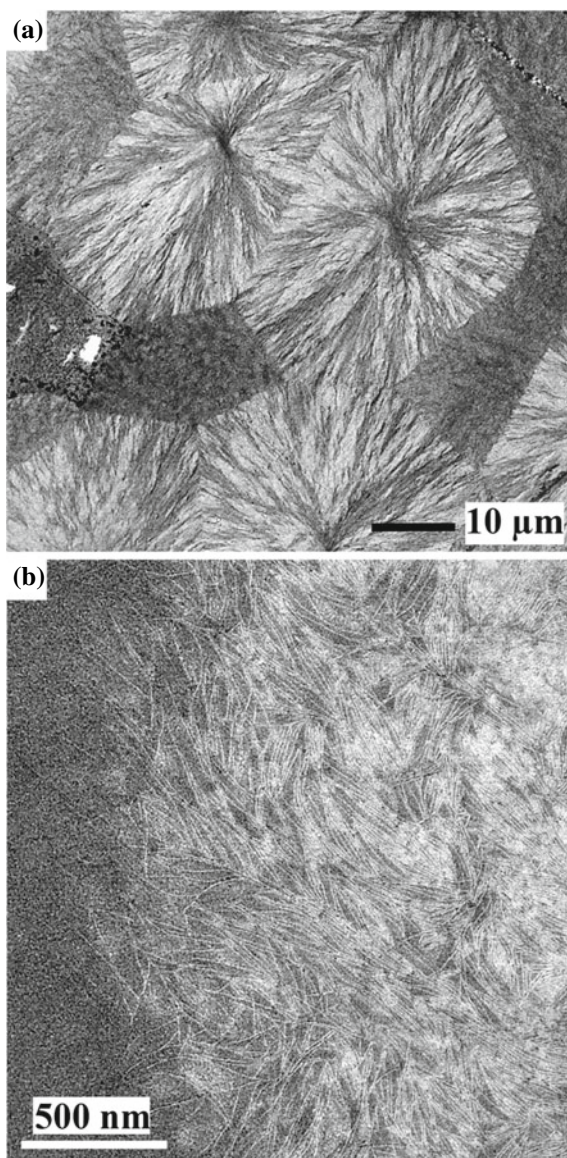
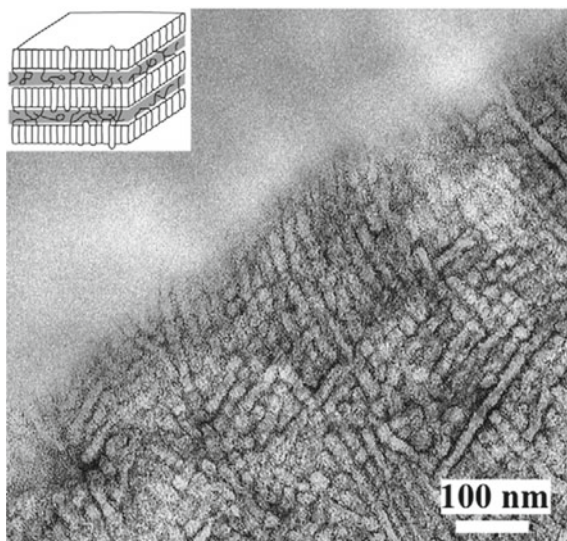


Figure 16 is an STEM-BF image showing the lamellae of isotactic PP (*i*PP) in the interfacial region, where an epoxy adhesive bonds to the *i*PP surface. As shown in the inset, the interlamellar amorphous region exists between the stacked lamellae in which the folded segments in a polymer chain are arranged parallel to the neighboring segments. These amorphous layers can be selectively stained, making the lamellae visible as the unstained region. Since the characteristics of the lamellae in contact with

Fig. 16 STEM-BF image showing the interfacial lamellar structure of *i*PP bonded to an epoxy adhesive. The inset illustrates the selective staining with RuO₄ of the interlamellar amorphous regions between the stacked lamellae



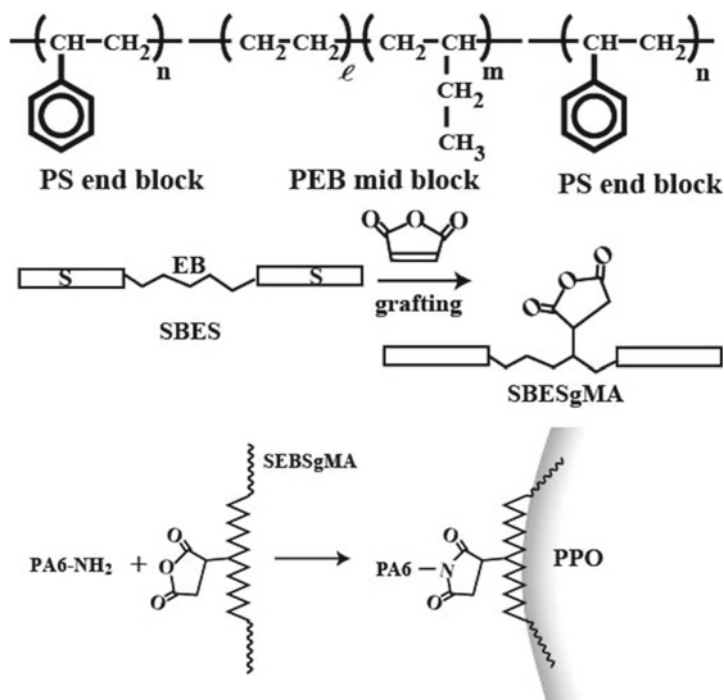
the adhesive are believed to affect the bonding properties greatly, we are concerned with the interfacial lamellar structures of *i*PP in terms of the orientation, length, width, and disordering to clarify the bonding mechanism, which will be described in Sects. 4 and 5 of “Interfacial Phenomena in Adhesion and Adhesive Bonding Investigated by Electron Microscopy” chapter.

3.2.3 Observation of Multi-phase Structures of a Polymer Blend by RuO₄ Section Staining

As an alternative to “block staining”, one can also directly stain sections of the samples. Ultrathin sections are stained using vapor of OsO₄ or RuO₄. The staining of thin polymer sections occurs quite rapidly compared to “block staining”. This method sometimes gives better results for polymer samples with complex phase-separated structures with multiple polymer components. Interfaces existing in the phase-separated structures of multi-component polymer materials are the issues to be highly concern for studying structure–property relationships of polymeric materials. Direct observation and analysis of interfaces localized in multi-phase polymer materials by TEM or STEM would be the promising approach for investigating the mechanism of outstanding properties that cannot be obtained in single-component materials. Melt blending of polyamide 6 (PA6), poly-(2,6-dimethyl-1,4-phenylene oxide) (PPO), and SEBS has complicated multi-phase morphologies. SEBS is an ABA triblock copolymer comprising of the polystyrene (PS) end blocks and the ethylene-butylene (PEB) mid-block as shown in Scheme 2 (top part), which has been used for a thermoplastic elastomer. SEBS can be functionalized by grafting maleic anhydride (MA) to the PEB mid-block (middle part in Scheme 2), which can

react to the $-\text{NH}_2$ terminal group of PA6 during the melt blending. The in situ chemical reaction between PA6 and SEBSgMA with 10–20 wt% SEBSgMA contents causes a remarkable reduction of the SEBS domain size, resulting in an impact strength approximately 20 times higher than PA6 [54]. PA6 and PPO, on the other hand, are incompatible and the simple blending of those two polymers results in poor mechanical properties due to the poor dispersion of the minor component and the poor interfacial strength between the matrix and the domains. The addition of SEBSgMA to the PA6/PPO (75/25 wt/wt) incompatible blend causes the localization of the SEBS elastomer phase at the PA6/PPO interface, as shown in Scheme 2 (bottom). This is because the combination of PS and PPO is a rare pair thermodynamically miscible in all compositions and temperatures. When the three polymers are melt-blended simultaneously, PA6 and SEBSgMA react to form a graft copolymer through imidization, while the PS block of SEBS penetrates the PPO phase. As a result, SEBS molecules are localized to the PA6/PPO interface and reinforce the interfaces.

The ternary PA6/SEBSgMA/PPO blend has a complicated heterogeneous multi-phase structure. Sectioning by ultramicrotomy for TEM investigation may cause distortion to the shape of the dispersed domains and the interfaces involved in the



Scheme 2 Chemical structure of SEBS (*top*), graft of MA onto the EB mid-block in SEBS (*middle*) and reaction between PA6 and SEBSgMA, and the localization of the PA6-SEBSgMA graft copolymer at PA6/PPO interface (*bottom*)

blend, so great care must be taken when preparing thin sections to preserve the original morphological features. For this purpose, sectioning by cryo-ultramicrotome followed by “section staining” is the best way to achieve reliable results. The wet sectioning with ethanol obtained the thin sections about 100 nm thick under a cryogenic condition at $-100\text{ }^{\circ}\text{C}$. Then the sections were stained with the RuO_4 vapor for 15 min. Figure 17 presents TEM micrographs showing the morphological structures. The staining was successfully employed to show the three phases with different contrast, as shown in Fig. 17: The PS domain of SEBS is the most intensely stained, and the PPO domain is the second most intensely stained. The PA6 matrix phase is less intensely stained, but the selective staining of the amorphous phase makes the lamellae visible, as shown in Fig. 17b. Figure 17b is a high-magnification image focusing on the interfacial region: A large number of SEBS domains are dispersed in the PA6 matrix, representing the nanodomain structure of a block copolymer where the stained PS domains and the PEB phases are arranged periodically with the distance of about 10 nm, and also the SEBS phase surrounds the PPO domains with the 10-nm-thick thin layer. It can also be found that a small number of SEBS domains are distributed in the PPO domains; this is caused by the micellization of the SEBS in the PPO domains. During the melt blending, a certain amount of SEBSgMA escapes from the interface toward the PPO domains instead of the reaction to PA6 due to the high miscibility of the PS and PPO. It can be confirmed that the dispersion of the SEBS domains in the PA6 matrix may enhance the impact resistivity of the PA6 matrix. At the same time, forming the SEBS thin layer at the PA6/PPO interface can improve the toughness of the interface. SEBSgMA acts as a compatibilization for the PA6/PPO blends.

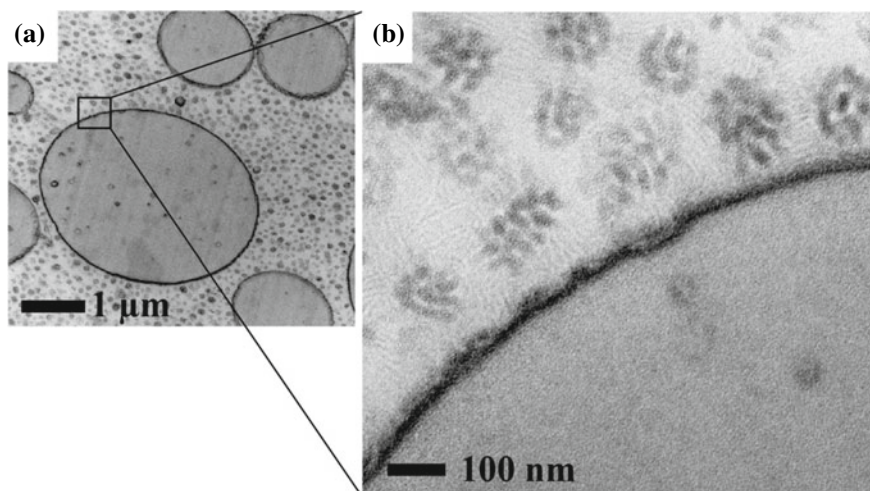


Fig. 17 TEM micrographs showing the multi-phase structure of PA6/PPO/SEBSgMA ternary blend stained with RuO_4 . **b** Is the magnified image of **a**. The images were taken as zero-loss images by EFTEM

3.3 Focused Ion Beam Fabrication (FIB)

Focused ion beam (FIB) is one of the methods of sampling a thin specimen from specific regions of a bulk sample for TEM and STEM imaging and microanalysis [55]. Unlike SEM, FIB systems use a focused beam of ions, usually Ga ions, to mill specific regions on the surface. The FIB/SEM system combines the two methods: SEM for high-resolution electron imaging and FIB for in situ milling of specific areas while monitoring the process with SEM. FIB specimen preparation can be applied to almost any material, hard or soft, or a combination of both.

Figure 18 demonstrates the micro-sampling process, consisting of several FIB steps, for sampling a thin specimen of a polymer composite coated with a thin copper film deposited by electroless plating: (1) surface protection; (2) peripheral milling; (3) bottom cutting; (4) precise probing processes of fixing the probe, micro-bridge cutting, picking up a micro-sample; (5) fixing the micro-sample to the TEM's specimen carrier and probe cutting; and (6) final thinning to create a thin window for electrons. Before cutting, a protective tungsten (W) layer is deposited onto the region of interest using electron beam-induced deposition. The rough-milling process creates trenches and extracts a thin chunk (a sample piece) from the bulk material, which is then welded to a nanomanipulator probe. The bridge of the chunk is cut, and the chunk is picked up and transferred to a TEM grid, where the final-milling process is employed. In the final-milling process, the chunk is thinned and polished down to around 100 nm in thickness. The process involves gradually reducing the FIB voltage and applying additional polishing to eliminate damaged layers on both sides of the specimen. Specifically, the FIB voltage is reduced from its initial value of 30–5 kV when the specimen thickness reaches approximately 200 nm. Subsequently, polishing is performed at voltages ranging from 0.6 to 1 kV to remove the damaged layers on both sides of the specimen. Finally, the electron-transparent window for TEM is prepared at the center of the lamella.

Thinning complex structures comprising various materials, including highly filled composites and layered materials, into electron-transparent lamellae suitable for TEM analysis can be accomplished using FIB. Such materials can be challenging to section by ultramicrotomy, resulting in cutting artifacts at the interface between the components. Another advantage is that FIB enables micro-sampling that can select specific regions accurately for the sampling using the SEM function coupled with an FIB system, making it a useful tool for microanalysis.

However, the drawbacks to FIB sample preparation are the ion implantation into the specimen and severe material damage caused by the ion collision. Moreover, the FIB process is time-consuming as compared to ultramicrotomy. The area of the electron-transparent window fabricated by FIB is usually limited to several ten microns, while the size of ultrathin sections prepared by ultramicrotomy is several hundred microns. Polymer samples are affected by the bombardment of the high-energy ion beam, which mainly produces noticeable effects on the chemical analysis by EELS. FIB has, therefore, limited applicability to polymers because many of them are sensitive to beam damage. Carbon fiber-reinforced plastic (CFRP) is a material

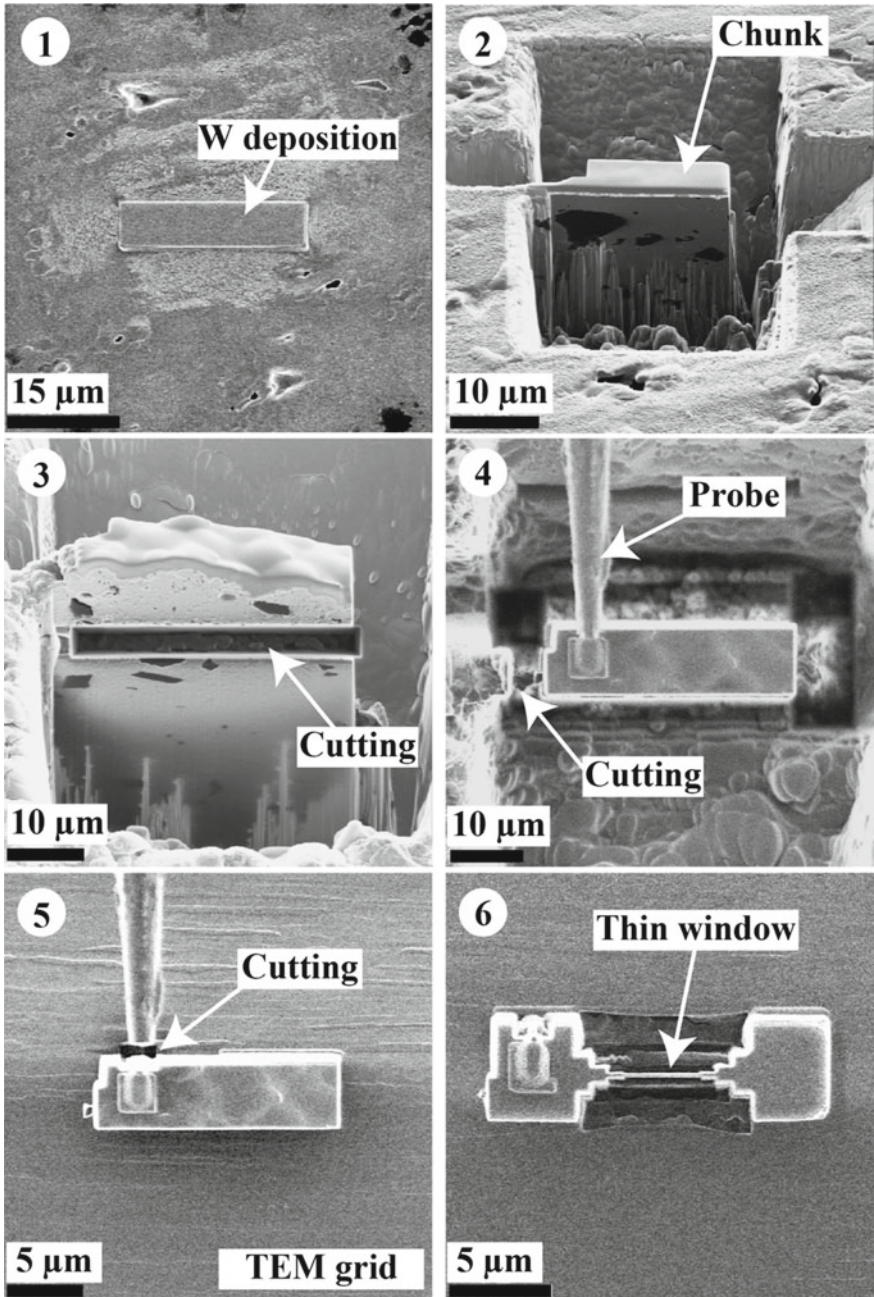


Fig. 18 SEM micrographs showing the stages of preparing a TEM specimen by FIB. 1: tungsten (W) coating; 2: rough-milling to prepare a chunk in bulk; 3: cutting off the bottom part to separate the chunk from the bulk; 4: in situ manipulator is fixed on the chunk; 5: the chunk is transferred and fixed on a TEM grid, and the FIB cuts the tip of the manipulator to release the sample; 6: the final thinning process to create a thin window for a final TEM specimen

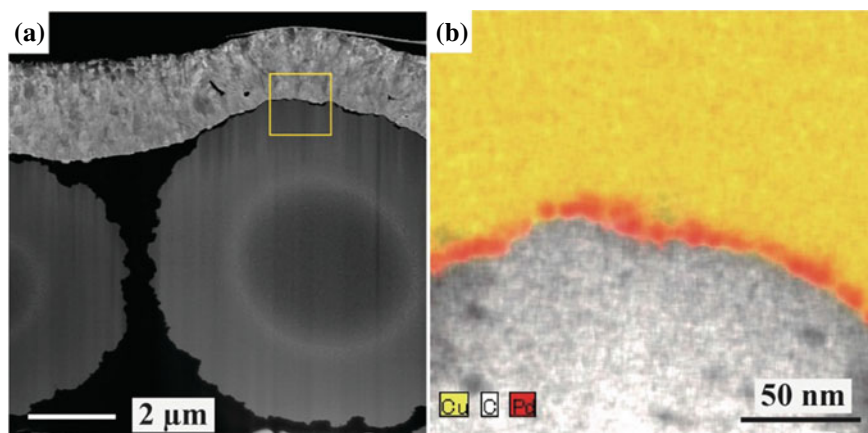


Fig. 19 Cross section of CFRP coated with electroless plated copper foil: **a** STEM-HAADF image; **b** STEM-EDX elemental map presenting Cu, C, and Pd distributions in the square area indicated in **a**

that is difficult to cut into a thin section for the TEM investigation by ultramicrotomy. At the same time, FIB allows to create a thin cross section with a smooth surface, as shown in Fig. 19. Figure 19a is an STEM-HAADF image showing the cross section of a CFRP coated with the copper film deposited by electroless plating. Cross sections of carbon fiber, matrix plastic, and copper films were successfully fabricated into a thin lamella of uniform thickness. Cross sections of carbon fiber, matrix plastic, and copper films were successfully fabricated into a thin lamella of uniform thickness. A slight gap between the electroless copper plating film and the carbon fiber can be confirmed to be filled with matrix resin. The CFRP surface is fully covered with the resin, and the copper plating film adheres to the matrix resin via the Pd nanoparticles. The STEM-EDX elemental mapping was performed, where the Pd nanoparticles act as the catalyst for the electroless plating of copper and are densely packed at the interface between the copper and CFRP.

3.4 Surface Replica

The method of replication involves the creation of a copy of a surface's topography through the use of casting or pressing techniques. This technique is commonly used when other methods of duplication are not feasible. One prevalent application of this technique is in metal replica-based electron microscopy, which allows for a high-resolution examination of the topography of biological structures. Another example of this method's use in biology is the freeze-fracture technique. A frozen biological sample is physically broken apart, and platinum-carbon is vacuum-deposited to produce a replica film that can be examined using TEM.

When investigating polymer surfaces that display structural changes after etching or fracture, SEM or atomic force microscopy (AFM) is typically used. However, the replica technique with TEM is employed when these surfaces are inaccessible using other techniques. A thin metal film evaporates onto the surface to produce a replica, and shadowing is carried out using heavy metal to enhance structure contrast. The metal is evaporated at an oblique angle to the surface, resulting in a lighter coating on the back of protrusions, creating the illusion of surface topography.

Figure 20 depicts the step-by-step process for creating surface replicas. A freeze-fracture device is used to vacuum deposit a mixture of platinum and carbon onto the sample surface (Fig. 20a). To preserve the original surface morphology during the deposition process, the specimen is fastened onto the cryo-stage at a temperature of $-144\text{ }^{\circ}\text{C}$. A 7-nm-thick layer of Pt is sputtered from a low angle of 25° , and then a 25-nm-thick carbon layer is deposited from another source at a 90° angle to reinforce the Pt film. The thickness of these films is monitored using a quartz crystal-thickness monitor. The specimen is rotated horizontally during deposition to achieve a semi-stereoscopic effect and to spread the deposit into the surface structures' finer spaces. After deposition, the coated specimen is transferred to room temperature in an atmosphere. A 30 wt% gelatin aqueous solution is poured onto the replica surface overnight to solidify. The gelatin layer is then peeled off from the replica films and floated on a 10 wt% aqueous potassium thiocyanate (KSCN) solution. After the gelatin layer dissolves entirely, the Pt-C replica film is washed with dilute H_2SO_4 and water and transferred onto a copper grid coated with collodion. The sample's surface topography can be precisely replicated, and the films can be examined using STEM in the HAADF mode. This technique is commonly utilized in examining biological materials [57] and has also been used in studying the tribological properties of polymer surfaces [58].

An example demonstrating the replica-STEM technique's effectiveness in examining semicrystalline polymer surface structures is presented in Fig. 21. The Pt-carbon replicas are produced from various locations on the backside of a plastic bottle screw cap made of iPP through injection molding. The STEM-HAADF images display two different lamellar morphologies: one exhibits randomly oriented and curved or spiral lamellae (top image). In contrast, the other part shows linear lamellae aligned in the same direction (bottom image). Additionally, the former lamellae are slightly thicker than the latter. This variation in the crystalline lamellae's morphology concerning the site may be due to the injection molding-induced orientation and the thermal histories during solidification in the mold. This technique allows for a clear view of the original specimen's surface features or topography without being concerned about electron beam irradiation-induced damage. Furthermore, combining the replica technique with STEM tomography allows for the development of three-dimensional surface structures, facilitating high-resolution fractography studies as outlined in Sects. 4 and 5 in "Interfacial Phenomena in Adhesion and Adhesive Bonding Investigated by Electron Microscopy" chapter [59].

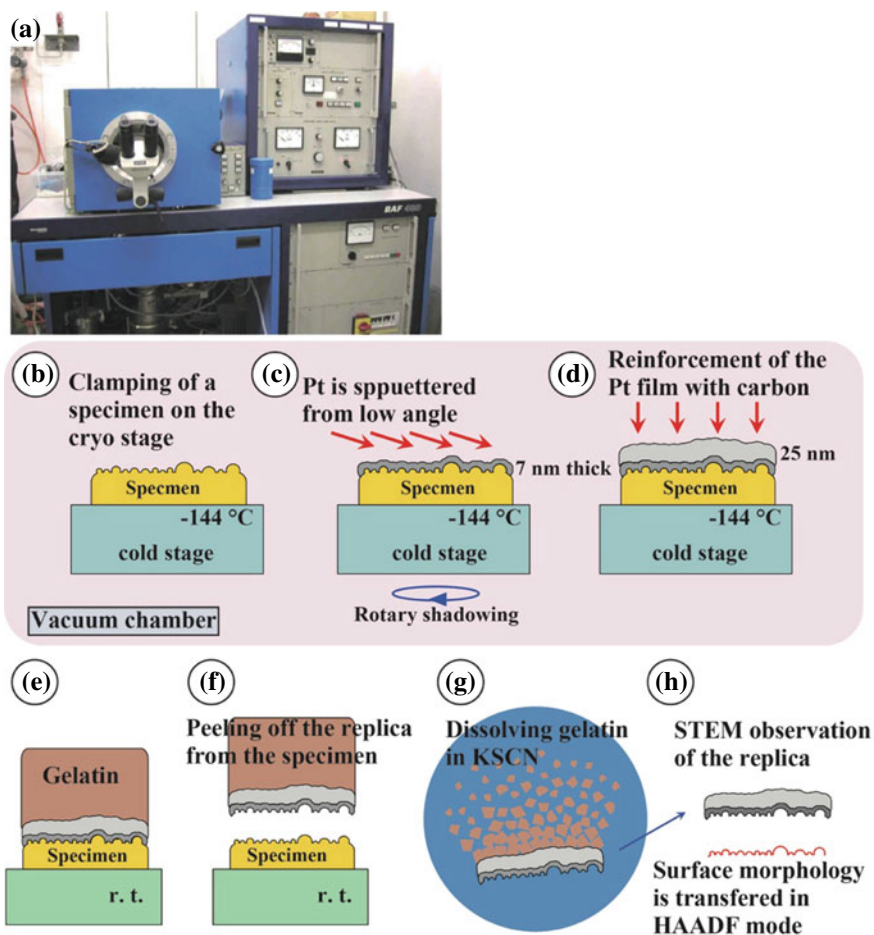


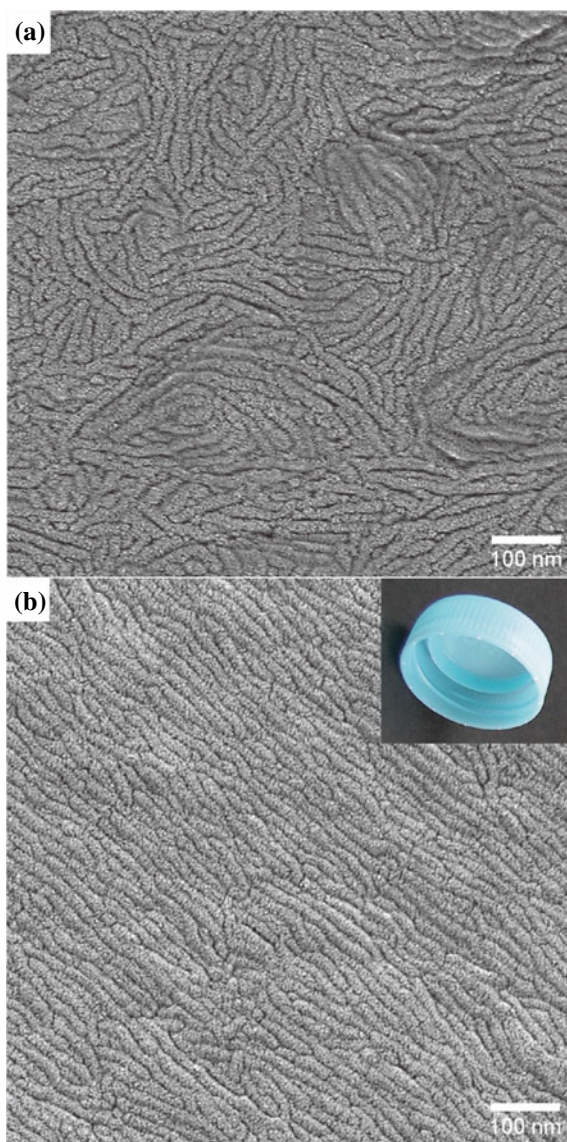
Fig. 20 Preparation procedure of replicated film of fracture or etched surfaces using a freeze-fracture apparatus: **a** appearance of a freeze replica apparatus (Balzers, BAF400D); **b** clamping of a specimen on the cryo-stage; **c** sputtering of Pt from low angle; **d** reinforcement of the Pt film with carbon; **e** drop of 30 wt% gelatin onto the replica; **f** peeling off the replica from the specimen; **g** dissolving gelatin in KSCN solution; **h** STEM-HAADF observation

4 EFTEM

4.1 Electron Spectroscopic Imaging (ESI) and Parallel EELS

Only electrons with large scattering angles contribute to contrast generation in CTEM, as they are selected for imaging solely through the objective aperture. The energy of the electrons and their energy differences are not considered, even though the chromatic aberration of the objective lens has a significant impact on contrast and

Fig. 21 STEM-HAADF images of Pt-carbon replica taken from the screw cap of a plastic bottle. **a, b** show location-dependence lamellar structures of the injection-molded article of *i*PP. Dr. Takayuki Uchida and Dr. Kazunori Kawasaki, AIST provide the data



resolution. As in CTEM, the image in EFTEM is produced by electron scattering in the specimen. However, EFTEM utilizes other interactions that need to be considered in CTEM. Figure 22 shows the electron beam path schematic diagram in an in-column-type EFTEM (LEO922 OMEGA, Carl Zeiss) [43]. In EFTEM, the transmitted electrons are not only selected according to their angle but also to their energy. An energy filter (Ω filter) disperses the inelastically scattered electrons according to their energy. Insertion of an energy-selecting slit in the energy-dispersive plane

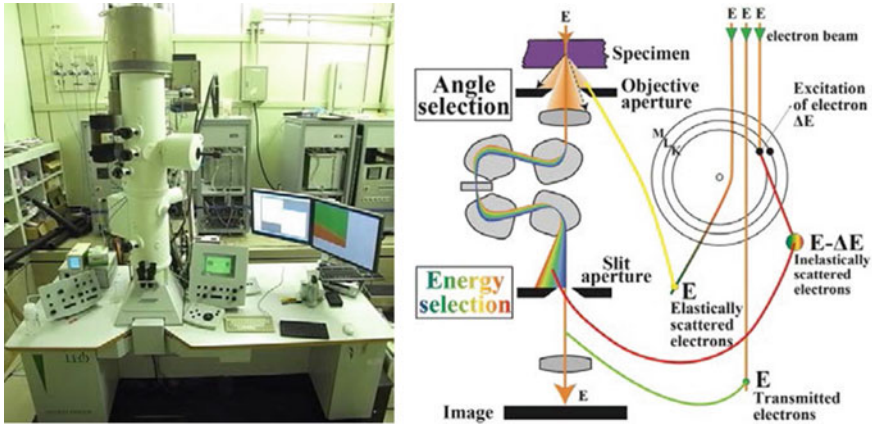


Fig. 22 Appearance of an in-column EFTEM, LEO922 OMEGA (Carl Zeiss) (*left*) and the schematic diagram of the selection of the electrons according to the scattering angles and the energy losses (*right*)

and subsequent projection of the corresponding image plane onto a screen allows energy-filtered imaging. Only electrons of a particular energy loss are transmitted, forming an energy-filtered image. This is most commonly known as electron spectroscopic imaging (ESI). Alternatively, when focusing the projector lens system on the energy-dispersive plane, an EEL spectrum can be seen on the screen, which permits EEL spectroscopy. This spectral acquisition method is named “parallel EELS” [60]. A spectrum can be obtained simultaneously in several ranges of 100 eV, which is imaged using a high-resolution CCD camera. An image analysis system measures the intensity and converts it into an energy-loss spectrum.

Dual electron selection by EFTEM results in considerably enhanced contrast. New information can be obtained with the structure-, thickness-, and element-specific contrast. In addition, ESI is capable of elemental mapping with rapid acquisition and high lateral resolution.

Figure 23 shows the three imaging modes available in EFTEM:

- **Global image**—The spectrometer disperses the electrons according to their energy (green with, red without energy loss), but the slit is not in the beam path. The second projective system combines all electrons into joint imaging. The results correspond to the quality of CTEM images, where the advantages of the filter are not utilized (left).
- **Zero-loss image**—The slit is in the beam path. High voltage is set to rated voltage, e.g., 200 kV. The slit allows only electrons without energy loss to pass. All electrons which have lost energy due to inelastic scattering are filtered out. This mode enhances the contrast for all imaging modes, such as bright field, dark field, and diffraction (center).
- **Energy loss image**—The slit is in the beam path. High voltage is increased by the required energy ΔE . The slit position and the spectrometer current remain

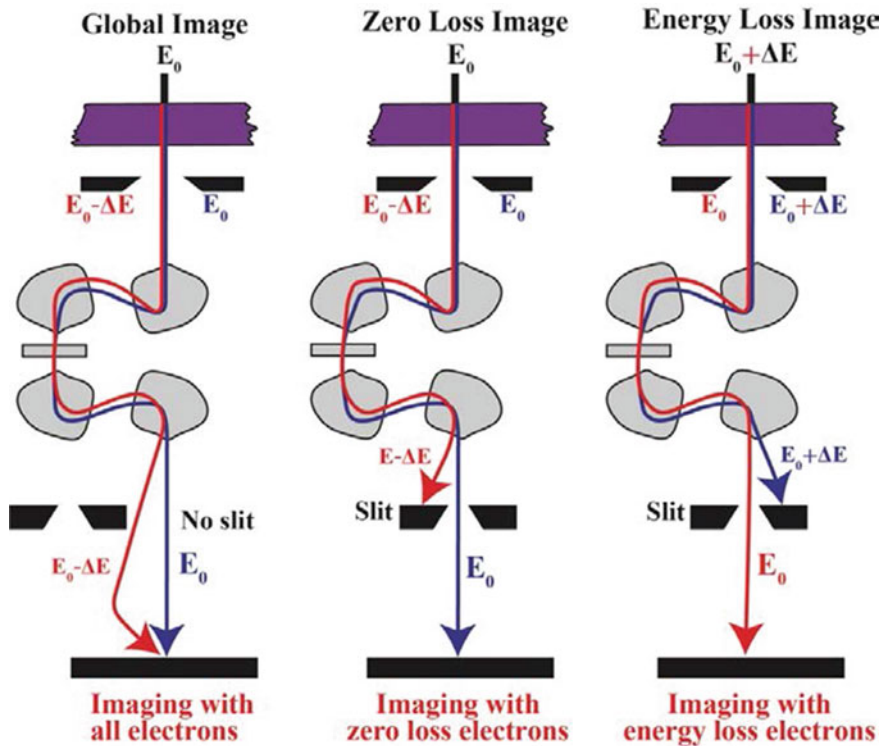


Fig. 23 Three imaging modes available in EFTEM

constant. The slit allows only electrons to pass that have lost the ΔE energy and are, therefore, back to the rated voltage. This mode is used for imaging with selective contrast on thin and thick specimens (right).

Different modes of ESI can be obtained by using energy-filtered images that are obtained by selecting electrons with a narrow energy width from different regions of an EELs spectrum. For the ESI of polymeric materials, energy windows ranging from 10 to 30 eV have commonly been used. The zero-loss imaging, as shown in Fig. 17, is a technique utilized to enhance the quality of bright-field images, although it does not provide element-specific information. The purpose of zero-loss imaging is to exclude all electrons that have been inelastically scattered, allowing only the elastically scattered and unscattered electrons that pass through the objective aperture to contribute to the image. Zero-loss imaging can improve resolution and increase contrast by minimizing chromatic aberration.

Energy loss imaging involves selecting electrons with a narrow energy width from the EEL spectrum. An energy window close to but not reaching the carbon K-edge (i.e., between approximately 150 and 280 eV) can be used to achieve structure-sensitive imaging. This window minimizes the scattering due to carbon atoms and

enhances the sensitivity and resolution of dark-field-like images, which are superior to elemental mapping. By selecting different energy-loss levels, the contrast in thicker specimens can be adjusted, and mass thickness effects such as cutting artifacts can be reduced or eliminated. The resulting contrast can be structure sensitive, phase sensitive, or element sensitive. Element-specific contrast allows for rapid visualization of element location by continuously varying the energy-loss values, causing areas containing a specific element to appear brighter in the image when the energy-loss value reaches the range where the element has its absorption edge.

4.2 Elemental Mapping and Image-EELS

In addition to element-sensitive imaging, elemental mapping representing the quantitative elemental distributions can be obtained. Elemental mapping is a very useful mode of EFTEM for identifying phases in heterogeneous materials. In conventional EDX mapping, the time required for recording an image of high-information content is very long because serial procedures are very time-consuming. With EFTEM, element distribution images are taken parallel, very fast, and with high local resolution. Elemental mapping is based on the fact that each core-loss edge of an EELS spectrum occurs at the energy characteristic of a specific element. A core-loss edge is superimposed on a strong decay as a background (BG) due to the plural scattering and extracting elemental information for mapping necessitates their separation from the BG contribution. Element-specific images (core-loss images) contain not only elemental information but also background information. They are, therefore, not taken directly but in several stages. First, an element-specific image is taken, then the background image below the ionization edges is calculated. Next, the background is subtracted from the element-specific image to obtain an element distribution image. As shown in Fig. 24a, several algorithms are available for background computation [61].

The two-window and three-window methods are employed for the calculation of the BG. In the two-window method, a single pre-edge image (at the energy loss of E_2) is scaled and then subtracted from the corresponding post-edge image (at the energy loss of E_{\max}) as expressed by Eq. (1) for an element of interest until there is zero net intensity in areas where that element is known to be absent.

$$S(E) = S(E_{\max}) - c \cdot S(E_2) \quad c < 1 \quad (1)$$

In the three-window method, the BG curve is estimated using the two-energy windows (E_1 and E_2) assuming power law (2) or exponential law (3) dependences as follows, where the factors A and r are calculated pixel by pixel from the signals $S(E_1)$ and $S(E_2)$.

$$S(E) = A \cdot E^{-r} \quad (2)$$

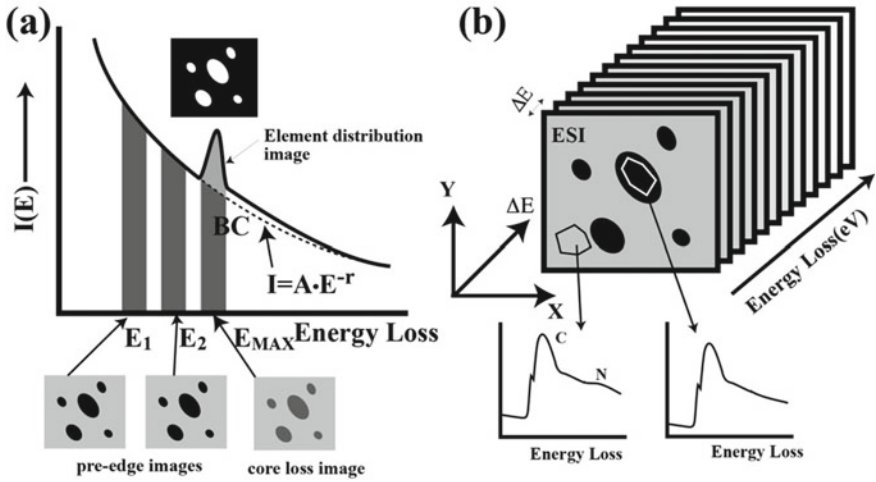


Fig. 24 Schematic illustration of the analytical modes available in EFTEM: **a** Elemental mapping; **b** Image-EELS

$$S(E) = A \cdot \exp(-r \cdot E) \tag{3}$$

A jump ratio image is generated by acquiring one pre-edge image and one post-edge image, which is then used to compute the ratio of the two. This produces a qualitative elemental distribution image related to the mass thickness of the element present. Jump ratio mapping is beneficial when there is a small amount of a substance in a relatively homogeneous matrix, and it reduces diffraction contrast created by metallic materials [62].

Image-EELS allows us to obtain EELS spectra from small and irregularly shaped objects chosen arbitrarily in an image [63–67]. As illustrated in Fig. 24b, tens of energy-loss images are captured sequentially over a broad range of energy loss to create a three-dimensional dataset containing spatial information ($I(x,y)$), obtained simultaneously, and spectral information ($I(E)$), obtained serially. EELS spectra from arbitrarily selected regions in an image can be synthesized by calculating the average gray values of the same pixels in each energy-loss image across the entire acquired image series. The image analysis system extracts the intensities at the same pixels in each image throughout the series. It constructs an EEL spectrum by plotting the intensities against the corresponding energy-loss values. To correct specimen drift, the individual images must be shifted pixel by pixel across the acquired image. A spectrum can be produced by summing neighboring pixels to improve the signal-to-noise ratio. This method is particularly suitable for analyzing minimal element concentrations on structures of any shape, and it can produce element distribution images from the image stack.

4.2.1 Elemental Mapping of Block Copolymer Nanodomain Structures

The successful application of the elemental mapping and the structure-sensitive imaging of a polymer sample is shown in Fig. 25. The specimen is an unstained thin cross section of an embedded film of a semi-rod-coil diblock copolymer of styrene (PS) and an isoprene with oligothiophene-modified side chains (POTI), namely, PS₄₀₀-*b*-POTI₂₅ (the subscripts indicate the number of repeating monomer units) as shown in Fig. 25a [68]. The experiments were carried out in an LEO 922 EFTEM with an integrated Ω -filter at an acceleration voltage of 200 kV. Figure 25b is an EELS spectrum taken by the parallel EELS, exhibiting the sulfur L_{2,3}-edge (S L_{2,3}-edge) at 160 eV energy losses after the BG subtraction. Although the as-taken spectrum seems to be a monotonical slope, the BG fitting using the energy range before the edge reveals the existence of the core-loss contribution. After subtracting the BG contribution, the core-loss peak of the S L_{2,3}-ionization edge can be seen, even though it is a noisy spectrum. The upper two images in Fig. 25c are the pre-edge and the post-edge (core-loss) images taken at the energy losses of 150 ± 10 and 200 ± 10 eV, respectively. The core-loss image clearly shows the well-ordered domains in the film, and thus it corresponds to the element-sensitive image of the sample. The elemental distribution images were then created by the BG subtraction in accordance with the two methods: the bottom left is created by the two-window method, while the bottom right is by the three-window method.

The map generated using the two-window method produces a clearer image with a higher signal-to-noise ratio (SNR) than the one generated using the three-window method. Inelastic scattering has a low cross section and is typically 10^2 to 10^6 times weaker than elastic scattering, resulting in inelastically scattered images with higher statistical fluctuations than elastically scattered images. Therefore, the three-window method is more susceptible to statistical errors associated with background extrapolation as two images are used for fitting. However, the map generated using the two-window method still displays some small objects in the film, indicated by arrows, which are removed from the map generated using the three-window method. This suggests the presence of some particles in the film. The contrast of these particles remains unchanged when the energy-loss position shifts from the pre-edge position to the post-edge position, suggesting that they may be inorganic contaminations. The inaccuracy in the map generated using the two-window method can be attributed to the polymer and the inorganic particles giving background curves with different slopes. The two-window method does not consider changes in background shape from one region of the specimen to another. Therefore, the two-window method cannot provide accurate elemental maps if the image involves components with different background features. On the other hand, the three-window method calculates the background curves pixel by pixel, enabling accurate subtraction of background intensities from the core-loss image for all pixels. This demonstration highlights the background subtraction process's influence on elemental mapping results. The three-window method should be used for performing quantitative elemental mapping.

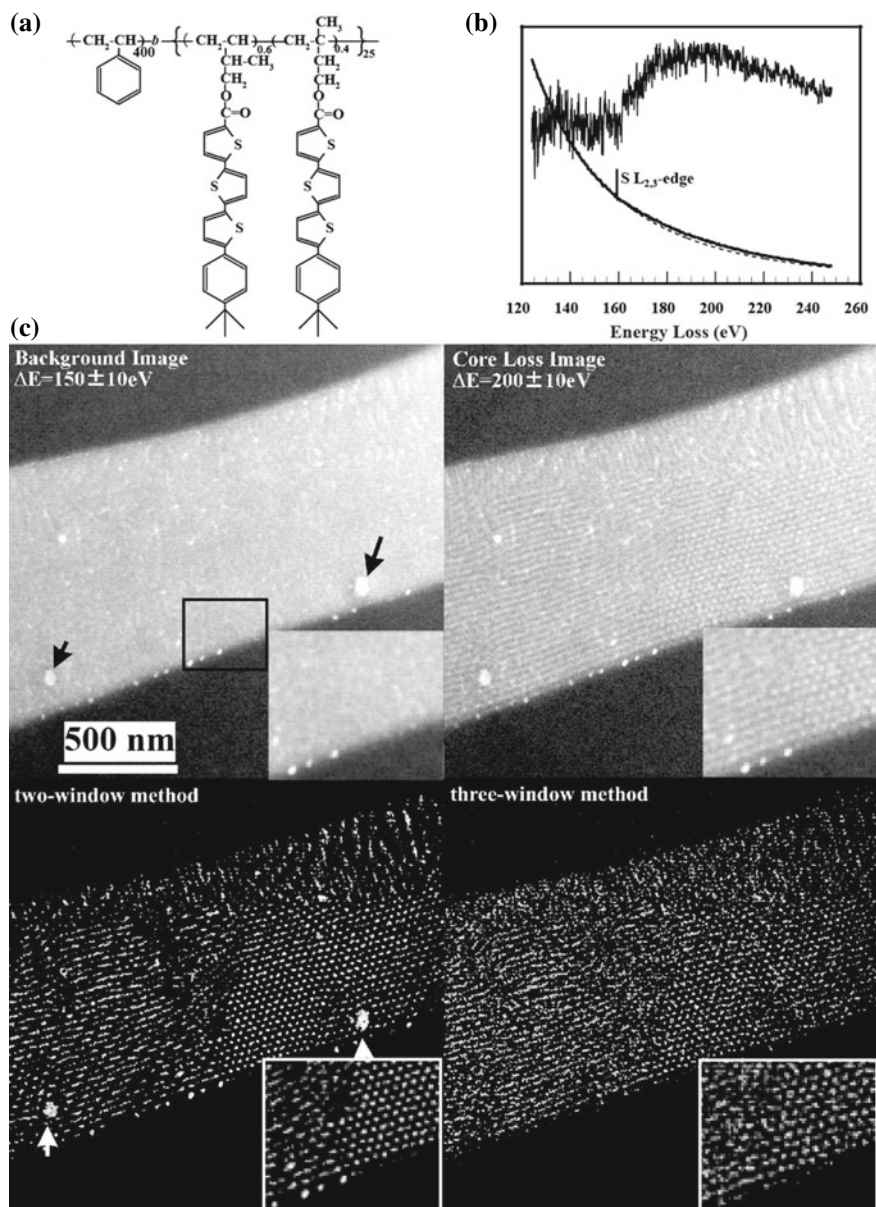


Fig. 25 Characterization of the phase-separated morphology of a diblock copolymer by elemental mapping: **a** chemical structure of a semi-rod-coil diblock copolymer of PS and an isoprene with oligothiophene-modified side chains (POT); **b** parallel EELS spectrum in the energy-loss region involving the sulfur $L_{2,3}$ -ionization and the core-loss edge appeared after the BG subtraction; **c** pre-edge and post-edge images of the cross section of the diblock copolymer film, and the sulfur distribution images calculated by the two-window and the three-window methods

4.2.2 Analysis of Rubber/Filler Interfaces by Image-EELS

Image-EELS was employed in the following study to investigate the interfaces between an inorganic filler and rubber in vulcanized rubber materials. Vulcanization, a crucial industrial process for cross-linking rubber molecules, involves accelerators and activators such as ZnO combined with stearic acid to accelerate the vulcanization reaction and enhance rubber properties. EFTEM was employed to examine the interactions between the rubber matrix and ZnO filler particles added as an activator in the accelerated vulcanization process [69]. The interactions between the rubber matrix and ZnO filler particles in the accelerated vulcanization process were investigated by EFTEM [70, 71].

Thin sections of the vulcanized styrene-butadiene-rubber (SBR) with 100 nm thickness were prepared by cryo-ultramicrotome at $-60\text{ }^{\circ}\text{C}$ after the vulcanization at $170\text{ }^{\circ}\text{C}$ for 10 min. Figure 26 presents the typical ZnO particles found in the vulcanized SBR. The upper row shows the zero-loss images, while the bottom row shows the corresponding structure-sensitive images at $250 \pm 10\text{ eV}$, revealing the presence of a phase surrounding the ZnO particles. The Image-EELS was used to characterize the product around the ZnO particles. The energy width and the energy increment for sulfur and oxygen were set at 5 and 3 eV, respectively. The energy width and increment of zinc were set at 10 and 5 eV, respectively. The Image-EELS enables the acquisition of EELS spectra from regions of interest in any shape in an image [70–72].

Figure 27a through d displays the energy-filtered image at $250 \pm 10\text{ eV}$ and the corresponding elemental distribution images of S, Zn, and O, respectively. The corresponding Image-EELS spectra obtained from the regions indicated in Fig. 27a are shown in the bottom row. The elemental mapping indicates that the phase formed around the ZnO particle contains S and Zn but not O. EELS spectra, including the core-loss edges of each element, are extracted from the region indicated in Fig. 27a, as shown below the corresponding images. The corresponding Image-EELS spectra allow semi-quantitative elemental analysis in the maps. The S $L_{2,3}$ -edges suggest that sulfur is distributed around the ZnO particles (regions 2 and 3) and the SBR matrix (region 4). The Zn $L_{2,3}$ -edges indicate that Zn is localized in the limited area around the ZnO particle and is not detected in the rubber matrix. Oxygen is distributed almost evenly in the SBR matrix, which may be attributed to stearic acid.

Therefore, the S- and Zn-rich phases around zinc oxide particles are not due to the fine dispersion of ZnO itself but are by-products formed due to the accelerated vulcanization reaction. In the complex accelerated vulcanization reaction mechanism, Zn^{2+} ions generated from zinc oxide by the addition of stearic acid are known to increase the efficiency of the cross-linking reaction of rubber through coordination with vulcanization accelerators. As a result, ZnS is produced as a by-product, and the EFTEM analysis clarifies its existence. The fact that ZnS is present surrounding the ZnO particles during accelerated vulcanization suggests that the reaction proceeds in the vicinity of the ZnO particles and that the crosslink density of the rubber is relatively higher around the ZnO particles. This result indirectly suggests the heterogeneity of the rubber network structures.

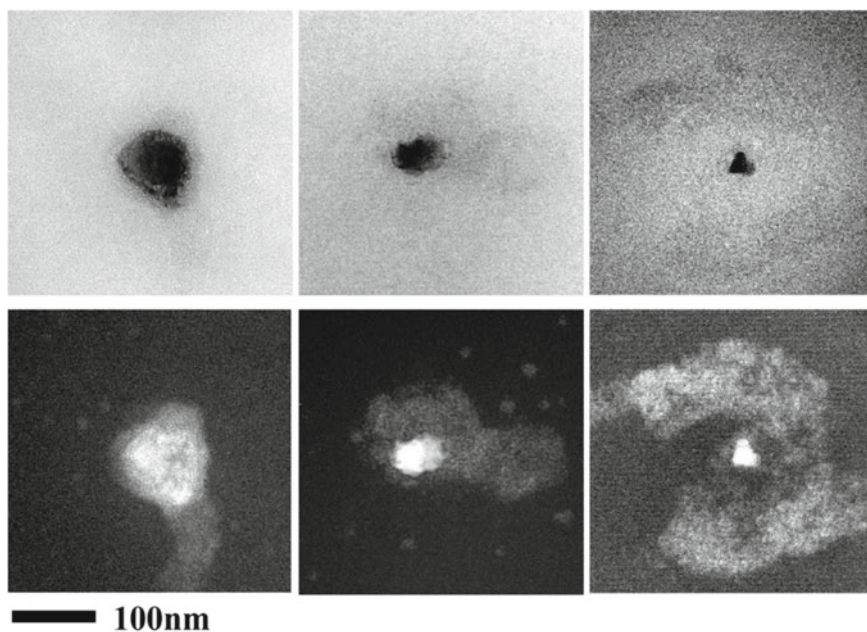


Fig. 26 Typical ZnO particles distribute in the SBR matrix after the vulcanization. The upper row shows the zero-loss images and the bottom row shows the corresponding structure-sensitive images at 250 ± 10 eV. Reprinted with permission from Ref. [70]. Copyright 2006, American Chemical Society. All Rights Reserved

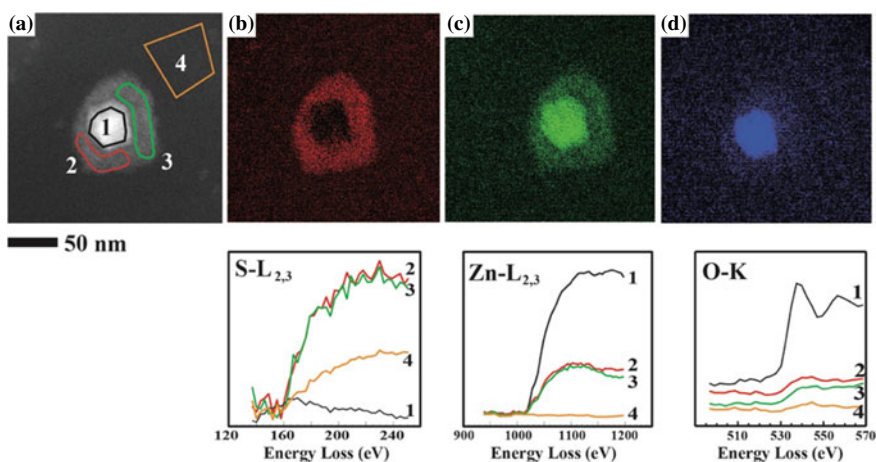


Fig. 27 Elemental maps and Image-EELS spectra obtained from the interface between a ZnO particle and SBR matrix: **a** Structure-sensitive image at 250 ± 10 eV; **b–d** Elemental distribution images of S, Zn, and O. The regions indicated in **a** are subjected to the Image-EELS analysis and the core-loss edges after the BG subtraction are shown below the corresponding images. Reprinted with permission from Ref. [70]. Copyright 2006, American Chemical Society. All Rights Reserved

4.2.3 Image-EELS Analysis of Reaction-Induced Phase Decomposition in Thermoset/Thermoplastic Polymer Blends

One of the processes involved in developing morphology in multi-component polymer systems is known as reaction-induced phase decomposition. During the polymerization of a monomer, a blend of a polymer and a monomer undergoes phase separation with an increase in molecular weight [73–83]. Utilizing a thermoset resin as a “reactive solvent” can be more environmentally friendly and efficient than common organic solvents since solvent removal is not required [84, 85]. As the curing reaction progresses, phase decomposition occurs in thermoset and thermoplastic (or rubber) blends, leading to unique multi-phase structures that can be used in high-performance composites and adhesives.

In this study, the samples analyzed are blends of poly(2,6-dimethyl-1,4-phenylene ether) (PPE) and 1,2-bis(vinyl phenyl)ethane (BVPE). PPE is a material that is attractive in the electronics industry due to its low dielectric constant (2.45), low dissipation factor (0.0007), and high glass transition temperature (T_g) of 210 °C. BVPE, on the other hand, is a styrene-type crosslinker with good thermal durability and dielectric properties and can be cured at relatively low temperatures without a curing agent [86]. The morphology development of PPE/BVPE blends through BVPE crosslinking was analyzed using Image-EELS [87]. The chemical structures of BVPE and PPE are similar, but only PPE contains oxygen, as shown in Fig. 28. The influences of composition and curing time on phase decomposition behavior were investigated by examining the intensity ratios of the O K-edges extracted from the two phases. Blending these two components is expected to yield materials with excellent dielectric properties, overcoming the drawbacks of the individual components. That is, the brittle nature of the cured product of BVPE could be improved by blending it with PPE, while the poor processability of PPE due to its high viscosity could be solved. In addition, the effect of the reaction between the two components on phase decomposition behavior was investigated by introducing a reactive allyl unit onto PPE. The blends had compositions of 25/75, 50/50, and 75/25 (PPE/BVPE) by weight, denoted as N25, N50, and N75 for the blends with non-reactive PPE and as R25, R50, and R75 for the blends with reactive allyl-PPE.

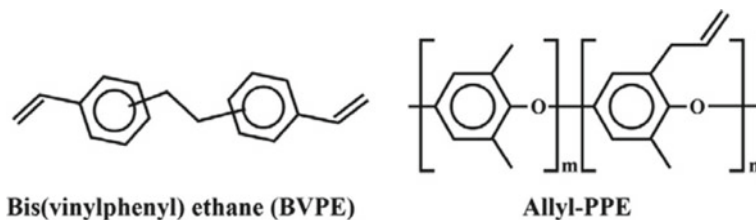


Fig. 28 Chemical structures of bis(vinyl phenyl) ethane (BVPE) and poly(2-allyl-6-methylphenol-co-2,6-dimethylphenol), (allyl-PPE). Reprinted with permission from Ref. [87]. Copyright 2007, Elsevier. All Rights Reserved

To prepare the samples for observation, ultramicrotomy was used to create thin sections with a thickness of approximately 60 nm at room temperature. Gold nanoparticles with 10 nm in diameter were then dropped onto the specimens to serve as markers for focus adjustment and drift correction during observation. High-resolution elemental mapping and quantitative EELS analysis were performed using Image-EELS. The energy-loss range was set to 450–600 eV, with a 5 eV energy width for each image and a 3 eV energy increment between neighboring images. Oxygen elemental maps were created by the “two-window jump ratio” method, which involved selecting two recorded images from those acquired by Image-EELS and dividing the energy-filtered image beyond the oxygen ionization edge at approximately 535 eV (post-edge image) by the energy-filtered image below the ionization edge (pre-edge image).

Figure 29a–d depicts the zero-loss image, the pre-edge image at 525 ± 2.5 eV, the post-edge image at 550 ± 2.5 eV, and the calculated oxygen elemental map, respectively, of N50 (a blend of PPE/BVPE with a weight ratio of 50/50) that was cured for 60 min. The oxygen elemental map reveals the phase-separated morphology due to the difference in the oxygen concentrations between the two phases, characterized as oxygen-rich (PPE-rich) and oxygen-poor (BVPE-rich) phases. Although the pre- and post-edge images exhibit no differences in the image contrast (Fig. 29b, c), the calculated oxygen elemental map presents the phase-separated morphology, which can identify the slight differences in the compositions between the two phases.

In Fig. 30, the phase decomposition of blends during curing is studied. The changes in oxygen distribution images are analyzed as the curing time increased for N25 (which is a BVPE-rich blend shown in Fig. 30a), N50 (shown in Fig. 30b), and R25 (shown in Fig. 30c), where R25 contained 10 mol% of the reactive unit in allyl-PPE. The samples were annealed at 230 °C for specific periods and then dipped into liquid nitrogen to freeze the developed phase-separated morphologies. All observations were conducted at room temperature. The oxygen maps for N25 show that oxygen-poor domains (BVPE-rich phase) are formed in the PPE-rich matrix during the early stages of curing and are coarsened as the curing time increases. However, the domain sizes of N50 remain unchanged during the curing process and are smaller than those in the BVPE-rich blend (N25). The growth of BVPE-rich domains during the curing of

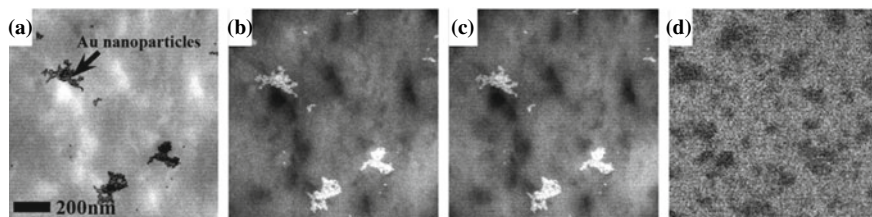


Fig. 29 A series of images of N50 showing zero-loss image (a), O K pre-edge image (b), O K core-loss image (c), and oxygen map (d) calculated by “two-window jump ratio” method in the same specimen region. Reprinted with permission from Ref. [87]. Copyright 2007, Elsevier. All Rights Reserved

R25 appears to be restrained compared to N25, suggesting that the reaction between the two components suppresses the phase decomposition.

To quantitatively estimate the differences in oxygen concentrations between the two phases, a method illustrated in Fig. 31 was employed. Firstly, the borders between the two phases in the oxygen map were identified precisely, as shown in Fig. 31a. Subsequently, the O K-edges were extracted from the two regions, as shown in Fig. 31b. Next, the background contributions were removed from the spectra using the power law function, and the oxygen core-loss peaks were obtained, as demonstrated in Fig. 31c. Finally, the integrated ratios of the two core-loss peaks, with an energy width of 60 eV, were calculated to determine the relative oxygen atomic ratios of the two phases.

The phase decomposition of the blends is characterized using two parameters: oxygen elemental ratios and the area fractions of the two phases. Figure 31d displays the plot of the oxygen atomic ratio as a function of curing time. The N25 blend exhibits

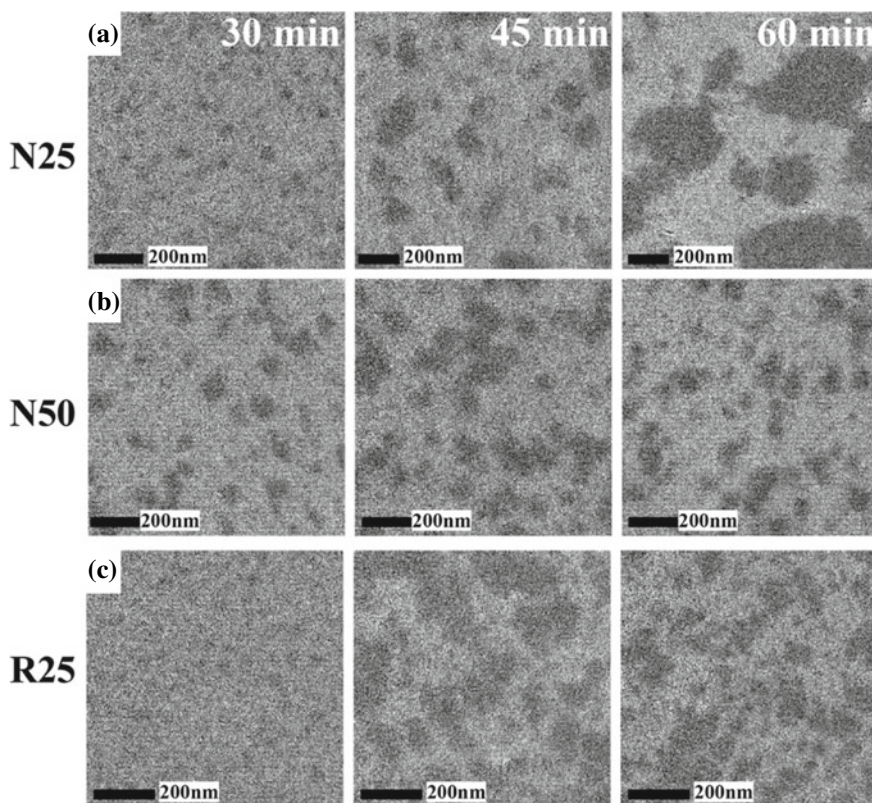


Fig. 30 Phase decomposition development of BVPE/Allyl-PPE blends: **a** oxygen distribution images of N25; **b** N50; **c** R25. Curing times are 30, 45, and 60 min for left, middle, and right columns, respectively. Reprinted with permission from Ref. [87]. Copyright 2007, Elsevier. All Rights Reserved

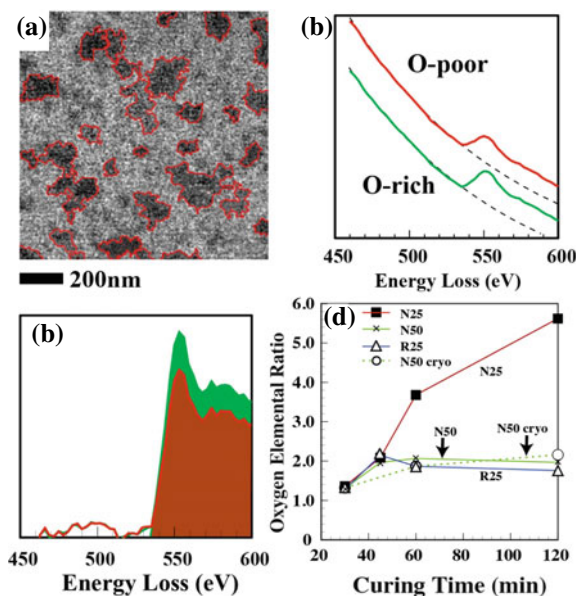


Fig. 31 Scheme for quantitative EELS analysis of the phase decomposition of PPE/BVPE blends: **a** an oxygen map classified accurately into the oxygen-rich and oxygen-poor regions; **b** EELS spectra extracted from the two regions (green and red spectra are acquired from the oxygen-rich and the oxygen-poor phases, respectively); **c** the integrated areas under the oxygen core-loss peaks calculated after the background subtraction; **d** oxygen elemental ratios between the two phases (ratio of PPE-rich phase to BVPE-rich phase) plotted against the curing time. Reprinted with permission from Ref. [87]. Copyright 2007, Elsevier. All Rights Reserved

a considerable increase in the oxygen atomic ratios between the two phases with increased curing time, while the other blends showed only a slight increase. The ratios of the compositions of the two phases are maintained at similar levels, approximately 2, except for N25, which suggests that the phase separation mechanism of N25 differs from those of the other blends.

The impact of radiation damage on the specimens during the Image-EELS data acquisition must be considered to ensure the results' reliability. It is inevitable to avoid damage to polymer specimens by the electron beam, which causes chain scission and mass loss. Therefore, observation under cryogenic conditions is recommended to minimize radiation damage. The results obtained under a cryogenic condition at $-160\text{ }^{\circ}\text{C}$ for N50 are also plotted in Fig. 31d, demonstrating that no significant differences were observed between the two observation conditions. Hence, even though the electron beam irradiation during TEM observation may change the chemical structures of the polymers, the elemental compositions may not be altered significantly. This allows us to perform quantitative EELS analysis of the phase decomposition processes at room temperature.

5 STEM

5.1 *Spectrum Imaging (SI) with Simultaneous EELS and EDX*

In STEM, the electron beam is focused into a spot with a spot size of less than 1 nm, and by rastering the beam across the sample, STEM can be used for techniques such as Z-contrast annular dark-field imaging, EDX and EELS [88]. The ray path in STEM is identical to that in TEM if the direction of the beam path in STEM is reversed. Despite this reciprocity principle, there are crucial differences between the image formation in both microscopes. In contrast to TEM, STEM does not need post-specimen lenses to magnify the image, as the transmitted electrons only need to be collected by a detector. Therefore, the image quality in STEM is unaffected by the chromatic aberration as it is in TEM. EELS and EDX, coupled with STEM, are powerful techniques that allow us to perform local elemental and chemical analysis in materials [48, 89–91]. Simultaneous acquisition of imaging and spectroscopy signals enables direct correlation between images and spectroscopic data. In EELS, an electron spectrometer attached at the bottom part of the column, as shown in Fig. 2b, measures the energy loss of the electrons in the beam through the interaction with the electrons in a specimen. STEM-EDX has been frequently employed for a quick overview of present elements. At the same time, EELS can be used for chemical analysis of elements of interest because the energy resolution in EELS is sufficient to allow the fine structure of ionization edges to be discussed. Especially, ELNES in EELS can offer chemical bonding information [89, 92]. It is expected to be a powerful approach to detecting chemical interaction at interfaces. EFTEM enables EELS to be performed in TEM mode, which involves irradiating a wide specimen area with the electron beam. In TEM mode, the energy density of the electron probe is significantly lower than in STEM mode, resulting in reduced radiation damage to the specimen. However, the spatial resolution of EELS analysis is restricted.

EDX and EELS can be worked together with the electron probe scanned pixel by pixel in the STEM mode. Spectral Imaging (SI) mode allows EDX/EELS simultaneous spectral acquisition with the annular dark-field imaging, significantly improving data-collection efficiency. Figure 32 shows an STEM instrument and the schematic illustration of the SI mode. Spectra are acquired in a spatially serial manner: EDX and EEL spectra are recorded for each position at the same time with a small probe scanned over two-dimensional (2D) regions in a specimen. Then, we can obtain a three-dimensional (3D) data cube consisting of 2D spatial position coordinates (x and y) and energy loss (ΔE) of the probe [49]. The Dual EELS system acquires the spectra, which allows recording both the low-loss and core-loss spectra nearly simultaneously at the same position before moving on to the next [93–95]. The low-loss region is captured in microseconds with a short dwell time to address the significant signal intensity disparity in the two energy-loss regions. In contrast, the core-loss regions are recorded in several seconds without modifying the beam conditions. Correcting the zero-loss peak's (ZLP) drift enables accurate energy-loss position

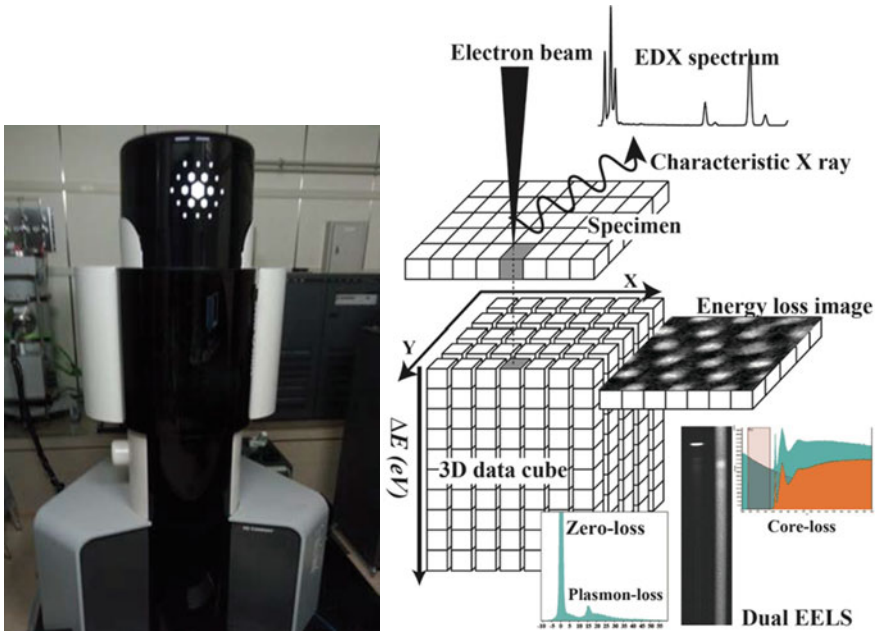


Fig. 32 An STEM instrument (TECNAI Osiris, FEI) used in this work and a schematic illustration of spectrum imaging (SI) data acquisition and processing scheme with dual EELS system

correction of the core-loss spectra. Fourier logarithmic deconvolution, employing the low-loss spectra shapes, can eliminate the influence of plural scattering in the core-loss region.

The 3D data cube can also be constructed by the TEM mode using the Image-EELS technique in EFTEM, but its scheme is different. In STEM-SI mode, the data cube is generated column by column, and the electron probe is scanned in a rectangular pixel array over the specimen. At the same time, the spectrum is collected in parallel. In EFTEM-Image-EELS mode, on the other hand, energy-loss images are collected successively in parallel across a wide range of energy loss with defined energy intervals. Those images are stacked in the data cube as depicted in Fig. 24b. Each approach has advantages and disadvantages: SI in STEM gives the highest spatial resolution and sensitivity. However, the image size is limited by the need to read the spectrum at each pixel. Image-EELS in the EFTEM provides a larger number of image pixels. Still, the spectral information is limited because the energy resolution of EEL spectra depends on the energy step in acquiring a series of energy-loss images.

5.1.1 STEM-EELS/EDX Simultaneous Analysis of Surface Oxide Layer of Aluminum Alloy

STEM measurements were conducted on a TECNAI Osiris microscope (FEI Company) equipped with an EELS spectrometer (Enfimum SE model 976, Gatan Inc.) and four windowless silicon-drift EDX detectors (FEI Super X). The measurements were performed at an accelerating voltage of 200 kV. To enhance the EDX detection efficiency and quickly detect low-Z elements in polymer materials, the four quadrant EDX detectors were symmetrically mounted above the specimen area along the optical axis [93, 95].

Figure 33 exemplifies how the STEM-SI mode provides elemental and chemical information with high spatial resolution. An oblique section of the surface of an Al6061 plate was obtained by ultramicrotomy and subjected to STEM analysis in SI mode. Three spectral information can be obtained: EELS low-loss, EELS core-loss, and EDX spectra. (a) The EELS low-loss spectrum contains a zero-loss peak at 0 eV energy loss and a plasmon-loss peak in 10–30 eV. Metallic Al gives a characteristic sharp peak at 16 eV [96]. The distribution of metallic Al can be created using the energy window at 16 ± 1 eV after the BG subtraction, as indicated by the red curve. (b) The EELS high-loss spectrum includes the O K-edge at 535 eV. An oxygen elemental map can be created using the 537–543 eV energy window and the BG subtraction as indicated by the red curve. The effects of plural scattering in the core-loss region are removed by Fourier logarithmic deconvolution using the shapes of the low-loss spectra and shown as a deconvoluted spectrum. A narrower energy window and choosing the energy-loss position permit a chemical map that can distinguish oxygen-containing Al compounds, as stated in Sect. 6 of “Interfacial Phenomena in Adhesion and Adhesive Bonding Investigated by Electron Microscopy” chapter. (c) According to the EDX spectrometry data, the aluminum surface region contains a small quantity of Mg, Si, P, and Cr, part of the aluminum alloy. The data also showed a minor amount of carbon, believed to be from atmospheric contamination during sample transportation in ambient air. Elemental maps created using EDX spectrometry reveal the Si, P, and Cr localization in the Al surface region, whereas Mg is localized in the metallic portion.

5.1.2 Mechanism of the Reactive Compatibilization of a Polymer Blend Investigated by STEM-EELS/EDX Analysis

Multi-component polymer systems can benefit from adding a small amount of a compatibilizer, which can interact with the polymer components physically or chemically to improve the strength of interfaces and the dispersion of phases [97, 98]. However, the challenge lies in locating the compatibilizer in the blends owing to its low concentration, typically less than a few weight percent. To address this issue, STEM-EDX/EELS analysis is demonstrated to evaluate the localization of the compatibilizer at the interfaces in immiscible polymer blends. As depicted in the top column in Fig. 34, this study uses a polyhedral oligomeric silsesquioxane

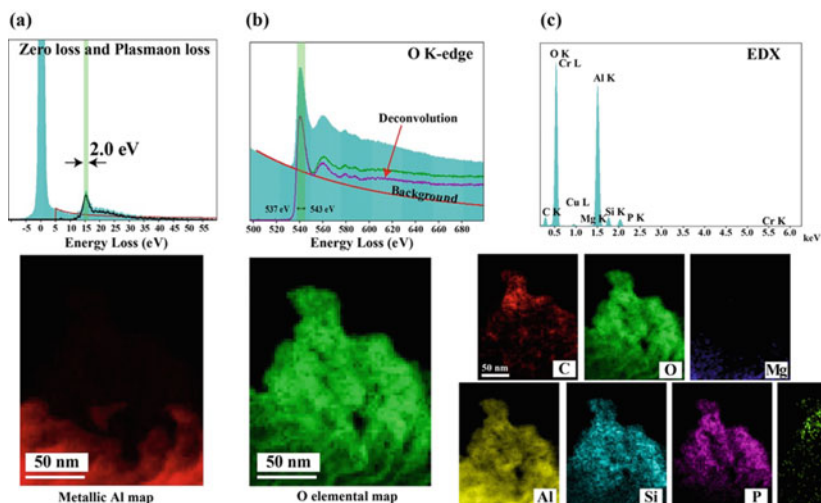


Fig. 33 STEM-EDX/EELS simultaneous analysis of the surface region of an Al6062 plate: **a** EELS low-loss region and metallic Al map; **b** EELS O K-edge and Al oxide map; **c** EDX spectrum and elemental maps. Reprinted with permission from Ref. [48]. Copyright 2022, Elsevier. All Rights Reserved

(POSS)-based compound as a compatibilizer in a PLLA/PVDF blend. The POSS molecule consists of eight silicon atoms, five connected to the epoxy groups. In contrast, the remaining three are connected to the PMMA chains, where the epoxide groups in the POSS derivatives react with the carboxyl end groups of PLLA. At the same time, the grafted PMMA unit is expected to be localized in the PVDF phase due to the thermodynamical miscibility of PMMA and PVDF as depicted in the middle column in Fig. 34 [99]. Therefore, the compatibilizer used in this study is labeled POSS(epoxy)₅-g-PMMA₃. The well-compatibilized PLLA/PVDF blends show a remarkable enhancement in elongation at break without decreasing the tensile modulus and strength [100]. Two-step mixing is used to obtain optimized properties (bottom in Fig. 34), where the POSS-compatibilizer is mixed with PLLA in the first step. Then the pre-mixed PLLA/compatibilizer is blended with PVDF, indicating that the location of the compatibilizer is significantly affected by the mixing sequence. STEM-EELS/EDX analysis is suitable for the PLLA/PVDF/POSS-compatibilizer multi-component polymer system because each component contains key elements for identifying their locations. That is, fluorine is for PVDF, oxygen is for PLLA, and silicon is for POSS. Also, oxygen is involved in the different chemical bonds in the polymers and the compatibilizer. In this study, the localization behaviors of the POSS-compatibilizers at the PLLA/PVDF interfaces, which are believed to be influenced by melt-blend conditions, are characterized by STEM-EELS/EDX analysis.

Figure 35 shows the STEM-BF images of the phase-separated morphologies of the PLLA/PVDF (50/50) blends. The blend films were firstly embedded in a light curable resin, LCR-D800 (Toagosei Corp.), and were cut by ultramicrotomy

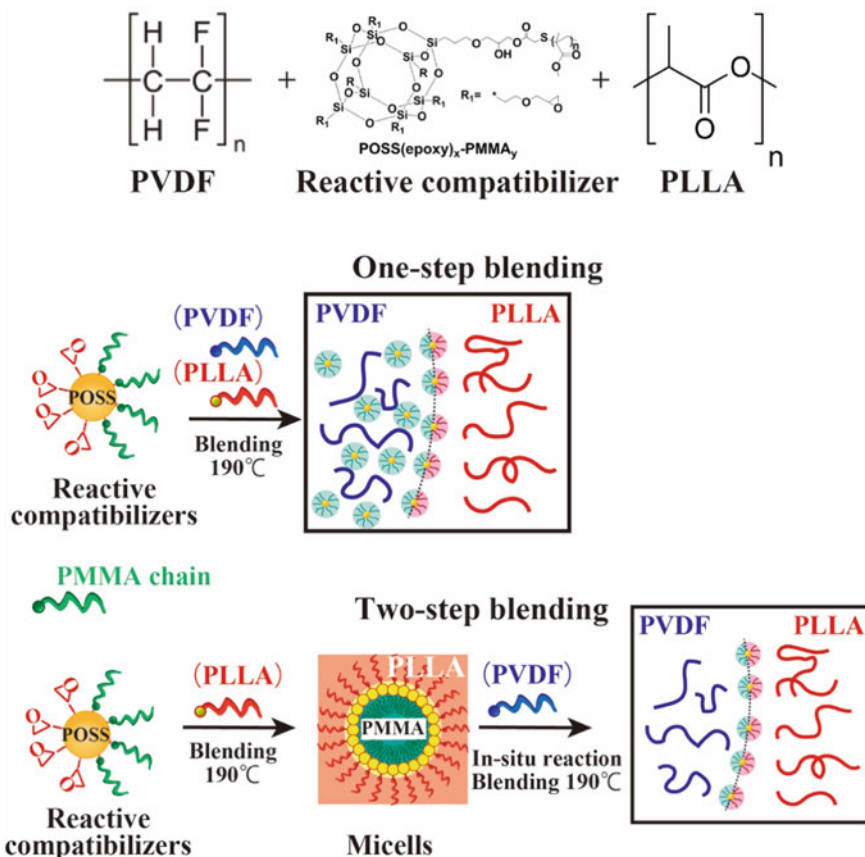


Fig. 34 Chemical structures of PVDF, POSS-compatibilizer, and PLLA (*top column*). One-step (*middle column*) and two-step (*bottom column*) blend sequences for PVDF/PLLA blends compatibilized with the POSS-compatibilizer

to obtain sections with a thickness of about 50 nm. The sections were collected on copper meshes covered with lacy carbon. The uncompatibilized PLLA/PVDF binary blend (Fig. 35a) shows the poor dispersion of the PVDF domains. In contrast, the blends with POSS(epoxy)₅-g-PMMA₃ prepared by one step (Fig. 35b) and two step (Fig. 35c) show remarkable improvements in the dispersion of the PVDF domains. The dispersity of the PVDF domains was quantitatively evaluated by the digital image analysis, which revealed that the average diameters and the standard deviations of the dispersed domains in one-step and two-step blends were 3.0 ± 0.13 and 2.2 ± 0.05 μm , respectively. The average diameters of those two blends are not significantly different, but the two-step blend shows uniform and fine dispersion of the domains, as was represented by the standard deviation.

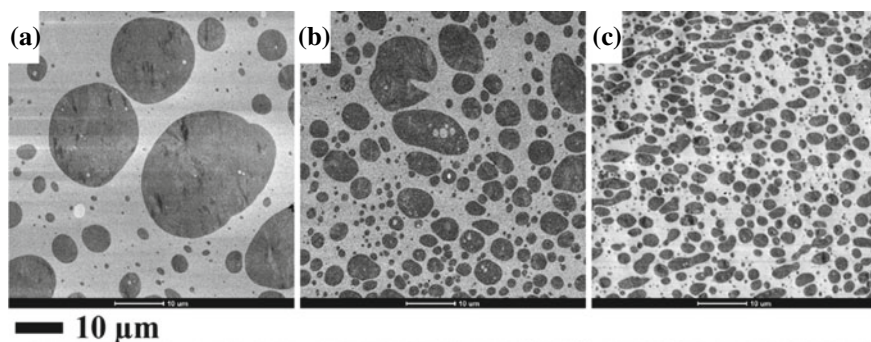


Fig. 35 STEM-BF images of PLLA/PVDF binary blend (a), one-step PLLA/PVDF blend with POSS-compatibilizer (b), and two-step PLLA/PVDF blend with POSS-compatibilizer (c). Reprinted with permission from Ref. [89]. Copyright 2019, American Chemical Society. All Rights Reserved

The PLLA/PVDF phase separation can be easily observed in all blends without heavy metal staining. The dark domains are found to be dispersed throughout the bright matrix. To confirm the assignment of the domains to the PVDF phase, EDX measurements were conducted, which revealed the presence of the fluorine (F)-K α peak at 0.68 keV. Additionally, the EDX measurement results indicate that the signal counts obtained from the PLLA phase are significantly lower than those obtained from the PVDF phase. This suggests that the PLLA underwent faster degradation by the electron beam, causing the chemical bonds of PLLA to be cleaved through either backbone main-chain scission or hydrogen abstraction, producing low-molar compounds that evaporated away from the specimen. This loss of mass of the PLLA phase results in high contrast between PLLA and PVDF in the STEM-BF images.

STEM-EDX analysis was employed to investigate the distribution of the POSS-compatibilizer in the blends. The STEM-HAADF images in Fig. 36 depict the bright phase as the PVDF phase, and the elemental maps of F, Si, and O in the PLLA/PVDF interfacial regions in the blends containing POSS are presented. In the one-step blend, the distribution of the POSS-compatibilizer is concentrated at the PLLA/PVDF boundaries, as shown in Fig. 36a–d. However, the small aggregates appear unevenly distributed along the interfacial region. Meanwhile, the two-step blend exhibits a more uniform distribution with the enriched compatibilizer along the PLLA/PVDF boundary (Fig. 36g). The POSS-compatibilizer is also found in the PVDF domains in the one-step blend (Fig. 36c), while it appears to be evenly distributed in both phases in the two-step blend (Fig. 36g). The thickness of the localized compatibilizer in the one-step blend is estimated to be about 30 nm, while it is about 100 nm in the two-step blend. It should be noted that the elemental maps are projections of the cross sections of spherical domains. Thus, the estimated interfacial thicknesses are larger than the actual values. Nevertheless, the results demonstrate differences in the interfacial structures regarding the POSS aggregation formed at the PDVF/PLLA boundary in one-step and two-step blends. The oxygen maps shown here primarily

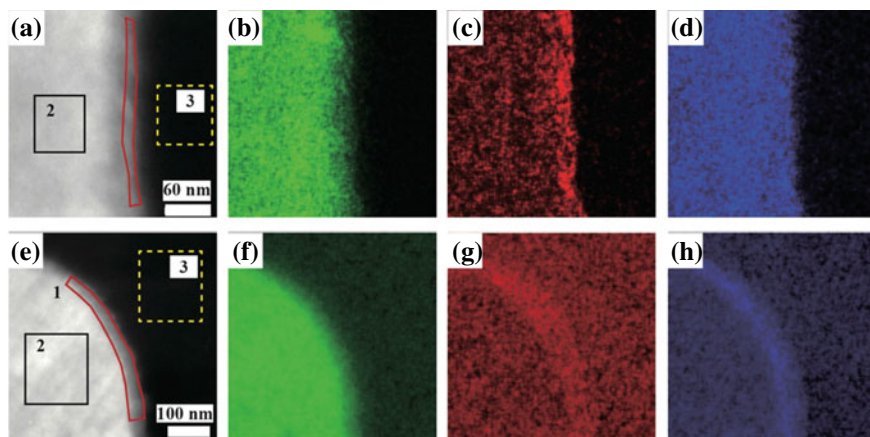


Fig. 36 STEM-HAADF images and STEM-EDX elemental maps of PLLA/PVDF/POSS(epoxy)₅-g-PMMA₃ blends: **a–d** one-step blend; **e–h** two-step blend. **a, e** STEM-HAADF images; **b–d** and **f–g** elemental distributions of F, Si, and O presenting green, red, and blue, respectively. Regions assigned by serial numbers in **a** and **e** are for acquiring EDX spectra in Fig. 37. Reprinted with permission from Ref. [89]. Copyright 2019, American Chemical Society. All Rights Reserved

represent the distribution of the POSS-compatible compatibilizers, not that of PLLA. Due to the degradation of PLLA, the contribution from PLLA to the O elemental maps is small compared to that from POSS.

Figure 37 illustrates the overall EDX spectra and the quantified Si-K α peaks extracted from selected regions highlighted in Fig. 36. The compatibilizer distributions are compared between the one-step and two-step blends. The Si-K α peak intensities shown in Fig. 37a, b indicate that the two blends have different compatibilizer distributions. In the one-step blend, the Si-K α peak intensities detected from three regions (interfacial, PVDF, and PLLA phases) differ, with the interfacial region exhibiting the highest intensity and the PLLA phase the lowest. On the contrary, in the two-step blend, the Si-K α peak intensity obtained from the interfacial region is the highest. In contrast, the other two regions show almost equal lower intensities. The EDX mapping and spectrometry confirm that the PMMA-grafted POSS-compatible compatibilizer can be effectively localized at the interfacial regions in both blends, but the blend sequence significantly influences the distribution of the compatibilizer.

The localization of POSS-compatible compatibilizers at the PLLA/PVDF boundary region can be effectively visualized and quantitatively analyzed using Si elemental mapping and EDX spectral analysis. However, detecting oxygen with high signal intensity is challenging in the EDX analysis due to the radiation damage of PLLA. STEM-EELS was conducted in SI mode to carry out a detailed chemical analysis of the phase-separated structures. To obtain the oxygen ionization K-edge of PLLA with a high signal-to-noise ratio, spectra were obtained from a 500 \times 500 nm area with a 50 nm interval and an acquisition time of 3 s. Therefore, the obtained spectra represent the average of 100 spectra. The beam condition was optimized with a beam size of

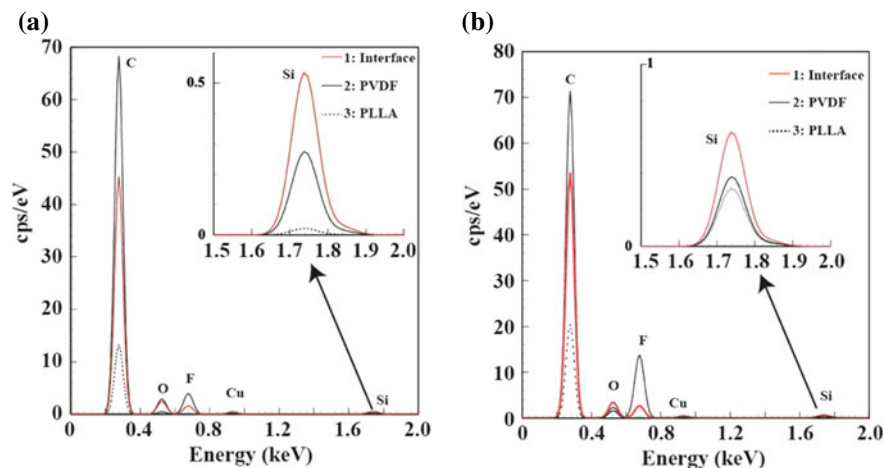


Fig. 37 STEM-EDX spectra extracted from the regions indicated in the STEM-HAADF images of Fig. 36. **a** One-step and **b** two-step blends of PLLA/PVDF blends with the reactive POSS-compatible compatibilizer. The insets display the Si-K α peaks that appeared in the quantified EDX spectra. Reprinted with permission from Ref. [89]. Copyright 2019, American Chemical Society. All Rights Reserved

0.74 nm and 0.293 nA beam current to get the highest jumping ratio of O K-edges. However, reducing the probe size to 0.66 nm resulted in a noisy spectrum with no core-loss signals. The EELS spectra acquisition was conducted at an accelerating voltage of 200 kV and at 110 K using a cryo-specimen holder to minimize the radiation damage to the specimens.

Figure 38 displays the O K-edge spectra obtained from the PLLA phase in the one-step and two-step blends. The O K-edge of the one-step blend shows two peaks at 533 and 543 eV, while the two-step blend reveals an additional peak at 537 eV. The O K-edge obtained from a POSS powder sample is also compared, demonstrating a shift of the edge to a higher energy-loss position and a sharp peak at 540 eV followed by a broad peak at 560 eV. The POSS powder sample's edge shape differs from those obtained in the two blend samples. Although the ester bonds of PLLA contribute to the O K-edges, they exhibit different ELNES features from each other. To investigate the cause of these differences, the impact of beam irradiation on the ELNES of the O K-edges of various oxygen-containing polymers was studied.

Different electron probe conditions were used to acquire the O K-edges of PLLA, PMMA, PET, and PPO, as presented in Fig. 39. The peak at 537 eV is highly sensitive to the beam condition. As the beam size and current increase, the peak gradually weakens and is ultimately eliminated in PLLA, PMMA, and PET. Notably, the intensity of the second peak in PLLA decreased much faster than in the other polymers, indicating poor stability of PLLA against the electron beam. Even after irradiation with a large probe, the peak in PET remains. All the investigated polymers, except for PPO, contain an ester bond, while PPO contains only an ether bond. Figure 39c

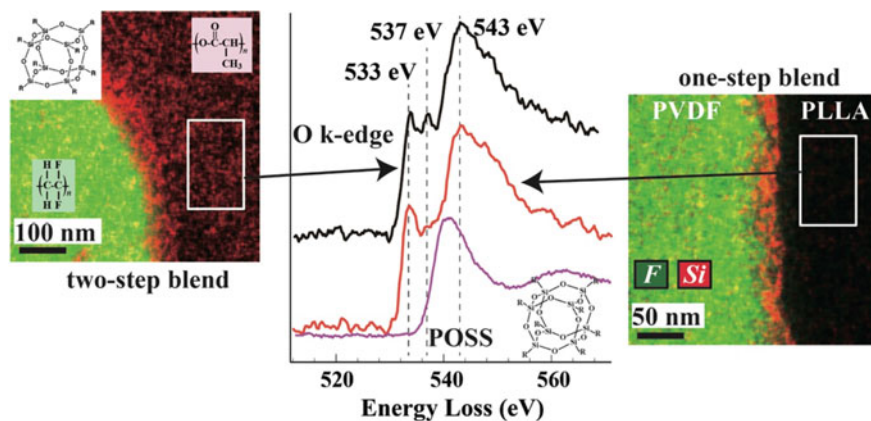


Fig. 38 STEM-EELS O K-edge spectra obtained from the PLLA phase in the one-step (*right*), two-step (*left*) PLLA/PVDF/POSS(epoxy)₅-g-PMMA₃ blends and from POSS. The images are STEM-EDX mixed maps, with green and red pixels corresponding to F and Si elemental distributions. Reprinted with permission from Ref. [89]. Copyright 2019, American Chemical Society. All Rights Reserved

shows a small peak at 537 eV for PPO, even with the smallest probe, indicating that the carbonyl group's oxygen mainly contributes to the beam-sensitive peak at 537 eV in the ester bond. The electron beam can easily cause chain scissions of the carbonyl group in the ester bond of the polymers, which can generate products like carbon oxide that evaporate away from the specimen.

The different O K-edge ELNES features obtained in the PLLA phases in the two blends shown in Fig. 38 are caused by the difference in the degradation behavior of PLLA. The small amount of the POSS-compatibilizer dissolved in the PLLA phase in the two-step blend can suppress the cleavage of the ester bonds, and thus the beam-sensitive peak in the O K-edge remains in the spectrum.

In Fig. 36, the Si elemental maps demonstrate that the POSS-compatibilizer selectively localizes at the interfaces of PLLA/PVDF in two different blends prepared using distinct mixing sequences. As previously mentioned, the interfacial layer formed by the compatibilizer in the two-step blend appears to be more uniform and thicker than that of the one-step blend. Moreover, the compatibilizer is mainly found in the PLLA side in the two-step blend, while it exists primarily in the PVDF phase in the one-step blend. However, analyzing oxygen by STEM-EDX is limited as PLLA and PMMA tend to degrade under STEM probe. To obtain sufficient signal gains in the EDX spectrum, scanning for an extended time with a relatively high-current probe is required. Conversely, STEM-EELS analysis using the low-current small probe permits the detection of the oxygen originating from PLLA and PMMA, as presented in Fig. 38. The results indicate that the compatibilizer is exclusively distributed in the PVDF phase in the one-step blend.

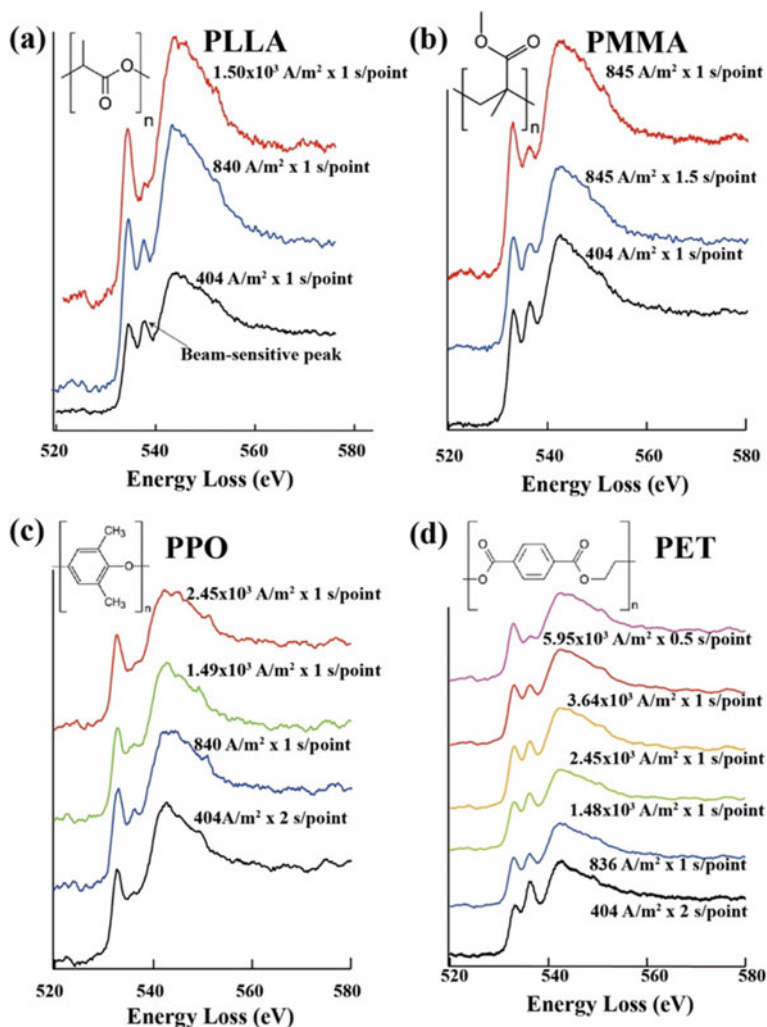
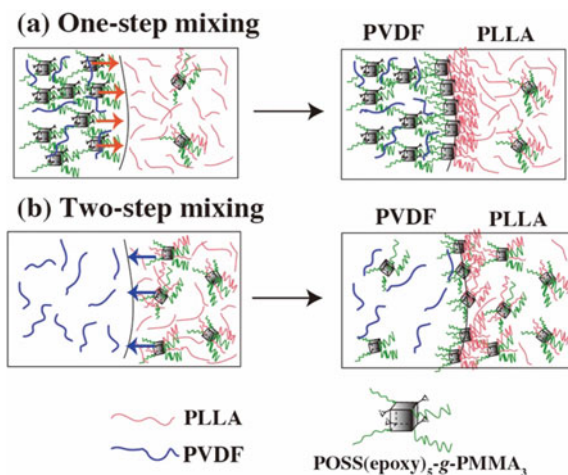


Fig. 39 O K-edge ELNES features of polymers taken with different electron probe conditions: **a** PLLA; **b** PMMA; **c** PET; **d** PPO. From the lower to upper spectrum, beam size and current are increased. The intensities of the spectra are normalized with the peak at 533 eV. Reprinted with permission from Ref. [89]. Copyright 2019, American Chemical Society. All Rights Reserved

Figure 40 illustrates the mechanism of the reactive compatibilization in blends with different mixing sequences, based on the findings. In the one-step blend (Fig. 40a), the compatibilizer tends to distribute in the PVDF phase due to the thermodynamic miscibility of PMMA and PVDF. However, when melt blending occurs, most of the compatibilizers close to the PLLA/PVDF boundary do not react with PLLA and, thus, are distributed in the PVDF phase, which does not enhance the PVDF phase dispersion in the PLLA matrix and the interfacial strength. In contrast,

Fig. 40 Illustration depicting the processes involved in the reactive compatibilization of PLLA/PVDF blends with POSS(epoxy)₃-g-PMMA₅: **a** one-step blend; **b** two-step blend. Reprinted with permission from Ref. [89]. Copyright 2019, American Chemical Society. All Rights Reserved



some compatibilizers may have reacted and become occluded in the PVDF phase. Figure 40b represents the two-step blending process, where PLLA and the compatibilizer are pre-mixed to retain significant compatibilizers in the PLLA phase. When the pre-mixed PLLA/compatibilizer is blended with PVDF, the compatibilizer moves toward the PVDF phase due to the thermodynamic affinity of the PMMA chains linked to POSS with the PVDF phase. However, the reaction between PLLA and the compatibilizer prevents the complete dissolution of the compatibilizer into the PVDF phase, and it can surround the PVDF domains in a thick and uniform layer. Unreacted compatibilizers from the first step may be distributed in the PVDF phase during the second step. The reactive compatibilizer creates an interfacial layer that improves the dispersion and interfacial strength by impeding the coalescence of the PVDF domains during melt mixing [101].

5.2 ELNES Phase Mapping

Chemical state identification can be achieved through EELS by analyzing the delicate modulations that appear in the higher energy-loss region, spanning an energy width of 50–100 eV, from the ionization edge. These modulations, called electron energy-loss near-edge structure (ELNES), provide high-resolution chemical information on the excited atom beyond simple elemental composition information obtained from integrated core-loss signals. ELNES can generate maps of different material phases based on differences in their spectra. Mapping phases composed of different chemical compounds can be achieved by multiple linear least-square (MLLS) fitting of the STEM-EELS SI dataset using multiple standard spectra. Standard spectra for the MLLS fitting can be obtained from known reference samples or extracted from the dataset being analyzed. ELNES phase mapping allows for separating and

quantifying different material phases using multiple reference spectra for the same ionization edge [102]. The Fourier-log deconvolution function can be applied to the entire STEM-EELS SI datasets, extracting the single-scattering distribution (SSD) at each pixel. MLLS fitting with reference SSD spectra provides superior quantification and accurate maps for specimens with thickness variations across the data.

Figure 41 is a typical result showing the successful separation of the thin surface layer in Al6061 alloy into three aluminum compounds. An oblique section was performed with an ultramicrotome to obtain a thin section with a broader surface thin layer. EEL spectra were acquired in the STEM-SI mode with 1 s per pixel exposure time with a point-to-point distance of 5 nm. The shapes of the O K-edge ELNES of the three oxygen-containing aluminum compounds are unique and characteristic, as shown in Fig. 5c. Using those three spectra as the standards (Fig. 41a–c), the MLLS fitting was applied to the individual spectrum in the whole SI data cube acquired from the region indicated in the STEM-HAADF image (Fig. 41d). The result clearly shows that the surface layer can be divided into three phases: Boehmite is the main compound (Fig. 41f), while small amounts of $\text{Al}(\text{OH})_3$ (Fig. 41e) and γ -alumina (Fig. 41g) are distributed. Typical fitting results of the two regions indicated in the phase maps are presented in Fig. 41h, i, which shows the core-loss edges with a 30 eV energy range, and can be well fitted with the standard spectra without noticeable errors. Thus, the compositional heterogeneity in the natural oxide layer of Al alloy can be characterized quantitatively.

As mentioned in Sect. 1.2 of “Analysis of Molecular Surface/Interfacial Layer by Sum-Frequency Generation (SFG) Spectroscopy” chapter, O K-edges of polymers exhibit ELNES features associated with the ester and the ether bonds in polymers.

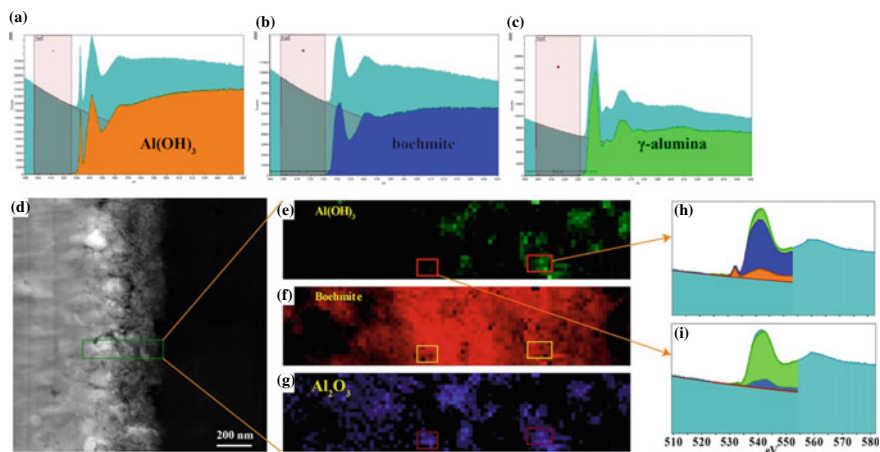
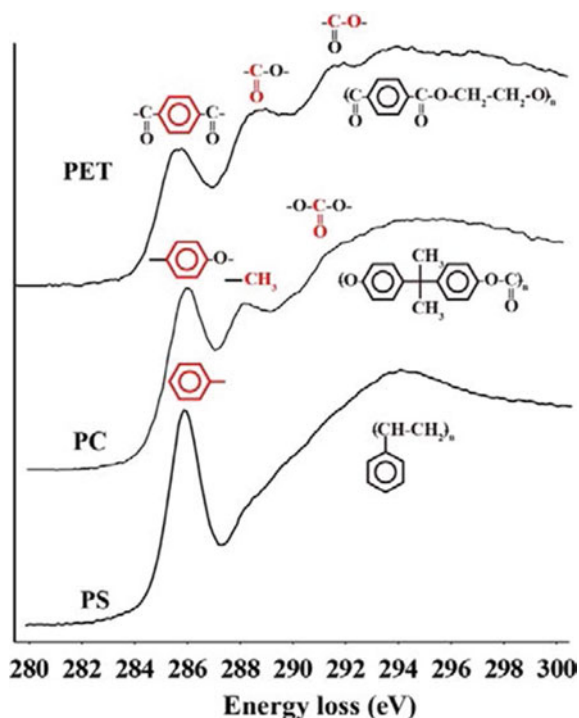


Fig. 41 ELNES phase mapping of Al6061 surface oxide layer: **a–c** standard spectra representing $\text{Al}(\text{OH})_3$, boehmite, and γ -alumina, respectively; **d** STEM-HAADF image showing the Al6061 surface region; **e–g** phase maps of ROI indicated in **d** representing the separation of $\text{Al}(\text{OH})_3$, boehmite, and γ -alumina phases, respectively; **h, i** results of the MLLS fitting of the EEL spectra extracted from the two regions in the phase maps

These represent the resistance of the polymers against the electron beam irradiation derived from their chemical structures, suggesting the possibility of the chemical identification of polymers with a high spatial resolution. The C K-edges of polymers contain ELNES that sensitively reflect chemical structures such as aromatic, carbonyl, ether, and methyl groups. Since carbon is the main element in most polymers, carbon ionization edges with high signal-to-noise ratios can be obtained with a lower electron dose than other elements, such as oxygen and nitrogen. Figure 42 shows typical examples of the C K-edges obtained from poly(ethylene terephthalate) (PET), PC, and PS. These spectra were acquired in the STEM-SI mode with an acquisition time of 100 ms and a point-to-point distance of 50 nm. After the post-acquisition processes of the BG subtraction and the deconvolution, 5×5 spectra in the SI data cube were summed into one spectrum. Then the ELNES reflecting the chemical structures of the polymers appeared in the C K-edges. According to the literature [103] and the spectra of other polymers we measured, the peaks can be assigned as shown therein. Careful attention should be paid to the effects of irradiation on ELNES. Upon irradiation with a higher dose, the characteristic features of ELNES may fade, resulting in similar core-loss peaks for all polymer samples. Therefore, standard spectra for the ELNES phase mapping of polymer samples should be prepared under the same condition as the SI data to be analyzed or extracted appropriately from the SI data cube being analyzed.

Fig. 42 C K-edge ELNESs of PET, PC, and PS with the assignments of the peaks to the chemical components



Figures 43 and 44 show the application of the ELNES phase mapping to the multi-phase structure of a PC/ABS blend. Figure 43a is an STEM-HAADF image of an unstained 50-nm-thick section, exhibiting the polybutadiene (PB) domains with the acrylonitrile-styrene (AS) copolymer occlusions, which are characteristics of the typical ABS polymer, and the presence of a light-gray phase surrounding the PB domains is confirmed. The spectral data was collected by STEM-SI mode with an acquisition time of 500 ms for one spectrum and a point-to-point distance of 10 nm. Figure 43b shows the standard spectra extracted from the three phases in the obtained SI data. These spectra exhibit distinct ELNES features in the energy-loss range from 284 to 290 eV: AS exhibits only the intense peak corresponding to the π - π^* transition of the aromatic group at 285.5 eV; PC exhibits the peak at around 288 eV corresponding to methyl group added to the peak at 286 eV assigned to the π - π^* transition of the aromatic group; and PB exhibits only the peak at 285.2 eV. Figure 44 shows the resulting maps computed by MLLS fitting using these three standard spectra, showing that the three components are successfully identified as distinct phases. The blend exhibits the multi-phase structure containing the PC phase (Fig. 44b) as the matrix and the AS phase (Fig. 44a) dispersed as the isolated domains and as the domains with the occluded PB domains (Fig. 44c). The result indicates the possibility of ELNES phase mapping with 10 nm resolution for polymer samples.

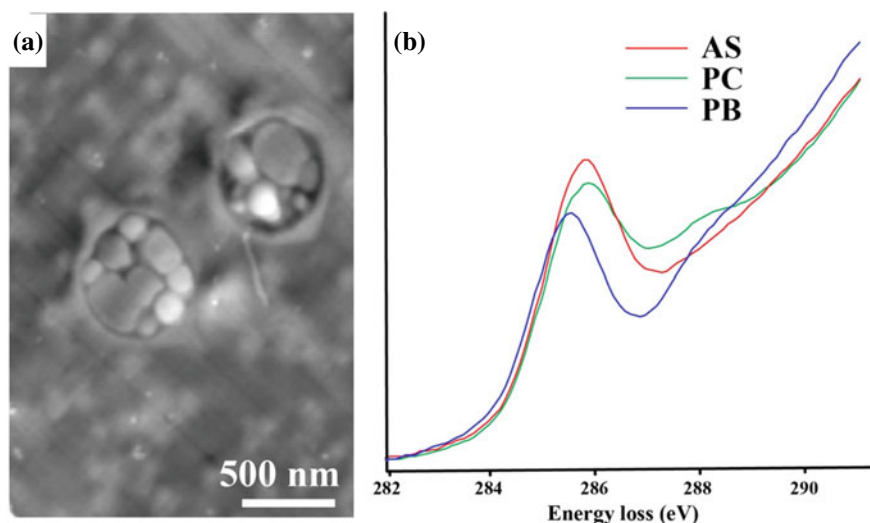


Fig. 43 STEM-HAADF image of ABS/PC blend (a) and C-K-edges taken from the three phases used as standard spectra for the MLLS fitting to perform ELNES phase mapping (b)

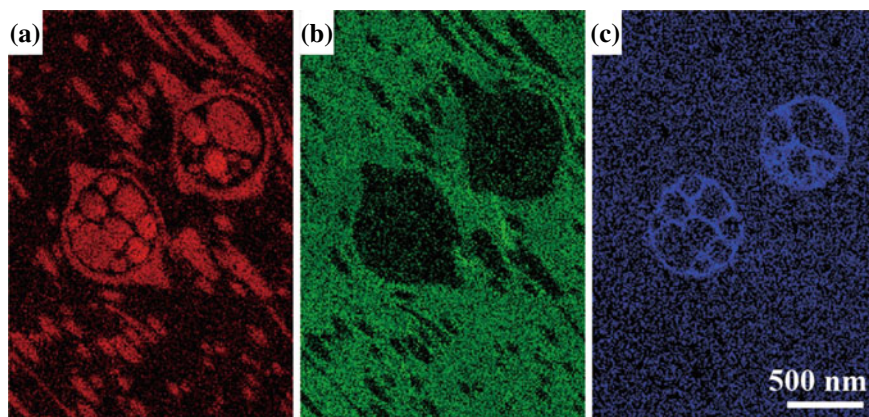


Fig. 44 a AS, b PC, and c PB phases in a PC/ABS blend created by ELNES phase mapping

5.3 Tomography and 3D Elemental Mapping

5.3.1 Advantages of STEM Tomography Over TEM Tomography

TEM is a technique that can be used to investigate structures at the nano-scale. However, this method only generates two-dimensional images of three-dimensional objects, which may lose information on their morphology and composition. Interpreting a three-dimensional structure based solely on two-dimensional projections may be unreliable or incomplete. Electron tomography, on the other hand, is a method that enables the reconstruction of an object's interior from its projections [104]. To perform TEM tomography, a tilt series is obtained by tilting the specimen sequentially about a single axis. Typically, the tilt series is acquired with angular increments of approximately 2° and a tilt range of $\pm 60^\circ$. The individual images are then aligned to a common tilt axis to remove residual shifts between them. Cross correlation of the images is used to carry out the alignment of each image. Measuring the projection yields a single central plane of the 3D Fourier transform of the object. By tilting an object, its Fourier transform can be collected into a bundle of planes intersecting each other on a single axis. Inverse Fourier can obtain the original object transform.

TEM tomography has been used to investigate the three-dimensional structures of polymers and composites [105–107] since applying tomographic principles to TEM has facilitated three-dimensional analysis [108, 109]. In electron tomography, the STEM mode has often been utilized for the 3D imaging of materials. STEM tomography provides several advantages over TEM tomography, including the ability to effectively image thick specimens, dynamic focusing, and linear contrast using an annular dark-field mode [110]. Autofocusing relies on detecting contrast differences in a focused series of a small sample area. Dynamic focusing can adjust the focus as a function of specimen tilt and the distance of the scanned probe from the tilt axis, effectively removing focus gradients present in normal images due to specimen

tilt. Figure 45 shows an example of the 3D nanostructure reconstructed by STEM tomography. The sample is a cross section of a triblock copolymer film composed of PS, PMMA, and poly(*ter*-butyl methacrylate) (*Pt*BuMA) with the block sequence of PS-*b*-PMMA-*b*-*Pt*BuMA. The molecular weights of each block are 100, 298, and 40×10^3 , respectively. Figure 45a is an STEM-BF image showing the 2D projection of the stained specimen with RuO₄ vapor for 30 min. PS, *Pt*BuMA, and PMMA phases appear dark gray, light gray, and white, respectively. Due to the complex phase-separated structure, the 3D structure is difficult to deduce from the 2D image. STEM tomography was performed in BF mode with an angular increment of 2.5° and a tilt range of ±60°. Acquisitions were performed under cryogenic conditions of 110 K to prevent sample shrinkage due to electron beam irradiation during the tilt-series acquisition. The reconstructed 3D data were divided into three phases based on the brightness of each voxel. A 3D structure was obtained as shown in Fig. 45b, with the PS and *Pt*BuMA phases shown in red and green, respectively. The volume fractions of each segment (23, 68, and 9 vol% for PS, PMMA, and *Pt*BuMA, respectively) agree with the calculated values based on the molecular weight ratio. The 3D data show that PS forms a continuous phase and the *Pt*BuMA phase is located between the PS and PMMA continuous phases. The detailed 3D nanostructure of the triblock copolymer can be seen in the video (Fig. 46), including the whole reconstruction procedure. In “[Interfacial Phenomena in Adhesion and Adhesive Bonding Investigated by Electron Microscopy](#)” chapter, the 3D nanostructures of the polymer/metal joint interfaces and the fracture surfaces are investigated by STEM tomography.

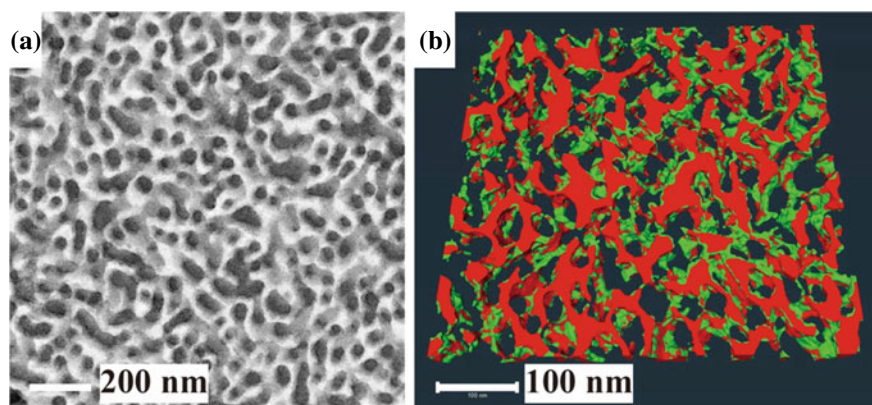


Fig. 45 STEM-BF image (a) and 3D reconstructed image (b) showing the nanodomain structure of a triblock copolymer of PS-*b*-PMMA-*b*-*Pt*BuMA. The thin section was stained with RuO₄ vapor. The red and green phases are PS and *Pt*BuMA, respectively

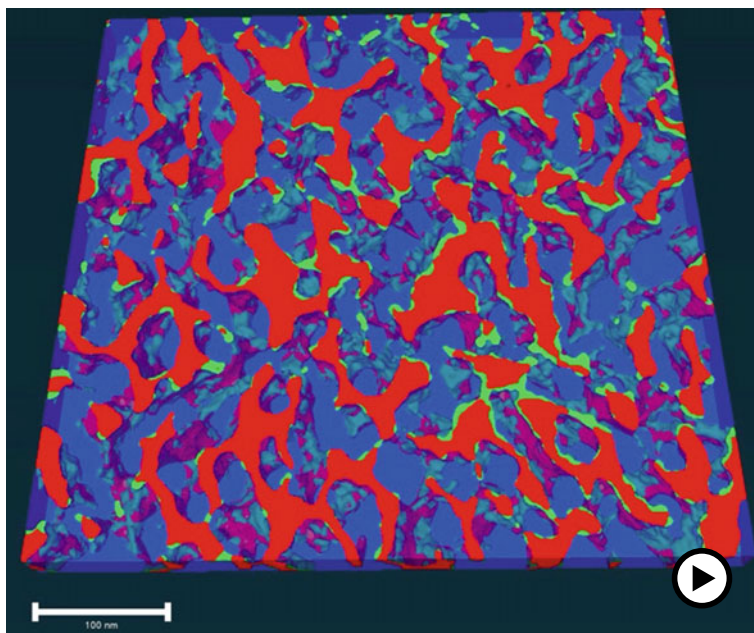


Fig. 46 Video showing the tilt series and the 3D reconstructed structure of PS-*b*-PMMA-*b*-PrBuMA triblock copolymer created by STEM tomography (► <https://doi.org/10.1007/000-ayd>)

5.3.2 3D Elemental Mapping of Rubber/Filler Blend Composites by STEM-EDX Tomography

Complex multi-component polymer systems often require detailed information about the distribution of specific elements, which can be obtained through 3D elemental mapping. This technique allows for locating components that contain specific elements within the structure. Nanoscale elemental mapping is possible using two electron microscopy methods: energy-filtered TEM (EFTEM) and STEM-EDX. As stated in the previous section, EFTEM allows us to perform elemental mapping based on electron energy-loss spectroscopy (EELS). Electron energy-loss spectroscopy (EELS)-based elemental mapping can be performed using EFTEM. However, the thickness of the specimen can strongly affect the EELS spectra, particularly during the acquisition of tilt-series images [111]. The increase in tilt angle results in increased thickness, which leads to changes in the contrast of the energy-loss images and difficulties in reconstructing 3D structures [112, 113]. As a result, EFTEM tomography is only suitable for specific specimen geometries such as cylindrical, spherical, or needle-like shapes.

Another technique used for elemental mapping is STEM-EDX. In conventional systems, X-rays emitted from the specimen are detected by a single detector located diagonally above the specimen. However, this setup can be strongly affected by the specimen tilting, resulting in the incomplete collection of emitted X-rays over the

range of tilt angles [114]. Due to shadowing effects, traditional STEM-EDX systems have difficulty detecting X-rays when the specimen is tilted away from the detector. To address this limitation, a new multidetector EDX system has been developed. This system features four silicon-drift detectors (SDDs) placed symmetrically around the optical axis near the specimen, enabling the acquisition of high-quality elemental maps with equal efficiency across the entire range of tilt angles [115, 116].

In this research, STEM-HAADF and STEM-EDX tomographies were combined to analyze the spatial distribution of silica nanofillers in two-phase immiscible polyisoprene/styrene-butadiene (IR/SBR) rubber blends and to evaluate the influence of silica loading on the phase-separated morphologies of the blends [117]. Different weight ratios of IR, SBR, and silica were melt-mixed, and thin sections (~150 nm) were produced by cryoultramicrotomy at a temperature of -130 °C. The sections were then stained with OsO_4 vapor for 15 h at 50 °C. STEM bright-field (BF) images of the IR/SBR/silica blend composites with IR/SBR weight ratios of 70/30 (Fig. 47a–d) and 30/70 (Fig. 47e–h) are shown in Fig. 47. The blends without silica (Fig. 47a, e) exhibit coarse phase separations with irregularly shaped domains. The SBR phase is stained relatively more strongly, resulting in the gray-colored phase in the STEM-BF images. OsO_4 staining cross-links the polymer chains by staining polymers containing carbon–carbon double bonds. Both rubber phases are stained, but the SBR phase is stained more strongly in the blends without silica. The small IR domains observed in the 30/70 IR/SBR blend (Fig. 47e) are stained much more strongly than the IR matrix, implying that OsO_4 staining depends on the domain size. OsO_4 staining enhances the elastic scattering of electrons and can help make IR/SBR phase separations visible by introducing the heavy atom. Additionally, it can improve the specimen's stability against beam irradiation to prevent shrinkage of the phase structures [52]. The phase separation and image contrast change when silica nanofillers are added at 25, 50, or 70 phr (weight parts per hundred rubber) to the 70/30 IR/SBR blend, as depicted in Fig. 47b–d, respectively. The SBR domains become smaller and appear brighter when silica is present. Identifying the IR/SBR phase separation is challenging when the silica content is 70 phr (Fig. 47d) because the volume fraction of the silica is high (23%). The same trend is observed for the SBR-rich blends (Fig. 47f–h), where the IR phase is stained more strongly than the SBR phase in the presence of silica. This phenomenon may be due to the reduced domain size and silica loading on the rubber phases' staining.

Relying solely on STEM-BF images does not allow for clear visualization of the silica distribution and the IR/SBR phase separations. When unstained, the silica is visible, but the two rubber phases cannot be distinguished. Staining with OsO_4 improves the visibility of the rubber phases, but the contrast between the two rubber phases and silica may be insufficient, making it challenging to identify the silica. Combining STEM-HAADF imaging and STEM-EDX elemental mapping could be the best way to distinguish the silica and the IR/SBR phase-separated morphologies. Figure 48a, b shows a STEM-HAADF image and the corresponding Si elemental map of a 50/50/50 IR/SBR/silica blend composite, respectively. The STEM-HAADF image exhibits a high contrast between the IR and SBR phases, in which the bright and dark phases correspond to the IR and SBR phases, respectively. The STEM-EDX

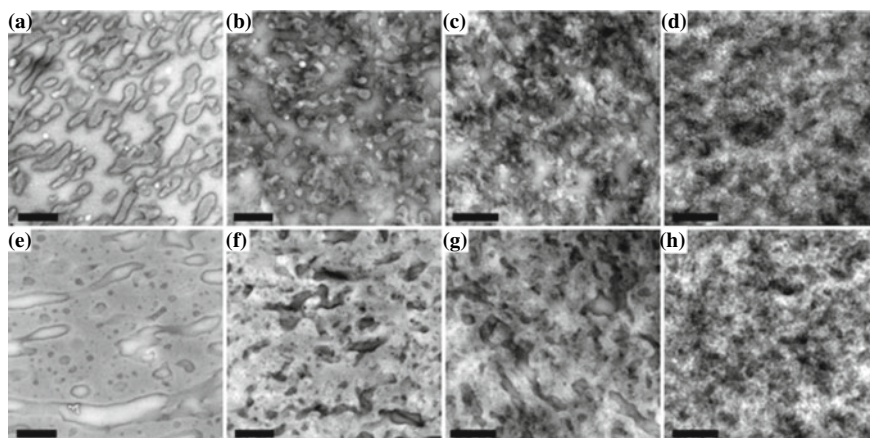


Fig. 47 OsO₄-stained STEM-BF images showing the impact of silica nanofiller loading on the phase-separated morphologies of IR/SBR rubber blends: **a–d** 70/30 (wt/wt) IR/SBR ratio; **e–h** 30/70 (wt/wt) IR/SBR ratio. The silica contents are 0 (**a, b**), 25 (**b, f**), 50 (**c, g**), and 70 phr (**d, h**). Scale bars represent 500 nm. Reprinted with permission from Ref. [117]. Copyright 2021, John Wiley & Sons. All Rights Reserved

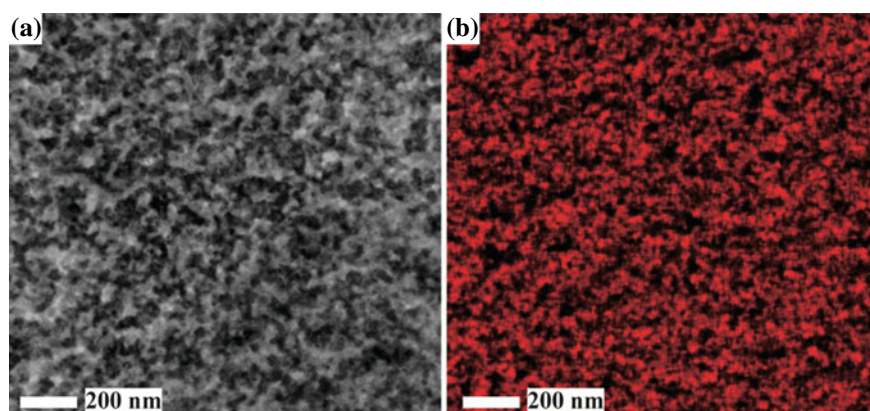


Fig. 48 STEM-HAADF (**a**) and STEM-EDX Si elemental distribution (**b**) images of 50/50/50 IR/SBR/silica blend composite. Reprinted with permission from Ref. [117]. Copyright 2021, John Wiley & Sons. All Rights Reserved

Si elemental map presents only the location of the silica, which cannot be seen in the STEM-HAADF image. The overlap of the Si elemental map onto the STEM-HAADF image could recognize that the silica is mainly distributed into the SBR phase. The combination of STEM-HAADF tomography and STEM-EDX tomography could be promising for quantifying the distribution of the silica in the two rubber phases three dimensionally.

Figure 49a, b displays the EDX spectra obtained at tilt angles of 0° and -55° , respectively. The spectra exhibit energy regions, including the Si, W, Os, and S peaks. The W peak originates from the specimen holder and is more significant at higher tilt angles. The Cliff–Lorimer method is used to separate the overlapping peaks [118]. Figure 50 presents the tilt-angle dependence of the deconvoluted Si $K\alpha$ peaks intensities for 30/70 IR/SBR blends with 70 phr silica contents. The EDX signals with sufficient intensities were collected symmetrically over the entire range of tilt angles. In contrast, a single detector yielded low EDX signal intensities, even at the highest silica content of 70 phr. The negative tilt angles did not yield any signals when the specimen was tilted to the opposite side of the detector (green data points in Fig. 50). Thus, the multidetector EDX system is essential for performing the 3D elemental mapping.

A video demonstrating the process for combined STEM-HAADF and STEM-EDX tomography is presented in Fig. 51. STEM-EDX tomography was performed using a 0.7 nm electron probe and 0.5 nA current, with a $30 \mu\text{s}/\text{pixel}$ dwell time. The resulting 512×512 pixel maps were obtained by scanning for 5 min and integrating the signals. The alignment of the tilt series of STEM-HAADF images and the Si elemental maps was performed in parallel using the same conditions. Then, the two tilt series were separately reconstructed into 3D volumes. The 3D structure reconstructed from the STEM-HAADF images represents the IR/SBR phase-separated morphology, classified into two segments corresponding to the IR and SBR phases. The Si 3D map is binarized to extract the silica part. Finally, these three parts are combined into a single 3D volume. The silica part is divided into two parts: distributed in the IR phase and the SBR phase.

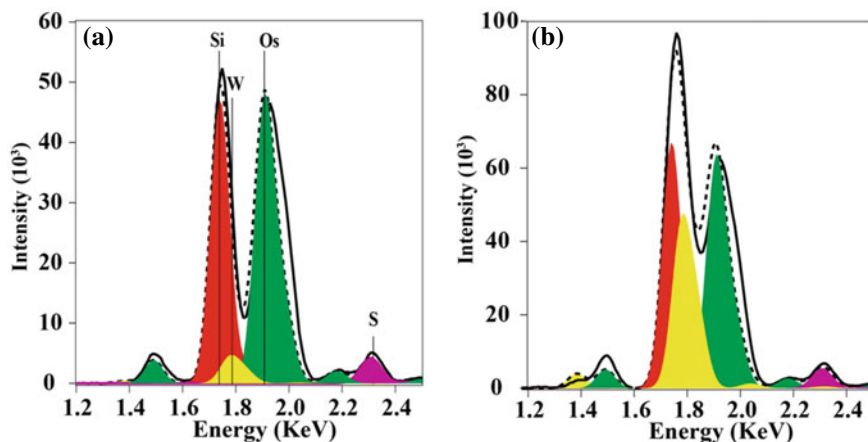


Fig. 49 EDX spectra showing the Si, W, Os, and S peaks of 30/70/50 IR/SBR/silica blend composite at tilt angles of 0° (a) and -55° (b). The peaks are separated by deconvolution. The solid and dotted lines are as-obtained and the sum of the deconvoluted spectra, respectively. Reprinted with permission from Ref. [117]. Copyright 2021, John Wiley & Sons. All Rights Reserved

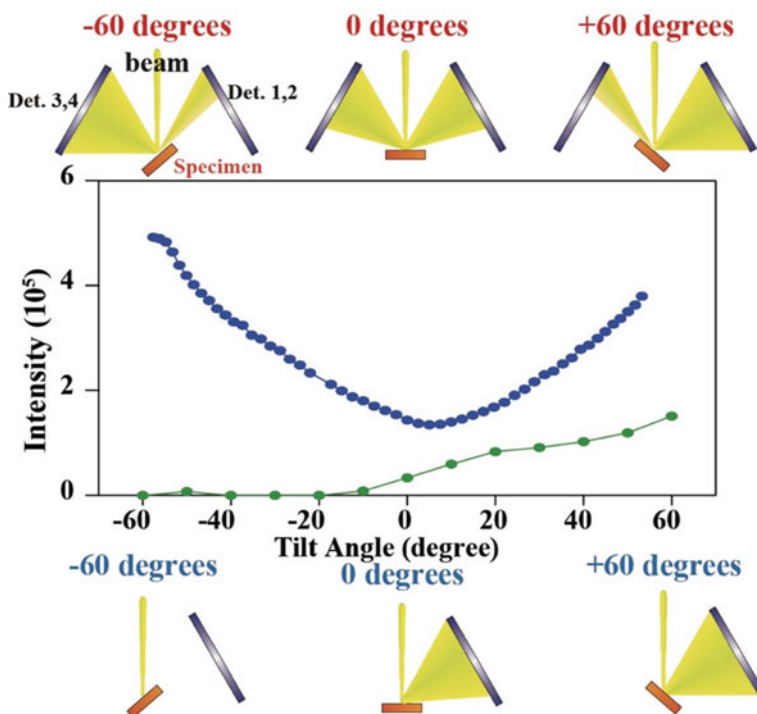


Fig. 50 Tilt-angle dependence of the Si $K\alpha$ peak intensities for 30/70 IR/SBR blends containing 70 phr silica (blue), and the signal intensities of 60/40/70 IR/SBR/silica obtained with a single detector (green dots). Angle dependence EDX signal detection in the multidetector (upper) and the single-detector (lower) systems are schematically illustrated

Figure 52 shows the distributions of silica and the effects of silica loading on the phase-separated morphologies of 30/70 and 70/30 IR/SBR blends. The dark blue, light blue, red, and yellow parts correspond to the SBR, IR, silica in SBR, and silica in IR, respectively. The figure clearly shows that silica is preferentially distributed in the SBR phase. Still, some silica also escapes into the IR phase when SBR is the minor component of the blend. It also shows that loading silica into the blends improved the dispersion of the minor rubber component.

A combination of STEM-HAADF and STEM-EDX tomography was utilized in this study to examine the 3D distribution of nano-sized silica in binary rubber blends. This approach enables the investigation of silica distribution between the rubber phases in highly silica-filled blends at 70 phr (23 vol%), which is not easily discernible using conventional 2D TEM. The quantification of silica distribution between the rubber phases demonstrates that silica is preferentially located in the SBR phase. Still, it can also be present in the IR phase when the IR fraction in the total rubber components is above 40 wt%. The phase-separated morphologies of IR/SBR blends are significantly impacted by silica loading, resulting in a fine

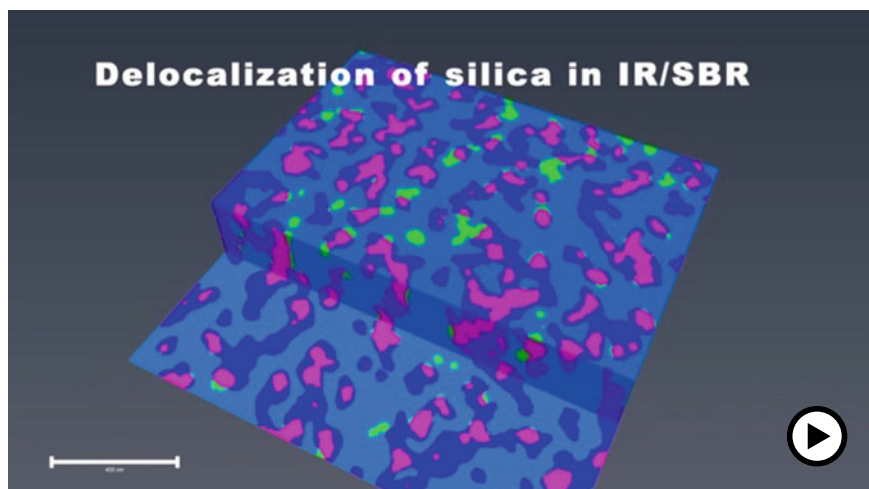


Fig. 51 Video showing the reconstruction procedure and the 3D image of the IR/SBR rubber blend with silica (► <https://doi.org/10.1007/000-ayb>)

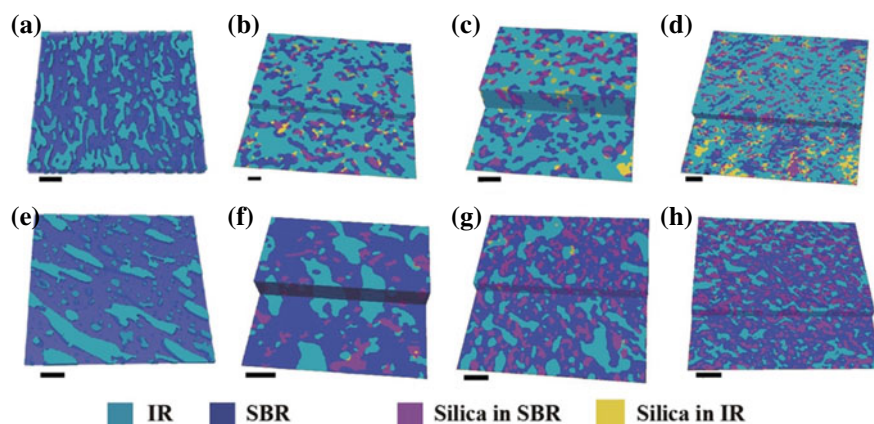


Fig. 52 Silica content dependence of the 3D structures of IR/SBR blends: **a–d** 70/30 (wt/wt) IR/SBR blend; **e–h** 30/70 (wt/wt) IR/SBR blend. The silica contents are 0 (**a, e**), 25 (**b, f**), 50 (**c, g**), and 70 (**d, h**) phr. Scale bars represent 200 nm. Reprinted with permission from Ref. [117]. Copyright 2021, John Wiley & Sons. All Rights Reserved

dispersion with high phase connectivity. This is due to the preferential distribution of silica in the SBR phase, which decreases the matrix/domain viscosity ratio. The manipulation of silica distribution in multi-phase polymer systems can be achieved by surface modification of silica, resulting in the optimization of rubber composite properties. The visualization method utilized in this study provides comprehensive structural information on multi-component polymer composite structures.

5.3.3 Multiple 3D Elemental Mapping by STEM-EDX Tomography of the Laser-Modified Galvanized Steel Surface

The surface modification of metallic substrates by laser irradiation has been recognized as a robust way to achieve adhesive bonding with high strength and durability [119–121]. Laser treatments with different power, wavelength, and scanning processes have constructed various surface topological structures. Galvanized steel sheets have been extensively used for automobiles. The steel sheet is covered with a uniform zinc-plated layer by controlling the amount of zinc coating. The zinc-plated layer itself is chemically treated, which ensures excellent corrosion resistance. Here, a laser-irradiated galvanized steel (Zn–Fe) surface is investigated to study the mechanism of the evolution of the laser-induced surface structures []. A low-magnification SEM micrograph (Fig. 53a) shows a topological surface structure created along the laser scanning direction. Deep trenches are formed by laser scanning, generating wavy threads and spherical objects between adjacent trenches. The spherical objects are created at periodic intervals on the thread. The high-magnification view of the spherical object surface shown in Fig. 53b indicates that the finer topological structure is built on the surface of the globules. FIB cross section along the line shown in Fig. 53b provides evidence that the globules are over 10 μm in height and that additional nanometer-scale topological structures have been created on the globule surface.

STEM-EDX elemental analysis was carried out with a thin specimen prepared by the FIB fabrication. Figure 54 shows the STEM-HAADF image and the 2D elemental distributions of O, Fe, and Zn in the surface layer created by laser irradiation on steel. The iron- and zinc-rich layers are involved in the oxygen-rich layers formed on steel. This layer is thought to be formed by the deposition of iron and zinc oxidation products vaporized by laser irradiation. Elemental distribution images of Fe and Zn suggest that the ZnO layer is first created on the steel substrate. Then the iron oxide layer is deposited on the ZnO layer. After the double-dense layer is formed, a porous layer with a Zn-rich top is formed. The 2D elemental maps, however, have limitations in understanding the true complex surface microstructures. Therefore, STEM tomography was performed to reconstruct the 3D surface structure created by

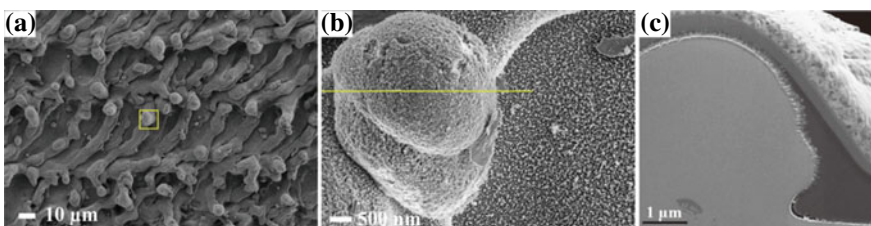


Fig. 53 SEM micrographs showing the surface topographic features of the Zn-coated steel created by laser irradiation. **a** Is a low-magnification image and **b** is the magnified view of the region indicated in **a**. **c** Is a cross section created by FIB along the line shown in **b**. Prof. S. Hartwig and Dr. C. Gndrach, Technische University Braunschweig, provided the sample

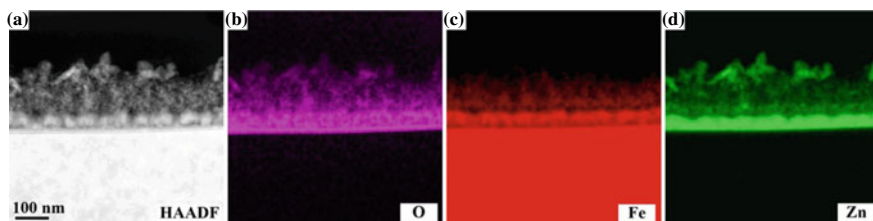


Fig. 54 Cross-sectional images of the laser-irradiated Zn-coated steel surface: **a** STEM-HAADF; **b–d** STEM-EDX elemental maps of O, Fe, and Zn, respectively

the laser irradiation, as shown in Fig. 55. A tilt series of the STEM-HAADF image (Fig. 55a) with the angular increment of 2.5° and the tilt range of $\pm 60^\circ$ was acquired, allowing the 3D reconstruction as displayed in Fig. 55b, c. The 3D image data makes viewing the structure at any angle, distance, or position possible. Looking at the 3D structure, we can see that the object existing in the upper layer is a thin plate. In the 2D image, the bottom bilayer looks like continuous film, but in the 3D image, we can confirm that these are porous.

Next, to know more about the 3D structure, the chemical structure of the surface layer was investigated by STEM-EDX tomography. STEM-EDX map data was acquired at each tilt angle using an electron probe of 0.7 nm diameter and 0.5 nA current with a $30 \mu\text{s}/\text{pixel}$ dwell time. 512×512 pixel EDX elemental map data was obtained by integrating the signals for 5 min scanning at each tilt angle. Figure 56 shows a video demonstrating the STEM-EDX tomography and the 3D viewing of the elemental maps. The Zn and Fe 3D elemental maps were constructed in parallel and then these two were combined into one 3D volume data. Figure 57 shows 3D views of the Fe and the Zn 3D elemental maps separately. The multiple 3D elemental maps are shown in Fig. 57c, where the Fe and Zn distributions are presented as red and green voxels, respectively. The yellow voxels represent the co-existing Fe and Zn elements. Thus, the multiple 3D elemental maps provide detailed structural information on the nano-scale regarding topological and chemical structures. We learned that the laser treatment on the galvanized steel could create a unique surface structure, including the co-continuous porous structure with the ZnO nanoflakes on the outermost part.

The steel surface is initially covered with a thick, uniform Zn-coated layer about $10 \mu\text{m}$ thick. Laser scanning locally heats the steel surface to a temperature high enough to melt it, creating micrometer-scale anisotropic topological structures due to the mechanical effect of the laser. At the same time, zinc and iron evaporate from the surface of the steel, oxidize in the air, and are deposited onto the molten iron surface. The porous structure is formed during the evaporation–deposition process, and finally the large zinc nanoplatelets are deposited.

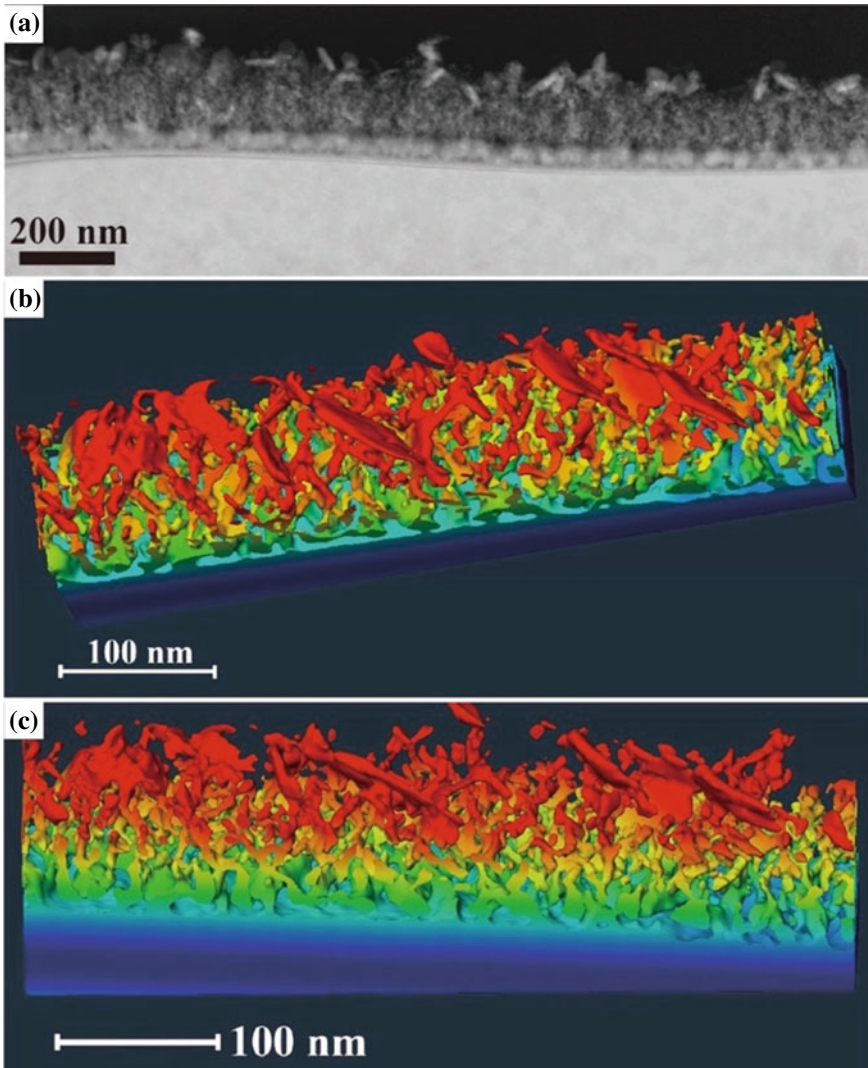


Fig. 55 TEM-HAADF tomography of the laser-irradiated Zn-coated steel surface: **a** STEM-HAADF image at 0° tilt angle; **b**, **c** 3D views obtained from the reconstructed 3D image data. The color represents the distance from the bottom plane

6 SEM

One method for producing a magnified image of a sample is SEM, which works by scanning an electron beam on a specimen surface and detecting the electrons that are emitted from its surface due to the interaction with the beam. As the electron beam scans line by line over the specimen, it generates various types of electrons

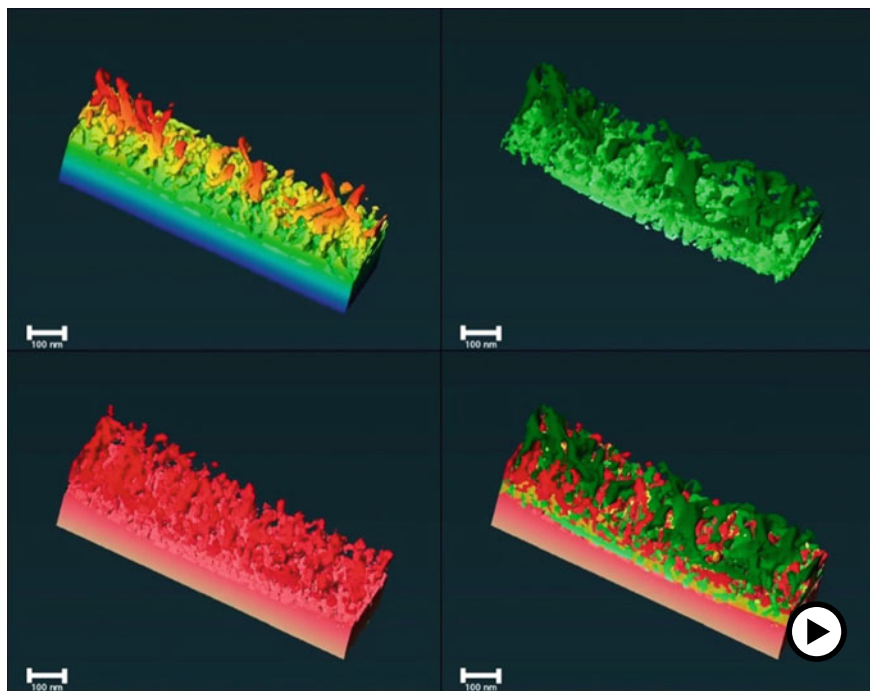


Fig. 56 Video demonstrating the STEM-EDX-tomography and the 3D viewing of the elemental maps of the laser-irradiated Zn-coated steel surface (► <https://doi.org/10.1007/000-ayf>)

that carry unique structural information about the sample, differing in origin, energy, and direction of travel. Several types of electrons are generated as the result of the energetic bombardment of the specimen by the primary beam electrons (PEs) as stated in Sect. 1. SEM imaging employs both secondary electrons (SEs) and back-scattered electrons (BSEs) that are emitted from the surface of the sample to produce contrast in the image. The contrast in BSE mode is primarily determined by the atomic number (material contrast). In contrast, SE mode is mainly based on the local surface inclination relative to the incident beam (topographic contrast). For imaging topographic features of surfaces in polymeric materials, the SE mode is often preferred. The SEs are low-energy electrons (<50 eV) that originate from the sample and play a role in forming the image.

Loosely bound electrons in the valence or conduction band of the sample atoms give rise to SE emission. When PEs interact inelastically with the sample atoms, they generate SEs that escape from the sample into the vacuum. The energy of SEs is very low, around 50 eV, which limits their mean free path in solid matter. As a result, SEs can only escape from the top few nanometers of the sample's surface. The signal from SEs is usually concentrated at the point where the primary electron beam impacts the sample. Two primary types of SEs, SE-I and SE-II, are generated from the sample, as illustrated in Fig. 58a [122]. SE-I originates from the direct interaction

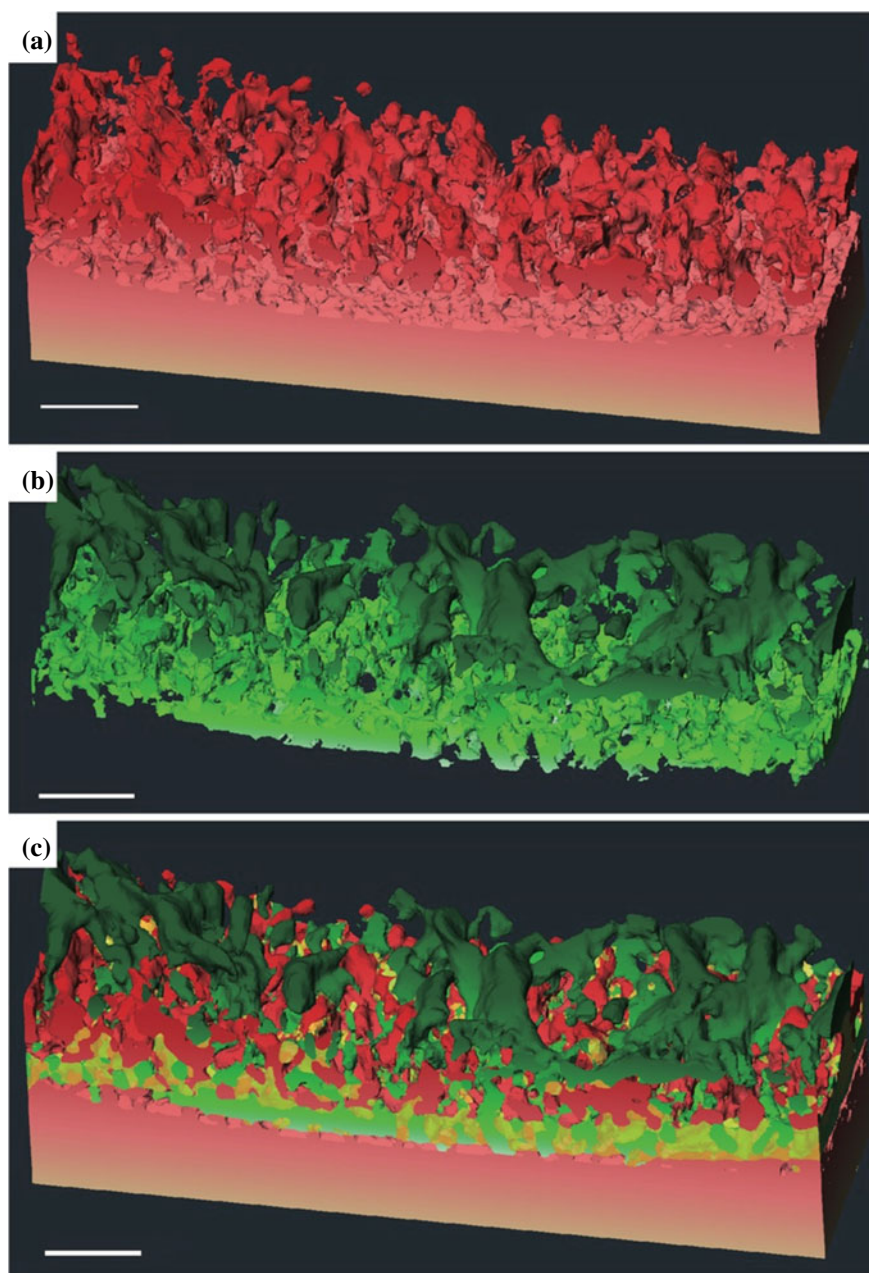


Fig. 57 3D elemental maps of the laser-irradiated Zn-coated steel surface created by STEM-EDX tomography: **a** Fe distribution image; **b** Zn distribution image; **c** mixed map of Fe (red), Zn (green), and Fe/Zn co-existing (yellow) region. Scale bars correspond to 100 nm

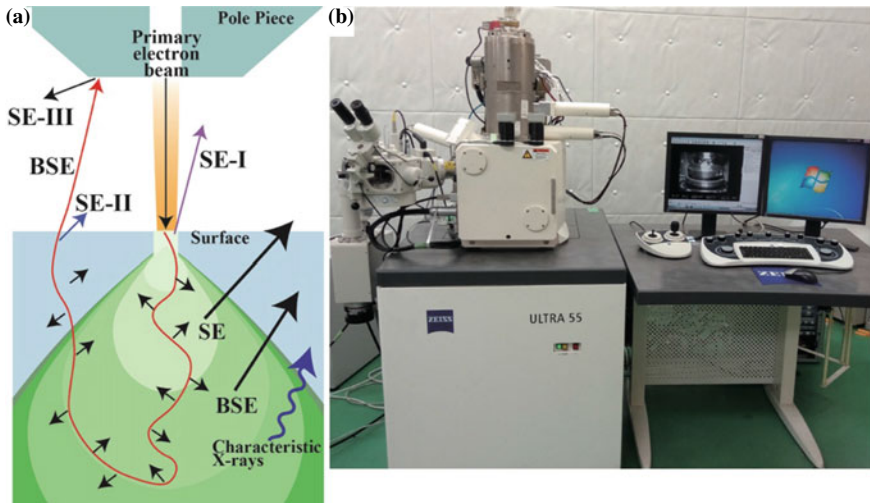


Fig. 58 Schematics of a typical specimen–electron interaction volume (a). SE-I is generated from the point of intact, while SE-II is generated by BSEs raveled in the sample. SE-IIIs are generated when high-energy BSEs from the sample strike the objective pole piece or the chamber walls and the appearance of an FE-SEM instrument, Ultra 55 (Carl Zeiss) (b)

of the primary electron beam with the sample near the beam impact point, while BSEs produce SE-II. The inelastic mean free path of SEs is relatively short, typically 1–3 nm and is energy dependent. When some PEs penetrate the sample, they lose energy through inelastic collisions before exiting the vacuum. Since BSEs, which create SE-II, also travel a certain distance within the sample, SE-II are emitted from the sample’s surface at locations significantly away from the primary beam impact point.

Apart from SE-I and SE-II, another type of SE, called SE-III, can also be generated. These electrons are produced when high-energy BSEs, which exit the sample, collide with the objective pole piece or the chamber walls, resulting in SEs from these surfaces. This background signal adds unwanted noise to the signal from the sample. SE-I provides high-resolution, surface-specific information about the sample since the spatial resolution depends on the size of the primary electron beam. On the other hand, SE-II is generated from a broader and deeper volume than SE-I and reflects at a lower angle, making it carry inherently lower resolution topographic information.

6.1 Energy-Filtered SE Imaging

As described in Fig. 2c, the column of the SEM instrument used in our study (Fig. 58b) integrates two detector systems for the collection of the SE signals: One is a conventional scintillator-type detector located outside the objective lens and the other is an

annular type positioned above the objective lens “on-axis”. Those two detectors are called the “chamber detector” and the “in-lens” detector, respectively. SEs emerging from the sample surface are attracted and accelerated by the positively biased electrode of the beam booster and finally projected onto the in-lens detector [123]. The electrostatic lens formed at the entrance of the objective lens accelerates the SE electrons backward and directs them into the in-lens detector. The in-lens detector mainly collects SE-I secondary electrons, while the chamber detector collects SE-II secondary electrons. Thus, the chamber detector is called the SE2 detector. Figure 59 presents a typical example for comparing the two SE images created by the two detectors at an acceleration voltage of 1.9 kV and a working distance of 3 mm. The specimen is a fracture surface of a welded interface between PS sheets that failed by the double beam cantilever (DCB) test, of which detail is shown in Sect. 3.2 of “Interfacial Phenomena in Adhesion and Adhesive Bonding Investigated by Electron Microscopy” chapter. It shows that the in-lens detector provides a higher resolution image (Fig. 59a) with detailed “nanofibrillar” structures visible clearly than the SE2 detector (Fig. 59b). The SEs collected with the in-lens detector originate from the very surface of the sample. The SE-I signal is commonly used to image surface details at the highest resolution at the expense of compositional information. The SE-II signals, on the other hand, are generated from a deeper and broader volume in the sample, resulting in poor image quality.

An interplay of accelerating voltage, detector selection, and working distance determines the quality of an SE image. The three imaging parameters should be optimized to obtain the best image quality for the samples under study. The influence of the three parameters on the SE image quality was investigated using a thin section of a semicrystalline polymer stained with RuO₄. The image quality discussed here is defined as “containing well discernable crystalline structural information” in an image. As stated in Sect. 3.2.2, the spherulites and the lamellae in PLA could be observed by the RuO₄ staining in the TEM mode. SEM can also provide a global image of the thin section fixed on a copper grid by the SE2 detector, as shown in Fig. 60. Figure 61a, b shows SE images detected by the in-lens detector and the SE2 detector, respectively, of the stained PLA section in the window of the copper grid. In contrast to high-resolution SE images of normal bulk polymer samples (Fig. 59), the two detectors have opposite effects on the resulting image quality. Because the in-lens detector mainly collects SE-I secondary electrons originating from the sample surface, the detector visualizes the electrons adsorbed on the sample surface like clouds due to the charging, which obscures to see the underlying structures. The negatively charged surface reflects many incoming electrons, creating very bright areas in the image. These regions deflect the electron beam, causing a blurring of the image. The SE2 detector, on the other hand, collects SE-II electrons generated from a deeper and wider volume within the sample. Because SE-II electrons have a considerable sample interaction depth, they contain topographical and compositional information. Therefore, the SE2 image represents the structure inside the section containing the compositional information produced by the selective staining.

The SE imaging with the two-detector system allows us to perform energy-filtered surface imaging, which offers the opportunity for high-resolution surface imaging

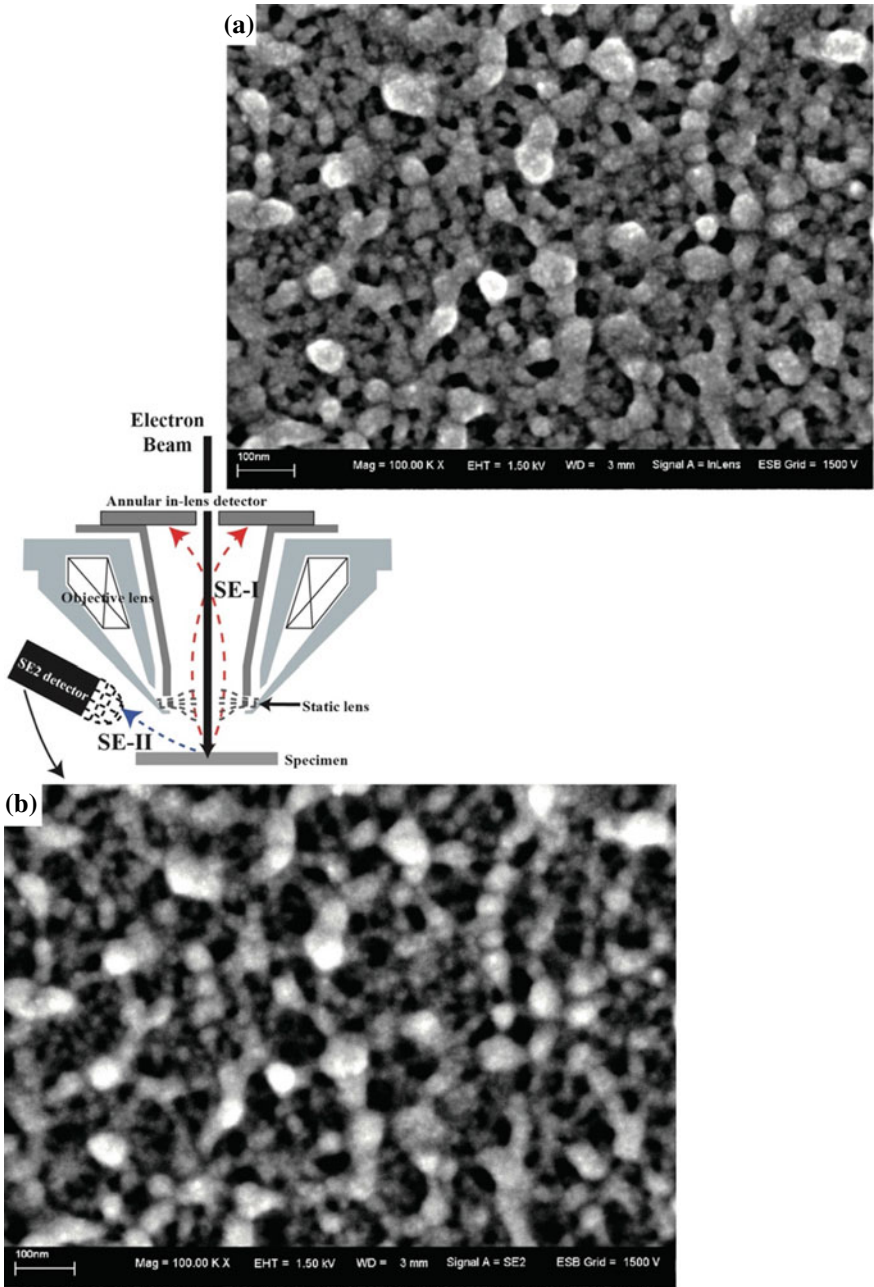


Fig. 59 SEM micrographs of the fracture surface developed in the failure of the welded PS interface in a DCB test: **a** SE image using the in-lens detector; **b** same region obtained using the SE2 detector

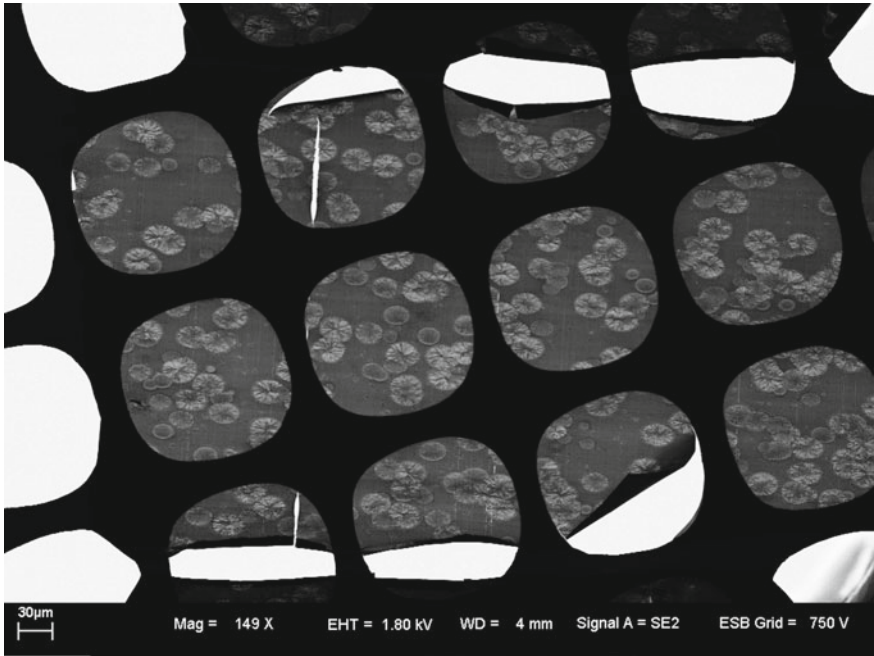


Fig. 60 SEM micrograph taken by the SE2 detector at 1.8 kV acceleration voltage showing a global image of the thin section of PLA stained with RuO₄

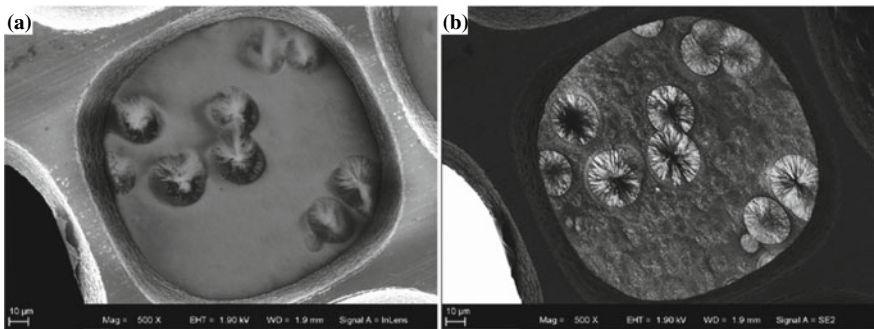


Fig. 61 SEM micrographs showing the spherulites of PLA distributed in the amorphous matrix: **a** SE image detected by the in-lens detector; **b** SE image detected by SE2 (chamber) detector (**b**)

of polymer specimens [124]. As mentioned above, SEs are the electrons that escape from the specimen surface with energies below about 50 eV, while BSEs are the primary electrons that undergo large deflections and leave the specimen surface with high energy similar to that of the primary electrons. The distribution of SEs into the two detectors according to their energy can be controlled by changing the working

distance. Figure 62 displays the series of in-lens (left column) and SE2 (middle column) images with varying working distances from 1.9 to 12.2 mm at the fixed accelerating voltage of 2.2 kV. As shown in Fig. 62i, j, the threshold energy, at which the SEs are divided into the two detectors, shifts from higher to lower when the working distance becomes longer. The in-lens image and the SE2 image at the same working distance vary with the threshold energy as shown by the changes from top to bottom in Fig. 62. With a large fraction of SEs distributed to the in-lens detector (Fig. 62i), the in-lens images represent the charging of the sample (Fig. 62a, b), while the SE2 image shows the underlying structure with good contrast (Fig. 62e, f). As the working distance increases, the in-lens images become darker and eventually, no brightness is gained at the working distance of 12.2 mm as shown in Fig. 62d. A longer working distance results in fewer SEs distributed to the in-lens detector. The SE2 images, on the other hand, become brighter as the working distance increases, and eventually the images become anomalously bright, and fine structures are obscured as shown in Fig. 62h. With a long working distance, most of the generated SEs, including SE-I, will be directed toward the SE2 detector and consequently unable to separate the charging contribution from the SE2 image. The threshold energy that splits the SEs between the two SE detectors can be optimized simply by changing the working distance, removing charging, and optimizing the contrast of the SE2 image.

As described above, the charging problem in the SE image of the PLA thin sections could be resolved by the energy filtering of the SEs. Next, using the same PLA specimen, we evaluated the effect of the accelerating voltage of the PE on the SE2 image. Figure 63 shows the changes in image quality of the SE2 image when the working distance is fixed at 3.9 mm which is determined in the above experiment and the accelerating voltage is varied in the range of 1.5–5.0 kV. A sufficiently bright image cannot be obtained at the experiment's lowest voltage due to the low SE yield. As the voltage is increased, the optimum quality is found to be obtained at 2.2 kV. When the accelerating voltage is further increased, the image brightness is too high to find the structural details in the specimen. To understand the effect of the PE energy on the SE image contrast, Monte Carlo simulations were employed to calculate an interaction volume where entering electrons interact with atoms in a 100-nm-thick carbon film as shown in Fig. 63. It demonstrates how this interaction volume is affected by accelerating voltage, where the blue lines represent the PEs spreading in the sample, and the red lines represent the BSEs generated and escaping from the surface. At the lowest PE energies (1.5 kV), electrons interact with sample atoms to a depth of about 40 nm. The PE pass distribution is pear shaped and spreads into the sample in the lateral direction. Therefore, the PEs cannot reach the bottom of the sample and go outside.

On the other hand, elevating the accelerating voltage increases the depth of penetration of the electrons into the section. When the PE energy is the highest at 5 kV, the PEs pass through the specimen without spreading significantly, suggesting that most PEs transmit the specimen without the interactions. The BSEs spread laterally, and thus the SE-II secondary electrons are generated far from the PE impact point, resulting in the loss of the spatial resolution. Thus the maximal compositional information could be obtained at the accelerating voltage of 2.2 kV. The image taken at

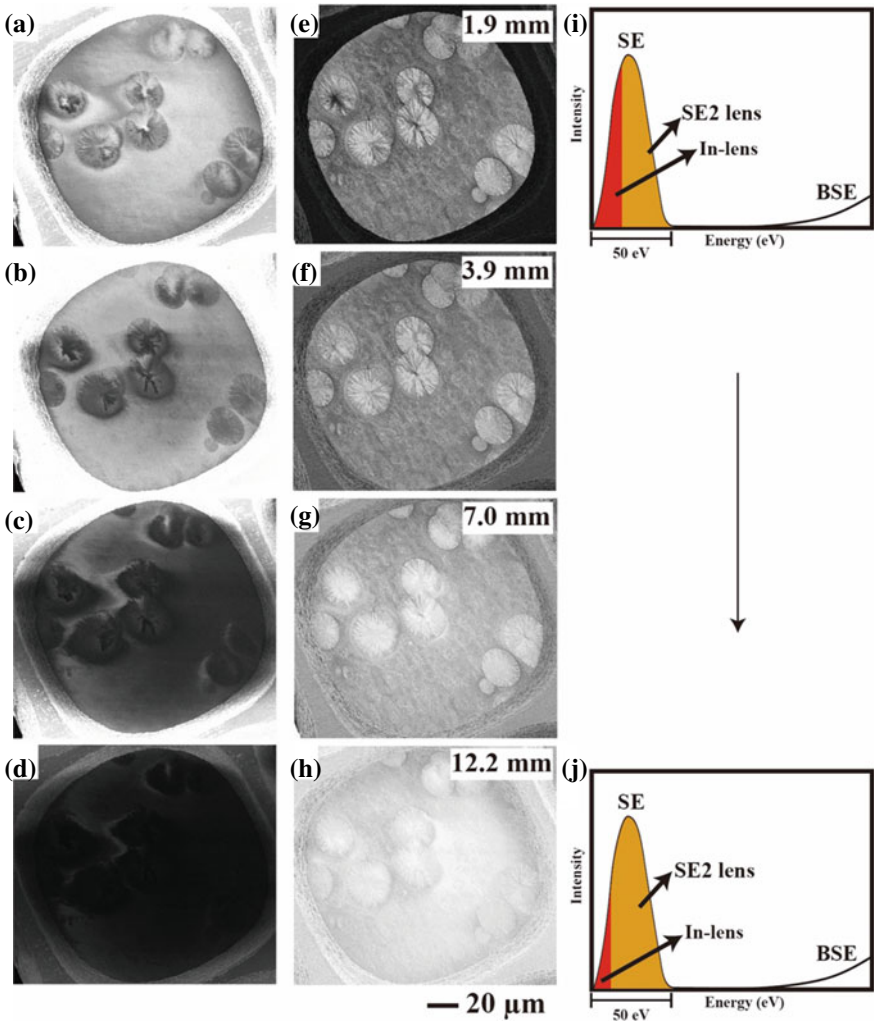


Fig. 62 Energy-filtered SE imaging of a semicrystalline PLA sections stained with RuO₄ with varied working distances: **a–d** in-lens images; **e–h** SE2 images; **i, g** schematic illustration depicting the distribution of SEs into the two detectors when the working distance is 1.9 and 12.2 mm, respectively

2.2 kV (Fig. 63c) resembles the image taken in TEM mode shown in Fig. 15. This means that this SE2 image mainly represents the internal structure of the section based on the difference in atomic composition and not on the surface topological features. The difference in the SE-II yield between RuO₄-stained and unstained areas is reflected in the contrast of the SE2 image shown in Fig. 63.

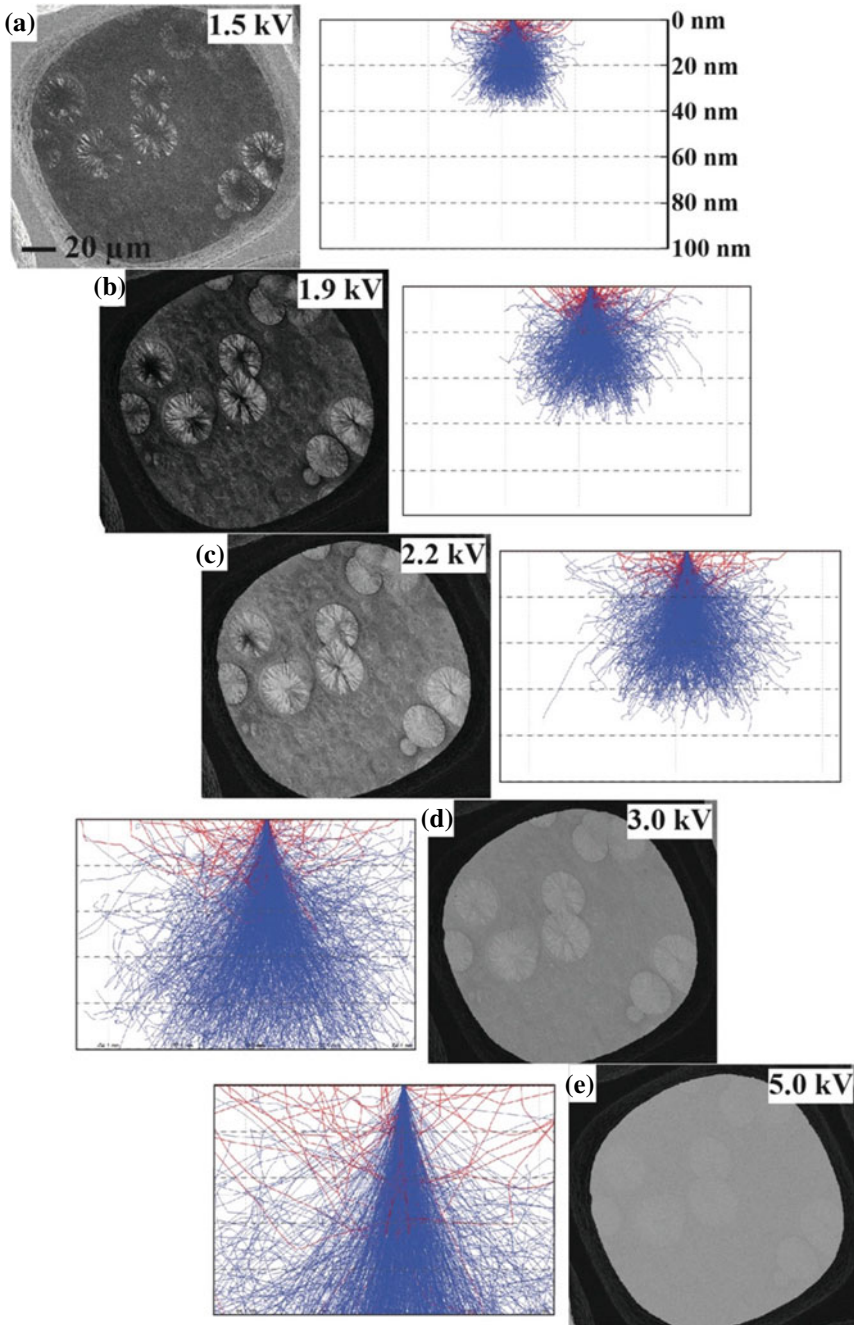


Fig. 63 Acceleration voltage dependence of the contrast in the SE2 images of the PLA thin section. Interaction volumes (blue) and BSEs paths (red) in a 100-nm-thick carbon sample created by Monte Carlo simulation

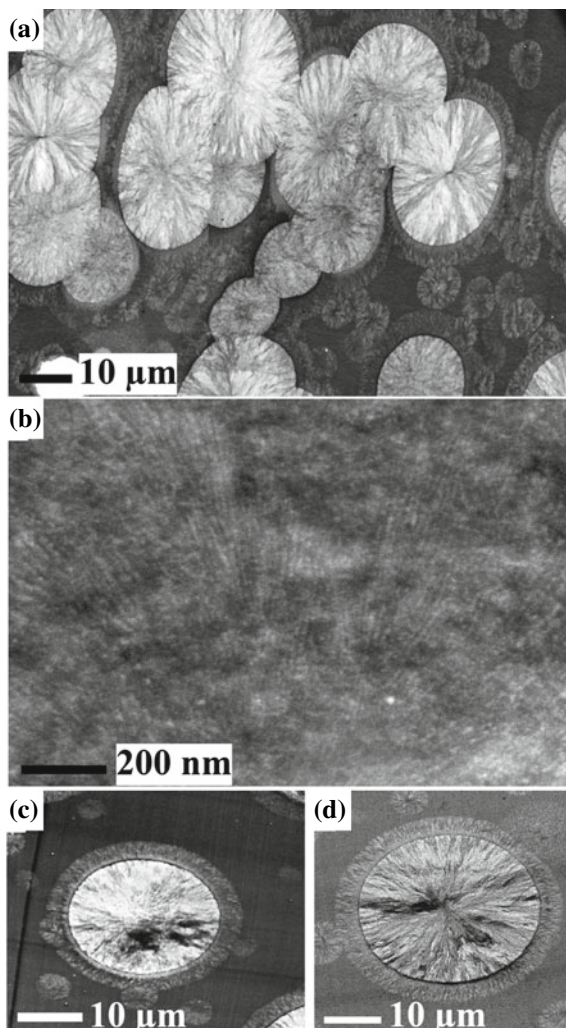
The conditions optimized for the SE imaging of the polymer thin section allow the acquisition of high-quality images of the structures developed within semicrystalline polymers that differ by as much as three orders of magnitude in structural scale, as shown in Fig. 64. One shows the global distribution of spherulites and their textures (Fig. 64a); the other is a high-resolution lamellar structure grown in the spherulites (Fig. 64b). Figure 64c, d shows the images showing the spherulites taken by the SEM and TEM, respectively. Even though the imaging principles are different, those two are similar. Figure 64a exhibits two types of spherulites with different sizes and appearances: One is large, with the typical spherulite texture found in common semicrystalline polymers, and the other is small, with an obscure but definite spherulite pattern, which is also present surrounding the large spherulites. In the former, lamellae are observed inside as shown in Fig. 64b, but not in the latter. We speculate that these two types of spherulites grow at different stages of the crystallization process. The former grows during annealing at a constant temperature in the mold for a certain period, and the latter produces during cooling to room temperature after removal from the mold. Thus, the latter may not have enough lamellae to be observable.

6.2 Correlative Raman Imaging and SEM

Correlative microscopy involves using multiple light or electron microscopy methods to analyze the same specimen area. One such technique is Correlative Raman Imaging and Scanning Electron (RISE) microscopy, which combines SEM and confocal Raman imaging. This correlative microscopy method links ultra-structural surface properties to molecular information. Confocal Raman imaging is a non-destructive spectroscopic method for analyzing molecular structures in a sample. The Raman effect is exhibited when light interacts with the chemical bonds in a material. This interaction causes a specific energy shift in the back-scattered light, which appears in a unique Raman spectrum that can be detected. By combining Raman spectroscopy with a confocal microscope, the confocal Raman imaging technique can detect and image the spatial distribution of chemical components within a sample. This technique can also analyze additional sample characteristics, such as the relative amount of a specific component, stress and strain states, or crystallinity.

RISE microscopy merges the benefits of two imaging methods into a single instrument. This enables the capture of detailed information about both the high-resolution surface structure and the molecular structures of the sample. The instrument automatically transfers and repositions the sample to alternate between the different measurement techniques. The results obtained from each method can be correlated and overlaid to produce composite images (Fig. 65) [125].

Fig. 64 SE2 image showing global spherulite distribution in the RuO₄-stained PLA thin section (a) and in-lens image showing the lamellae in the spherulite (b). c, d Are the spherulites in the PLA thin section taken by SEM and by TEM, respectively



RISE microscopy was performed to investigate an interface formed by adhesive bonding of *i*PP and alkylborane (AB)-initiated acrylic adhesive. As described in Sect. 4 in “Interfacial Phenomena in Adhesion and Adhesive Bonding Investigated by Electron Microscopy” chapter, the bonding mechanism of the surface treatments of *i*PP was investigated. The acrylic adhesive using alkylborane as an initiator yields strong bonding to *i*PP through the chemical reaction between the acrylic monomer and the *i*PP, which produces the acrylate polymers grafted onto the *i*PP main chains at the interface. Figure 66a shows an STEM-BF image showing the interfacial region between the AB-initiated acrylic adhesive and *i*PP by the staining with RuO₄. The radical species produced by the oxidation of alkylborane preferentially attacks the

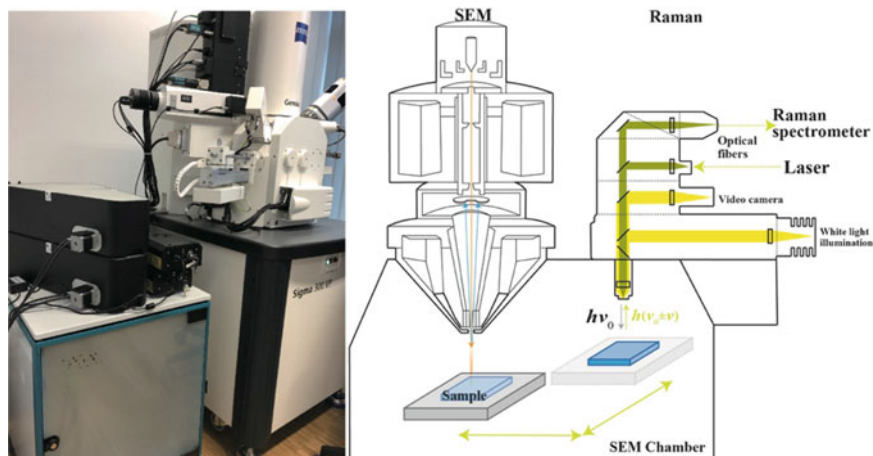


Fig. 65 The appearance of RISE microscope with a combination of SEM (ZEISS Sigma300) and Raman microscope system (WITec) (a) and the principle of its operation (b)

amorphous phase of alkylborane PP and initiates the polymerization of the acrylic monomers. The acrylate monomers erode the amorphous region of *i*PP and initiate graft polymerization onto the lamellae, disrupting the lamellar structure and etching the *i*PP surface. The micrograph shows the three regions: the left side (I) is the *i*PP substrate containing the dispersed rubber domains, the right side (III) is the adhesive layer including the stained small objects that are presumed to be the *i*PP eroded from the *i*PP surface owing to the highly reactive acrylic radicals, and the central part (II) is unknown to be produced as a result of the chemical reaction between *i*PP and the adhesive.

A smooth cross section was prepared by cryoultramicrotomy for analysis with the SEM-Raman system. The sample is first imaged with the SEM microscope to locate the region to be analyzed by the subsequent Raman imaging, as shown in Fig. 66b, showing the three regions as found by STEM. After the SEM measurement, the sample was automatically transferred and re-positioned for confocal Raman imaging within the vacuum chamber of the electron microscope. Then, 240×80 spectra were acquired for an area of $40 \times 20 \mu\text{m}$ with a 532 nm, 14.534 mW laser. The acquisition time for one spectrum is 0.5 s. The spectra extracted from the *i*PP, the adhesive layer, and the rubber domains in the *i*PP are shown in Fig. 66d. Using these three spectra as standard spectra and the MLLS fitting was employed for the acquired individual spectra. By mapping the three components shown in Fig. 66c, region II can be known to be the co-existing layer of *i*PP (red) and adhesive (blue) with no rubber particles (yellow). The dispersed rubber particles of several hundred nanometers can be identified only in the *i*PP substrate (Region I).

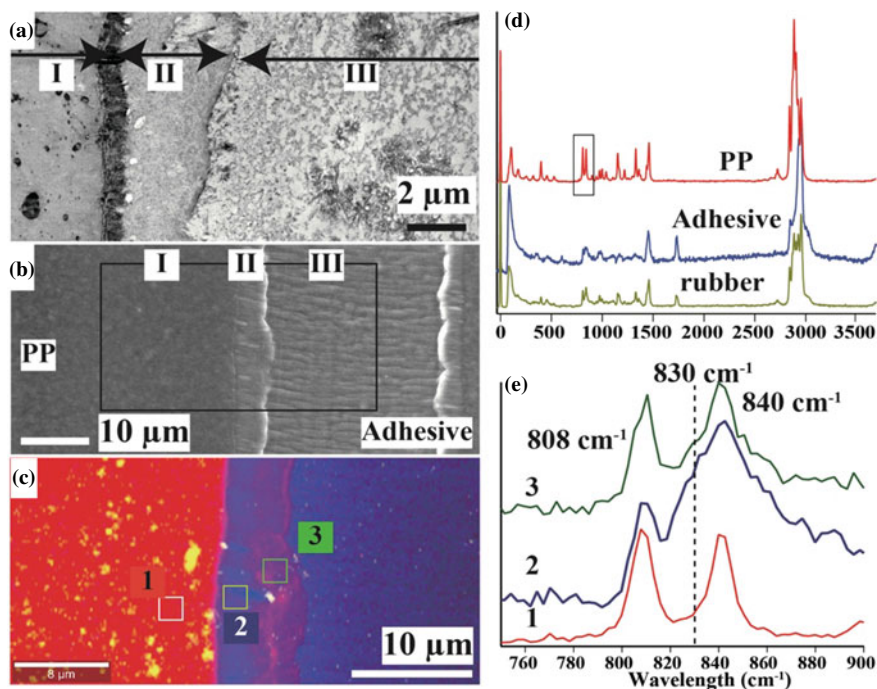


Fig. 66 RISE microscopy analysis of the interfacial region between *i*PP and the alkylborane-initiated acrylic adhesive: **a** STEM-BF image showing the interfacial region by the staining with RuO_4 ; **b** SEM image of the cross section of the interfacial region; **c** Raman image displaying the chemical maps *i*PP (red), adhesive (blue) and rubber (yellow); **d** The corresponding color-coded Raman spectra of the three components for the map; **e** The peaks in the Raman spectra in the region indicated in **d** representing the local crystallinity of *i*PP extracted from the ROIs shown in **c**. The data acquisition was supported by Dr. Ute Schmidt (WITec) and Dr. Fang Zhou (Carl Zeiss)

It is known that confocal Raman spectroscopy makes it possible to evaluate the local crystallinity of *i*PP using the peaks at 808 and 840 cm^{-1} assigned to helical chains and shorter chains within the crystalline phase, respectively, while the peak at 830 cm^{-1} assigned to non-helical amorphous phase [59, 126]. Figure 66e presents the peaks in the Raman spectra corresponding to the local crystallinity of *i*PP extracted from the ROIs indicated in Fig. 66c. The peak at 830 cm^{-1} can be identified as a shoulder of the peak at 840 cm^{-1} in the spectra extracted from ROI-2 and ROI-3. These results indicate that the interfacial chemical reaction between the acrylic monomer and *i*PP produced a thick interfacial layer, including *i*PP with low crystallinity, of which thickness was estimated to be ~ 5 μm . Through RISE microscopy, it is possible to link surface morphology with molecular information. This combination enables new possibilities in comprehensive interface characterization.

7 In Situ TEM

Studying bonding mechanisms and evaluating joint performance requires investigating the failure of interfaces. Optical or scanning electron microscopy has been used to speculate on failure behaviors of joint interfaces, but this classical fractography method has limitations in understanding complicated bonding mechanisms and properties [59, 127, 128]. Direct observation of failure behavior under high-resolution electron microscopy can provide information on complicated failure processes in joint interfaces. A new specimen holder has been developed to perform in situ tensile testing under TEM observation, allowing direct observation of interface failures. This microscopy technique has only been applied to observing deformation and microcrack propagation in metallic and ceramic bulk materials [129–131]. The failure of an adhesive interface between an aluminum alloy (Al5052) and an epoxy adhesive was investigated through the in situ tensile test using this new equipment, visualizing the different stages before the macroscopic failure of the interfaces. Figure 67 shows the specimen holder equipped with a device for the in situ tensile experiments manufactured by Mel-Build Corp. (Fukuoka, Japan). The specimen is mounted on an isolated thin metal cartridge (Fig. 67c). A small device for applying a tensile force to the specimen is built into the tip of the sample holder (Fig. 67a), as illustrated in Fig. 67b. Pushing the cartridge by the actuator with 100 nm/s can open the slit fabricated in the cartridge as shown in Fig. 67d, and tensile load can be applied into the specimen fixed on the slit. The sample used for the experiment is the Al bonded with an epoxy adhesive. 2-mm-thick Al5052 plates were preliminarily treated with sodium hydroxide aqueous solution (pH12) at 60 °C for 10 s and then with nitric acid for 10 s. Those two plates were bonded with an epoxy adhesive, comprising bisphenol-A epoxy and triethylenetetramine (TETA), by curing at 100 °C for 30 min. The in situ experiment used a thin section of 200 μm in length and width and 100 nm in thickness, containing a pre-crack at one end in the center of the specimen. The thin section was cut with a diamond knife by ultramicrotomy. Figure 67e shows an STEM-HAADF image of the slit part, where the specimen is fixed on the slit with the interface aligned parallel to the longitudinal direction of the slit with a width of 20 μm . The mounting of the thin sections floating on water onto the slit of the cartridge is demonstrated in Fig. 68.

Figure 69 displays STEM-HAADF images demonstrating failure at the Al/epoxy adhesive interface. Figure 70 provides a schematic illustration depicting the observed failure behavior of the epoxy/Al adhesive interface under an in situ tensile experiment conducted under STEM observation. The initial pre-crack is visible in Fig. 69a, b through d presents high-magnification images of the early stages of crack initiation. Figure 69e–g shows the zoomed images of Fig. 69b–d, respectively. The damaged zone was found to occur before crack generation at the pre-crack tip in the epoxy side near the interface, which then transformed into a crack and grew toward the Al surface, as seen in Fig. 69f. Once the crack reached the Al surface, it propagated along the interface, resulting in failure. A small amount of adhesive remained on the Al surface after failure, as shown in Fig. 69g. Micro-voids ahead of the crack were also

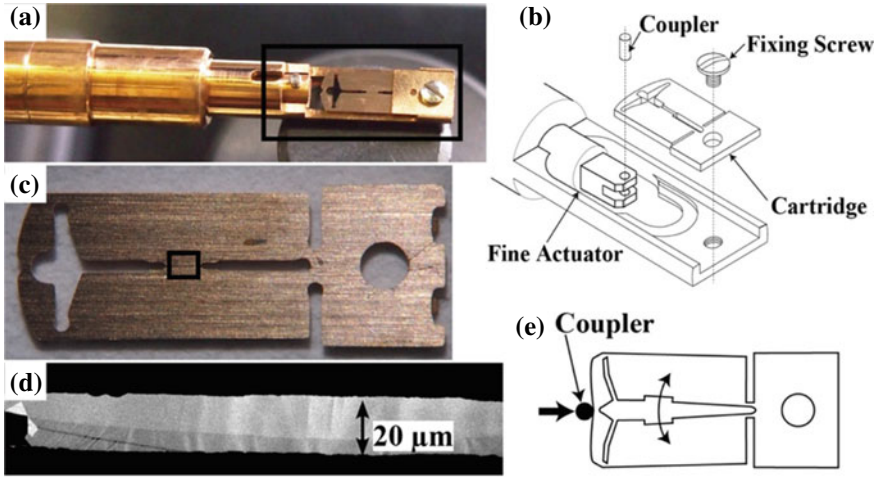


Fig. 67 Nano-order tensile specimen holder for STEM: **a** head part of the specimen holder; **b** illustration of the tensile loading device indicated in **a**; **c** specimen cartridge connected to the fine actuator built in the holder device; **d** illustration representing the deformation of the cartridge to widen the slit by pushing with the coupler; **e** STEM-HAADF image showing the thin section fixed on the slit of the cartridge. Reprinted with permission from Ref. [132]. Copyright 2021, Elsevier. All Rights Reserved

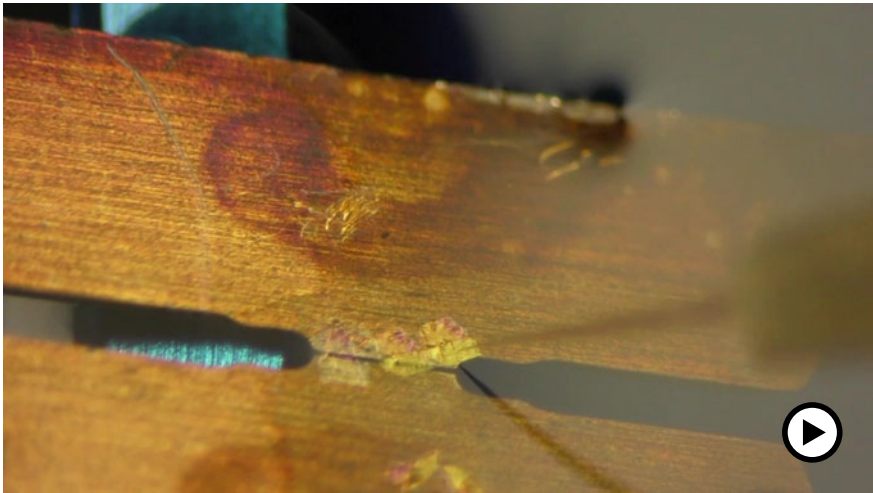


Fig. 68 Video demonstrating the placement of the thin sections on the slit of the cartridge (► <https://doi.org/10.1007/000-ayg>)

produced before crack propagation, as shown in Fig. 69c. The failure process from crack generation to propagation and the final interface failure is displayed in the video in Fig. 71. In Sect. 7 of “Interfacial Phenomena in Adhesion and Adhesive Bonding Investigated by Electron Microscopy” chapter, it is described that the in situ straining in STEM allowed for the dynamic observation of the failure process, including plastic deformation preceding crack initiation, crazing in polymer, micro-voids ahead of the crack, and crack propagation along interfaces [132].

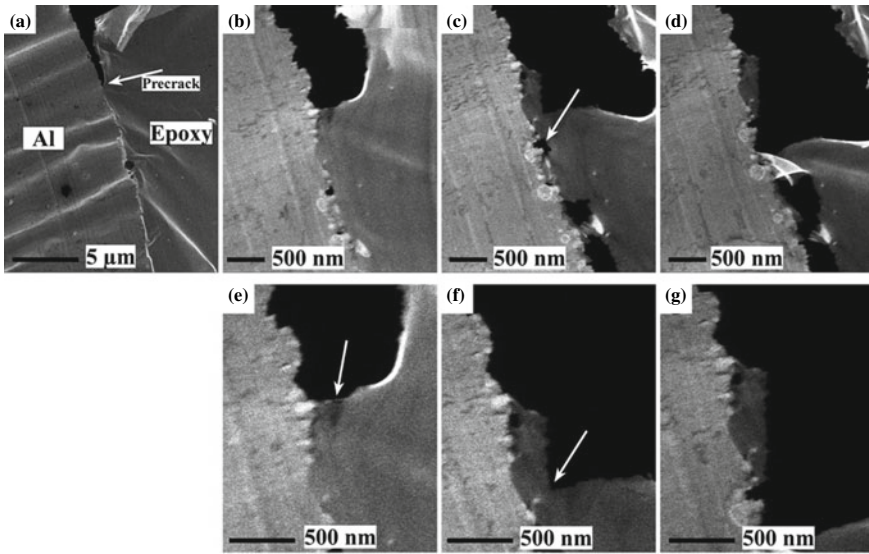


Fig. 69 STEM-HAADF images of the in situ observation of the crack propagation of Al5052/epoxy adhesive interface under tensile loading. The left and the right sides correspond to the Al and adhesive, respectively: **a** shows the interface with pre-crack before applying tensile load. **b–d** Show the failure process at the crack tip. **e–g** Are the high-magnification views of **b–d**, respectively. Reprinted with permission from Ref. [132] Copyright 2021, Elsevier. All Rights Reserved

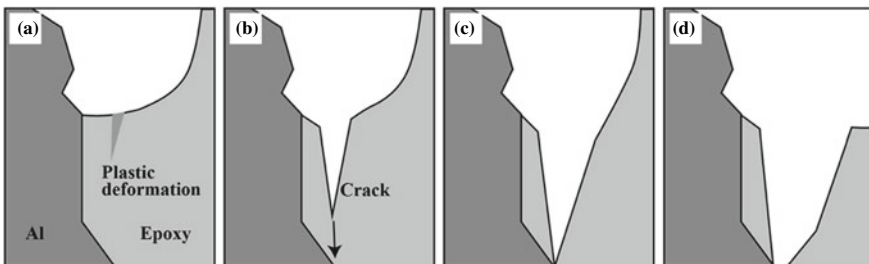


Fig. 70 Schematic illustration presenting the failure behavior of the epoxy/Al adhesive interface as was observed by in situ tensile experiment under the STEM observation

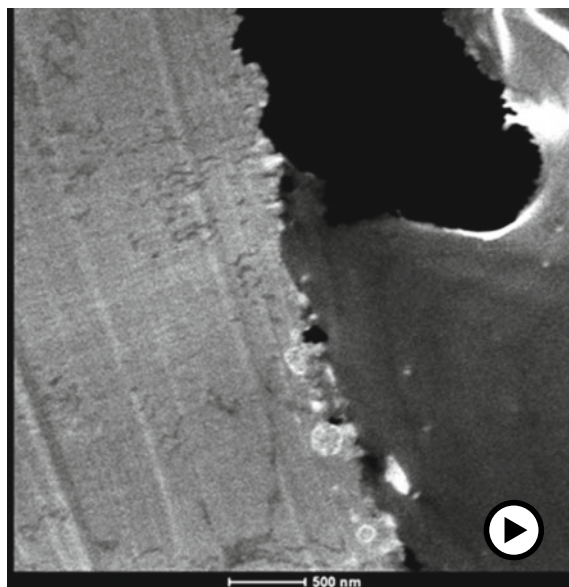


Fig. 71 Video presenting the in situ tensile experiment under STEM observation exhibiting the failure of the interface between Al6061 and an epoxy adhesive (► <https://doi.org/10.1007/000-ayh>)

8 Specimen Damages by Electron Beam Irradiation

Electron beam irradiation poses a significant challenge for investigating polymers, which are highly sensitive to it due to their organic nature. The literature has extensively discussed the effects of irradiation on polymers, with many papers and reviews dedicated to the topic [133]. The primary damage process is inelastic scattering, which results in molecular excitation or ionization. This energy dissipation can produce molecular vibrations (heat) or cause bond scission, such as hydrogen loss and forming radicals. Secondary effects include chain scission or cross-linking, mass loss, reduced crystallinity, and heat generation. The imaging of soft materials has spatial resolution limitations due to radiation damage to the specimens. Unlike the TEM studies of inorganic materials, where the spatial resolution is primarily limited by electron optics, soft-material imaging's resolution limit depends on the total electron dose they can withstand before undergoing structural changes.

The scission of carbon chains and side units can inflict significant damage on polymer specimens, forming low molecular weight molecules and radicals. Aliphatic chains are more prone to C–H bond breakage than aromatic compounds that can dissipate energy through the π -electron system of benzene rings. The low molecular weight molecules and radicals can also lead to reactions with radicals, thermal diffusion, and evaporation of low atomic weight fragmented atoms and molecules like H_2 , CH_4 , CO_2 , and NH_3 . The degradation of PMMA and PS under radiation has been extensively studied, and their degradation schemes have been proposed [134,

135]. PMMA undergoes main-chain scission and pendant unit removal, forming methyl and formyl radicals. Breakage of the main chain causes a decrease in molecular weight, and the low molecular weight PMMA terminal group can be either a C=C double bond or a tertiary radical. In contrast, PS undergoes cross-linking, with breakage of the phenyl ring [136].

Another problem that limits high-resolution imaging and analysis is the specimen contamination induced by electron beam irradiation. When a small specimen area is irradiated, the hydrocarbon molecules are highly prone to diffusion on the surface and subsequent cracking, ultimately leading to fixation by the electron beam. Here, our investigations associated with the specimen damages of polymers by electron beam irradiation are summarized.

8.1 Mass Loss in Polymer Thin Sections

The effect of electron beam irradiation on polymer specimens was studied by evaluating the changes in specimen thickness as a function of dose. The local thickness (t) of the specimen is estimated from an EELS spectrum using the formula:

$$t/\lambda = \ln(I_t/I_0), \quad (4)$$

where I_0 is the area under the zero-loss peak, I_t is the total area beneath the overall spectrum, and λ is the total mean free path for inelastic scattering [137]. Thin polymer films of polymethyl methacrylate (PMMA) and styrene-acrylonitrile random copolymer (SAN), with 40 and 50 nm thicknesses, respectively, were prepared by spin-coating on cleaved NaCl crystals from dilute solutions and transferred onto TEM meshes after lifting off with water. The relative thicknesses t/λ estimated from the EELS spectra are plotted against the radiation dose in Fig. 72 [72]. The films were measured by ellipsometry to determine their thicknesses. The figure indicates that the specimens with the same thickness irradiated at room temperature and 120 K exhibit quite different relative thicknesses. Their relative thicknesses were estimated from the EELS spectra. The results indicate that the PMMA and SAN films show lower relative thicknesses when irradiated at room temperature than at 120 K. The thicknesses of the films irradiated at room temperature remain almost constant with the increase in dose, while those irradiated at 120 K gradually decrease in thickness. This suggests that the degradation process causing a mass loss in the specimen is completed at a significantly lower dose at room temperature, whereas cooling the specimen retards the degradation process. The results also show that PMMA tends to degrade much faster than SAN.

The study suggests that cryogenic conditions effectively retard radiation damage but cannot prevent the damage completely. This experiment shows that electron beam irradiation should be minimized, even in cryogenic conditions, to avoid the damaging effect on polymer specimens.

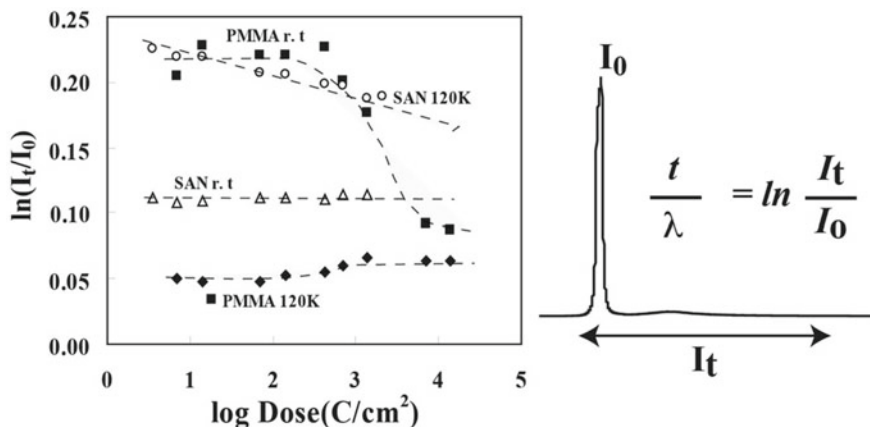


Fig. 72 The plot of the relative thicknesses of PMMA and SAN films versus the irradiation dose at room temperature and 120 K. Reprinted with permission from Ref. [72]. Copyright 2005, John Wiley & Sons. All Rights Reserved

Cooling the specimen results in a cage or frozen-in effect, which is the most effective way of reducing secondary processes at low temperatures. In some instances, cooling can increase the likelihood of scission products recombining or cross-linking before leaving the specimen. Nonetheless, primary processes remain unaffected by temperature and cannot be prevented by cooling the specimen.

8.2 Chemical Damages of Polymers Evaluated by ELNES

As mentioned in Sect. 5.2, the C K-edges of polymers contain ELNES that sensitively reflect chemical structures such as aromatic, carbonyl, ether, and methyl groups. Changes in the structure of molecules can be detected by their influence on the ELNES. O K-edges of the oxygen-containing polymers also exhibited the ELNES features that were sensitive to the polyester's chemical structures. The elimination of the particular peak in the O K-edge ELNES reflects the resistivity of the polymers against the dose of the electron beam, as shown in Fig. 39. To investigate chemical damage caused by electron beam irradiation in polymer specimens, C K-edge ELNES of several polymers was acquired under different acquisition conditions by varying the acquisition time and point-to-point distance in STEM-SI mode at 200 kV. Figure 73 displays the C K-edge ELNES of aromatic (left column) and non-aromatic (right column) polymers. The measurements were carried out in a cryogenic condition at 110 K with a beam size of 0.74 nm and a beam current of 0.293 nA. 10×10 spectra were acquired and summed up into one spectrum with the acquisition time for one spectrum of 100 ms. Therefore, the exhibited spectra are the average of 100 spectra. Two spectra are shown for each polymer acquired with long (black)

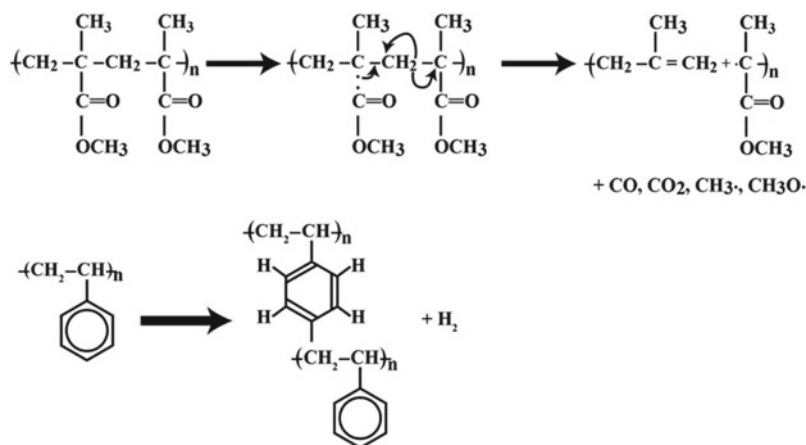
and short (red) point-to-point distances with an acquisition time of 100 ms for one spectrum.

The presence of oxygen in PET and PBT leads to an increase in the number of peaks when compared to saturated polyolefins. PBT and PET bond assignments can be carried out using previously reported EELS results [103]. When the point-to-point distance is 50 nm, the first and most prominent peak at 286 eV is assigned to the π^* C=C transition in the phenyl ring. The second and third peaks at 289 ± 0.5 and 292 ± 0.5 eV, respectively, are assigned to the π^* C=O transitions and the σ^* C–O transition. The peak assigned to the π^* C=O transition can also be detected as a broad shoulder in the poly(benzyl methacrylate) (PBzMA). The second and third peaks are eliminated when the point-to-point distance is decreased to 2 nm. A broad peak at around 287–288 eV is generated instead, indicating that the spectral acquisition at the narrow interval significantly caused chemical damage to the polymers. It is known that both chain scission and cross-linking occur when PET undergoes electron beam damage [138]. It has been said that intramolecular dehydrogenation occurs, leading to carbonyl group rearrangement.

PS contains a phenyl pendant group on every alternating carbon in the main hydrocarbon chain. The first peak at around 285 eV is a signature of π^* transition in the phenyl group. According to the radiation damage mechanism shown in Scheme 3, PS undergoes cross-linking, which changes the environment of the main-chain C–C bonds. The damage effect can be seen in the spectral features associated with the first peak assigned to the π^* C=C transition, which becomes broader and shifts to lower energy.

PC and PPO show the peak at 288.0 eV in addition to the intense peak at 286.0 eV assigned to the π^* C=C transition in the phenyl ring, which is attributed to the σ^* C–H transition in the methyl groups. This ELNES feature can be identified in the spectra taken with a 50 nm point-to-point distance. In contrast, with the narrow interval of 10 nm, the peak in PPO eliminates, suggesting that the methyl groups attached to the phenyl ring are lost due to the scission of the bonds. As observed in PS, the π^* C=C transition at 286 eV becomes broader and shifts to lower energy in PPO. It is therefore suggested that the phenyl rings are cross-linked after removing the methyl groups. Polyphenylene sulfide (PPS) exhibits no peak elimination and shifts with minor changes in the peak heights by decreasing the spectral acquisition interval. Therefore, PPS is the highest resistivity against electron beam irradiation among the polymers evaluated in this study.

The C K-edge ENLEs of PMMA and poly(*tert*-butyl methacrylate) (*Pt*BuMA) show similar features. The first peak at 285 is a characteristic of π^* C=C transition. Since no such bond is present, this spectral feature implies degradation under the electron beam, as shown in Scheme 2. The second peak at 289.5 eV is a signature of the carbonyl group. For PMMA, we observed slight increases and decreases in the peak heights at 286 ± 0.5 and 289 ± 0.5 eV, respectively, and no dramatic changes due to the reduced acquisition intervals. In contrast, for *Pt*BuMA, the peak at 286 eV is enlarged and the peak at 289.5 eV disappears. These results suggest that acquiring damage-free C K-edge ELNES for both methacrylate polymers is challenging.



Scheme 3 The degradation processes of PMMA and PS under electron beam irradiation

Polyethylene and PP are fully saturated and therefore expected to display relatively simple C K-edges. These two polymers are structurally different due to a methyl group on every other carbon atom. EELS measurements of PE and PP reveal that the processed spectra can be decomposed into three peaks for each polymer. The first peak at 285.0 eV in both polymers corresponds to the π^* C=C transition. These unsaturated bonds are created due to electron beam damage during irradiation. The second peak at 288.5 ± 1 is attributed to the σ^* C-H transition. The third peak at 292.0 eV in both polymers is associated with the σ^* C-C transitions. Under beam irradiation, the second peak disappears and the height of the π^* C=C transition peak increases.

POM showed two distinct peaks at 288 and 291.5 eV when the point-to-point distance is 40 nm. These peaks can be assigned to σ^* C-H and σ^* C-C transitions, respectively, according to X-ray absorption spectroscopy (NEXAFS) of polyethylene oxide [139]. The characteristic peaks are unfortunately eliminated by the reduction of the acquisition interval to the spectra to 2 nm and only the peak of the π^* C=C transition at 286 eV can be seen as a result of the damage.

As discussed in Sect. 5.2, ELNES phase mapping in STEM-SI mode is a powerful technique for imaging polymer nanostructures. To improve the spatial resolution of the mapping, the acquisition of EEL spectra should be performed with a distance between points as small as possible. The results indicate that the ELNES features of the C K-edge are lost when the distance is less than 10 nm. Therefore, phase mapping using C K-edge ELNES in polymers is challenging.

8.3 Electron-Induced Contamination

The spatial resolution has limits in the imaging of soft materials, mainly due to radiation damage. Additionally, specimen contamination can cause a loss of resolution, which is especially pronounced when imaging soft materials. This contamination manifests as a carbonaceous layer deposited on the specimen surface due to electron bombardment. The contamination arises from the hydrocarbons present in the TEM chamber that react with the electron beam to form hydrocarbon ions that condense and form a carbon-rich, polymerized film on the irradiated area. Figure 74a shows contamination spots created on a thin carbon foil by an electron beam with an intensity of 5.6×10^4 el/nm s at an accelerating voltage of 200 kV. The thickness of the contamination spots can be estimated using EELS, as shown in Fig. 74b. As the irradiation period increased, the intensity of the zero-loss peak decreased, but the overall intensities in the energy-loss regions of the spectra increased. The thickness (D) of the contamination can be estimated using Eq. (4). The thickness of the contamination rises and reaches about 600 nm with 10 min of irradiation.

Hydrocarbons in a TEM chamber can come from various sources, such as vacuum pump oils, outgassing specimens, or poor vacuum practices. Even with ultra-high vacuum conditions, some sources of contamination can remain and cannot be easily removed. Carbon is a principal element in organic compounds, and utilizing carbon ionizations in ESI and EELS could result in higher data-collection efficiency.

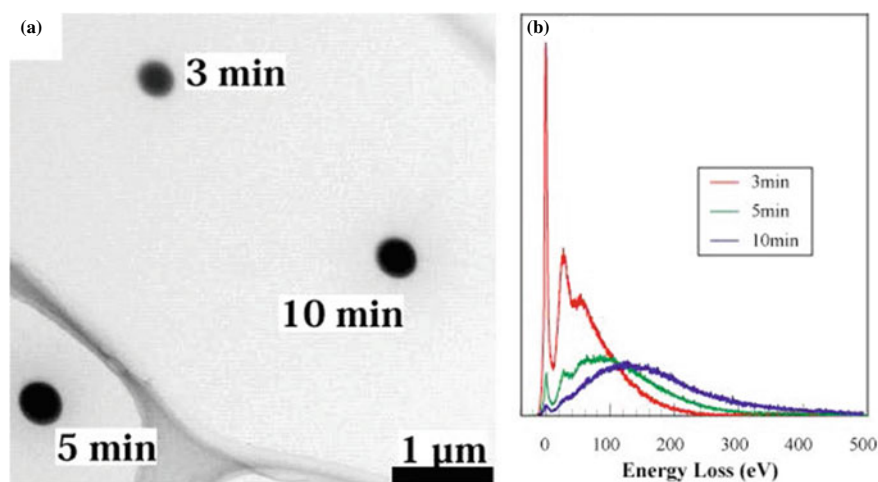


Fig. 74 The electron beam, with an intensity of 5.6×10^4 el/nm s, resulted in the production of beam-induced specimen contamination on a carbon thin foil through irradiation: **a** TEM micrograph showing the contamination spots created by irradiation for 3, 5, and 10 min; **b** EELS spectra acquired from the contamination spots. Reprinted with permission from Ref. [140] Copyright 2009, American Chemical Society. All Rights Reserved

However, the presence of specimen contamination leads to the formation of carbon-rich deposits in areas of interest, which disrupts carbon analysis and imaging of the specimen.

A process for cleaning the TEM chamber has been developed, utilizing activated oxygen radicals [140]. To achieve this, a low-temperature plasma generator (Evac-tron 45, XEI Scientific, Inc., USA) was installed on one of the accessory ports near the specimen chamber, as shown in Fig. 75a. The device produces oxygen radicals from the air, which can chemically etch the contaminants from the interior of a vacuum chamber [141]. The oxygen radicals oxidized hydrocarbons and other organic compounds, forming volatile oxides that can be easily pumped out of the TEM chamber. The plasma was confined within the generator chamber, preventing ion bombardment damage to the microscope. This device has also been used successfully to clean SEM. The oxygen radicals were carried by convection flow from the plasma into the specimen chamber and then toward the roughing pump. Although using a plasma generator to produce oxygen radicals could clean a TEM chamber's interior, it was ineffective in reducing beam-induced specimen contamination. This is because the narrow vacuum path of the TEM doesn't allow enough oxygen radicals to enter the chamber through the roughing pump alone. To overcome this limitation, an additional pumping system was installed at the objective aperture port (see Fig. 75b). This system created a viscous flow of oxygen radicals that reacted with hydrocarbons in the chamber atmosphere and surfaces. To clean the chamber, a high-frequency power of 10 Watts was applied to generate plasma using room air as the feed gas. The chamber was gently cleaned for 3 min, and then nitrogen gas was purged to flush out the reactant products. This cleaning/purging cycle was repeated 20 times while maintaining a pressure of 0.4 torr at the objective aperture port.

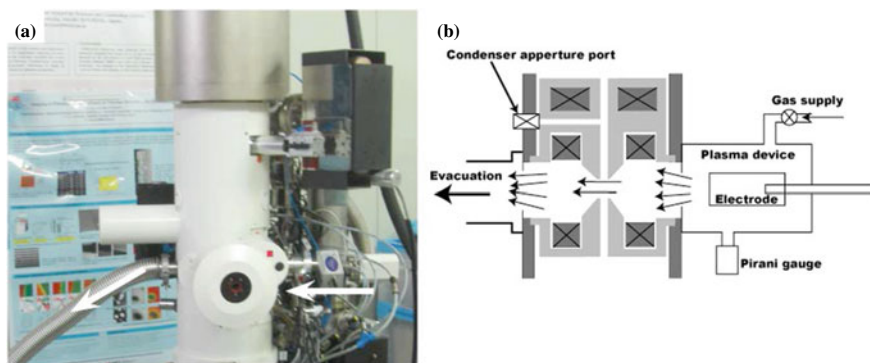


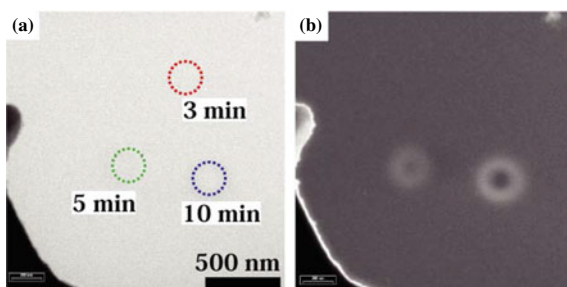
Fig. 75 Cleaning of a TEM chamber using a compact plasma generator: **a** A picture displaying the plasma generator installed on an accessory port near the specimen chamber. Arrows indicate the direction of the flow of activated oxygen radicals; **b** Schematic illustration shows the flow of activated oxygen radicals in the TEM chamber. Reprinted with permission from Ref. [140] Copyright 2009, American Chemical Society. All Rights Reserved

After cleaning, we observed no signs of contamination even after exposing the electron beam for 30 min without using an anticontamination device. Figure 76 depicts contamination spots formed on a plasma-polymerized thin osmium tetroxide (OsO_4) film. Due to the carbon-rich nature of the contamination, the non-carbon supporting film presents the contamination as high-contrast areas. However, the contamination spots are thin and barely discernible in the zero-loss image (Fig. 76a). However, they can be slightly enhanced when viewed as an energy-filtered image at the 50 ± 10 eV energy loss (Fig. 76b).

Through gentle chemical cleaning of the specimen chamber with activated oxygen radicals, we can achieve a “contamination-free TEM”. To demonstrate the benefits of this approach, we investigated the structure of a single polymer layer immobilized on the surface of a silica nanoparticle (SiNP), as depicted in Fig. 77. The surface initiator (2-bromo-2-methyl) propionyloxyhexyltriethoxysilane (BHE) was immobilized on the SiNP surface. Then poly(2-methacryloyloxyethyl phosphorylcholine) (PMPC) was grafted onto the BHE-immobilized SiNP using surface-initiated atom-transfer radical polymerization. The hydrodynamic radius of the PMPC-immobilized SiNP (PMPC-SiNP) in water was estimated at 48.1 nm using dynamic light scattering. The dimensions of the PMPC polymer chains immobilized on SiNP are much larger than those of the corresponding free polymer, indicating that the PMPC chains form a “polymer brush” where the radially oriented chains stretch perpendicularly against the silica surface [142]. We obtained a PMPC-SiNP distribution on an OsO_4 thin film, where only the SiNPs were visible.

Figure 78a, b exhibits images of a single PMPC-SiNP particle obtained by the ESI technique, capturing an individual particle with energy losses of 270 ± 10 and 315 ± 10 eV, respectively, corresponding to pre- and post-edge images for the carbon K-edge at 285 eV. The contrast change observed beyond the carbon K-edge indicates the presence of the PMPC brush layer surrounding the SiNP. Using “contamination-free TEM”, it is possible to observe the polymer chains extending from the SiNP surface. Comparing the two images, it is apparent that the pre-edge image (Fig. 78a) shows only the silica particle. In contrast, the post-edge image (Fig. 78b) reveals the complete PMPC-SiNP structure. Figure 78c displays intensity profiles of the gray value measured along a horizontal line across the center of the SiNP. The pre-edge image’s profile (green line) shows an SiNP diameter of around 20 nm, while the post-edge image’s profile (red line) estimates the PMPC brush thickness at approximately

Fig. 76 Contamination marks produced on an OsO_4 thin film after cleaning recognized in zero-loss image (a) and energy-filtered image at 50 ± 10 eV (b). Reprinted with permission from Ref. [140]. Copyright 2009, American Chemical Society. All Rights Reserved



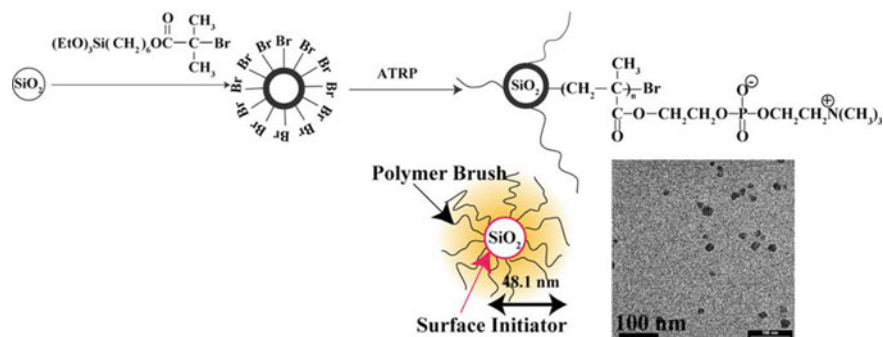


Fig. 77 Synthesis process of PMPC brushes on SiNPs, an illustration of the PMPC-SiNPs brush structure, and a global TEM image that displays the distribution of PMPC-SiNPs on an OsO_4 thin film. Reprinted with permission from Ref. [140]. Copyright 2009, American Chemical Society. All Rights Reserved

40 nm. The intensity profile from the post-edge image also shows two peaks at the SiNP edge, representing the bright ring surrounding the SiNP, which is believed to be the surface initiator (BHE) immobilized on the SiNP surface. Therefore, the surface initiator can be differentiated from the polymer brush layer, and its thickness can be estimated at approximately 5 nm.

The polymer brushes to modify inorganic surfaces have improved materials' dispersion, wetting, and adhesion properties, making them a promising method for industrial development. In the context of EFTEM analysis of polymers, carbon is more accessible to detect than other light elements due to its high concentration. As a result, images with a high signal-to-noise ratio can be obtained with lower electron doses compared to other elements. This suggests that EELS carbon analysis with

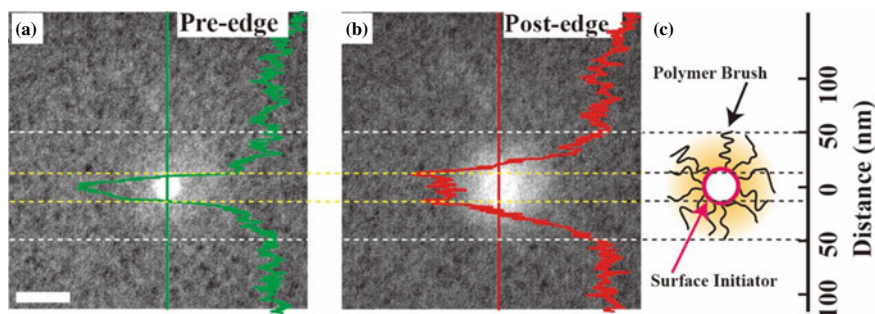


Fig. 78 The intensity profiles of pixels measured by taking horizontal lines across the center of the PMPC-SiNP in pre-edge (a) and post-edge (b) images. The red and green lines represent the profiles obtained from the respective images. An illustration depicting the hypothesized structure, featuring the initiator and polymer brush portions, is also provided (c). The scale bar corresponds to 50 nm. Reprinted with permission from Ref. [140]. Copyright 2009, American Chemical Society. All Rights Reserved

the high spatial resolution has the potential to advance the field of nano-analysis for soft materials. Additionally, contamination-free TEM can assist in various analytical techniques that require extended exposure times, such as electron tomography, EELS, and nanobeam diffraction.

9 Conclusions

This chapter provided an overview of electron microscopy techniques to investigate the interfaces present in polymeric materials and adhesive bonds. The basic components of EFTEM, STEM, and SEM instruments and EELS and EDX spectroscopy principles were explained. To perform the techniques, it is necessary to prepare artifact-free specimens. Ultramicrotomy is preferred for making thin sections of polymers and polymer/metal interfaces. The use of FIB should be limited to the samples that are difficult to cut by ultramicrotomy, such as composite materials containing large amounts of carbon fibers and inorganic fillers. Advanced electron microscopy techniques such as STEM-EDX tomography, ELNES phase mapping, energy-filtered SE imaging, and in situ tensile TEM were also introduced with the applications to the surface and interface characterizations of polymer alloys and composites, crystalline polymer, adhesive bonds, and metal substrates. Polymers are particularly sensitive to electron beam irradiation. This is a significant problem for polymer analysis by electron microscopy, especially for EELS. Scission of chemical bonds and cross-linking by electron beam irradiation cannot be avoided. It should be noted that imaging and analysis of polymers at high spatial resolution is limited due to structural changes upon electron beam irradiation rather than instrumental performance. In the next chapter, these electron microscopy techniques are used to discuss interfacial phenomena and mechanisms of adhesion and adhesive bonding.

Acknowledgements SH thanks Mr. Hideki Hakukawa, Ms. Yuri Shigemto, Dr. Takeshi Hanada, Dr. Kazunori Kawasaki, Dr. Yida Liu, Dr. Lingyun Lyu (AIST), Prof. Yongjin Li (Hangzhou Normal University), and Prof. Yonggui Liao (Huazhong University of Science and Technology) for their contribution to the works described in this chapter. Parts of the work were commissioned by JST-Mirai Program Grant Number JPMJMI18A2, Japan (Sects. 5.2, 7, and 8.3) and by the New Energy and Industrial Technology Development Organization (NEDO) Grant Numbers JPNP16010, Japan (Sects. 5.1.2 and 5.3.2) and JPNP20005, Japan (Sect. 5.5.3).

References

1. J. van den Brand, P.C. Snijders, W.G. Sloof, H. Terryn, J.H.W. de Wit, *J. Phys. Chem. B* **108**, 6017–6024 (2004)
2. S. Horiuchi, N. Terasaki, M. Itabashi, *Manuf. Rev.* **7**, 11 (2020)
3. K. Shimizu, C. Phanopoulos, R. Loenders, M.L. Abel, J.F. Watts, *Sur. Interface Anal.* **42**, 1432–1444 (2010)

4. M.L. Abel, J.F. Watts, *Surf. Interface Anal.* **41**, 508–516 (2009)
5. H. Téllez, J.M. Vadillo, J.J. Laserna, *Rapid Commun. Mass Spectrom.* **23**, 2357–2362 (2009)
6. T.N. Zittberg, J.D. Wolf, P.S. Wang, *J. Mater. Sci.* **23**, 1745–1747 (1988)
7. P.M.A. Sherwood, *Surf. Sci. Spectra* **5**, 1–3 (1998)
8. H. Dunlop, M. Benmalek, *J. Phys. IV* **7**, C6-163–C6-174 (1997)
9. M. Amstutz, M. Textor, *Surf. Interface Anal.* **19**, 595–600 (1992)
10. A. Kurian, S. Prasad, A. Dhinojwala, *Langmuir* **26**, 17804–17807 (2010)
11. T. Miyamae, H. Nozoye, *Appl. Phys. Lett.* **85**, 4373–4375 (2004)
12. J. van den Brand, O. Blajiev, P.C.J. Beentjes, H. Terryn, J.H.W. de Wit, *Langmuir* **20**, 6318–6326 (2004)
13. P. Taheri, J.R. Flores, F. Hannour, J.H.W. de Wit, H. Terryn, J.M.C. Mol, *J. Phys. Chem. C* **117**, 3374–3382 (2013)
14. B. Salgin, O. Özkanat, J.M.C. Mol, H. Terryn, M. Rohwerder, *J. Phys. Chem. C* **117**, 4480–4487 (2013)
15. R.J. Composto, E.J. Kramer, *J. Mater. Sci.* **26**, 2815–2822 (1991)
16. E.L. Jablonski, R.E. Gorga, B. Narasimhan, *Polymer* **44**, 729–741 (2003)
17. T.P. Lodge, *Phys. Rev. Lett.* **83**, 3218–3221 (1999)
18. P.F. Nealey, R.E. Cohen, A.S. Argon, *Macromolecules* **26**, 1287–1292 (1993)
19. R.J. Composto, E.J. Kramer, *Macromolecules* **25**, 4167–4174 (1992)
20. E. Kim, W.C. Wu, P.D. Garrett, *Polymer* **35**, 5706–5715 (1994)
21. E. Kim, E.J. Kramer, J.O. Osby, *Macromolecules* **28**, 1979–1989 (1995)
22. R.J. Composto, E.J. Kramer, *Polymer* **31**, 2320–2328 (1990)
23. P.F. Green, B.L. Doyle, *Macromolecules* **20**, 2471–2474 (1987)
24. N.C. Stoffel, C.A. Dai, E.J. Kramer, T.P. Russell, V. Deline, W. Volksen, W. Wu, S. Satija, *Macromolecules* **29**, 6880–6891 (1996)
25. M. Sferrazza, C. Xiao, R.A.L. Jones, D.G. Bucknall, J. Webster, J. Penfold, *Phys. Rev. Lett.* **78**, 3693–3696 (1997)
26. D.G. Bucknall, S.A. Butler, J.S. Higgins, *Macromolecules* **32**, 5453–5456 (1999)
27. B.B. Sauer, D.J. Walsh, *Macromolecules* **24**, 5948–5955 (1991)
28. J. Klein, *Science* **250**, 640–646 (1990)
29. T.E. Shearmur, A.S. Clough, D.W. Drew, M.G.D. van der Grinten, R.A.L. Jones, *Macromolecules* **29**, 7269–7275 (1996)
30. T.E. Shearmur, A.S. Clough, D.W. Drew, M.G.D. van der Grinten, R.A.L. Jones, *Phys. Rev. E* **55**, R3840–3843 (1997)
31. N. Clarke, F.R. Colley, S.A. Collins, L.R. Hutchings, R.L. Thompson, *Macromolecules* **39**, 1290–1296 (2006)
32. H. Qiu, M. Bousmina, *Macromolecules* **33**, 6588–6594 (2000)
33. M. Bousmina, H. Qiu, M. Grmela, J.E. Klemberg-Sapieha, *Macromolecules* **31**, 8273–8280 (1998)
34. S.E. Harton, T. Koga, F.A. Stevie, T. Araki, H. Ade, *Macromolecules* **38**, 10511–10515 (2005)
35. S. Hüttenbach, M. Stamm, G. Reiter, M. Foster, *Langmuir* **7**, 2438–2442 (1991)
36. G.A. O’Neil, J.M. Torkelson, *Macromolecules* **30**, 5560–5562 (1997)
37. J.P.S. Farinha, O. Vorobyova, M.A. Winnik, *Macromolecules* **33**, 5863–5873 (2000)
38. A. Ohshima, A. Yamagata, T. Sato, A. Teramoto, *Macromolecules* **32**, 8645–8654 (1999)
39. G. Dlubek, J. Pionteck, V. Bondarenko, G. Pompe, C. Taesler, K. Petters, R. Krause-Rehberg, *Macromolecules* **35**, 6313–6323 (2002)
40. S. Wang, E.D. von Meerwall, S.Q. Wang, A. Halasa, W.-L. Hsu, J.P. Zhou, R.P. Quirk, *Macromolecules* **37**, 1641–1651 (2004)
41. K.E. Price, S.J. Broadwater, A.R. Bogdan, I. Keresztes, J.L. Steinbacher, D.T. McQuade, *Macromolecules* **39**, 7681–7685 (2006)
42. L. Reimer (ed.), *Energy-Filtering Transmission Electron Microscopy* (Springer, Berlin, 1995), pp. 347–400
43. R. Brydson, *Electron Energy Loss Spectroscopy* (Taylor and Francis, London and New York, 2006), pp. 39–58

44. M. Kociak, O. Stéphan, M.G. Wall, M. Ténce, C. Colliex, in *Scanning Transmission Electron Microscopy, Imaging and Analysis*, ed. by S.J. Pennycook, P.D. Nellist (Springer, 2011), pp. 163–206
45. R. Pal, A.K. Sikder, K. Saito, A.M. Funston, J.R. Bellare, *Polym. Chem.* **8**, 6927–6937 (2017)
46. F. Hofer, P. Warbichler, in *Transmission Electron Energy Loss Spectroscopy in Material Science and the EELS ATLAS*, 2nd edn, ed. by C. Ahn (Wiley-VCH, Weinheim, 2004), p. 159
47. R. Brydson, *Electron Energy Loss Spectroscopy* (Taylor and Francis, London and New York, 2001), pp. 79–96
48. S. Horiuchi, Y. Liu, T. Hanada, A. Akiyama, *Appl. Surf. Sci.* **599**, 153964 (2022)
49. R. Leapman, in *Transmission Electron Energy Loss Spectrometry in Materials Science and the EELS ATLAS*, ed. by C.C. Ahn (Wiley-VCH, Weinheim, Germany, 2004), pp. 49–96
50. L.C. Sawyer, D.T. Grubb, G.F. Meyers, *Polymer Microscopy*, 3rd edn. (Chapman and Hall, London, 2008), pp. 146–160
51. G.H. Michler, *Electron Microscopy of Polymers* (Springer, Berlin, 2008), pp. 199–217
52. L.C. Sawyer, D.T. Grubb, G.F. Meyers, *Polymer Microscopy*, 3rd edn. (Chapman and Hall, London, 2008), pp. 160–180
53. J.S. Trent, J.I. Scheinbeim, P.R. Couchman, *Macromolecules* **16**, 589–598 (1983)
54. S. Horiuchi, N. Matchariyakul, K. Yase, T. Kitano, *Macromolecules* **30**, 3664–3670 (1997)
55. L.A. Giannuzzi, F.A. Stevie (eds.), *Introduction to Focused Ion Beams* (Springer, Berlin, 2005)
56. N.J. Severs, *Nat. Protoc.* **2**, 547–576 (2007)
57. J.A. Zasadzinski, J. Schneir, J. Gurley, V. Elings, P.K. Hansma, *Science* **239**, 1013–1015 (1988)
58. A. Igarashi, T. Terasawa, M. Kanie, T. Yamanobe, T. Komoto, *Polym. J.* **37**, 522–528 (2005)
59. Y. Liu, Y. Shigemoto, T. Hanada, T. Miyamae, K. Kawasaki, S. Horiuchi, *A.C.S. Appl. Mater. Interfaces* **13**, 11497–11506 (2021)
60. R. Brydson, *Electron Energy Loss Spectroscopy* (Taylor and Francis, London and New York, 2001), p. 46
61. L. Reimer, in *Energy-Filtering Transmission Electron Microscopy*, 1st edn, ed. by L. Reimer (Springer, Berlin, 1995), p. 383
62. R. Brydson, *Electron Energy Loss Spectroscopy* (Taylor and Francis, London and New York, 2001), pp. 101–109
63. K.H. Körtje, *Scanning Microsc.* **8**, 22 (1994)
64. S. Abolhas Sani-Dadras, G.H. Vázquez-Nin, O.M. Echeverría, S. Fakan, *J. Microsc.* **183**, 215–222 (1996)
65. P.J. Thomas, P.A. Midgley, *Ultramicroscopy* **88**, 179–186 (2001)
66. S. Horiuchi, T. Hamanaka, T. Aoki, T. Miyakawa, R. Narita, H. Wakabayashi, *J. Electron. Microsc.* **52**, 255–266 (2003)
67. S. Horiuchi, T. Fujita, T. Hayakawa, Y. Nakao, *Langmuir* **19**, 2963–2973 (2003)
68. S. Horiuchi, T. Hayakawa, *Angew. Chem. Int. Ed.* **42**, 2285–2289 (2003)
69. M.R. Krejsa, J.L. Koenig, in *Rubber Technology Handbook*, ed. by N.P. Cheremisinoff (CRC Press, Boca Raton, Florida, 1993), p. 476
70. S. Horiuchi, H. Dohi, *Langmuir* **22**, 4607–4614 (2006)
71. H. Dohi, S. Horiuchi, *Polymer* **48**, 2526–2530 (2007)
72. S. Horiuchi, D. Yin, T. Ougizawa, *Macromol. Chem. Phys.* **206**, 725–731 (2005)
73. S. Goossens, B. Goderis, G. Groeninckx, *Macromolecules* **39**, 2953–2963 (2006)
74. G.A. Buxton, N. Clarke, *Macromolecules* **38**, 8929–8938 (2005)
75. J.B. Nephew, T.C. Nihei, S.A. Carter, *Phys. Rev. Lett.* **80**, 3276–3279 (1998)
76. Q. Tran-Cong, A. Harada, *Phys. Rev. Lett.* **76**, 1162–1165 (1996)
77. H. Furukawa, *J. Phys. Soc. Jpn.* **63**, 3744–3750 (1994)
78. A. Harada, Q. Tran-Cong, *Macromolecules* **30**, 1643–1650 (1997)
79. K. Kimura, H. Inoue, S.I. Kohama, Y. Yamashita, Y. Sakaguchi, *Macromolecules* **36**, 7721–7729 (2003)
80. E. Girard-Reydet, J.P. Pascault, *Macromolecules* **33**, 3084–3091 (2000)

81. W. Li, A.J. Ryan, I.K. Meier, *Macromolecules* **35**, 5034–5042 (2002)
82. V. Rebizant, A.S. Venet, F. Tournilhac, E. Girard-Reydet, C. Navarro, J.P. Pascault, L. Leibler, *Macromolecules* **37**, 8017–8027 (2004)
83. S. Swier, B. Van Mele, *Macromolecules* **36**, 4424–4435 (2003)
84. Y. Ishii, A.J. Ryan, *Macromolecules* **33**, 158–166 (2000)
85. R.W. Venderbosch, H.E.H. Meijer, P.J. Lemstra, *Polymer* **35**, 4349–4357 (1994)
86. J. Nunoshige, Y. Shibasaki, M. Ueda, *Chem. Lett.* **36**, 238–239 (2007)
87. Y. Liao, S. Horiuchi, J. Nunoshige, H. Akahoshi, M. Ueda, *Polymer* **48**, 3749–3758 (2007)
88. A.E. Coode, A.E. Porter, M.M. Klosowski, M.P. Ryan, S. Heutz, D.W. McComb, *Curr. Opin. Solid State Mater. Sci.* **21**, 55–67 (2017)
89. W. Dong, H. Hakukawa, N. Yamahira, Y. Li, S. Horiuchi, *ACS Appl. Polym. Mater.* **1**, 815–824 (2019)
90. Y. Liu, A.L. Hamon, P. Haghi-Ashtiani, T. Reiss, B. Fan, D. He, J. Bai, A.C.S. Appl. Mater. Interfaces **8**, 34151–34158 (2016)
91. J. Bertho, V. Stolojan, M.L. Able, J.F. Watts, *Micron* **41**, 130–134 (2010)
92. G. Radtke, G.A. Botton, in *Scanning Transmission Electron Microscopy: Imaging and Analysis*, ed. by S.J. Pennycook, P.D. Nellist (Springer, Berlin, 2011), pp. 207–245
93. R. Arenal, F. de la Peña, O. Stéphan, M. Walls, M. Tencé, A. Loiseau, C. Colliex, *Ultramicroscopy* **109**, 32–38 (2008)
94. J. Scott, P.J. Thomas, M. MacKenzie, S. McFadzean, J. Wilbrink, A.J. Craven, W.A.P. Nicholson, *Ultramicroscopy* **108**, 1586–1594 (2008)
95. J. Bodynko, I. Maclaren, A.J. Craven, *Ultramicroscopy* **149**, 9–20 (2015)
96. F. Voisard, N. Brodusch, M.L. Trudeau, H. Demers, K. Zaghib, R. Gauvin, *Microsc. Microanal.* **24**, 464–465 (2018)
97. D.R. Paul, J.W. Barlow, H. Keskkula, in *Encyclopedia of Polymer Science and Engineering*, vol. 1, 2, 2nd edn., ed. by J.I. Kroschwitz (Wiley, New York, 1988)
98. W. Baker, C. Scott, G.H. Hu, *Reactive Polymer Blending* (Hanser Publisher, Munich, 2001), pp. 1–279
99. S. Wu, H.-K. Chung, *J. Polym. Sci. Polym. Phys.* **24**, 148–169 (1986)
100. Z. Fu, H. Wang, X. Zhao, S. Horiuchi, Y. Li, *Polymer* **132**, 353–361 (2017)
101. U. Sundararaj, C.W. Macosko, *Macromolecules* **28**, 2647–2657 (1995)
102. B. Schaffner, L. Spillner, P.J. Thomas, *Microsc. Microanal.* **25**, 648–649 (2019)
103. R. Pal, L. Bourgeois, M. Weyland, A.K. Sikder, K. Saito, A.K. Funstron, J.R. Bellare, *ACS Omega* **6**, 23934–23942 (2021)
104. J. Frank, *Electron Tomography* (Springer, New York, 2006)
105. P. Ercius, O. Alaidi, M.J. Rames, *Adv. Mater.* **27**, 5638–5663 (2015)
106. H. Jinnai, Y. Shinbori, T. Kitaoka, *Macromolecules* **40**, 6758–6764 (2007)
107. M. Weyland, P.A. Midgley, *Mater. Today* **7**, 32–40 (2004)
108. R.D.J. De, A. Klug, *Nature* **217**, 130–134 (1968)
109. R.G. Hart, *Science* **159**, 1464–1467 (1968)
110. P.A. Midgley, R.E. Dunin-Borkowski, *Nat. Mater.* **8**, 271–280 (2009)
111. R. Brydson, *Electron Energy Loss Spectroscopy* (Taylor & Francis, London & New York, 2001), p. 60
112. P.A. Midgley, M. Weyland, *Ultramicroscopy* **96**, 413–431 (2003)
113. G. Möbus, R.C. Doole, B.J. Inkson, *Ultramicroscopy* **96**, 433–451 (2003)
114. S.M. Collins, P.A. Midgley, *Ultramicroscopy* **180**, 133–141 (2017)
115. T.J.A. Slater, A. Janssen, P.H.C. Camargo, M.G. Burke, N.J. Zaluzec, S.J. Haigh, *Ultramicroscopy* **162**, 61–73 (2016)
116. P. Burdet, Z. Saghii, A.N. Filippin, A. Borrás, P.A. Midgley, *Ultramicroscopy* **160**, 118–129 (2016)
117. L. Lyu, T. Hanada, N. Yamahira, J. Morita, R. Yamamoto, K. Itomi, T. Adachi, S. Kubouchi, S. Horiuchi, *J. Appl. Polym. Sci.* **138**, e51443 (2021). <https://doi.org/10.1002/app.51443>
118. H. Hoefelt, P. Schwaab, *X-Ray Spectrom.* **17**, 201–208 (1988)

119. R. Sundar, P. Ganesh, R.K. Gupta, G. Raghendra, B.K. Pant, V. Kain, K. Ranganathan, R. Kaul, K.S. Bindra, *Lasers Manuf. Mater. Process.* **6**, 421–463 (2019)
120. A. Fukuda, H. Matsukawa, H. Goto, M. Suzuki, M. Nakamoto, R. Matsumoto, H. Utsunomiya, T. Tanaka, *Mater. Trans.* **56**, 1852–1856 (2015)
121. P. Ganesh, R. Sundar, H. Kumar, R. Kaul, K. Ranganathan, P. Hedaoo, P. Tiwari, L.M. Kukreja, S.M. Oak, S. Dasari, G. Raghavendra, *Opt. Laser. Eng.* **50**, 678–686 (2012)
122. L. Reimer, *Scanning Electron Microscopy*, 2nd edn. (Springer, Berlin, 1998), p. 164
123. K. Kumagai, T. Sekiguchi, *Ultramicroscopy* **109**, 368–372 (2009)
124. R. Rasch, A. Stricher, R.W. Truss, *J. Appl. Polym. Sci.* **131**, 39572 (2014)
125. O. Hollricher, U. Schmidt, S. Breuninger, *Microsc. Today* **22**, 36–39 (2014)
126. U. Schmidt, J. Muller, J. Koenen, *Confocal Raman Microscopy*, 2nd edn., ed. by J. Toporski, T. Dieing, O. Hooricher (Springer, Berlin, 2011), pp. 487–492
127. S. Horiuchi, A. Nakagawa, Y. Liao, *Macromolecules* **41**, 8063–8071 (2008)
128. S. Horiuchi, H. Hakukawa, Y.J. Kim, H. Nagata, H. Sugimura, *Polym. J.* **48**, 473–479 (2016)
129. Y. Wang, Z. Guo, R. Ma, G. Hao, Y. Zhang, J. Lin, M. Sui, *Prog. Nat. Sci.* **24**, 121–127 (2014)
130. Z.Q. Feng, Y.Q. Yang, Y.X. Chen, B. Huang, M.S. Fu, M.H. Li, J.G. Ru, *Mater. Sci. Eng. A* **586**, 259–266 (2013)
131. A. Nie, H. Wang, *Mater. Lett.* **65**, 3380–3383 (2011)
132. S. Horiuchi, Y. Liu, Y. Shigemoto, T. Hanada, K. Shimamoto, *Inter. J. Adhes. Adhes.* **117**(Part B), 103003 (2022)
133. L. Reimer, *Transmission Electron Microscopy*, 4th edn. (Springer, Berlin, 1997), pp. 463–493
134. K. Varlot, J.M. Martin, D. Gonbeau, C. Quet, *Polymer* **40**, 5691–5697 (1999)
135. K. Varlot, J.M. Martin, C. Quet, *Micron* **32**, 371–378 (2001)
136. K. Varlot, J.M. Martin, C. Quet, *J. Microsc.* **191**, 187–194 (1998)
137. R. Brydson, *Electron Energy Loss Spectroscopy* (Taylor and Francis, London and New York, 2001), pp. 59–68
138. L. Bourgeois, M. Weyland, A.K. Sikder, K. Saito, A.M. Funston, J.R. Bellare, *Polym. Chem.* **11**, 5484–5492 (2020)
139. J. Kikuma, B.P. Tonner, *J. Electron. Spectrosc. Relat. Phenom.* **82**, 53–60 (1996)
140. S. Horiuchi, T. Hanada, M. Ebisawa, Y. Matsuda, M. Kobayashi, A. Takahara, *ACS Nano* **3**, 1297–1304 (2009)
141. R. Vane, V. Carlino, *Microsc. Microanal.* **11**, 900–901 (2005)
142. Y. Matsuda, M. Kobayashi, M. Annaka, K. Ishihara, A. Takahara, *Langmuir* **24**, 8772–8778 (2008)

Open Access This chapter is licensed under the terms of the Creative Commons Attribution 4.0 International License (<http://creativecommons.org/licenses/by/4.0/>), which permits use, sharing, adaptation, distribution and reproduction in any medium or format, as long as you give appropriate credit to the original author(s) and the source, provide a link to the Creative Commons license and indicate if changes were made.

The images or other third party material in this chapter are included in the chapter's Creative Commons license, unless indicated otherwise in a credit line to the material. If material is not included in the chapter's Creative Commons license and your intended use is not permitted by statutory regulation or exceeds the permitted use, you will need to obtain permission directly from the copyright holder.



Interfacial Phenomena in Adhesion and Adhesive Bonding Investigated by Electron Microscopy



Shin Horiuchi

Abstract Using electron microscopy techniques described in Chap. 2, we investigate interfacial phenomena in adhesion and adhesive bonding. Polymer–polymer interfaces formed via interdiffusion are visualized and characterized by EFTEM. Fractographic studies using high-resolution SEM investigate entanglements at the polymer–polymer interfaces, and the adhesion mechanism is discussed about the interfacial entanglements. The effect of surface treatments of polymers for adhesion improvement is studied in terms of the surface roughness and the chemical functionality of the adherend created by the surface pretreatments. We then describe the role of chemical interactions between polymers and metals on bonding by the analysis of fracture surfaces by the STEM-replica technique. Bonding mechanisms of adhesive bonding and recently developed direct bonding of metal and plastic are also investigated by STEM-EELS/ELNES and STEM-tomography. Finally, we evaluate the toughness and durability of adhesive joints between metal and carbon fiber reinforced plastics (CFRP) and discuss the durability of the adhesive bonding.

Keywords Adhesion · Bonding · Interface · Diffusion · Entanglement · Fracture · Electron microscopy · EELS · EDX · Tomography

Supplementary Information The online version contains supplementary material available at https://doi.org/10.1007/978-981-99-4456-9_3. The videos can be accessed individually by clicking the DOI link in the accompanying figure caption or by scanning this link with the SN More Media App.

S. Horiuchi (✉)

Research Laboratory for Adhesion and Interfacial Phenomena (AIRL), National Institute of Advanced Industrial Science and Technology (AIST), 1-1-1, Higashi, Tsukuba 305-8565, Ibaraki, Japan

e-mail: s.horiuchi@aist.go.jp

© The Author(s) 2024

S. Horiuchi et al. (eds.), *Interfacial Phenomena in Adhesion and Adhesive Bonding*, https://doi.org/10.1007/978-981-99-4456-9_3

1 Visualization of Homopolymer/Random Copolymer Interfaces by EFTEM

Polymer interdiffusion is important for both fundamental research [1–3] and practical applications, such as adhesion, welding, coating, and laminated films. The success of these applications depends on the interfacial layer's entanglement structure formed via inter-chain penetration during the interdiffusion process. Although Transmission Electron Microscopy (TEM) is a potential tool for polymer material morphology characterization, it requires heavy metal staining to obtain sufficient phase contrasts due to the low yields of elastically scattered electrons in organic polymer specimens. However, heavy metal staining may alter the original structure. Therefore, an alternative technique with high spatial resolution, real space observation, non-toxic preprocessing, and no limitations on specimen geometry could be a promising approach to studying polymer interdiffusion.

We employ energy-filtering transmission electron microscopy (EFTEM) for the development of advanced applications of TEM for the investigation of polymer structures. Interfaces formed via diffusion of dissimilar polymers were characterized by transmission electron microscopy (TEM) equipped with an imaging filter [4–7]. A type of microscope known as Energy Filtering TEM (EFTEM) allows for the acquisition of images showing the two-dimensional intensity distribution of inelastically scattered electrons within a given energy-loss range [8]. This Electron Spectroscopic Imaging (ESI) technique allows for mapping chemical elements with almost the same resolution as TEM.

In this study, we examine the adhesion and interfaces created between poly(methyl methacrylate) (PMMA) and styrene-acrylonitrile random copolymers (SAN). This system helps explore the correlation between adhesion and interfacial thickness because the miscibility between PMMA and SAN can be adjusted by the acrylonitrile (AN) content in SAN. The “repulsive effect” of random copolymers, which causes highly favorable interactions between its blends with homopolymers, affects the miscibility of blends with homopolymers. SAN possesses positive and negative interaction parameters, χ , depending on the AN content in SAN [9]. Flory–Huggins χ parameter describes the excess free energy of mixing and governs phase behaviors of polymer blends. The χ parameter of homopolymer (A)/random copolymer (B) blends, where copolymer B is composed of monomers C and D, is expressed by Eq. (1), where φ is the composition of homopolymer A. The high segmental repulsive effect in the random copolymer, which gives a high positive χ_{CD} , results in a negative χ_{AB} value.

$$x_{AB} = \varphi x_{AC} + (1 - \varphi)x_{AD} - \varphi(1 - \varphi)x_{CD}. \quad (1)$$

Figure 1a shows the χ_{AB} values as a function of AN content in SAN calculated by three groups, indicating that PMMA is miscible with SAN containing 10–35 wt% AN [9, 10]. Figure 1b is a phase diagram of the blend of PMMA and SAN with 33 wt% AN content, showing a lower critical solution temperature (LCST)-type phase diagram [11]. Thus, various interfacial situations can be created by adjusting the SAN composition and annealing temperature in this system. EFTEM is employed to visualize the interfacial formations between PMMA/SAN while varying the AN content in SAN. The PMMA and SAN plates were prepared by compression molding between silicon wafers at 150 °C to create smooth-surfaced sheets. The PMMA/SAN laminates were annealed in the air under slight pressure at 140 °C for 2 h to ensure contact between the plates. After the specimens were quenched to room temperature to terminate the interdiffusion, they were cut into thin sections of approximately 50 nm thickness perpendicularly to the interface using ultramicrotomy. To aid in focus adjustment during TEM operation and drift correction for element mapping, 10 nm diameter gold nanoparticles were spread onto the thin sections by dropping a thin gold colloid solution onto them.

To perform the imaging and spectral recording, we use an in-column energy-filtering transmission electron microscope with a LaB₆ cathode and an Omega-type energy filter at an accelerating voltage of 200 keV. A 2 K × 2 K slow-scan CCD camera records the energy-filtered images and ELES spectra, and 512 × 512-pixel images are acquired by summing up 4 × 4 pixels into one effective pixel to gain sensitivity. All observations are performed cryogenically at 120 K to minimize radiation damage to the specimens.

This study aims to generate high spatial-resolution oxygen and nitrogen maps. When two polymers are thermodynamically immiscible, their interface has a thickness in the nanometer range. To examine such thin interfaces using EFTEM,

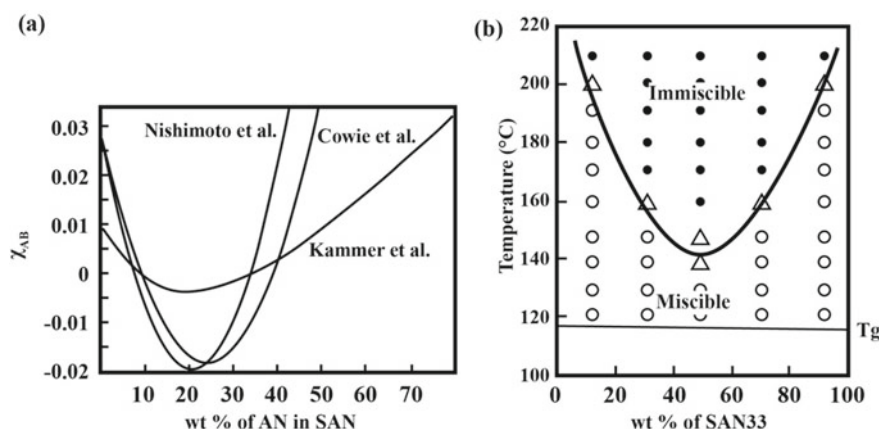


Fig. 1 AN content dependence of χ parameter of PMMA/SAN blends (a) and phase diagram of PMMA/SAN33 (b)

improving the spatial resolution and quantitiveness of elemental maps is necessary. Image-EELS techniques and elemental mapping to visualize the interfaces are used for that purpose. Elemental mapping relies on the fact that each core-loss edge of an EELS spectrum occurs at an energy characteristic of a particular chemical element. Extracting elemental information for mapping requires separation from the background (BG), which is superimposed on the core-loss edge due to plural scattering. The two-window and three-window methods are utilized to calculate the BG components [12]. In the three-window process, the BG curve is estimated by assuming power law (2) or exponential law (3) dependences using the two energy windows (E_1 and E_2), where the factors A and r are calculated pixel by pixel from the signals $S(E_1)$ and $S(E_2)$.

Power law

$$S(E) = A \cdot E^{-r} \quad (2)$$

Exponential law

$$S(E) = A \cdot \exp(-r \cdot E) \quad (3)$$

In this study, we perform Image-EELS to obtain EELS spectra from small areas with arbitrary shapes and locations in an image [7, 13–15]. As illustrated in Fig. 2, tens of energy-filtered images are recorded sequentially across a broad energy loss range to build a three-dimensional dataset containing spatial information $I(x, y)$, acquired in parallel, and spectral information $I(E)$, which is recorded serially. The average gray values of the same pixels are calculated in each energy-filtered image across the whole range of acquired images, giving an EELS spectrum from a chosen region in the image. A typical condition for Image-EELS is an energy width of 5 eV and an energy increment of 4 eV. A series of energy-filtered images sequentially across a broad energy loss range is taken with such a condition. The images are acquired, for example, with magnification at 50,000 and the acquisition time for each image of 5 s. These images are stacked and extracted the intensities at the same pixel in each image across the series to construct an EELS spectrum by plotting the intensities against the corresponding energy loss values. To correct the drift of the specimen, the individual images have to be shifted pixelwise over the entire acquired images.

To enhance the quality of elemental maps, it is essential to increase the signal-to-noise ratio (SNR). A method to achieve this is by utilizing the three-window approach, which involves selecting suitable widths and energetic positions for elemental mapping. In this particular investigation, Image-EELS is utilized to pick energy windows and background fitting methods for elemental maps that covered the nitrogen and oxygen K-edges. The interfacial region of the PMMA/SAN laminate is imaged by applying an energy loss range of 350–600 eV, while the zero-loss image, which lacks specific features and has low contrast, is not suitable for focus adjustment. Instead, the focus can be adjusted on gold nanoparticles located outside of the interfacial region to avoid damage from radiation. EELS spectra are generated

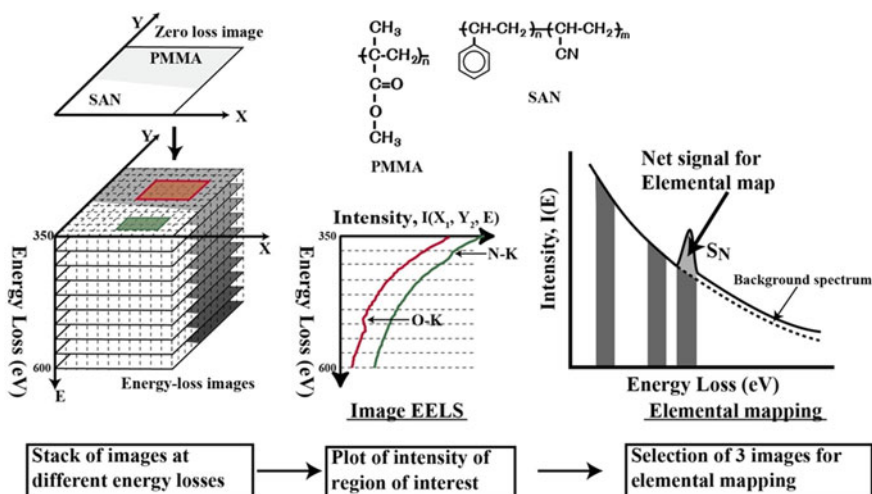


Fig. 2 The procedure for the creation of EELS spectra and elemental maps from the stack of energy-filtered images by Image-EELS

from the PMMA and the SAN regions by utilizing a series of images collected using Image-EELS. The nitrogen and oxygen ionization edges are noticeable at approximately 400 and 530 eV, respectively. Based on these spectra, energy windows for the core-loss image and background images for curve fittings can be determined appropriately. As illustrated in Fig. 3b, the exponential law is more effective in fitting the background curves compared to the power law.

Figure 3c and d display the nitrogen maps generated using the two-window and three-window methods, respectively. The two-window method provides a nitrogen map with better clarity and higher SNR than the three-window method. This is due to the higher statistical fluctuation of inelastically scattered images compared to elastically scattered images, as inelastic scattering has a lower cross section. However, in the nitrogen map produced by the two-window method, the gold nanoparticles are still present, whereas they are eliminated in the nitrogen map created using the three-window method. This inaccuracy in the two-window map can be attributed to the dissimilar slopes of the background curves for the polymer and the gold nanoparticles. In contrast, the three-window method computes the background curves on a pixel-by-pixel basis, which accurately subtracts the background contribution from the core-loss image. Therefore, for precise elemental mapping analysis, the three-window method should be utilized. Additionally, the successful removal of 10 nm gold nanoparticles in the elemental map confirms that the map has a spatial resolution exceeding 10 nm.

A range of energy-filtered images is taken from the region around the interface of the sample that is annealed for 2 h at 140 °C, with energy losses ranging from 350 to 600 eV. Next, spectra are extracted from the areas with 10 nm in diameter

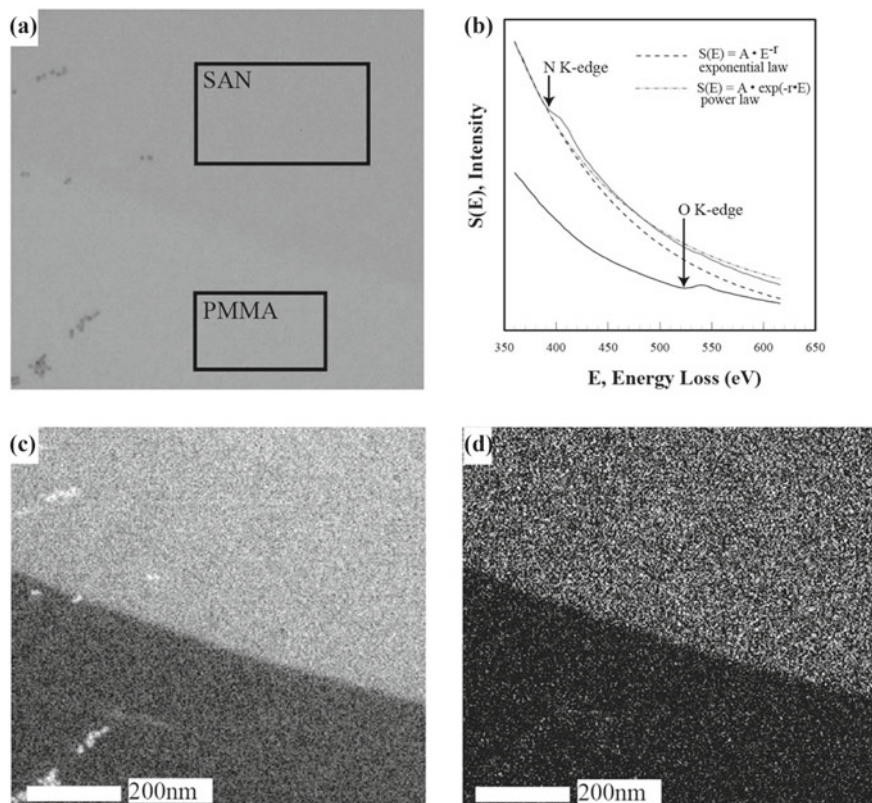


Fig. 3 Zero-loss image of the PMMA/SAN laminate annealed at 160 °C (a) and Image-EELS spectra (b) obtained from the regions shown in (a) with BG fitting curves for the nitrogen K-edge calculated by the exponential and power laws (b). Nitrogen maps created by the two-window (c) and the three-window exponential (d) methods. Reprinted with permission from [16]. Copyright 2005 John Wiley & Sons. All Rights Reserved

arranged across the interface, as presented in Fig. 4a. The nitrogen and oxygen K-edges are observed in areas 2 and 4, respectively, from which spectroscopy analysis of the interfacial region is performed with a spatial resolution exceeding 10 nm. In Fig. 4b, the nitrogen and oxygen K-edges are displayed after curve fitting based on the exponential law and background (BG) intensity subtraction. The width of the region where both polymers coexist was estimated to be approximately 65 nm.

In the next step, the interfacial regions are analyzed by elemental mapping—three suitable images for nitrogen and oxygen maps from the stack of energy-filtered images obtained by Image EELS. The energy windows, including the nitrogen and oxygen ionization edges, are chosen from the spectra and the BG fitting method. We select one pre-edge image close to the ionization edges and another with a broad energy range for a safer fit. An energy window for the core-loss image is determined to yield a high signal-to-noise ratio (SNR) elemental map. The concept

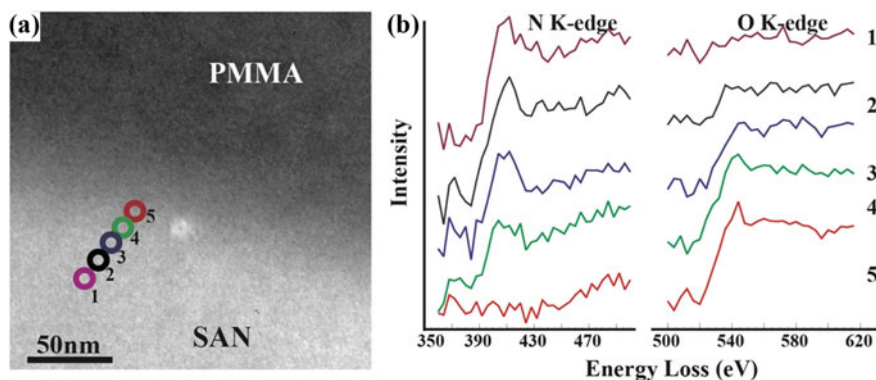


Fig. 4 Structure-sensitive image at 250 ± 10 eV energy loss of the PMMA/SAN laminate annealed at 140°C (a). Image-EELS spectra of the nitrogen and the oxygen K-edges after subtracting the BG contributions (b) acquired from the regions marked in (a). Reprinted with permission from [16]. Copyright 2005 John Wiley & Sons. All Rights Reserved

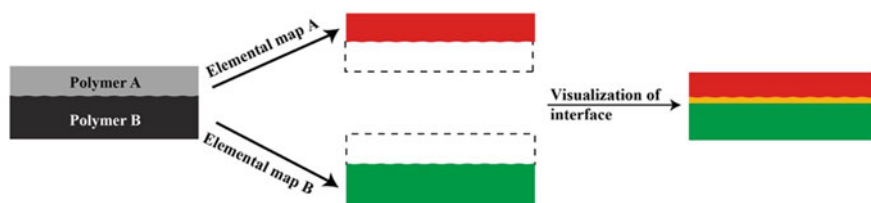


Fig. 5 Visualization of an interface by the simple RGB technique with two elemental maps

for the visualization of an interface is shown in Fig. 5. Using the RGB (red–green–blue) method, one of the basic color components represents the nitrogen map (green). In contrast, the oxygen map is represented in red. Combining the two maps displays the interfacial area as yellow due to the overlap of green and red pixels.

Figure 6's top section displays the RGB-composition images formed from the nitrogen (red) and oxygen (green) maps of the lamination of PMMA and SAN with varying AN content. Figure 6a, b and c correspond to the laminations containing 29, 34, and 40 wt% AN contents, respectively. The intensity profiles along the lanes highlighted in the maps are presented underneath their corresponding images (middle part). These profiles show the intensity variations in the nitrogen and oxygen maps across the interfaces and their ratios (O/N). The images and the profiles reveal that the interfacial width increased as the AN content decreased. Using Image-EELS, EELS spectra are generated from the spots on the interfacial regions. The nitrogen and oxygen core-loss peaks obtained after the background subtraction are shown in the bottom part. The intensity of the nitrogen core-loss peaks gradually decreases from left to right in their images, whereas the opposite trend is seen for the oxygen core-loss peaks. This result confirms that the pixel intensities in the elemental maps

represent the elemental concentrations. Although the two original intensity profiles are noisy and fluctuating, smooth curves with reduced noises are obtained from their ratios. These ratios allow us to estimate the interfacial widths: approximately 130, 50, and 20 nm for SAN29, 34, and 40, respectively. This finding indicates that the fluctuation in the original profiles of the specimens is due to variations in the specimen thickness.

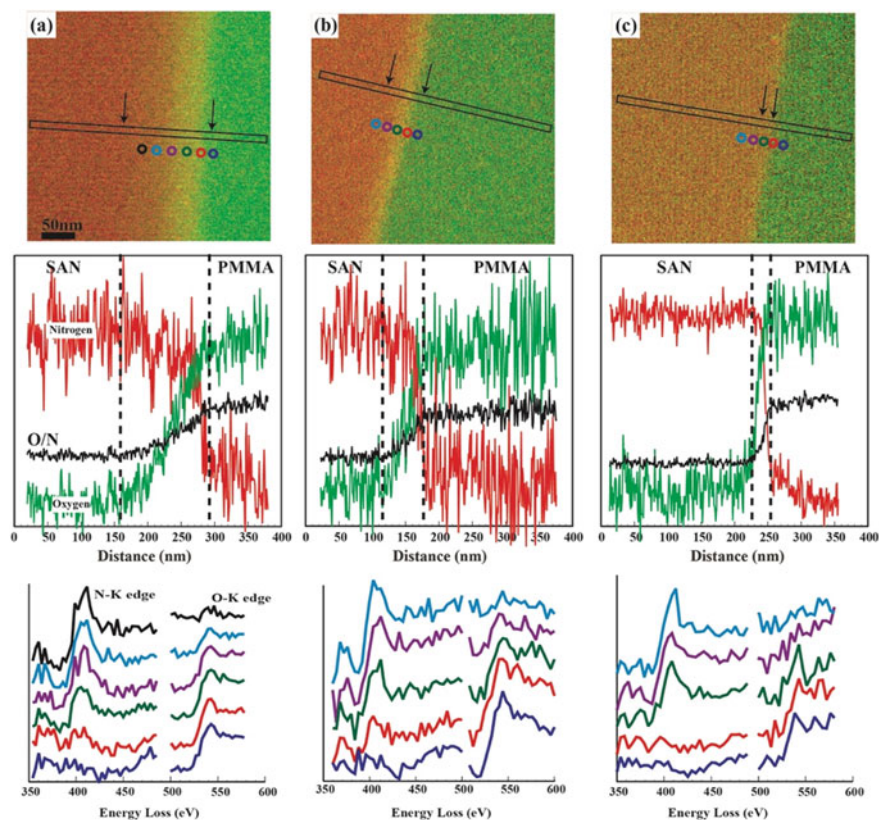


Fig. 6 Results of EFTEM analyses of PMMA/SAN interfaces; **a** SAN29; **b** SAN34; **c** SAN40. The top row features RGB composite images, with nitrogen and oxygen maps displayed in red and green, respectively. The maps were combined to highlight the formation of yellow interphase resulting from the overlap of red and green pixels. Arrows in the corresponding top images indicate the interfacial regions. The middle row exhibits intensity profiles acquired from the areas shown in oxygen and nitrogen maps and their ratios (O/N). The bottom row shows the changes in the intensities of nitrogen and oxygen core-loss peaks. The data was obtained using Image-EELS from the spots shown in the corresponding images. Reprinted with permission from [17]. Copyright 2007 John Wiley & Sons. All Rights Reserved

2 Thermodynamic Acceleration of Interdiffusion in Miscible Polymer Pairs

As presented in the previous section, the interfaces formed by the interdiffusion of PMMA and SAN can be visualized and the composition profiles across the interfaces were presented [17]. Here, the dynamics of interdiffusion in a miscible polymer pair (PMMA/SAN29) are discussed [18]. Figure 7 presents the developments of the interfacial layer between PMMA and SAN29 by thermal annealing with different periods and temperatures. The interfacial layer is visible as yellow due to overlapping green (oxygen) and red (nitrogen) pixels in the RGB composite images. The figure displays the development of the interfacial layer with welding time at temperatures above the glass transition temperatures (T_{gs}) of both polymers. The composition profiles across the interfaces for the relatively short welding times (Fig. 7a, b, and e) exhibit smooth single gradients that can be well-described by a hyperbolic tangent function [19]. As the welding time increases, the interfacial zones are widened with the profiles exhibiting two-step gradients with a plateau part in the middle. During the interdiffusion process, an equivalent composition of PMMA/SAN is formed at the central part of the layer. This layer appears after 12 h at 130 °C (Fig. 7c), while at 140 °C, it appears after only 4 h (Fig. 7f). The higher temperature accelerates the diffusion and promotes the plateau layer's formation. At temperatures significantly above the T_{gs} , the composition profiles with the plateaus at the midpoint are obtained in the earlier stage of the diffusion (Fig. 7 h and i, respectively).

Image-EELS enables to estimate the composition variation across the interface by the intensity ratios of the two core-loss peaks at the points of interest on the image [17]. In Fig. 8, the intensity changes of the nitrogen and oxygen core-loss peaks across the interface of the sample welded for 12 h at 130 °C are displayed, with the analyzed spots marked in the image. The integrated areas under the oxygen core-loss peak are compared to those of nitrogen using an energy window of 60 eV, giving the S_O/S_N ratios. It is evident from the data that the integrated intensity ratios of the core-loss peaks remain fairly constant in the central region with a plateau in the profile.

The following Eq. (4) describes the atomic ratios of two elements by the calculation of the ratio of the integrated intensities of the core-loss peaks (S_i) in an EELS spectrum:

$$\frac{N_1}{N_2} = \frac{S_1(\Delta, \alpha) \sigma_2(\Delta, \alpha)}{S_2(\Delta, \alpha) \sigma_1(\Delta, \alpha)} \quad (4)$$

where σ_i is the inelastic partial cross section, Δ is the energy window, and α is the collection angle. The core-loss peak ratios for oxygen and nitrogen (S_O/S_N) are determined experimentally via EELS using PMMA/SAN homogeneous blend films with known compositions. Subsequently, a master curve was constructed to represent the PMMA/SAN composition dependence of the integrated intensity ratio of the core-loss peaks, as depicted in Fig. 9. To ensure a specimen thickness of 50 nm, a

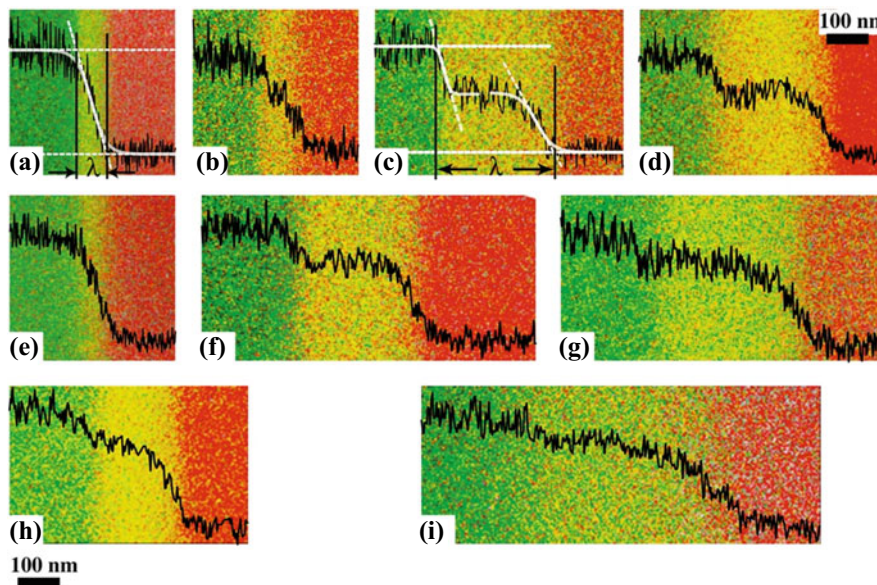


Fig. 7 RGB composite images of PMMA/SAN29 laminates, with green representing oxygen maps and red representing nitrogen maps. The laminates were annealed at various temperatures and times: **a**) 130 °C for 1 h; **b**) 130 °C for 4 h; **c**) 130 °C for 12 h; **d**) 130 °C for 24 h; **e**) 140 °C for 1 h; **f**) 140 °C for 4 h; **g**) 140 °C for 8 h; **h**) 150 °C for 2 h; **i**) 160 °C for 2 h. The oxygen-to-nitrogen concentration profiles are overlaid on the corresponding image. **a** and **c** demonstrate the process of determining the interface width (λ) by fitting the profiles with a hyperbolic tangent function. Reprinted with permission from [18]. Copyright 2007 American Chemical Society. All Rights Reserved

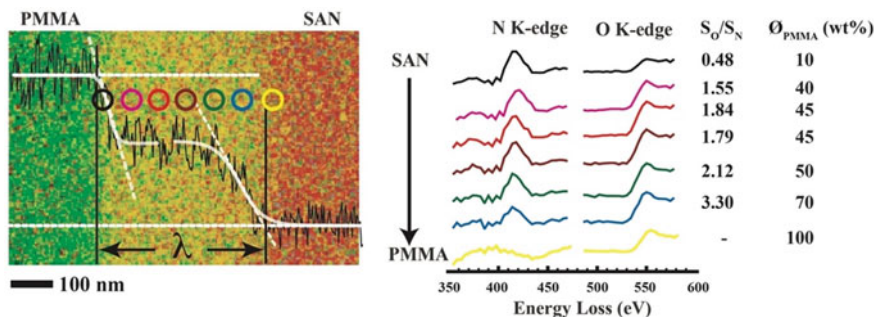
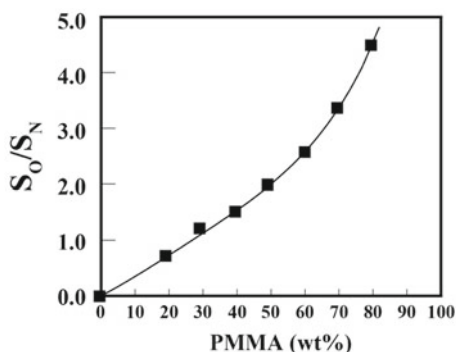


Fig. 8 The variations in N and O K-edges across the interface of a PMMA/SAN29 laminate annealed at 130 °C for 12 h (*middle*) and the ratios of integrated intensities (S_O/S_N) and estimated PMMA compositions (O_{PMMA}) (*right*). The analyzed positions are highlighted in the image (*left*), with the same colors as the corresponding spectra. Reprinted with permission from [18]. Copyright 2007 American Chemical Society. All Rights Reserved

Fig. 9 Ratio of the integrated intensities of N and O core-loss peaks (S_O/S_N) in EELS versus the PMMA composition in blend films of PMMA/SAN acquired by parallel EELS. Reprinted with permission from [18]. Copyright 2007 American Chemical Society. All Rights Reserved



THF solution was utilized for spin-coating onto a cleaved NaCl single crystal. Based on the findings, we were able to estimate the approximate compositions (ϕ_{PMMA}) in the interfacial region, which revealed that the central part of the interface with a low composition gradient contained PMMA at 40–50 wt%, as shown in Fig. 8. Similar levels of composition were also estimated for the other samples along the low gradient profile.

At temperatures above the T_g s of both PMMA/SAN polymers, their interdiffusion reveals unique composition profiles that differ from the classical profile by Fick's law, which is characterized by a constant diffusion coefficient and a maximum composition gradient at the profile midpoint. The occurrence of the unique composition profile obtained in this study is known to be the thermodynamic "acceleration". This acceleration arises from attractive interactions between the different segments, greatly enhancing the interdiffusion process relative to self-diffusion. The attractive interactions are proportional to the Flory–Huggins interaction parameter, χ , and the volume fraction of one polymer, ν , multiplied by $(1-\nu)$. The composition-dependent diffusion coefficient, $D_m(\nu)$, exhibits a maximum value at $\nu = 0.5$. The expression for $D_m(\nu)$ is obtained through an analysis of Flory–Huggins theory for the free energy of mixing of a polymer blend [3]:

$$D_m(\nu) = D_0[1 - 2\chi N\nu(1 - \nu)], \quad (5)$$

where D_0 represents the self-diffusion coefficient when the materials have the same mobility. When the absolute value of χ is roughly one order greater than $1/N$, where N stands for the polymerization index for PMMA or SAN, the second term in (5), i.e., the enthalpy term, becomes dominant, except for extremely low concentrations. This induces a thermodynamic "acceleration" diffusion behavior and results in a mutual diffusion coefficient D_m that varies with concentration, exhibiting a much higher diffusion constant in the middle of the concentration range [20].

Poly(vinyl chloride)/poly(ϵ -caprolactone) (PVC/PCL) is an example of this occurs where a notable negative χ parameter (-0.38) leads to a mutual diffusion coefficient (D_m) that is highly dependent on composition and diffusion constants that are much higher in the central concentration range [21]. Consequently, interdiffusion is hastened in the middle of the interfacial zone, resulting in a zone with an equivalent composition. The interaction parameter between PMMA and SAN can be calculated using Eq. (1) with the segmental interaction parameters obtained from the literature, which are -0.021, -0.028, -0.028, and -0.012 at temperatures of 130, 140, 150, and 160 °C, respectively. Though the χ parameters are not large negative values as those of PVC/PCL, they are still considerably higher than $1/N$, which is the primary reason for the thermodynamic “acceleration” phenomenon.

Polymer interdiffusion can be classified into normal Fickian diffusion (Case-I) and Case-II diffusion [22], based on diffusion and segmental relaxation rates. Case-I occurs when the diffusion rate is much lower than segmental relaxation, as in liquid–liquid interdiffusion. This type of diffusion can be described by the reptation model proposed by Edwards [1] and de Gennes [2], where polymer chains move within a virtual tube made up of the entanglement network of surrounding chains, constrained by this tube. These chains move in a Rouse-type motion [23] along their contour within the tube, and normal Fickian diffusion is observed after a time longer than the reptation time, according to equation [3],

$$\lambda = 2(D_m t)^{1/2}. \quad (6)$$

In contrast to normal Fickian diffusion, Case-II diffusion occurs when the diffusion rate is faster than the segmental relaxation rate. In the case of liquid/glassy polymer pairs, the diffusion is influenced by the polymer’s time-dependent mechanical response to the osmotic swelling stress at the penetrant diffusion front. This forms the core aspect of Case-II diffusion, where the interfacial width scales with time ($\lambda \sim t$).

To determine the interfacial width in our study, we calculated the tangent at the inflection point of the fitted curves to form a wedge shape and defined the interfacial width (λ) as shown in Fig. 7a. In situations where the composition profile has a middle plateau part, the profile was divided into two single hyperbolic tangent shapes and individually fitted by the function shown in Fig. 7c. Figure 10a illustrates that λ grows linearly with the square root of the welding time ($t^{1/2}$). Despite the local diffusion being driven by a thermodynamic “acceleration” mechanism resulting in an “anti-Fickian” profile, the overall interdiffusion in our study appears to obey Fickian diffusion, rather than Case-II diffusion with a scaling of $\lambda \sim t$ [3]. Using Eq. (7), we can calculate the apparent D_m as 4.26×10^{-15} , 1.66×10^{-14} , 3.76×10^{-14} , 1.82×10^{-13} cm²/s at 130, 140, 150, and 160 °C, respectively. The data in Fig. 10b is fitted with an Arrhenius expression, and the resulting solid line represents the best fit. The activation energy, E_a , was calculated to be 175 ± 15 kJ/mol.

$$D_m = D_0 \exp(E_a/RT) \quad (7)$$

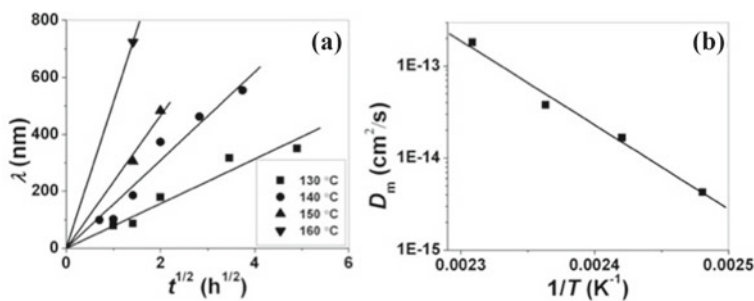
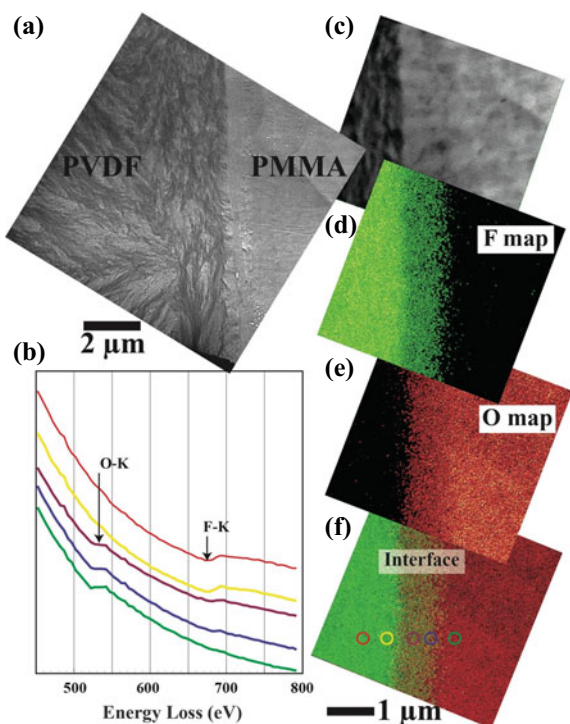


Fig. 10 Interfacial width (λ) versus square root of diffusion time for PMMA/SAN interfaces annealed at various annealing temperatures (a) and semilogarithmic plot of mutual diffusion coefficient (D_m) as a function of $1/T$ (b), where the solid line represents the best fit of an Arrhenius equation. Reprinted with permission from [18]. Copyright 2007 American Chemical Society. All Rights Reserved

To compare our findings to previously reported data, we utilized the approach proposed by Qiu and Bousmina [24], converting all four values of D_m to the reference temperature of 120 °C. These converted values ranged from 0.62 to 2.43×10^{-16} cm²/s, which were roughly one order of magnitude higher than the results obtained by Kim et al. (1.1×10^{-17} cm²/s) [25] using FRES and are in agreement with the values obtained by Yukioka et al. (1.0×10^{-16} cm²/s) [26, 27] using ellipsometry and by Qiu et al. (3.7×10^{-16} cm²/s) using rheometry [24]. These results suggest that EFTEM is a highly effective method for studying polymer interdiffusion.

The next section states that interfacial diffusion between identical polymers is extremely slow compared to dissimilar miscible polymer pairs. For example, when PS is bonded together, the thickness is 8 nm after 45 min at 120 °C and 15 nm after 36 h [28, 29]. On the other hand, PMMA/SAN29 forms a diffusion layer with an extraordinarily thick layer with 100 nm or more in 1 h. PMMA/polyvinylidene fluoride (PVDF) [30] is a unique miscible combination. It is possible to characterize the interfacial diffusion behavior by analyzing oxygen and fluorine elemental distributions by Image EELS. As shown in Fig. 11a, since PVDF is a crystalline polymer, it exhibits a morphological feature derived from spherulites, making it easy to identify the boundary as the crystalline/amorphous interface. The diffusion of each polymer can be characterized by the combination of oxygen (O) and fluorine (F) distributions. Both O and F ionization edges appear in the 500–800 eV energy loss range as shown in Fig. 11b, which were extracted from the spots indicated in Fig. 11f. Superimposing the F map, representing the PVDF location, on the energy-loss image shown in Fig. 11c indicates that PVDF diffuses toward the PMMA side over the crystalline/amorphous boundary (Fig. 11d). No penetration of PMMA into the crystalline PVDF phase seems to be taken place, as shown in Fig. 11e. It was found that an extremely thick interfacial layer with a thickness of about 1 μ m was formed in a very short time (Fig. 11f). Diffusion between identical polymers is caused only by the contribution of combinatorial entropy change, which is relatively small for high molecular weight polymers. As no significant increase in entropy is expected for diffusion between

Fig. 11 Image-EELS analysis of thermally-treated PMMA/PVDF interface at 180 °C for 5 min: **a** TEM image of the cross section; **b** energy-filtered image at 70 ± 10 eV energy losses; **c** fluorine map, **d** oxygen map, **e** RGB composite image with overlaying fluorine map (green) and oxygen map (red) on the energy-filtered image



polymers, interdiffusion is slowed. On the other hand, mixing dissimilar miscible polymer pairs adds the effect of exothermic interaction (negative χ parameter), and this enthalpic effect promotes fast diffusion.

3 Role of Interfacial Entanglements on Interfacial Toughness Studied by Nanofractography

3.1 Interfacial Thickness and Toughness in PMMA/SAN Interfaces

The entanglement structure is a crucial feature of polymer materials. However, the detailed topological structure still needs to be fully understood, as it cannot be observed experimentally even with high-resolution electron microscopes. It is especially difficult to characterize the local entanglement structures formed through the interdiffusion of polymers. The correlation between the structure of polymer chains at the interface and its resistance to crack propagation is significant for practical applications and scientific investigations. The adhesion between polymers is

controlled by intermolecular chain entanglements across the interface, which can provide physical links. The work of adhesion can be calculated based on surface and interfacial energies between two polymers. Still, experimental adhesion values are much higher than the calculated work of adhesion, indicating the significant contribution of polymer chain entanglements to the toughness of the interface [28, 29, 31–35]. For example, the work of adhesion between polystyrene (PS) and poly(methyl methacrylate) (PMMA) was measured to be 78.6 mJ/m^2 [36], while the measured interfacial toughness was 12 J/m^2 which is more than two orders of magnitude [28]. This means that the contribution of polymer chain entanglements to the toughness of the interface is significantly essential.

This study investigates the correlation between adhesion property and interfacial structure between PMMA and SAN, considering interfacial thickness and diffusion. The interfacial toughness is evaluated by an asymmetric double-beam cantilever (ADBC) test. The failure behavior in the test is inspected by the observation of fracture surfaces by high-resolution SEM. The interfacial fracture toughness (G_c) is measured by using asymmetric double cantilever beam (ADCB) specimen geometry as illustrated in Fig. 12a [37, 38]. This method has proved to be a simple but effective way of testing the toughness of interfaces between two polymer sheets. The specimens were prepared by compression molding of PMMA and SAN between silicon wafers. The interfacial toughness was measured by propagating an interfacial crack from a pre-crack inserted in a thin film of PTFE. The minimum G_c value was found by varying the thickness of the PMMA beams, and the appropriate thickness ratio of the two beams was determined to calculate the interfacial toughness using Eq. (6), where a is crack length, Δ is the thickness of the razor blade, E_i is the elastic modulus, h_i is the beam thickness, and $C_i = 1 + 0.64(h_i/a)$. The subscripts 1 and 2 refer to the PMMA and the SAN beams, respectively.

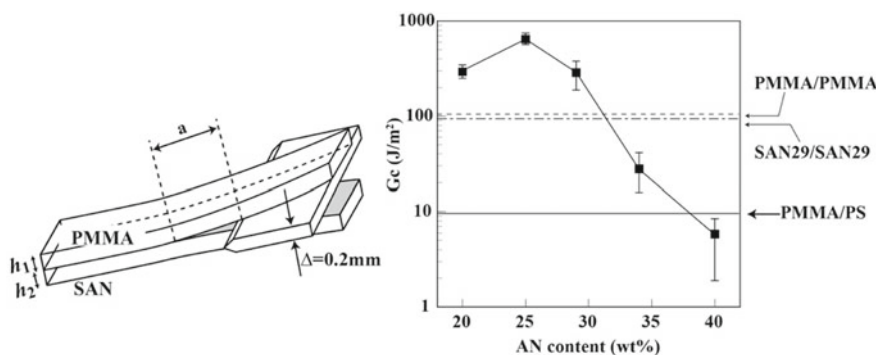


Fig. 12 Schematic drawing of the ADCB test specimen (left) and fracture toughness (G_c) of PMMA/SAN interfaces as a function of AN content in SAN annealed at $140 \text{ }^\circ\text{C}$ for 2 h (right). 8–10 measurements were taken for each polymer pair, and average values with maximum and minimum values are shown. Reprinted with permission from [17]. Copyright 2007 John Wiley & Sons. All Rights Reserved

To ensure contact between the two plates, the specimens underwent annealing at 140 °C for 2 h in the air under slight pressure. The interdiffusion was terminated by rapidly cooling the specimens to room temperature. A razor blade was pushed into the pre-crack to propagate an interfacial crack. Upon cessation of the crack propagation, the length ahead of the blade was measured with a microscope to determine the critical energy release rate, G_c . To determine the appropriate thickness ratio of the two beams so that the crack propagates along the interfacial plane, G_c values are calculated by varying the thickness of the PMMA beams between 1.7 to 2.3 mm, while the thickness of the SAN beams is fixed at 1.7 mm. Among these measurements, the minimum value is defined as interfacial toughness.

$$G_c = \frac{3\Delta^2 E_1 h_1^3 E_2 h_2^3}{8a^4} \frac{E_1 h_1^3 C_2^2 + E_2 h_2^3 C_1^2}{(E_1 h_1^3 C_2^3 + E_2 h_2^3 C_1^3)^2} \quad (8)$$

$$C_i = 1 + 0.64(h_i/a) \quad (9)$$

The ADBC test was performed to investigate how interfacial toughness is affected by the composition of random copolymer SAN. Figure 12 shows the specimen geometry in the left panel and the plot of G_c values against the AN content in SAN in the right panel. A significant increase in interfacial toughness is achieved as the AN content in SAN decreased, indicating that the interfacial toughness between PMMA and SAN is highly sensitive to the composition of SAN. The G_c values for PMMA/SAN29 were notably higher than those for identical polymers, i.e., PMMA/PMMA and SAN29/SAN29. In contrast, PMMA/PS showed a poor adhesion level similar to PMMA/SAN40, suggesting that the maximum adhesion strength could be achieved with AN content of 29 wt% or less. The high interfacial toughness of PMMA/SAN29 indicates that the interdiffusion is more rapid in the miscible pair than in the identical polymer pairs. This finding is attributed to the polymer pair with a negative χ parameter providing an additional favorable enthalpic driving force for a highly tough interface as mentioned in Sect. 2.

The EFTEM analyses of the PMMA/SAN interfaces indicate that increasing the interfacial width by around 100 nm significantly improves interfacial toughness. To investigate the cause of this improvement, we examined the fractured surfaces using SEM. SEM micrographs of the fractured surfaces of AN29, SAN34, and SAN40 are presented in Fig. 13a, b, and c, respectively. These micrographs were obtained near the crack tips after coating with OsO₄ plasma polymerized film to prevent charging, which is advantageous for high-resolution imaging by SEM due to its ability to provide sufficient conductivity with thinner films than the conventional gold-sputtered film [39]. The samples display various surface features, and the opposite PMMA surfaces show similar features as the counterpart SAN surfaces. The fracture surface of SAN29 contains numerous cell-like units of approximately 5 μm, identical to those found in bulk material fractures.

In contrast, SAN34 and SAN40 exhibit a macroscopically uniform and smooth surface. At the same time, higher magnification images reveal the presence of many

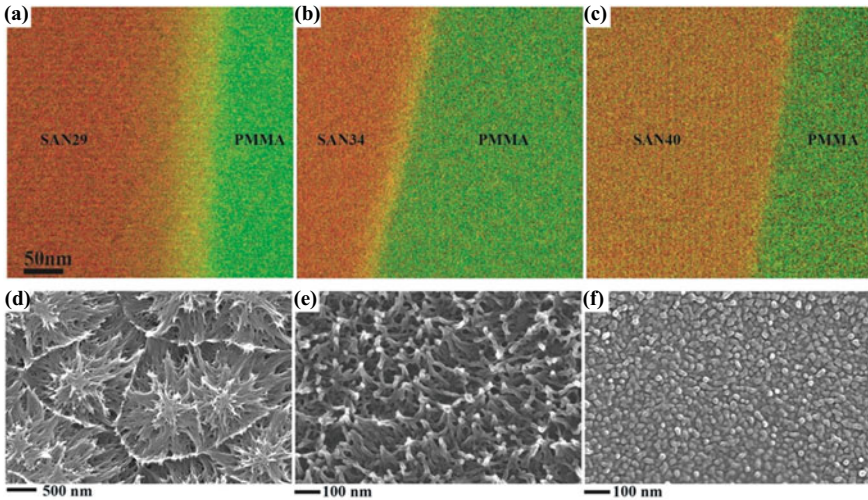


Fig. 13 Visualization of PMMA/SAN interfaces by EFTEM (*upper row*) and SEM micrographs showing fracture surfaces (*bottom row*): **a, d** SAN29; **b, e** SAN34; **c, f** SAN40; nitrogen and oxygen maps represented as red and green, respectively, and the yellow layers correspond to the interfacial layers

small fibrils with diameters of approximately 20 nm over the entire surface. These fibrils are elongated normally to the smooth surface, as shown in Fig. 13e and f. The length of the fibrils of SAN34 is greater than that of SAN40, suggesting that higher toughness could yield more extended elongation. These fine features on the fracture surface with relatively low toughness are observed for the first time using the high-resolution SEM (HR-SEM, Carl Zeiss, Ultra 55) technique with the in-lens SE detector and OsO₄ coating described in Sect. 2.6.1. According to the fractographic characteristics of SAN29, crack nucleation appears at the cell centers, followed by propagation from the inside outwards. The crack propagation process could involve several “crack nucleation and growth” cycles, which lead to cell-like patterns on the fractured surface. Ahead of the primary crack, microvoids may merge to form a continuous crack. The resulting dimple pattern is assumed to be produced from the combination of the primary crack front that develops due to the interface separation process, and the secondary crack generated by the microvoids’ nucleation ahead of the primary crack, as suggested by reference [40].

To understand this drastic change, the fracture surfaces of PMMA/SAN29 and PC/SAN29 are compared. The former is a miscible system, while the latter is an immiscible system. The G_c values of PMMA/SAN29 and PC/SAN29 are 290 and 10 J/m², respectively. The fracture behavior of immiscible PC/SAN29 differs from that of miscible PMMA/SAN29. The difference in the miscibility of those two systems exhibits significantly different failure appearances. The PC/SAN29 has a weak interfacial toughness due to its immiscibility. The fracture surface is so smooth that no topographic features can be seen in the micrometer scale (Fig. 14a). However, a

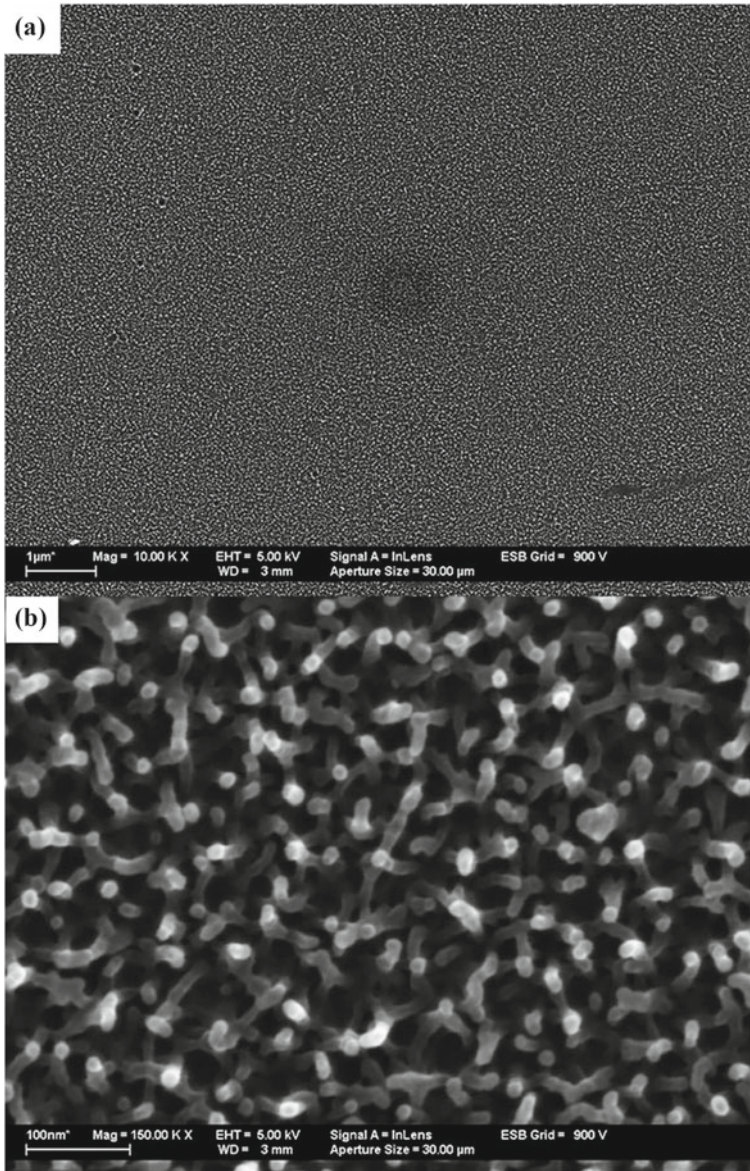


Fig. 14 SEM micrographs showing the fracture surface of SAN29 produced in the failure of PC/SAN29 interface. **b** is a magnified image of the central part of **(a)**

high-magnification view allows us to find the formation of nano-fibrils with approximately 20 nm diameter (Fig. 14b). XPS measurements of the fracture surfaces of PMMA/SAN29 showed comparable intensities of N1s and O1s peaks on both fracture surfaces, while the SAN29 surface was extremely rich in nitrogen, and the PC side was vice versa in PC/SAN29. This indicates that cohesive failure, where the crack progressed within the thick interfacial layer, occurred in PMMA/SAN29, while interfacial failure is the primary failure mode in PC/SAN29. Therefore, it can be mentioned that the transition from the micrometer-scale “dimple pattern” to the “nano-fibrous pattern” in fracture surfaces represents the changes in the miscibility of polymers.

3.2 *Interfacial Entanglements at PS/PS Welded Interfaces*

When interfaces fracture via interfacial failure, a “nanofibrillar” structure forms on the surface. A simple system is used for a basic study to understand the mechanism for the formation of this structure and its relationship with the interfacial entanglement structure. The system varying m involves welding two sheets of the same homopolymer with a narrow molecular weight distribution for periods at a temperature above T_g . This symmetrical system can clarify the criteria for producing the “nanofibrillar” surface structure when the interface fails.

Our study aims to examine the relationship between fracture surface patterns, interfacial width, and toughness by conducting welding experiments between identical molecular weights between the PS sheets [41]. The polymer chains diffuse across the interface during the experiment, increasing interfacial thickness over the welding time. Figure 15 depicts a double logarithmic plot of the interfacial toughness between the PS sheets, which have an M_w of 541 k and M_w/M_n of 1.07, versus welding time at 120 °C. Additionally, the figure includes HR-SEM images of the fracture surfaces obtained at various welding times. Schnell et al. conducted a study to explore the correlation between interfacial toughness and PS/PS interface thickness utilizing neutron reflectivity and fracture toughness measurement techniques [28]. The interfacial thicknesses they measured between protonated PS (752 k) and deuterated PS (660 k) are plotted on the same figure [42].

Schnell et al. proposed a three-stage model to explain the dependence of G_c on welding time [29]. In the first stage, G_c increases slowly and steadily. During the second stage, G_c increases rapidly within a short time, reaching a value close to that of bulk PS’s toughness. In the third stage, G_c remains constant and independent of welding time. Our findings show a similar trend, but the fracture toughness values during the initial stage are lower than those reported in the literature where the adhesion energy of 93 J/m² was measured after only 6 min. This may be due to the induction period for softening and wetting the thick (2 mm) specimens used in the ADCB test, which mainly occurs before chain interdiffusion is allowed, resulting in relatively lower interfacial toughness values. However, the measured G_c values are comparable to those attained with various immiscible polymer pairs with interfacial

thicknesses less than 10 nm [29, 32]. For example, the G_c between PS and PMMA is about 12 J/m^2 with an interfacial thickness of 5 nm. The toughness enhancement during the second stage occurs over a narrow range of interfacial thicknesses between 9 and 12 nm. Further polymer interdiffusion contributes little to the enhancement, consistent with Schnell et al.'s findings [29]. The HR-SEM images depict the dynamic change of fracture surface patterns with welding time and the relationship between interfacial toughness and the fracture surface. Figure 16a shows the production of the “nanofibrillar” pattern during the early stage when the interdiffusion and toughness are relatively low (90 min). In the second stage, the fibrils become elongated as G_c increases, as seen in Fig. 16b (5 h), followed by the appearance of micrometer-scale dimples in the later part of the second stage (6 h). Finally, during the third stage, the “nanofibrillar” surface disappears, and the micrometer-scale dimple pattern dominates, as observed in the PMMA/SAN29 miscible pair (Fig. 13).

According to previous research, a significant increase in interfacial toughness is associated with a change in the molecular failure mechanism [29]. Specifically, the fracture mechanism transitions from “chain pullout” to crazing at the critical interfacial thickness. Therefore, the “nanofibrillar” pattern is formed when “chain pullout” is the primary failure mechanism. In the second stage, when the interfacial toughness increases rapidly with increasing interfacial thickness, the transition from

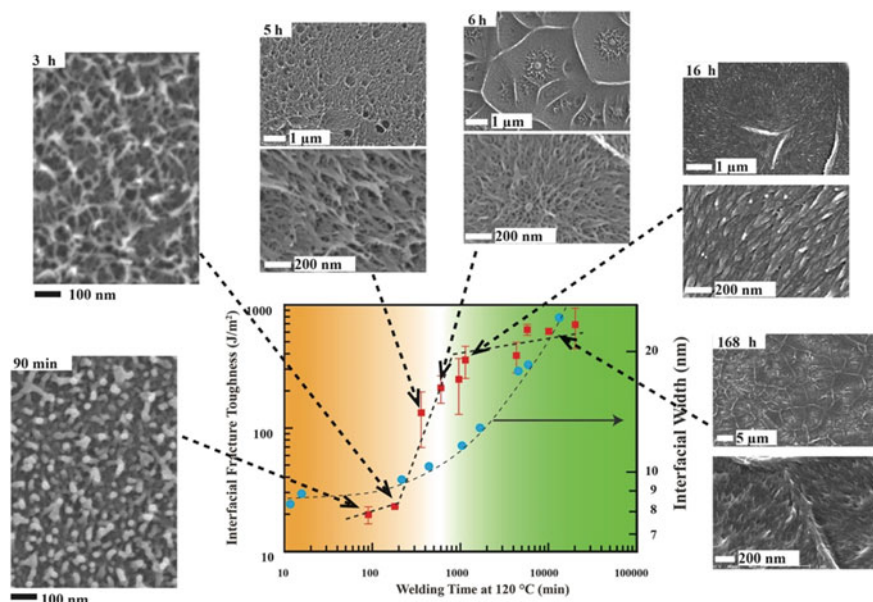


Fig. 15 The plot displaying the interfacial toughness (G_c) of PS/PS 541 k as a function of welding time at 120 °C. The corresponding SEM micrographs of the fracture surface at different welding times are also presented. The plot additionally includes interfacial thickness measurements by Stamm et al. [42] using neutron reflectivity. Reprinted with permission from [41] Copyright 2008 American Chemical Society. All Rights Reserved

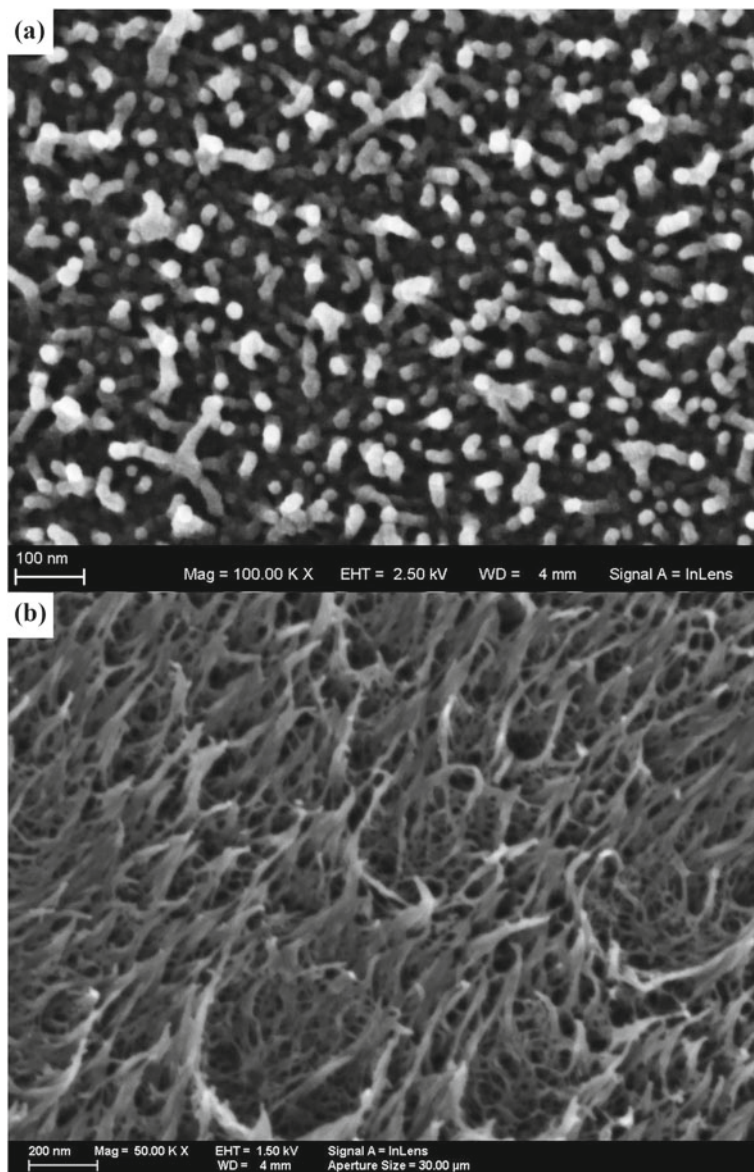


Fig. 16 SEM micrographs showing the fracture surface of PS-PS interfaces annealed at 120 °C for 90 min (a) and 5 h (b)

“chain pullout” to crazing occurs, and the fracture surface exhibits a combination of “nanofibrillar” and “dimple” features. As demonstrated in Fig. 17, the interfacial toughness of the polymer interface increases following an *S*-shaped curve as the interface thickness increases. It has been reported that when the interface thickness exceeds 10–15 nm, polymer chains become sufficiently entangled at the interface to form a plastic deformation zone at the crack tip, leading to toughness comparable to that of the bulk. In this plastic deformation region, crazing occurs, producing interpenetrating microvoids, cross-ties fibrils, and dissipating a significant amount of energy before the interface fails. It is believed that the nanofibrillar structure is formed when a thin interface separates with the disentanglement of polymer chains before crazing initiation.

The range of the critical interfacial thickness, which leads to a significant increase in interfacial toughness, is between 9 and 12 nm. This thickness is closely related to the average distance between the entanglement points in PS, estimated at 9.3 nm [43]. Thus, it is possible to achieve sufficient interfacial toughness with narrow interfaces that are considerably smaller than the radius of gyration of the polymer molecules, which is around 21.3 nm for 570 k PS [28]. These findings suggest that the polymer

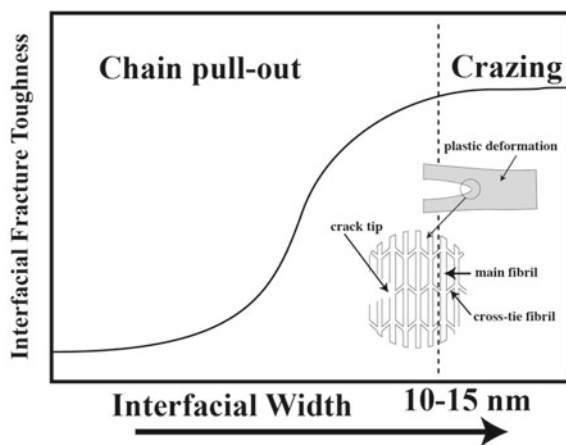


Fig. 17 Correlation between interfacial toughness and interfacial thickness

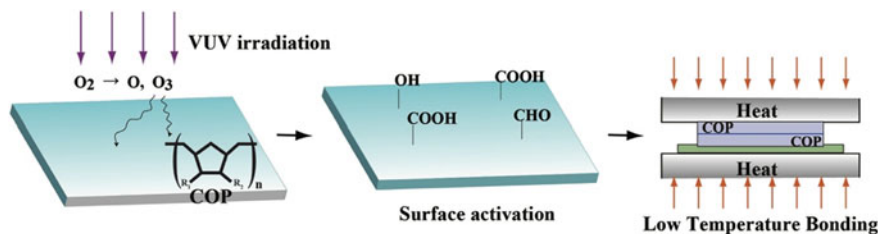


Fig. 3.18 Process of the low-temperature bonding of COP plates

chains must penetrate only roughly one entanglement distance to achieve optimum interfacial toughness.

Silvestri et al. proposed the term “partial crazing” to describe a scenario where crazing begins but does not fully develop, resulting in the breaking of some load-bearing strands during plastic deformation without creating cross-tie fibrils to transfer lateral stress [31]. The early stage of toughness development involves plastic deformation, and even in this initial stage, fracture energies are significantly larger than the work of adhesion, indicating the need for plastic deformation to dissipate a large amount of fracture energy. It is believed that the nanoscale fibrils result from plastic deformation created in the partial crazing regime before complete crazing occurs. In cases where polymer chains are not sufficiently entangled at the interface to initiate crazing, plastic deformation may occur at the crack tip, but the polymer chains may slip away, resulting in failure without forming lateral cross-tie fibrils. The diameter of craze fibrils is reported to be 5–30 nm, similar to the thickness of nanofibrils formed by chain pullout. The nanofibrils formed by the failure of thin interfaces are thought to be remnants of partial crazing. When crazing does occur, the fibrils elongate until they become thin enough that their traces are not visible.

To achieve an interfacial toughness (G_c) value similar to the bulk PS fracture energy (approximately 600 J/m²), annealing of the identical PS interface is required for over 10 h [28]. This indicates that in identical high molecular weight polymers, the driving force for diffusion is primarily the combinatorial entropy change, which is relatively low.

The “nanofibrillar” pattern found in narrow interfaces corresponds to the local entanglement structures that are similar to the entanglement spacing. This kind of surface feature has been observed in the failure of narrow dissimilar interfaces between immiscible polymers with block copolymers localized at the interface [44]. Classical fractography can only provide information on fracture mechanisms at micrometer scales, whereas HR-SEM enables the study of interfacial entanglement structures, which enables us to perform “Nanofractography.” This method has the potential to advance our understanding of adhesion and bonding mechanisms.

3.3 Mechanism of Low-Temperature Bonding of VUV-Activated COP

Surface structures similar to nanofibrils are observed in the failure of the interfaces in surface-activated cyclo-olefin polymer (COP). COP is a low-cost amorphous polymer with high transparency, heat resistance, and low water absorption [45]. However, due to its simple chemical structure lacking effective polar functional groups for adhesion, surface modification is necessary for achieving high adhesion strength. Sugimura et al. investigated the COP surface activation by vacuum ultraviolet (VUV) treatment, which generates oxygen-containing ether, ketone, and carboxyl units on the surface to produce a hydrophilic surface and enable adhesive-less direct bonding

at low temperatures below the T_g [46]. Low-temperature bonding is an effective method for preserving sub-micrometer-scale features created in the COP plates, but the detailed bonding mechanism remains unknown [47]. This bonding mechanism is presumed to involve attractive interactions between chemical functional groups on the surface, enabling bonding without sufficient interdiffusion.

The bonding mechanism of low-temperature surface-activated COP is investigated by the nanofractography technique [48]. Figure 19 presents the influence of the VUV irradiation on the interfacial toughness acquired by bonding at 110 °C. To assess the interfacial toughness, the DCB test was employed with the symmetric DCB specimen geometry, where 1 mm thick COP plates were bonded. In this situation, Eq. (8) is simplified as Eq. (10) to compute G_c .

$$G_c = \frac{3\Delta^2 E h^3}{16a^4 C^4} \quad (10)$$

When a razor blade is inserted into the interface in the bonded laminates, the crack propagates ahead of the blade, and no significant crack propagation is observed after an hour. The initial G_c values are calculated based on the crack length thus obtained. The results indicate that the maximum G_c can be achieved with a 5-min VUV irradiation, and prolonged exposure does not result in further enhancement but rather

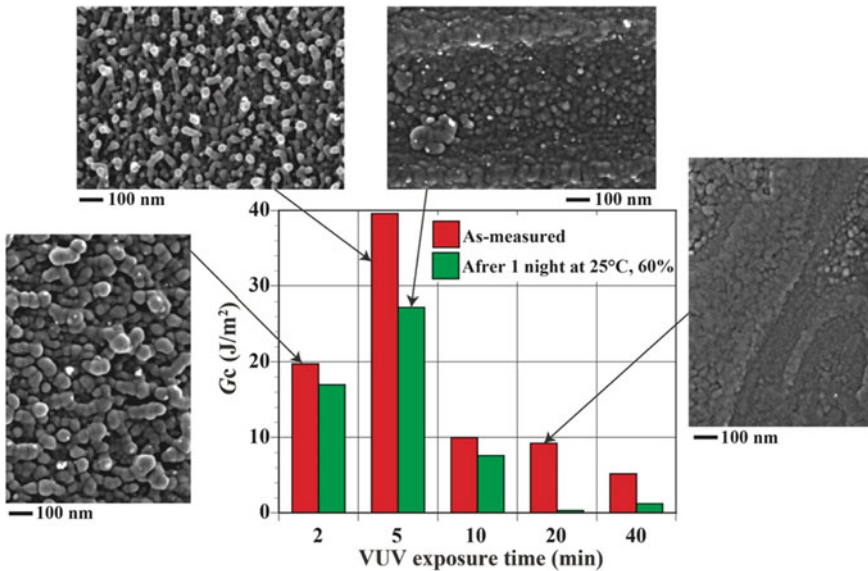


Fig. 19 Effect of VUV irradiation period and a high humidity environment on interfacial fracture toughness (G_c) of low-temperature bonding of COP. The average and standard deviations were calculated with at least ten data points for each laminate. SEM micrographs shown on upper side of the graph are fracture surfaces produced in the indicated conditions. Reprinted with permission from [48]. Copyright 2016, The Society of Polymer Science, Japan, All Rights Reserved

causes a decrease in G_c . To assess the effect of humidity on interfacial toughness, crack growth was measured after the specimens were left at 25 °C and 60%RH for 12 h. The G_c values decrease from their initial values for all VUV irradiation conditions in such a humid condition. The crack continues to propagate slowly as the specimen with the inserted razor blade was left under the humid condition, indicating that water vapor degraded the interfacial toughness. According to Sugimura and colleagues, the content of oxygen-containing functional groups on the COP surfaces increased with increasing VUV irradiation time of up to 40 min, and the water contact angle decreased [46]. These findings suggest that the optimal condition for bonding is not necessarily the same as that for the degree of surface activation.

In Fig. 19, SEM micrographs present the fracture surfaces of the DCB test specimens. The specimens VUV-irradiated for 2, 5, and 20 min, and the specimen exposed to the high humidity conditions after 5 min VUV-irradiation are shown. Before bonding, no surface features are observed on the surface of the VUV-irradiated specimens. The SEM micrographs indicate that many nano-fibrils are present on the fracture surfaces of the specimens irradiated for 2 and 5 min, which have relatively high G_c values. The results suggest that the surface-activated COPs exhibit similar surface features to those produced on the fracture surface of interfaces formed in melt conditions. The elongation, thickness, and density of the fibrils characterize their features. Conversely, the fracture surfaces of the specimens irradiated for 20 min, which have an extremely low G_c value, exhibit barely visible fibrils. Additionally, the fracture surface produced during exposure to high humidity conditions displays surface features significantly different from those produced in the as-irradiated specimen. Although surface features with similar length scales are produced, the height of the fibrils is relatively low.

The fact that the 2 and 5 min VUV-irradiated COPs produce the nano-fibrils on their fracture surfaces suggests that the interfaces failed via “chain pullout”. Since the bonding temperature (110 °C) is much lower than the T_g of COP (140 °C) and the bonding time is short (10 min), there is not enough mutual interdiffusion to form sufficient entanglement at the interface. It is presumed that hydrogen bonds at the interface between the oxygen-containing polar functional groups bridge the polymer chains across the interface. These polymer chains can reinforce the interface and be pulled out during the fracture.

Increased VUV irradiation results in more polar functional groups on the surface, which could produce more polymer chains across the interface. However, prolonged VUV irradiation also leads to polymer degradation beneath the activated surface, making fragments with lower molecular weight than the average molar weight between entanglement points. Despite an increase in the number of polymer chains across the interface, effective interfacial entanglement cannot be formed under such conditions, resulting in poor interfacial toughness. Exposure to high humidity allows water molecules to penetrate the interface and disrupt the hydrogen bonds formed at the interface, decreasing interfacial toughness.

Two analytical electron microscopy techniques were performed to inspect the interfaces of the COP bilayer specimens. Directly imaging the interfaces between identical polymers by conventional TEM is difficult since no contrast can be obtained

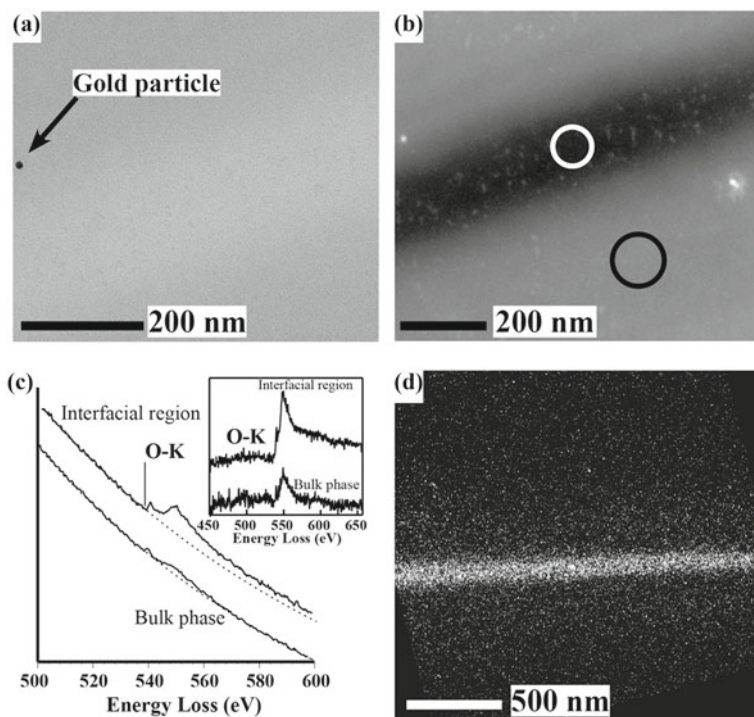


Fig. 20 EFTEM analysis of the interface between the 5 min VUV-irradiated COPs formed by the low-temperature bonding: **a** zero-loss image; **b** structure-sensitive image at 150 ± 5 eV energy loss; **c** O K-edges in EELS spectra acquired inside and outside the interfacial region shown in **b** with an inset of the background-subtracted O K-edges; **d** oxygen map created by three-window method. Reprinted with permission from [48]. Copyright 2016, The Society of Polymer Science, Japan, All Rights Reserved

between the COP plates. However, in our case, oxygen is introduced only in the region underneath the surface with a certain depth, allowing for the possibility of imaging the VUV-modified region by tracing the location of the oxygen element. In Fig. 20a and b, energy-filtered images by EFTEM of the specimen VUV-irradiated for 5 min are shown, one of which is a zero-loss image (ΔE is 0 ± 5) and another of which is a structure-sensitive image at 150 ± 5 eV. The interfacial region appears as a dark, approximately 200 nm thick layer in the energy-filtered image at 150 eV, while the zero-loss image does not clearly show the interfacial region. The EELS spectra acquired from the areas inside and outside the interfacial region are shown in Fig. 20b and c, respectively. The core-loss peaks of the O K-edges are shown in the inset of Fig. 20c, which are created by the subtraction of the BG component calculated by the power-law function shown as the dotted curves drawn along the as-measured spectra. The localization of oxygen in the interfacial region is due to the polar functional groups produced by the VUV irradiation. A small amount of oxygen is also detected over the entire area in the specimen, which may be derived

from the stabilizing agent contained in the gold colloid. An oxygen elemental map in Fig. 20d is calculated by the three-window method using three energy-loss images at 450 ± 5 , 500 ± 5 , and 550 ± 5 eV, which indicates the formation of a uniform interphase with a thickness of about 200 nm. This leads to an estimation of the depth of the surface activation of about 100 nm.

The interfacial region is also visualized using STEM-EDX, and the resulting images are presented in Fig. 21a and b as bright field (BF) and annular dark field (ADF) images, respectively. The BF and ADF images show the interfacial layer, which is similar to what was observed with EFTEM. The BF image can sufficiently identify the interfacial region, while the ADF image provides a much clearer contrast due to the difference in chemical composition between the interfacial region and the bulk part. The ADF image's contrast is related to the mass thickness and atomic numbers in the specimen. STEM allows the creation of an image by detecting signals at each probe position without an objective lens, resulting in a relatively minor effect of chromatic aberration on image quality. EDX microanalysis conducted on points within and outside the interfacial layer shows the presence of oxygen as shown in Fig. 21c, confirming the bright layer in the ADF image to be an oxygen-rich region. The ADF image of the sample prepared by VUV irradiation for 40 min is displayed in Fig. 21d, demonstrating that longer irradiation does not significantly increase the thickness of the activated layer. The VUV treatment remains confined to a depth of 100 nm below the surface, even with prolonged irradiation.

The proposed mechanism for the low-temperature bonding of VUV-irradiated COP is presented in Fig. 22. VUV irradiation generates polar functional groups such as $-\text{OH}$, CHO , COOH , etc., with a modification depth of about 100 nm, which is almost independent of the irradiation time. Shorter VUV irradiation times (less than 5 min) result in the formation of hydrogen bonds between functionalized polymer chains on both sides of the interface, reinforcing the interface and allowing energy dissipation during fracture via chain pullout of the coupled polymer chains. However, exposure to humidity can cause the hydrogen bonds to break, decreasing toughness. Longer VUV irradiation times generate more functional polar groups but can also cause polymer degradation, resulting in low molecular weight species. As a result, the polymer chains across the interface cannot achieve effective entanglements, leading to low interface toughness. The interfacial fracture toughness is greatly reduced by 10-min VUV irradiation, with the molecular weight decreasing below the critical value of the molecular weight between the entanglement points of COP.

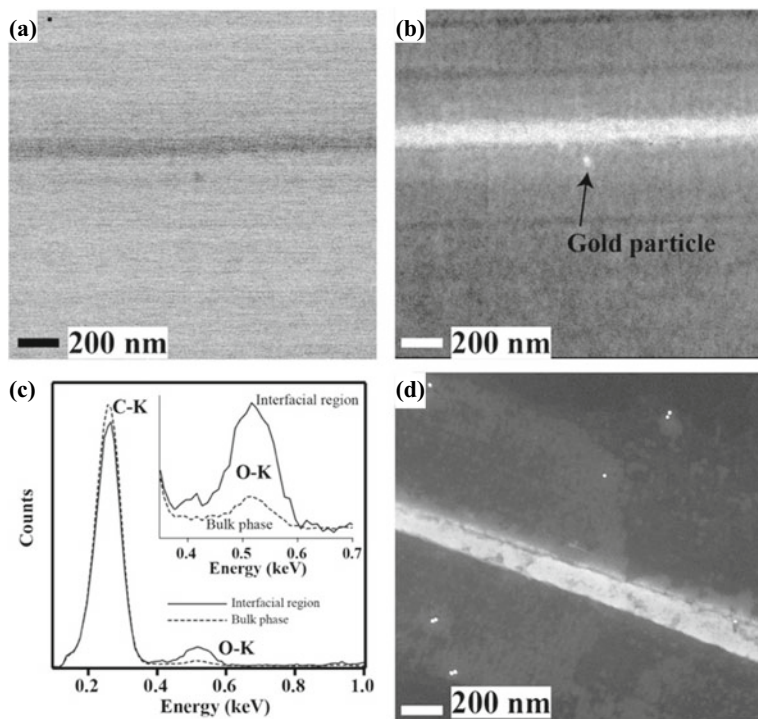


Fig. 21 STEM-EDX analysis of the interface between the COP laminate VUV-irradiated for 5 min: **a** STEM-BF image; **b** STEM-ADF image; **c** EDX spectra taken from the points inside (straight line) and outside (dotted line) the interfacial region; **d** STEM-ADF image showing the interfacial region between the COP plates surface-activated by 40 min VUV irradiation. Reprinted with permission from [48]. Copyright 2016, The Society of Polymer Science, Japan, All Rights Reserved

4 Adhesive Bonding by Surface and Interface Modifications of Polypropylene—Effect of Chemical Bonding and Mechanical Interlocking

Polypropylene (PP) is an important plastic material for the industry due to its high environmental durability, excellent heat resistance, and lightweight and inexpensive. The low surface energy of PP inhibits adhesion to most adhesive and coating formulations. The poor adhesion property of PP limits its use in various applications. Thus, different surface treatment techniques for adhesion improvement have been developed. However, the mechanisms of the surface pretreatment effect have yet to be fully understood. In this study, flame treatment and plasma treatment for the adhesion improvement of PP with an epoxy adhesive are evaluated and that mechanism is considered.

The interface between PP and adhesive involves multiscale structures with length scales ranging from Å to μm. The surface treatments of PP cause changes in the

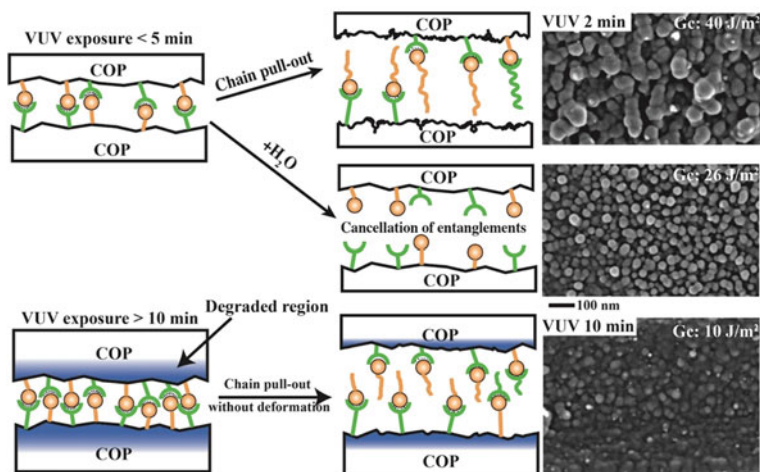


Fig. 22 Schematic illustrations describing the mechanism of low-temperature bonding of VUV-irradiated COP. Reprinted with permission from [48]. Copyright 2016, The Society of Polymer Science, Japan, All Rights Reserved

molecular structures and the crystallinity of the surface and create surface topography with the features of nanometer to micrometer scales. We are investigating such multi-scale interfacial structures formed between the adhesive and PP by electron microscopy [49, 50].

Commercial isotactic polypropylene (*i*PP) is press-molded at 200 °C into 3 mm thick plates between silicon wafers to obtain a flat surface to exclude the effect of initial surface roughness on adhesion behavior. The plasma treatment uses an atmospheric damage-free plasma source with N₂ gas, PF-DFMJ01, developed by Plasma Concept Tokyo Inc., Japan. The plasma source is scanned twice over the *i*PP plate with a 5 mm/s scanning speed and a 5 mm gap between the plasma source and the sample, as shown in Fig. 23a and the associated video. Flame treatment is employed by briefly exposing blue flame over the *i*PP surface by scanning the sample twice under the flame with 60 mm/s, as shown in Fig. 23b and the associated video. Those surface-treated and non-treated *i*PP plates are laminated with two-component epoxy adhesive, Denatite 2204 (Nagase ChemteX Corp.), and cured at 45 °C for 12 h.

Interfaces between *i*PP and the epoxy adhesive are investigated by STEM at an accelerating voltage of 200 kV. Thin cross sections of the interface are cut from the laminates by ultramicrotomy after staining with RuO₄. Surface morphologies before bonding are also investigated by the replica-STEM technique. As described in Sect. 2.3.3, a thin film of Pt with a thickness of 6.5 nm is deposited by sputtering at a low angle of 25°. To strengthen the Pt film, a carbon layer with a thickness of 25 nm is coated by sputtering at a high angle of 90°. The specimen is horizontally rotated during deposition to ensure that the deposit fills small spaces on the surfaces. After deposition, a 30 wt% aqueous gelatin solution is applied to the carbon surface and

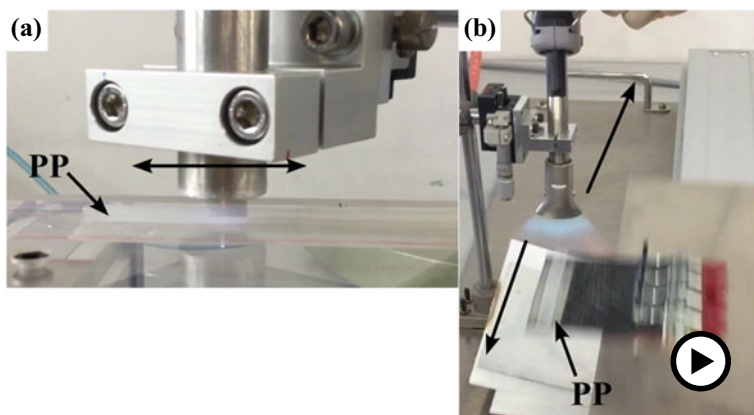


Fig. 23 Video showing atmospheric plasma (a) and flame (b) pretreatments of *i*PP surface employed for adhesion improvement (▶ <https://doi.org/10.1007/000-ayn>)

allowed to dry overnight under ambient conditions. The resulting solidified gelatin layer is removed along with the replica film from the substrate and immersed in an aqueous potassium thiocyanate (KSCN) solution to dissolve the gelatin layer. Following the complete dissolution of the gelatin layer, the Pt-carbon replica film is washed using dilute H_2SO_4 and water before being transferred onto copper grids coated with collodion. Finally, the replica film is observed by STEM.

Figure 24a–c shows STEM annular dark field (ADF) images of the replica films produced from the non-treated, flame, and plasma-treated *i*PP sheets, respectively. The replica from the non-treated sample (Fig. 24a) exhibits the lamellar feature of the *i*PP surface, indicating that the crystalline structures of the *i*PP surface are successfully transferred to the replica. The replica from the flame-treated sample (Fig. 24b), on the other hand, shows flat but no crystalline features, suggesting that an amorphous layer is formed after the flame treatment, and a replica of the plasma-treated sample (Fig. 24c) shows a very rough surface with pores of about 100 nm. Therefore, we can recognize that the two different surface treatments produce significantly different surface structures.

Figure 25 shows cross-sectional STEM-bright field (BF) micrographs of the interfacial regions between the adhesive and the surface-treated *i*PPs. As shown in Fig. 25a, the flame-treated *i*PP shows a relatively smooth interface where the strongly RuO_4 -stained layer with 50 nm thickness is formed. This result agrees well with the surface structure deduced by the replica experiment. The high-magnification view of Fig. 25a shows the lamellae of *i*PP in the bulk part underneath the interfacial amorphous layer. It can be interpreted that the rapid scanning of high-temperature flame over the *i*PP substrate melts the surface region of *i*PP and freeze the melted structure upon the rapid cooling from the melted state. The T_g of the amorphous part of *i*PP is lower than at room temperature; thus, this soft layer may form entanglements with the epoxy adhesive.

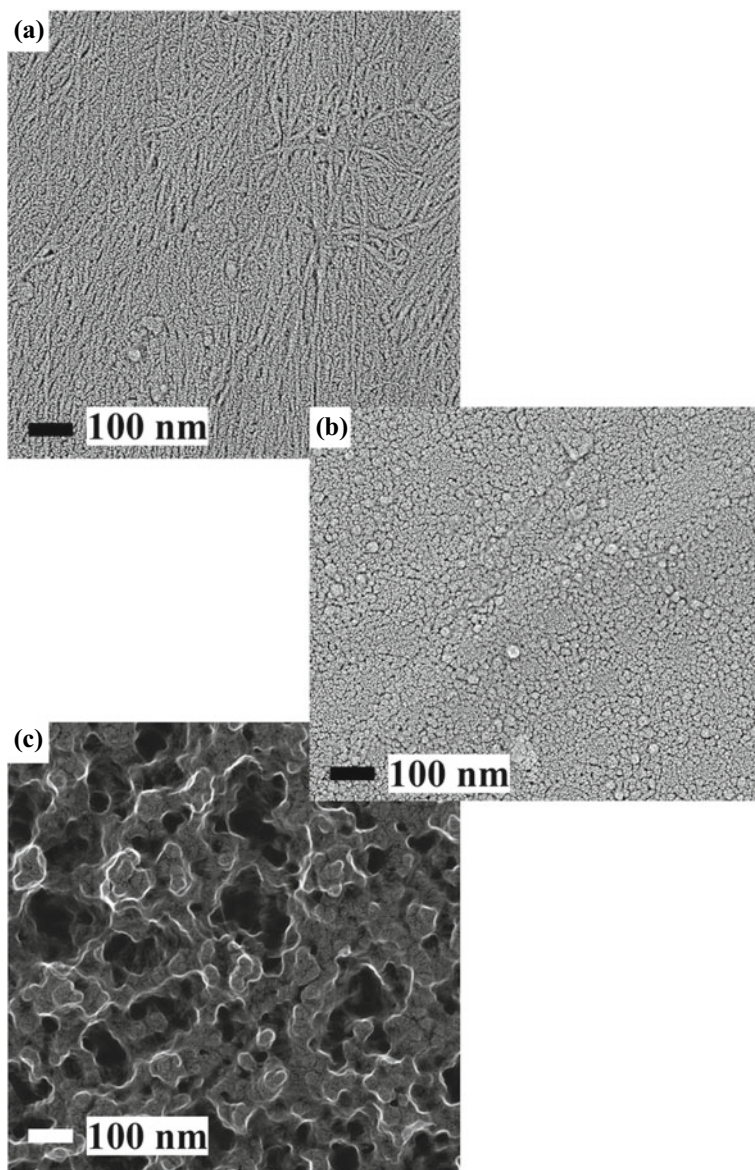
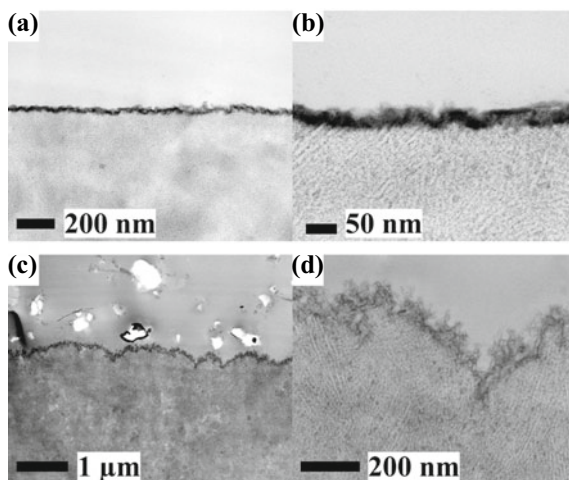


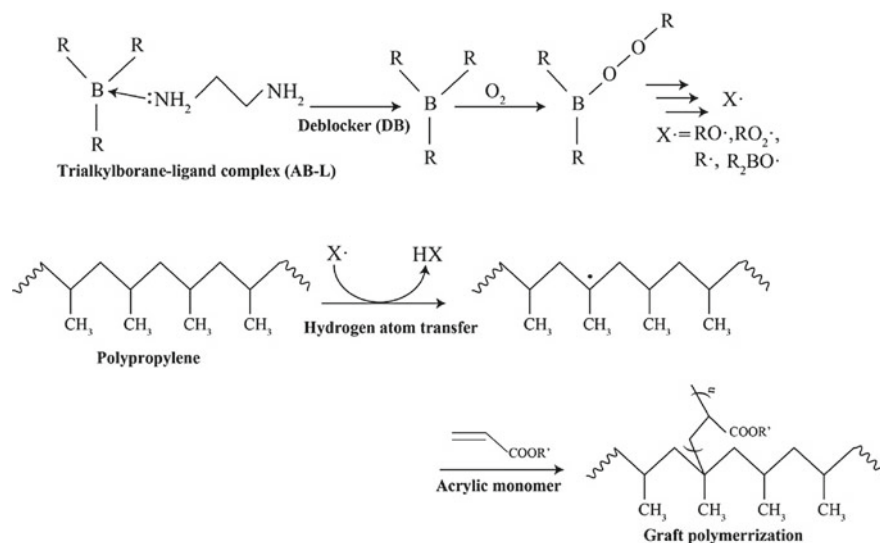
Fig. 24 STEM-ADF micrographs of replicas films showing the surface morphologies of *iPP*: **a** no treatment; **b** flame treatment; **c** plasma treatment

Fig. 25 STEM-BF micrographs showing the interfaces between *i*PP and adhesive: **a** flame treatment; **c** plasma treatment; **b**, **d** magnified images of **a** and **c**, respectively. The holes seen in the adhesive layer in **c** correspond to the traces of the inorganic fillers dropped off during the sectioning by ultramicrotomy



The plasma-treated *i*PP, on the other hand, exhibits an interface involving two different topological structures with different length scales, as shown in Fig. 25c and d. One is a rough feature having about 1 μm periodicity, while the other exhibits roughness with about 10 nm periodicity. The plasma treatment may etch the surface in two different processes simultaneously. The physical attack of plasma may create the micrometer scale etched surface. In contrast, the nanometer scale topological feature may be created chemically by the reactive species produced by the plasma. Figure 25d indicates that the roughness is almost equal to the lamellar thickness. It is therefore speculated that the amorphous part between the lamellae, called tie molecules, can be selectively etched chemically owing to the difference in the resistivity against the plasma between the amorphous and crystal parts. One can also recognize that the thin layer at the interface is relatively stained and more robust than the inside, suggesting that a thin layer with low crystallinity is formed at the surface. The crystalline structures of *i*PP are preserved under the modified skin layer. This means the plasma treatment can largely change the surface topographic features without losing the original polymer structures. And also, the adhesive can penetrate the complicated rough surface without voids.

We also evaluate the interfacial modification of *i*PP by an alkylborane-initiated acrylate-based adhesive. The chemical concept is shown in Scheme 1. In the first step, an alkylborane-ligand complex (AB-L) containing a monomer solution is mixed with another mixture of a deblocker (DB) and the monomer. Diisocyanate is used for the deblocker in this experiment. The complexed alkylboranes are deblocked in this process, generating uncomplexed trialkylborane, which is oxidized and produces several types of radicals. In the second step, the generated radicals initiate free-radical polymerization and graft polymerization from the *i*PP substrate. In the third step, an interfacial chemical reaction occurs between the adhesive and the substrate through hydrogen atom transfer, introducing radicals onto the *i*PP's backbone, where graft polymerization is initiated [51, 52].



Scheme 1 Reaction and adhesion process via complexed alkylborane

The adhesive mixture is placed between two *i*PP sheets at room temperature for 1 h, giving a strictly bonded plate. Figure 26 shows STEM-ADF images showing the interfacial region between *i*PP and the adhesive, where the bottom is the *i*PP substrate. The low magnification view (Fig. 26a) indicates that the adhesive creates a rough interface. The high magnification image (Fig. 26b) shows that the lamellae are partially cleaved from the substrate, producing disordered crystal structures. The stained region appears bright in the ADF images, corresponding to the amorphous part of *i*PP. Therefore, the highest magnification image (Fig. 26c) implies that the radical species produced by the oxidation of alkylborane attacks the amorphous phase between the lamellae and cleave the lamellae from the *i*PP substrate. In the next step, the acrylate monomers invade the amorphous part of *i*PP and initiate graft polymerization onto the lamellae. The STEM-ADF images present evidence of chemical interaction between the alkylborane (AB) initiated adhesive and *i*PP. Still, it is not a simple phenomenon, creating a heterogeneous thick interphase comprising the *i*PP lamellae, the amorphous *i*PP, and the grafted acrylate polymers.

The DCB test evaluates interfacial toughness. Untreated *i*PP does not bond at all and thus cannot be tested. Flame and plasma treatments, on the other hand, improve bond strength and allow testing, showing G_c values of 60 and 150 J/m², respectively. The AB-initiated adhesive offers excellent adhesion performance in the DCB test. The crack is not produced at the interface when the razor blade is inserted into the interface and the *i*PP plate fails.

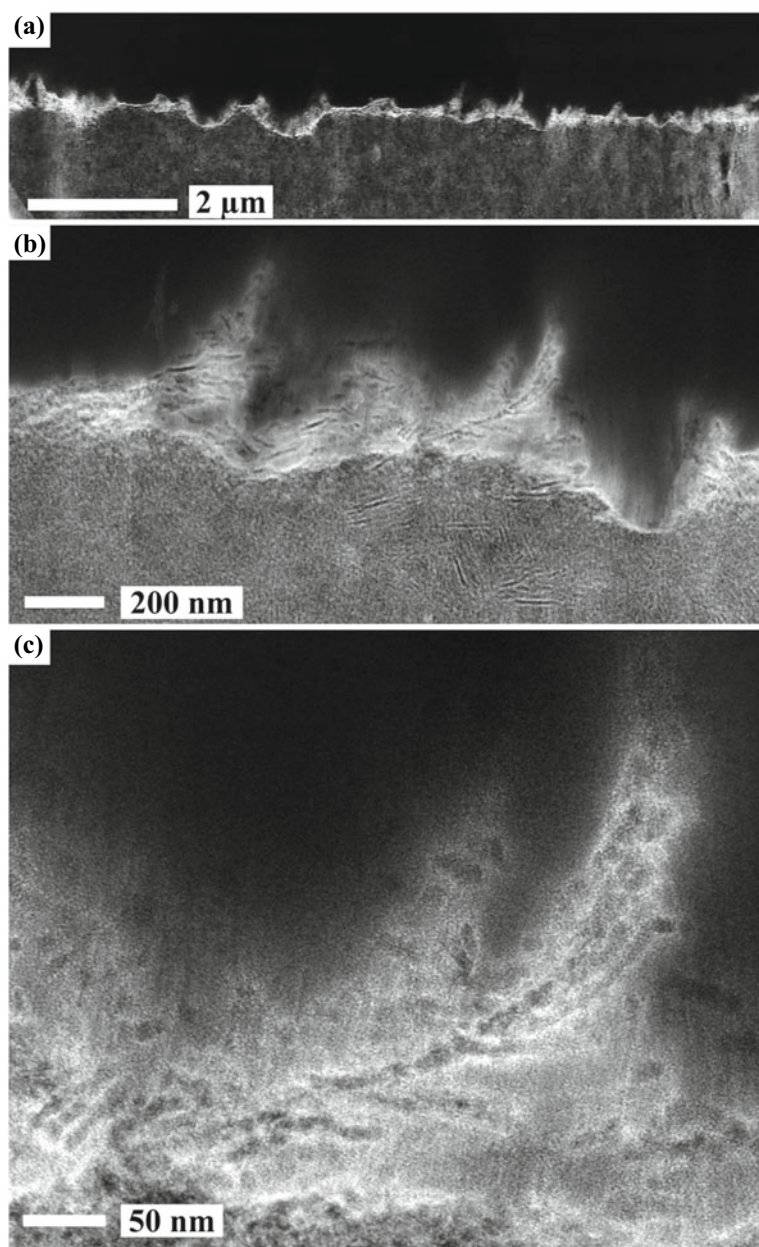


Fig. 26 STEM-ADF micrographs showing the interfacial region created by the alkylborane-initiated acrylate adhesive. The magnification increases in the order of **a**, **b**, and **c**

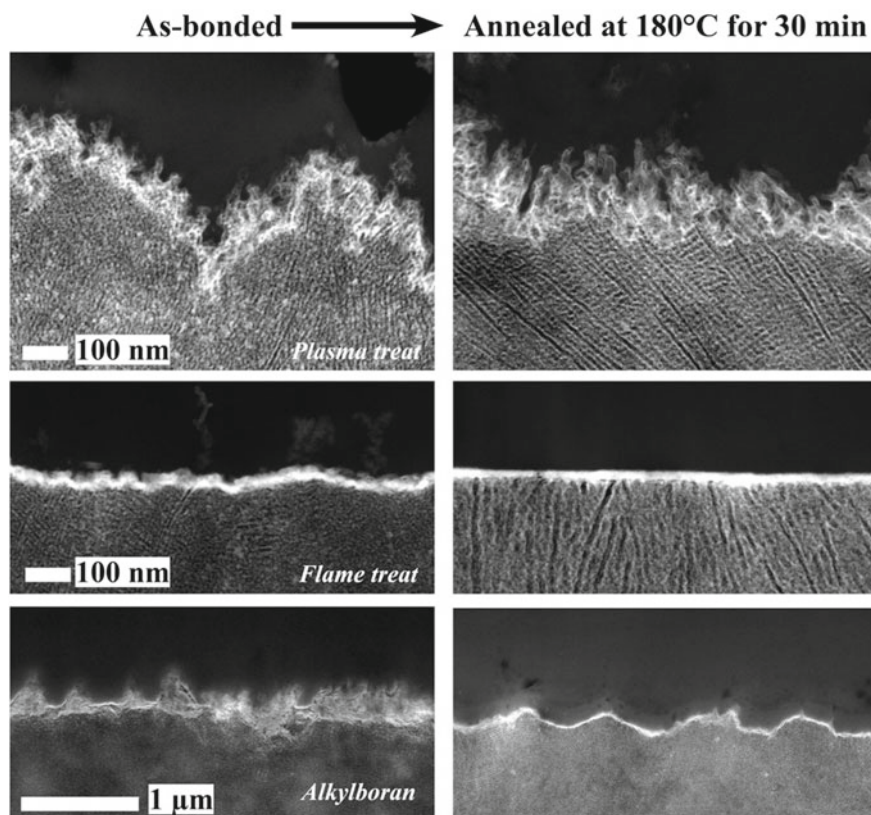


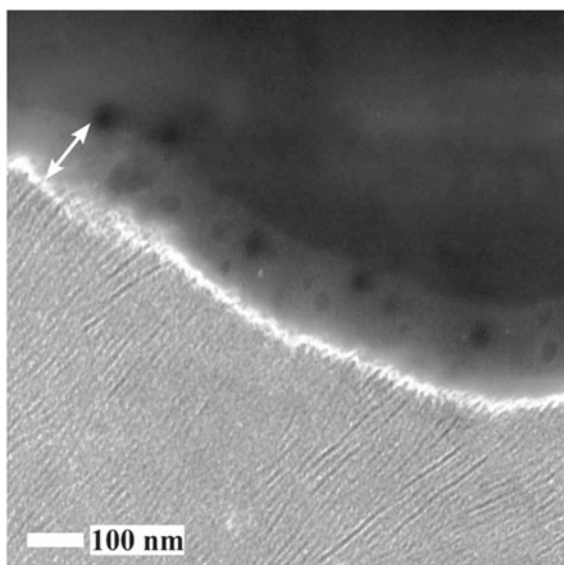
Fig. 27 STEM-ADF micrographs showing the changes of the interfacial region by thermal treatment at 180 °C for 30 min and subsequent cooling: plasma treatment (upper row); flame treatment (middle row); alkylborane-initiated adhesive (bottom row). The left column shows the interfaces of the as-bonded specimens, while the right column shows the interfaces after the thermal treatment at 180 °C for 30 min

We conduct further experiments to study the adhesion mechanism of the three surface and interface modification techniques. The bonded plates are annealed at 180 °C for 30 min and then cooled to room temperature. During this thermal treatment, the *i*PP melts and recrystallizes. The interfacial structures before and after the thermal treatment are inspected by STEM as shown in Fig. 27: The plasma-treated sample loses the micrometer level roughness features and flattened the interface with retaining nanometer-scale roughness after the thermal treatment (*upper row*). In the flame-treated sample, the thermal treatment makes the thin amorphous layer smooth (*middle row*). At the interface modified by the AB-initiated adhesive, the disordered lamellae produced by graft polymerization disappear while maintaining the micrometer-level roughness features (*bottom row*). The fact that the plasma-treated sample changes the morphology of the interface significantly suggests that the interface is loosely bonded. A similar trend is indicated in the flame-treated sample. Flame

treatment forms an amorphous layer and simultaneously causes chemical structure changes in *i*PP. The flat layer that forms after recrystallization comprises chemically modified compounds. The *i*PP that maintains the original structure included in the initial amorphous layer may be able to take part in recrystallization. Therefore, a thinner and flat interfacial layer is formed after the thermal treatment. In contrast to the plasma and flame pretreatments, the micrometer-scale roughness of the interface created by the AB-initiated adhesive remains the same even after the thermal treatment, indicating that the chemical bonding between *i*PP and the adhesive fixes the interface. The graft polymers developed onto the *i*PP main chains, produced by the AB-initiated adhesive, may disturb the recrystallization. Therefore, alternatively, a 100 nm thick layer is formed between the *i*PP crystalline phase and the adhesive, occluding domains of the adhesive composition as shown in Fig. 28, which is the high-magnification image of the bottom right image in Fig. 27. It should be mentioned that the lamellae can be seen clearly and tend to align perpendicular to the interface in all three samples after the thermal treatment. This means that the crystallization starts from the interface and grows inside.

The flame and atmospheric plasma treatments are effective for the adhesion of *i*PP, but the mechanism for those surface treatments differs. The flame treatment creates a thin amorphous layer on the surface which may promote the penetration of the epoxy adhesive and form molecular entanglement. This physical interaction is the main reason for the adhesion enhancement. The plasma treatment produces complicated surface roughness without the loss of the crystalline structure of *i*PP. This surface roughness mainly contributes to the adhesion increment to facilitate mechanical interlocking. Therefore, the chemical reactions between the adhesive and the substrate are not the first reason for the adhesion improvements. On the other

Fig. 28 STEM ADF micrograph showing the interfacial layer and the lamellar orientation formed after the thermal treatment in the interfacial region between the AB-initiated adhesive and *i*PP. The arrow indicated the amorphous layer formed by the graft polymer



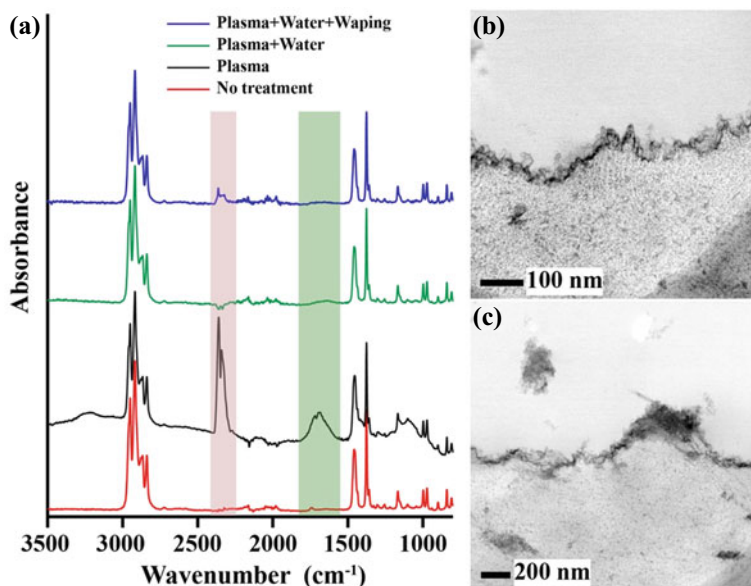


Fig. 29 ATR-IR spectra of as-prepared *i*PP (red), plasma-treated *i*PP (black), plasma-treated *i*PP washed with water (green), and plasma-treated *i*PP washed with water and rubbed subsequently with tissue paper (blue) (a). STEM-BF images of the interfaces between *i*PP and the adhesive: **b** after washing with water; **c** after rubbing with tissue paper

hand, the AB-initiated adhesive creates chemical bonds to *i*PP, which enhances the interfacial toughness remarkably.

Detailed surface chemical spectroscopy analyses are described in Chap. 5. Here, one typical result indicating the role of the chemical functional groups on adhesion is shown in Fig. 29a, which shows the ATR-IR spectra of non-treated (bottom) and plasma treated (second from the bottom). The ATR-IR spectra indicate carbonyl and hydroxyl functional group production after the plasma treatment. The third one from the bottom was obtained after washing the plasma-treated sample with water, showing the elimination of the peaks corresponding to the functional groups produced by the plasma treatment. This means that the plasma treatment causes the fragmentation of the polymers, which can be washed away from the substrate. The lap-shear bonding strength of the plasma-treated sample is 6.18 MPa, while it is 5.60 MPa after washing with water. Even with the elimination of the functional groups from the surface, the reduction of the bonding strength is limited. However, rubbing the surface with tissue paper after washing with water substantially reduced the bonding strength to be 3.13 MPa. Figure 29b and c are STEM-BF images of the interfacial region after washing with water and subsequent rubbing, respectively. No remarkable differences can be observed after washing with water in terms of the roughness of the interface, whereas, after rubbing, the roughness feature of the *i*PP surface is lost, and some fragments produced by the plasma treatment are detached from the *i*PP surface and

floated in the adhesive phase. This result strongly supports that chemical functional groups generated by plasma treatment have a limited role in adhesion enhancement.

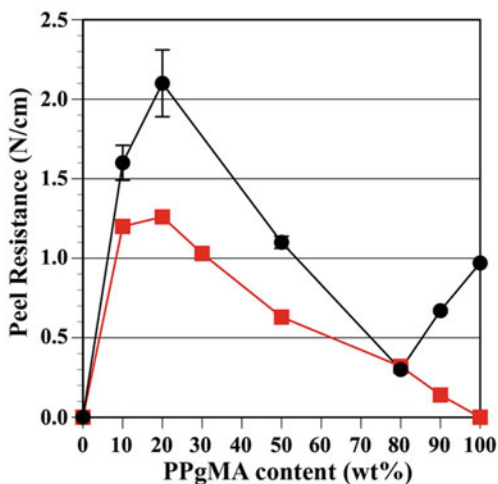
5 Formation of the Interphase Between Aluminum and Polypropylene—The Role of Reactive Functionality on Metal Bonding

The polymer–metal hybrid materials have been widely used in various industrial applications, leading to improved product design flexibility, product weight reduction, and protection of metallic surfaces in harsh environmental conditions. Polymers have been modified with chemically reactive groups to improve adhesion to the metallic adherend. It is generally believed that the formation of chemical bonds at the metal/polymer interface is the primary factor that enhances adhesion. Although detecting chemical bonding at adhesion interfaces is important in elucidating the bonding mechanism and assuring bonding reliability, obtaining direct evidence of covalent bonding is analytically challenging. In addition, adhesion performance is influenced not only by the two-dimensional metal/polymer interface but also by a three-dimensional (3D) “interphase” or “interfacial region” that possesses different properties and structural characteristics extending into the bulk materials [54, 55]. The thickness of this region remains unknown and has been the focus of extensive research. It is crucial to understand the bonding mechanism to identify the interfacial area and determine how it is created in the bonding process.

We conducted a simple adhesion experiment [53]. In this experiment, polymer films of the blends of *i*PP and PP grafted with maleic anhydride (PPgMA) are hot-pressed onto an Al sheet. The influence of the PPgMA content on adhesion is presented in Fig. 30: Pure *i*PP exhibit no adhesion to Al, but incorporating a small amount of PPgMA into *i*PP shows a remarkable increase in peeling resistance. Nevertheless, the bonding strength is reduced with a further increase in the fraction of PPgMA in the *i*PP/PPgMA blends. Based on the findings, adhesion enhancement may not be primarily attributed to interfacial chemical bonding between PPgMA and the Al surface.

The study uses *i*PP with an average molecular weight (M_n) of 67,000 and weight average molecular weight (M_w) of 250,000. PPgMA with different molecular weights are also used: One has an M_w of 9100 and a 3 wt.% MA content (*l*-PPgMA), while the other had an M_w of 153,000 and 3 wt.% MA content (*h*-PPgMA). The PPgMA was synthesized through free radical grafting of MA onto the PP backbone with peroxide during melt compounding. It is assumed that MA is mainly grafted onto the tertiary carbon of the PP backbone [56]. The *i*PP and PPgMA were melt-blended for 10 min at 300 rpm using an extruder. Subsequently, the resulting blend was molded into 300 μm thick films through hot-pressing between silicon wafers at 200 °C. The films were then hot-pressed between a 0.1 mm thick Al foil and a Si

Fig. 30 T-peel resistance to Al of the blend of *i*PP and PPgMA as a function of *i*PP/PPgMA ratio. Peeling resistance is plotted against the contents of *l*-PPgMA (red) and *h*-PPgMA (black) in the *i*PP/PPgMA blends. Reprinted with permission from [53]. Copyright 2021, American Chemical Society. All Rights Reserved



wafer. According to the DSC measurements, the *i*PP/PPgMA blends are miscible as a single peak corresponding to the melting temperature is observed [57].

The experiment involved heating the samples to 210 °C at a pressure of 10 MPa for 60 min, cooling them to 100 °C with the same pressure for 10 min, and finally cooling them to room temperature. The Si wafer was easily peeled off from the PP film after cooling. The T-peel resistance of adhesive bonds was measured according to the ISO11339:2010 [58] test method to measure the bonding strength. The relationship between the PPgMA content and peel resistance was similar for *h*-PPgMA and *l*-PPgMA, with *h*-PPgMA consistently exhibiting higher peel resistance. The maximum bonding strength is observed at 20 wt.% of PPgMA, and further increases lead to a steady decrease until the PPgMA content reached 80 wt.%. For *l*-PPgMA, the peel resistance decreases continuously with increasing content until it reaches zero with pure *l*-PPgMA. However, for *h*-PPgMA, a slight increase is exhibited in peel resistance when the content increased from 80 to 100 wt.%.

5.1 Bonding Mechanism Investigated by Replica-STEM Tomography

We thoroughly examine the fracture surfaces generated during the peeling test to investigate how adding reactive functional groups to *i*PP enhances its adhesion to Al. In Sect. 2, we utilized HR-SEM to find the nanoscale failure behavior of the fracture surfaces in the polymer interfaces. In this study, we perform the replica-STEM method to quantitatively evaluate the topographical surface features, allowing us to construct accurate 3D surface structures by STEM tomography using Pt/carbon replicas as described in Sect. 2.3.3.

To study the impact of PP_gMA on the adhesion between PP and Al, we initially examined the fracture surfaces' topological structures. Four fracture surfaces are produced, as illustrated in Fig. 31i when peeling the test specimens: an Al surface (FS-I); a PP surface separated from Al (FS-II); a PP surface detached from the silicon wafer (FS-III); a Si wafer surface (FS-IV). The replica-STEM technique accurately transfers the surface topological structures to the Pt-carbon thin replica films. The films are examined using STEM in the HAADF mode with an accelerating voltage of 200 kV. As the molecular weight does not impact the bonding properties, only *h*-PP_gMA-containing blend samples are investigated in the following. In the rest of this study, *h*-PP_gMA is referred to as PP_gMA.

Figure 31a–d depict STEM-HAADF micrographs of the replica films obtained from the four fracture surfaces between *i*PP and Al (*i*PP/Al). In Fig. 31b and c, surface lamellar morphologies with widths of approximately 10 nm can be observed on both sides of the *i*PP (FS-II and FS-III). The Al and Si wafer surfaces are presented

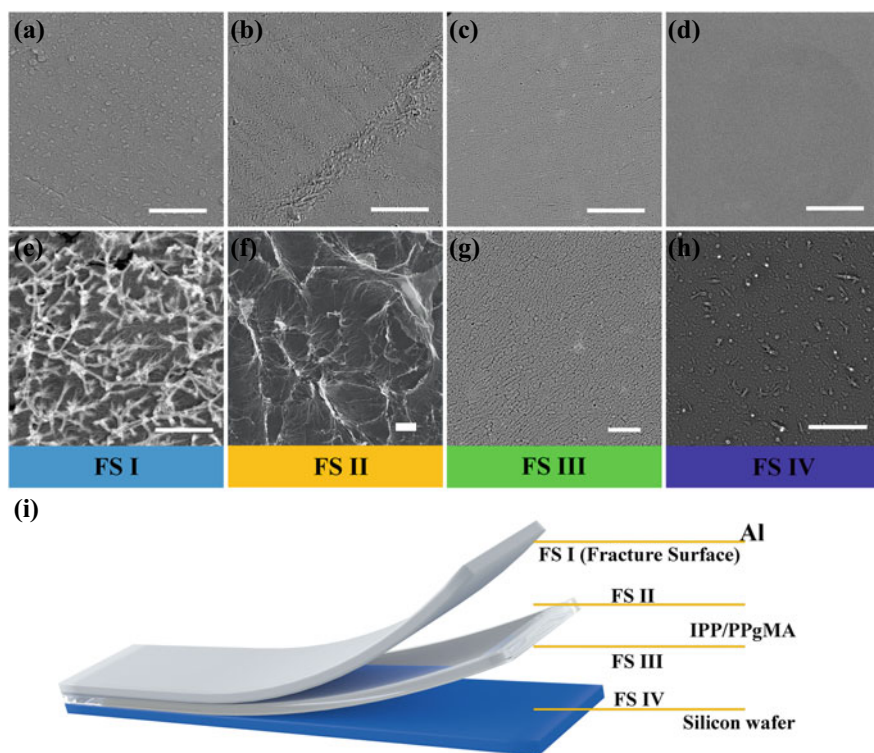


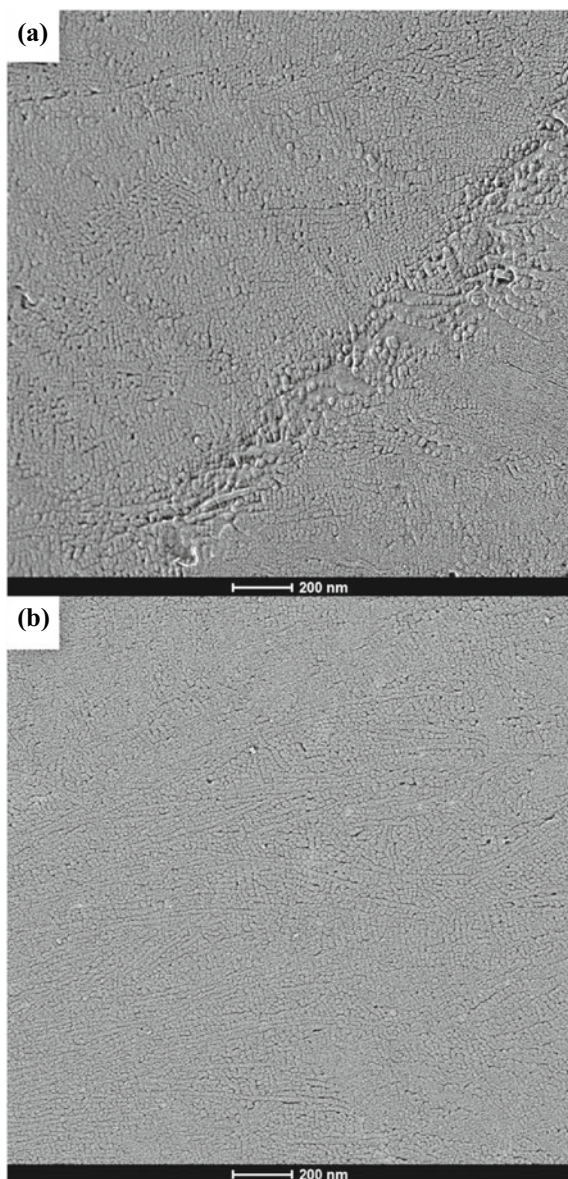
Fig. 31 STEM-HAADF images of the replica films taken from the fracture surfaces of the Al/ (*i*PP/PP_gMA)/Si wafer laminates as defined in (i): a–d fracture surfaces of an Al/*i*PP/Si wafer; e–h fracture surfaces of the lamination with the *i*PP/PP_gMA (80/20). Scale bars represent 500 nm. Reprinted with permission from [53]. Copyright 2021, American Chemical Society. All Rights Reserved

in Fig. 31a and d, respectively (FS-I and FS-IV), which appear smooth. Figure 32 provides enlarged images of Fig. 31b and c, demonstrating that the lamellar orientations on FS-II and FS-III exhibit distinct features. Specifically, the *i*PP failed from the Al foil consists of shorter lamellae, while that failed from the Si wafer contains longer lamellae. This discrepancy suggests that substrate surfaces can influence the crystallization of *i*PP despite the absence of adhesion. The lamellae on the surface attached to the Al foil grow from the Al surface, whereas those in contact with the Si wafer are randomly oriented. The Al surface significantly impacts the *i*PP crystallization more than the Si wafer. The replica images also highlight differences in the roughness of the *i*PP surface attached to the Al versus the Si wafer, reflecting the roughness of the Al foil and the Si wafer. The replica obtained from FS-I indicates the existence of small bumps less than 50 nm in diameter on the Al surface (Fig. 31a), while the FS-IV exhibits an entirely flat surface of the Si wafer (Fig. 31d). The results suggest that delicate surface structures of *i*PP can be successfully transferred to the replica, enabling observation of the crystallinity and topological features of the outermost surface of *i*PP. The Al/*i*PP interface is separated via interfacial failure, indicating no adhesion.

The incorporation of 10 wt.% of PPgMA leads to a significant improvement in the adhesion of PP to Al, as shown in Fig. 30. The fracture surfaces created by peeling the *i*PP/PPgMA (90/10) blend film from the Al substrate and from the Si wafer are shown in Fig. 31e-h. The addition of PPgMA causes substantial changes in the fracture surfaces, especially in FS-I and FS-II, where a large number of fibril-like fragments with widths of approximately 10 nm is generated on FS-I (Fig. 31e), and significant deformation of the *i*PP/PPgMA surface is observed on FS-II (Fig. 31f). In visual inspection, all samples' Al surfaces (FS-I) exhibit uniform metallic luster, implying interfacial failure. However, the STEM-replica technique indicates that a thin polymer layer with nanoscale fibril-like fragments is formed (Fig. 31e) in the failure process between the *i*PP/PPgMA blend film and the Al. Figure 33a, a zoomed-in image of Fig. 31e, shows that the entire Al surface (FS-I) is covered with *i*PP/PPgMA. Additionally, the Al/(*i*PP/PPgMA) interface exhibits asymmetric failure, as demonstrated in Fig. 31e and f. Figure 31b is a high-magnification image displaying the deformed *i*PP/PPgMA fibrils on FS-II, which are significantly larger than those observed on the Al surface FS-I. In contrast, the fracture surface of *i*PP/PPgMA separated from the Si wafer (FS-III) shows a lamellar morphology (Fig. 31g), and even with no adhesion, a small quantity of polymer adheres to the Si wafer FS-IV (Fig. 31h).

The results above suggest that the fine features on the fracture surfaces can be replicated onto thin film. While surface structures can be observed directly by SEM, of which resolution is limited due to specimen charging and damage caused by the electron beam. Conductive coatings can prevent charging but hinder the observation of fine structures, and convergent electron beams can penetrate below the surface, making it difficult to obtain true surface images [59]. In contrast, the replica-STEM technique overcomes these drawbacks and enables 3D visualization of surfaces through tomography. The video presented in Fig. 34 displays a sequence of STEM-HAADF tilt images that are obtained by incrementally tilting the sample from -60° to

Fig. 32 STEM-HAADF images of the replica films showing the surface lamellar morphologies of *i*PP: **a** *i*PP separated from the Al substrate; **b** *i*PP separated from the silicon wafer. Reprinted with permission from [53]. Copyright 2021, American Chemical Society. All Rights Reserved



+ 60° with a 2.5° interval. These images are used to reconstruct a 3D image through alignment and statistical analysis. In Fig. 35a–f, bird’s-eye and side views of the 3D reconstructed fracture surfaces of the Al sides after peeling off *i*PP/PPgMA blend films with various ratios are displayed. These images show the spatial distribution of the fibrils produced on the Al substrate. The 80/20 blend exhibits the highest density

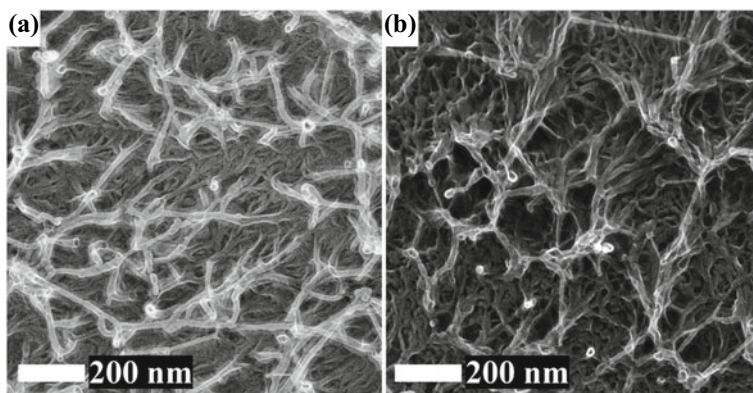


Fig. 33 Magnified STEM-HAADF images of the replicas shown in Fig. 31e and f: **a** the fracture surface of Al; **b** PP surface of *iPP/PPgMA* (90/10) blend. Reprinted with permission from [53]. Copyright 2021, American Chemical Society. All Rights Reserved

of fibrils, whereas the 100/0 blend shows no polymer fragments. The 3D visualizations also provide information on the fibrils' length, shapes, and branching, which are then transformed into thin filaments using skeletonization. Statistical analysis shows that the average thickness of the fibrils is 9.4 ± 5.1 nm.

The failure of the interfaces between the Al and *iPP/PPgMA* blend is asymmetric, as demonstrated by the highly elongated fibrils along the direction of the crack opening on the PP side of *iPP/PPgMA* 90/10, as shown in Fig. 37. The lamellar

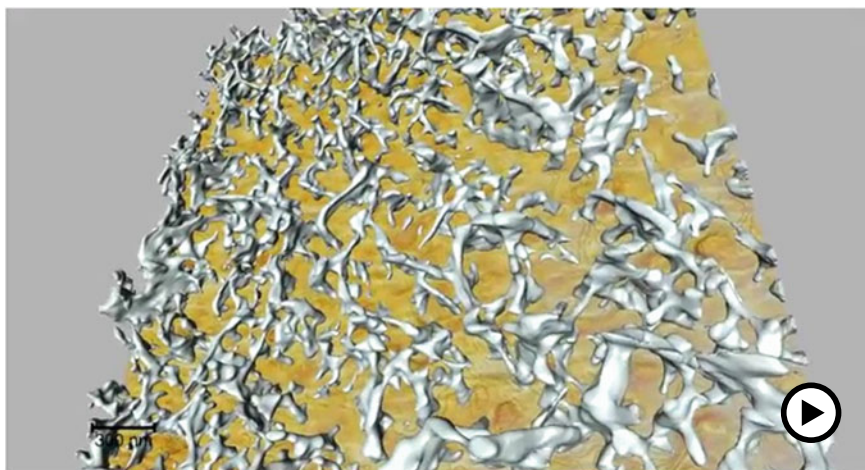


Fig. 34 A video showing a series of the STEM-HAADF tilt images acquired from -60° to $+60^\circ$ degrees with a 2.5° step, and the 3D image reconstructed after the alignment of the tilt images followed by quantitative and statistical analyses. Reprinted with permission from [53]. Copyright 2021, American Chemical Society. All Rights Reserved (► <https://doi.org/10.1007/000-ayk>)

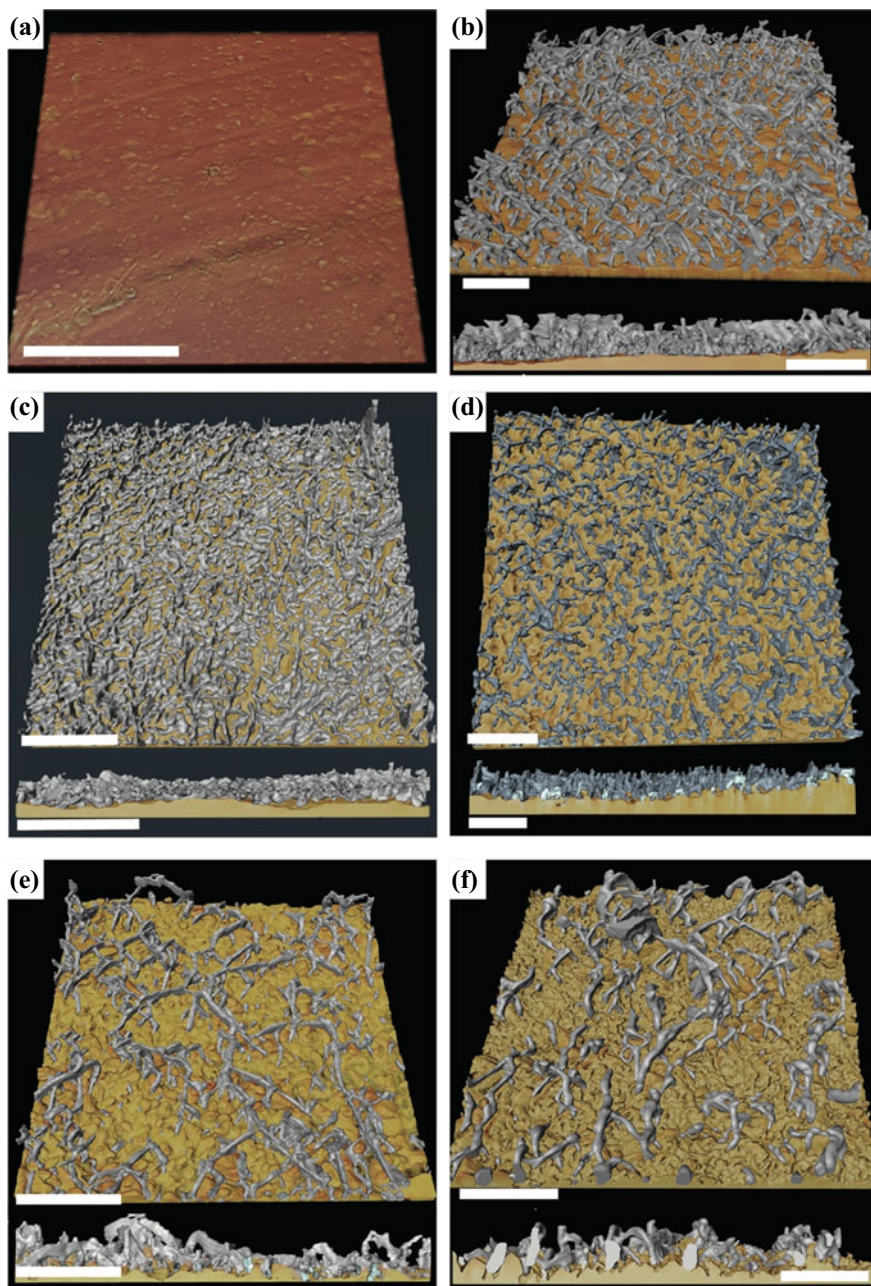
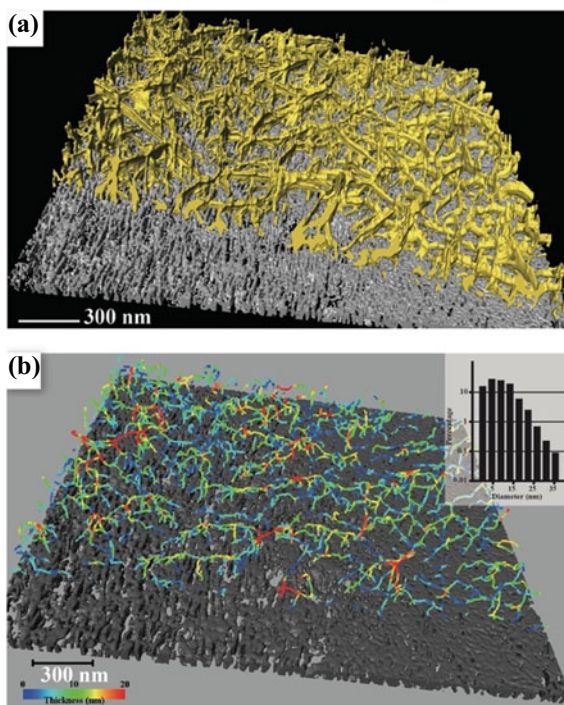


Fig. 35 Bird's-eye and side views of fracture surfaces of the Al substrate reconstructed by STEM-tomography of the replicas. Panels (a) through (f) correspond to *i*PP/PPgMA blend ratios of 100/0, 90/10, 80/20, 50/50, 10/90, and 0/100, respectively. Scale bars represent 500 nm. Reprinted with permission from [53]. Copyright 2021, American Chemical Society. All Rights Reserved

Fig. 36 3D re-constructed image of the replica representing the fracture surface of the Al surface bonded to the *i*PP/PPgMA (90/10) laminate (a) and the color map representing the fibril's thickness distribution (b). The Inset in (b) is a histogram showing the distribution of the thickness of the fibrils. Reprinted with permission from [53]. Copyright 2021, American Chemical Society. All Rights Reserved



structure with elongation along the crack opening direction is retained in the bottom part (gray), while the upper part (yellow) is largely elongated, making the crystalline structure unrecognizable. The STEM-replica technique can visualize this deep and complicated structure using rotary shadowing, which allows Pt-C deposition to reach into narrow spaces, as shown in the video (Fig. 38) [60].

Figure 39 illustrates the plot of bonding strength versus blend ratio, where the fracture surfaces of the Al side are displayed, and the corresponding images reveal the qualitative links between bonding strength and nanofibrillar formation. The 3D visualization presented in Fig. 35 enables an approximation of the volume fractions of the fibrils generated on the Al surfaces in the region predominantly occupied by the fibrils. The association between the volume fraction of the fibrils and peeling resistance is demonstrated in Fig. 40a, suggesting that the bonding strength rises as the volume fraction of fibrils increases.

Similar surface features have been observed in the failure of interfaces between glassy polymers, as discussed in Sect. 3 and reported in previous studies [17, 41, 44, 48]. In the welding of PS, for example, the thickness of the interface increases due to interdiffusion, and nano-fibrils are generated in the failure of the interfaces that form in the early stages of interdiffusion, where entanglements are insufficient to trigger crazing. The length and number of fibrils increase with increasing interfacial toughness before the failure mode transition, concluding that these nano-sized fibrils are associated with the failure of weak interfaces resulting from the interdiffusion of

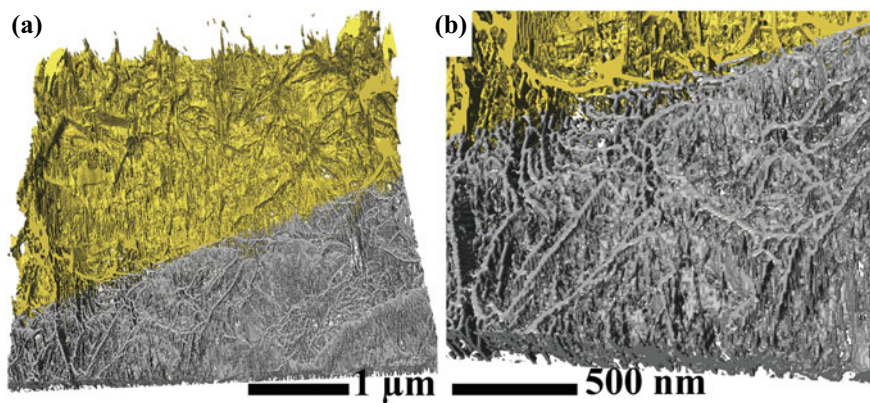


Fig. 37 The fracture surface of the PP in (*i*PP/PPgMA (90/10))/Al laminate. The yellow portion represents the outermost fractured surface, while the gray part indicates the inner parts with lamellar structures. A magnified view of (a) is shown in (b). Reprinted with permission from [53]. Copyright 2021, American Chemical Society. All Rights Reserved

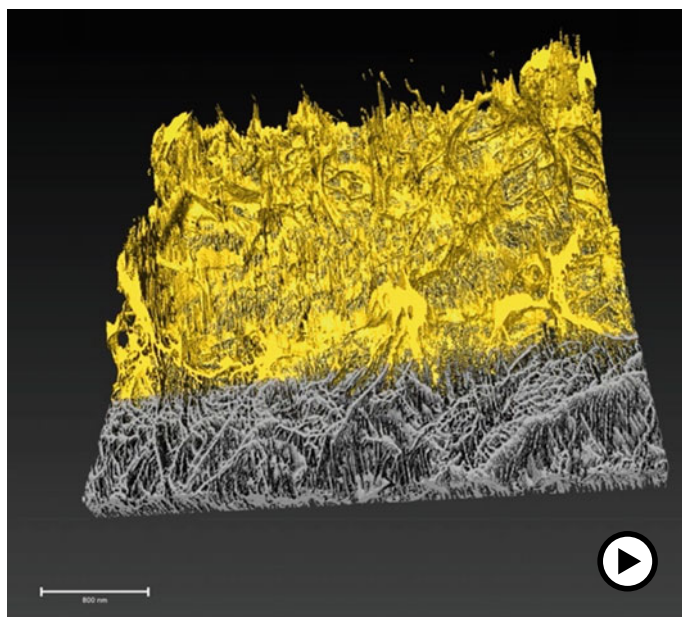


Fig. 38 A video showing the 3D structure of the fracture surface on the PP side of *i*PP/PPgMA 90/10 (▶ <https://doi.org/10.1007/000-aym>)

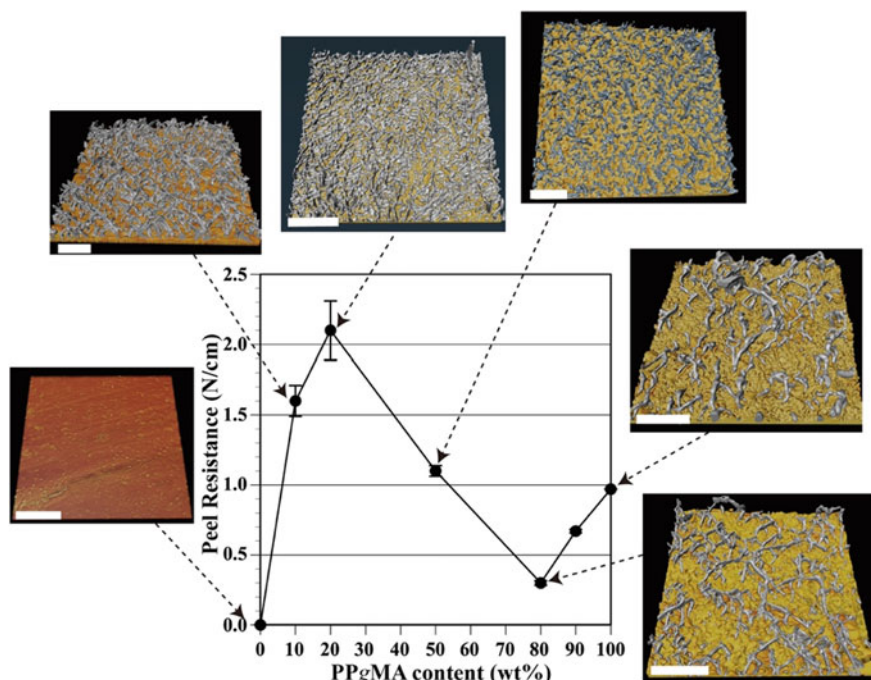


Fig. 39 Correlation between the 3D fracture surfaces constructed by replica-STEM tomography and the bonding strength between Al and *i*PP/PPgMA

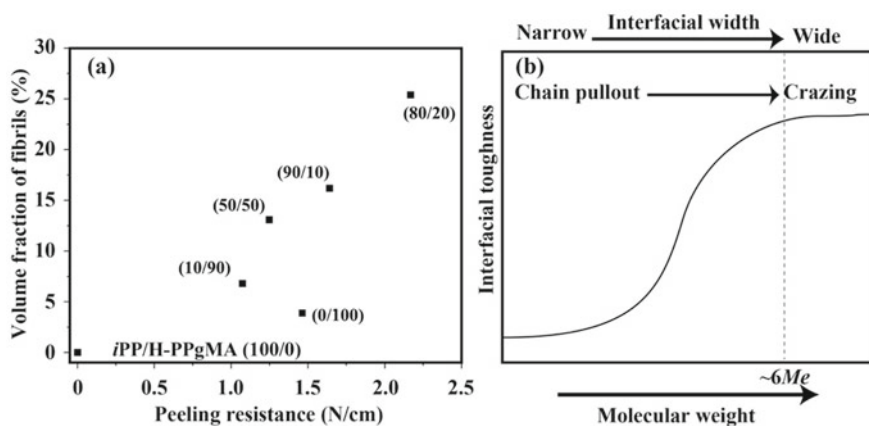


Fig. 40 Relationship between volume percentage of the fibrils produced on the Al fracture surfaces versus peeling resistance (a) and schematic representation of the dramatic increase in interfacial toughness resulting from a shift in failure mode (b). Reprinted with permission from [53]. Copyright 2021, American Chemical Society. All Rights Reserved

glassy polymers. In contrast, in the bonding of polymers to metals, interface diffusion is not possible.

Once again, we examine the bonding mechanism using the *S*-shaped curve as demonstrated in Fig. 17. For polymer–polymer adhesion, where entanglements play a crucial role, the interfacial toughness typically depends on the interfacial width. In contrast, the interfacial toughness is linked to the polymer’s molecular weight for polymer–metal adhesion, as indicated in Fig. 40b. According to the scaling analysis, failure mode transition occurs when the chain length exceeds the length associated with a molecular weight of $6Me$, where Me is the molecular weight between entanglement points. For instance, the Me of PS was reported to be 18,000, whereas that of *i*PP was 5,100–8,100. In this case, it is likely that a low-molecular-weight glassy or low-crystallinity layer formed in the region near the metal/polymer interfaces, leading to failure within that layer.

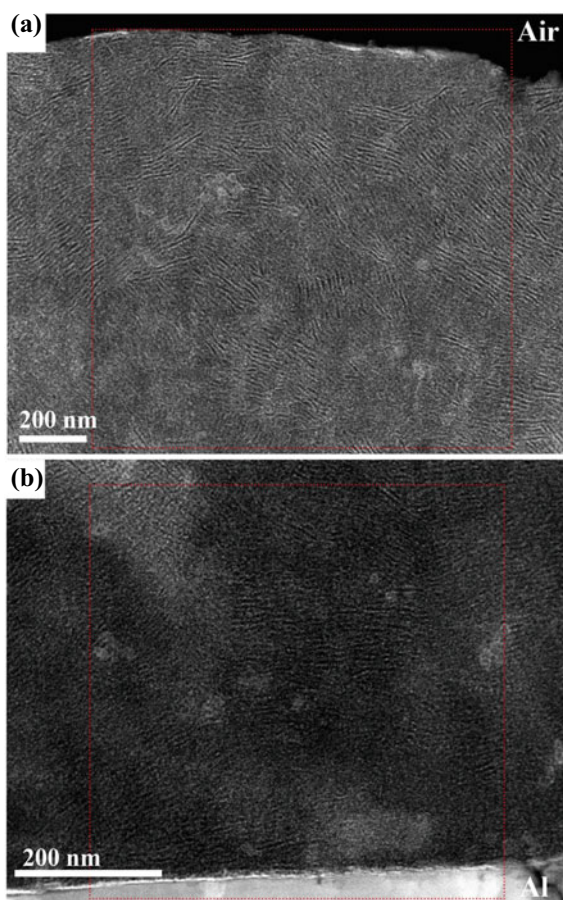
The replica-STEM technique enables us to find the generation of the nano-sized fibrils on the Al substrate when peeling off the lamination. This technique is especially effective in the point that the 3D visualization of the occurrence of the surface deformation on failure is visible. Additionally, it is interesting that the failure of polymer/metal-bonded interfaces produces surface features similar to entanglement-based polymer/polymer adhesion. We discover that a low-crystallinity and low-molecular-weight layer forms in the interfacial region, which is responsible for improving adhesion. We believe that this “soft layer” is produced due to the interfacial chemical reaction of PPgMA to the reactive moieties, such as -OH or adsorbed water on the Al surface. Furthermore, MA and Al surface’s interfacial chemical reaction leads to *i*PP with grafted carboxylic acid groups (-COOH), which may be excluded from the *i*PP crystal lamellae. The asymmetrical features of the Al and PP side’s fracture surfaces suggest gradient structures in the “soft layer” in terms of crystallinity and molecular weight. Structures with relatively low molecular weights and lower crystallinity are likely formed on the Al side, which segregates PPgMA when it is added as a minor component in the blend up to 20 wt%. The adhesion strength depends on the toughness of the “soft layer,” mainly determined by its molecular weight and crystallinity. Therefore, we conclude that chemical bonding does not achieve the enhancement of the metal/polymer adhesion. Still, chemical bonding is needed to induce the segregation of PPgMA from *i*PP, which causes the formation of the “soft layer”.

5.2 Mechanism of Interphase Formation

The replica-STEM fractography study indicated that forming a low-crystallinity and low-molecular-weight layer at the interfacial region is responsible for improving adhesion. This layer is likely produced via crystallization in the end of the hot-melt bonding process. It is likely accompanied by a change in the miscibility between *i*PP and PPgMA induced by the interfacial reaction between PPgMA and the Al surface.

The lamellae of the 80/20 wt/wt *i*PP/PP_gMA blend at the interfacial region and at the free surface are inspected by STEM (Fig. 41). The lamellae of PP can be visualized by staining with RuO₄ because the amorphous region can be stained preferentially. The interlamellar amorphous region exists between the stacked lamellae in which the folded segments in a polymer chain are arranged parallel to the neighboring segments. These amorphous layers can be selectively stained, making the lamellae visible as the unstained region. Therefore, the lamellae are visible to be dark filaments between the bright amorphous layers in the HAADF mode in STEM. Notably, the visibility of lamellae in the region below the surface (Fig. 41a) is markedly clear compared to that in the interfacial region (Fig. 41b), implying that the interfacial region contains disordered lamellae. Additionally, the lamellae in the interfacial region prefer parallel orientation to the Al surface plane, while no particular lamellae orientation can be found in the region below the surface. Specifically, the “flat-on” lamellae are grown in the interfacial region, in which the chain axis is normal to the Al substrate.

Fig. 41 STEM-HAADF images showing the lamellae of *i*PP/PP_gMA (80/20) blend: **a** surface side; **b** interfacial region. FFT calculations were performed for the red frames



Fast Fourier transformation (FFT) of an image allows the determination of its periodic components and their corresponding frequencies. Moreover, it identifies the preferred orientation direction of the structures within the image [61]. The FFT analyses of the lamellar structures were performed as shown in Fig. 42, which allows us to evaluate the orientation and thickness of the lamellae of PP. The FFT images were created from the area in the red flames shown in Fig. 41. The FFT image on the surface side is characterized by a broad pair of arcs (Fig. 42a), whereas that in the interfacial region is characterized by a pair of bright spots (Fig. 42b). The inverse Fourier transformations of the areas including the reflexes (peripheral arcs and spots) in the FFT images (as demonstrated in Fig. 42c and d) can produce clarified images representing the periodical structures, as depicted in Fig. 42c and d. The images also highlight the difference in lamellar orientation between the surface side and the interfacial region.

These findings suggest that the interaction between the Al surface and the *i*PP/PPgMA blend affects the growth of the lamellar during the crystallization from the isotropic melts. It has been known that lamellar crystallites exhibit preferential orientation in thin films because of their confinement and interactions with the

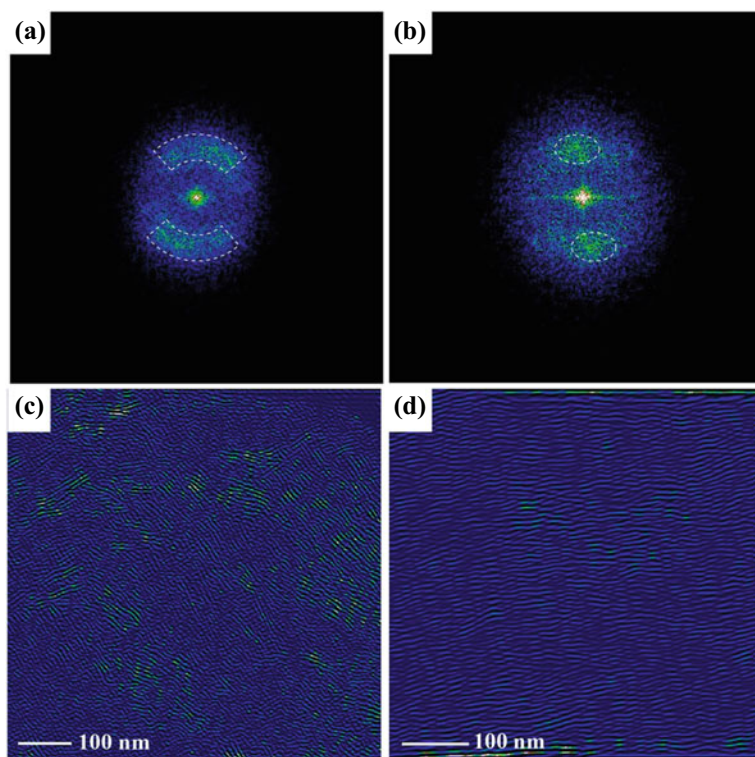


Fig. 42 FFT images (a, b) and inverse Fourier transformed images (c, d) for the regions marked by red flames in Fig. 41: a, c surface side; b, d interfacial region

substrate [62–64]. In a film with thicknesses of 100–1000 nm, they usually form “edge-on” lamellae, where the chain alignment can be parallel. They usually form flat-on lamellae in a much thinner film with thicknesses less than 100 nm. The film is much thicker than these critical thicknesses in the situation studied here. It is, therefore, presumed that the preferential “flat-on” lamellae in the interfacial region are produced by the chemical interaction between PPgMA and the Al surface.

Further details of the interphases were investigated by the localized thermomechanical responses of the cross sections of the *i*PP/PPgMA blend bonded to the Al [65]. The localized thermomechanical analysis was performed using an atomic force microscopy (AFM) instrument with a thermal probe tip to heat locally on PP, called NanoTA. NanoTA is a local analytical technique that combines the high-spatial-resolution imaging capabilities of AFM with the ability to obtain high-spatial-resolution information on the thermomechanical behavior of materials at specified positions [66, 67]. The local thermomechanical analysis by NanoTA could successfully identify the interphase between *i*PP/PPgMA blends and the Al substrate. The thermomechanical behavior near the Al/PP interface exhibited distinct differences compared to the bulk region or even the surface side of PP. The interphase extended approximately 10 μm away from the Al/PP interface towards the bulk region of PP, as described in [65].

Observations using STEM revealed that the interphase consisted of disordered “flat-on” lamellae when examining lamellar crystals. The wide interphase formation, triggered by a chemical reaction between PPgMA and the Al surface, occurs through phase separation of the blend. It’s important to note that the interfacial chemical reaction doesn’t directly enhance bonding strength but instead creates the interphase, which plays a critical role in improving bonding strength. The elucidated bonding mechanism highlights the need for careful control of cooling conditions in the bonding process to create an optimized interphase for desired bonding properties. Figure 43 illustrates the mechanism behind interphase formation during the bonding process.

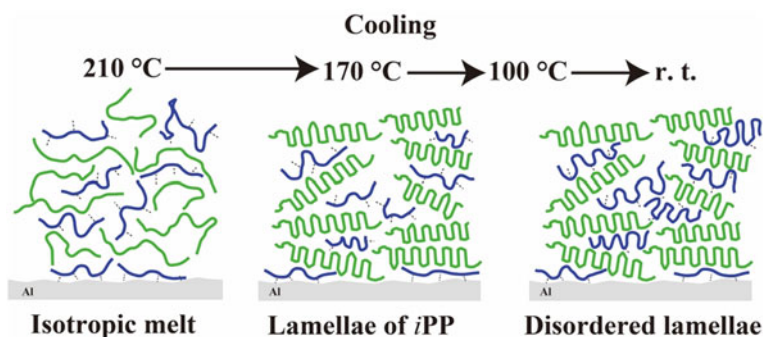


Fig. 43 Schematic illustration depicting the interphase formation during the *i*PP/PPgMA blend bonding to Al. The blue and red represent *i*PP and PPgMA chains, respectively

According to the proposed explanation, a chemical reaction takes place between PPgMA and the —OH functional groups on the Al oxide surface, as well as the adsorbed water molecules, converting MA to dicarboxylic acid. When the blend film is hot-pressed onto the Al foil at 210 °C, PPgMA selectively adheres and immobilizes on the Al surface due to the MA-Al oxide surface reaction. This preferential adsorption serves as nucleation sites for *i*PP crystallization, leading to the growth of “flat-on” lamellae in the interfacial region. As the sample cools, *i*PP initiates crystallization, forming ordered lamellae, while the converted PPgMA is expelled from the *i*PP lamellae and becomes encapsulated by them. During subsequent cooling stages, PPgMA gradually crystallizes until the sample reaches room temperature. However, the presence of surrounding ordered *i*PP lamellae may disrupt the chain folding of dicarboxylic acid-grafted PP, resulting in the production of disordered lamellae. This situation occurs when PPgMA is a minor component in the blend, typically with a composition of less than 20 wt% to achieve enhanced bonding strength.

6 Mechanism of Adhesive Bonding of Aluminum Alloys Studied by STEM-EELS/ELNES

Due to the excellent combination of mean density, high strength, and good corrosion resistance, aluminum alloys will be crucial for constructing lightweight car bodies. To understand the bonding mechanism of aluminum, the heterogeneous structures in the aluminum surface layer and its molecular-level chemistry in the bonding process must be well understood. The natural aluminum surface possesses thin oxide and/or hydroxide compounds with porous structures, of which the thickness is less than 10 nm [68]. In this work, we study chemistry at the interfaces in the adhesive bonding process of aluminum alloy with an epoxy adhesive by STEM-EELS and study the bonding mechanism [69].

6.1 Mechanism of Steam Treatment in Improving Adhesion Bonding of Aluminum

To achieve robust adhesion with durability in adhesive bonding, it is essential to identify practical, cost-effective, safe, and environmentally friendly surface treatment methods. Pretreating Al surfaces by immersing them in boiling water has been known as a suitable technique [70, 71]. We found that the bond strength of Al alloys and epoxy adhesives can be improved by a straightforward steam treatment approach, in which the Al surface is exposed to hot steam created by a commercial steam cleaner for 5 min. The effectiveness of the steam treatment on Al–Al adhesive bonding is evaluated using technical grade sheets of Al6061 alloy with a thickness of 2 mm, and lap shear strength tests are conducted using epoxy adhesives. The epoxy adhesive

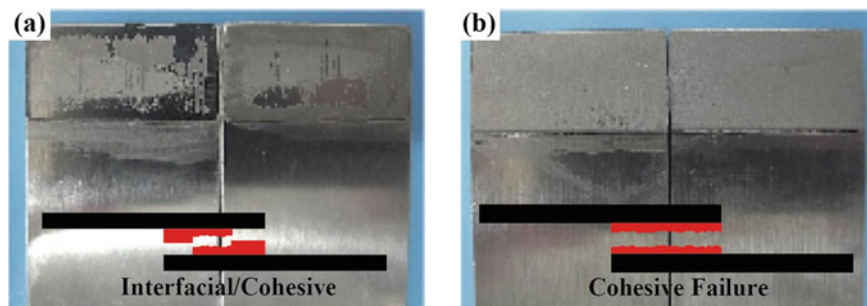


Fig. 44 Photographs of fracture surfaces showing interfacial failure with the degreased aluminum (a) and cohesive failure with the steam-treated aluminum (b). Reprinted with permission from [69]. Copyright 2022, Elsevier. All Rights Reserved

used in this study is a simple mixture of bisphenol A diglycidyl ether (DGEBA) and diphenyl diamino sulfone (DDS). When aluminum is sonicated with chloroform for degreasing, the lap shear strength is 10.8 ± 3.2 MPa. In contrast, steam-treated Al yielded 19.9 ± 1.1 and 22.8 ± 1.2 MPa. Subsequent macroscopic observation of the fracture surface revealed that the improved bond strength resulted from a change in failure mode, as shown in Fig. 44. The degreased aluminum showed a mixed “interfacial” and “cohesive” failure (Fig. 44a), while the steamed aluminum showed complete cohesive failure (Fig. 44b).

The aluminum/adhesive interfaces were inspected by STEM to investigate the mechanism of adhesive strength improvement by steam treatment. When the specimen was cut perpendicular to the interface, the projected two-dimensional (2D) image overlapped the three-dimensional (3D) structure within the interface region, so that interface details could not be observed (Fig. 45a). To address this issue, samples were prepared by cutting at an angle to the interface. The detailed procedure is depicted in Fig. 9 in Chap. 2. This gave an oblique projection showing very thin aluminum oxide regions (Fig. 45b). The interfacial structural details could be seen, revealing the roughness and porosity of the thin layer on the aluminum surface. STEM-tomography reconstruction using tilted series images of obliquely sectioned samples reveals the porous features of the aluminum oxide surface in 3D, showing that the aluminum surface exhibits a complex structure with densely packed pores of size 10–20 nm (Fig. 45c). The natural aluminum surface of industrial aluminum plates is coated with a porous 10 nm layer of oxides and/or hydroxides [69], so the surface is not atomically flat. When the surface of the used aluminum plate was observed by SEM, no significant difference was observed before and after the steam treatment.

The STEM-EDX elemental maps of C, O, and Al of the adhesive interfaces formed with either steam-treated or degreased Al are shown in Fig. 45d and e, respectively. The STEM-HAADF images on the left in each series show the surface roughness of the aluminum that the oblique sectioning can see. The Al and O elemental maps allow for identifying the oxygen-containing Al parts on the surface, and the C elemental

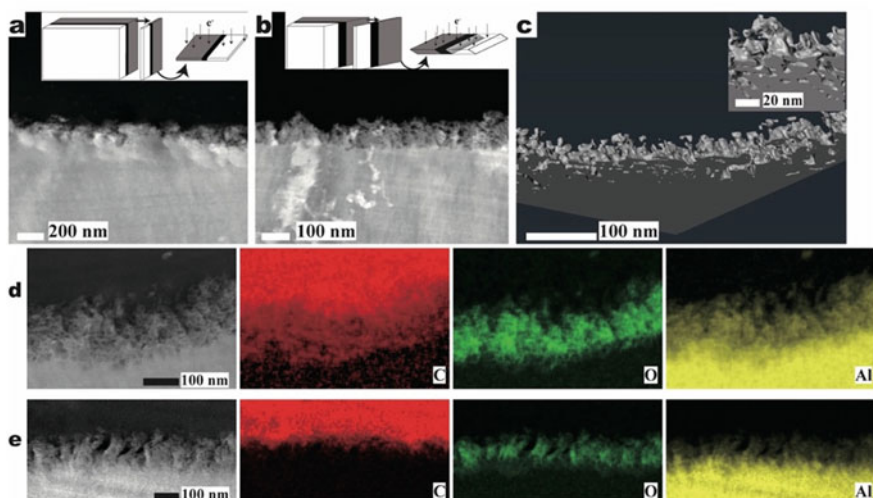


Fig. 45 Cross-sectional images of adhesive interfaces: **a, b** STEM-HAADF images of the adhesive interfaces of the steam-treated Al with a cross section (**a**) and an oblique section (**b**) at 30° to the interfacial plane as depicted in the insets in **a** and **b**; **c** 3D Al surface image re-constructed by STEM-tomography; **d, e** STEM-HAADF image and EDX elemental maps of carbon, oxygen, and aluminum of adhesive interfaces of steam-treated (**d**) and degreased aluminum (**e**). Reprinted with permission from [69]. Copyright 2022, Elsevier. All Rights Reserved

maps represent the location of the adhesive. In steam-treated aluminum, the adhesive diffuses and infiltrates the micropores of the oxide layer. In contrast, in the degreased aluminum, the adhesive only makes contact with the Al surface and does not penetrate the pores.

To examine the chemical composition of the Al plate's surface layer before bonding, thin cross sections were made from the Al plate before and after steam treatment using ultramicrotomy. These cross sections were analyzed by STEM-EELS in SI mode [72–75]. Two EELS spectra are acquired nearly simultaneously in dual EELS mode, one for the low-loss region and another for the high-loss region, including the O K-edge. The core-loss spectra's accurate energy-loss positions are obtained by drift correction of the zero-loss peak. To remove the plural scattering effects in the core-loss region using the shapes of the low-loss spectra, Fourier logarithmic deconvolution is applied to the obtained spectra. The chemical structures of the Al surface layer produced due to steam treatment are investigated using O K-edge ELNES and are shown in Fig. 46. Before steam treatment, a STEM image in HAADF mode was taken, and spectral data were obtained from the ROI shown in Fig. 46a. The maps representing the intensities in the narrow energy window of 530–535 eV are created (Fig. 46b, e and h), corresponding to the small peak in the energy loss region shown as green-shaded boxes in Fig. 46c, f, and i before the edge of the main peak. The results demonstrate that the Al surface layer underwent chemical changes due to steam treatment, as evidenced by the increased population and intensity of the small

peak in the 530–535 eV energy loss region. The results after steam treatment for 1 and 3 min are presented in Fig. 46d through 46i.

EELS spectra of various oxygen-containing Al compounds were obtained to investigate the ELNES characteristics of the O K-edge in the Al surface layer.

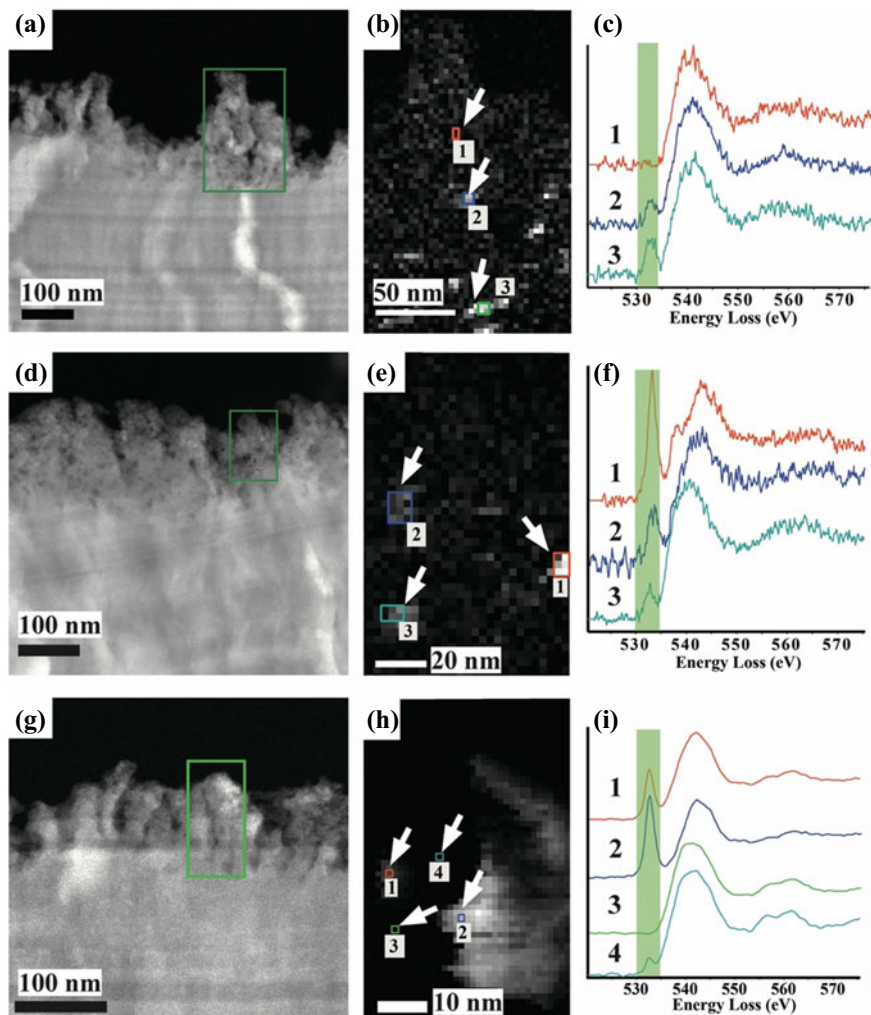


Fig. 46 STEM-EELS analysis of Al surface: **a–c** before steam treatment; **d–f** steam treatment for 1 min; **g–h** steam treatment for 3 min. The left column shows the STEM-HAADF images of the oblique sections of the surface layers. The middle column shows the chemical maps showing the distribution of Al(OH)₃ created with the 530–535 eV energy window. The right column shows the O K-edges extracted from the ROIs indicated in the corresponding chemical maps. The green-shaded boxes indicate the 530–535 eV energy window used for the mapping. Reprinted with permission from [69]. Copyright 2022, Elsevier. All Rights Reserved

Figure 47 illustrates the O K-edges of γ -alumina (Al_2O_3), boehmite ($\text{AlO}(\text{OH})$), and aluminum hydroxide ($\text{Al}(\text{OH})_3$) powders under various irradiation conditions. The spectra were collected in the SI mode, with an interval of 10 nm and from 10×10 points, and then summed into a single spectrum. The ELNES characteristics of the O K-edges varied significantly among the three oxygen-containing compounds. γ -alumina exhibits two peaks at 550 and 563 eV energy losses, followed by the primary peak at 542 eV (Fig. 47a). Boehmite displays a broadened first peak, followed by only one peak at an energy loss of 560 eV (Fig. 47b). $\text{Al}(\text{OH})_3$ shows an intense characteristic peak at 532.6 eV, followed by two peaks at 540 and 560 eV energy losses (Fig. 47c). Despite significantly higher irradiation doses than the sample acquisition condition (a probe current of 160 pA for 500 ms), no significant changes in the ELNES features are observed. Thus, the O K-edge ELNES can be utilized to identify the chemical compositions produced in the Al surface layers, as these characteristic features are often utilized as fingerprints for chemical characterization by EELS and ELNES. They can assist in identifying those compounds in the thin, heterogeneous surface layer of technical Al substrates [76]. The emergence of peaks in the 530–535 eV energy loss region in Fig. 46 suggests $\text{Al}(\text{OH})_3$ in the ROIs indicates that the steam treatment produces -OH functional groups in the Al surface. Hydroxylation of aluminum surfaces has increased their wettability and chemical reactivity [70, 71, 77, 78]. Therefore, introducing hydroxyl functional groups through the steam treatment is responsible for improving adhesion strength.

It is challenging to differentiate between $\text{Al}(\text{OH})_3$ and $\text{AlO}(\text{OH})$ in XPS spectra because their spectroscopic information is usually similar. However, in EELS, the chemical states of aluminum in metallic, oxide, and hydroxide Al compounds are

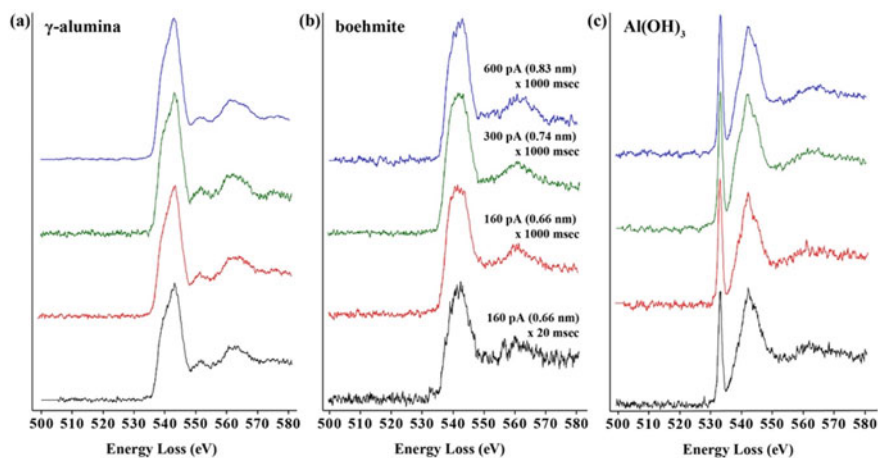


Fig. 47 O K-edge ELNES obtained from the powder samples: **a** γ -alumina; **b** $\text{AlO}(\text{OH})$ (boehmite); **c** $\text{Al}(\text{OH})_3$. Irradiation dose increases from lower to upper. All the spectra are presented after the background subtraction by fitting the pre-edge regions with a power law function. Reprinted with permission from [69]. Copyright 2022, Elsevier. All Rights Reserved

reflected in the plasmons-loss and core-loss regions of Al L_{23} - and O K-ionizations as shown in Fig. 2.5 in Sect. 2. The Al L_{23} -edges clearly show that the ionization edge of metallic aluminum appears at a lower energy (72 eV) than aluminum compounds. The three aluminum compounds exhibit ionization edges between 75 and 76 eV and two major peaks near the edges at about 80 eV and 84 eV. The peak at the onset of the edge consists of the shoulder on the lower energy side. Introducing a hydroxyl group into γ -alumina causes the peak at 79.5 eV to shift towards higher energies, resulting in another peak at 77.5 eV in $\text{Al}(\text{OH})_3$. The fine structures in the Al L_{23} -edges of the three Al compounds represent the difference in Al atomic coordination. A first-principles calculation of γ -alumina revealed that the two peaks near the edge at 77.5 and 79.5 eV originate from tetrahedrally and octahedrally coordinated Al, respectively [79].

STEM-EELS/EDX simultaneous analysis was employed with a point-to-point distance of 3 nm and an acquisition time of 0.5 s to examine the interface after bonding. Figure 48 presents the EDX elemental maps and O K-edges obtained from different regions at varying distances from the interface. The STEM-EDX elemental maps of C, O, and Al (middle panel) demonstrate that the adhesive molecules fill the nanopores in the Al surface layer. The O K-edge acquired from the ROI in close proximity to the interface (upper spectrum) shows ionization edge at 530 eV before the edge at 535 eV, which originates from the oxygen in the epoxy. The characteristic sharp peak at 532.6 eV vanished entirely when compared with the EELS spectra collected from the sample before bonding as shown in Fig. 46. The hydroxyl functional group in $\text{Al}(\text{OH})_3$ is removed after bonding, indicating that the Al surface is dehydrated. As a result, a chemical interaction between the hydroxylated aluminum surface and the epoxy adhesive arises after bonding.

To explore the interfacial interaction, the ELNES of Al L_{23} -edges in the adhesive bonding of the steam-treated and the degreased aluminum are examined carefully, as shown in Fig. 49. These were obtained by recording EELS and EDX spectra simultaneously in dual EELS- and SI-mode, with a point-to-point distance of 1 nm

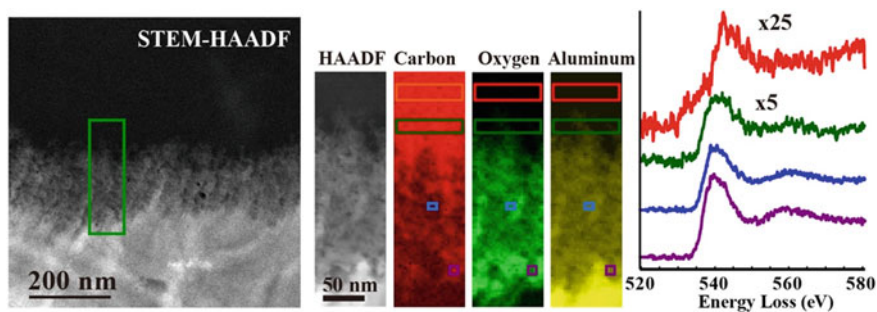


Fig. 48 A global STEM-HAADF image, STEM-EDX elemental maps for the ROI marked in the global STEM-HAADF image, and EELS O K-edges extracted from the ROIs indicated in the EDX elemental maps of the interfacial region between the adhesive and steam-treated A. Reprinted with permission from [69]. Copyright 2022, Elsevier. All Rights Reserved

and an acquisition time of 0.1 s. In the steam-treated sample (Fig. 49a), most of the spectra except for the lowest one display a characteristic ELNES consisting of two distinct peaks at 85 and 88 eV in the energy range of 85–90 eV indicated as the green-shaded boxes. Conversely, the degreased sample has no apparent characteristic ELNES (Fig. 49b). This ELNES pattern is likely the outcome of the interaction between the hydroxy groups on the Al surface and the adhesive, which differs from the ELNES acquired in the reference aluminum compounds presented in Fig. 2.5.

To gain a deeper understanding of the ELNES observed in the Al L_{23} -edge spectra, STEM analyses were performed for the single component of the epoxy (DGEBA) and the amine (DDS). The Al plates were coated with liquid DGEBA, 10 wt% DDS acetone solutions, or an organophosphate (HDPA), followed by annealing at 100 °C for 1 h. HDPA has been known to be effective in promoting the adhesion of epoxy adhesives to Al [80]. After rinsing the surfaces by ultrasonication with toluene, acetone, and ethanol, thin cross sections containing the aluminum surface were examined using STEM-EELS/EDX in SI mode. Figure 50a shows the surface region of steam-treated Al before bonding, where the metallic and oxide parts are differentiated. Despite vigorous rinsing, small amounts of each coated material are found on the Al surface (Fig. 50b–d), as evidenced by EDX elemental mapping, where

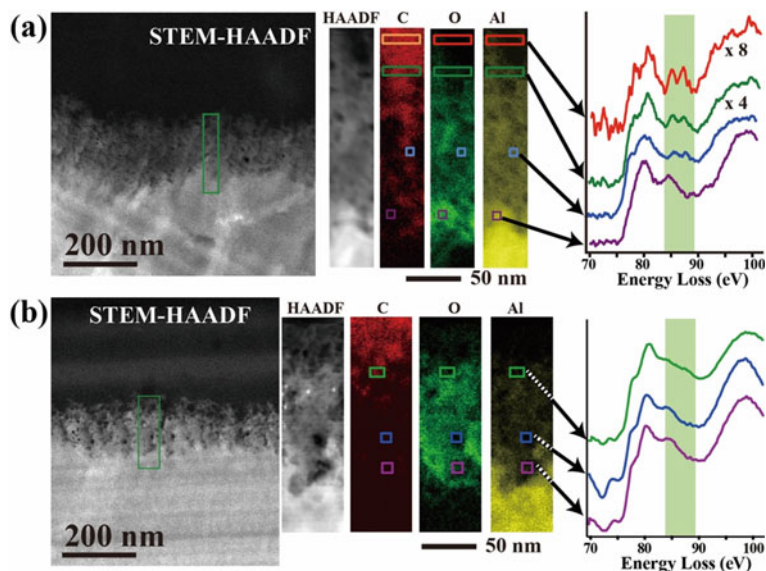


Fig. 49 The EELS spectra of Al L_{23} -edges obtained from the interfacial area: **a** interface between steam-treated Al and the adhesive; **b** interface between degreased Al and the adhesive. Each panel displays a global STEM-HAADF image (*left*), a STEM-HAADF image, and STEM-EDX elemental maps for the ROI specified in the global STEM-HAADF image (*middle*), and the Al L_{23} -edges extracted from the ROIs indicated in the EDX elemental maps (*right*). The ELNES feature indicating the interfacial chemical interaction is shown in green-shaded boxes. Reprinted with permission from [69]. Copyright 2022, Elsevier. All Rights Reserved

red pixels indicate metallic aluminum, green indicates oxygen, and blue indicates carbon. Figure 50b and c show the location of DGEBA and DDS, respectively. In Fig. 50d, it can be observed that HDPA adsorbs onto the oxygen-rich aluminum layer, depicted as a phosphor (P) elemental distribution. The ELNES characteristics of Al L_{23} -edges from these samples are compared to those of the Al/(DGEBA/DDS) interface in Fig. 50e. No distinct features are detected in the 85–90 eV energy loss region from the surface region of the Al (top spectrum) before bonding. However, two 86 and 88 eV peaks are observed in that same region after bonding (second top spectrum). While the ELNES feature in the 85–90 eV energy loss region is visible in the spectra for DDS alone, it is absent in the spectra for DGEBA alone. This suggests that the interaction between the amine and hydroxy groups present on the aluminum surface primarily drives the chemical interaction.

The O K-edge ELNES results of the aluminum surface treated with steam indicate the absence of surface hydroxy groups after bonding. The Al L_{23} -edge ELNES studies suggest that the bonding between the epoxy/amine adhesive and the aluminum occurs primarily due to the hydroxy groups on the aluminum surface and the amine component in the adhesive. Considering the surface-activation scheme of HDPA as

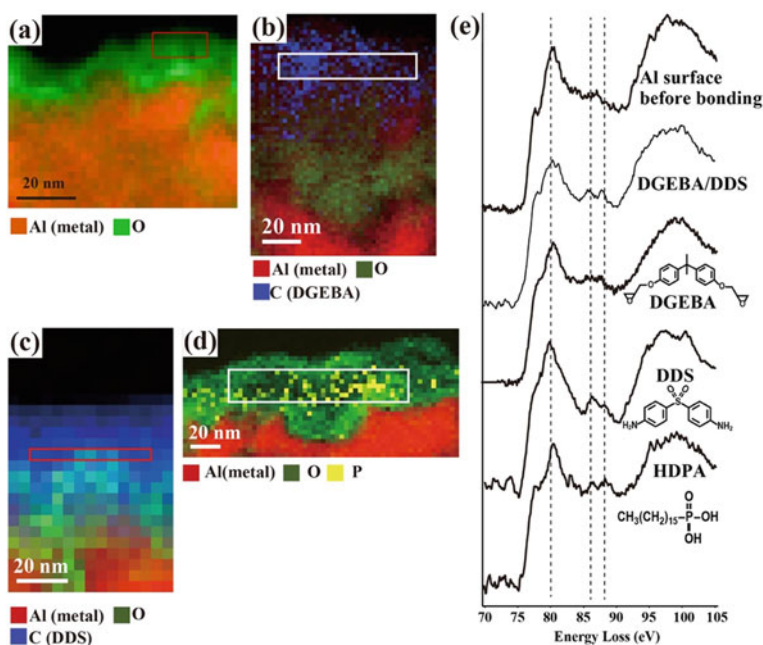


Fig. 50 Compositional maps of cross sections of aluminum surfaces: **a** before bonding; **b, c, d** after the adsorption of DGEBA, DDS, and HDPA, respectively. Red pixels represent the metallic Al distributions by EELS, and the green, blue, and yellow pixels represent O, C, and P elemental distributions by STEM-EDX; **e** ELNES of Al L_{23} -edges extracted from the ROIs indicated in the corresponding images. Reprinted with permission from [69]. Copyright 2022, Elsevier. All Rights Reserved

proposed in Fig. 51a [80], and based on the ELNES analysis and the previous SKP [70] and SFG studies [81], it can be inferred that chemical bonding at the adhesive interface occurs via acid–base interaction between the hydroxyl group on the aluminum surface and the secondary or tertiary amine in the adhesive molecules as shown in Fig. 51b. However, such bonding might not be sufficient to enhance adhesion strength, as the interaction energy of the bond is much lower than that of covalent bonds. In reality, the improvement in adhesion strength is achieved by the diffusion of adhesive molecules into the nanopores of the Al surface layer rich in hydroxy groups, which increases mechanical resistivity against applied shear stress, resulting in cohesive failure. Although acid–base interaction plays a crucial role in facilitating the diffusion of adhesive molecules into the Al porous surface layer, it does not directly enhance adhesion strength. The enthalpy-driven diffusion of adhesive molecules into the micropores of the Al surface layer results in the spontaneous diffusion of the adhesive molecules due to the acid–base interaction. Regarding polymer–polymer diffusion at the interface, dissimilar miscible polymer pairs demonstrate fast interdiffusion due to thermodynamic acceleration as stated in Sect. 2. In such cases, the positive enthalpy gained by mixing leads to more rapid diffusion compared to entropy-based interdiffusion between identical polymer pairs.

According to our findings, surface hydroxylation by steam treatment is a straightforward approach to improving the bonding strength of technical aluminum alloy substrates. Our analysis of the O K-edges using ELNES reveals the heterogeneous chemical nature of the oxide/hydroxide layer on the aluminum surface, which displays intricate nanoporous structures with a spatial resolution of less than 5 nm. The observed increase in adhesion strength is due to the penetration of adhesive molecules into the nanopores on the aluminum surface, leading to a shift from interfacial failure to cohesive failure. ELNES analysis of the Al L₂₃-edges allowed us to identify the chemical bonds created through acid–base interactions between the

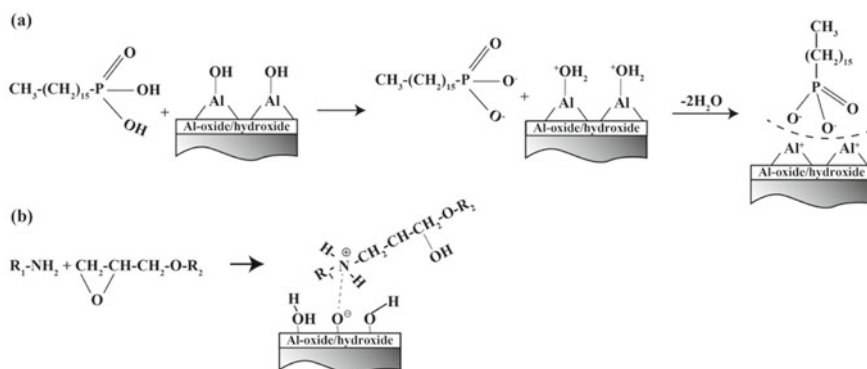


Fig. 51 Schematic representation of the acid–base interactions between adsorbed molecules and a hydroxylated aluminum surface: **a** Al surface adsorbs HDPA; **b** hydroxyl groups on the aluminum surface interact with the secondary amine in an epoxy adhesive. Reprinted with permission from [69]. Copyright 2022, Elsevier. All Rights Reserved

amino group of the adhesive and the hydroxyl groups on the aluminum surface. Although this weak bonding may not directly contribute to the improved adhesion strength, it facilitates the spontaneous penetration of adhesive molecules into the pores by means of thermodynamically favored acid–base interfacial interactions [18, 30, 82, 83].

6.2 Role of the Chemical Bonding on Interfacial Toughness Between Aluminum and Epoxy Adhesive

The extent to which chemical bonding and mechanical interlocking contribute to the bonding strength attained has yet to be completely comprehended. To address this concern, more comprehensive EELS/ELNES research was employed with an atomically flat aluminum oxide substrate, with a discussion on the impact of surface roughness and chemical bonding on adhesive bonding [84]. DGEBA, triethylenetetramine (TETA), and 2,4,6-tris(dimethylaminomethyl)phenol (TDAMP) were mixed stoichiometry at the molar ratio of 3/1 (5.7/0.72 wt/wt) and with 3 wt% of TDAMP. The curing condition of the adhesive was at 100 °C for 30 min. 50–100 nm thick oxidized Al thin film sputtered on a CaF₂ plate was used for a naturally oxidized Al model surface. The CaF₂ substrate with coated oxidized Al was ultrasonicated in ethanol for 10 min, followed by UV/ozone treatment for at least 20 min to serve a hydrocarbon-contamination-free surface before the coating of the adhesive.

Figure 52a shows a STEM image of a cross section of the specimen in STEM-HAADF mode, where the cured adhesive is coated on the AlO_x thin film sputtered on the CaF₂ substrate. Observing the cross section confirms that the uniform sputtered Al film is formed on the CaF₂ substrate without noticeable defects. A ROI indicated as a green box in Fig. 52a was inspected by STEM-EDX/EELS simultaneous analysis with a point-to-point distance of 2 nm and the acquisition time of 0.1 s, providing 86 × 25 EDX and EELS spectra. Figure 52b is an EDX elemental map of the ROI showing the carbon (red) and aluminum (blue) elemental distributions. Al L₂₃-edges were extracted from the regions with 2 nm width parallel to the interface as indicated in Fig. 52b. Figure 52c shows the background-subtracted Al L₂₃-edges extracted from the three regions, where the regions and the corresponding spectra are shown with the same colors. Those spectra show intensity fluctuations in the energy loss region beyond the ionization edge at 75 eV, especially in the energy loss range from 85 to 90 eV. As found in the technical Al alloy plate, the spectra extracted from the interface (orange) exhibit a characteristic ELNES in the energy range of 85–90 eV, where two distinct peaks at 85 and 88 eV are presented. The second layer (green) from the interface exhibits the same feature, but the intensities of those peaks become lower, while in the bulk part (blue), those peaks disappear, and a broad peak appeared instead. It is also noticed that the maximum peak at 79.5 eV in the spectra extracted from the interfacial region is shifted toward higher energy. The Al L₂₃-edge ELNES,

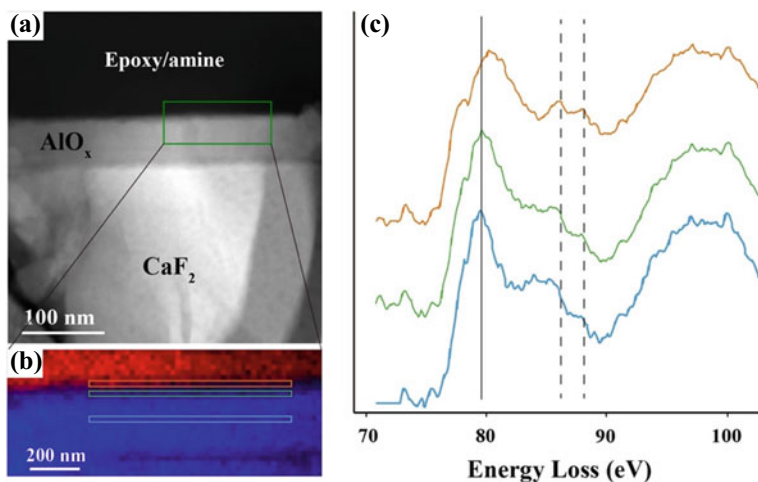


Fig. 52 STEM-EELS/ELNES analysis of the interface between the cured adhesive and the oxidized Al thin film: **a** STEM-HAADF image of a cross section of Al-sputtered film on CaF_2 covered with adhesive; **b** STEM-EDX elemental map representing carbon (red) and aluminum (blue) distributions in the ROI indicated in **a**; **c** Al L_{23} -edge EELS spectra extracted from the regions indicated in **b**. The spectra and the regions are shown as the same color

therefore, indicates that the chemical interaction between the sputtered AlO_x film and the adhesive influences the Al atomic coordination.

Figure 53 shows the O K-edge ELNES analysis of a cross section including the adhesive layer, sputtered Al thin film, and CaF_2 plate. An ROI indicated in the STEM-HAADF image (Fig. 53a) was inspected with a point-to-point distance of 5 nm and an acquisition time of 0.5 s, which provided 20×7 EDX and EELS spectra. Figure 53b shows the EDX elemental maps showing the oxygen, aluminum, carbon, and calcium distributions, and O K-edge EELS spectra extracted from the 5 nm thick layers as indicated in the EDX oxygen map (left panel in Fig. 53b) are presented in Fig. 53c. The extracted four spectra exhibit different ELNES features. The sharp peak at 532.6 eV is shown with different intensities, and the following broad peak in the 535–545 eV energy loss range exhibits different shapes. The upper layer contact with the adhesive (layer 1) does not have the sharp peak at 532.6 eV, while the second and the third layer (layers 2 and 3, respectively) shows the peak with the highest intensity of the third layer. Considering the ELNES features of O K-edges of the three reference samples, we can identify that the extracted EELS spectra 1 is similar to the boehmite spectra, and spectra 3 is identical to the $\text{Al}(\text{OH})_3$ spectra. The fact that only the interfacial layer contact with the adhesive gives the boehmite-like ELNES feature indicates that the hydroxy groups on the Al-sputtered thin film surface are consumed due to the chemical reaction with the adhesive.

STEM-EELS/ELNES analysis of the flat interface formed between the model Al oxide sputtered film and the epoxy/amine curing mixture can more clearly reproduce the results obtained with the technical Al plate as stated in Sect. 6.1. The sample used

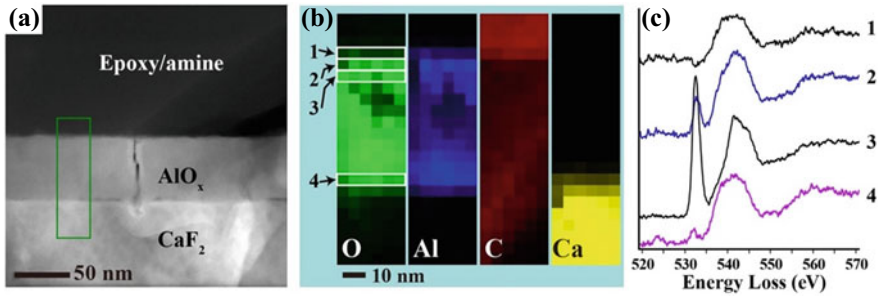


Fig. 53 O K-edge STEM-EELS/ELNES analysis of the interface between the cured epoxy/amine and AlO_x : **a** STEM-HAADF image of a cross section of AlO_x sputtered film on CaF_2 covered with epoxy/amine-cured adhesive; **b** STEM-EDX elemental maps representing oxygen (green), aluminum (blue), carbon (red) and calcium (yellow) distributions in the ROI indicated in; **c** O K-edge EELS spectra extracted from the regions shown in (b)

in this experiment can be used for other instrumental measurements, such as XPS, SFG, and Kelvin probe measurements, which support the results obtained in this study. The details will be reported elsewhere.

To evaluate the contribution of the chemical bonding, the interfacial fracture toughness between the AlO_x sputtered film and the epoxy was measured using the specimen geometry depicted in Fig. 54a, and the ADCB test was carried out. The Al thin film was sputtered on a polycarbonate (PC) plate, and the adhesive was molded onto the PC plate using a silicone rubber mold. The test was performed by the procedure stated in Sect. 3. The G_C values of the adhesive joint of technical Al plate (Al1000) were also measured by the wedge-test [85] using the symmetrical DCB specimens as shown in Fig. 54b, where the thickness, width, and length of the specimen are 3, 25, and 150 mm, respectively. The plates were preliminarily treated with sodium hydroxide aqueous solution (ph12) at 60 °C for 10 s and then with nitric acid for 10 s to remove the natural oxide layer, followed by UV/ozone treatment before bonding. After bonding, an Al wedge having 25 mm width, 30 mm length, and 1 mm thick is driven into pre-crack 30 mm from the edge to create an interfacial crack. After the initial crack made by the insertion of the wedge is stabilized, G_C is calculated.

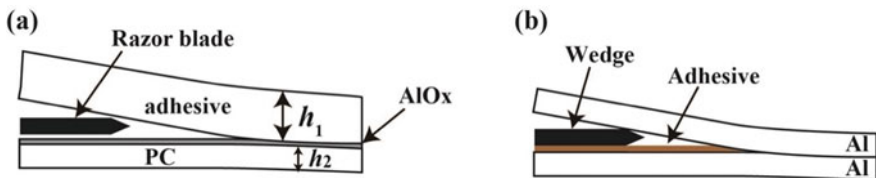


Fig. 54 Schematic illustrations of the specimens for the interfacial critical energy release rate measurements, G_C , for adhesive/sputtered Al thin film interface (a) and technical Al plate/adhesive interface (b)

The test was performed with five specimens and obtained G_c values of $3.8 \pm 1.5 \text{ J/m}^2$. After the tests, the fracture surfaces were inspected by SEM, and no topographic surface features were found on both surface. This suggests that the failure occurs at the adhesive/ AlO_x interface without noticeable deformation of the adhesive. The interfacial toughness between the technical Al plates, on the other hand, is calculated to be $129.2 \pm 17.9 \text{ J/m}^2$.

Work of adhesion (W_{adh}) can be estimated by measuring contact angles using three probe liquids. Surface energies of the sputtered Al substrates (γ_{Al}) and the cured adhesive (γ_{ad}) are determined from contact angles of water, diiodooctane, and ethylene glycol in the framework of acid–base theory [86] In this theory, total surface energy (γ^{total}) is given by

$$\gamma^{\text{total}} = \gamma^{\text{LW}} + 2\sqrt{\gamma^+ \gamma^-} \quad (11)$$

where γ^{LW} , γ^+ , and γ^- denote Lifshitz–van der Waals, Lewis acid, and Lewis base components, respectively. Using the Young–Dupré Eq. (12), respective components of the surface energies of a substrate ($\gamma_{\text{S}}^{\text{LW}}$, γ_{S}^+ , γ_{S}^-) were calculated from the parameters of the three probe liquids ($\gamma_{\text{L}}^{\text{LW}}$, γ_{L}^+ , γ_{L}^-) and experimental contact angles (θ) of respective liquids.

$$\frac{\gamma_{\text{L}}^{\text{total}}(1 + \cos \theta)}{2} = \sqrt{\gamma_{\text{S}}^{\text{LW}} \gamma_{\text{L}}^{\text{LW}}} + \sqrt{\gamma_{\text{S}}^+ \gamma_{\text{L}}^-} + \sqrt{\gamma_{\text{S}}^- \gamma_{\text{L}}^+}. \quad (12)$$

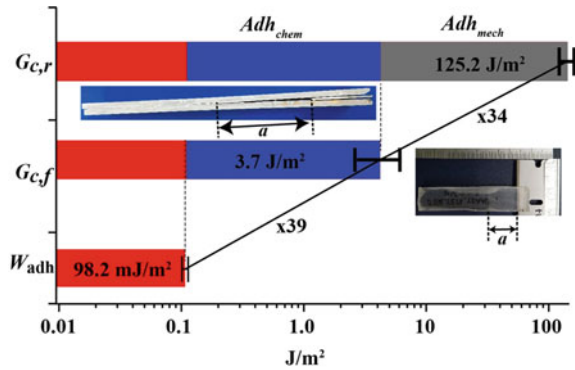
The values are used to calculate W_{adh} using the following Eq. (13):

$$W_{\text{adh}} = 2\sqrt{\gamma_{\text{Al}}^{\text{LW}} \gamma_{\text{ad}}^{\text{LW}}} + 2\sqrt{\gamma_{\text{Al}}^+ \gamma_{\text{ad}}^-} + 2\sqrt{\gamma_{\text{Al}}^- \gamma_{\text{ad}}^+}. \quad (13)$$

Figure 55 compares three adhesion energies obtained throughout the experiments. The interfacial fracture energy between the flat AlO_x substrate and the adhesive ($G_{c,f}$) is 39 times larger than the W_{adh} represented by Lifshitz–van der Waals and Lewis acid/base interactions. The contribution of chemical bonding may achieve this enhancement. The interfacial fracture energy between the technical Al plates and the epoxy adhesive ($G_{c,r}$), on the other hand, is 34 times larger than $G_{c,f}$. Therefore, the contribution of the mechanical bonding owing to the surface roughness of the Al plate is significantly more significant than that of the chemical bonding.

The toughness of interfaces between dissimilar polymers has been well investigated by the reinforcement of block copolymers (BC), of which components are identical to the polymers to be bonded. The interface between polymer A and polymer B reinforced with an A–B diblock polymer can be considered a model of the interface strengthened by chemical bonding, and the relationship between the areal density of BC at the interface and the interfacial toughness has been extensively discussed [87, 88]. In the polymer/polymer adhesion reinforced by BC, the interfacial toughness can be enhanced to more than 100 J/m^2 due to the energy dissipation through the deformation of the polymers at the crack tip via crazing if the BC chains are well

Fig. 55 Roles of the chemical and the mechanical bonding on the adhesion of Al and an epoxy adhesive. The work of adhesion (W_{adh}), the interfacial fracture energies between the flat oxide Al substrate and the epoxy adhesive ($G_{c,f}$), and between the Al technical plate and the epoxy adhesive ($G_{c,r}$) are compared. The corresponding test specimens are shown therein



entangled at the interface between the polymers. In contrast to the polymer/polymer adhesion, the interfacial toughness between the AlO_x and the adhesive was not sufficiently enhanced by the chemical bonding. This suggests that sufficient deformation of the metal/polymer interface is not expected by chemical bonding. Our result indicates that the effect of the chemical bonding is limited for the adhesion of Al, and the mechanical bonding achieved by the surface roughness is more effective.

7 Metal–plastic Direct Bonding by Injection Nano-Molding—Interfacial Structures and Testing Joint Performance

A novel technique for joining metal and plastic without adhesive has been developed, utilizing a surface treatment process that creates small pores on the metal surface. Known as Nano-Molding Technology (NMT), this is a method of directly molding plastic by inserting surface-modified metal into a mold [89–91]. Metal–plastic hybrids can be created using various combinations of metals such as Al, Cu, Ti, Mg, and plastics such as polyphenylene sulfide (PPS), polyamide (PA), and PP. The polymer chains infiltrate the nano-sized pores on the metal, yielding strong joint strength. This technique allows for fast assembly of metal and plastic with high design flexibility, but the size of the products is mainly limited by mold size. Another attractive feature of this joining technique is that cost reduction can be achieved in the case of many products being repeatedly manufactured. The new joint technology requires a thorough understanding of the joint mechanism and proper evaluation methodology to ensure safety and reliability. In this study, the joint process of PPS and Al5052 is investigated by STEM and XPS, and new test methods to evaluate the joint performance and assess environmental durability are developed.

The test specimens for the evaluation were prepared by insert-injection molding of PPS onto a surface-modified Al5052 plate at the process temperatures of 290–330 °C and the mold temperature of 120 °C. Two types of surface structures of Al5052 were

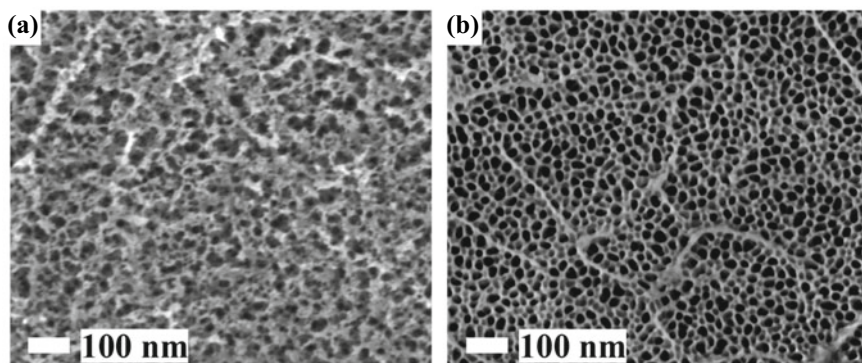


Fig. 56 SEM micrographs showing the aluminum surface porous features: **a** NMT1; **b** NMT2. Reprinted with permission from [78]. Copyright 2020, EDP Sciences. All Rights Reserved

prepared by the chemical treatment developed by Taisei Plas Co., Ltd. [89]. Those two are different in terms of the pore size, the depth of the treated layer, and the 3D interconnected structures inside the layers. The PPS/Al5052 joint performances were evaluated by ISO19095 [92].

To investigate the bonding mechanism, two distinct Al5052 surface structures named NMT-1 and NMT-2, which have different pore sizes and shapes, thicknesses of modified layers, and internal pore connectivity, were employed [78]. SEM micrographs of the Al5052 surfaces of NMT-1 and NMT-2 are presented in Fig. 56a and b, respectively. The Al surface in both treatments is characterized by tiny pores approximately 20 nm in diameter. The pores of NMT-1 are relatively smaller than those of NMT-2, and the pores of NMT-1 are irregularly shaped, while those of NMT-2 are uniformly distributed.

In Fig. 57, the PPS/Al5052 joint interface of NMT-1 is depicted through both a STEM-HAADF image (Fig. 57a) and STEM-EDX elemental maps of Al, sulfur (S), and oxygen (O) (Fig. 57b, c, and d, respectively). The surface-modified layer's depth, around 100 nm, is visible in the HAADF image. The elemental maps indicate that the surface-modified layer comprises aluminum and oxygen and that the S map (Fig. 57c) signifies the penetration of PPS into the Al surface pores. In contrast, Fig. 58 shows that NMT-2 has a roughly 500 nm thick interfacial layer. The STEM bright field (BF) image shows that PPS has only penetrated the upper part of the layer, with a depth of around 100 nm, and the majority of the layer is comprised of empty holes.

By using STEM tomography, we can better understand the porous structures formed on the surface of Al. The 3D reconstructed images of NMT1 and NMT2 are displayed in a video in Fig. 59. These images reveal that the pores on NMT1 are interconnected and create 3D continuous hollows with a space of 10–20 nm (Fig. 59a). In contrast, NMT-2 exhibits isolated pores growing perpendicular to the substrate (Fig. 59b). In NMT-1, the complex narrow and deep hollows allow polymer chains to enter during the injection molding process within minutes. The continuous

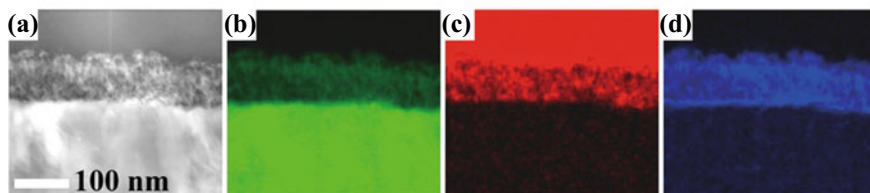


Fig. 57 Cross-sectional views of a PPS/Al5052 joint interfacial region with NMT-1 surface treatment: **a** STEM-HAADF image; **b, c, d** EDX elemental maps of Al, S, and O, respectively. Reprinted with permission from [78]. Copyright 2020, EDP Sciences. All Rights Reserved

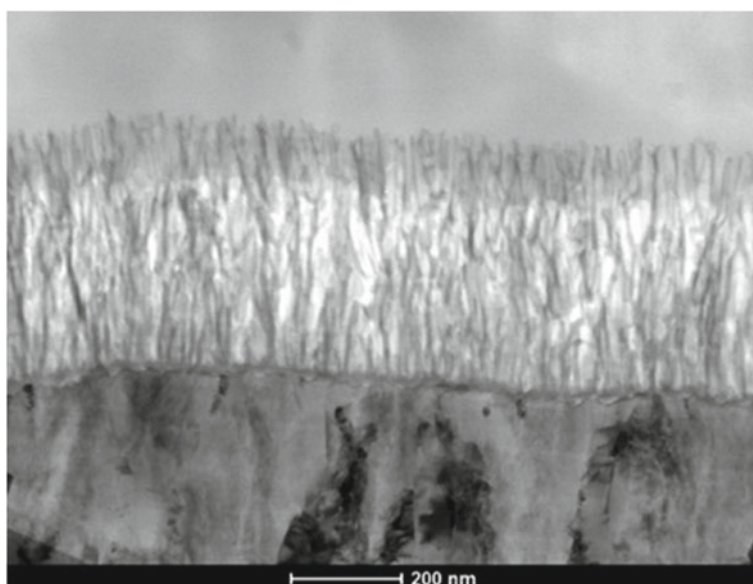


Fig. 58 STEM-BF micrograph showing PPS/Al5052 joint interface with NMT-2 surface treatment

porous structure enables air to escape from the pores, facilitating the replacement of the air with polymer chains. Conversely, NMT-2 has a narrow one-way space, and PPS polymer chains cannot displace the air from the pores. As a result, the penetration of polymer chains is limited to the upper portion of the layer.

XPS depth profiles are measured to examine the chemical interactions between metal and polymer. Figure 60a displays the XPS depth profiles, including the Al 2p peaks acquired from the NMT-1 surface before bonding. Within the first minute, the peak shifted towards higher binding energy, and another peak emerged. Ultimately, after 11 min of sputtering, only the single peak assigned to metallic Al (73 eV) remained. The depth profiles mean that the chemical state of the oxygen-containing modified layer varies from the outermost surface to the interior of the Al plate, suggesting that the surface layer possesses a chemical gradient structure and a porous

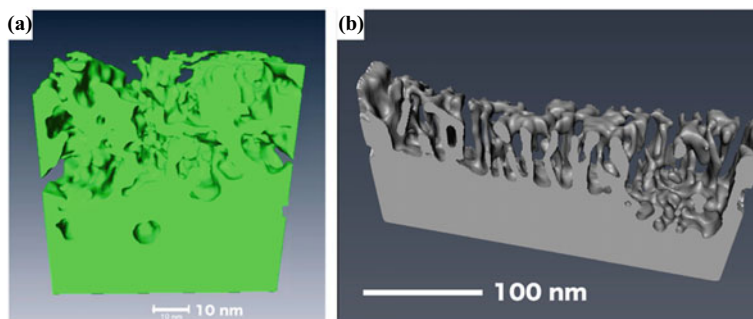


Fig. 59 A video presenting the 3D reconstructed views of NMT-1 (a) and NMT-2 (b) showing the internal porous structures created on the Al surface. Reprinted with permission from [78]. Copyright 2020, EDP Sciences. All Rights Reserved

structure. Figure 60b shows the XPS depth profiles of the PPS/Al5052 joint interface after rinsing the Al part by HCl etching. Despite the etching, a trace of Al persists on the PPS, and the Al 2p peaks are detectable during the sputtering. The binding energies at which the Al 2p peaks appear are relatively constant, independent of the sputtering time, which differs from the profiles acquired before bonding. These observations suggest that bonding PPS to Al induces changes in the chemical state of the oxygen-containing Al surface layer.

Figure 61 is the plots of the O/Al atomic ratios as a function of sputtering time, calculated by integrating Al 2p and O 1s peaks from depth profiles. The results indicate that the oxygen content is higher in the entire depth of the modified layer before bonding. In particular, the outermost surface of the modified Al before bonding has the highest O/Al ratio, which is almost equivalent to the atomic ratio of $\text{Al}(\text{OH})_3$, and gradually decreases to approximately 2.0. Therefore, the chemical shift of the Al 2p peaks observed before bonding (Fig. 60a) is caused by gradual changes in the chemical structure from the surface to the inner part.

It was known that the dehydration reactions of $\text{Al}(\text{OH})_3$ to $\text{AlO}(\text{OH})$ and $\text{AlO}(\text{OH})$ to Al_2O_3 occur when exposed to high temperatures above 253 °C and 500 °C, respectively. These endothermic reactions have 15.70 and 0.20 kJ/mole activation energies, respectively. Upon contact with the hot molten polymer, these dehydration reactions occur and absorb heat from the polymer. This heat transfer can promote the spontaneous penetration of polymer chains into the pores. Since the space provided by the pores is only slightly larger than the size of a polymer molecule, it may be challenging for highly viscous polymer melt to penetrate these tiny pores, even with high pressure applied during injection molding. The 3D continuous hollow structure likely plays a critical role in forming the metal/polymer hybrid interface, allowing the metal pores to be filled with polymer. At the same time, the air escapes from the pores during the penetration of polymer chains.

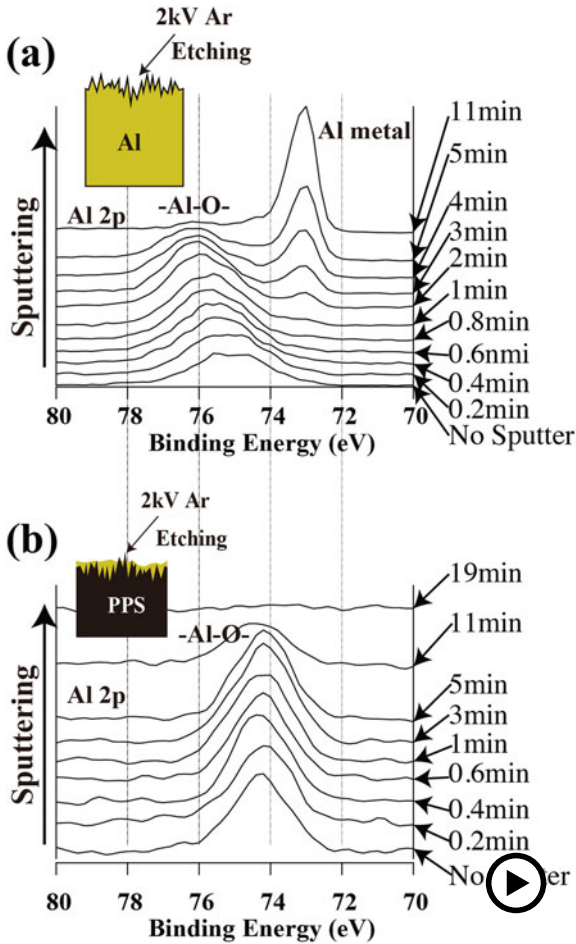
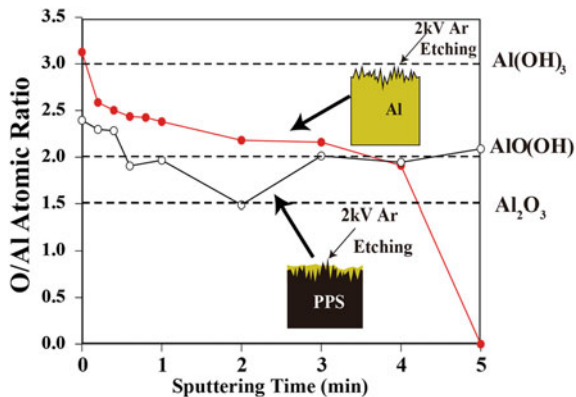


Fig. 60 XPS depth profiles of Al 2p signals of the Al surface before the bonding (a) and the Al/PPS interface after removing Al by HCl etching (b). Reprinted with permission from [78]. Copyright 2020, EDP Sciences. All Rights Reserved (▶ <https://doi.org/10.1007/000-ayj>)

Figure 62 depicts the durability of the PPS/Al5052 joint with the NMT-1 under a high humidity condition (85 °C 85%RH) and after repeated temperature cycles of a rapid-rate change. The butt-joint specimens before and after the measurement of the joint strength are also presented in Fig. 62a. The specimens are fractured near the metal/plastic joint interface, and the initial tensile strength of about 45 MPa is maintained for 3000 h. The measured strengths represent the interfacial region’s strengths because the value is significantly lower than the tensile strength of the PPS (about 120 MPa). Figure 62b presents the thermal shock resistance under two conditions. The joint strengths are maintained even after 1500 cycles of the rapid-rate temperature changes between -40 and 85 °C. It decreases to about 25 MPa with

Fig. 61 Sputtering time dependence of the atomic ratios of O/Al determined by the ratios of the integral peak intensities of Al 2p and O 1 s before bonding (Al surface) and after bonding (PPS/Al5052 interface). Reprinted with permission from [78]. Copyright 2020, EDP Sciences. All Rights Reserved



significant large scatterings of the results between 500 and 1000 cycles in the more significant temperature gap from -40 to 120 °C. The peel resistance measurement gives a typical force-distance curve, as shown in Fig. 63a, demonstrating steady peeling keeping the force of about 180 N/25 mm. The geometry of the lap joint specimen and the specimen before and after the measurement are shown in Fig. 63b, which is measured to be 44.2 ± 1.2 MPa. The failure occurred near the interface, where a small amount of PPS is partly fixed on the Al plate. In all the measurements, a small amount of PPS remains on the fracture surface of Al, implying that PPS forms a weak boundary layer near the interface during the joint process. The difference in the cooling rate of PPS in the interfacial region close to the metal and in the bulk part causes the joint strength reduction. The PPS undergoes rapid cooling when injected on the Al plate at 120 °C after melting at 290 – 330 °C in the injection molding machine. This results in different crystallization behavior near the interface than the bulk part. It can be inferred that the crystallinity of PPS near the interface is lower than that of the bulk part due to this rapid cooling. The excellent joint performance of the PPS/Al5052 joint is demonstrated under various test conditions, except for the thermal shock with a significant temperature gap, which can be attributed to the large difference in the thermal expansion coefficient between the metal and plastic.

To comprehend the failure mechanism of the joint, in situ STEM is performed to observe the failure behavior directly [93]. As discussed in Chap. 2, this technique involves subjecting thin sections that include the joint interfaces to tensile load using a specially designed specimen holder for the in situ tensile experiments under STEM. Figure 64 is a video demonstrating the failure behavior of the PPS/Al direct joint in STEM bright-field (BF) mode, while Fig. 65 presents selected images captured from the movie. In Fig. 65a and d, dark strands appear due to wrinkles produced during specimen preparation by ultramicrotomy. Rubber domains dispersed in the PPS matrix to improve injection moldability and impact strength of molded articles can also be observed. Upon applying a tensile load to pull the specimen perpendicular to the interface, the PPS part stretched and the wrinkles disappeared. Microcavities were observed to form preferentially inside the rubber domains (Fig. 65b and e), and

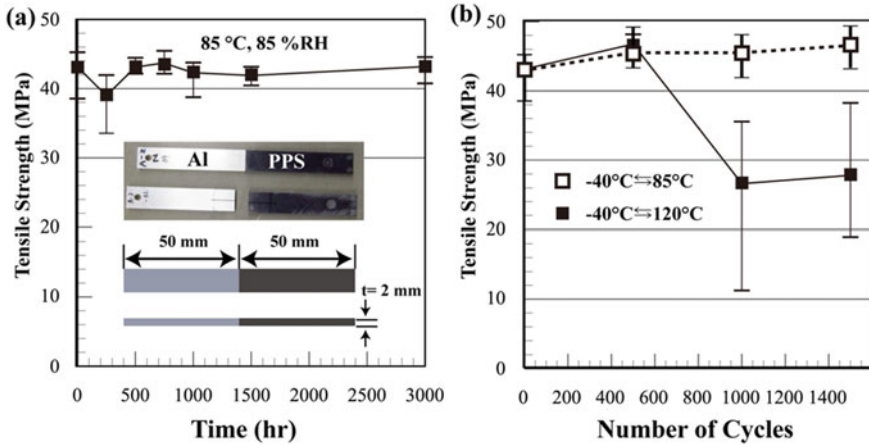


Fig. 62 The PPS/Al5052 tensile joint strength as a function of residence time under accelerated environmental conditions: **a** durability at 85 °C and 85%RH and the butt-joint test specimen before and after the test; **b** thermal shock resistivity under the temperature jumps from -40 to 85 °C and from -40 to 120 °C as a function of the cycles. Reprinted with permission from [78]. Copyright 2020, EDP Sciences. All Rights Reserved

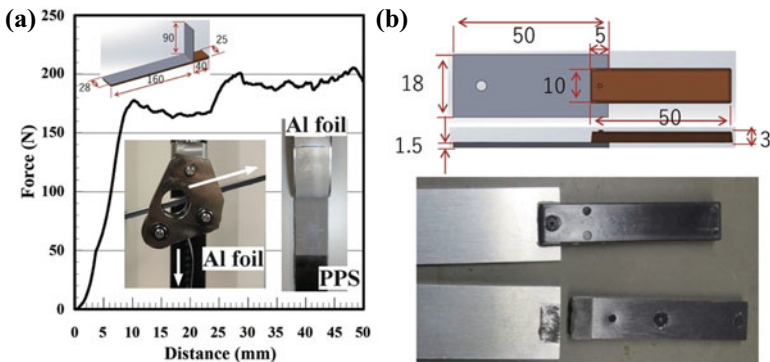


Fig. 63 Force vs. distance curve obtained in the peeling resistivity test of Al/PPS laminate with NMT1 surface treatment, the specimen geometry, a floating roller jig, and the specimen after the test (a). The specimen geometry of the PPS/Al5052 lap joint and the test specimens before and after the test (b). Reprinted with permission from [78]. Copyright 2020, EDP Sciences. All Rights Reserved

microcracks in the PPS matrix connecting neighboring domains were produced. The failure’s final stage before the specimen’s complete fracture is shown in Fig. 65c and f, revealing that the elastomer domains near the interface underwent significant deformation and then ruptured. Finally, the PPS part is separated from the Al part.

The interpretation of failure behavior observed by the in situ TEM tensile experiment is described as shown in Fig. 66. When tensile stress is applied to the joint

Fig. 64 Video showing the failure behavior of the PPS/Al direct joint in STEM bright-field (BF) mode



specimen, the plastic part preferentially elongates along the tensile direction, and microcavities are generated inside the rubber domains (Fig. 66a). As a result, the plastic deformation of the PPS matrix around the rubber domains is promoted, and crazes are generated between the rubber domains (Fig. 66b). At the same time, the plastic experiences a compressive stress perpendicular to the tensile direction. In the region close to the interface, the deformation of the plastic part is constrained by the strong bonding with Al (Fig. 66c). Therefore, the stress concentrates in the interfacial area in the plastic, causing the specimen to rupture (Fig. 66d).

The interfacial fracture energies of PPS/Al5052 joints can be characterized using a test specimen designed based on the compact tensile (CT) test specimen geometry described in ISO 13586 [94] for measuring the fracture toughness of bulk plastics. The joint laminate is produced by bonding metal and plastic plates, each with a thickness of 2 ± 0.1 mm, together, leaving a non-bonded region on one side to serve as a pre-crack as shown in Fig. 67a. To apply stress to the pre-crack tip, the laminate is sandwiched between two aluminum blocks using an epoxy adhesive, as shown in Fig. 67b. The surface of the metal substrate was masked to reduce the bond area of the laminate by 50%, ensuring that failure initiates from the pre-crack rather than the interface between the load block and the metal/plastic laminate. The pins inserted into the two holes of the load blocks were used to apply a crack opening stress to the specimen at a testing speed of 10 mm/min.

A force–displacement curve for a PPS/Al5052 laminate treated with the NMT1 is shown in Fig. 68. This curve displays an abrupt linear increase in force with a drop at the moment of crack initiation. The energy required to fracture the specimen is

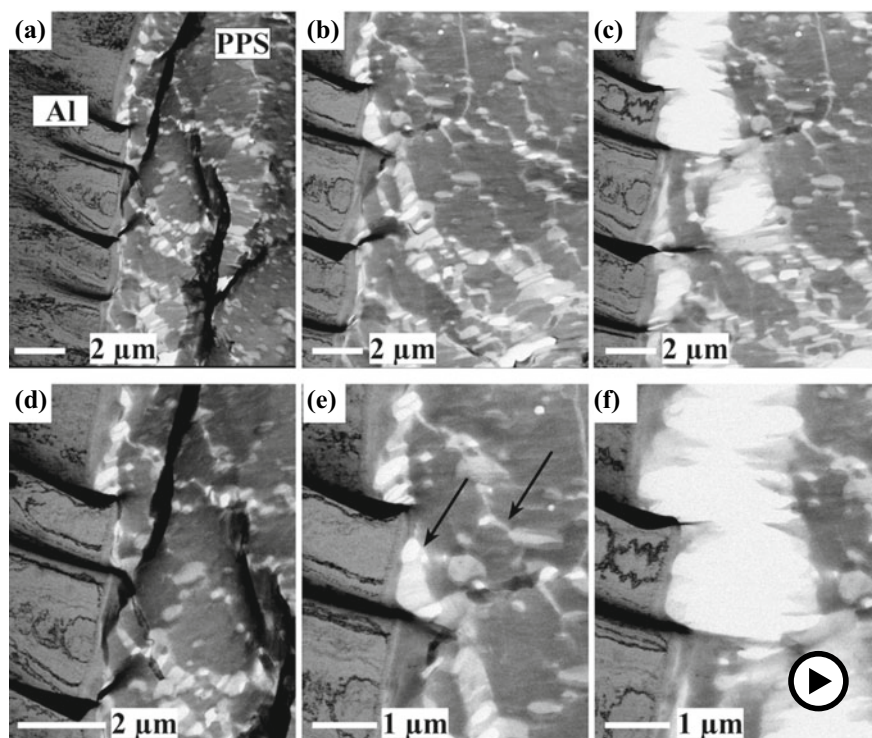


Fig. 65 In situ STEM-BF images of the PPS/Al direct joint interface under tensile load showing the failure of the interface: **a** initial state before applying the tensile load; **b** evolution of cavity and craze before the failure; **c** crack generated in the interfacial region. **(d)**, **(e)**, and **(f)** are the high-magnification images of **(a)**, **(b)**, and **(c)**, respectively. The arrows indicate the microcavity in the elastomer domains and the crazes between neighboring domains. Reprinted with permission from [93] (► <https://doi.org/10.1007/000-ayp>). Copyright 2021, Elsevier. All Rights Reserved

determined by calculating the area under the linear portion of the force–displacement curve.

The findings of this study are summarized in Table 1. The data demonstrate that the NMT-1 surface treatment yields slightly higher values than the NMT-2 under all test conditions. Although the penetration of PPS into the surface pores in NMT-2 is incomplete, it shows high joint strength. Additionally, it shows that direct Al/PPS bonding produces significantly higher joint strength than adhesive bonding.

The failure mechanism of the joints is investigated with the cross section of the fracture surfaces. Figure 69a shows a largely deformed PPS attached to the Al surface with the NMT-2 surface treatment in the upper part of the image. A mixed elemental map of S, O, and Al shown in Fig. 69b reveals that PPS is not pulled off from the Al surface pores. In Fig. 70a and b, STEM-HAADF and EDX mixed elemental maps of the fracture surface near the crack tip of the Al with the NMT-1 treatment are displayed, respectively. These images indicate the largely deformed PPS

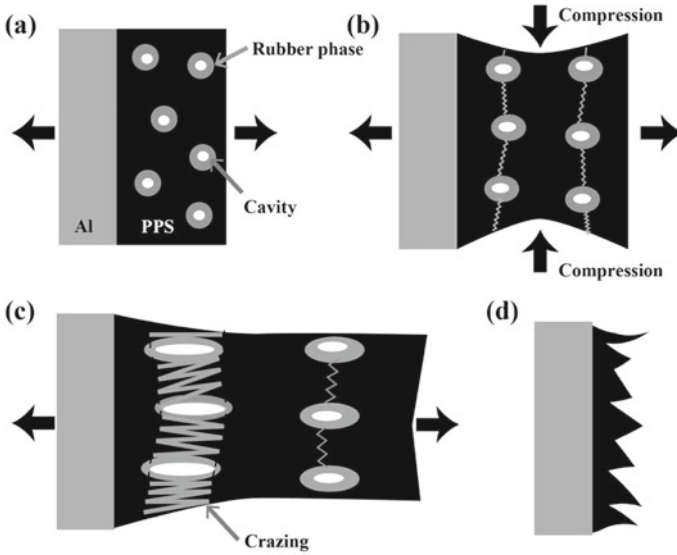


Fig. 66 Schematic illustration presenting the failure behavior of the PPS/Al direct joint interface

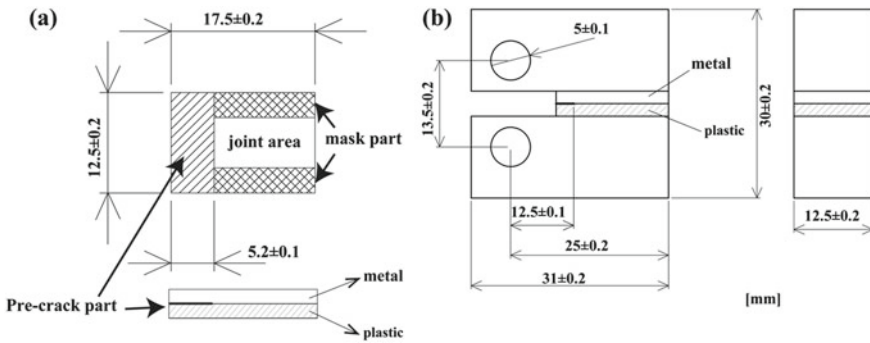


Fig. 67 Test specimen geometry and size for measuring interfacial fracture energy: a metal/plastic laminate; b the test specimen for the fracture test. Reprinted with permission from [78]. Copyright 2020, EDP Sciences. All Rights Reserved

attaches to the Al surface. Figure 70c is a magnified view of the interfacial region of Fig. 70a, which reveals that the surface-modified layer is partially damaged with voids produced inside the surface layer. The S elemental map (Fig. 70d) indicates that PPS remains inside the pores even though the layer is damaged. Based on these findings, it is concluded that once PPS diffuses into the pores, it cannot be pulled off from the pores in the surface layer, and instead, the interfacial layer is damaged to create voids. This failure behavior explains why the joint strength of NMT-1 is higher than that of NMT-2.

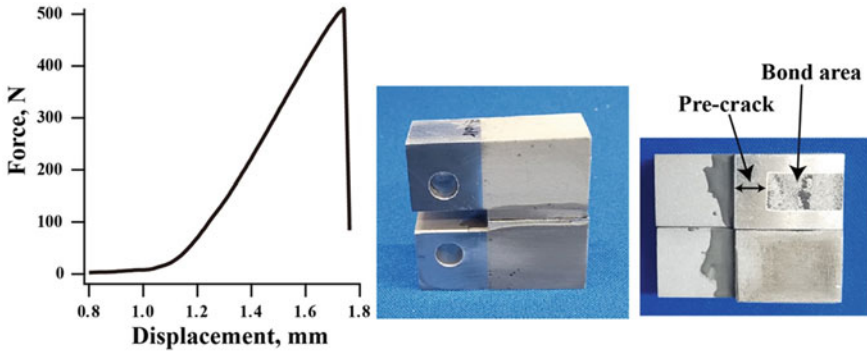


Fig. 68 The typical force–displacement curve obtained with a PPS/Al5052 laminate with NMT1 surface treatment and fracture surfaces of the test specimen

Table 1 Summary of the joint properties of the PPS/Al5052 joints with the NMT-1 and NMT-2 surface treatment

Surface treatment	NMT1 (Direct bonding)	NMT2 (Direct bonding)	NMT1 (Adhesive bonding)
Fracture energy (J/m)	12.3 ± 1.0	11.6 ± 1.1	3.20 ± 0.08
Lap shear strength (MPa)	44.2 ± 1.2	42.3 ± 0.52	10.8 ± 0.22
Tensile strength	43.0 ± 2.5	41.2 ± 2.2	18.5 ± 1.2

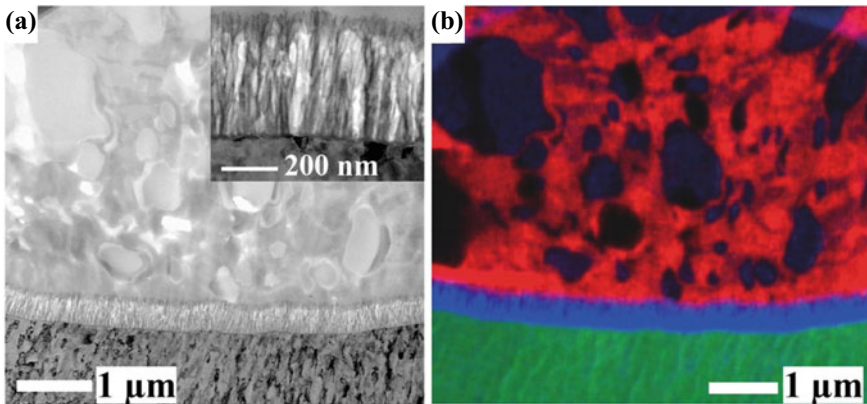


Fig. 69 STEM-HAADF and STEM-EDX elemental maps of the cross sections of the fracture surface of the Al with NMT-2 treatment after the fracture energy measurement: **a** STEM-BF cross-sectional image; **b** STEM-EDX mixed map of S (red), O (blue), and Al (green). Inset in **(a)** is a magnified image of the interfacial region. Reprinted with permission from [78]. Copyright 2020, EDP Sciences. All Rights Reserved

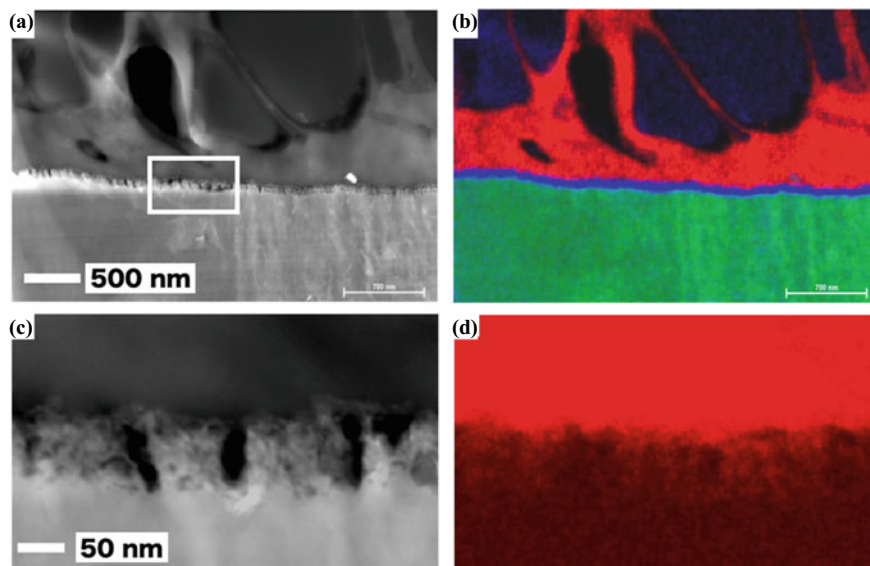


Fig. 70 STEM-HAADF and STEM-EDX elemental maps of the cross sections of the fracture surface of the Al with NMT-1 treatment after the fracture energy measurement: **a** STEM-HAADF image; **b** STEM-EDX mixed map of S (red), O (blue), and Al (green); **c** magnified image of **a**; **d** magnified image of the STEM-EDX S map representing the PPS distribution. Reprinted with permission from [78]. Copyright 2020, EDP Sciences. All Rights Reserved

Direct bonding of plastic and Al via insert injection molding provides high joint strength. This high joint performance can be achieved by the surface pretreatment of Al substrate, creating porous surface structures of 30–50 nm. The small pores are filled with molten polymers in the injection molding process in a short time. This study investigates the bonding mechanism between Al and PPS with two different surface treatments with different 3D connectivity in the modified surface layer. STEM tomography allows us to observe the interconnectivity of the pores at the joint interfaces. NMT-1 has three-dimensionally co-connected pores, while NMT-2 has isolated two-dimensional pores perpendicular to the metal substrate. It was found that the 3D-connected porous structure in NMT-1 facilitates polymer chain penetration. Due to dehydration, we observed a chemical reaction during the bonding process that converts meta-stable aluminum hydroxide into more stable alumina. The 3D porous structure and dehydration process are essential in creating a polymer/metal strong joint. Although incomplete penetration of PPS into the pores, sufficient joint strength can be achieved. These findings suggest that the nano-sized porous metal structures yield robust adhesion of polymer chains with metal.

8 Toughness and Durability of Interfaces in Dissimilar Adhesive Joints of Aluminum and Carbon-Fiber Reinforced Thermoplastics

Thermosetting polymers like epoxy and polyester resins have been widely studied as matrices for carbon fiber-reinforced plastics (CFRP) [95, 96]. However, these composites are not recyclable due to the characteristics of thermosetting polymers. In contrast, thermoplastic polymers have gained significant attention as a matrix because of no heat curing process needed, less hazardous chemical compositions, better recyclability, and mass production capabilities. By combining thermoplastic polymers with unidirectional and discontinuous carbon fibers, composite materials can be produced. Carbon fiber-reinforced thermoplastic polymers (CFRTP) offer a weight reduction of approximately 50% compared to steel and 20% to aluminum [97, 98].

CFRTPs have been identified as a promising composite for various industrial applications, including in the automotive, renewable energy, and aerospace industries. Their exceptional properties, such as high strength-to-weight ratio, wear resistance, and stiffness, give them an edge over traditional materials like metals. CFRTPs are better suited for mass production in the automotive industry. They can be easily manufactured using conventional molding methods like injection, rotational, extrusion, vacuum, and compression molding. Unlike traditional CFRP, the molding process for CFRTP is shorter, requiring only a few simple steps. Moreover, the shape of CFRTP can be altered after molding, enabling recycling through reuse, reforming, or other means, thereby improving production efficiency.

As a result, the demand for reliable techniques for joining metals and CFRTP is increasing. Adhesive bonding is a preferred option due to its lower weight, cost-effectiveness [99, 100], ability to prevent electrolytic corrosion [101, 102], and uniform stress distribution over the entire bonding area, as opposed to mechanical joining techniques such as welding, riveting, and bolt fastening. However, great concerns arise regarding the durability and mechanical resistance of adhesive bonding under severe service conditions, as adhesives are believed to be weak against heat than mechanical joining. Therefore, establishing a methodology to ensure the reliability of adhesive bonding is crucial.

A thorough evaluation of adhesive interfaces is required to guarantee the safety of adhesive bonding. The dissimilar adhesive joints of metal and CFRTP involve two interfaces, one between the adhesive and CFRTP, and the other between the adhesive and metal [103, 104]. The failure of joints can occur at any of the interfaces, within the adhesive layer, or a combination of all three. Accurately characterizing the interfacial region in adhesive joints is essential for appropriate system design by selecting surface pretreatments for adherents and adhesives.

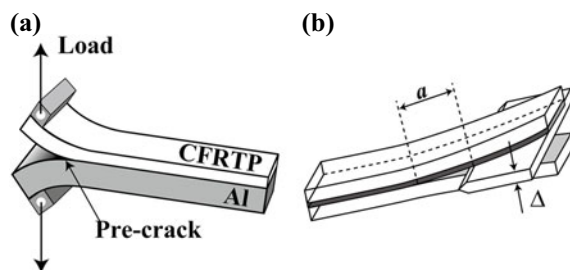
Accurate interfacial characteristics cannot be extracted from the measured data by traditional engineering tests such as lap shear and peel adhesion tests because these tests are sensitive to inelastic deformations in adherend and adhesive away from the interface. The double cantilever beam (DCB) geometry is suitable for estimating

the fracture resistance of adhesive interfaces subjected to tensile opening force as the crack grows along the interface [105, 106]. This study aims to investigate the fracture toughness and durability of different adhesive interfaces in joints of Al and CFRTP with a polyamide-6 (PA6) matrix under high humidity and temperature conditions, using an optimized DCB specimen geometry, as shown in Fig. 71 [85]. By continuously pulling the specimen apart at a constant velocity (Fig. 71a) or displacement by inserting a wedge (Fig. 71b), the locus of failure is inspected, and the bonding mechanism of surface pre-treatments of CFRTP is discussed.

The TEPEX® product, manufactured by LANXESS, is a CFRTP consisting of plain woven carbon fiber continuous fabric impregnated with PA6 with a bending modulus of 50 GPa. NMT-1 was used to prepare surface-treated aluminum alloy (Al5052) plates with a bending modulus of 65 GPa, and their surface properties are described in Sect. 7. Three types of commercial paste adhesives (epoxy, acrylic, and urethane) were used to join the CFRTP and Al. The two-component epoxy adhesive (Denatite 2204, Nagase ChemteX Corp.) was cured at 25 °C for 1.5 h and 100 °C for 1 h. The second-generation acrylic (SGA) adhesive (HARDLOC C-335–20, Denka corp.) was cured at room temperature for 1 h and then at 80 °C for 1 h. The two-component urethane adhesive was cured at 25 °C for 1.5 h and 80 °C for 1 h.

Two methods are used to pretreat the CFRTP surface: acetic acid treatment, where the substrate is rubbed with cotton containing acetic acid, and flame treatment, which is detailed in Sect. 4. To control the thickness of the adhesive layer, 200 μm diameter glass spheres are added after coating the adhesive onto both adherents. Before lamination, an 80 μm thick PTFE film is placed on one end of the substrate, which creates a 50 mm long non-bonded area. This area is used as a pre-crack for the initiation of the crack in the DCB test. After curing, rectangular coupons with a length of 250 mm and a width of 25 mm are cut out from the bonded laminates. These specimens include a non-bonded part at one end.

Fig. 71 Schematic illustrations of the specimens for ADCB test (a) and wedge test (b). Reprinted with permission from [85]. Copyright 2020 American Chemical Society, All Rights Reserved



8.1 Evaluation of Interfacial Fracture Toughness by ADCB Test

To assess the toughness of dissimilar joint interfaces, a universal testing machine is utilized to apply a tensile opening load to a pre-crack of the specimen, as shown in Fig. 71a. An asymmetric double cantilever beam (ADCB) test [107] is employed using specimens of 10 mm thick Al and 4 mm thick CFRTP beams to obtain reliable interfacial toughness values. The modulus mismatch of the dissimilar joint makes it necessary to achieve the reliability of the results. When using a conventional DCB specimen with beams of equal thickness for dissimilar joints, the crack could escape from the interface and calculated fracture energy is overestimated. Therefore, the appropriate Al/CFRTP thickness combination have to find by testing specimens with different thickness ratios, as presented in Fig. 72. In the DCB test with the same Al/CFRTP thicknesses beams, the crack propagation accompanies significant plastic deformation of the Al beam, which makes it difficult to interpret the calculated data. Increasing the Al/CFRTP thickness ratio decreases the plastic deformation of the Al beam, and a ratio of 5/2 mm shows negligible plastic deformation, enabling the test to be performed within the elastic deformation of both beams. The thermal expansion coefficient mismatch between Al and CFRTP is another concern that causes specimen warping. When cooled from a cure temperature to room temperature, residual thermal stress in the specimen impacts the calculation of fracture energies. The specimens with 10 mm thick Al and 4 mm thick CFRTP make specimen warping negligible.

One-component epoxy (Scotch-Weld, EW-2040, 3 M, USA) is used to adhesively bond the load blocks to one end of the specimens following ISO 25217 [108], and they are set to the testing instrument via loading blocks. All tests are performed at room temperature with a constant crosshead speed of 1 mm/min. The mechanoluminescence (ML) technique is introduced to monitor the crack's progress during the ADCB test [109], which detail is described in Chap. 4. The force measured by a universal testing machine and the crack length measured by the assistance of ML are plotted against the crack opening displacement (COD), measured by the displacement of the crosshead. The interfacial fracture toughness is calculated by using a method described later.

Detecting the crack tip accurately is essential to obtain precise fracture toughness values by the ADCB test. The conventional method to detect the crack tip is to apply white paint to the side of the specimen, as described in ISO 25217. However, the crack tip may not always be detectable. In contrast, the ML technique effectively identifies the crack tip precisely. The ML particles act as a sensitive mechanical sensor that emitted bright light under mechanical stimuli, revealing the specimen's dynamical strain/stress distribution as demonstrated in Fig. 73a. The ML-assisted DCB test allows us to observe the crack frontline within the adhesive layer from outside the adherend.

Figure 73b–d display the load and crack length versus COD for the non-treated, acetic acid-treated, and flame-treated specimens. The tensile load initially increases linearly but deviates from this slope before reaching the maximum load point. The



Fig. 72 Al/CFRTP thickness ratio dependence on the plastic deformation of the Al beams after the DCB test of the Al/CFRTP adhesive joints. The total thickness is fixed at 7 mm and the thickness ratio is varied. Reprinted with permission from [85]. Copyright 2020, American Chemical Society. All Rights Reserved

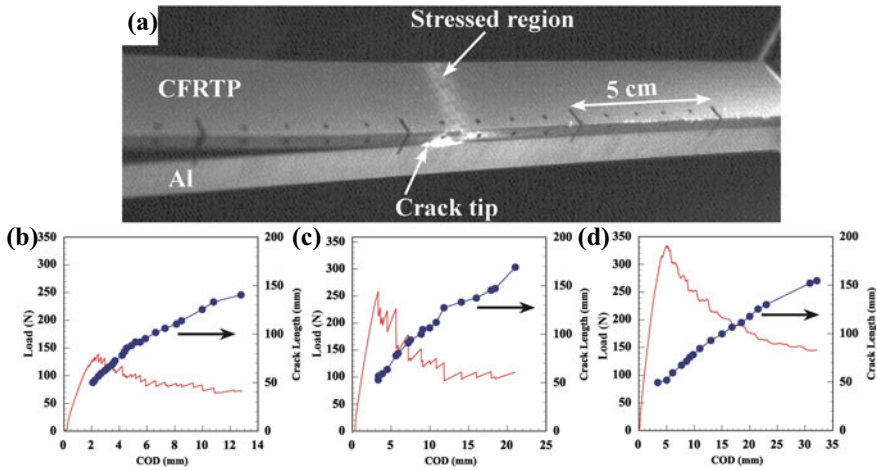


Fig. 73 ML emission seen in a test specimen for the ADCB test of the dissimilar adhesive joints of CFRTP and Al (a). The load and crack length versus COD plots obtained for the non-treated (b), acetic acid-treated (c), and flame-treated (d) specimens through the ADCB test. Reprinted with permission from [85]. Copyright 2020, American Chemical Society. All Rights Reserved

crack begins shortly before the maximum load is reached and continues to grow with a gradual decrease in load in all tests [110]. After passing the maximum load point, the load-COD curves for the non-treated (Fig. 73b) and acetic acid-treated (Fig. 73c) specimens exhibit similar features, showing gradual decay with small random fluctuations as the crack propagated. In contrast, the load for the flame-treated specimen (Fig. 73d) shows a smooth decay during crack propagation. Figure 74 is a video demonstrating that the cracks in the non-treated and acetic acid-treated specimens progress unstably with repeated “initiation and arrest”. In contrast, the flame-treated specimen exhibits continuous and steady crack growth. Furthermore, it can be found that the crack propagation rate is the fastest for the non-treated specimen, slower for the acetic acid-treated specimen, and slowest for the flame-treated specimen. These results indicate that both fracture toughness and fracture behavior are affected by the surface treatment of the CFRTP.

The modified beam theory is used to estimate the interfacial fracture energies of the ADCB specimens. To introduce an equivalent stiffness (EI_{eq}), the cubic root of compliance, C , as defined by Eq. (14) is plotted against the crack length, a , as shown in Fig. 75. All points on the graph are on the linear slopes produced by least squares fitting. The negative X-intercept of the linear fits provided Δ values, while the linear fit slope represented the specimen’s stiffness, defined as $(1/EI_{eq})^{1/3}$. The interfacial fracture energy, G , can be calculated using Eq. (15), with B representing the specimen width and Δ serving as the calibration parameter.

$$C = \frac{\delta}{P} \tag{14}$$

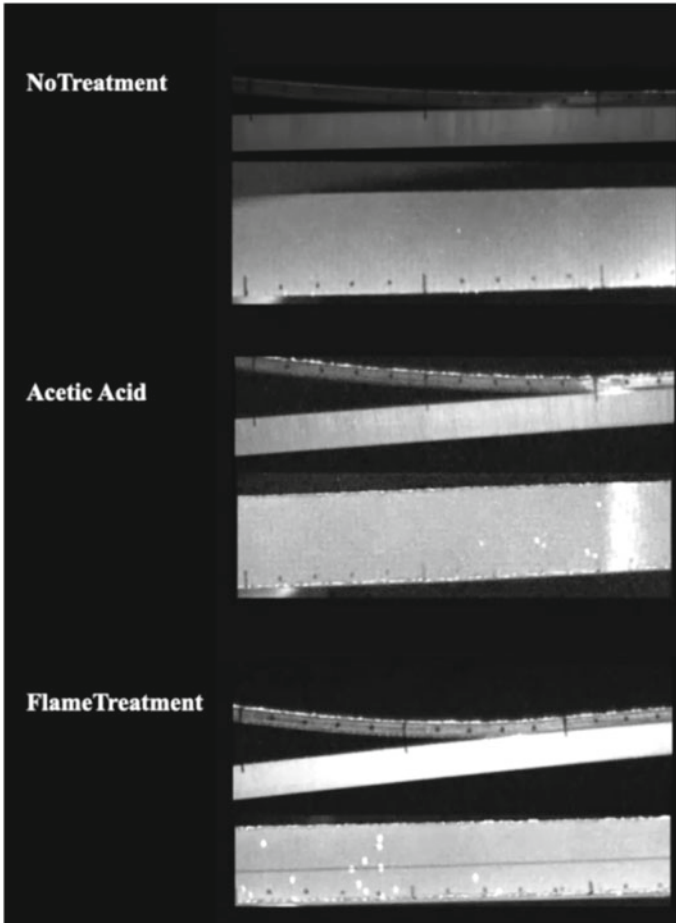
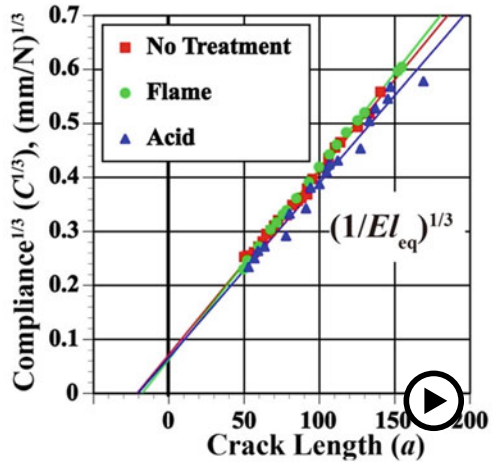


Fig. 74 A video showing the cracks progressed in ADCB tests of the non-treated, the acetic acid-treated and the flame-treated specimens. Reprinted with permission from [85]. Copyright 2020, American Chemical Society. All Rights Reserved

$$G = \frac{3P^2(a + \Delta)^2}{2B(EI)_{eq}} \quad (15)$$

The toughness of the Al/CFRTP dissimilar joint interfaces is evaluated by plotting G values against the crack length in the crack growth resistance curves (R-curve), as shown in Fig. 76. The influence of the surface pretreatments on the interface toughness is found to be adhesive-dependent. The interfacial fracture toughness of the epoxy adhesive joint is significantly enhanced by flame treatment. In contrast, the acetic acid treatment improved the joint toughness to some extent but showed

Fig. 75 Plots of $C^{1/3}$ versus crack length, a , for determining the equivalent stiffness, EI_{eq} , and the calibration parameter, Δ . Reprinted with permission from [85]. Copyright 2020, American Chemical Society. All Rights Reserved
 (▶ <https://doi.org/10.1007/000-ayq>)



fluctuations in the values during crack propagation. The lowest G values in the R-curves of the flame-treated and non-treated specimens are attributed to the energy required for crack initiation. The slight increase in G values with increasing crack length suggests the growth of a plastic zone around the crack tip, which makes the interfaces more ductile. Surface treatments are necessary for bonding with the SGA, and the acid treatment is the most effective, followed by the flame treatment. On the other hand, high bonding performance is observed for the urethane adhesive joint, regardless of surface treatment.

To investigate the mechanism of the surface pretreatments for CFRP, the interfaces between pristine PA6 and the epoxy adhesive were investigated. As stated in Sect. 4, the flame treatment produces a 10 nm thick amorphous layer on the PA6 surface. The absorption band at 1710 cm^{-1} observed in FT-IR spectra of acetic acid-treated PA6 is attributed to the $\text{C}=\text{O}$ stretch of acetic acid [111], indicating

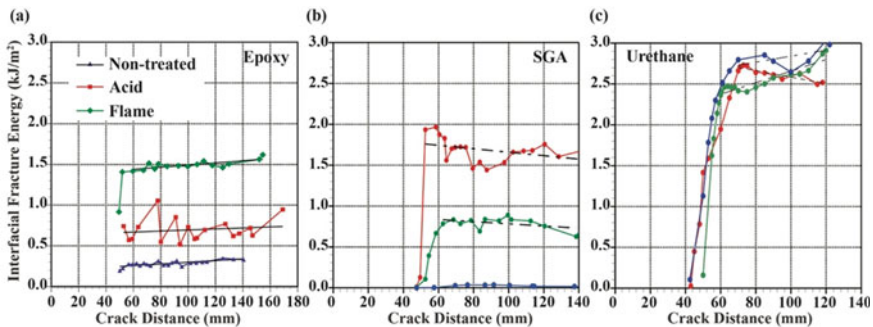


Fig. 76 Crack growth resistance curves of no treated (blue), acetic acid treated (red), and flame treated (green) specimens: **a** epoxy adhesive; **b** SGA; **c** urethane adhesive. Reprinted with permission from [85]. Copyright 2020, American Chemical Society. All Rights Reserved

the absorption of acetic acid into PA6 [112]. STEM-EDX results demonstrated that acetic acid treatment suppresses the segregation of silica, which is contained in the epoxy adhesive, on the interface, thereby promoting contact between the adhesive and PA6 and enhancing adhesion. The authors suggest that the acetic acid treatment may improve the affinity of PA6 to the epoxy adhesive, as evidenced by contact angle measurements that showed enhanced wettability of the PA6 surface. The flame treatment did not produce specific functional groups on PA6; the amorphous layer may improve surface mobility at the curing temperature, allowing for diffusion of the liquid state adhesive into the PA6 layer and entanglement with PA6. Although the mechanism for SGA and urethane adhesives is unknown, the authors recommend using the ADCB test with appropriate beam thickness combinations to quantitatively evaluate the effects of adhesive and surface treatment on dissimilar adhesive joints.

8.2 Evaluation of Durability of Adhesive Interfaces Under High Humidity Environment by Wedge Test

In the wedge test, the interface is cleaved by pulling apart the edge of the specimen at a constant displacement, as illustrated in Fig. 71b. It is a simple test that requires no specialized equipment, making it suitable for use in different environmental conditions where a testing machine is difficult to be used. After the wedge is inserted into the interface, a crack is initiated and stabilized. If the environmental conditions change, the crack may expand afterward, which allows for assessing interface durability under specified environmental conditions. An equation that is discussed in Sect. 3 can be used to relate the fracture energy directly to the crack length.

Figure 77a displays a side view of an Al/CFRTP wedge test specimen, where Al and non-treated CFRTP are bonded with the epoxy adhesive. When the Al wedge is inserted into the pre-crack, the crack is extended and then terminated within a 12-h. The specimen is subjected to a high temperature and high humidity environment of 85 °C and 85%RH. Water penetrates the interfaces when the adhesive layer is exposed to these conditions under the stress applied by the wedge. Water invades the adhesive layer at the crack tip, resulting in further crack extension along the interface. As illustrated in Fig. 77b, this significantly decreases interfacial fracture toughness within the first few hours. The decrease in interfacial toughness is primarily attributed to the high humidity, which appeared independent of the surface pretreatment condition. Subsequent exposure to these conditions resulted in a gradual decline in toughness values, G_{wet} . A test is also conducted under dry conditions at 85 °C, which indicates that heat damage to the interfacial region is negligible and the decrease in interfacial toughness is primarily caused by high humidity.

Figure 77c through 77e depict the visual examination of fracture surfaces following the wedge tests of non-treated, acetic acid-treated, and flame-treated specimens. The non-treated specimen (Fig. 77c) exhibits an apparent fracture between the adhesive and the CFRTP interface. In the acetic acid-treated specimen (Fig. 77d),

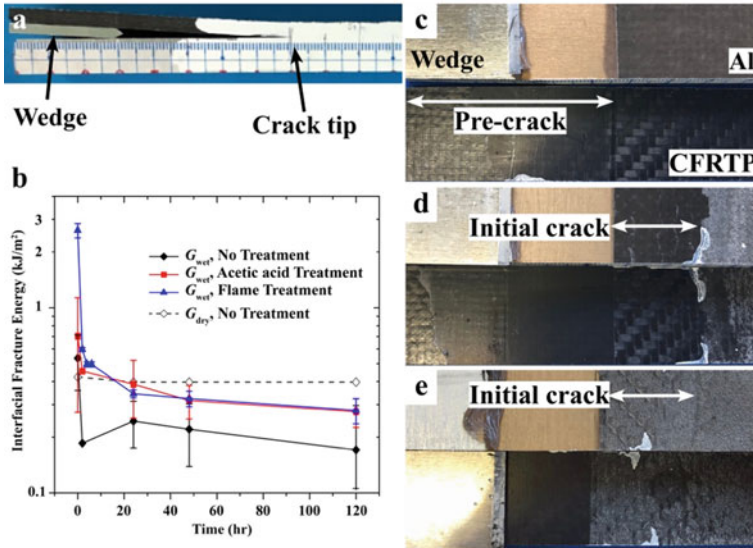


Fig. 77 Wedge-test of Al/CFRTP adhesive joints with the epoxy adhesive: **a** side view of the specimen after the wedge insertion; **b** semi-log plot of interfacial fracture energy under wet, G_{wet} , and dry, G_{dry} , conditions as a function of residence time in high humidity condition at 85 °C and 85% RH; **c** fracture surfaces of the non-treated specimen; **d** acetic acid-treated specimen; **e** flame-treated specimen. Reprinted with permission from [85]. Copyright 2020, American Chemical Society. All Rights Reserved

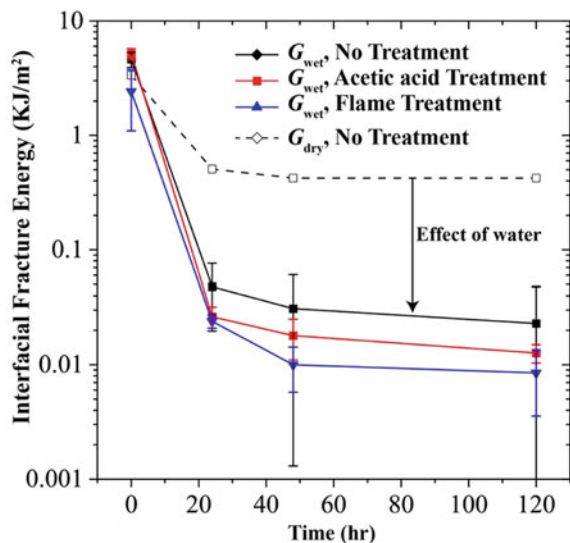
the locus of failure shifts from the interfacial to the cohesive at the period when the crack extension starts in the high humidity environment, indicating successful toughening of the CFRTP/adhesive interface and preventing water invasion into the interface. In contrast, water is absorbed into the epoxy adhesive, not into the interface, causing degradation of the adhesive and significantly reducing the interfacial toughness. Therefore, the interfacial fracture toughness of the acetic-acid-treated and flame-treated specimens under wet conditions, G_{wet} , are nearly identical, while the non-treated specimen exhibited much lower values. The flame-treated specimen did not fail at the CFRTP/adhesive interface (Fig. 77e), indicating the critical role of physical bonding created via entanglements in interface toughness.

The adhesive joints with the urethane adhesive are also evaluated under the same condition. The urethane adhesive exhibits the initial high bonding performance regardless of the CFRTP surface pretreatment, as shown in Fig. 76c. However, the crack extends along the interface once the specimen is brought into the high-humidity environment. This means the urethane adhesive is much weaker than the epoxy under high humidity conditions, although the initial adhesion strength is remarkably high. According to Fig. 78, the initial interfacial toughness values are higher than the epoxy adhesive, but the interfacial fracture toughness decreased significantly within the first 24 h. The interfacial toughness was also measured in a dry condition at 85 °C. Although it reduces, the reduction is not as significant as in the wet condition

and differed from the behavior of the epoxy adhesive. This difference highlights the impact of water on the interfacial toughness with the urethane adhesive. The results indicate that the urethane adhesive exhibits weaker performance in wet conditions when compared to the epoxy adhesive. Furthermore, the surface treatments exhibit negative effect on the durability. Unlike the epoxy adhesive, the surface pretreatments of CFRTP shows no chance to improve the durability under the high-humidity condition for the urethane adhesive.

To gain further insight, a detailed investigation was conducted using STEM with thin cross sections of the fracture surfaces of the Al sides. Figure 79a, b, and c exhibit STEM-HAADF images of the non-treated, acetic-acid-treated, and flame-treated specimens, respectively. Significant changes are observed in the Al surface structures of the non-treated specimens (Fig. 79a) and the acetic acid-treated (Fig. 79b). In contrast, the original porous structure on the Al plate is preserved in the flame-treated specimen (Fig. 79c). In the non-treated specimen, the Al surface oxide layer is highly elongated along the crack opening direction, with a 300–400 nm length, confirmed in the corresponding EDX elemental maps (Fig. 79d). The acetic acid-treated surface appears to have been significantly damaged, with voids generated within the layer, which seems to be partially separated from the Al metal part (Fig. 79e). The wedge test conducted under high humidity conditions reveals that water preferred to invade the Al/adhesive interfaces in the non-treated and acetic acid-treated specimens, resulting in the growth of thick oxide layers. Although the urethane adhesive used in the study exhibited high initial adhesive strength and did not require surface treatment, its strength considerably decreased when exposed to high humidity. Previous experiments have shown that isocyanate can chemically bond with glycidyl groups on solid substrates [113], implying the possibility of chemical bonding between isocyanate

Fig. 78 The semi-log plot of interfacial fracture energy of the urethane adhesive under wet, G_{wet} , and dry, G_{dry} , conditions as a function of residence time in the high humidity condition at 85 °C and 85 RH%. Reprinted with permission from [85]. Copyright 2020, American Chemical Society. All Rights Reserved



and PA6. However, the harmful effects of flame treatment on the urethane adhesive remain unclear and require further investigation.

Two different test methods were employed to assess the toughness and durability of dissimilar adhesive joints between CFRTP and Al alloy under high humidity conditions. The first is the ADCB test, in which the specimens are pulled apart continuously at a constant velocity, while the second is the wedge test, in which they are pulled apart at a constant displacement. The ML-assisting ADCB test allows for accurate detection of the crack tip and visualization of micro-deformations around it, revealing plastic deformation and failure inside the CFRTP. Combining ADCB and wedge tests provides insight into the effects of surface pretreatments and adhesive types on adhesive interface characteristics. Various failure modes are observed, as summarized in Table 2. Notably, using epoxy adhesive with acetic acid treatment results in a switch

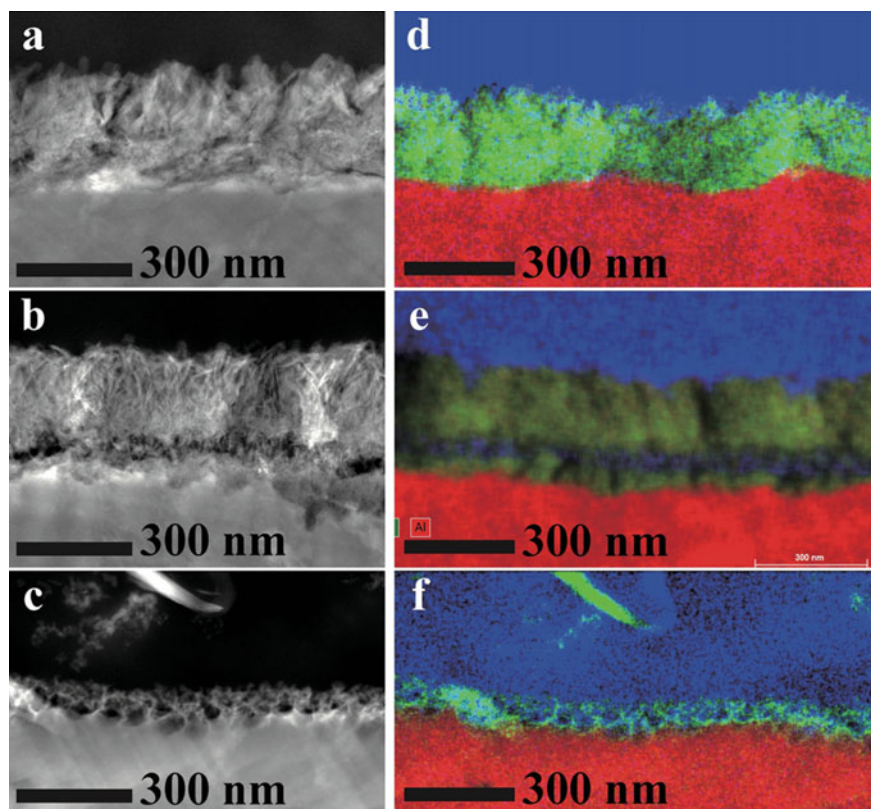






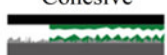


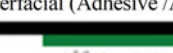




Fig. 79 STEM-HAADF (a–c) images and STEM-EDX elemental maps (d–f) of the cross sections of the Al fracture surfaces: **a, d** non-treated; **b, e** acetic acid treated; **c, f** flame treated specimens. Blue, green, and red represent carbon, oxygen, and aluminum distributions in the STEM-EDX maps. Reprinted with permission from [85]. Copyright 2020, American Chemical Society. All Rights Reserved

Table 2 Loci of failure in the test conditions employed in this study and schematic illustrations representing the failure mode. Reprinted with permission from [85]. Copyright 2020, American Chemical Society. All Rights Reserved

Adhesive	Surface Treatment on CFRTP	Locus of Failure	
		DCB	Wedge
Epoxy	No	Interfacial (CFRTP/Adhesive) 	Interfacial (CFRTP/Adhesive) 
	Acetic acid	Interfacial (CFRTP/Adhesive) 	Cohesive 
	Flame	Cohesive 	Cohesive 
Urethane	No	Cohesive 	Interfacial (Adhesive/Al) 
	Acetic acid	Cohesive 	Interfacial (Adhesive/Al) 
	Flame	Cohesive 	Interfacial (CFRTP/Adhesive) 

from “interfacial” to “cohesive” failure when the environment changes from atmospheric to high humidity. Under high humidity conditions, failure of the urethane adhesive occurs at the Al/adhesive interface with significant deformation of the Al surface layer. This study aims to establish a correlation between interfacial structure and mechanical joint properties, regardless of joint design or size. The results do not represent adhesive-type properties and require further data collection. The durability of adhesive joints under high humidity conditions remains a challenge, and future efforts will focus on developing appropriate surface treatments and highly durable adhesives.

8.3 Stress-Induced Corrosion at Adhesive Interfaces

As shown in Fig. 79, the cross-sectional STEM observations of aluminum fracture surfaces indicate the formation of a novel structure within the thick oxide layer, suggesting that the Al/adhesive interfaces are severely attacked by moisture. The wedge test was employed with an Al/Al similar adhesive joint with an epoxy adhesive

to find the chemical phenomena at the Al adhesive interface. The wedge inserted into the pre-crack produced a crack along the interface, as shown in Fig. 80a. The two Al plates were separated after the test for 24 h and both sides showed the fracture surfaces as shown in Fig. 80b. It shows that the adhesive remains on one side of the Al plates, indicating failure along the interface. The initial crack, propagated after the insertion of the wedge, and the crack progressed under the high humidity condition are clearly distinguished on the fracture surface as shown in the upper plate of Fig. 80b. The surface created by the initial crack is glossy, while the surface produced after the crack propagation under a humid environment appears white and cloudy.

The three ROIs on the fracture surfaces were selected, as shown in Fig. 80b. Figure 80c shows the STEM-HAADF image, STEM-ELNES phase map, and STEM-EDX elemental map of the cross section of ROI-I, which was produced under the high-humidity condition. An oxide layer of 500 nm or more thickness is formed on the fracture surface. As mentioned in Sect. 6, the ELNES phase mapping allows us to distinguish aluminum oxide compounds by the ELNES of O K-edges in EELS. All the spectra included in the ROI are fitted with the O K-edges of $\text{Al}(\text{OH})_3$ and $\text{AlO}(\text{OH})$ as standard spectra. The distribution of the two compounds is obtained as a phase map according to the ratio of those compounds obtained by fitting. The obtained ELNES phase map (middle panel of Fig. 80c) shows that the oxide layer comprises two parts: the bottom part is $\text{Al}(\text{OH})_3$ -rich and the upper part is boehmite-rich. The STEM-EDX elemental map (right panel of Fig. 80c) indicates that the chlorine element is in the bottom part of the oxide layer.

The cross section of ROI-II, which is below the initial crack, shows different features compared to ROI-I. Even though ROI-II was exposed to the high-humidity environment, the oxide layer is not as thick as produced in ROI-I, which is close to the crack tip. And also, the two-layer structure with $\text{Al}(\text{OH})_3$ and boehmite as found in ROI-I was not formed and $\text{Al}(\text{OH})_3$ was produced less than the ROI-I. Chlorine element was also detected in this region but was not concentrated as much as ROI-I. ROI-III is the opposite part of ROI-I, where the adhesive layer is attached to the surface and no thick oxide layer is produced, as shown in Fig. 80e.

In the wedge test, water invaded mainly into the Al/epoxy interface at the crack tip and an extremely thick oxide layer was produced in 24 h. The STEM-ELNES mapping revealed that a two-component layer structure with $\text{Al}(\text{OH})_3$ and boehmite was formed with Cl-rich bottom $\text{Al}(\text{OH})_3$ part. It is indicated that corrosion is likely to occur at the highly stressed crack tip. The Al oxide layer can prevent corrosion, but bending stress applied to the oxide layer may destroy the oxide layer, and the metal part below is oxidized. We will investigate the detailed mechanism of this stress-induced corrosion.

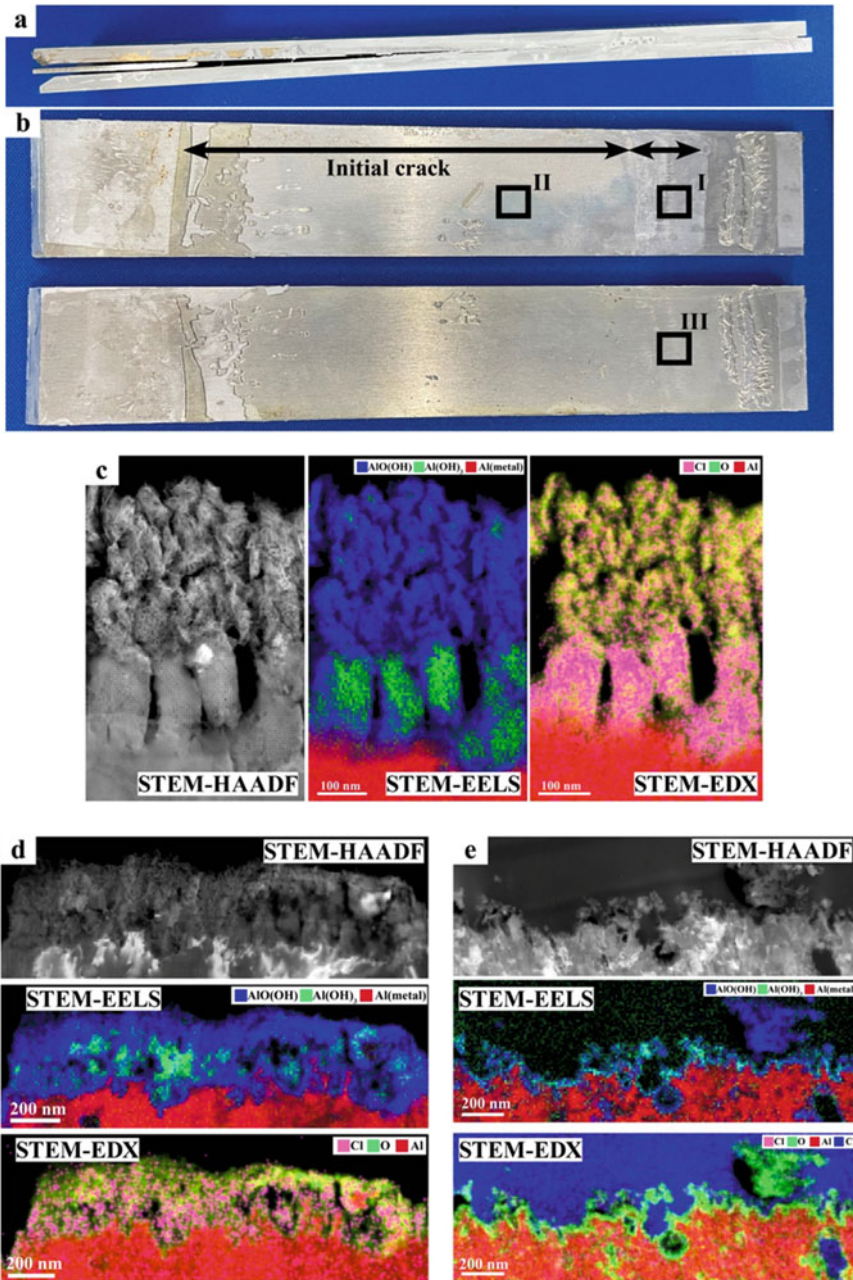


Fig. 80 Side view (a) and fracture surfaces (b) of the wedge-test specimen of the adhesive joint of Al exposed to 85 °C, 85%RH condition for 24 h. c, d, and e are cross-sectional images of the ROIs I, II, and III, respectively, marked in b. Each panel shows STEM-HAADF, STEM-ELNES phase map, and STEM-EDX elemental map

9 Concluding Remark

Polymer–polymer dissimilar interfaces formed via interdiffusion can be visualized and characterized by the elemental mapping and Image EELS techniques of EFTEM. The concentration profiles can estimate the interfacial thickness across the interfaces with a spatial resolution of 10 nm. The enthalpy-driven thermodynamic acceleration causes ultrafast interdiffusion in miscible polymer pairs. On the other hand, the interfacial diffusion between identical polymers is extremely slow because the diffusion between identical polymers is caused only by the contribution of combinatorial entropy change, which is relatively tiny for high molecular weight polymers.

The observation of the fracture surfaces by HR-SEM revealed that the failure of interfaces between polymers creates about 10 nm thick fibrils when they failed in the earlier diffusion stage. The nanofibrillar structure is formed when a thin interface is separated with the disentanglement of polymer chains before the initiation of crazing. This nanofibrillar surface feature is a signature of the failure of thin interfaces via “chain-pullout” and represents the entanglement structure at the interface. A similar nanofibrillar pattern on fracture surfaces is also found in the failure of the interfaces between metal and polymer. This indicates that an interfacial layer is formed with the low-molecular-weight polymer, and the entanglement structure within this layer determines the bonding strength. It was found that the interfacial toughness is determined by entanglement rather than thickness from the relationship between interfacial toughness and interface thickness.

Using STEM-EELS/ELNES, we clarified the chemical reaction at the Al adhesive interface with a resolution of 5 nm. We found that the main reason for the strong bonding is the diffusion of the adhesive molecules into tiny pores spaced about 10 nm on the aluminum oxide surface. This shows a similarity to polymer–polymer entanglement at the interface. The acid–base interaction between the amino moiety of the epoxy/amine adhesive and the hydroxyl unit on the Al oxide surface is the origin of the chemical bonding between Al and epoxy adhesive. This bond itself is weak and makes a small contribution to the increase in adhesive strength, but the enthalpic drive of acid–base interfacial interactions may cause spontaneous diffusion of adhesion molecules into the pores.

Acknowledgements SH thanks Mr. Hideki Hakukawa, Ms. Yuri Shigemto, Dr. Takeshi Hanada, Dr. Kazunori Kawasaki, Dr. Yida Liu, Dr. Lingyun Lyu (AIST), Prof. Yongjin Li (Hangzhou Normal University), and Prof. Yonggui Liao (Huazhong University of Science and Technology) for their contributions to the works. Part of this work was commissioned by JST-Mirai Program Grant Number JPMJMI18A2, Japan (Sects. 5, 6, and 7) and by the New Energy and Industrial Technology Development Organization (NEDO) Grant Number JPNP14014, Japan (Sect 8).

References

1. S.F. Edwards, *Proc. Phys. Soc.* **92**, 9–16 (1967)

2. P.G. de Gennes, *J. Chem. Phys.* **55**, 572–579 (1971)
3. F. Brochard, J. Jouffroy, P. Levinson, *Macromolecules* **16**, 1638–1641 (1983)
4. S. Horiuchi, Y. Ishii, *Polymer J.* **32**, 339–347 (2000)
5. T. Hayakawa, S. Horiuchi, *Angew. Chem. Int. Ed.* **42**, 2285–2289 (2003)
6. S. Horiuchi, T. Hanada, K. Yase, T. Ougizawa, *Macromolecules* **32**, 1312–1314 (1999)
7. S. Horiuchi, T. Hamanaka, T. Aoki, T. Miyakawa, T. Narita, H. Wakabayashi, *J. Electron Microsc.* **52**, 255–266 (2003)
8. L. Reimer, *Energy-Filtering Transmission Electron Microscopy*, 1st edn., ed. by L. Reimer (Springer, Berlin, 1995) pp. 347–400
9. N. Higashida, J. Kressler, S. Yukioka, T. Inoue, *Macromolecules* **25**, 5259–5262 (1992)
10. M.E. Fowler, J.W. Barlow, D.R. Paul, *Polymer* **28**, 1177–1184 (1987)
11. M. Suess, J. Kressler, H.W. Kammer, *Polymer* **28**, 957–960 (1987)
12. L. Reimer, *Energy-Filtering Transmission Electron Microscopy*, 1st edn., ed. by L. Reimer (Springer, Berlin, 1995) pp. 383–388
13. K.H. Körtje, *Scanning Microsc.* **8**, 22 (1994)
14. P.J. Thomas, P.A. Midgley, *Ultramicroscopy* **88**, 179–186 (2001)
15. S. Horiuchi, T. Fujita, T. Hayakawa, Y. Nakao, *Langmuir* **19**, 2963–2973 (2003)
16. S. Horiuchi, D. Yin, T. Ougizawa, *Macromol. Chem. Phys.* **206**, 725–731 (2005)
17. S. Horiuchi, D.H. Yin, Y.G. Liao, T. Ougizawa, *Macromol. Rapid Commun.* **28**, 915–921 (2007)
18. Y. Liao, A. Nakagawa, S. Horiuchi, T. Ougizawa, *Macromolecules* **40**, 7966–7972 (2007)
19. J. Kressler, N. Higashida, T. Inoue, W. Heckmann, F. Seitz, *Macromolecules* **26**, 2090–2094 (1993)
20. J. Klein, *Science* **250**, 640–646 (1990)
21. M.A. Parker, D. Vesely, *J. Polym. Sci. Polym. Phys.* **24**, 1869–1878 (1986)
22. H.C. Lin, I.F. Tsai, A.C.-M. Yang, M.S. Hsu, Y.C. Ling, *Macromolecules* **36**, 2464–2474 (2003)
23. P.E. Rouse, *J. Chem. Phys.* **21**, 1272–1280 (1953)
24. H. Qiu, M. Bousmina, *Macromolecules* **33**, 6588–6594 (2000)
25. E. Kim, E.J. Kramer, W.C. Wu, P.D. Garrett, *Polymer* **35**, 5706–5715 (1994)
26. S. Yukioka, K. Nagato, T. Inoue, *Polymer* **33**, 1171–1176 (1992)
27. S. Yukioka, T. Inoue, *Polym. Comm.* **32**, 17–19 (1991)
28. R. Schnell, M. Stamm, C. Creton, *Macromolecules* **32**, 3420–3425 (1999)
29. R. Schnell, M. Stamm, C. Creton, *Macromolecules* **31**, 2284–2292 (1998)
30. S. Wu, H.-K. Chung, *J. Polym. Sci. Polym. Phys.* **24**, 148–169 (1986)
31. L. Silvestri, H.R. Brown, S. Carrà, S. Carrà, *J. Chem. Phys.* **119**, 8140–8149 (2003)
32. P.J. Cole, R.F. Cook, C.W. Macosko, *Macromolecules* **36**, 2808–2815 (2003)
33. H.R. Brown, *J. Adhes.* **82**, 1013–1032 (2006)
34. J. Zhang, P.J. Cole, U. Nagpal, C.W. Macosko, *J. Adhes.* **82**, 887–902 (2006)
35. W.S. Gutowski, *J. Adhes.* **79**, 445–482 (2003)
36. S. Wu, *Polymer Interface and Adhesion* (Marcel Dekker: New York, 1982) p. 111
37. C. Creton, E.J. Kramer, C.Y. Hui, H.R. Brown, *Macromolecules* **25**, 3075–3088 (1992)
38. V. Janarthanan, R.S. Stein, P.D. Garret, *Macromolecules* **27**, 4855–4858 (1994)
39. A. Tanaka, *J. Electron Microsc.* **43**, 177–182 (1994)
40. D. Hull, *Fractography: Observing, Measuring and Interpreting Fracture Structure Topography* (Cambridge University Press, Cambridge, 1999) pp. 139–142
41. S. Horiuchi, A. Nakagawa, Y. Liao, T. Ougizawa, *Macromolecules* **41**, 8063–8071 (2008)
42. M. Stamm, S. Hüttenbach, G. Reiter, T. Spronger, *Europhys. Lett.* **14**, 451–456 (1991)
43. Z. Xu, N. Hadjichristidis, L.J. Fetters, J.W. Mays, *Adv. Polym. Sci.* **120**, 1–50 (1995)
44. S. Horiuchi, *Kobunshi Ronbunshu* **69**, 326–333 (2012)
45. M. Yamazaki, *J. Mol. Catal. A: Chem.* **213**, 81–87 (2004)
46. Y.J. Kim, Y. Taniguchi, K. Murase, Y. Taguchi, H. Sugimura, *App. Surface Sci.* **255**, 3648–3654 (2009)

47. Y. Taguchi, Y.J. Kim, M. Hagioi, Y. Taniguchi, H. Sugimura, *Hyoumen Gijutsu* **65**, 234–239 (2014)
48. S. Horiuchi, H. Hakukawa, Y. Jong Kim, H. Nagata, H. Sugimura, *Polym. J.* **48**, 473–479 (2016).
49. T. Sato, H. Akiyama, S. Horiuchi, T. Miyamae, *Surf. Sci.* **677**, 93–98 (2018)
50. T. Sato, S. Ise, S. Horiuchi, H. Akiyama, T. Miyamae, *Int. J. Adhe. Adhes.* **93**, 102322–102322 (2019)
51. M.F. Sonnenschein, S.P. Webb, P.E. Kastl, D.J. Arriola, B.L. Wendt, D.R. Harrington, *Macromolecules* **37**, 7974–7978 (2004)
52. O.R. Wilson, D.J. Borrelli, A.J.W. Magenau, *ACS Omega* **7**, 28636–28645 (2022)
53. Y. Liu, Y. Shigemoto, T. Hanada, T. Miyamae, K. Kawasaki, S. Horiuchi, *A.C.S. Appl. Mater. Interfaces* **13**, 11497–11506 (2021)
54. H. Leidheiser, P.D. Deck, *Science* **241**, 1176–1181 (1988)
55. J. Cognard, *Inter. J. Adhe. Adhes.* **11**, 114–116 (1991)
56. B.A. Calderón, J. Soule, M.J. Sobkowicz, *J. Appl. Polym. Sci.* **136**, 47553 (2019)
57. Z. Qiu, T. Ikehara, T. Nishi, *Polymer* **44**, 2799–2806 (2003)
58. International Standardization Organization. *ISO11339: 2010: Adhesives-T-peel test for flexible-to-flexible bonded assemblies* (2010)
59. R.F. Egerton, P. Li, M. Malac, *Micron* **35**, 399–409 (2004)
60. N.J. Severs, *Nat. Protoc.* **2**, 547–576 (2007)
61. G.H. Michler, *Electron Microscopy of Polymers* (Springer, Berlin, 2008), pp.165–171
62. Y. Chen, T. Gan, C. Ma, L. Wang, G., *J. Phys. Chem. B*, **120**, 4715–4722 (2016)
63. Q. Liu, X. Sun, H. Li, S. Yan, *Polymer* **54**, 4404–4421 (2013)
64. K. Uchida, K. Mita, Y. Higaki, K. Kojio, A. Takahara, *Polymer J.* **51**, 183–188 (2019)
65. S. Horiuchi, Y. Liu, Y. Shigemoto, T. Hanada, *Mater. Today Commun.* **36**, 106637 (2023)
66. W.P. King, T.W. Kenny, K.E. Goodson, G. Cross, M. Despont, U. Dürig, H. Rothuizen, G.K. Binnig, *P. Vettiger, Appl. Phys. Lett.* **78**, 1300–1302 (2001)
67. F. Tang, P. Bao, A. Roy, Y. Wang, Z. Su, *Polymer* **142**, 155–163 (2018)
68. J. Zähr, S. Oswald, M. Türpe, H.J. Ullrich, U. Füssel, *Vacuum* **86**, 1216–1219 (2012)
69. S. Horiuchi, Y. Liu, T. Hanada, H. Akiyama, *Appl. Surf. Sci.* **599**, 153964 (2022)
70. A. Strålin, T. Hjertberg, *Appl. Surf. Sci.* **74**, 263–275 (1994)
71. A.N. Rider, *J. Adh. Sci. Tech.* **15**, 395–422 (2001)
72. R. Leapman, *EELS Quantitative Analysis*, C.C. Ahn, ed., *Transmission Electron Energy Loss Spectrometry in Materials Science and the EELS ATLAS*, Wiley-VCH (Weinheim, Germany, 2004) pp. 49–96
73. R. Arenal, F. de la Peña, O. Stéphan, M. Walls, M. Tencé, A. Louseau, C. Colliex, *Ultramicroscopy* **109**, 32–38 (2008)
74. J. Scott, P.J. Thomas, M. MacKenzie, S. McFadzean, J. Wilbrink, A.J. Craven, W.A.P. Nicholson, *Ultramicroscopy* **108**, 1586–1594 (2008)
75. J. Bobynko, I. Maclaren, A.J. Craven, *Ultramicroscopy* **149**, 9–20 (2015)
76. R. Brydson, H. Sauer, W. Engel, In *Transmission Electron Energy Loss Spectrometry in Materials Science and the EELS ATLAS*, C.C. Ahn, ed., (Wiley-VCH, Weinheim, Germany, 2004) pp 223–270
77. R.U. Din, K. Piotrowska, V.C. Gudla, M.S. Jellesen, R. Ambat, *Appl. Surf. Sci.* **355**, 820–831 (2015)
78. S. Horiuchi, N. Terasaki, M. Itabashi, *Manuf., Rev.* **7**, 11 (2020)
79. K. Kimoto, K. Ishizuka, T. Mizoguchi, I. Tanaka, Y. Matsui, *J. Electron Microsc.* **52**, 299–303 (2003)
80. K. Wapner, M. Stratmann, G. Grundmeier, *Inter. J. Adhe. Adhes.* **28**, 59–70 (2007)
81. A. Kurian, S. Prasad, A. Dhinojwala, *Langmuir* **26**, 17804–17807 (2018)
82. D. Wang, T.P. Russell, T. Nishi, K. Nakajima, *ACS Macro Lett.* **2**, 757–760 (2013)
83. Y. Liao, M.J. Peng, F.Z. Liu, X.L. Xie, *Chinese. J. Polym. Sci.* **31**, 870–878 (2013)
84. K. Akaike, Y. Shimoi, S. Horiuchi, *Langmuir* **39**, 10625–10637 (2023)

85. L. Lyu, Y. Ohnuma, Y. Shigemoto, T. Hanada, T. Fukada, H. Akiyama, N. Terasaki, S. Horiuchi, *Langmuir* **36**, 14046–14057 (2020)
86. R.J. Good, In *Contact Angle, Wettability and Adhesion*, K.L. Mittal, ed. Utrecht, Vol. 3 (1993)
87. J. Washiyama, E.J. Kramer, C.-Y. Hui, *Macromolecules* **26**, 2928–2934 (1993)
88. C. Creton, H.R. Brown, V.R. Deline, *Macromolecules* **27**, 1774–1780 (1994)
89. <https://taiseiplas.jp/nmt/> (accessed 2023–01–28)
90. S. Horiuchi, T. Hanada, T. Miyamae, T. Ymanaka, K. Osumi, N. Ando, M. Naritomi, *J. Adhesion Soc. Japn.* **48**, 322–330 (2012)
91. Composite material of aluminum alloy and resin and production method therefore. Inventors: M. Naritomi, N. Ando, M. Takahashi and M. Shiraishi, EP1459882A1. 2004–09–22
92. International Standardization Organization. *ISO19095:2015: Plastics-Evaluation of the adhesion interface performance in plastic-metal assemblies* (2015)
93. S. Horiuchi, Y. Liu, Y. Shigemoto, T. Hanada, K. Shimamoto, *Inter. J. Adh. Adhes.*, **117**, Part B, 103003 (2022)
94. International Standardization Organization. *ISO 13586:2018: Plastics—Determination of fracture toughness (G_{IC} and K_{IC})—Linear elastic fracture mechanics (LEFM) approach* (2018)
95. S.-S. Yao, F.-L. Jin, K.Y. Rhee, D. Hui, S.-J. Park, *Compos. Part B Eng.* **142**, 241–250 (2018)
96. K. Stoeffler, S. Andjelic, N. Legros, J. Roberge, S.B. Schougaard, *Compos. Sci. Technol.* **84**, 65–71 (2013)
97. B.A. Alshammari, M.S. Alsuhybani, A.M. Almushaikeh, B.M. Alotaibi, A.M. Alenad, N.B. Alqahtani, A.G. Alharbi, *Polymers* **13**, 2474 (2021). <https://doi.org/10.3390/polym13152474>
98. T. Ishikawa, K. Amaoka, Y. Masubuchi, T. Yamamoto, A. Yamanaka, M. Arai, J. Takahashi, *Compos. Sci. Technol.* **155**, 221–246 (2018)
99. M.D. Banea, L.F.M. Da Silva, *Proc. Inst. Mech. Eng.*, L. **223**, 1–18 (2009)
100. M.D. Banea, M. Rosioara, R.J.C. Carbas, L.F.M. Da Silva, *Compos. Part B: Eng.* **151**, 71–77 (2018)
101. O. Haga, H. Koyama, K. Kawada, *Adv. Compos. Mater.* **5**, 139–149 (1996)
102. P. Molitor, V. Barron, T. Young, *Int. J. Adhes. Adhes.* **21**, 129–136 (2001)
103. E.H. Andrews, A.J. Kinloch, *Proc. R. Soc. London. A. Math. Phys. Sci.* **332**, 401–414 (1973)
104. E.H. Andrews, A.J. Kinloch, *Proc. R. Soc. London. A. Math. Phys. Sci.* **332**, 385–399 (1973)
105. B.R.K. Blackman, In *Testing Adhesive Joints*, L.F.M. Da Silva, D.A. Dillard, etc., eds., Wiley-VCH, Weinheim Germany, **12**, p 55–62 (2012)
106. B.R.K. Blackman, *Quasi-Static Fracture Tests. Testing Adhesive Joints*. Eds. by L.F.M. Da Silva, D.A. Dillard, B.R.K Blackman, R.D. Adams, (Wiley-VCH, Weinheim Germany, 2012) pp 169–172
107. F. Xiao, C.Y. Hui, E.J. Kramer, *J. Mater. Sci.* **28**, 5620–5629 (1993)
108. International Standardization Organization. *ISO 25217:2009: Adhesives-Determination of the mode I adhesive fracture energy of structural adhesive joints using double cantilever beam and tapered double cantilever beam specimens* (2009)
109. N. Terasaki, Y. Fujio, S. Horiuchi, H. Akiyama, *Int. J. Adh. Adhes.* **93**, 102328 (2019)
110. V. Tvergaard, J.W. Hutchinson, *J. Mech. Phys. Solids* **40**, 1377–1397 (1992)
111. C.M. Johnson, E. Tyrode, S. Baldelli, M.W. Rutland, C. Leygraf, *J. Phys. Chem. B* **109**, 321–328 (2005)
112. P. Supaphol, C. Mit-uppatham, M. Nithianakul, *Macromol. Mater. Eng.* **290**, 933–942 (2005)
113. K. Sensui, T. Tarui, T. Miyamae, C. Sato, *Chem. Commun.* **55**, 14833–14836 (2019)

Open Access This chapter is licensed under the terms of the Creative Commons Attribution 4.0 International License (<http://creativecommons.org/licenses/by/4.0/>), which permits use, sharing, adaptation, distribution and reproduction in any medium or format, as long as you give appropriate credit to the original author(s) and the source, provide a link to the Creative Commons license and indicate if changes were made.

The images or other third party material in this chapter are included in the chapter's Creative Commons license, unless indicated otherwise in a credit line to the material. If material is not included in the chapter's Creative Commons license and your intended use is not permitted by statutory regulation or exceeds the permitted use, you will need to obtain permission directly from the copyright holder.



Direct Visualization of Mechanical Behavior During Adhesive Bonding Failure Using Mechanoluminescence (ML)



Nao Terasaki

Abstract In this chapter, we introduce recent progress in direct visualization of mechanical behavior in the failure process of adhesive bonding by mechanoluminescence (ML). Firstly, basic mechanoluminescence technologies are introduced in terms of materials, sensors, sensing technologies in Sects. 1 and 2. Then, for considering effective application of ML sensing that takes advantage of technological features, (Sect. 3) structural health monitoring (SHM)/Conditioning based monitoring (CBM), and (Sect. 4) innovation in design and prediction are discussed from the viewpoint of visualizing mechanical behavior, deterioration, and failure process as killer application of ML sensing. Furthermore, visualizing the mechanical behavior of adhesive joints, fracture initiation points, and fracture processes will be introduced based on time-series information of mechanoluminescence (ML) images, using internationally standardized adhesion strength tests.

Keywords Mechanoluminescence · Visualization · Mechanical behavior · Adhesion · Bonding · Lightweight material · Failure process · Crack propagation

1 Introduction of Mechanoluminescence—Materials, Sensor and Sensing Concept

In bonding and joining, it is essential to obtain the necessary force within the required period of time. However, the mechanical behavior cannot be determined based on the “force” information. Therefore, the appropriate information needs to be predicted

Supplementary Information The online version contains supplementary material available at https://doi.org/10.1007/978-981-99-4456-9_4. The videos can be accessed individually by clicking the DOI link in the accompanying figure caption or by scanning this link with the SN More Media App.

N. Terasaki (✉)

Sensing System Research Center (SSRC), National Institute of Advanced Industrial Science and Technology (AIST), 807-1 Shuku-machi, Tosu 841-0052, Saga, Japan
e-mail: nao-terasaki@aist.go.jp

© The Author(s) 2024

S. Horiuchi et al. (eds.), *Interfacial Phenomena in Adhesion and Adhesive Bonding*,
https://doi.org/10.1007/978-981-99-4456-9_4

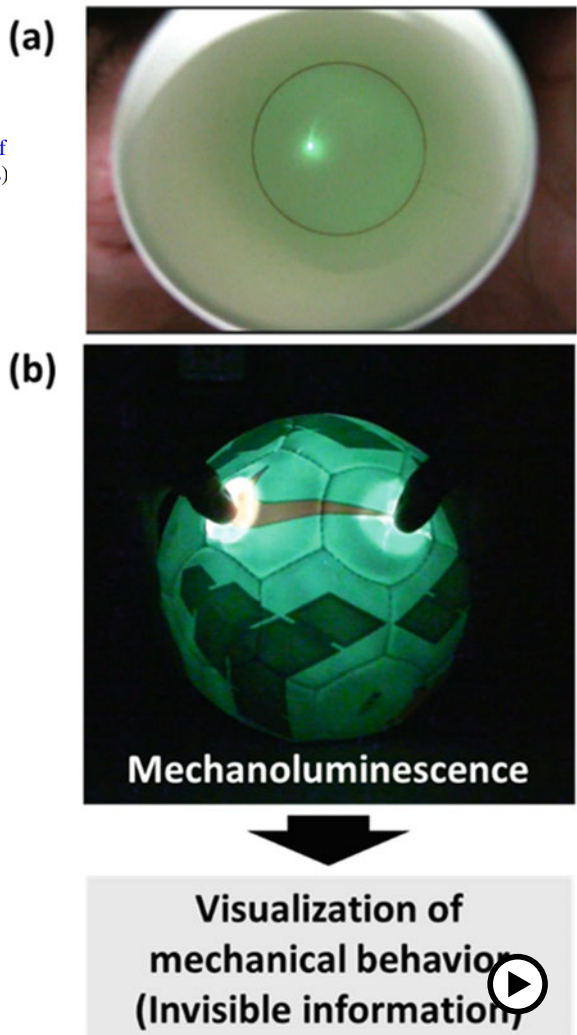
209

based on expert experience and knowledge and reflected in the design, and strength prediction and simulation should be performed based on a database with accumulated experience. However, it is not known whether the previous knowledge, simulations, and designs are accurate. Are there any assumptions in the knowledge? Is there any information that was not considered? These questions still remain.

To address this issue, independently developed mechanoluminescence technology (Fig. 1) [1–9] that can visualize dynamic strain distribution was utilized to visualize the “force information (strain distribution information)” originating from the adhesive bonding area and its interface.

Fig. 1 Introduction of mechanoluminescence, which is a visual sensing method to visualize dynamic strain distribution

- ▶ <https://doi.org/10.1007/000-azf>
- ▶ <https://doi.org/10.1007/000-ays>



Therefore, the basic mechanoluminescence technologies are first introduced in this section considering the materials, sensors, sensing technologies, and killer applications (structural health monitoring, innovation in design, and prediction) that make use of the technological features. Subsequently, the mechanical behavior of adhesive joints, fracture initiation points, and fracture processes is visualized based on time-series information using internationally standardized adhesion strength tests. The purpose of this study is to demonstrate the invisible mechanical behavior of adhesive joints, which is becoming increasingly important in multi-material lightweight design, and to contribute to the confidence in the conventional experience and inspire the development of completely different designs and predictions.

2 Mechanoluminescence (ML) Technology—Visualization of the Dynamic Strain Information

2.1 Mechanoluminescence (ML) Materials

The core of mechanoluminescence (ML) technology is the mechanoluminescent functional ceramic particles, wherein a typical material is $\text{SrAl}_2\text{O}_4:\text{Eu}^{2+}$, a green luminescent material abbreviated as SAOE [1–9] (Fig. 2). Mechanoluminescence (ML) materials have undergone various improvements, refinements, nano-, multi-color, and polymorphisms since their initial discovery in 1999 by our research group [1–20], and in the 2010s, the development of ML material have been investigated worldwide [21–28]. Typically, they are synthesized using a solid-phase synthesis method wherein the carbonates of each required element are weighed, provisionally calcined, and sintered. For ease of use, particles are typically pulverized to a few microns, and the commercially available products are further pulverized to an average size of approximately 1 μm using a more sophisticated pulverization process. These particles are then further pulverized using an atomic force microscope (AFM) to reduce the size of the primary particles to approximately 50 nm [29, 30]. However, because the mechanoluminescence performance is deactivated during the pulverization process, the size of the particles was maintained at approximately 1 μm and used in the sensor. Although nanoparticles are formed when the atomized solution is calcined in a draft, micrometer-sized mechanoluminescence particles were used for sensing owing to their ease of handling and high sensing performance.

For the evaluation of the mechanoluminescence (ML) performance of ML materials, a sensor film was developed on an aluminum foil via screen printing. Subsequently, a 10 mm^2 sensor film was cut and attached to a test specimen (SUS plate) using rapid instant adhesive, and its mechanoluminescence characteristics were measured under tensile load and strain from a sensor usage perspective. Subsequently, the ML luminescence characteristics are then summarized against the strain information (evaluation method).

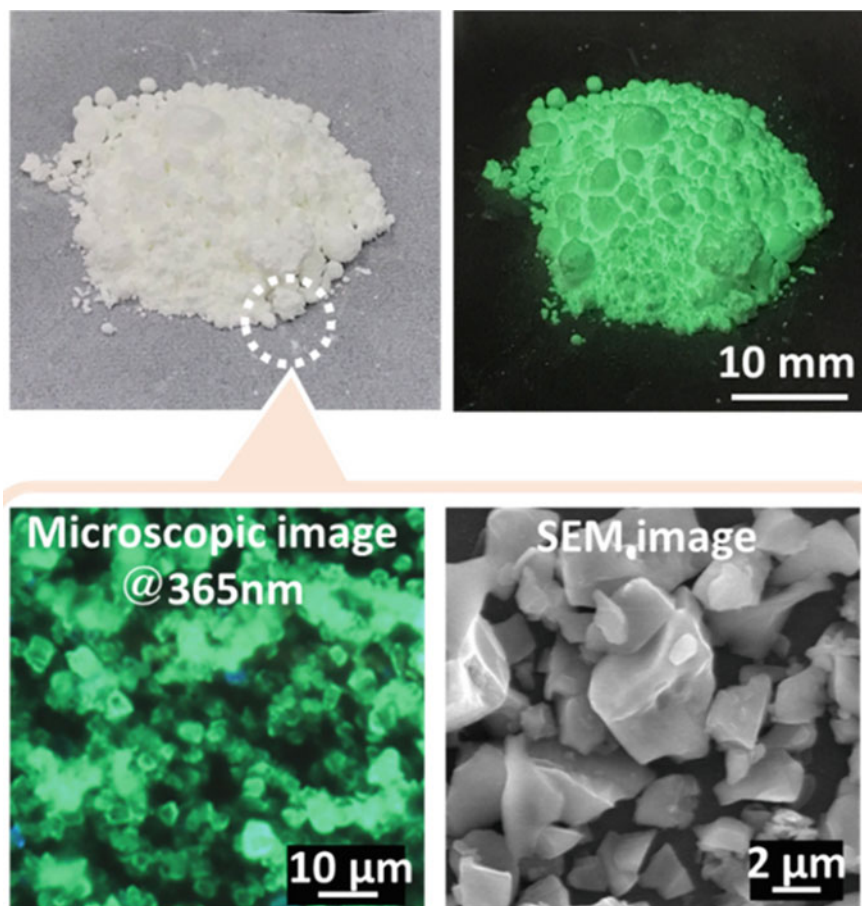


Fig. 2 Mechanoluminescent material. **a** Photo and **b** microscopic image under an irradiation of 365 nm. **c** SEM image

However, during the early stages of mechanoluminescence development in the 2000s and in laboratories that were purely engaged in material development, ML ceramic material cylinders molded using epoxy resin and circular standardized pellets were compressed in a compression testing machine and the resulting luminescence was measured [1–4]. Naturally, there is a strain distribution due to compression; thus, a luminescence pattern (uneven luminescence) is obtained. However, because stress is concentrated at the ground, low-performance or primitive ML materials are often used because they can be evaluated. As shown in Fig. 3, when a mechanoluminescence (ML) material with high luminescence performance is used, the mechanoluminescence and its distribution can even be determined in an environment bright enough to see the upper and lower compression plates.

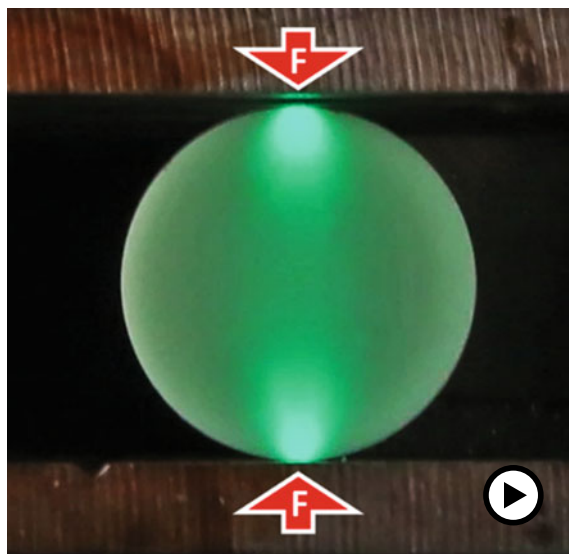


Fig. 3 Mechanoluminescence (ML) evaluation based on compression loading using a cylindrical pellet consisting of ML ceramic material and epoxy resin (► <https://doi.org/10.1007/000-ayt>)

Figure 4 shows a schematic of the mechanoluminescence mechanism that was employed. In previous studies, it has been proven using thermoluminescence (TL) measurements that for long-participant phosphors, the presence of carrier traps is strongly related to the mechanoluminescence performance. In addition, the peaks of the mechanoluminescence (ML) and photoluminescence (PL) spectra are almost similar, indicating that they are mediated by the same emission center. Based on this, the following mechanoluminescence mechanism can be assumed [1–9, 24, 28].

- (1) Excitation using a light at the luminescent center (such as Eu^{2+}).
- (2) Carrier transfer and supplementation of the host material (such as SrAl_2O_4).
- (3) Re-excitation and carrier transfer via mechanical stimulation.
- (4) Emissions via recombination at the emission center.

In the case of long-participant phosphors, it was proposed that carrier release from the trap occurs owing to thermal energy. However, it is currently speculated that they are released owing to the energy produced during mechanical stimulation. In addition, although the majority of the mechanoluminescence (ML) materials have an afterglow, they retain their ML performance even after the afterglow has stabilized, which typically requires a long waiting time or heat treatment. Therefore, it is considered that mechanoluminescence involves traps with a higher energy order than that of the afterglow.

As mentioned above, the emission color of $\text{SrAl}_2\text{O}_4:\text{Eu}^{2+}$ is green due to the $4f^7-4f^65d^1$ transition in Eu^{2+} , which shows a broad emission peak around 520 nm because it is easily affected by the surrounding crystal field. In other words, the

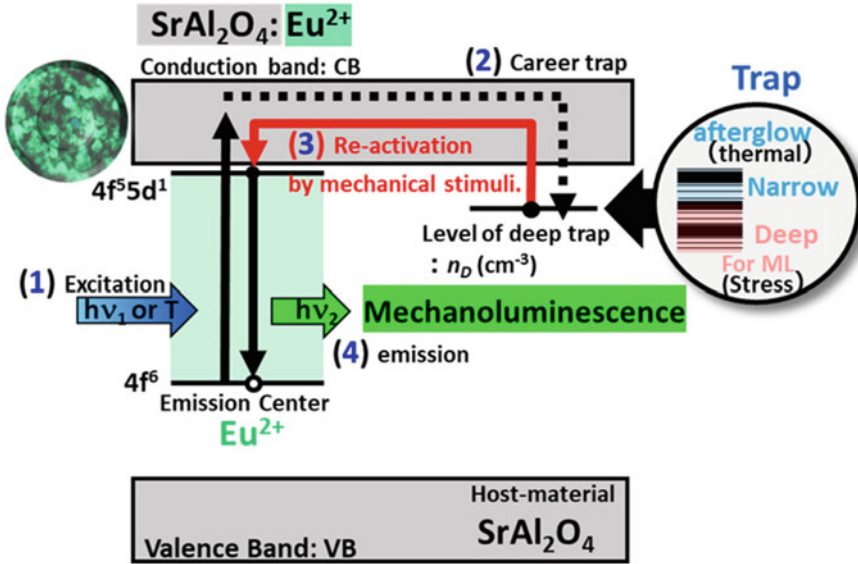


Fig. 4 Mechanism of mechanoluminescence in $\text{SrAl}_2\text{O}_4:\text{Eu}^{2+}$, in the case of as represented ML material

emission color can be set by changing the host material to intentionally vary the interaction between the crystal field and emission center metal ion. For example, in Fig. 5, even if the same luminescent center Eu^{2+} is used, the emission color can still be changed to 437 nm (blue), 489 nm (blue), 489 nm (greenish blue), 524 nm (green), and 540 nm (yellow) by modifying the host material to materials such as $\text{CaGdAl}_3\text{O}_7$, CaYAl_3O_7 , $\text{CaLaAl}_3\text{O}_7$, $\text{Sr}_2\text{MgSi}_2\text{O}_7$, $\text{SrCaMgSi}_2\text{O}_7$, $\text{Ca}_2\text{MgSi}_2\text{O}_7$, or Sr_2SiO_4 [3, 11–17].

The emission color can also be controlled by changing the emission center metal ion from Eu^{2+} to Ce^{3+} (375 nm, UV [12]) or Mn^{2+} (red [21]), etc. In other words, the luminescent color can be controlled based on the selection of the luminescent ion, host material, and their combination.

In addition, a near-infrared mechanoluminescence material that emits infrared and near-infrared light was successfully synthesized by mixing several luminescent center metals using down-conversion (Fig. 6) [20]. Figure 2a shows the photoluminescence (PL) spectra of the prepared $\text{SrAl}_2\text{O}_4:\text{Eu}^{2+}\text{Cr}^{3+}\text{Nd}^{3+}$ powder. Under light irradiation corresponding to the excitation spectra of Eu^{2+} , green emission at 516 nm and NIR emissions at 695, 729, and 881 nm can be observed, originating from the $4f^65d^1$ transition state of the Eu^{2+} ion [1–7], ^2E , and $^4\text{T}_2$ transition states of the Cr^{3+} ion [31–33], and $^4\text{F}_{3/2}$ transition state of the Nd^{3+} ion [34, 35], respectively, as shown in the energy diagrams in Fig. 6a and b. In the excitation spectrum for the NIR emission of Nd^{3+} at 881 nm, three main peaks that are consistent with the peak positions of the excitation spectra of Eu^{2+} and Cr^{3+} are observed at 361, 419, and 560 nm, which are assigned to the absorption bands between the $4f^7$ and $4f^65d$

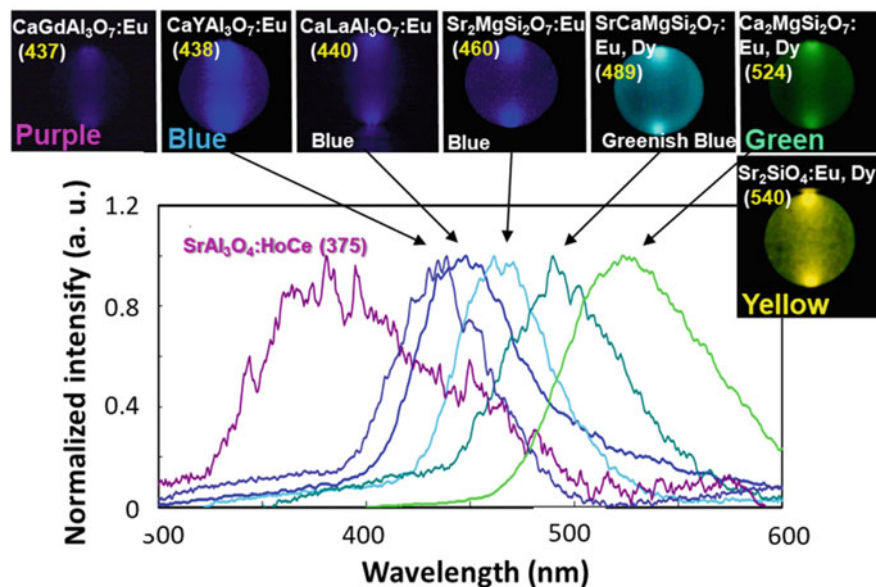


Fig. 5 ML spectra and photo pictures of UV, blue, green, and yellow color emissive ML materials

states of Eu^{2+} (or conduction band of SAOE) and between the $^4\text{A}_2$ and $^4\text{T}_1$ or $^4\text{T}_2$ states of Cr^{3+} , respectively. This indicates that the excited state of Nd^{3+} for the NIR emission at 881 nm can be generated through the excitation of either Eu^{2+} or Cr^{3+} . This can also be explained by the fact that the emission spectrum of Eu^{2+} overlaps with the excitation spectrum of Cr^{3+} and that the Cr^{3+} ion is known to be an effective photosensitizer for the Nd^{3+} emission ion [36, 37]. From these results, it can be concluded that the origin of the NIR emission at 695, 729, and 881 nm, which is within the in vivo optical window, is the excitation of Eu^{2+} and the subsequent down-conversion process along the energy diagram, as described in Fig. 6b. The synthesis of a near-infrared ML material with an emission wavelength of 700–1000 nm as the in vivo optical window [38, 39] makes it possible to use the sample as a light source for measuring the bio-penetrating image of the living body, as shown in Fig. 6c. In this case, a hand was placed on a cylindrical pellet of $\text{SrAl}_2\text{O}_4:\text{Eu}^{2+}\text{Cr}^{3+}\text{Nd}^{3+}$ ceramic powder molded using epoxy resin and measured with a camera based on the NIR afterglow emitted from the pellet light source. As a result, a human tissue transmission image was obtained, wherein the blood vessels that absorbed more light appeared darker.

In addition, human tissue transmission images were successfully obtained using the NIR-ML material (Fig. 6d(a–e)). The experimental set-up and positional correlation are shown in Fig. 6d(b–d). The SAOEuCrNd composite ML pellet was covered with an optical black paper with a 1 cm^2 window to limit the emission area (b), and the window was covered using the thumb to focus imaging (c). Moreover, the dashed line circle and squares show the position of the ML pellet and window, respectively,

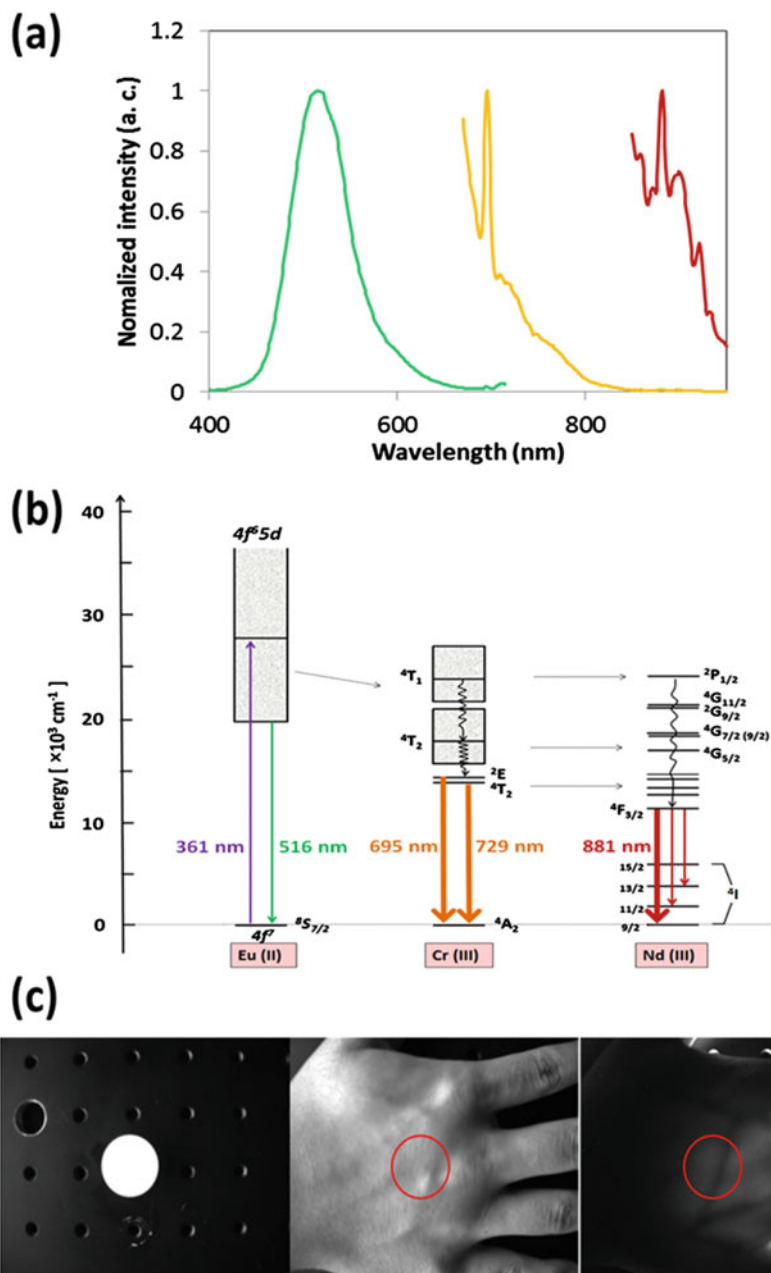


Fig. 6 Near infrared (NIR) mechanoluminescence (ML) material. (a) Normalized PL spectra and (b) energy diagram for $\text{SrAl}_2\text{O}_4:\text{Eu}^{2+}\text{Cr}^{3+}\text{Nd}^{3+}$, λ_{ex} : 361 nm. Human tissue transmission image using the NIR (c) afterglow (AG) and (d) mechanoluminescence (ML) as the light sources (e) ML response curves at ROI1 of (d) d

(d)

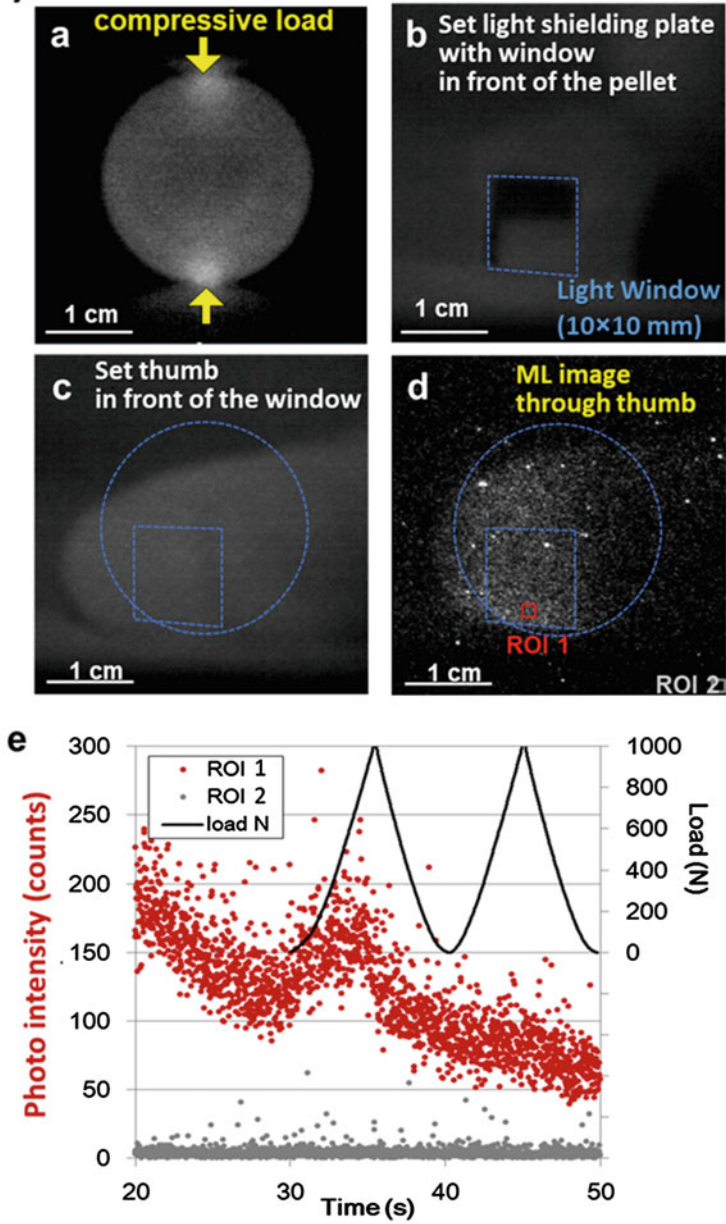


Fig. 6 (continued)

Table 1 Mechanoluminescent materials used worldwide

Company	User				
	USA	China	Korea	Israel	Japan
<i>ZnS series</i>					
Osram Sylvania Inc. ZnS:Cu	✓		✓		
Osram Sylvania Inc. ZnS:Cu,Mn			✓		
LONCO Company Limited ZnS:Cu			✓		
Global Tungsten & Powders Co. ZnS:Cu, ZnS:Al,Cu		✓	✓		
Phosphor Technology Ltd. ZnS:Mn	✓			✓	
<i>SAO series</i>					
Shenzhen Yaodexing Technology Ltd. SAOED		✓			
United Mineral and Chemical Co. (LumiNova G300M)	✓				
Taiko Refractories Co., Ltd., (TAIKO-ML-1)					✓
Sakai Chemical Industry Co., Ltd., SAOE (ML032 etc.)					✓

and the bright and ML images were captured using an NIR light-responsive CCD camera with the same field of view. By applying the compressional load using the conditions shown in Fig. 6d(a) to generate the NIR-ML, a clear biotransmission image with a visible thumb shape was successfully recorded (Fig. 6d(d)). This was probably due to diffraction of light and/or scattering by the tissue thumb in spite of the NIR-ML emitting through the 1 cm² square window [38, 39]. From the response curves shown in Fig. 6d(e), the detected NIR emission signal that was analyzed from ROI 1 is consistent with the load signal (straight line), whereas the load application is independent of the environmental optical conditions based on ROI 2. Therefore, it can be concluded that the increase in the emission signal that accompanied the load originated from NIR-ML from the SAOEuCrNd composite ML pellet and transmission through the thumb.

Recently, mechanoluminescence research has been progressing worldwide, and the number of synthetic developments, commercial products, and users has been increasing. Table 1 shows a list of representative commercial products, which can be used in future experiments on mechanoluminescence.

2.2 Mechanoluminescence (ML) Sensors

To fabricate a sensor for mechanoluminescence (ML) sensing, a paint consisting of an ML ceramic material and a resin (epoxy resin, urethane resin, silicon resin, etc.)

was first prepared, as shown in Fig. 7a. Subsequently, mechanoluminescence paint was either directly applied to the sample using a spray can or using an air spray to form an ML sensor film on the measurement object (Fig. 7b). Alternatively, the ML sheet can be prepared in advance by evenly spraying or screen-printing the paint onto an aluminum foil, employing it as a sensor by attaching it to the point of measurement using instant rapid adhesion (Fig. 7c) [2, 40–45].

The former is effective for measuring complex shapes such as test specimens and 3D-printed objects, joints, and structures. In contrast, the latter is effective for large structures because it is possible to create a uniform sensor with a large area in advance, its characteristics can be evaluated, it is highly reliable, and it is simple to apply to the sheet on-site.

One of the main mechanisms through which mechanoluminescence (ML) sensors can visualize the dynamic strain distribution is based on the emission pattern because each mechanoluminescent material ceramic particle functions as a sensor that emits light in response to the surrounding mechanical behavior. Moreover, the load was applied to the $\text{SrAl}_2\text{O}_4:\text{Eu}^{2+}$ microparticles using an AFM cantilever, the light was measured using a photomultiplier, and when the load was applied to a single ML particle, luminescence was observed (Fig. 8a) [30]. In addition, the analysis of the ML test results of an ML film sensor fabricated by dispersing an extremely low concentration of it in epoxy resin to distinguish it from the single particle showed that the luminescence performance of a single mechanoluminescence microparticle is equivalent to 3.4 nW/cm^2 at a deformation of 0.12 (Fig. 8b) [46]. This is because mechanoluminescence (ML) sensors such as the coated film and sheet type are developed by dispersing and applying ML particles, which then act as sensors that vary their luminescence intensity in response to the surrounding mechanical conditions in a single particle, thereby allowing the dynamic strain distribution to be visualized.

As an evaluation method for the mechanoluminescence (ML) sensor performance of ML materials, a sensor film was developed on aluminum foil via screen printing, and a 10 mm^2 sensor film was cut and attached to a test specimen (SUS plate) using a rapid instant adhesive. Subsequently, its mechanoluminescence characteristics under tensile load was investigated against the strain from a sensor use perspective [2, 3, 47]. For the ML evaluation test, a camera was mounted on the front face of the ML sensors located on the surface of the specimen or object. However, if a specimen exhibits different mechanical behaviors on all four faces, as in the case of a specimen comprising a dissimilar material that is adhesively bonded, the camera is mounted on the front faces of the four faces to measure the mechanoluminescence, as shown in Fig. 9.

Subsequently, the ML luminescence characteristics were compared to the strain information.

Various correlation evaluations were conducted between the mechanoluminescence performance and strain values, strain rate, stress, and principal stress to evaluate the mechanoluminescence characteristics. As a result, a correlation was found between the mechanoluminescence (mcd/m^2) and Mises strain value ($\%$, μst), particularly the proportional relationship that exists with the strain energy, as shown in Fig. 10. Using this relationship, it is possible to determine the strain distribution from

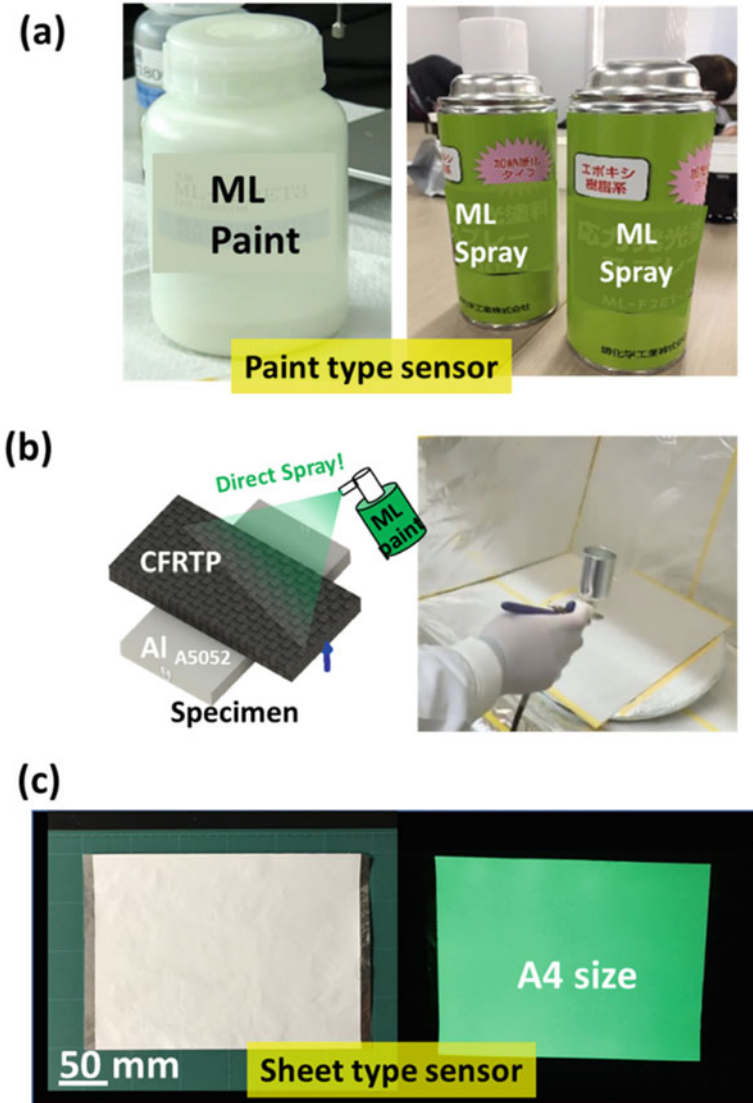


Fig. 7 ML sensors. a ML paint-type sensor. b Directly air spraying ML paint to form ML sensor. c ML sheet-type sensor

the mechanoluminescence emission pattern. Although the ML intensity is proportional to the strain energy, the ML intensity gradually decreases according to load cycles [2, 47], as shown in Fig. 11a. This phenomenon can be explained using the mechanism depicted in Fig. 4, wherein carriers that were supplemented and stored at the trap level in advance gradually decrease with the generation of luminescence due to repeated loading. However, mechanoluminescence can be completely recovered

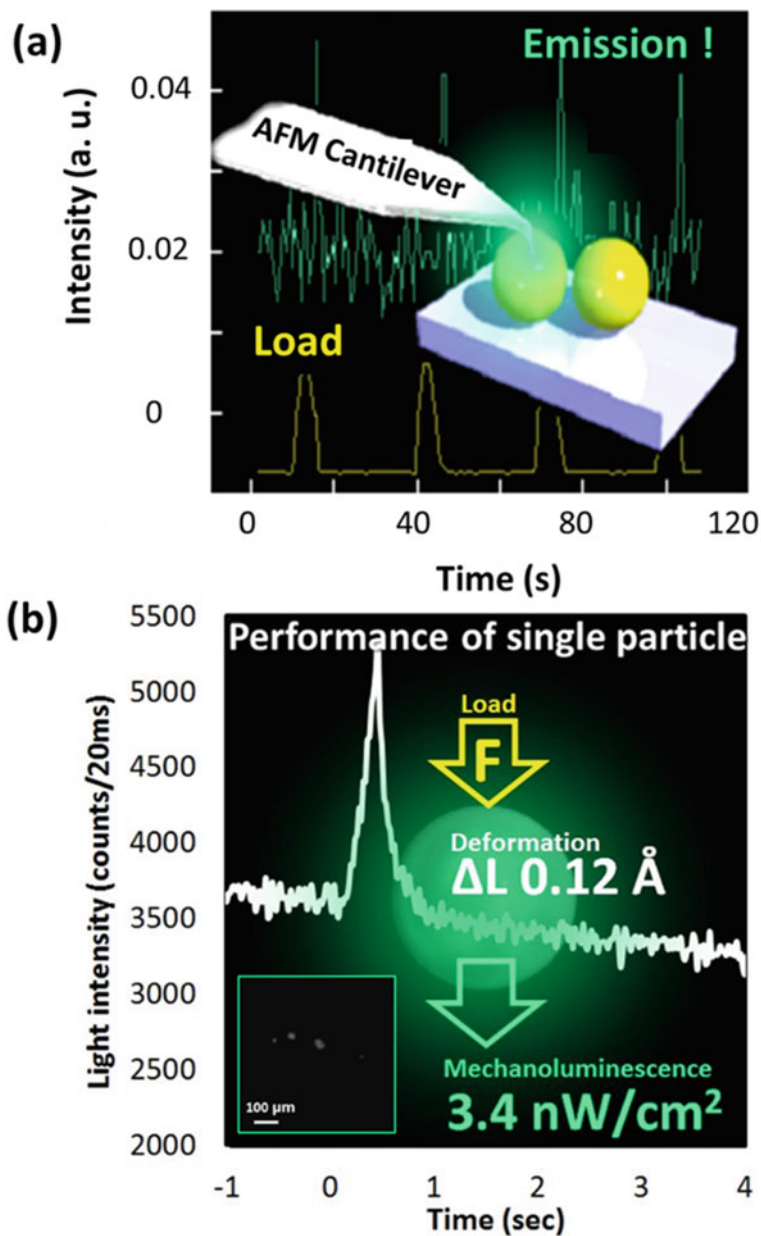


Fig. 8 Evaluation of the performance of single $\text{SrAl}_2\text{O}_4:\text{Eu}^{2+}$ microparticles using the **a** AFM cantilever and photomultiplier and **b** low-concentration ML film under microscopic observation

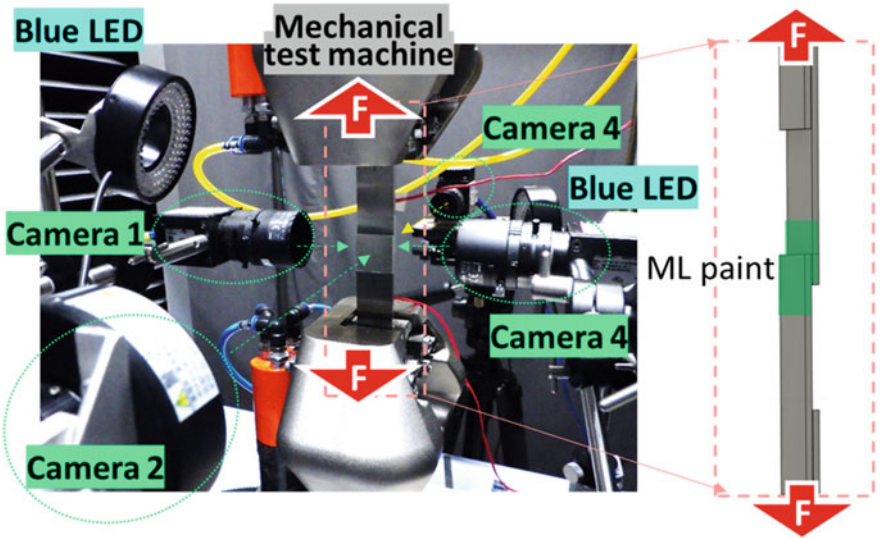


Fig. 9 Example of an experimental set-up for mechanoluminescence using a 4-way camera system

via irradiation using excitation light (for example, 470 nm blue light, 0.5 mW/cm²) even if it is reduced. Therefore, when quantitatively evaluating mechanoluminescence, measurements should be performed after the carrier trap is filled when the sample is irradiated with excitation light for several seconds or 1 min.

Fig. 10 Relationship between the ML luminance and strain energy. Material: SrAl₂O₄:Eu²⁺

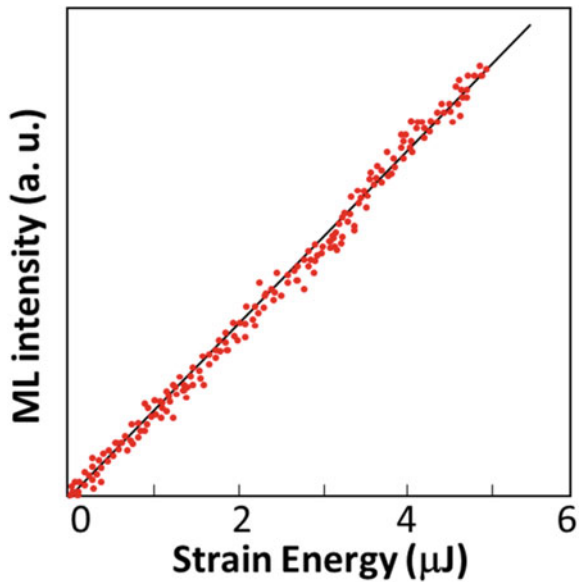
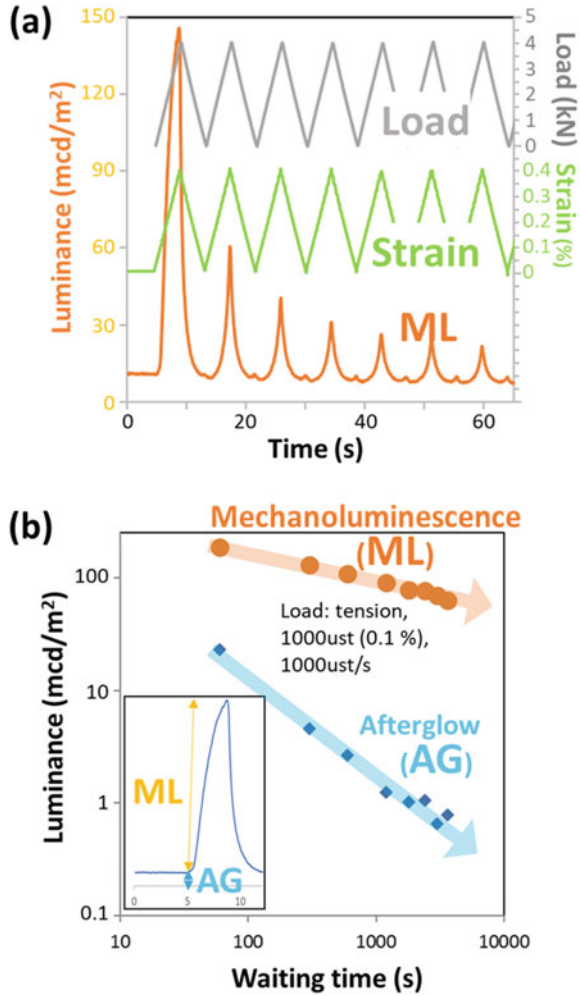


Fig. 11 Basic performance of the $\text{SrAl}_2\text{O}_4:\text{Eu}^{2+}$ ML sensor. **a** ML intensity accompanied by the cyclic load and strain. **b** Relationship between the ML and AG intensities, and waiting time after excitation using the blue LED. Inset illustrates the definition of the ML and AG intensities



The ML sensor shows the afterglow (AG) after excitation as a long-persistent phosphor and mechanoluminescence at the load application, as shown in Fig. 11b. Therefore, a sufficient waiting time after excitation and correct camera conditions are essential for ensuring that the ML/AG ratio (also called ML index) is sufficiently high because the afterglow functions as the base noise and the ML pattern as the measurement signal.

To achieve better quantitative mechanoluminescence testing, a dark environment should be used, photoexcitation should be done prior to testing, and an appropriate waiting time should be selected. As mentioned above, mechanoluminescence (ML) luminance is correlated to the von Mises strain. Thus, the ML pattern is consistent with the simulation results for the von Mises strain distribution (Fig. 12). From

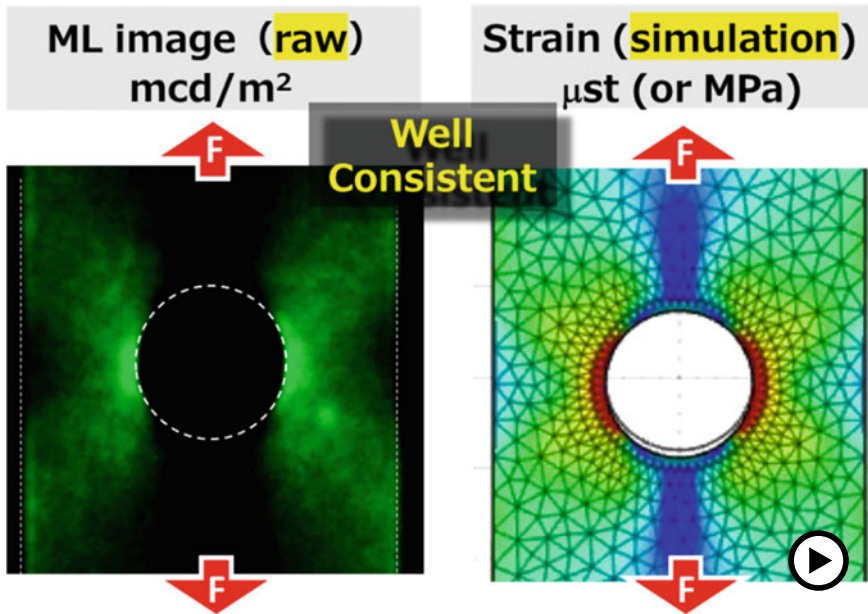


Fig. 12 Comparison of the mechanoluminescence pattern of perforated SUS631 and simulated von Mises strain distribution under a tensile load (► <https://doi.org/10.1007/000-ayv>)

the opposite perspective, the strain distribution can be calculated based on this mechanoluminescence pattern and the correlation between ML luminance and strain.

In general, mechanoluminescence sensors are often used for the quantitative analysis of the strain distribution. However, focusing on the ML pattern two-dimensional information, the sensor can be used as a tool for searching for and tracking the existence of unexpected and invisible stress concentrations, as well as changes in mechanical behavior due to deterioration, crack initiation, and propagation, which are difficult to see. Furthermore, regarding the four-dimensional information, including the time variation of the mechanoluminescence pattern, the sensor can be used as a tool for feature extraction that allows the prediction of the remaining lifetime of materials, structural members such as the joints, and structures by capturing the degradation process and events that occur at that the time of the change in the mechanical behavior of the structure.

In addition, a notable feature of mechanoluminescence-based visualization strategies is their real-time properties. For example, a two-dimensional strain distribution can be obtained using array strain sensors. In addition, as will be shown in a comparison later, technologies that can analyze the strain distribution such as digital image correlation (DIC) have also been widely used in recent years. In contrast, from the perspective of visualization strategies, mechanoluminescence has the advantage of simply converting invisible mechanical information into luminous information by applying it. In other words, it has the advantage of being directly visible without

the need for an analytical device. To make the most of this advantage, efforts for recognizing the degree of damage and danger based on the color change during mechanoluminescence are promoted [3].

As mentioned above, mechanoluminescent materials come in a variety of colors and have different luminescence characteristics in response to strain. Some materials emit light with high sensitivity at low strains, while others emit light at slightly higher strains but show high luminescence brightness. Figure 13 shows the results of mechanoluminescence under compression using cylindrical pellets composed of two types of mechanoluminescent (ML) ceramic powders ($\text{SrAl}_2\text{O}_4:\text{Eu}^{2+}$: green, $\text{CaYAl}_3\text{O}_7:\text{Eu}^{2+}$: blue) that were mixed and molded in epoxy resin and have different strain sensitivity curves. It was confirmed that the color of the mechanoluminescence at the stress concentration point at the ground point changed in conjunction with the increase in strain owing to the application of a compressive load to the pellet (Fig. 13a). By setting the region-of-interest (ROI) at this point (Fig. 13b) and evaluating the color and intensity of the luminescence, blue emission is predominant in the early stages of strain, and green emission is predominant in the 0.15–0.2% strain region, which is a rough indication that the metallic structural material is entering plasticity. This indicates the possibility that the high-strain region that causes structural plastic deformation (danger region) can be visually recognized on-site or using a camera and based on the luminescence color.

Mechanoluminescence sensors emit light in response to external forces that cause strains. For example, in addition to common compression, tension, and torsion, high-speed strain propagation owing to shock, impact, and vibration can also be visualized [2, 5, 7–9]. Moreover, both the mechanoluminescence powder and sensor film emit light in response to ultrasonic irradiation, and the ML intensity changes with the ultrasonic intensity, as shown in Fig. 14. [48, 49]. The ultrasonic wave can penetrate the human body, thus is an expected useful stimulation method for mechanoluminescence (ML) particle to generate emission even in bio-body as a ubiquitous light source [48–51].

As a summary of Sect. 1, I would like to mention the benchmarking result from the viewpoint of the most frequent questions in my past lectures with representative strain-measurement techniques. Figure 15 shows a comparison of the strain gauge, digital image correlation (DIC), and mechanoluminescence.

Strain gauges are commonly used as strain-measurement sensors. The most important feature of strain gauges is their reliability; they can stably measure and monitor strains as small as 0.0001% (one micro strain) or less. The three-axis strain gauges shown in the photograph provide the values necessary for evaluation and design, such as principal stress values and directions, as well as scalar values such as von Mises stress and strain. Strain gauges are mechanoluminescence (ML) measurements. However, because strain gauges are point sensors, they do not respond if there is even a slight deviation from the point of strain generation or concentration. Therefore, the strain gauge has an advantage when the point to be monitored is clear; however, it is not always easy to determine where to monitor. In addition, because wiring is required for strain gauges, it is not suitable for sites that are unsuitable for electrical systems, or sites where noise is likely to occur or decrease.

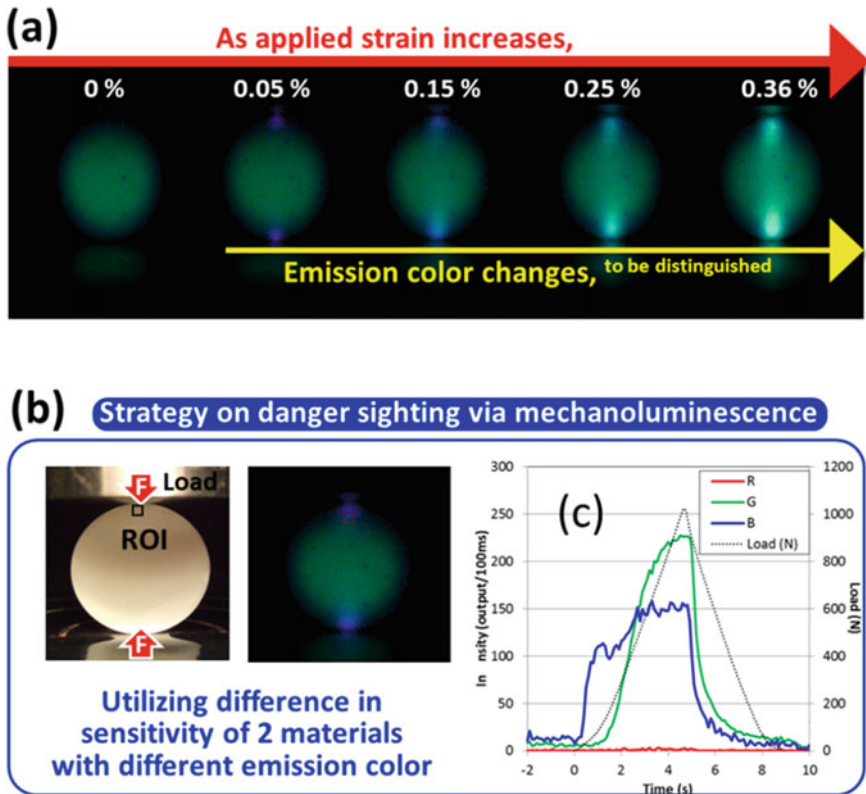
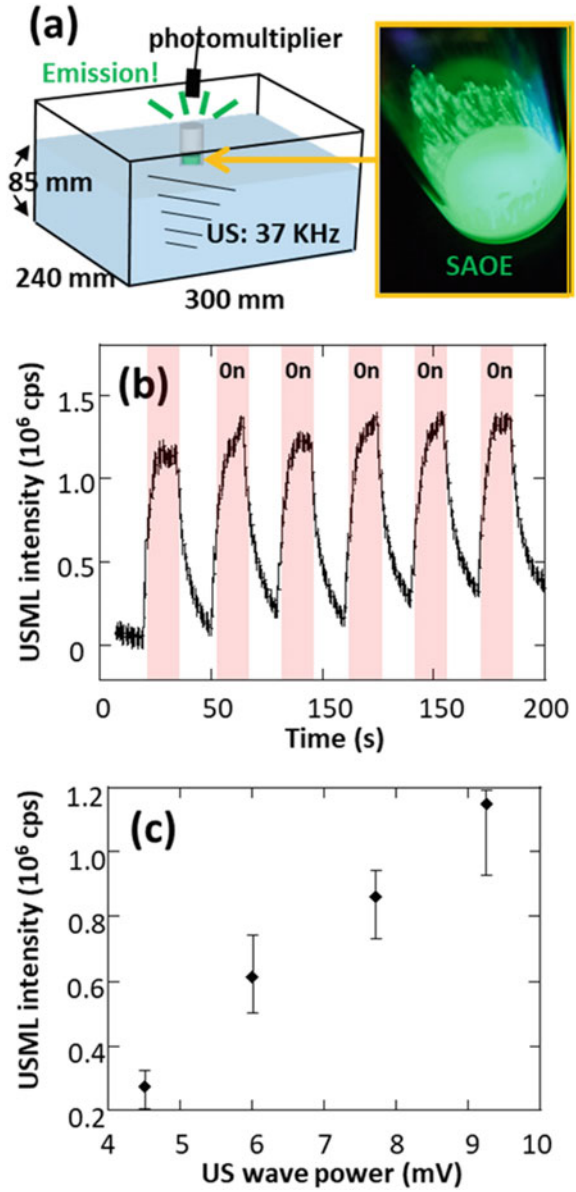


Fig. 13 Danger sighting based on the changing color of the mechanoluminescence. **a** Mechanoluminescence time course for the load applied on the $\text{SrAl}_2\text{O}_4:\text{Eu}^{2+}$ -embedded ML pellet (green ML material) and $\text{CaYAl}_3\text{O}_7:\text{Eu}^{2+}$ (blue ML material). **b** ROI area in the photo, and **c** blue and green light intensity using RGB CCD device

Digital image correlation (DIC) is a method of obtaining the strain distribution by forming a dot pattern on a test specimen in advance and using a camera to capture and analyze how the dot pattern moves in a certain region, called a subset. Mechanoluminescence is stronger in high-speed phenomena than in slow deformation because it produces stronger ML luminescence owing to the high-strain energy. Conversely, DIC has an advantage, even in slow deformation phenomena, where the dot pattern can be clearly photographed. In addition, since the information is digitized, DIC has an advantage in that it can classify and display strain values and directions in each coordinate direction, including the principal stresses. However, it is difficult to capture high-speed phenomena in which the dot pattern becomes blurred, or crack propagation in which the dot pattern disappears.

Mechanoluminescence requires a dark environment for measurements and other conditions for quantification. In contrast, mechanoluminescence is particularly good for phenomena that are difficult to measure with other techniques, such as crack tips

Fig. 14 Ultrasonic wave-induced mechanoluminescence (USML). **a** Experimental set-up. **b** Luminance response accompanied by cyclic ultrasonic wave irradiation. **c** Relationship between intensity of mechanoluminescence and ultrasonic wave (37 kHz)



where extreme stress concentration occurs, high speed with high-strain energy, and vibrational phenomena. It also has features such as real-time performance, multiscale performance by simply applying paint, and remote monitoring using luminescence.

Therefore, a combination of the strengths of the abovementioned technologies is currently being used in appropriate places and at the right time to solve problems.


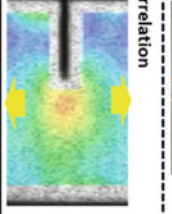
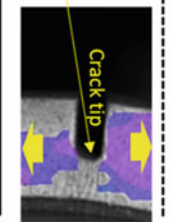
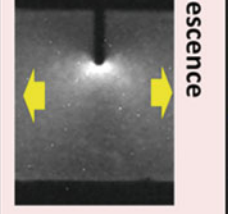
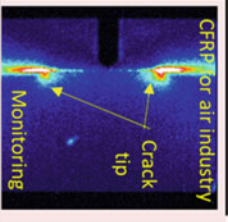
name	Element	Sensitivity	Distribution	Failure monitoring
Strain gauge 	Reliable <input checked="" type="radio"/> 0.0001% (benchmark)	× Point measurement	△ Eventually in the case, crack pass very	
DIC Digital Image Correlation 	<input type="radio"/> 0.01%	<input checked="" type="radio"/> 2D visualization um-Km	<input type="radio"/> Enable analysis - at crack tip - Noto real time	 Crack tip
Mechanoluminescence 	<input type="radio"/> 0.01%	<input checked="" type="radio"/> 2D visualization um-Km Detection of failure origin	<input checked="" type="radio"/> Emphasize with luminescence - Real time - Inner information	 CFRP for air industry Crack tip Monitoring

Fig. 15 Benchmarking of the strain-measurement sensing, strain gauge, DIC, and mechanoluminescence

3 Killer Application of Mechanoluminescence 1: Detection of Crack and Defects in Structural Health Monitoring (SHM)

In the previous section, the materials, sensors, and mechanoluminescence (ML) technology used to visualize dynamic strain as light-emission patterns were described. In this chapter, the application of ML technology to structural health monitoring (SHM) as a killer application of mechanoluminescence is discussed.

3.1 Mechanoluminescence (ML) Detection of the Origin to Deduce the Integrity

Mechanoluminescence is a powerful technique for detecting excessive stress concentrations, fatigue, plastic deformation, crack initiation, crack propagation, and fracture, which are factors that reduce the integrity of a structure (Fig. 16).

In general, the design of a structure is based on proper stress/strain dispersion and rigidity to withstand external forces, and mechanoluminescence sensing can only provide weak and uniform light-emission patterns. In contrast, higher intense stress/strain concentrations occur in a narrower area during the stage of damage factor generation, which means that the structural integrity is degraded. In addition, the crack initiation, propagation, and failure processes create a localized high-strain energy that exceeds the material strength and is required for failure propagation at the last stage of a structure and structural material. Normally, although stress/strain concentration or crack tips are invisible or only visible with careful observation, mechanoluminescence (ML) technology, which emits a high luminous intensity proportional to the strain energy, is more advantageous for detecting them clearly as the luminescence becomes stronger and more specific in pattern (Fig. 16). Therefore, structural health monitoring is considered an important application in mechanoluminescence technology [2, 3, 42–45].

In addition, the ability to visualize information on the predictive signs of failure and mechanical behavior associated with failure can be used to make repair decisions. By chronologically visualizing the fracture process with the mechanical behavior, it is possible to understand the stress concentration behavior and fracture origin, that is, why the structure broke, which cannot be determined based on prediction or experience, leading to the design of structures with high resistance to damage. Figure 17 shows the ML monitoring of the fracture behavior under seismic-stimulated wave inputs for seismic-resistant reinforced concrete members used as building materials [2, 4].

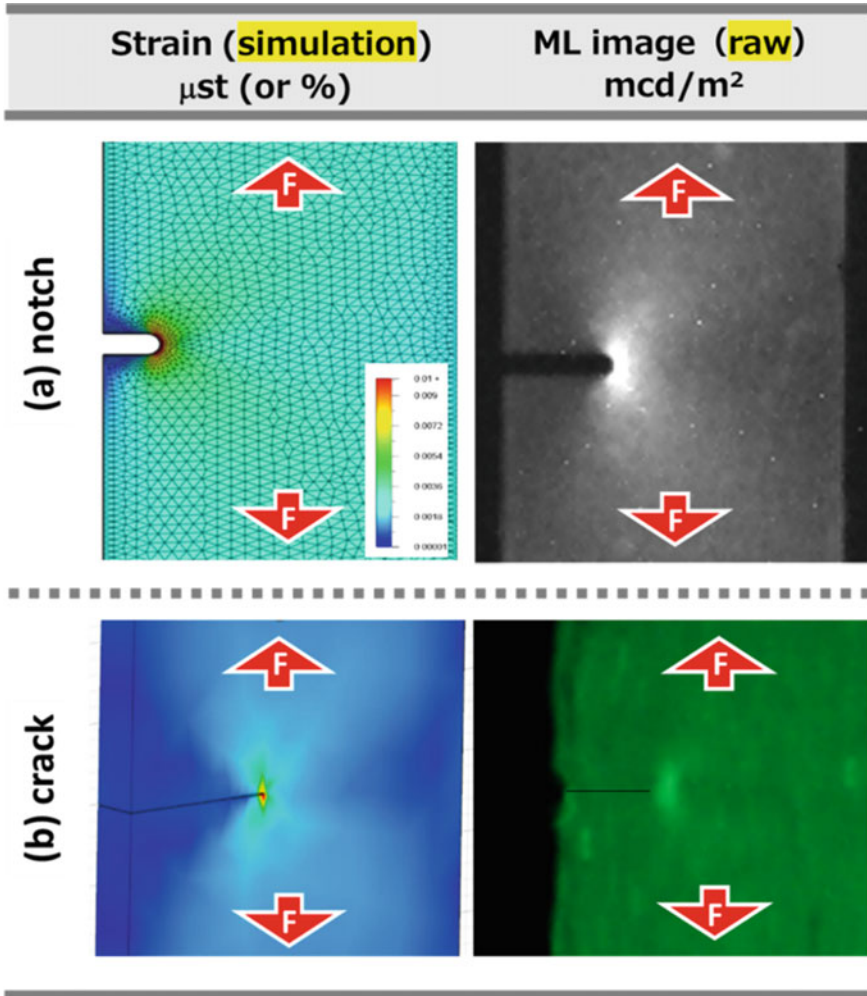


Fig. 16 ML detection of crack initiation and propagation under dynamic loading and fatigue

After seismic vibration induction, mechanoluminescence analysis clearly shows that shear forces are generated between the structure and girders, and cracks are propagated in the 45° direction of vibration (Fig. 17) and in the more direct -45° direction, as measured based on the high-speed vibration of seismic waves.

To accurately track the position of tips using mechanoluminescence, it is recommended to perform contour map processing on raw ML images using image processing software. Figure 18 shows the ML images of crack propagation during a double cantilever beam (DCB) test to determine the fracture toughness of an adhesively bonded structural member. In the raw image (black-and-white image), the location of the crack can be roughly identified based on the intense ML emission

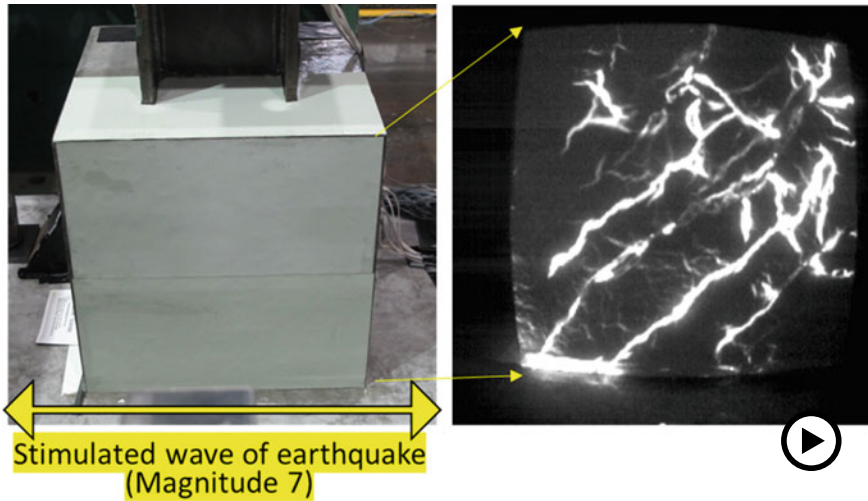


Fig. 17 ML monitoring of the fracture behavior based on seismic-stimulated wave inputs for seismic-resistant reinforced concrete members used as building material (► <https://doi.org/10.1007/000-ayw>)

area near the crack tip; however, it is difficult how to distinguish the highest ML point from the crack tip, as shown in Fig. 18a. In contrast, the highest ML luminance points are highlighted in red in the contour image, making it easy to locate the crack tip position (Fig. 18b). Therefore, an ML contour map is used in many cases to observe the behavior of cracks and fractures [47].

Crack tip sharpening using mechanoluminescence is useful for both static and dynamic tests such as fatigue tests. Figure 19 shows the mechanoluminescence (ML) monitoring of crack initiation and propagation in metal fatigue under cyclic loading [42]. For the fatigue crack growth detection experiment, a test piece (SUS430, $225 \times 25 \times 3$ mm) was notched in advance at the center position of the side edge, and a fatigue crack was prepared from the notch and propagated by applying a cyclic tensional load using a mechanical testing machine (MTS Systems Co.; Fig. 19a). ML paint was directly applied to cover the area including the notch and pre-prepared fatigue crack with a length of 8.4 mm on the test piece, which was used as an ML paint film sensor (20×10 mm, Fig. 19b). Pre-prepared fatigue cracks were then observed to record the growth length on the backside using microscopy (Fig. 19c) and mechanoluminescence (Fig. 19d).

It is noteworthy that before the ML test piece ruptured, fatigue crack growth and tensile cycles were observed. The rupture was confirmed via visual inspection and through the dramatic change in the displacement and load value (Fig. 19e). The stress intensity factor (K) is used in fracture mechanics to predict the stress intensity near the tip of a crack caused by a remote load or residual stresses [52], and it was

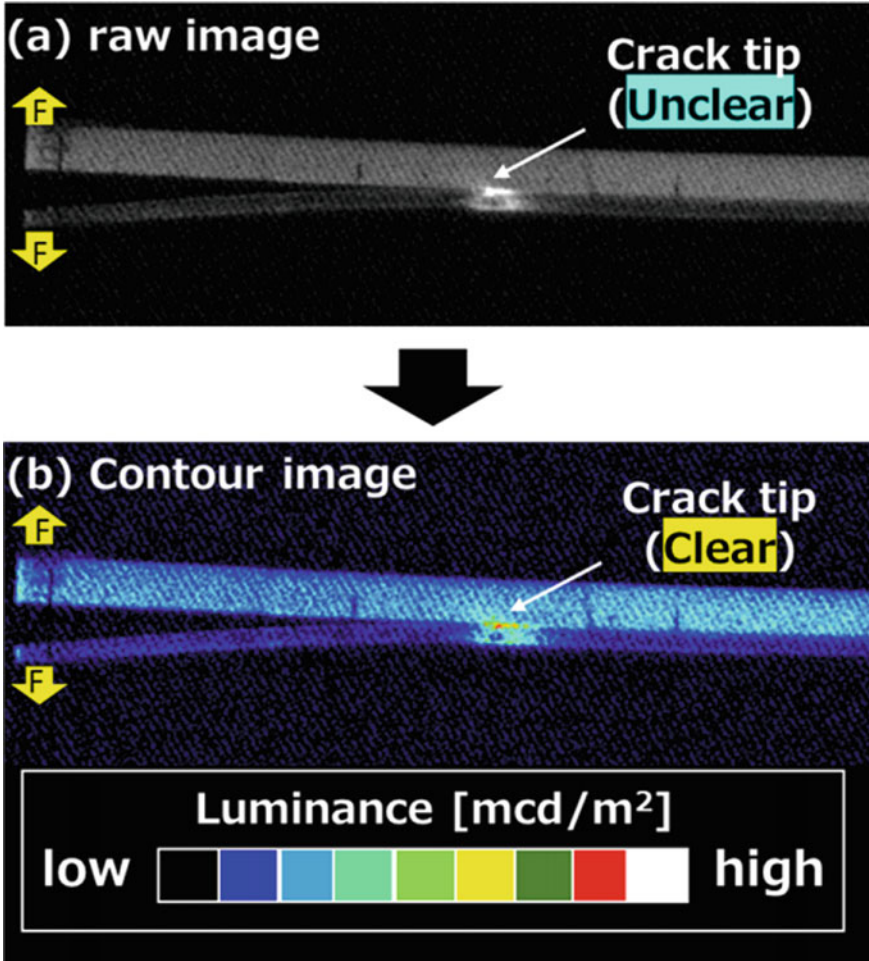


Fig. 18 Method of crack tip sharpening using a mechanoluminescence contour image. Comparison of the **a** raw image and **b** contour image of mechanoluminescence

calculated based on Eq. (1).

$$K = F(\xi)\sigma\sqrt{\pi\alpha} \tag{1}$$

$$F(\xi) = 1.12 - 0.231\xi + 10.55\xi^2 - 21.72\xi^3 + 30.39\xi^4$$

$$\xi = \alpha/W$$

where σ is the uniform remote stress, α is the crack length, W is the width of the specimen, and $F(\xi)$ is a dimensionless shape factor [53–55].

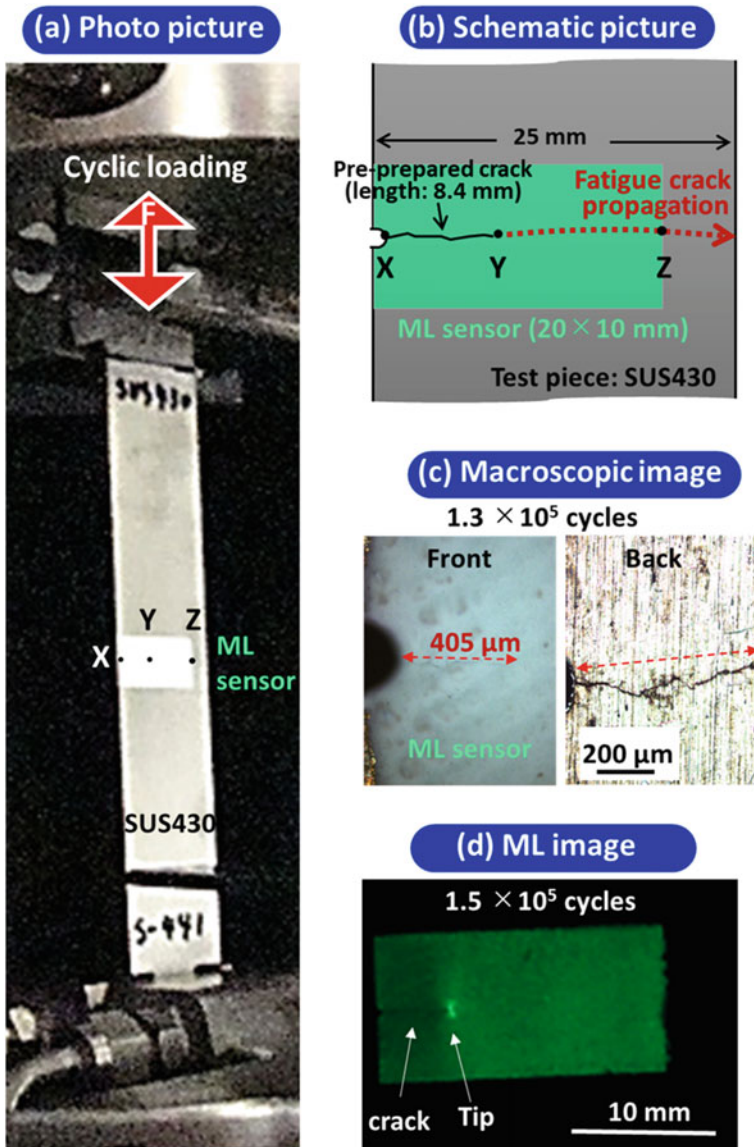


Fig. 19 Mechanoluminescence detection of crack initiation and propagation in a metal fatigue under cyclic loading. **a** Photograph. **b** Schematic. **c** Microscopic image of specimen. **d** ML image during cyclic loading. **e** ML image monitoring of fatigue crack propagation during cyclic loading. Here, the displacement and load values were monitored using a mechanical machine, and the stress intensity factor (K) was calculated. **f** Relationship between the ML intensity and stress intensity factor (K)

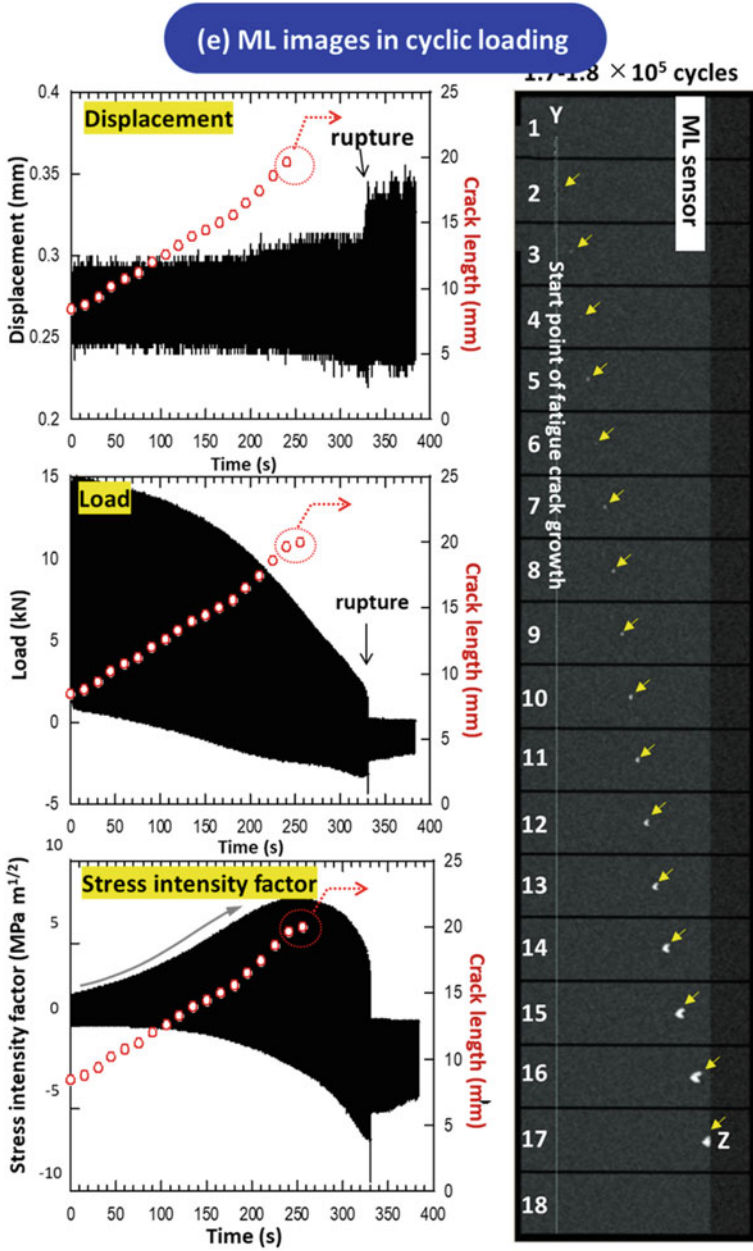


Fig. 19 (continued)

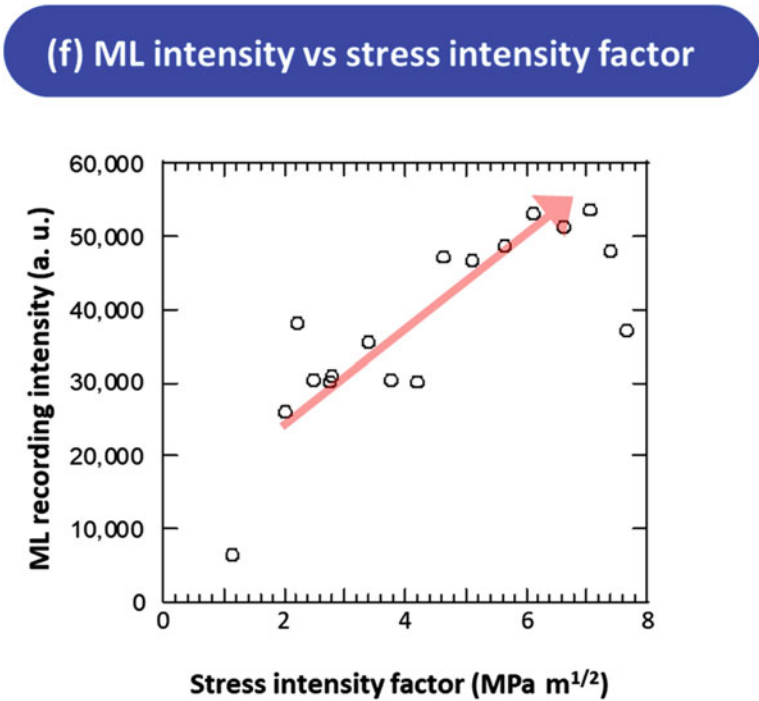


Fig. 19 (continued)

The consecutive real-time ML images taken by the CCD camera in Fig. 19e show that fatigue crack growth from point Y to Z was successfully monitored using the bright ML point from its origin at the crack tip where there is stress concentration. In addition, the ML point gradually became brighter and larger, and the cyclic loading and fatigue crack growth increased as the stress intensity factor gradually increased. Figure 19f shows the relationship between the ML intensity and stress intensity factor (K), which indicates that the ML intensity at the crack tip has the potential to be a rough index of the stress intensity factor (K) for evaluating and predicting crack growth.

Metallic materials are often used in infrastructure. These metallic materials undergo elastic deformation, stress concentration, fatigue, plastic deformation, yielding, and rupture. Therefore, the early detection of the stress concentration, which is a predictive sign of degradation, is important for the diagnosis of plastic deformation, which directly leads to yielding and rupture. In response to this, by applying mechanoluminescence (ML) paint to the metal specimens, the occurrence of the plastic phenomenon in the rudder zone during tensile loading was successfully visualized (Fig. 20a; photo shows aluminum A6061). A specific wrinkles-like ML pattern is also observed in the steel materials in the responding area where the strain value reaches plastic deformation in the strain gauges. It is expected that although the

origin of the pattern is under further investigation, the use of such a specific emission pattern will aid in the identification of the plastic deformation region [2].

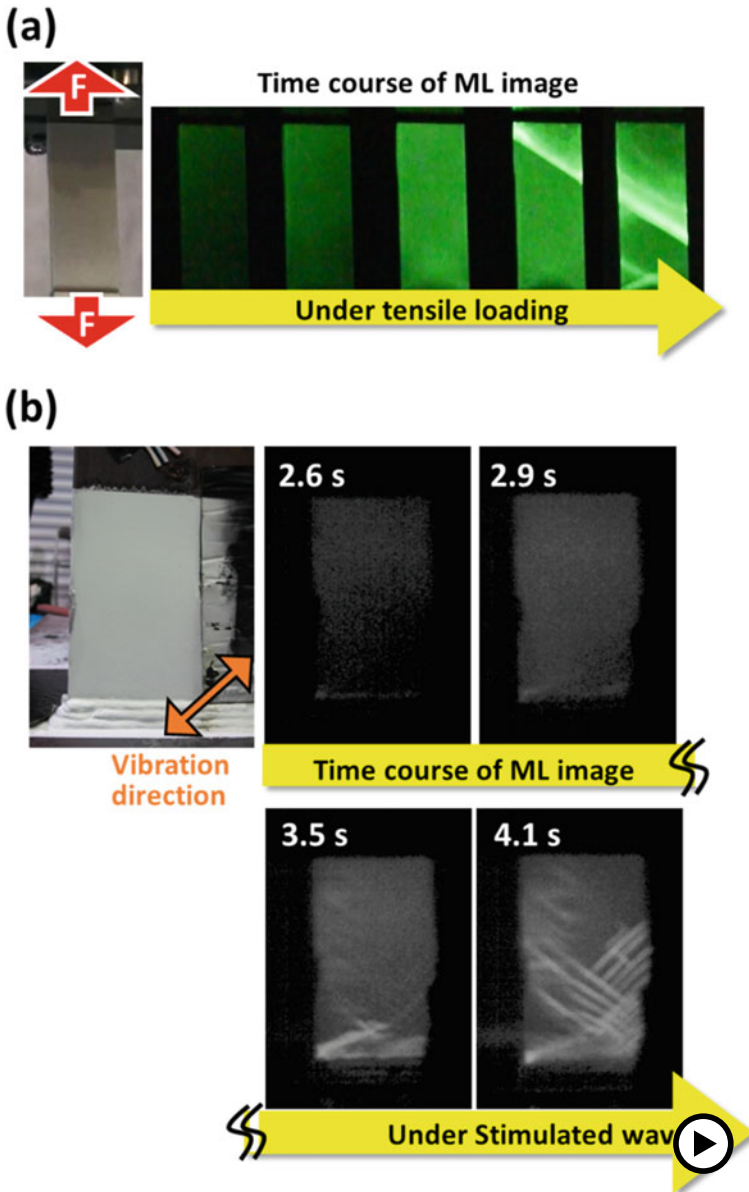


Fig. 20 Detection of mechanoluminescence in the Lueders zone and plastic deformation regions (► <https://doi.org/10.1007/000-ayx>)

3.2 *Mechanoluminescence (ML) Sensing in Real Infrastructures*

Here, the adaptation of mechanoluminescence to detect deterioration in structures and materials is introduced, beginning with the existing social implementation examples for various infrastructures.

Buildings and bridges are important social infrastructures that use steel and concrete as structural materials. Steel is used to enhance the bearing capacity of structures; however, the alkali-silica reaction (a type of moisture degradation known as an ASR reaction) in concrete causes crack development and water penetration, which corrodes the steel and reduces its bearing capacity. Additionally, diagnosis is difficult because steel is contained inside the concrete. Thus, the diagnostic standard for cracks is 0.2 mm wide, which requires high precision to ensure perfect inspection. Figure 21 shows the results of the structural health monitoring (SHM) of social infrastructure (bridges in use) using ML sensors [2, 42, 43]. For this experiment, a heavily trafficked bridge that was built more than 50 years ago was selected (Fig. 21a). The center of the piers (length: 13 m) is the most vulnerable to deflection and cracking because of the dynamic three-point bending load acting on it when a car passes by. An ML sheet-type sensor (70 × 40 cm) was attached using a rapid instant adhesive to the sidewall of the floor plate at this location, and visual and camera recordings were taken. According to the photograph of the responding area where the ML sensors are attached, as shown in Fig. 21b, a slight crack is present from the upper floor plate downward. Although it was noted above that all cracks with an opening equal to or wider than 0.2 mm are subject to marking, the width of the cracks is not constant, and there are many areas where the cracks are perfectly closed. This is considered the reason why some cracks were not noticeable. In contrast, when an ML sheet was attached to take measurements, clear ML luminescence with a varied intensity depending on the size (load) and speed of the vehicle was uniformly obtained along the crack (Fig. 21c). Comparing this ML behavior with the crack mouth opening displacement (CMOD) behavior, the ML intensity is highest when the crack opens. Moreover, this mechanoluminescence is caused by the opening of the crack, which distorts the luminescent sheet above it, and the maximum luminescence is reached at the point where the deformation (strain) energy is highest. If a mechanoluminescence (ML) sheet is laid on the bridge, the ML sheet is pulled from the point of opening displacement, and light is emitted along the crack opening (Fig. 21s). Because this diagnosis involves the application of ML sheet sensors to the surface of the structure, and the opening crack is clearly visible through the mechanoluminescence pattern, it can be concluded that an unskilled diagnosis of cracks has been realized.

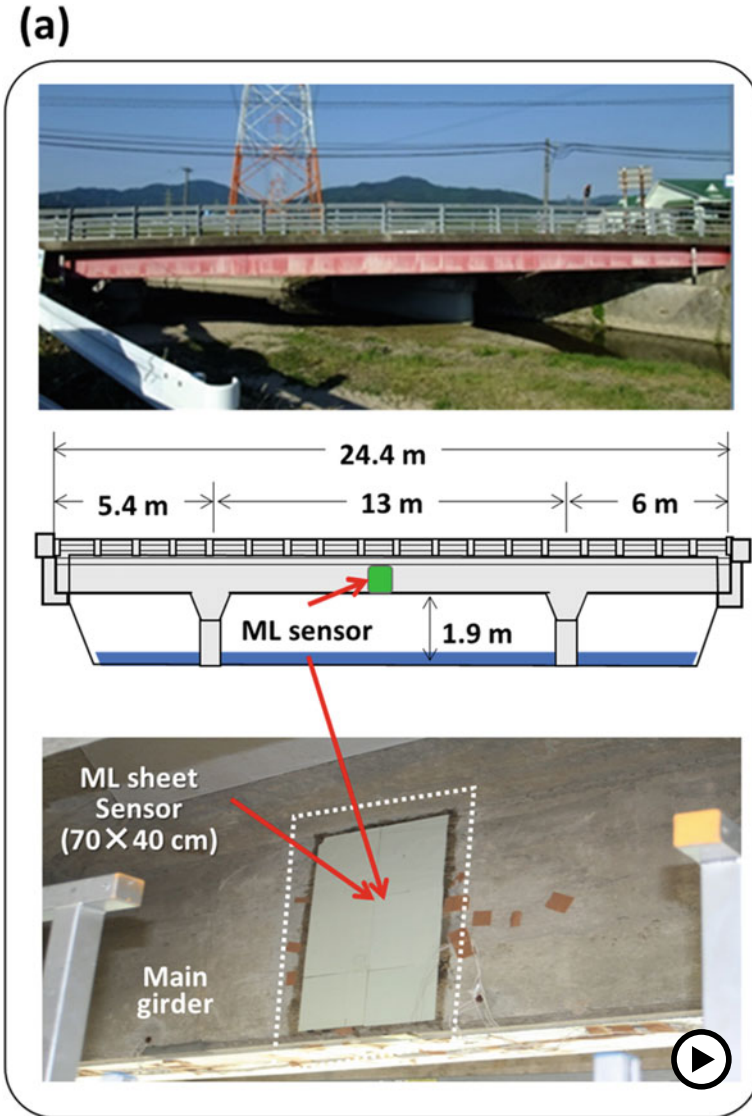


Fig. 21 Structural health monitoring (SHM) of the social infrastructure (bridges in use). **a** Monitoring site, **b** picture of the crack for ML monitoring, **c** results of ML monitoring and crack mouth opening displacement (CMOD), and **d** mechanism of the ML monitoring of the crack (► <https://doi.org/10.1007/000-ayy>)

(b)

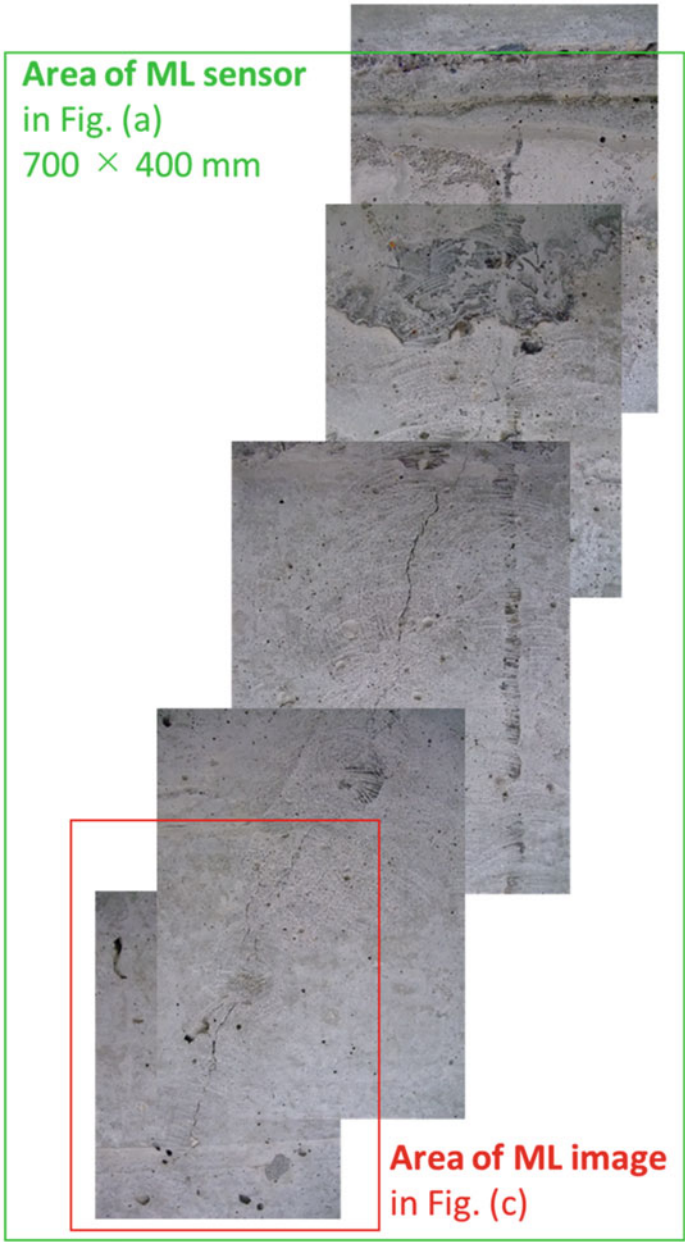


Fig. 21 (continued)

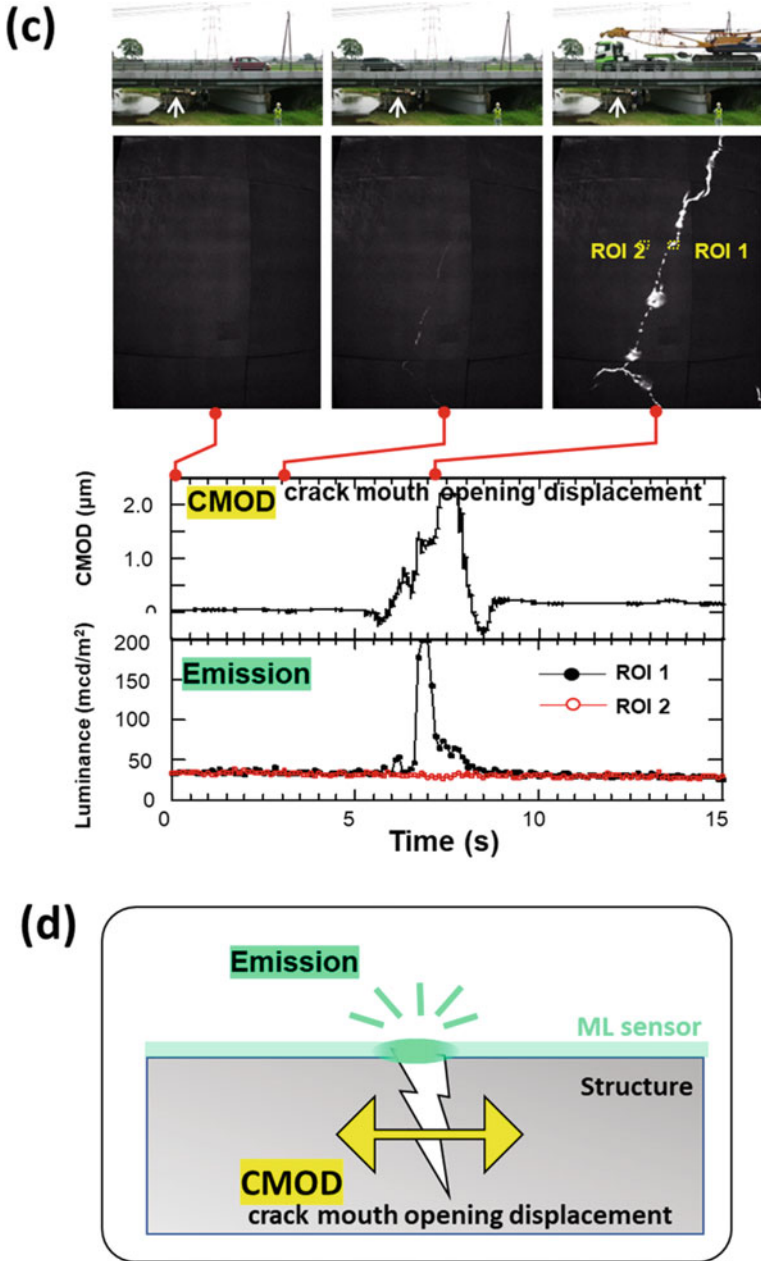


Fig. 21 (continued)

Figure 22 shows the results of mechanoluminescence (ML) monitoring at the back of the floor plate of a bridge located near a warehouse district in Tokyo. Figure 22a shows a crack photographed at a distance of 1 m. As shown in the figure, the crack can hardly be identified without marking it with a pencil. However, when an ML sheet is attached to the bridge and the emission is measured under the dynamic load of a moving vehicle, a clear ML pattern that perfectly matches the crack shape is obtained, as shown in Fig. 22a. The monitoring of the bridge was conducted using wireless equipment from the Kyushu area, which is 1000 km away, and ML monitoring was performed over a six-month period using a bridge-monitoring application. It was also proved that the ML sheet was damaged along the cracks in areas with a large CMOD, but the luminescence pattern is completely recovered by removing the sheet and applying a new ML sheet.

Furthermore, it has been successfully demonstrated that ML monitoring can be applied in both fast demonstrations accompanied by active loading based on moving vehicles, and extremely slow daily deformations and crack mouth opening displacements.

Figure 23 shows photos of the monitoring site (building) and ML sensors attached to the crack at the monitoring point. For this ML monitoring test on the slow deformation phenomena, a CCD camera with long-exposure performance was used instead of the high-speed or general CCD camera to detect long-persistence slight mechanoluminescence that responded to the slow deformation in an integral image. The ML measurement for integral (long-exposure) ML images was performed after UV light (365 nm, 0.7 mW/cm²) irradiation and heat treatment to reset the performance of the ML sensor [2, 46].

As shown in Fig. 23, the maximum CMOD value was estimated a100 nm in one daily cycle. However, despite such an extremely small and slow CMOD, clear ML images were successfully recorded every day at a specific time and at the same position along the crack. To clarify the origin of the mechanoluminescence, the time course of the ML intensity, CMOD value, and the temperatures were summarized, as shown in Fig. 23, where it can be seen that the ML pattern is synchronized and originates from the change in temperature and follows the CMOD caused by the thermal strain of the structure.

Furthermore, the degradation of the ML sensor sheets and ML spray-type sensors was observed for two years and found to be negligible in the practical field. New crack propagations were also recorded using the same conditions used in ML sensing owing to the daily thermal effect of sunlight on the building.

However, it is time-consuming to monitor such slow deformation in CMOD and the crack propagation caused by thermal effects in buildings during the day. In addition, the resulting crack propagation is extremely slow, which makes frequent real-time monitoring unnecessary. This is generally true for infrastructure monitoring, and many professionals in the field believe that it is sufficient to only know how much damage or stress has accumulated due to loading once every few months or years.

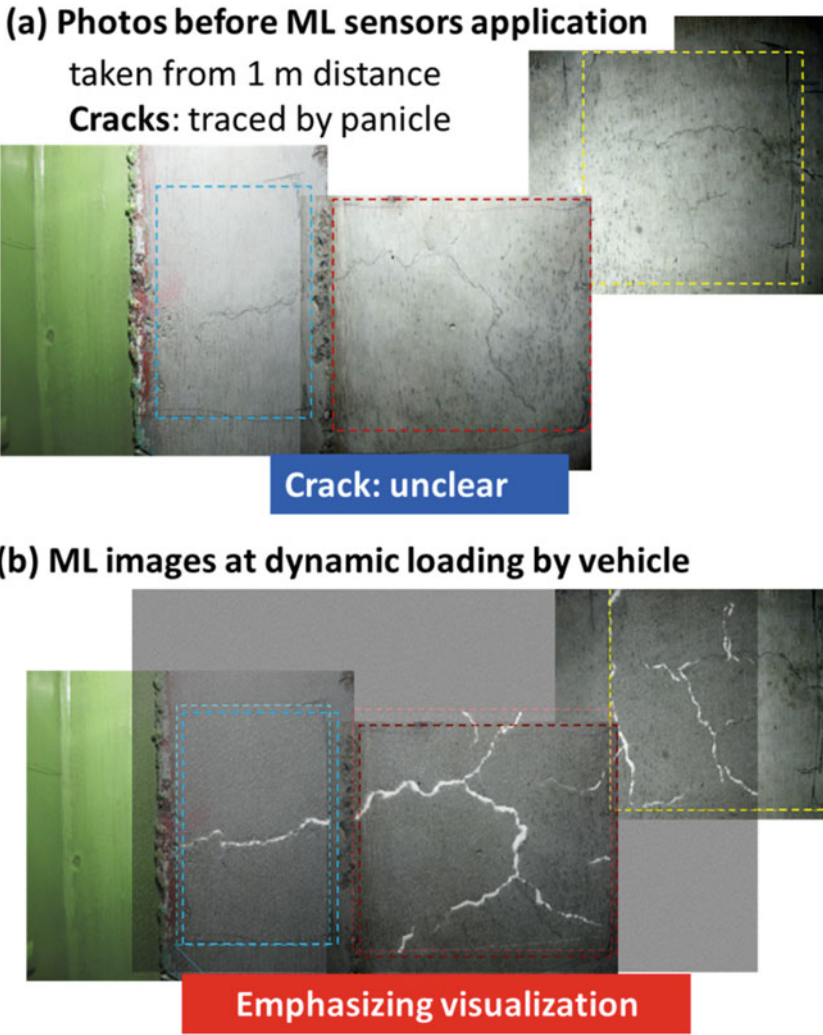


Fig. 22 Emphasizing visualization of the crack on the floorboards of the bridge in use. **a** Photos before ML sensor application, and **b** ML images after being exerted to the dynamic loading of vehicles

To meet this need, a stress history system was developed using a mechanoluminescence (ML) sensor and optical reaction layers, as shown in Fig. 24 [2, 41, 42, 46]. In this system, the light emitted from the ML layer functions as a light source, and the photoreactive layer reacts and changes color to obtain the stress history (Fig. 24a). Additionally, a stress integration recording system was employed on the extremely slow daily COMD in the old building, as shown in Fig. 24a. As a result, after 20 h of long-term history recording in one daily cycle, an integral ML recording pattern was

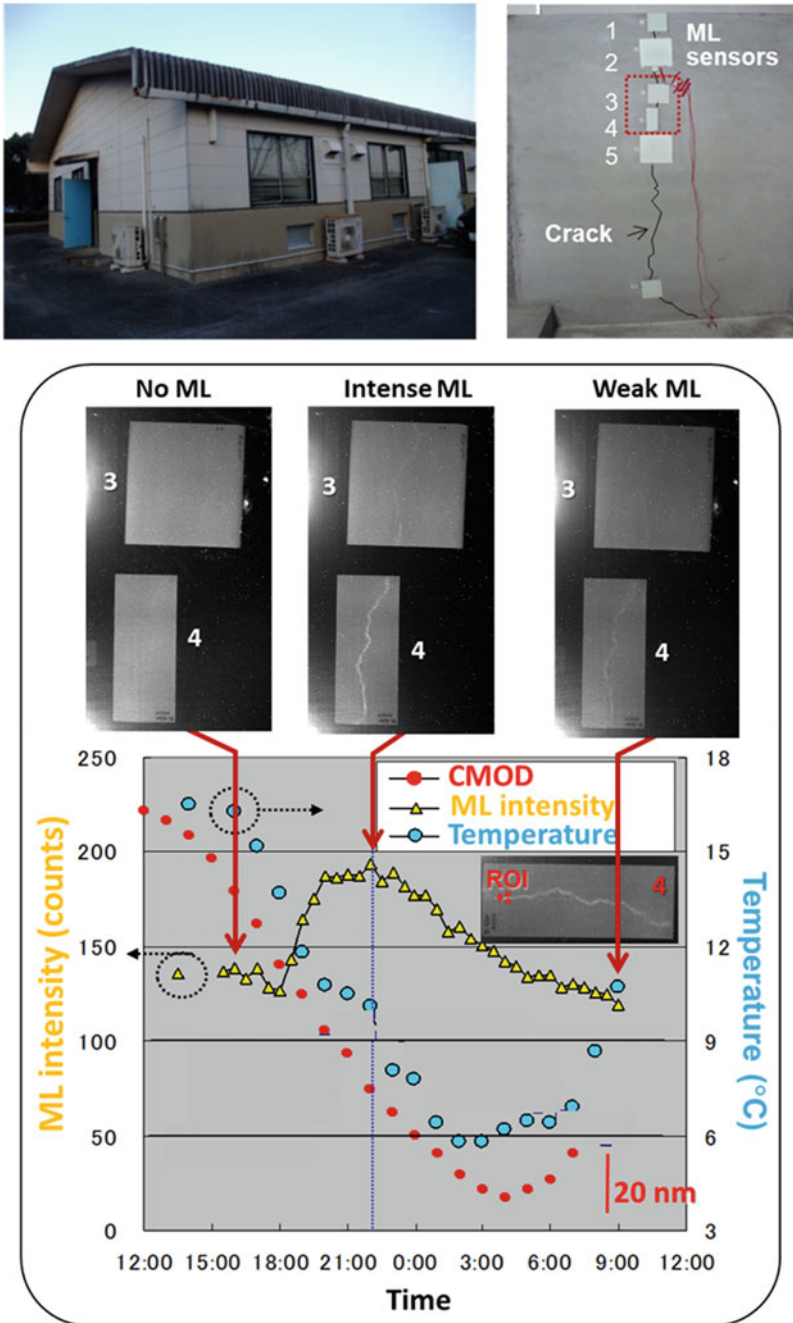


Fig. 23 Structural health monitoring (SHM) of the extremely slow daily deformation crack behavior in buildings using an ML sensor

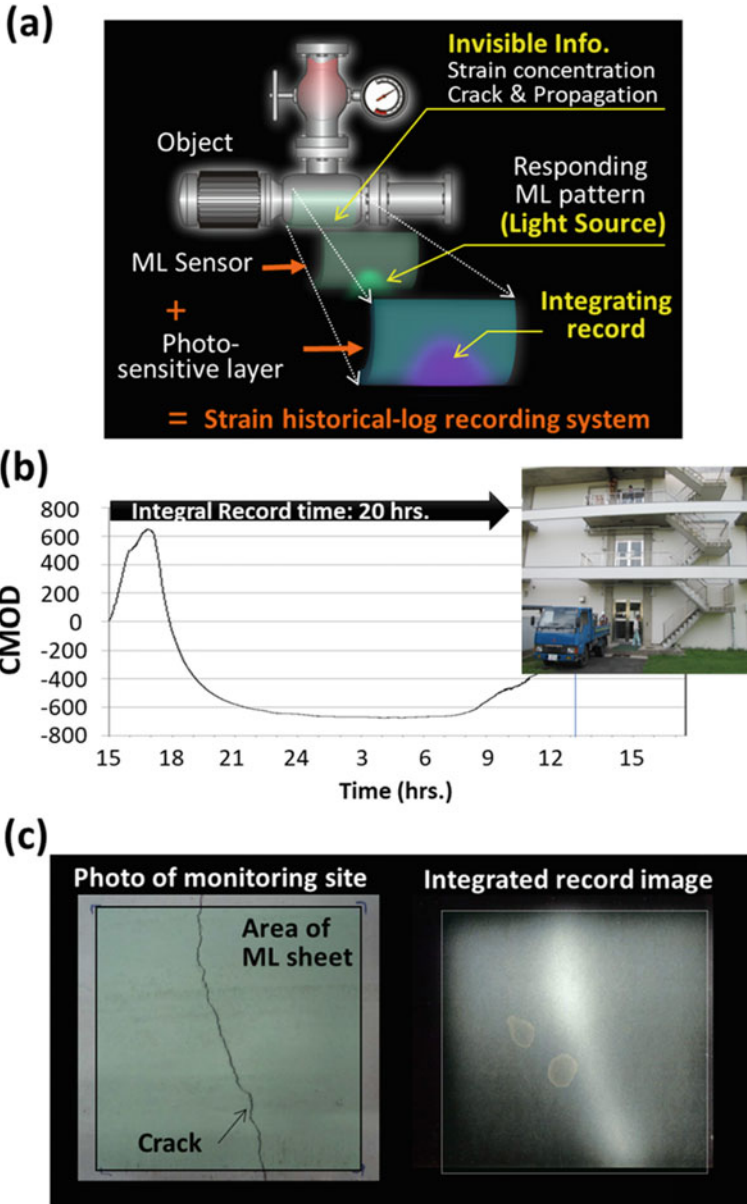


Fig. 24 Integrated recording of the ML sensor using a photosensitive material. **a** Concept, **b** CMOD of the crack in the building, and **c** integrated recorded image of the crack behaviors using the ML sensor and photo of the monitoring site

derived based on the slow CMOD emission. Moreover, the stress-recording system has been successfully applied for bridge monitoring in different scenarios. However, a challenge still remains in determining the stability of the photosensitive layer for long-term monitoring, which allows stable and reproducible results to be obtained in any monitoring opportunity or environmental condition. Thus, this system cannot be considered a quantitative monitoring system for stress, but a quality monitoring system that can be used as an indicator of crack propagation.

Thus far, the mechanoluminescence (ML) monitoring of cracks and defects on the surface of structures has been discussed. Figure 25 shows the results of the ML inspection and remaining life diagnosis of a high-pressure hydrogen vessel, which is an infrastructure used in the rapidly growing hydrogen energy field [56–58]. Hydrogen vessels are now being increased from 35 to 70 MPa, and the first-generation metal vessels are being replaced by third- and fourth-generation metal vessels made of resin and fiber-reinforced plastic. However, in Fig. 25, the detection of internal fatigue cracks in a steel vessel was examined for ease of experimentation. Because the upper limit of this tank was 35 MPa, the test was conducted by varying the sinusoidal internal water pressure up to 5/3 times the upper limit. When there is damage inside the tank, it is common to externally inspect the vessel via ultrasonic inspection; however, this is time-consuming and its accuracy is questionable, thus shortening the inspection time is a problem. In contrast, an ML paint sensor was directly attached to the outside of the high-pressure tank and a camera was used to capture images from three directions to enable the omnidirectional measurement of the vessel condition after applying a predetermined internal pressure, as shown in Fig. 25a. Additionally, based on Fig. 25b, when a vessel with no inner crack is used, uniform mechanoluminescence is obtained when internal pressure is applied. However, when vessels with artificial damage (axial slit damage) or fatigue cracks are used, the ML sensor film in the area corresponding to the inner cracks shows a peculiar splitting ML emission pattern. Furthermore, because the fatigue crack propagated by repeatedly applying internal pressure, the ML pattern that had been split into two became brighter and clearer and moved closer to being narrow. Interestingly, a linear correlation between the distance of the split ML pattern and crack length was obtained in subsequent experiments.

By considering the mechanism of this phenomenon on the basis of simulations (Fig. 25c), the following conclusions regarding the monitoring of the inner damage were reached. The mechanism through which internal damage can be visualized using ML sensors attached to the outside of the structure is based on strain concentration that occurs at the inner crack tip owing to the loading in the vessel's circumferential direction because of internal water pressure loading. This strain distribution propagates outward while reducing in the inside of the structure, causing the distortion of the ML sensor readings when producing an ML pattern. If the distance from the surface of the structure to the crack tip is large, the distance between the split at the surface of the ML pattern becomes wider because the strain distribution is mainly in an oblique direction from the crack tip. In contrast, if the distance between the crack tip and surface decreases as the fatigue crack propagates, the strain distribution reaches the structural surface without spreading, resulting in a narrow ML pattern.

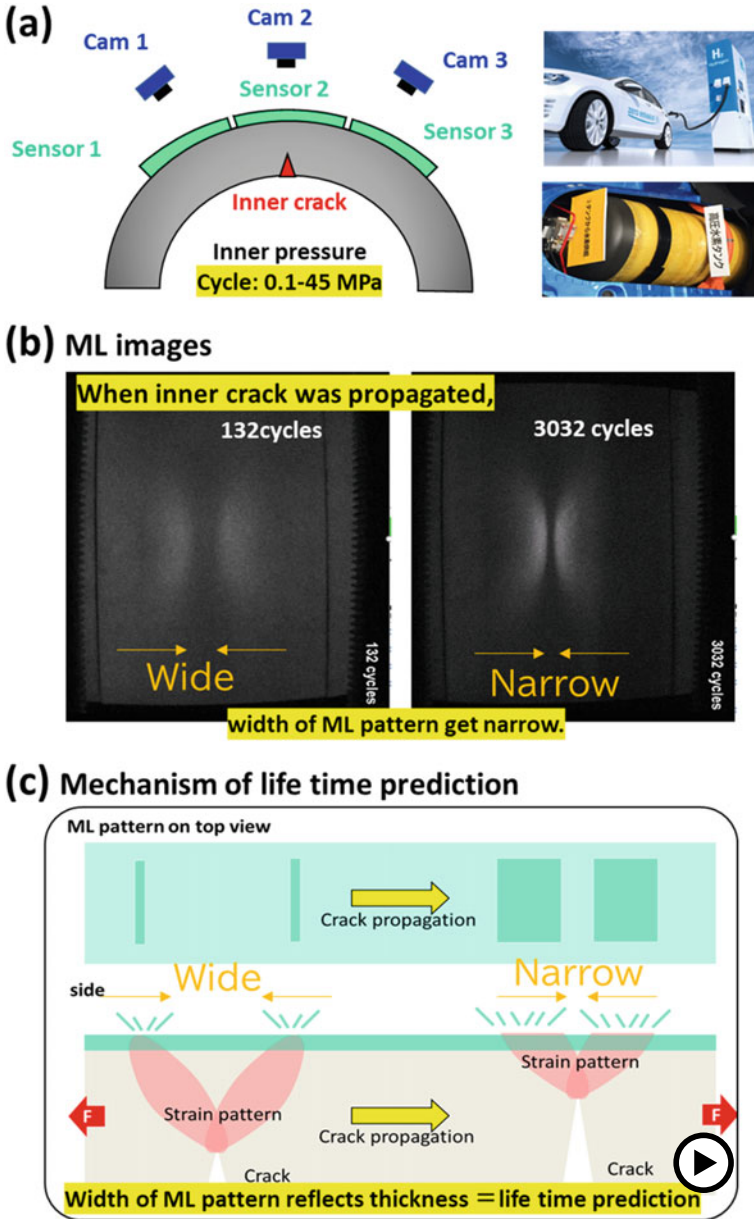


Fig. 25 Lifetime prediction and condition-based monitoring (CMB) of the energy infrastructure (hydrogen high-pressure vessel). **a** Schematic illustration, **b** ML images at the point where inner pressure was applied, and **c** mechanism of light time prediction based on the change in the ML pattern (► <https://doi.org/10.1007/000-ayz>)

Because the surface is closer to the crack tip, the stress intensity factor is higher, the strain is correspondingly higher, and the relaxation is reduced, resulting in a sharper and stronger ML pattern. In other words, the distance between the split ML pattern functions as an indicator of the location of the crack tip (depth information of the crack).

This is the first study to present the possibility of conditioning-based monitoring (CBM), which can be used as an indicator of the degradation events during a particular lifetime by focusing on the changes in the light-emission pattern, and the mechanoluminescence can be considered an indicator of the strain intensity distribution. This is a notable achievement.

3.3 Visualization of Repair Effect Using Mechanoluminescence (ML)

Here, the adaptation of mechanoluminescence is discussed to evaluate the repairing effect using mechanoluminescence from the viewpoint of mechanical behavior.

Depending on the deterioration diagnosis of the structure, repairs or other construction may be necessary. For example, cracks in bridges are sealed by injecting epoxy adhesives, and CFRP or metal plates are bonded and reinforced [59–63]. For aerospace CFRP structures, it has been proposed to scarf sand the damaged area and fill it with repair patches. The effectiveness of repairs is evaluated based on the porosity obtained using ultrasonic testing [64, 65], but it is still unclear whether the effectiveness of repair can be evaluated and predicted from the viewpoint of mechanical behavior (strength). Therefore, investigations were performed to visualize the effect of mechanoluminescence on the functional recovery.

In the actual experiment, as shown in Fig. 26, a flat plate with a thickness of 3 mm was made by molding epoxy adhesive, and pseudo-damage of 1 mm depth was formed by processing, followed by repair to fill the pseudo-damage with the same epoxy adhesive as the base material. First, the strain distribution-related mechanoluminescence (ML) pattern was investigated in advance using numerical analysis (simulation), as shown in Fig. 26a. Subsequently, the ML paint sensor was applied to the backside of the pseudo-damage, and the ML pattern was verified during the repair process of the sound specimen, pseudo-damage formation (three locations), and each repair location. Consequently, as shown in Fig. 26b, a uniform ML pattern was observed in the sound sample, whereas a peculiar pattern was observed in the pseudo-damaged sample (three locations), with three black streaks directly behind the pseudo-damage and high ML luminescence in the surrounding area. Furthermore, as the number of repair sites increased from one to three, specific black streaks at the repair sites were no longer observed, and eventually a uniform luminescence pattern was observed again. The simulation results indicate that the black streaks obtained in the pseudo-damaged material reflect the original tensile load and offset of strain due to the stress concentration in the damaged area and the generation of compression

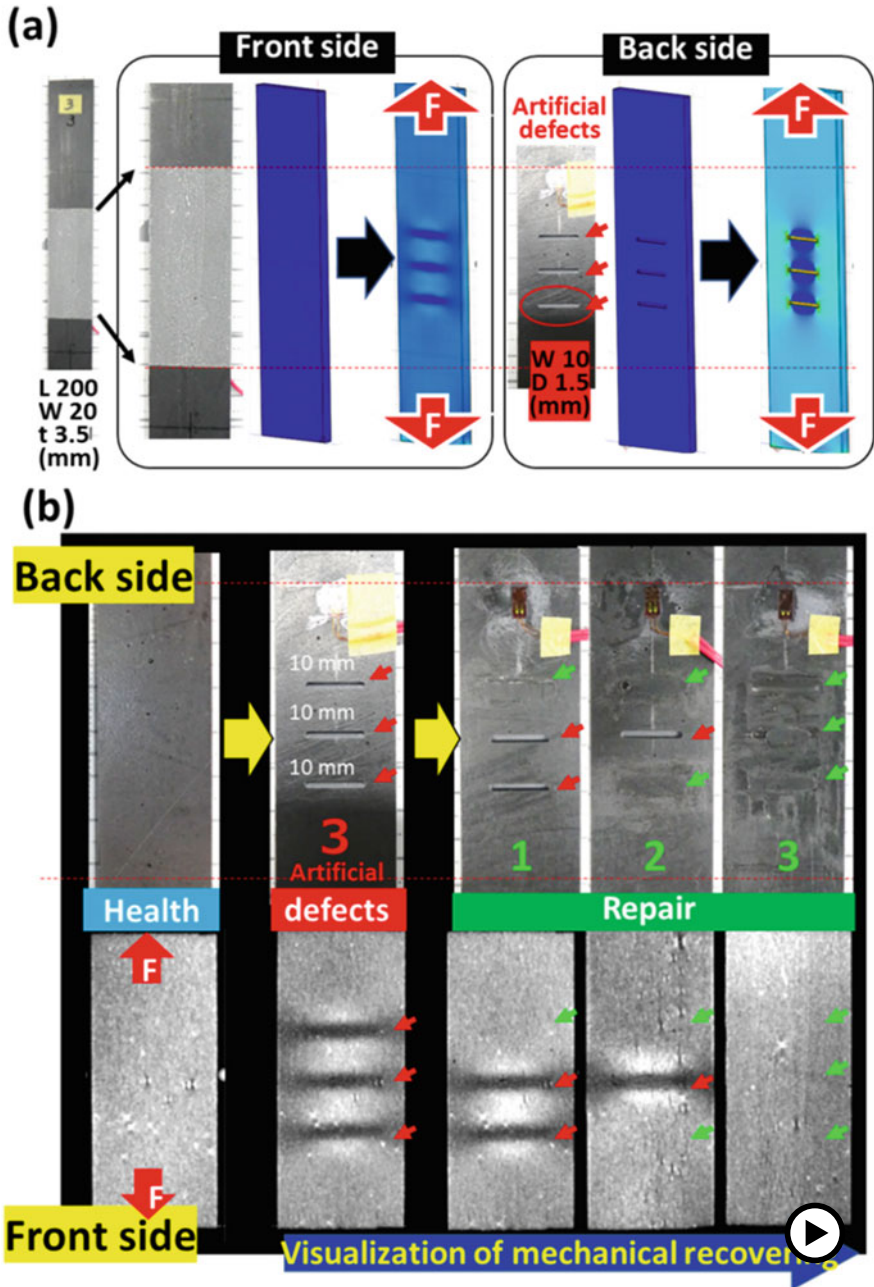


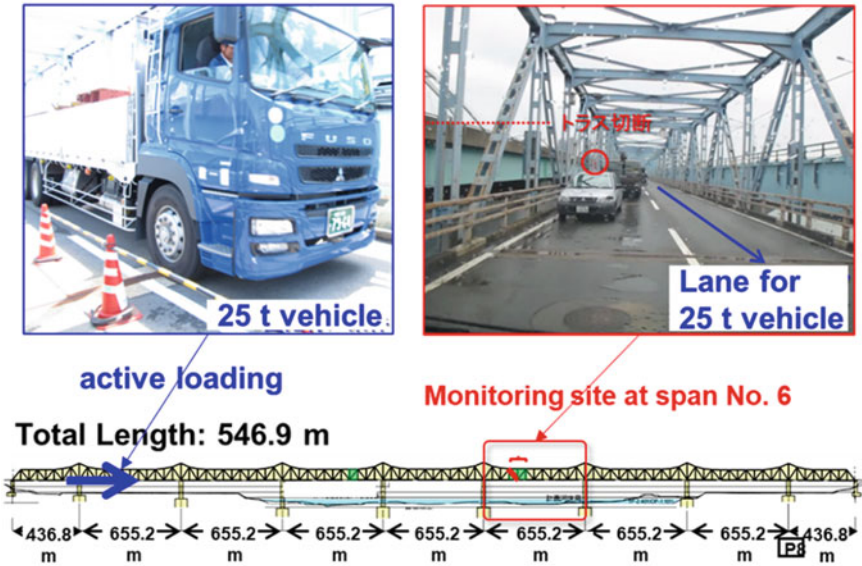
Fig. 26 Visualization of the repairing effect and recovery of the mechanical performance during the lab-level demonstration. **a** Simulation of the strain distribution around the artificial defects on the specimen during tensile loading. **b** Photographs of the backside of specimens with artificial defects and repairing, and front side of ML images. The red arrows represent the defects, and the green arrows represent the repairing sites (► <https://doi.org/10.1007/000-az0>)

due to local bending in this area. In other words, the uniform ML pattern obtained by repair indicates that the specific mechanical state caused by the damage is restored to a state of healthy stress dispersion by the repair.

The next example is the mechanoluminescence evaluation of the damage resistance measures on actual bridges [45]. The target bridge for mechanoluminescence (ML) monitoring was the Torikai big bridge (Osaka Prefecture, Japan, Fig. 27a), which is a nine-span continuous-Gerber-truss-type steel bridge (through bridge, length: 550 m). This bridge was used by the public in 1954. After continual use for over 50 years, fatigue cracks, degradation, and corrosion became prominent with increasing traffic. Consequently, an alternative new bridge was constructed alongside the old one, and its construction was completed in 2010. The old bridge could be used for diagnosis investigation before removal. We sprayed ML paint sensors around the stop hole or each of the fatigue cracks in span no. 6 on the old bridge, as shown in Fig. 27b. A stop hole is used when a crack is found in a steel structure. By drilling a hole near the crack tip, the crack tip was eliminated, thereby eliminating extreme stress concentrations and stopping crack propagation. ML measurements were performed during dynamic load testing using a heavy moving vehicle (over 25 t). As a result, mechanoluminescence was used to visualize the CMOD of the original fatigue crack at b and c with a broken line. In addition, a slight ML emission can be recognized at the edge of the stop hole, originating from the stress dispersion from the original crack tip to the wider area of the stop hole. This can be considered a positive effect of the stop-hole procedure. In contrast, interestingly, an intense ML line was observed at point d, which can be considered as the new crack generation. Before ML monitoring, no new crack generation was noticed, indicating that ML sensors are powerful tools for detecting unexpected defects and damage during monitoring.

In this section, the application of mechanoluminescence (ML) technology to structural health monitoring (SHM) is introduced as a killer application of mechanoluminescence. Accompanied by various types of dynamic loading, structural materials undergo elastic deformation and stress concentration because of their geometry. However, cyclic loading degrades the integrity by generating fatigue and crack initiation and propagation, plastic deformation, yield, and rupture, as shown in Fig. 28. Remarkably, it was demonstrated that these types of deterioration origins such as various defect signs and mechanical events, can be detected using ML visual sensing to distinguish them from the specific ML pattern. In general, ML sensors have been used for the quantitative analysis of strain distributions. However, focusing on the two-dimensional information of the ML pattern, another aspect of the sensor was found to be a powerful tool to search for and track the existence of unexpected and invisible stress concentrations, as well as changes in the mechanical behavior due to deterioration and crack initiation and propagation, which are difficult to observe. Furthermore, focusing on the four-dimensional information, including the time variation of the mechanoluminescence pattern, features can be extracted for AI analysis, which enables the prediction of the remaining lifetime of materials, structural members including joints, and structures, by capturing the degradation process and

(a)



(b)

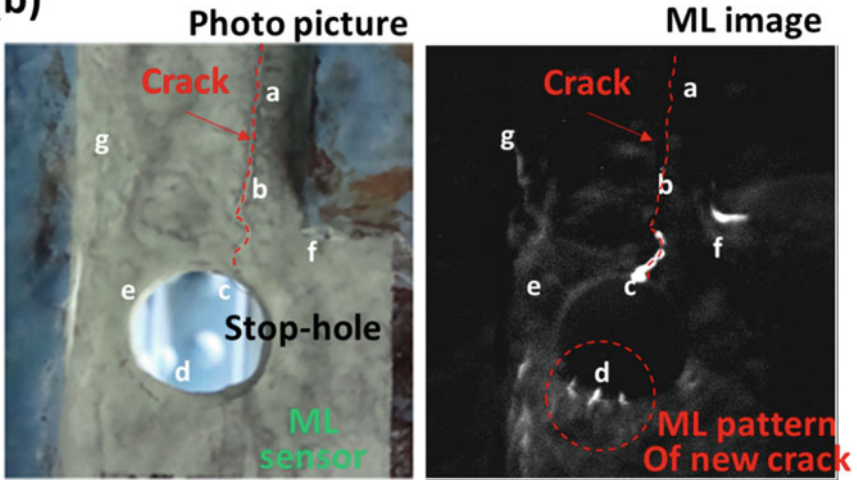


Fig. 27 Visualization of the repairing effects for a bridge in use. a Schematic illustration of the monitoring site on the bridge. b Photographs and ML image of the stop hole where repairs were made to stop crack propagation in the steel bridge

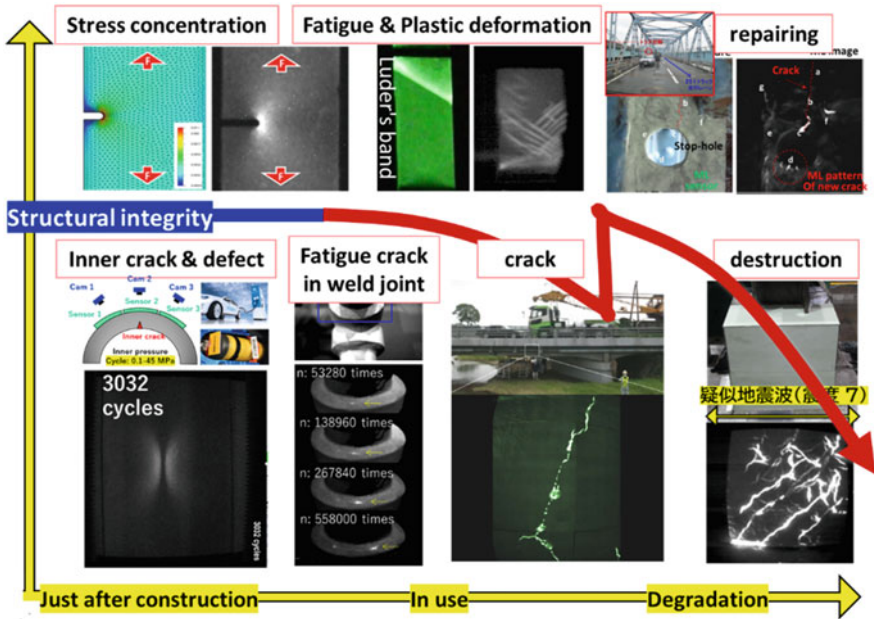


Fig. 28 Concept of conditioning-based monitoring (CBM) using ML images and the change in the feature extraction of the life cycle event in structure and structural material

events that occur at that time, which typically influence the mechanical behavior of the structure. This case is the first to present the possibility of conditioning-based monitoring (CBM), which can provide an indicator of degradation events during a lifetime by focusing on changes in the light-emission pattern.

4 Killer Application of Mechanoluminescence 2: Innovation in Design and Prediction

In this section, another innovative application of ML technology for design and prediction is introduced. As an approach for design and set-up using mechanoluminescence (ML) sensing, structural members that are difficult to predict were targeted and are being addressed from the viewpoint of the visualization of mechanical behavior. In this section, focus is placed on:

- (1) Carbon fiber-reinforced plastic (CFRP), which is still in the development phase and difficult to simulate for design owing to its complex structure.
- (2) Simulation sophistication.

- (3) Rapid simulation (gears, bridge models, etc.) that can be handled by workers using 3D printing devices; and
- (4) Setting mechanical conditions in sports equipments, where the setting of mechanical conditions can create enormous value.

4.1 Mechanoluminescence (ML) Sensing in CFRP Composite Material

CFRP is a composite material composed of carbon fiber and resin with excellent mechanical properties, light weight, and strength [66]. Its greatest feature is that the strength anisotropy can be designed by the fiber direction, weave, and lamination direction. To accelerate the sophistication and shorten the design time, the mechanoluminescence visualization of CFRP composite materials is currently being actively investigated, focusing on the stress distribution, which is a characteristic of CFRP, although it is sometimes difficult to simulate. Although the method is simple and involves the installation and measurement of appropriate mechanoluminescence sensors, the changes in the stress distribution pattern in response to an applied load were successfully visualized, as well as changes in specific mechanical information during the fracture process, on the order of tens of microseconds (Fig. 4a). In addition, the method succeeded in visualizing the predictive signs of failure (transverse crack initiation, zero-degree split, correlated delamination, and fiber breakage) and is effective as an evaluation method for designing high damage resistance [67].

Figure 29 shows the strain distribution visualization of the twill-weave CFRP using a mechanoluminescence (ML) paint sensor. In fact, when checking CFRP strain-measurement methods in standards, it is stated that strain gauges should be placed near the center of the material. When the strain distribution is measured using strain gauges, it was found that the strain values differed only by the location of the strain gauges. The direction of the fibers is clearly visible from the surface, and intuitively, the strain behavior does not seem to be uniform.

Subsequently twill-weave CFRP was then covered by the ML paint sensor, and a tensile or torsional load was applied to the specimen to check the strain distribution. Consequently, an emission pattern similar to the twill-weave pattern was obtained in the tensile load application, and the ML emission was strong only in the same fiber direction, indicating that the strain behavior was different in the fiber direction. However, when a torsional load was applied, mechanoluminescence was uniformly obtained from areas in both the vertical and horizontal fiber directions, indicating a uniform strain distribution. This shows that CFRP is a complex system in which the strain distribution varies depending on the internal fiber direction and loading direction, even in such a simple strain measurement.

The failure process of CFRP laminates involves not only fiber breakage but also microscopic damage such as transverse cracks and delamination [68]. In particular, transverse cracks in off-axis plies occur at a much lower stress than the ultimate tensile strength of laminates. Therefore, it is important to detect the occurrence of

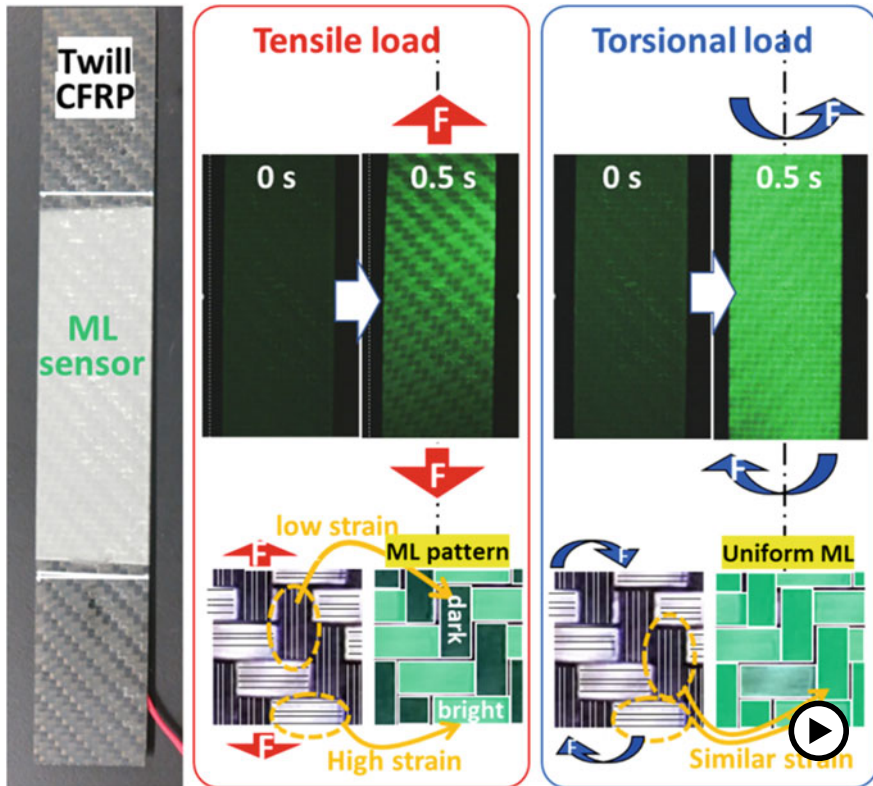


Fig. 29 Mechanoluminescence (ML) visualization of strain distribution in CFRP (1), which is difficult to predict, under tensile and torsional load (► <https://doi.org/10.1007/000-az1>)

transverse cracks as portents of CFRP destruction in real time for the reliability of the CFRP laminates in use, and ML detection of transverse generation has been investigated. The laminate configuration of the CFRP was a cross-ply $[0_2/90_4/0_2]$. An ML sheet was placed on the surface using commercial adhesive. From the preliminary experiments, as shown in Fig. 30a. It is known that the first transverse crack is generated at approximately 0.8% strain (8000 μst) at a tensional loading rate of 1 mm/min. At the early stage, in the range of low strain such as 0–0.3% strain (3000 μst , Fig. 30c), mechanoluminescence was observed from entire area without specific pattern accompanied by tensional load, as shown in Fig. 30b because of no transverse crack generation during this stage. In contrast, from approximately 0.8% strain (8000 μst), specific straight ML emission patterns were gradually recorded in the perpendicular direction to the tensional loading.

After the specific ML emissions, the ML specimen was unloaded immediately, and the entire cross-section of the CFRP specimen was carefully observed using a digital microscope (KEYENCE, VHX-5000), as shown in Fig. 30d. As a result, transverse cracks were confirmed in the cross-sectional microscopic image only at

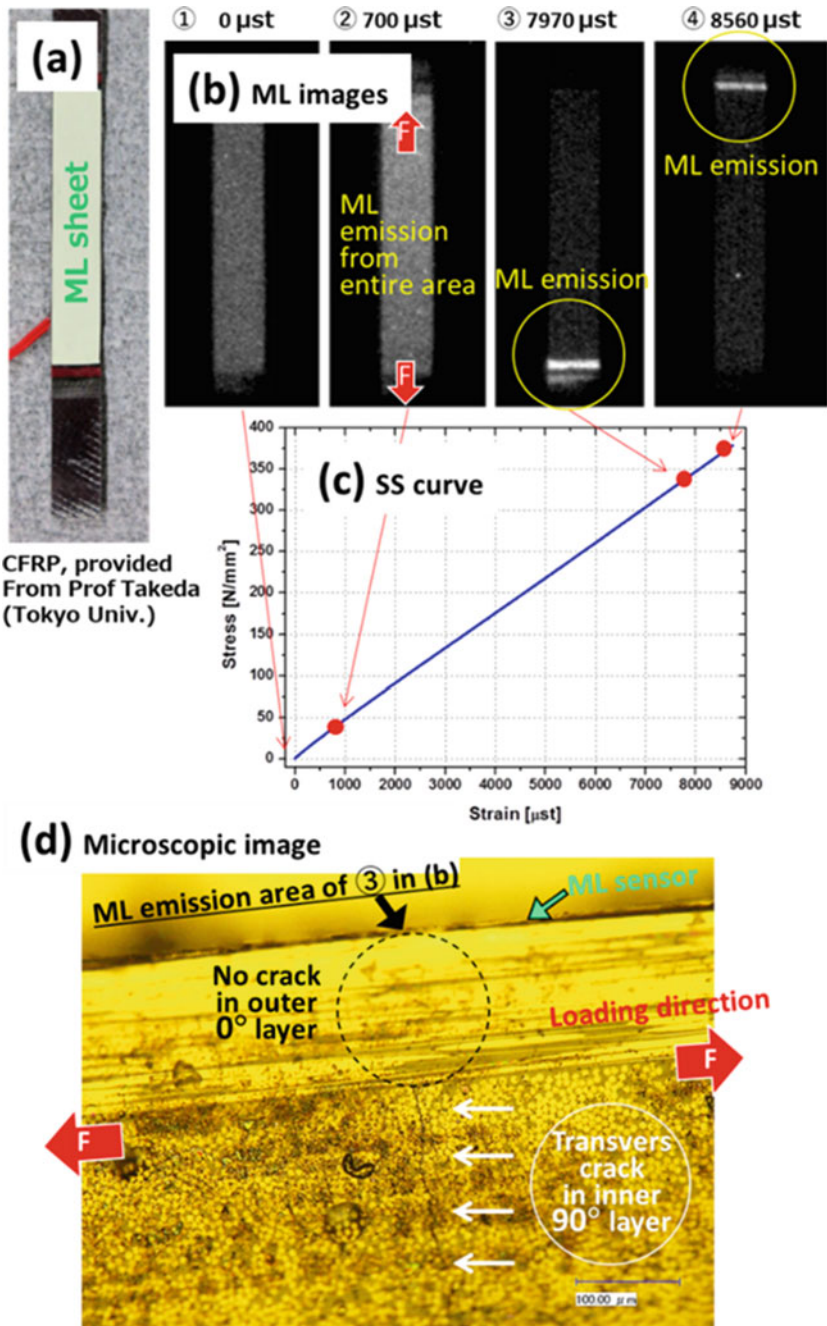


Fig. 30 Mechanoluminescence (ML) visualization of strain distribution in CFRP (2), CFRP for aerospace applications: detection of inner transverse crack generation from outside. **a** photo of the specimen with ML sensor, **b** ML images during tensile load shown in **c** SS curve. **d** Microscopic image at ML emission area at a side view of the specimen after tensile test

positions corresponding to the ML emissions, as shown in Fig. 30d. This clearly shows the usefulness of ML sensing for the real-time monitoring of transverse crack occurrence in terms of position and timing.

Furthermore, mechanoluminescence (ML) monitoring of the strain behavior of twill woven CFRP during a high-speed fracture process was also successfully performed. In bright images, a high-speed camera image of a CFRP fracture shows that a crack propagates from a notch, which defines the crack propagation point, in only 16 μs (Fig. 31 upper panel), when a tensile load is applied [68]. However, when the same situation is measured by applying mechanoluminescence, as shown in Fig. 31, the strain concentration at the tip of the notch leads to the concentration of strain on a single CFRP bundle (longitudinal ML emission pattern). When this bundle breaks, the next single CFRP bundle emits light, and when it reaches the opposite side of the plate, it ruptures. This ML emission pattern differed significantly from the strain concentration pattern at the tip of the notch when metallic materials were used. The luminescence pattern also changes if the weave of the CFRP internal fibers changes. In other words, it can be said that the pattern reflects the mechanical behavior derived from the internal reinforcing fibers.

In contrast, despite having the same geometry in the notch susceptibility test, the case with aircraft-grade CFRP (T800-3900-2B, unidirectional, 16 ply) showed a completely different ML emission behavior in Fig. 32 from that in the case of twill-weave CFRP (Fig. 31). The X-ray CT results showed the occurrence of 0° splitting

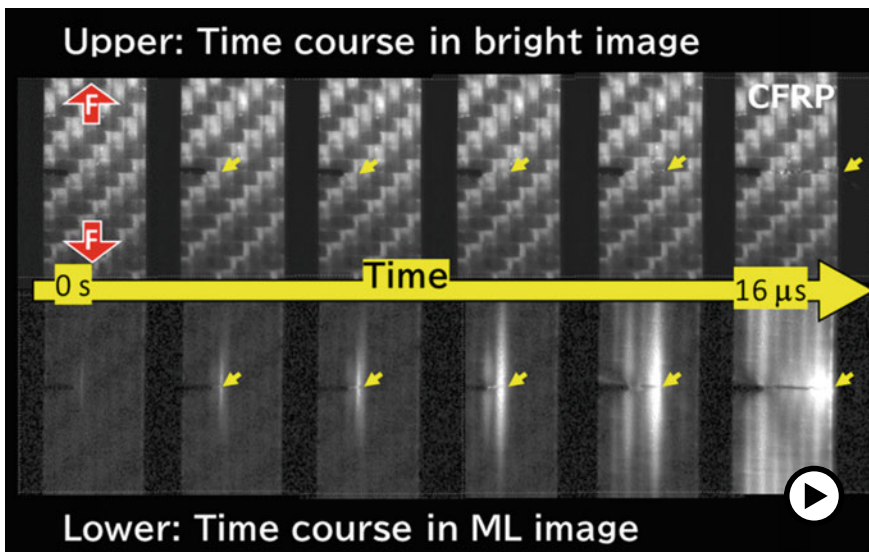


Fig. 31 Mechanoluminescence (ML) visualization of strain distribution in CFRP (3), high-speed destruction process of CFRP. Arrows means position of crack tip (► <https://doi.org/10.1007/000-az2>)

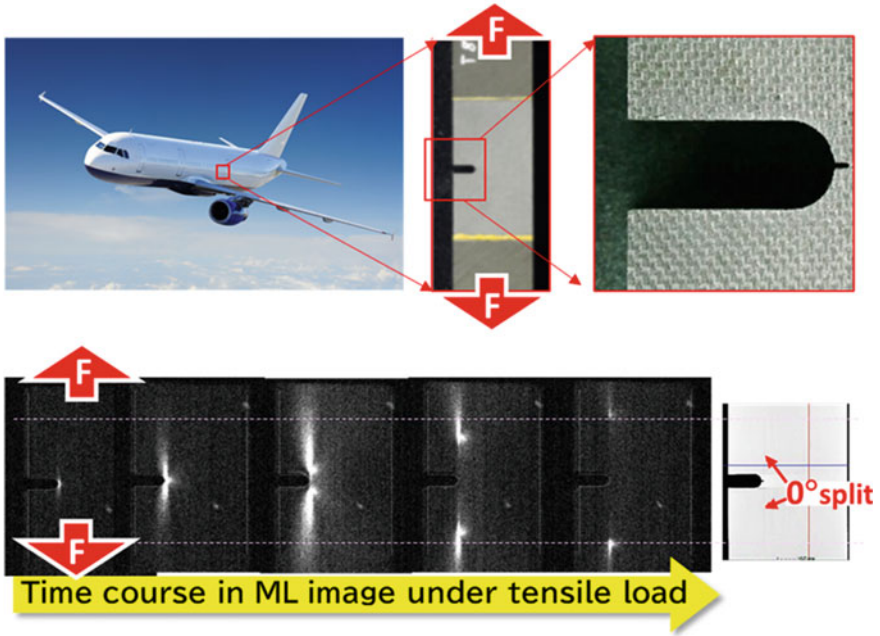


Fig. 32 Mechanoluminescence (ML) monitoring of minor damage progress in CFRP for aviation application

along the fiber direction, that is, internal delamination, at the point corresponding to the line where the ML emission point moved.

4.2 Simulation Sophistication Using Mechanoluminescence (ML)

Advancement of simulation is a challenge to “assumption of what should be visible. In fact, during the development of mechanoluminescence (ML) sensors, many experts and professors, especially in the mechanical field, said that the stress/strain distribution was well understood through experience and that visualization technology was not necessary. Furthermore, the stress and strain distributions can be visualized graphically as simulation (prediction) results through CAE (computer-aided design engineering (CAE)). Although visual information may give the impression of a good understanding, a completely different solution can be obtained even with a slight change in the loading conditions, including direction and frequency. However, because the loading conditions are always the same in the drill in the simulation, it is not uncommon to assume that the stress concentration pattern is always the same, especially for an immature person. In addition, the mechanical behavior in

experience and CAE are extremely effective, but the reality is often different in the case of fatigue and dynamic tests. This is especially true for advanced materials and composite materials (for which there are few databases) that are being developed in the agile cycle for the purpose of multi-materials in aircraft, automobiles, etc., where weight reduction is progressing. Therefore, it is extremely effective to “visualize” the actual information and reconsider the model and loading conditions in the simulation.

Figure 33 is the subject of a lap-shear test using adhesives with different Young’s moduli, and the methods of improving the accuracy of the simulation to a great extent are being investigated. After confirming the mechanical behavior through ML movies, strength calculations were performed with a high accuracy prediction within 95%, even for three different single-wrap adhesive joints with significantly different strain concentration conditions [69, 70].

In addition, Terasaki et al. gained a lot of experience that visualization information from mechanoluminescence can lead to simulation worker to be manure as education. In this sense, the ML luminescence information was provided as teaching data for the design prediction of industrial products [6, 48], and also conducted educational seminars to foster workers’ intuition on the type of loading or mechanical behavior using 3D-printed instruments of industrial products coated with ML paint sensors as a rapid simulation tool (Fig. 34).

However, the setting optimization using mechanoluminescence is discussed. Without sports, no other field has established a system that actively incorporates sensing such as “visualization” and provides feedback to settings in real. The mechanical design and setting (condition setting) of sporting tools are effective applications of mechanoluminescence. For example, the strain distribution in the gut of a tennis racket is visualized by mechanoluminescence while hitting a ball, as shown in Fig. 35a [5, 48]. This ML pattern and intensity reflects not only the product design of the racket, but also the gut-setting conditions. Furthermore, the ML pattern and balance also depend on the point where the tennis ball was hit; it must relate to the feeling of a pleasant smash. In other words, the physical conditions of design and setting visualized by mechanoluminescence can be correlated with the player’s condition, sensation, and results and can be used for AI learning to set conditions with a high probability of winning.

We also propose a novel method for filling a gap in the originally invisible mechanical behavior in modeling, an evaluation method that imitates real information and products using mechanoluminescent (ML) visual sensing [71]. To demonstrate the effect of the method, mechanical information was evaluated in the folding test of the flexible electronics film, as shown in Fig. 36.

Consequently, the appearance of strain concentration was successfully visualized based on mechanoluminescence, and complex dynamic mechanical information was instinctively understood from the time course of the ML patterns. In addition, the ML pattern clearly depends on the sticking situation of the flexible film on a folding plate with gripping tape even under the same test conditions, such as folding radius, material, and thickness, which are major factors affecting mechanical behavior during folding. Moreover, microcrack generation was detected during the folding cycle as

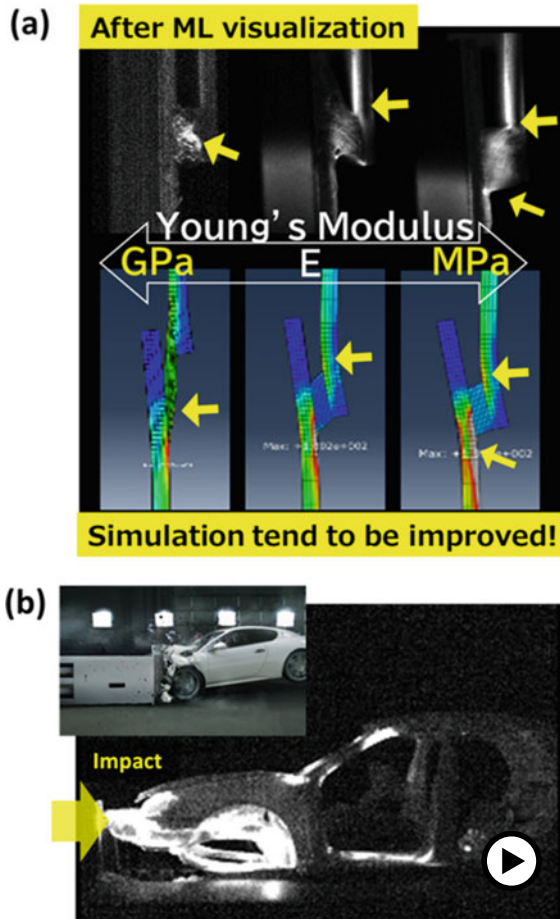


Fig. 33 Mechanoluminescence (ML) studies for advanced simulation. **a** Tensile load for single lap adhesive joints with various Young's modulus. **b** Impact test and high-speed strain propagation in car body at a car crash (► <https://doi.org/10.1007/000-az3>)

blinking of ML points, and it occurred even after 10 cycles of fatigue of the flexible film in the endurance folding test.

In the topics of optimizing design [72–77], it can also be introduced that mechanical properties of processing design on surgical epiphysis plates were investigated using a mechanoluminescence (ML) sensor as shown in Fig. 37 [78, 79]. Small dots with diameters of 1 and 2 mm were processed on the epiphysis plates using forceps from the viewpoint of operability. Through conventional mechanical tests using strain gauges, the strain of the processed epiphysis plates was remaining within 110% of the original plate.

In contrast, through mechanoluminescent evaluation, it was clarified that the strain was concentrated even around the processed small dots; however, the ML luminance

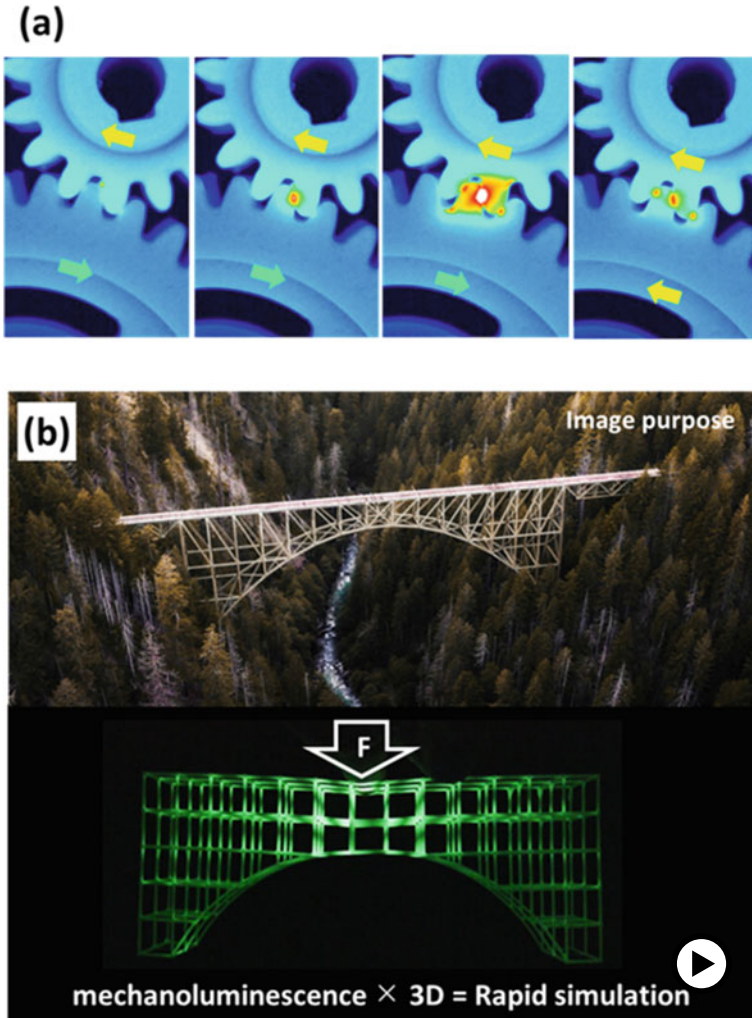


Fig. 34 3D-printed models \times mechanoluminescence = rapid simulation. **a** Dynamic strain behavior of gear, and **b** bridge (► <https://doi.org/10.1007/000-az4>)

reflecting the strain value at ROI 3 was much less than that around the tapped holes, which was processed originally on the epiphysis plates at ROI 1 and 2. Thus, the processing of small dots does not cause serious mechanical effects, such as stiffness reduction, and smaller dots are more appropriate for this purpose. From the results, it was successfully demonstrated that mechanoluminescence has high potential for the design of medical and surgical equipment.

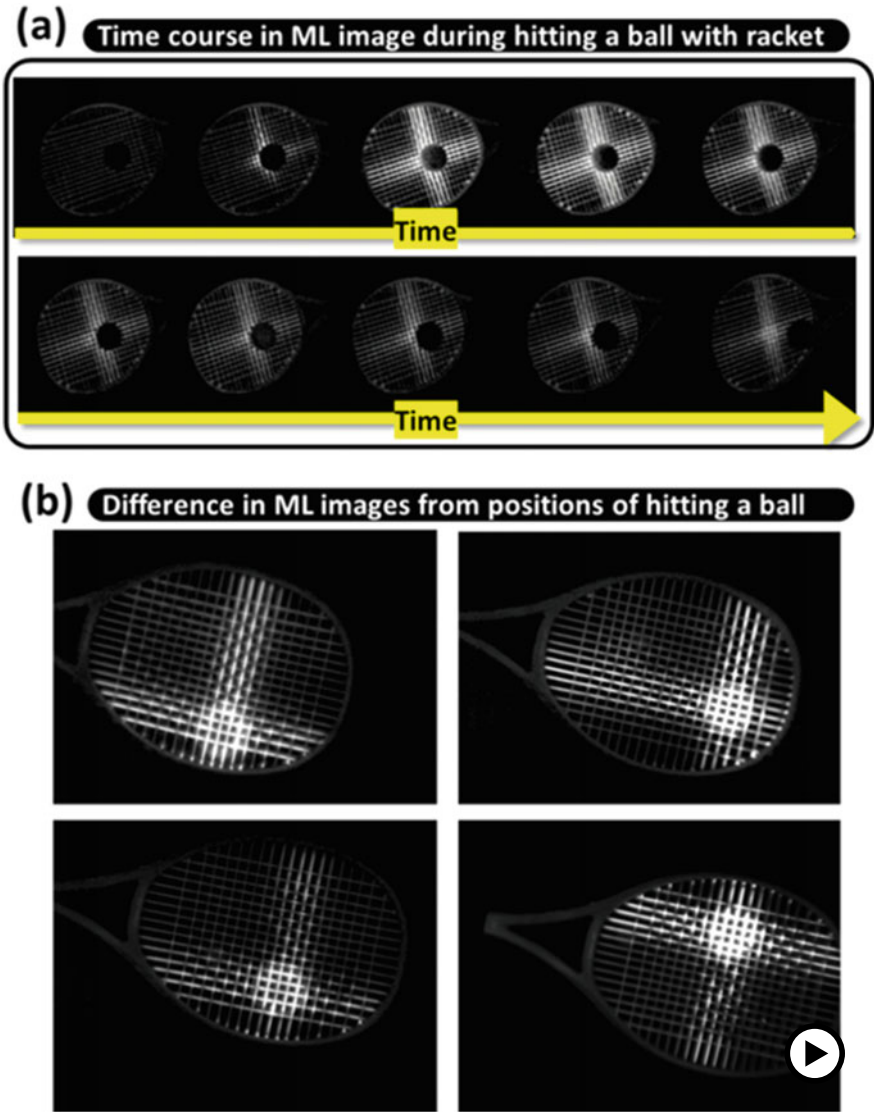


Fig. 35 Visualization of mechanical behavior during use for improved configuration of sports equipment. **a** Time course in ML image during hitting a ball with a tennis racket, **b** difference in ML images from positions of hitting a ball (▶ <https://doi.org/10.1007/000-az5>)

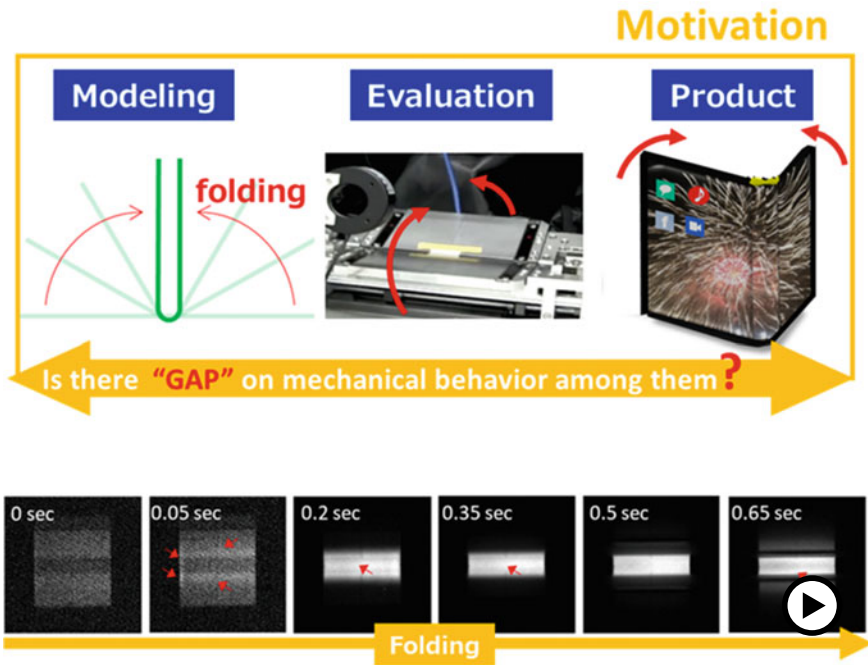


Fig. 36 New concept for filling a gap among modeling, evaluation, and product from the viewpoint of visualizing mechanical behavior. Conditions: mechanoluminescence (ML) images during folding process, 20 fps. Brightness: optimized for recognizing the ML pattern (► <https://doi.org/10.1007/000-az6>)

5 Mechanoluminescent (ML) Visualization in the Evaluation of Adhesive Joint

The most important factor in adhesion and adhesive bonding is whether the required “force” can be obtained within the required period. Therefore, in the evaluation of the adhesive strength, the fracture phenomenon, which causes deterioration beyond the elastic deformation region, is considered to be directly related to the strength.

In contrast, important information such as crack initiation and fracture processes that occur during adhesive strength evaluation, the stress/strain distribution that changes during the fracture process, and the correlation between the stress/strain distribution and load-stroke diagram (mechanical information), cannot be realistically observed. Therefore, the required information, which is difficult to visualize using mechanoluminescence, was extracted based on the mechanical behavior information to be used in the adhesion strength tests based on international standards (Fig. 38), and to determine which points correlate with the fracture or adhesive strength [48, 80–84]. In this chapter, the ML investigation process is introduced with

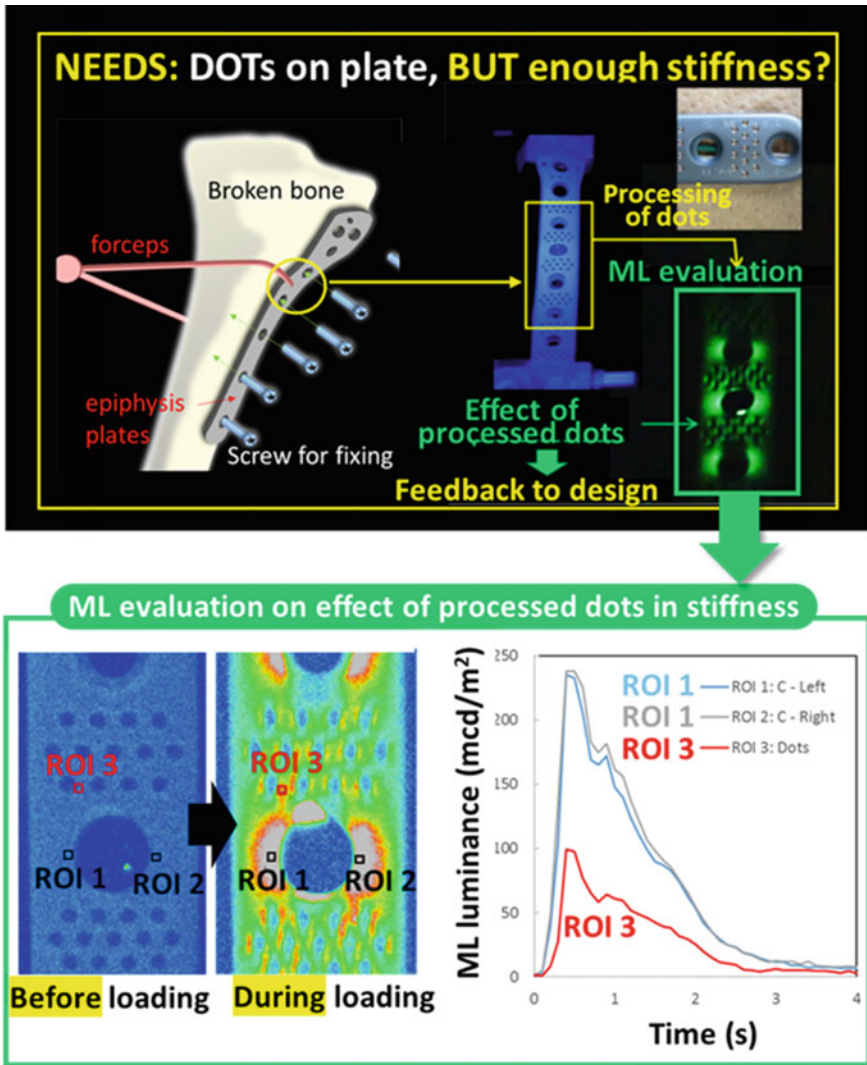


Fig. 37 Mechanoluminescence assisting agile optimization of processing design on surgical epiphysis plates

a particular focus on the following three tests that are frequently used in adhesion evaluation.

- (1) Fracture toughness (G_{Ic}) for mode I crack propagation
The weakest force leads to fracture, and it is severe at the interface.
- (2) Tensile shear strength (TSS)
Most common joint strength in actual structural designs.
- (3) Cross-tensile strength (CTS)

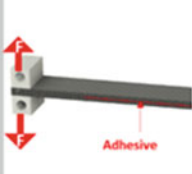
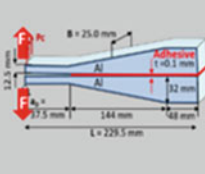
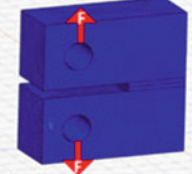
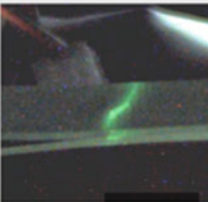
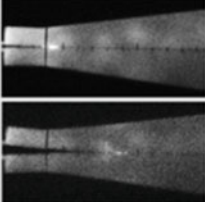
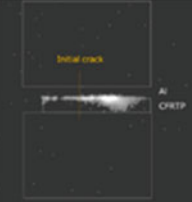
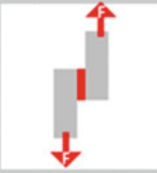

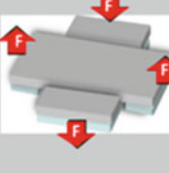
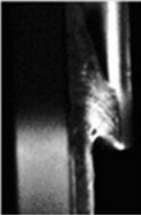

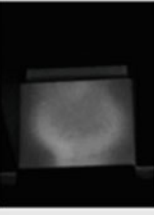
		Fracture Toughness energy		
		G_c		
		ISO 15024:2001 ISO 22838: 2020	ISO 25217:2009	ISO/DIS 19095-5
Geometry		DCB 	T-DCB 	Compact tension 
ML image				
		Tensile Shear stress	Peel Strength	Cross tension
		TSS	Peel	CTS
		ISO 22838:2020 ISO 25217:2009	ISO 11339	ISO 24360:2022 ISO 14272
Geometry		Lap-Shear 	T-peel test 	Cross tension 
ML image				

Fig. 38 International standards for adhesive strength evaluation and ML studies

Important for the comparison of car body spot welds.

(4) Others.

5.1 Fracture Toughness for Crack Propagation

The double cantilever bead (DCB) test for bonded fracture toughness was performed using the interlaminar fracture toughness test of carbon fiber-reinforced plastics (CFRP) as a reference. Recently, the methods for determining the fracture toughness values of bonded joints have been extended to not only similar-material adhesive joints but also dissimilar-material adhesive joints [85–98].

- **JIS. K 7086:1993**, Interlaminar fracture toughness test method for carbon fiber-reinforced plastics.
- **ISO 15024:2001**, Fiber-reinforced plastic composites—Determination of mode I interlaminar fracture toughness, GIC, for unidirectionally reinforced materials.
- **ASTMD 5528-01**, Standard Test Method for Mode I Interlaminar Fracture Toughness of Unidirectional Fiber-Reinforced Polymer Matrix Composites; ASTM: West Conshohocken, PA, USA, 2001.
- **ISO 25217:2009**, Adhesives—Determination of the mode 1 adhesive fracture energy of structural adhesive joints using double cantilever beam and tapered double cantilever beam specimens.
- **ISO 22838:2020**, Composites and reinforcements fibers—Determination of the fracture energy of bonded plates of carbon fiber reinforced plastics (CFRPs) and metal using double cantilever beam specimens.

The details for the fracture toughness (G_{1c}) evaluation tests of Mode I are outlined in other studies [85, 94]. The parameter that is directly related to the fracture toughness value (G_{1c}) when a load is applied to the adherend in the vertical direction is the crack propagation rate, and it is important to precisely determine the crack tip location. However, the crack tip is very small and difficult to see, and the conventional method of visual inspection is not only labor-intensive, but also potentially prone to human error. To solve this problem, stress luminescence paint was simply applied to the DCB specimen as shown in Fig. 39a. The proposed method can be successfully employed to detect the crack tip location and fracture front with a high accuracy by visualizing the stress concentration at the crack tip in the bond line using mechanoluminescence, as shown in Fig. 39b [82].

This result supports the fact that the ML point reflects the crack tip accompanied by the fracture, crack propagation, and delamination of the DCB specimen. Using these experimental values, the sample values, and Eq. (2) [82, 85, 94], the fracture toughness G_{1c} (kJ/m^2) was calculated, as shown in Fig. 39c.

$$G_{1c} = \frac{3}{4H} \left(\frac{Pc}{B} \right)^2 \frac{(B\lambda)^{\frac{2}{3}}}{\alpha_1} \quad (2)$$

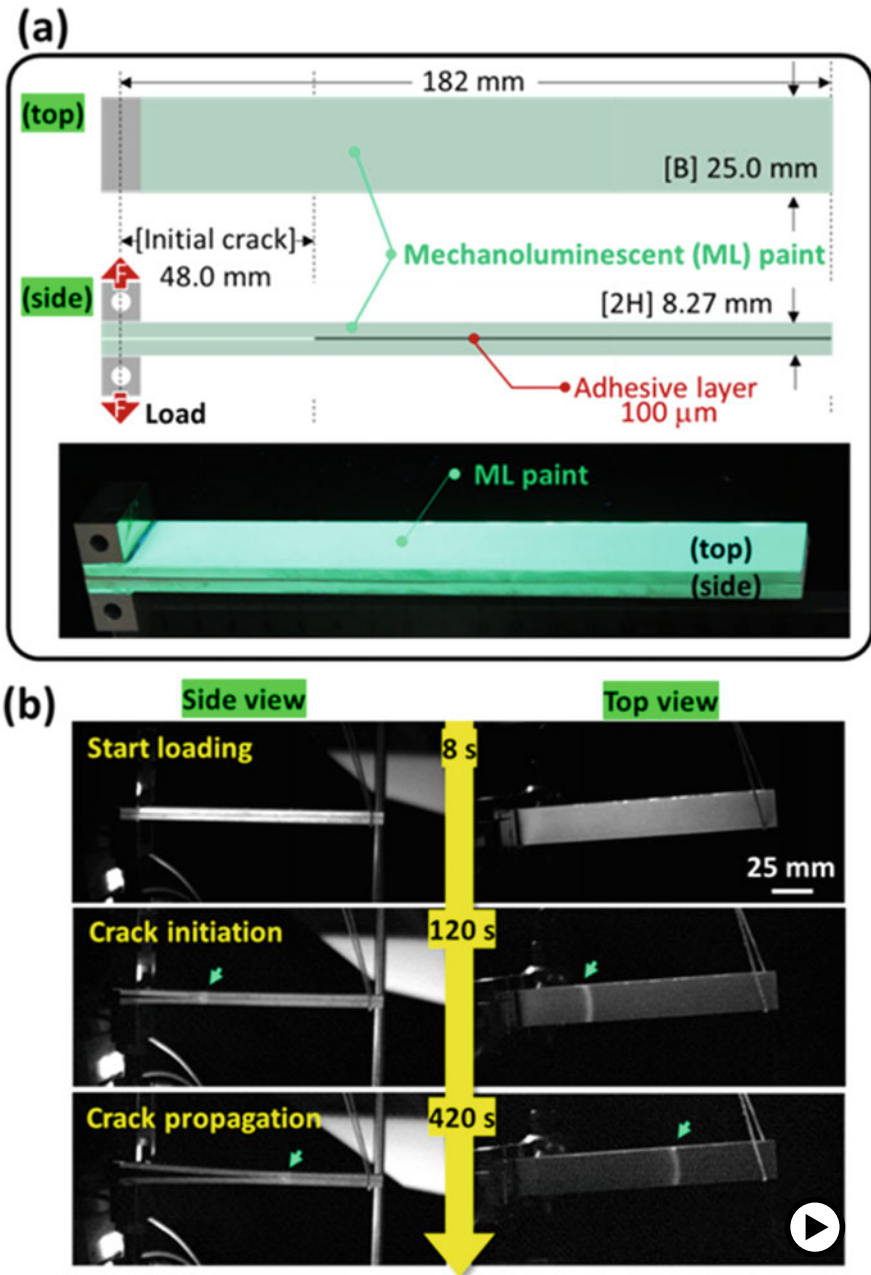


Fig. 39 Mechanoluminescence visualization of the mechanical behavior related to the adhesion using a double cantilever beam (DCB) test, that is, mode I Fracture toughness value evaluation (► <https://doi.org/10.1007/000-az7>)

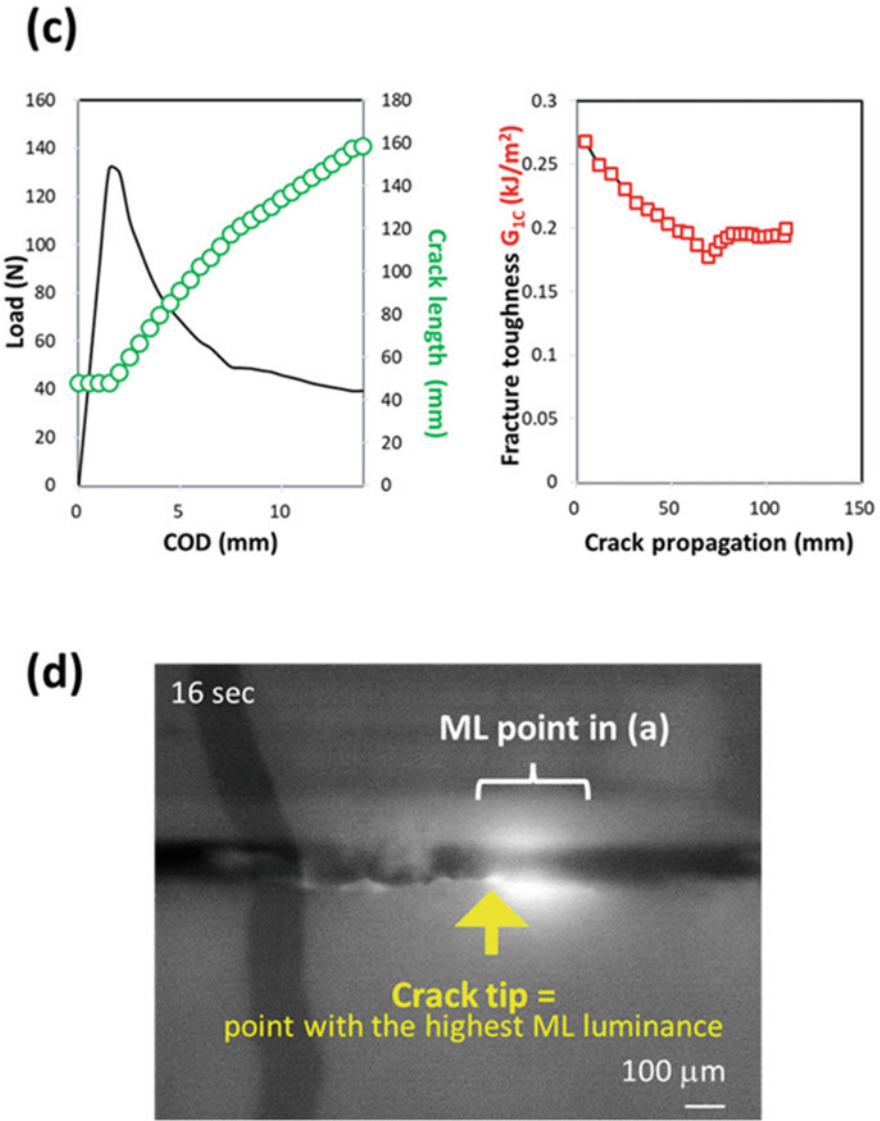


Fig. 39 (continued)

where $2H$ is the thickness (mm) of the DCB specimen, P_c is the load (N), B is the width of the specimen, λ is the COD compliance (mm/N), and α_1 is the slope of $(a/2H)$ and $(B/\lambda)^{1/3}$.

To demonstrate the accuracy of the ML method in identifying the crack tip using mechanoluminescence, microscopic observations were performed on the sidewall of the specimen during the mechanoluminescence-assisted DCB test. Notably, the point

with the highest mechanoluminescence could be observed approximately 0–20 μm in front of the crack tip, as shown in Fig. 39d. This result clearly demonstrates that mechanoluminescence accurately reflects the position of the crack tip even on a microscopic scale. In addition, intense mechanoluminescence was observed 0–300 μm in front of the crack tip, which may be due to the effect of microcracks in the process zone [85, 92].

Subsequently, to clarify the origin of mechanoluminescence (ML) line in the top view as the failure front propagated at the inner bond line in Fig. 39b in chapter “Interfacial Phenomena in Adhesion and Adhesive Bonding Investigated by Electron Microscopy”, ML sensing in the top view and bright image monitoring from the bottom view were simultaneously performed in the new DCB test, as shown in Fig. 40 [83].

For this experiment, DCB specimen was made of polycarbonate (PC) transparent substrate and 2-component epoxy adhesive, ML paint sensor was applied on the only upper surface, and the bottom surface was intently maintained clear to be able to monitor the failure front at inner bond line from outside as shown in Fig. 40a. For stable recording of the bright images (BI) with ML simultaneous sensing was performed using a red LED with a wavelength of 633 nm as the light source, as shown in Fig. 40b. Red light with wavelength values higher than 600 nm have no influence on the $\text{SrAl}_2\text{O}_4:\text{Eu}^{2+}$ ML material and its emission behavior; however, their used results in noisy when recorded using a CCD camera. Therefore, a bandpass filter was applied to CCD 1, allowing only green mechanoluminescence to be captured and cutting off red light from the LED (633 nm).

Consequently, the ML line on the outside surface of the adherend was found to perfectly synchronize with the failure front for deamination occurring in the bond line during the entire DCB test, as shown in Fig. 40c [83].

The ML line originates from the strain concentration owing to the bending deformation of the adherend with a crack-opening displacement. These results are supported by the study results on the substrate deflection within the crack vicinity [98], and those on the crack front process zone [92]. Based on the results, it can be concluded that: (1) the ML line reflects the shape of the adhesive failure front line as a balance point for the strain concentration in the adherend, and (2) the ML sensing of the top view of the adherend can be utilized as a monitoring indicator for the behavior and fracture toughness distribution at the crack front line from the outside surface of the adherend.

To confirm the coverage of the crack propagation mechanoluminescent (ML) visualization method for joint evaluation, the proposed method was applied in the DCB test using adhesive specimens and various types and combinations of materials, thickness, and surface pre-treatment to confirm the mechanoluminescent visualization of crack propagation, as shown in Fig. 41.

The method for determining the fracture toughness energy (G_c) is summarized in the international standard for dissimilar-material joints [94].

For a case whereby the deformation energy factor and difference in the bending stiffness of both adherends need to be excluded, a tapered DCB test has been proposed for the evaluation of the fracture toughness [99, 100].

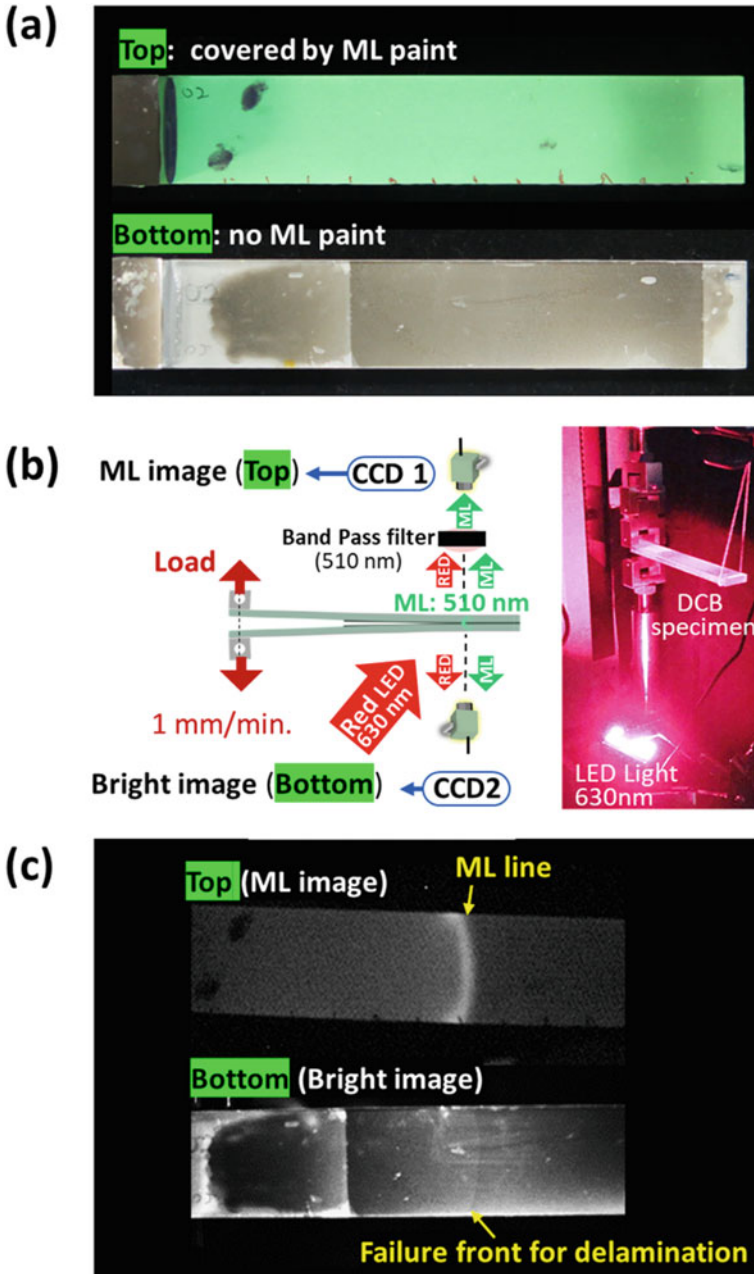


Fig. 40 Mechanoluminescence visualization of the delamination failure front at the inner adhesive layer from the outside of the adherend. **a** Photo of the specimen, **b** schematic illustration of the experimental set-up, and **c** comparison of the ML image of the top view and bright image of the bottom view

	GC	adherend 1			adhesive		adherend 2			ML results
	NokJ/m ²	Material	Thickness (mm)	Pre-treatment	adhesive	Thickness (mm)	Material	Thickness (mm)	Pre-treatment	
Similar material bonding	1	Aluminum A5052	3	nano-molding tech. (NMT)	2C-Epoxy (Denatite 2204)	0.1	Aluminum A5052	3	NMT	
	2					1				
	3				0.1					
	4				1					
	5	0.31	HTSS (980 MPa class)	1.6	NMT	2C-Epoxy	0.1	HTSS (980 MPa class)	1.6	
	6	0.52				2C-Urethane	0.1			
	7	0.08	CFRTP (twill)	3	Flame	2C-Epoxy (Denatite 2204)	0.1	CFRTP (twill)	3	
	8	0.11					1			
	9	1.48				0.1				
	10	0.81				1				
Dissimilar material bonding	11	CFRTP (twill)	3	Flame	2C-Epoxy (Denatite 2204)	0.1	A5052	5	NMT	
	12		0.15					4		4
	13		0.17					2		5
	14	0.14	CFRTP (twill)	3	Flame	2C-Epoxy (Denatite 2204)	1	A5052	5	
	15	0.12		4					4	
	16	0.14		2					5	
	17	1.61	CFRTP (twill)	3	Flame	2C-Urethane (E-TEC, MG5000)	0.1	A5052	5	
	18	2.21		4					4	
	19	1.21		2					5	
	20	1.35	CFRTP (twill)	3	Flame	2C-Urethane (E-TEC, MG5000)	1	A5052	5	
	21	1.18		4					4	
	22	0.95		2					5	
	23	-	CFRTP (UD)	3	Flame	2C-Urethane (E-TEC, MG5000)	0.1	A5052	5	
	24	-					1			
	25	0.18	CFRTP (twill)	3	Flame	2C-Epoxy (Denatite 2204)	0.1	A5052	5	
	26	0.09		4					4	
	27	0.17		2					5	

Fig. 41 Sample list for confirming the usability of the mechanoluminescent visualization method of the crack propagation for joint evaluation

Figure 42 shows the load-COD curves, microscopic ML images in (1)–(3), and ML images recorded at the time shown in (4)–(7) using the TDCB specimen.

The load–COD curves show a linear behavior owing to the designed curve shape of the adherends during the TDCB test, in which $d\lambda/da$ remained constant throughout all propagation stages [83].

This result is similar to that in the ML observations wherein only a slight mechanoluminescence is observed from the adherend itself, and that wherein the mechanoluminescence is only observed from the area of the bond line, as shown in Fig. 42 (4)–(7). This indicates that a small strain occurs on the adherend during the TDCB test, and most of the loading energy must be provided for the adhesive to be deformed and for rupture to occur for crack propagation. Regarding the ML behavior on the bond line, the ML area (ca. 10 mm) in the TDCB test is much longer than that used in the DCB test (ca. 200 μm), as shown in Fig. 38, even under the same material conditions using aluminum (Al) and an epoxy adhesive (Denatite 2204, Nagase Chem.). To clarify the deformation and rupture phenomena in the long ML area, microscopic observations were performed, as shown in Fig. 42 (1)–(3). In the case of the DCB specimen, the ML area was located immediately in front of the crack tip, even in the microscopic image, as shown in Fig. 39d. In contrast, many microcracks were simultaneously generated in the wide failure process zone (FPZ) accompanied by mechanoluminescence, as recorded in sub-figures (1) and (2) of Fig. 42, and the cracks generated connected to create an open crack, as shown in sub-figure (3) of Fig. 42. For example, although the failure process zone tends to become longer in the case of a thinner bond line [30], the adhesive thickness is almost the same for both the DCB and TDCB specimens. Thus, it can be considered that the long ML area originated from a much smaller crack-opening displacement and angle in the case of the TDCB specimen because of the higher stiffness in the adherend compared to that in the DCB specimen.

Furthermore, mode II crack propagation was successfully monitored for the first time using mechanoluminescence in the end-notch flexure (ENF) test, which is a mode II fracture toughness evaluation method (Fig. 43). In investigation of mode II crack propagation using methods such as the ENF test, only shear forces are generated at the crack tip, and crack expansion does not occur at all. Therefore, detecting the crack tip using this method is more difficult and requires more skill than using the DCB tests with an opening mode load. However, the calculation of mode II fracture toughness (G_{2c}) requires information on the crack length, as shown in Eq. (3), and crack tip monitoring is indispensable.

$$G_{2c} = \frac{9P^2Ca^2}{2B(2L^3 + 3a^3)} \quad (3)$$

where $2H$ is the thickness (mm) of the DCB specimen, Pc is the load (N), B is the width of the specimen, λ is the COD compliance (mm/N), and α_1 is the slope of $(a/2H)$ and $(B/\lambda)^{1/3}$.

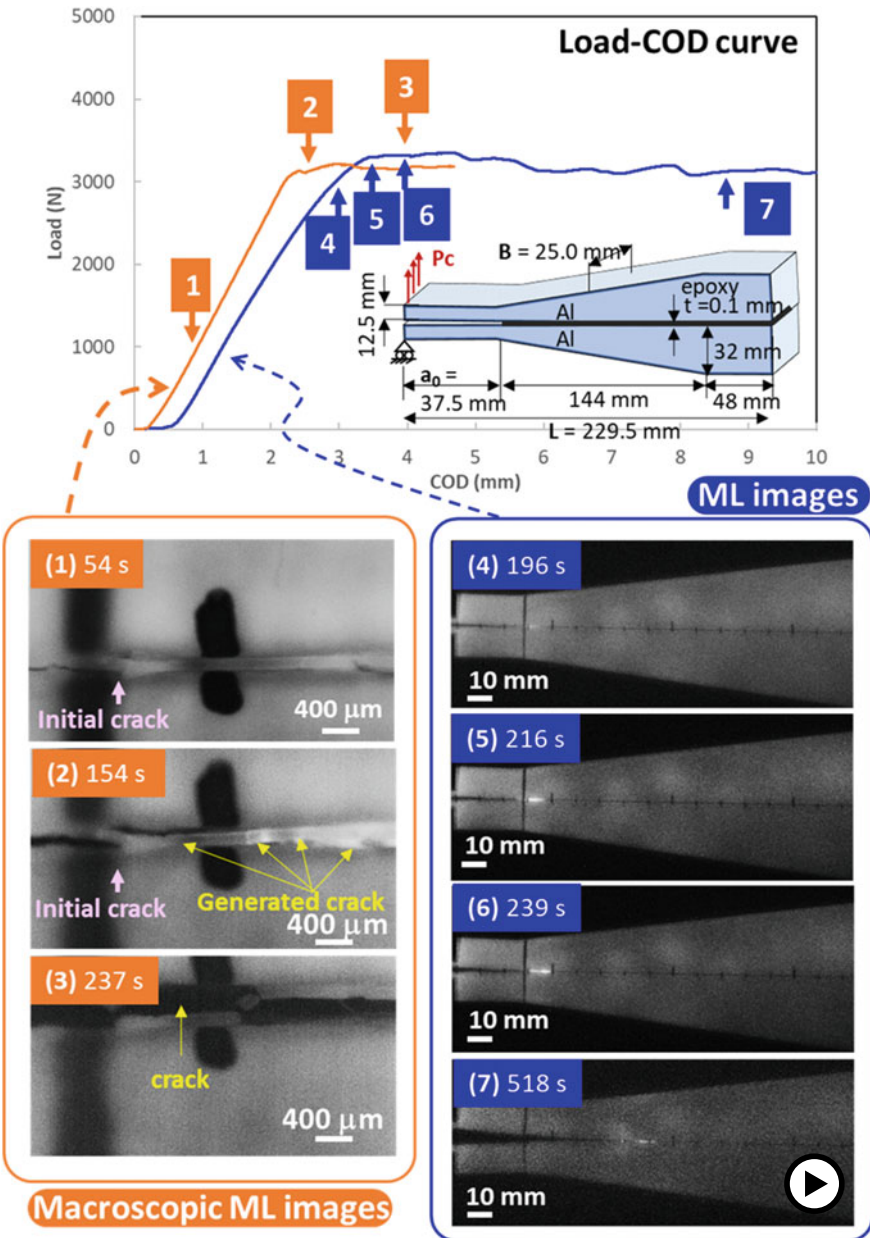


Fig. 42 ML studies of the TDCB test: a load–COD curves using TDCB specimens, b microscopic ML images, and c macroscopic ML images (► <https://doi.org/10.1007/000-az8>)

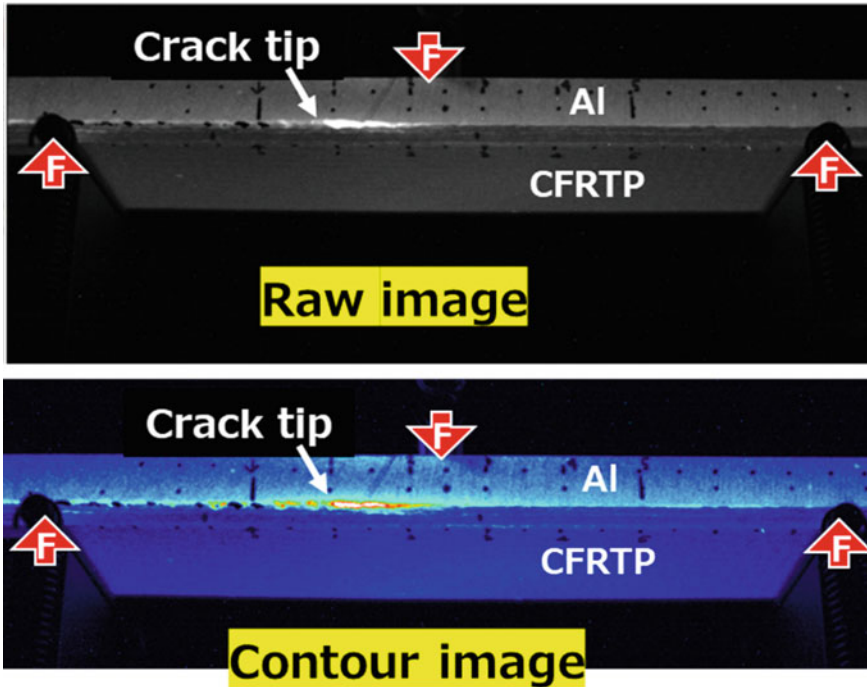


Fig. 43 Mechanoluminescence (ML) visualization of crack tip in propagation during ENF test, to obtain mode II fracture toughness

Mechanoluminescence (ML) monitoring was conducted based on the assumption that ML sensing is a method for detecting the strain concentration, not the presence of a crack, which is highly detectable. Figure 43 shows the ML crack monitoring of an aluminum substrate (A5052) and thermoplastic CFRTP cured using a two-component epoxy adhesive to which an ML paint sensor was applied and loaded under the loading conditions of a typical ENF test.

The results showed that a long ML pattern originating from the shear force in the adhesive layer around the crack tip is observed along the bond line. A careful inspection of the upper adherend surface reveals that there is ML emission in the compression plane (upper side) and tension plane (lower side) around the loading point, and no ML emission occurs in the stress-neutral plane. Additionally, the crack tip was successfully identified as the tail of the ML emission line (highlighted by the arrow) in the raw and counter images, which was confirmed by microscopic observations. This achievement is expected to make a significant contribution to the composite and adhesive industries, where interlaminar fracture toughness is frequently evaluated.

5.2 Tensile Shear Strength (TSS) Test of Adhesive Joint

The tensile shear strength (TSS) test (lap-shear test) was performed on the adhesive joints in accordance with the following international standards [48, 85, 101–108].

- **ISO 4587:2003**, Adhesives—Determination of tensile lap-shear strength of rigid-to-rigid bonded assemblies.
- **JIS K 6850**, Adhesives—Determination of tensile lap-shear strength of rigid-to-rigid bonded assemblies, consistent with ISO 4587.
- **ASTM D5868-01(2014)**, Standard Test Method for Lap Shear Adhesion for Fiber-Reinforced Plastic (FRP) Bonding.
- **ISO 22841:2021**, Composites and reinforcements fibers—Carbon fiber reinforced plastics (CFRPs) and metal assemblies—Determination of the tensile lap-shear strength.

Lap-shear adhesive joints are used in the majority of industrial adhesive-bonded members. Because shear forces, which require a strong external force for fracture, are applied, and because the stiffness can be controlled based on the bonding area, tensile loads and shear forces are incorporated into the design bonded joint. However, when a tensile load is applied to a simply bonded joint, a high-stress concentration is originally generated at the edge of the lapped adhesive area, and a bending moment is generated causing crack initiation and delamination from the edge; thus, it is said that fracture is induced with a weaker force. Therefore, the key point of the design should be to suppress the occurrence of stress concentration and, in particular, the occurrence of cracks. As mentioned above, since this is the most commonly used adhesive material form in industry, many studies have been conducted on the effects of adhesives, adherends, and surface treatment, and the adhesive thickness, lap-length of the adhesive area, simulation, and fracture mechanism analysis. Although there are various results and considerations regarding this, there are no examples of actual observations of the mechanical behavior during fracture. Therefore, the visualization of the mechanical behavior using mechanoluminescence is proposed.

Figure 44 shows an example of the mechanoluminescence (ML) evaluation during the lap-shear test. The specimens comprised sandblasted aluminum plates (A6061) bonded using a structural epoxy adhesive (adhesive layer thickness of 100 μm and TSS of 22 MPa) [48]. An ML coating sensor was applied near the adhesive bonding area of interest, and mechanoluminescence during tensile load application was recorded from four specimen directions (front, back, right side, and left side) using the four-way camera system shown in Fig. 9. Figure 44b shows the time course of the ML images obtained from the four specimen directions, which is presented as a contour image to easily distinguish the change in the ML pattern and luminance. Figure 44b shows that, along with the strain distribution on the adherend, there is a strong stress concentration at the top and bottom edges of the adhesive layer (2.7 s), peel propagation from the top and bottom edges of the adhesive layer toward the center (5.7–10.3 s), and adhesive rupture (13.8 s or later) where the cracks connect at the center. Interestingly, apart from the strain concentration at the top and bottom edges,

the crack propagated across the adhesive layer (5.7 s) and cohesive failure of the thin layer near the adhesive interface were observed in real time via mechanoluminescence. In addition, the ML lines on the front and back surfaces moved from the top and bottom edges to the center (5.7–10.8 s) in conjunction with the mechanoluminescence observed on the right and left sides, which was derived from the crack propagation on the top and bottom edges to the center. Similar to the DCB test, this was considered to be an external observation of crack and delamination propagation within the adhesive layer. Crack propagation across the adhesive layer at 5.7 s was observed in real time via ML measurement under a microscope (Fig. 44c). From the results of the examination of the remaining adhesive layer thickness, and the optical and microscopic observations of the fracture surface, it is clear that the failure mode is thin-layer cohesive failure (TCF), which is consistent with the failure process considerations in previous studies. The mechanoluminescence results presented here are the first examples of the real-time monitoring of mechanical and crack propagation behaviors during the fracture process.

The mechanism described above, that is, stress concentration at the edge, crack propagation toward the center, and rupture across the adhesive layer, is invisible in well-fabricated structural adhesive members. This is because when the interface strength and fracture toughness value are sufficiently high, the crack propagates and ruptures rapidly after crack initiation. To clarify this phenomenon, a mechanoluminescence (ML) test was performed using a low-strength specimen (TSS value of 0.8 MPa) consisting of polycarbonate (PC) bonded with the same structural epoxy adhesive (adhesive layer thickness: 100 μm) and without any pre-surface treatment, as shown Fig. 45 [48].

Generally, the TSS value is typically employed as the index for the adhesive strength; however, insufficient research has been conducted on the events in the load-stroke diagram, which are not required to be reported in the standards. In contrast, when checking the mechanoluminescence in the failure process, the mechanical behavior during the lap-shear test can be visualized and events in load-stroke curves and changes in the ML patterns can be considered. In reality, the stress is first concentrated at the top and bottom edges as shown in range A in the load-stroke curve. Subsequently, cracks and delamination propagate near the adhesive layer from the top and bottom edges to the center, as shown in range B, and to obtain the TSS value, the adhesive is loaded and ruptures along the adhesive layer at the center (range C) from the crack connection. Using ML visual sensing as an example, the mechanical events behind the adhesive strength index, referred to as the TSS value, can be intuitively visualized to instinctively understand and respond to the changes in the load-stroke diagram.

Similar to the lap-shear test, the peel test is often used in the industrial adhesion evaluation of tape or thin adherend joints [109]. This test is effective for measuring the strength under loading conditions that imitate those of actual structural members. In addition, it supports the use of a general tensile testing machine without a special jig and allows the determination of the peel strength from the load value at a constant load state in the load-stroke curve. However, similar to the lap-shear test, it is difficult to capture the energy theory because all the input energy is not used to fracture

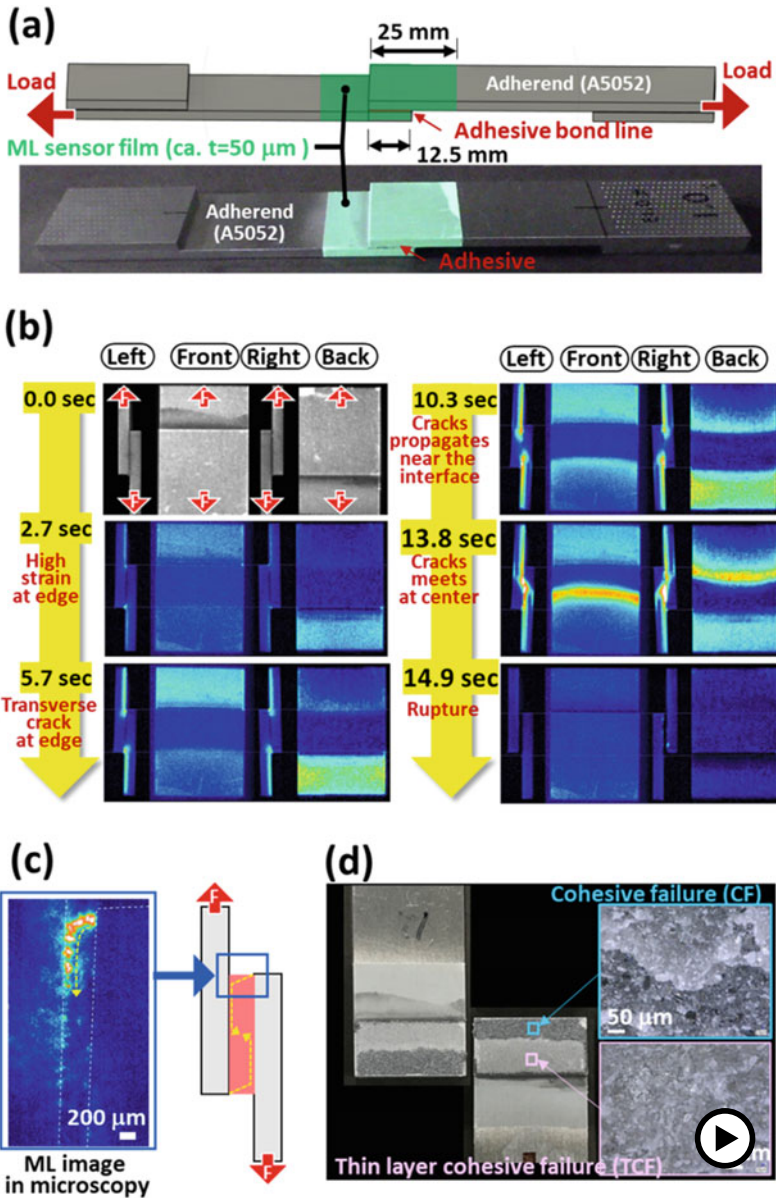


Fig. 44 ML visualization of the lap-shear (LS) tensile shear strength test for a single lap adhesive joint. **a** Illustration and photo of the specimen used in the LS mechanoluminescence (ML) test. **b** Time course for the ML image during the LS test. **c** Microscopic ML observation and illustration of the destruction process in the adhesive layer. **d** Photos and microscopic observations of the fracture surface (► <https://doi.org/10.1007/000-az9>)

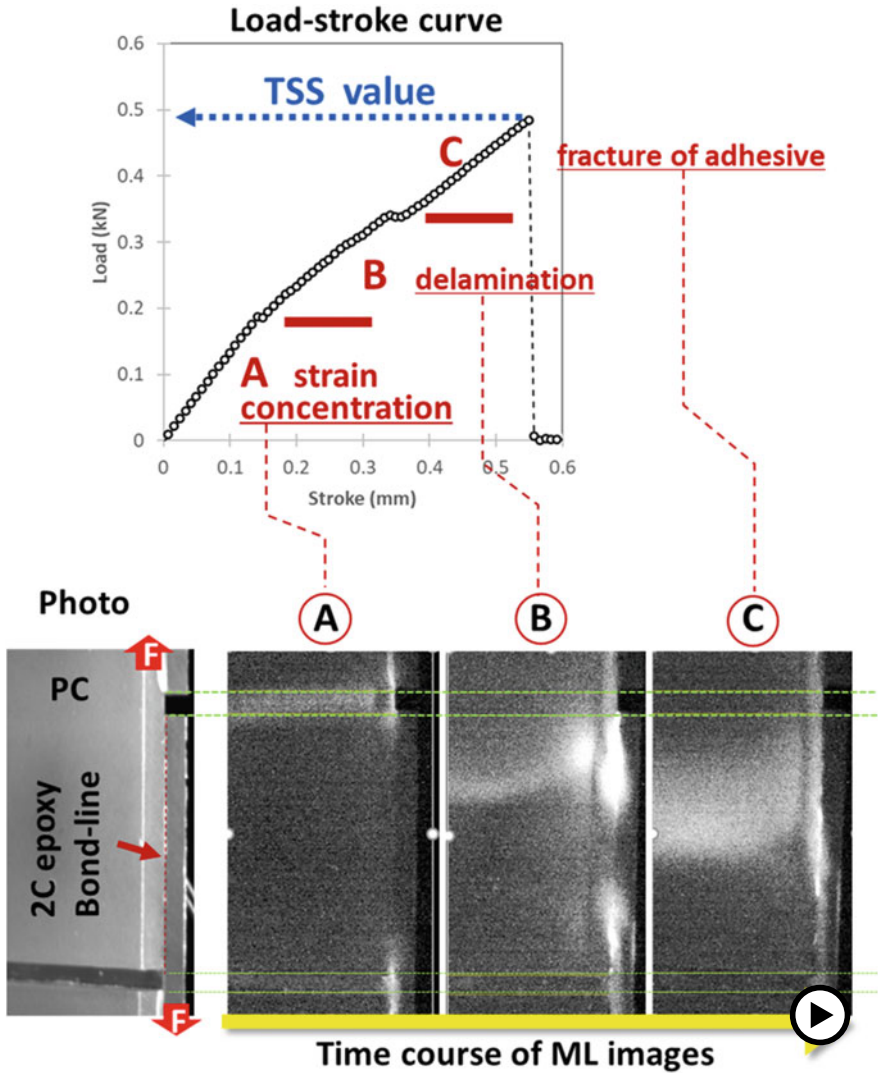


Fig. 45 Visualization of mechanical behavior during lap-shear test through mechano-luminescence to consider event in load-stroke curve and change in ML patterns (► <https://doi.org/10.1007/000-aza>)

the adhesive layer because some of it is used for the deformation of the specimen. Therefore, the input energy is mainly used for the deformation and vertical movement of the adherend rather than for peel propagation in the adhesive layer (Fig. 46). This indicates that it is important to use the peel strength as the strength index to consider the deformation of the adherend.

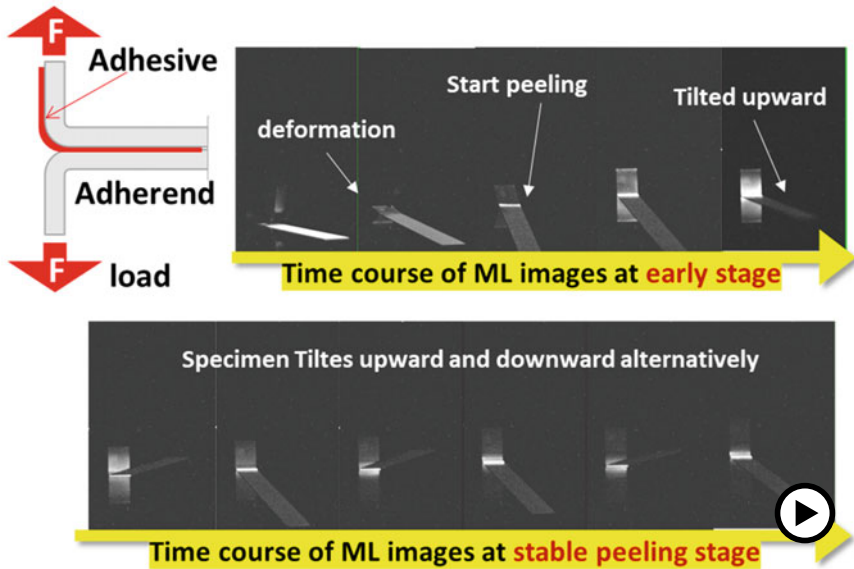


Fig. 46 ML visualization during peel tests. The adherend is an Al thin substrate with a thickness of 0.5 mm (► <https://doi.org/10.1007/000-azb>)

5.3 Cross-Tension Strength (CTS) Test of Adhesive Joint

Cross-tension strength (CTS) tests are often used for resistance spot welding in the automotive industry. A CTS test is required even for adhesive joints and is tested in accordance with the following international standards [110].

- **ISO 24360:2022**, Composites and reinforcements fibers—Carbon fiber reinforced plastics (CFRPs) and metal assemblies—Determination of the cross-tension strength.
- **ISO 14272:2016**, Resistance welding—Destructive testing of welds—Specimen dimensions and procedure for cross-tension testing of resistance spot and embossed projection welds.

Figure 47 shows the results of a study on the optimization of test specimens for the evaluation of the cross-tension tests on dissimilar-material bonded joints using carbon fiber-reinforced plastic (CFRTP) and aluminum substrate as adherends. The evaluation was performed according to strength tests, mechanical simulations, and mechanoluminescence using bonding areas of different shapes and sizes. In the strength test, the specimens with square bonding areas, which are often used in adhesive specimens, had significantly scattered CTS values, and those with circular bonding areas were successful in minimizing scattering [84].

The simulation results suggest that the stress concentration occurs evenly with the load (up and down arrows) from the four corners in the adhesive layer (Fig. 47;

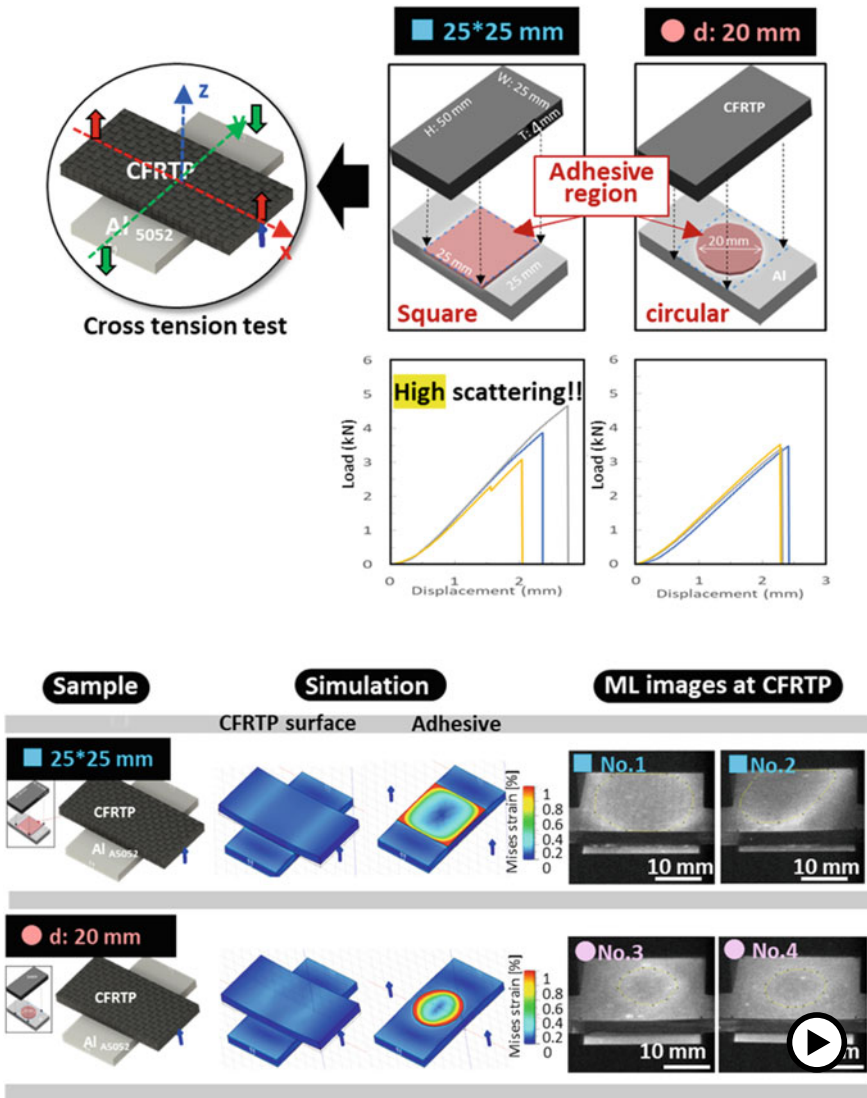


Fig. 47 Cross-tension test for the adhesive-bonded joint. Optimization of the joint design through mechanical testing, simulation, and mechanoluminescence (ML) visualization for dissimilar-material joints such as Al and thermoset CFRP (CFRTP) (► <https://doi.org/10.1007/000-azc>)

red area in the simulation image) and spreads to the four edges to induce uniform peeling from the four corners. Similarly, in the mechanoluminescence (ML) image, the luminescence from each of the four corners and four edges connect to form an ML circle that decreases in size and moves toward the center before breaking (Fig. 47; ML image for sample No. 1). This suggests that exfoliation occurs from the outer

periphery and propagates toward the center before rupture occurs. In contrast, the problem with performing the cross-tensile test using adhesion is that the CTS value is not constant even though the specimens were prepared in the same way. This was further verified using mechanoluminescence, where it was shown that in specimen **No. 1**, the ML circles are evenly generated from the periphery and move toward the center, whereas in specimen **No. 2**, the ML circles are unevenly distributed in one corner, which can easily lead to uneven delamination and large scattering of the CTS values. To solve the scattering caused by the uneven stress distribution and crack propagation, circular-shaped bonding areas were created. As a result, the ML circle generates a similar size and shape in every specimen as those in the examples of specimens **No. 3** and **No. 4**, before gradually decreasing in size with the tensile load, leading to rupture and causing the minimization of the scattering in the CTS value.

This result has been reflected in international standards and is a notable example of how the visualization of the stress/strain distribution is utilized to establish rules for testing.

5.4 Mapping of Weak Bond and Local Fracture Toughness

The disbonding areas and detection of the kissing bond in the adhesive layer, which are not visible from the outside, are described. Because adhesion defects cause various serious failures and accidents [111], X-ray and ultrasonic images are used to perform precise inspections during aircraft inspection, automobile manufacturing, and structural material manufacturing [64, 65]. However, although X-ray and ultrasonic images are promising for detecting delamination and voids, it is still difficult to detect the “kissing bonds,” the areas that appear to be bonded but do not exhibit adhesive strength, and the areas without defects or delamination. Therefore, a new method based on new principles is required for detecting “weak bonding adhesion.” To address this issue, the use of mechanoluminescence as a new detection method was proposed, and different mechanoluminescence (ML) patterns representing good and bad adhesion were successfully obtained (Fig. 48) [68, 80].

In this case, transparent polycarbonate (PC) was intentionally used as the adherend, and epoxy adhesive (black) was used to bond the adherend so that adhesive defects could be observed. Figure 48 shows the ML patterns of good and disbonded samples during tensile testing using the ML sensor sheet attached to adhesive joints, visual photographs, and numerical analysis of the von Mises strain distribution (FEM) results. First, mechanoluminescence was observed in the entire tangential region of well-bonded specimens with all the joint parts safely glued together (Fig. 48a).

However, for the specimen with adhesive failure in the center of the joint area, a specific ML pattern was observed only in the area corresponding to the adhesive area (in this case, the edge of the tangent joint area) (Fig. 48b). This ML emission pattern changes when the adhesion area is changed and is effective in detecting disbonding areas. The presence of a disbonding area inhibits the propagation of stress/strain from the relative adherend, reflecting a change in the strain distribution on the outer

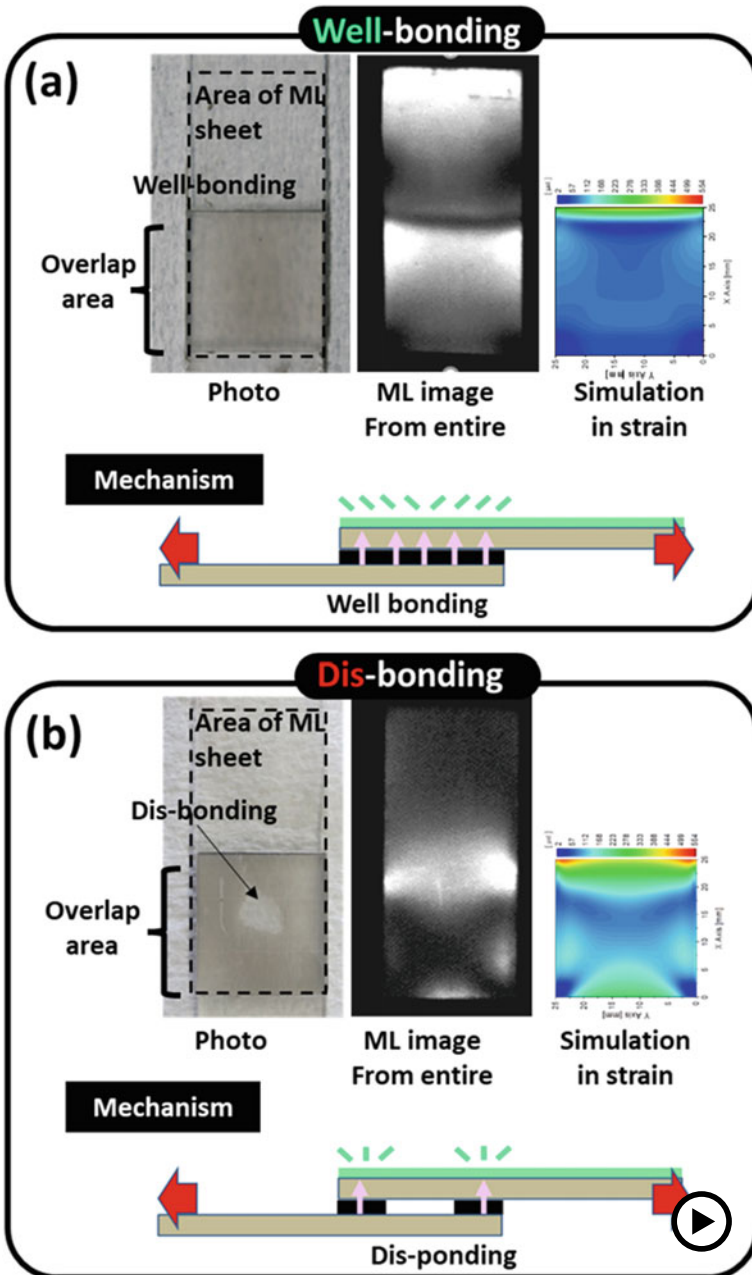


Fig. 48 Mechanoluminescence (ML) visual detection of the adhesion defects at the inner adhesive layer and mechanics for distinguishing them. **a** Good bonding, and **b** disbonding (► <https://doi.org/10.1007/000-azd>)

surface of the adherend to create a specific ML pattern, which is supported by the FEM analysis of the strain.

Additionally, adhesion strength tests using mechanoluminescence have been found to be effective even when using actual structural material systems. For example, in Fig. 49, an attempt was made to detect the local bond strength and interlaminar strength as the local fracture toughness in an actual aircraft-grade adhesively bonded member.

The target was a DCB specimen made of aircraft-grade CFRP (T800s/3900-2B, [45/0/-45/90]2s) and an epoxy adhesive sheet (FM309-1M, Solvay) assembly and prepared under aircraft-grade manufacturing conditions. For the mechanoluminescence (ML) test, an ML paint sensor was directly applied via air spraying. As mentioned earlier in Fig. 40, in a typical DCB test, the ML points associated with the crack tip at the lateral bond lines were monitored to calculate the fracture toughness value (G_{1c}) from the crack propagation rate.

However, to discuss the local fracture toughness of the adhesive assembly, mechanoluminescence from the top surface of the adherend was used in the analysis, which is associated with the failure front in the adhesive layer. Figure 49 shows an image of the mechanoluminescence at a certain time after starting the DCB test, a photograph of the fracture surface after the end of the DCB test, and a composite of both images.

In fact, local adhesion strength inspections often confirm the failure mode at the fracture surface, and there are many reports on the automation and use of AI analysis to promote quality assurance. Therefore, a comparative analysis between the mechanoluminescence (ML) images and fracture surface observation photographs was performed, and it was revealed that the strong ML line is in the cohesive failure (CF) region, and the weak ML line is in perfect agreement with the interlaminar failure (ILF) region at the fiber. Because of the different fracture toughness values in these regions, the cohesive fracture regions have a stronger ML luminescence and the luminescence lines progress more slowly.

The use of mechanoluminescence (ML) sensing is advantageous because it provides actual local fracture toughness mapping rather than just a value of the fracture toughness for each failure mode reported in other studies. In addition, adhesion evaluation tests that calculate the energy values such as the DCB and ENF tests should be performed under the assumption that all input energy is used to fracture the adhesive joint. In contrast, it has been found that mechanoluminescence can be used to externally detect unexpected and hard-to-notice microcracks, internal failures, and fiber fractures during the test. This proves that ML sensing is a promising method for effective adhesion evaluation.

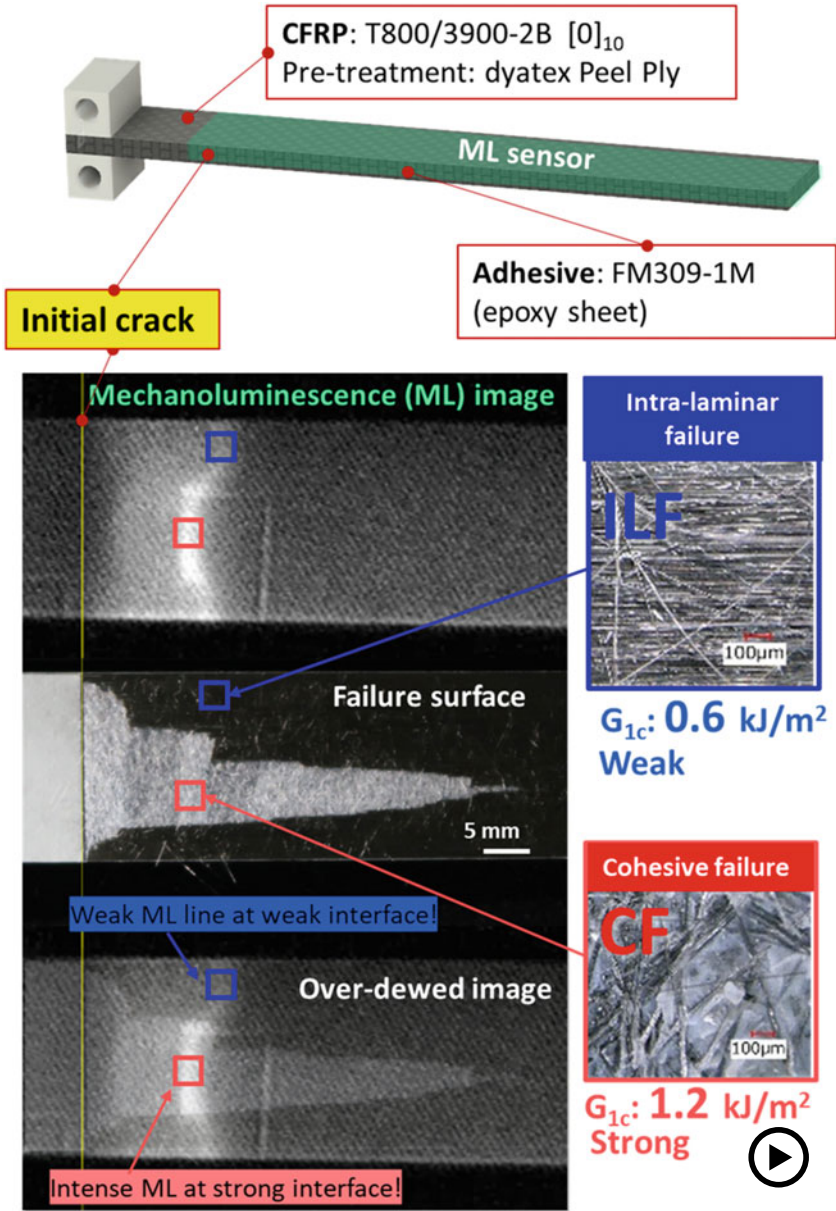


Fig. 49 Mechanoluminescent (ML) study of the local destruction mode and local fracture toughness on the aircraft CFRP-epoxy adhesive sheet assembly (► <https://doi.org/10.1007/000-aze>)

6 New Challenge for the Invisible Information on the Lightweight Structure

6.1 Toward the Appropriate Choice of Joints in the Multi-material Concept

Here, the mechanoluminescence (ML) studies on the appropriate choice of the various types of joints for lightweight structures in multi-material concepts are discussed.

The use of adhesives in automobiles is increasing every year [112]. In addition to controlling the rigidity and stiffness of the joints, adhesive bonding has the potential to be used for a variety of functions such as shock absorption, vibration absorption, sealing, and protection against electrical corrosion [74]. However, a combination of hybridization with other joining methods is currently the most promising approach. Therefore, mechanoluminescence (ML) sensing was used to reveal the advantages of hybrid joining by showing the advantages of each joint and its hybrid from a mechanical behavior visualization perspective.

Figure 50 shows a comparison of the mechanoluminescence during tensile testing for various joints such as adhesion, spot welding, and friction stir welding (FSW) [70]. Among these, adhesion was expected to have a stress-dispersing effect because mechanoluminescence is dispersed over the overlapped bonded area. However, once crack propagation begins at both ends of the bonded area, rupture can easily occur. The key to this design is to control the stress concentration, and the crack initiation and propagation. In contrast, spot welding and friction stir welding (FSW) exhibit extremely strong mechanoluminescence in the vicinity of the joining area, indicating a strong stress concentration as well as a strong joining strength. Therefore, the hybridization of strong joining and stress-dispersive adhesive bonding is a promising and smart approach. In the future, we plan on publishing results on the types of cases that show positive effects when hybrid bonding is used.

6.2 Static Electricity in Light Weighting Structure

In recent years, automobiles, airplanes, and flying vehicles have become lighter and more electrically powered and are now equipped with many plastic materials and sensitive semiconductors. As a result, the importance of antistatic electrostatic measures has increased, in addition to the importance of the mechanical behavior we have introduced so far. Static electricity generation is an extremely common phenomenon. Most people probably felt the spark (electrostatic discharge) when a charged object (such as a charged finger) was brought close to a metal, as shown in Fig. 51 [113, 114]. However, the electrostatic evaluation remains elusive. Conventional electrostatic sensors have difficulty measuring objects with uneven surfaces,

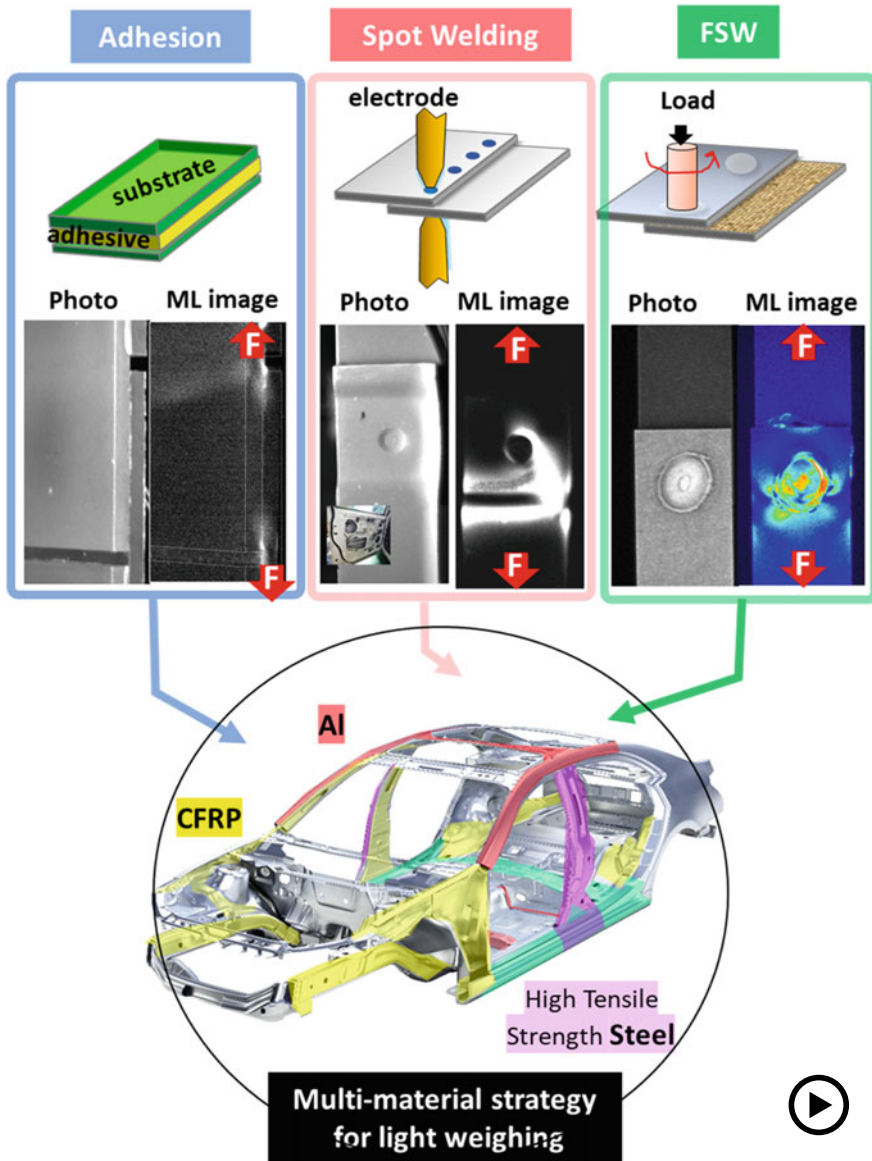


Fig. 50 Mechanoluminescence (ML) study on the appropriate choice of the various type of joints for lightweight structures in the multi-material concept (▶ <https://doi.org/10.1007/000-ayr>)

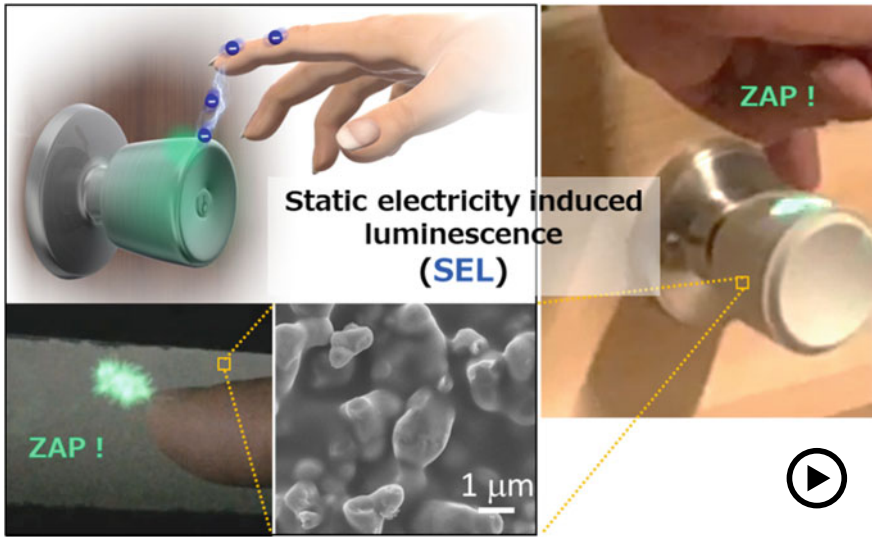


Fig. 51 Static electricity-induced luminescence (SEL): material and sensing (► <https://doi.org/10.1007/000-azg>)

moving objects, and objects in changing environments. Above all, the lack of intuitive means to understand static electricity, such as seeing it with the eyes or taking pictures with a camera, has made it a difficult problem to solve. This is also the reason why there are many industrial requirements for the inspection of static electricity. In contrast, we recently discovered that certain $\text{SrAl}_2\text{O}_4:\text{Eu}^{2+}$ (ceramic particles) function as static electricity-induced luminescence (SEL) materials for the first time in the world, emitting light in response to weak electricity from ions and charged particles in air. When the SEL sensor film was irradiated with corona discharge from an experimental static electricity-generating gun, green luminescence spread radially. When the surface potential distribution was measured after observation using a conventional sensor, the charged and luminous areas coincided. We also succeeded in detecting electrostatic discharges from the human hand, as shown in Fig. 51. In this way, the “invisible” problem that arises can be solved using adhesive bonding to contribute to the next generation of transportation such as in automobiles, aircraft, and railroads.

7 Concluding Remark

In this chapter, mechanoluminescence (ML) sensing technology that can visualize the mechanical behavior (strain distribution) that is inherently invisible to the naked eye is introduced. To understand the properties of ML sensing technology, innovative applications for infrastructure structural health monitoring (SHM) and advanced

design and prediction are introduced. Subsequently, to address the main issue in this chapter, the ML visualization of the mechanical behavior of adhesive joints and interfaces, fracture initiation points, and fracture processes, is performed according to internationally standardized adhesion strength evaluation tests. This is done to determine an index for representing the mechanical behavior behind the strength, thereby enabling it to be reflected in improvement, design, and prediction; in contrast to the current situation where only the adhesive strength is the primary focus. For this reason, there is increased interest to use mechanoluminescence as an international standard for bond strength testing and crack monitoring [115].

Furthermore, it is clear that the use of mechanoluminescence is a promising approach for visualizing the mechanical behavior at multiple scales and on different adhesive interfaces wherein the mechanical behavior cannot be directly evaluated.

In addition, discrepancies between the actual and predicted values, particularly in stress wave propagation during collision, high-strain deformation, composite fracture, and standing waves owing to different vibration modes, are challenges that should be addressed during the development of the next generation of lightweight and electrified mobility. The contents of this chapter indicate the ability and expectation of mechanoluminescence in contributing to solving the challenging issues mentioned above, where the frontier for the long-term stability of the adhesion is an essential specification for users.

Acknowledgements N. T. is grateful to Dr. Y. Fujio and Y. Sakata as collaborators, Ms. Y. Nogami and Ms. H. Kawahara for spraying the ML paint for ML testing. Additionally, N. T. is grateful to Ms. Y. Kato, Ms. M. Iseki, Ms. Y. Sugawa, Ms. C. Hirakawa, Ms. Y. Sakamoto, and Ms. S. Sano for assisting with ML measurements and analysis in the 4D visual sensing team (AIST) Part of this work was supported by New Energy and Industrial Technology Development Organization (NEDO) and the Research and Development Program for Promoting Innovative Clean Energy Technologies through International Collaboration (JPNP20005) commissioned by NEDO, a Grant-in Aid for Scientific Research, Innovative Science and Technology Initiative for Security, ATLA, Japan. and strategic innovation program (SIP).

References

1. C.N. Xu, T. Watanabe, M. Akiyama, X.G. Zheng, *Appl. Phys. Lett.* **74**, 2414–2417 (1999)
2. C.N. Xu, N. Ueno, N. Terasaki, H. Yamada, *Mechanoluminescence and Novel Structural Health Diagnosis* (NTS, Tokyo, 2012).
3. N. Terasaki, *Sens. Mater.* **28**(8), 827–836 (2016)
4. N. Terasaki, Movies of mechanoluminescence sensing, <https://www.youtube.com/watch?v=7fsA-POmKjA>
5. Mechanoluminescence (ML) Introduction in science view, broadcasted by NHK world, Protecting Infrastructure by Visualizing Stress, <https://www3.nhk.or.jp/nhkworld/en/tv/scienceview/20220222/2015274/>

6. ML movies in AIST official account on YouTube. (a) Mechanoluminescence paper cup, <https://www.youtube.com/watch?v=ose3T1Gd2SU>. (b) Mechanoluminescence under tensile load for perforated SUS631 specimen, <https://www.youtube.com/watch?v=PSzTvntGTM4>. (c) Mechanoluminescence during front collision test, <https://www.youtube.com/watch?v=JEIP-4Zv15w>
7. C.N. Xu, T. Watanabe, M. Akiyama, X.G. Zheng, *Appl. Phys. Lett.* **74**, 1236–1239 (1999)
8. C.N. Xu, X.G. Zheng, M. Akiyama, K. Nonaka, T. Watanabe, *Appl. Phys. Lett.* **76**, 179–181 (2000)
9. C.N. Xu, *Coatings. Encycl. Smart Mater.* **1–2**, 190–201 (2002)
10. Z. Hongwu, H. Yamada, N. Terasaki, C.N. Xu, *Electrochem. Solid State Lett.* **10**, 129 (2007)
11. Z. Hongwu, H. Yamada, N. Terasaki, C.N. Xu, *J. Electrochem. Soc.* **155**, J55 (2007)
12. Z. Hongwu, H. Yamada, N. Terasaki, C.N. Xu, *Appl. Phys. Lett.* **91**, 081905_1 (2007)
13. Z. Hongwu, H. Yamada, N. Terasaki, C.N. Xu, *Key. Eng. Mater.* **368**(372), 359 (2008)
14. Z. Hongwu, H. Yamada, N. Terasaki, C.N. Xu, *J. Electrochem. Soc.* **155**, J128 (2008)
15. Z. Hongwu, N. Terasaki, H. Yamada, C.N. Xu, *Int. J. Mod. Phys. B* **23**, 1028 (2009)
16. Z. Hongwu, N. Terasaki, H. Yamada, C.N. Xu, *Thin Solid Films* **518**, 610 (2009)
17. Z. Hongwu, N. Terasaki, H. Yamada, C.N. Xu, *Phys. E* **42**, 2872 (2010)
18. Y. Fujio, C.N. Xu, N. Terasaki, N. Ueno, *J. Lumin.* **148**, 89 (2014)
19. Y. Fujio, C.N. Xu, N. Terasaki, *ECS Trans.* **98**, 61 (2020)
20. Y. Fujio, C.-N. Xu, N. Terasaki, *J. Electrochem. Soc.* **168**, 047508 (2021)
21. X. Wang, C.-N. Xu, H. Yamada, K. Nishikubo, X.-G. Zheng, *Adv. Mater.* **17**(10), 1254–1258 (2005)
22. S.M. Jeong, S. Song, S.-K. Lee, N.Y. Ha, *Adv. Mater.* **25**, 6194–6200 (2013)
23. K.-S. Sohn, M.Y. Cho, M. Kim, J.S. Kim, *Opt. Express* **23**, 6073 (2015)
24. (As review) A. Feng, P.F. Smet, *Material* **11**, 484 (2018)
25. Z. Monette, A.K. Kasar, P.L. Menezes, *J. Mater. Sci. Mater. Electron.* **30**, 19675–19690 (2019)
26. M.V. Mukhina, J. Tresback, J.C. Ondry, A. Akey, A.P. Alivisatos, N. Kleckner, *ACS Nano* **15**(3), 4115–4133 (2021)
27. C. Li, Q. He, Y. Wang, Z. Wang, Z. Wang, R. Annapooranan, M.I. Latz, S. Cai, *Nat. Commun.* **13**, 3914 (2022)
28. (As review) Z. Huang, B. Chen, B. Ren, D. Tu, Z. Wang, C. Wang, Y. Zheng, X. Li, D. Wang, Z. Ren, S. Qu, Z. Chen, C. Xu, Y. Fu, D. Peng, *Adv. Sci.* **10**, 2204925 (2023)
29. K. Sakai, T. Koga, Y. Imai, S. Maehara, C.-N. Xu, *Phys. Chem. Chem. Phys.* **8**, 2819–2822 (2006)
30. N. Terasaki, K. Sakai, T. Koga, C. Li, Y. Imai, H. Yamada, Y. Adachi, K. Nishikubo, C.-N. Xu, *MRS Online Proc. Libr.* **951**, 933 (2006)
31. L.S. Forster, *Chem. Rev.* **90**, 331–353 (1997)
32. M. Grinberg, *Opt. Mater.* **19**, 37–45 (2002)
33. Z. Pan, Y.Y. Lu, F. Liu, *Nat. Mater.* **11**, 58–63 (2011)
34. T. Som, B. Karmakar, *J. Alloys Compd.* **476**, 383–389 (2009)
35. M.C. Silva, F.H. Cristovan, C.M. Nascimento, M.J.V. Bell, W.O. Cruz, A. Marletta, *J. Non-Cryst. Solids* **352**, 5296–5300 (2006)
36. P. Hong, X.X. Zhang, C.W. Struck, B.D. Bartolo, *Appl. Phys. Lett.* **78**, 4659–4667 (1995)
37. L.A.-Sorgho, H. Nozary, A. Aebischer, J.C.G. Bünzli, P.Y. Morgantini, K.R. Kittilstved, A. Hauser, V. Svetlana, S. Petoud, C. Piguët, *J. Am. Chem. Soc.* **134**, 12675–12684 (2012)
38. R. Weissleder, *Nat. Biotech.* **19**, 316–317 (2001)
39. P. Taroni, A. Pifferi, A. Torricelli, D. Comelli, R. Cubeddu, *Photochem. Photobiol. Sci.* **2**, 124–129 (2003)
40. C. Li, C.N. Xu, L. Zhang, H. Yamada, Y. Imai, *J. Vis.* **11**, 329 (2008)
41. N. Terasaki, C.N. Xu, H. Yamada, Y. Imai, *Jpn. J. Appl. Phys.* **46**, 2385 (2007)
42. N. Terasaki, C.N. Xu, *IEEE Sens. J.* **13**(10), 3999–4004 (2013)
43. N. Terasaki, C.N. Xu, C. Li, L. Zhang, C. Li, D. Ono, M. Tsubai, Y. Adachi, Y. Imai, N. Ueno, T. Shinokawa, *Proc. SPIE* **8348**, 2012, 8348D1 (2012)

44. A.I. Zad, M.R. Rahimi, G.J. Yun, Quantitative full-field strain measurements by SAOED (SrAl₂O₄:Eu²⁺, Dy³⁺) mechanoluminescent materials. *Smart Mater. Struct.* **25**(9), 095032–095046 (2016)
45. N. Terasaki, C.N. Xu, C. Li, L. Zhang, Y. Sakata, N. Ueno, K. Yasuda, L. Ichinose, in *Proceedings of 6th International Conference on Bridge Maintenance, Safety and Management*, vol. 6, (2012), p. 2542
46. N. Terasaki, C. Li, L. Zhang, C.N. Xu, in *Proceedings of the IEEE Sensors Applications Symposium 2012*, vol. 77 (2012)
47. N. Terasaki, C.N. Xu, *J. Colloid Interface Sci.* **427**, 62 (2014)
48. N. Terasaki, Y. Fujio, *J. Vis. Exp.* **191**, e64118 (2023). <https://doi.org/10.3791/64118>
49. N. Terasaki, C.N. Xu, *Thin Solid Films* **518**, 473 (2009)
50. N. Terasaki, Z. Hongwu, H. Yamada, C.N. Xu, *Chem. Commun.* **47**, 8034 (2011)
51. N. Terasaki, C.N. Xu, *Catal. Today* **201**, 203 (2013)
52. N. Terasaki Z. Hongwu, H. Yamada, C.N. Xu, *Jpn. J. Appl. Phys.* **49**, 04C150 (2009)
53. R.J. Sanford, *Principles of Fracture Mechanics* (Pearson Education Inc., New Jersey, 2003)
54. Y. Murakami, *Stress Intensity Factors Handbook* (Pergamon Press, Oxford, 1987)
55. A. Shimamoto, H. Ohkawara, S.M. Yang, D.K. Choi, S. Akamatsu, *J. Jpn. Inst. Metals* **73**(7), 542–547 (2009)
56. Y. Fujio, C.N. Xu, Y. Terasawa, Y. Sakata, J. Yamabe, N. Ueno, N. Terasaki, A. Yoshida, S. Watanabe, Y. Murakami, *Int. J. Hydrogen Energy* **41**, 1333–1340 (2015)
57. Y. Fujio, C.-N. Xu, Y. Sakata, N. Ueno, N. Terasaki, *J. Alloys Compd.* **832**, 1 (2020)
58. Y. Fujio, C.N. Xu, M. Nishibori, Y. Teraoka, K. Kamitani, N. Terasaki, N. Ueno, *J. Adv. Dielectr.* **4**, 1450016 (2014)
59. C.M. Dry, in *Proceedings of the SPIE, Smart Structures and Materials 1999: Smart Systems for Bridges, Structures, and Highways*, vol. 3671 (1999), pp. 253–256
60. C.M. Dry, *Cem. Concr. Res.* **30**, 1969–1977 (2000)
61. T.C. Miller, M.J. Chajes, D.R. Mertz, J.N. Hastings, *J. Bridge Eng.* **6**(514), 0702 (2001)
62. U. Meier, *Appl. Compos. Mater.* **7**, 75–94 (2000)
63. K.B. Katnam, L.F.M. Da Silva, T.M. Young, *Prog. Aerosp. Sci.* **61**, 26–42 (2013)
64. P. Puthillath, J.L. Rose, *Int. J. Adhes. Adhe.* **30**, 5 (2010)
65. K. Diamanti, C. Soutis, *Prog. Aerosp. Sci.* **46**, 342–352 (2010)
66. K. Uzwa, *Forefront of CFRP Shaping, Processing, and Recycling Technologies* (NTS, Tokyo, 2015)
67. N. Terasaki, in *Proceedings of the International Committee on Aeronautical Fatigue and Structural Integrity, 2017* (2017), p. 1964
68. N. Terasaki, Y. Fujio, Y. Sakata, in *Proceedings of 29th International Committee on Aeronautical Fatigue and Structural Integrity (ICAF2017) Symposium*, vol. 75 (2017), p. 1961
69. N. Terasaki, Y. Fujio, Y. Sakata, S. Horiuchi, H. Akiyama, M. Abe, Y. Matsuki, H. Matuda, in *Extended Abstract of Annual Meeting of America Adhesion Society* (2019)
70. N. Terasaki, in *Proceedings of Joining in Car Body Engineering 2019*, vol. D1 (2019)
71. N. Terasaki, N. Ando, K. Hyodo, *Jpn. J. Appl. Phys.* **61**(SE), SE1009-1–SE1009-6 (2022)
72. N. Miyachik, D. Yugue, T. Fukazawa, Y. Nakamura, H. Mimura, M. Etoh, K. Akiyama, *Orthop. Traumatol.* **35**, 178 (1986)
73. A. Goel, V. Laheri, *Acta Neurochir.* **129**, 47 (1994)
74. A.D. Palma, F. Sollitto, D. Loizzi, F.D. Gennaro, D. Scarascia, A. Carlucci, G. Giudice, A. Armenio, R. Ludovico, M. Loizzi, *J. Thorac. Dis.* **8**, 490 (2016)
75. E. Munting, M. Verhelpen, *J. Biomech.* **28**, 949 (1995)
76. S. Märdiana, W. Schmölz, K.D. Schaser, G.N. Duda, M. Heylan, *Clin. Biomech.* **30**, 814 (2015)
77. M. Sonohata, Japan Patent P4572301 (2010)
78. T. Toyomasu, M. Sonohata, N. Terasaki, in *Extended Abstract of the International Conference on Solid State Devices and Materials, 2017* (2017), p. 955
79. N. Terasaki, T. Toyomasu, M. Sonohata, *Jpn. J. Appl. Phys.* **57**, 04FM10 (2018)
80. N. Terasaki, Y. Fujio, Y. Sakata, M. Uehara, T. Tabaru, *ECS Trans.* **75**, 9–16 (2017)

81. Y. Fujio, C.N. Xu, Y. Sakata, A. Yoshida, N. Ueno, N. Terasaki, *ECS Trans.* **45**, 23 (2017)
82. N. Terasaki, Y. Fujio, Y. Sakata, S. Horiuchi, H. Akiyama, *J. Adhes.*, **94**, 867–879 (2018) (Open access)
83. N. Terasaki, Y. Fujio, Y. Sakata, S. Horiuchi, H. Akiyama, *Int. J. Adhes. Adhes.* **93**, 40–46 (2019) (Open access)
84. N. Terasaki, Y. Fujio, H. Akiyama, S. Horiuchi, M. Itabashi, *J. Adhes.* **98**, 6, 637–646 (2022)
85. L.F.M. D da Silva, A. Öchsner, R. Adams, *Handbook of Adhesion Technology* (Berlin, Springer, 2011), which is published as 2nd edition in 2018
86. O. Ishai, H. Rosenthal, N. Sela, E. Drukker, *Composites* **19**, 49–54 (1988)
87. M.D. Bane, L.F.M. da Silva, R.D.S.G. Campilho, *J. Adhes. Sci. Technol.* **26**, 939–953 (2012)
88. Z. Chen, R. Adams, L.F.M. da Silva, *Int. J. Fract.* **167**, 221–234 (2011)
89. R. Trummer, E.A. Marques, F.J.P. Chaves, J.M.R.S. Tavares, L.F.M. da Silva, P.M.S.T. de Castro, *Materialwiss. Werkstofftech.* **42**, 452–459 (2011)
90. F.J.P. Chaves, L.F.M. da Silva, M.F.S.F.D. Moura, A.D. Dillard, V.H.C. Esteves, *J. Adhes.* **90**, 955–992 (2014)
91. M.F.S.F. Moura, J.P.M. Gonçalves, A.G. Magalhães, *Int. J. Adhes. Adhes.* **39**, 54–59 (2012)
92. N.B. Salem, M.K. Budzik, J. Jumel, M.E.R. Shanahan, F. Lavelle, *Eng. Fract. Mech.* **98**, 272–283 (2013)
93. C. Sarrado, A. Turon, J. Costa, J. Renart, *Int. J. Solids Struct.* **81**, 110–116 (2016)
94. Standardization documents. For example, (a) ISO 25217 “Adhesives—determination of the mode I adhesive fracture energy of structural adhesive joints using double cantilever beam and tapered double cantilever beam specimens”, (b) ASTM D5528-13 “Standard test method for mode I interlaminar fracture toughness of unidirectional fiber-reinforced polymer matrix composites”, (c) JIS K7086 “Testing methods for interlaminar fracture toughness of carbon fiber reinforced plastics”, (d) ISO 15024 “Fiber-reinforced plastic composites—determination of mode I interlaminar fracture toughness, GIC, for unidirectionally reinforced materials” etc.
95. T.K. O’Brien, *Compos. B* **298**, 57–62 (1998)
96. S. Horiuchi, H. Hakukawa, Y.J. Kim, H. Nagata, H. Sugimura, *Polym. J.* **48**, 473–479 (2016)
97. L. Ye, *Composites. Sci. Technol.* **43**, 49–54 (1992)
98. M.K. Budzik, J. Jumel, M.E.R. Shanahan, *J. Adhes.* **87**, 967–988 (2011)
99. P. Qiao, J. Wang, J.F. Davalos, *Eng. Fract. Mech.* **70**(2), 339–353 (2003)
100. J.M.D. Teixeira, R.D.S.G. Campilho, F.J.G. da Silva, *J. Adhes.* **94**, 951–973 (2018)
101. Standardization documents. For example, ISO 4587:2003, Adhesives—determination of tensile lap-shear strength of rigid-to-rigid bonded assemblies, (b) JIS K 6850, Adhesives—determination of tensile lap-shear strength of rigid-to-rigid bonded assemblies, consistent with ISO 4587, (c) ASTM D5868-01(2014), Standard test method for lap shear adhesion for fiber reinforced plastic (FRP) bonding, (d) ISO 22841:2021, Composites and reinforcements fibres—carbon fibre reinforced plastics (CFRPs) and metal assemblies—determination of the tensile lap-shear strength
102. R.D. Adams, N.A. Peppiatt, *J. Strain Anal. Eng. Des.* **9**, 185 (1974)
103. L.F.M. da Silva, *J. Adhes.* **82**, 1091 (2006)
104. A.A.-Safar, *Int. J. Solids Struct.* 109–189 (2017)
105. L.D.R. Grant, R.D. Adams, L.F.M. Da Silva, *Int. J. Adhes. Adhes.* **29**, 535 (2009)
106. J.H. Song, *Metals Mater. Int.* **7**, 467 (2001)
107. F. Kadioglu, *Mater. Sci. Eng.* **369**, 012034 (2018)
108. G. Li, *J. Manuf. Process.* **56**, 238 (2020)
109. Standardization documents. For example, (a) ISO 11339:2010, Adhesives—T-peel test for flexible-to-flexible bonded assemblies, (b) ISO 11339:1993 Adhesives—180 degree peel test for flexible-to-flexible bonded assemblies (T-peel test)
110. Standardization documents. For example, (a) ISO 24360:2022, Composites and reinforcements fibres—carbon fibre reinforced plastics (CFRPs) and metal assemblies—determination of the cross-tension strength, (b) ISO 14272:2016, Resistance welding—destructive testing of welds—specimen dimensions and procedure for cross tension testing of resistance spot and embossed projection welds

111. Aviation Investigation Report A05F0047, Loss of Rudder in flight
112. Adhesives and sealants market size, share & trends analysis report by technology, by product, by application, by region (North America, Europe, APAC, CSA, MEA), and segment forecasts, 2022–2030
113. K. Kikunaga, N. Terasaki **12**, 8524 (2022)
114. AIST press release, Direct visualization of invisible electrostatic distribution by emitting light (2022.6), https://www.aist.go.jp/aist_j/press_release/pr2022/pr20220602/pr20220602.html
115. ISO/CD 8065(en), Composites and reinforcements fibres—Mechanoluminescent visualization method of crack propagation for joint evaluation
116. N. Terasaki, K. Takagi, in Proceedings of 2nd International Conference on Industrial Applications of Adhesives, IAA2022 (2022), <https://web.fe.up.pt/~iaa2022/img/IAA2022%20Prog.pdf>

Open Access This chapter is licensed under the terms of the Creative Commons Attribution 4.0 International License (<http://creativecommons.org/licenses/by/4.0/>), which permits use, sharing, adaptation, distribution and reproduction in any medium or format, as long as you give appropriate credit to the original author(s) and the source, provide a link to the Creative Commons license and indicate if changes were made.

The images or other third party material in this chapter are included in the chapter's Creative Commons license, unless indicated otherwise in a credit line to the material. If material is not included in the chapter's Creative Commons license and your intended use is not permitted by statutory regulation or exceeds the permitted use, you will need to obtain permission directly from the copyright holder.



Analysis of Molecular Surface/Interfacial Layer by Sum-Frequency Generation (SFG) Spectroscopy



Takayuki Miyamae and Kouki Akaike

Abstract This chapter reviews recent progress in polymer surfaces and interface studies using sum-frequency generation (SFG) vibrational spectroscopy. SFG is a surface-specific vibrational spectroscopic technique that has spread on a worldwide scale since it was first reported in 1987. The SFG principles, instruments, techniques, and experiments are presented in detail, and recent results on interfacial physics and chemistry at jointed interfaces are described. It focuses on SFG studies of the surfaces and buried interfaces of polymeric materials, such as modification of polymer surfaces, polymer-water, polymer-metal, and polymer-polymer interfaces. This review demonstrates that SFG is a powerful technique for nondestructive, in situ measurement of molecular level understanding at complex polymer surfaces and interfaces.

Keywords Sum-frequency generation · Surface · Interface · Polymer · Molecular orientation

T. Miyamae (✉)

School of Engineering, Chiba University, 1-33 Yayoi-Cho, Inage-ku, Chiba 263-8522, Japan
e-mail: t-miyamae@chiba-u.jp

Molecular Chirality Research Center, Chiba University, 1-33 Yayoi-Cho, Inage-ku,
Chiba 263-8522, Japan

Soft Molecular Activation Research Center, Chiba University, 1-33 Yayoi-Cho, Inage-ku,
Chiba 263-8522, Japan

K. Akaike

Research Laboratory for Adhesion and Interfacial Phenomena (AIRL), National Institute of
Advanced Industrial Science and Technology (AIST), 1-1-1, Higashi, Tsukuba 305-8565, Ibaraki,
Japan

© The Author(s) 2024

S. Horiuchi et al. (eds.), *Interfacial Phenomena in Adhesion and Adhesive Bonding*,
https://doi.org/10.1007/978-981-99-4456-9_5

291

1 Introduction

Surface/interfacial properties play dominating roles in many applications, such as biomedical implants, coatings, packaging materials, adhesives, lubricants, etc. Among them, adhesion is extremely important in many industrial applications, from the automotive and aircraft industries to the housing and the microelectronics industry. In the microelectronics industry, for example, epoxy polymeric underfills are commonly used to enhance the long-term drive reliability of microelectronics chip assemblies, and the buried interface structure of the underfill is critical to the lifetime of the device. Adhesion failures at this buried metal/epoxy interface can lead to premature and unexpected device failures. Therefore, understanding the relationship between adherent and adhesive interfacial structure and property is critical to improving microelectronics device performance.

Generally, polymer surface properties are believed to be determined by molecular surface structures. Therefore, it is crucial to characterize polymer surface structures at the molecular level for developing polymer surfaces with desired properties. In the last few decades, a variety of surface-sensitive analytical techniques have been developed. However, most such techniques often require a high vacuum to operate and the conductivity of the samples, cannot probe molecular level surface structure, or lack desired surface specificity. Therefore, probing polymer surface structures at the molecular level in situ in real-time is still not easy. Furthermore, particularly concerning the adhesion, it is expected that the structural changes of the adhesives, which are in a liquid state in the initial stages of adhesion and then turn into a solid state at the interface with curing, significantly affect the adhesive strength. However, it is not easy to nondestructively investigate the molecular structural changes at interfaces between liquids and solids, or buried interfaces of solids.

Recently sum-frequency generation (SFG) vibrational spectroscopy has been developed into a powerful and unique technique to investigate surface structures of various kinds of material surfaces. SFG is a second-order nonlinear optical effect, which requires high-energy pulses to generate enough signal for detection. SFG vibrational spectroscopy first appeared in publication in 1987, developed by Shen et al. at the University of California, Berkeley [1, 2]. In addition to the surface studies in the air such as polymeric materials surfaces [3, 4], block copolymer surfaces [5], resin [6], and polymer blends [7], buried interfaces such as polymers in water [8], polymer–polymer interfaces [9], and polymer–solid interfaces [10–12] have also been examined using SFG. Furthermore, SFG has been used to investigate molecular interactions between polymers and adhesion promoters and the structural changes at the interfaces to understand the molecular mechanisms of the adhesion of polymers.

The primary advantage of SFG spectroscopy is that vibrational resonances can be label-free probes. Because this technique is inherently a probe of broken centrosymmetry, surface specificity is not dependent on the shallow penetration of the infrared (IR) beam, as is the case with near-field wave probes such as in the cases of the grazing angle experiments or attenuated total reflection (ATR) IR spectroscopy. As a result, a potential application is where the molecule of interest at surfaces is the same

as the molecule in the adjacent bulk. For example, at the polymer-water interface, SFG can probe the polymer chains at the surface on their own, excluding the contribution of the bulk polymers. Water molecules at the interface can be also studied in the same experiments without the contribution of the bulk water phase.

Currently, many books [13–15] and review articles [16–24] have been published covering the basic principles of vibrational SFG spectroscopy. Here, we present a schematic overview of SFG spectroscopy at the interface of materials, especially at polymeric surfaces and interfaces, as well as physical and molecular scientific approaches to reveal the true nature of the interfaces by combining SFG and other analytical techniques toward the target of the buried adhesive interface. With the purpose of this session, basic issues about SFG will be explained.

Before reviewing applications of SFG spectroscopy to study buried adhesion interfaces, we summarize in brief the basic theory and the experimental implementation of SFG as a methodology.

2 Basic Theory for Surface/Interface Sum-Frequency Generation

(A) *Nonlinear optics*

SFG vibrational spectroscopy has developed based on advancements in nonlinear optics and vibrational spectroscopy, and the early work by Y. R. Shen and his collaborators established the theoretical and the experimental basis for the development of the SFG field of research [13, 15].

In nonlinear optics, the optical induced polarization $P(t)$ of a material is nonlinearly dependent on the input electric field strength, which can be expressed as

$$P(t) = \chi^{(1)}E(t) + \chi^{(2)}E^2(t) + \chi^{(3)}E^3(t) \dots \quad (1)$$

Here, $E(t)$ is the input optical field, and $\chi^{(1)}$, $\chi^{(2)}$, and $\chi^{(3)}$ are, respectively, the linear susceptibility, the second-order, and the third-order nonlinear susceptibility of the material of interest. The generation of SFG signal arises from $P^{(2)} = \chi^{(2)}E^2(t)$, which is the second-order nonlinear polarization of the second term in Eq. (1), and it involves two distinct input optical frequency components. If we assume that the second-order nonlinear polarization is proportional to the square of the optical field,

$$P^{(2)}(t) \propto [E(t)]^2 \quad (2)$$

If the light electric field is constituted by two frequency components, the nonlinear polarization can be written as follows.

$$E(t) = E_1 \cos \omega_1 t + E_2 \cos \omega_2 t \quad (3)$$

Then the nonlinear polarization is,

$$\begin{aligned} P(t) &\propto E_1^2 \cos^2 \omega_1 t + E_2^2 \cos^2 \omega_2 t + 2E_1 E_2 \cos \omega_1 t \cos \omega_2 t \\ &= \frac{E_1^2}{2} (1 + \cos 2\omega_1 t) + \frac{E_2^2}{2} (1 + \cos 2\omega_2 t) + 2E_1 E_2 [\cos(\omega_1 + \omega_2)t \\ &\quad + \cos(\omega_1 - \omega_2)t] \end{aligned} \quad (4)$$

From Eq. (4), second-order nonlinear optical effects enable the frequency conversion. This equation also indicates that the frequencies of the converted lights are the frequency doubles, the sum-frequency, and the difference frequency of the two input light frequencies, respectively.

(B) *Symmetry argument and the selection rule*

A schematic of the energy diagram of the SFG is shown in Fig. 1 (left). A frequency fixed visible (ω_1) beam and a frequency-tunable infrared (ω_2) beam temporally and spatially overlap at a surface or interface to generate a sum-frequency ($\omega = \omega_1 + \omega_2$) signal which can be measured by a detection system (e.g., monochromator/photomultiplier tube (PMT)). When the IR frequency is tuned across a vibrational transition of the surface/interfacial molecules, the sum-frequency signal intensity is resonantly enhanced. An SFG spectrum can be acquired by plotting the SFG signal intensity as a function of the IR frequency. Under the electric dipole approximation, this process can occur only in the absence of inversion symmetry. When the inversion operation is applied to the isotropic material, nonlinear susceptibility $\chi^{(n)}$ does not change even if r is set to $-r$ due to the existence of an inversion center. On the other hand, the polarization P becomes $-P$ and the electric field E becomes $-E$. Therefore, $\chi^{(n)} = (-1)^{(n-1)} \chi^{(n)}$ holds, and the nonlinear susceptibilities $\chi^{(2)}, \chi^{(4)}, \dots$ of even-order become zero in a medium with inversion symmetry. This means that no SFG is generated from the isotropically oriented bulk. However, surfaces and interfaces necessarily lack inversion symmetry with respect to the normal direction, which allows $\chi^{(2)}$ to have a certain value under dipole approximation. In other words, if we can rule out significant quadrupolar contributions to the induced polarization, the second-order susceptibility $\chi^{(2)}$ is nonzero when there is no inversion symmetry. This is why second-order nonlinear spectroscopy such as SFG is a surface- and interface-specific technique. The intensity I_{SFG} detected at the sum-frequency is then given by

$$I_{SFG} \propto |\chi^{(2)}|^2 I_{VIS} I_{IR} \quad (5)$$

where I_{VIS} and I_{IR} are the intensities of the incident visible and infrared beams, respectively. As shown, SFG signal intensity is proportional to the square of a property, second-order nonlinear susceptibility $\chi^{(2)}$, of the material. Here, the effective susceptibility $\chi_{eff}^{(2)}$, which is related to the actual susceptibility, can be obtained by considering the electric field from the laser at the point where the SFG is generated. These local fields are what govern the SFG process. These local electric fields may differ from the fields of the incident electromagnetic waves, such as transmission or reflection at the surface, or propagation through the phase to reach the buried interface. In general, one can write

$$\chi_{ijk,eff}^{(2)} = l_{ii}l_{jj}l_{kk}\chi_{ijk}^{(2)} \quad (6)$$

where l are the so-called local field correction factors and the indices i, j , and k refer to any of the laboratory frame Cartesian coordinates x, y , or z . These are merely the macroscopic part of the local field correction, a complete consideration of the local fields near the molecules also requires microscopic factors. In the coordinate system used here, P-polarized light has its electric field in the xz -plane, so the components of the field along x and z depend on the angle of incidence, θ . S-polarized light then has an electric field along y . A local field correction factor such as l_{yy} , for S-polarized light, is the ratio between the y -component of the field at the point of interest and the y -component of the incident light infinitely far from the surface.

SFG is equivalent to the second term in Eq. (1) as a second-order nonlinear optical process. The energy level diagram of the SFG process is illustrated in Fig. 1 (left). SFG resonance is a combination of an IR absorption and an anti-Stokes Raman scattering process. Thus the transition polarizability describing an SFG process, termed as hyperpolarizability or second-order polarizability, can be expressed by the infrared transition dipole moment (μ) and Raman polarizability tensor (α) as follows,

$$\beta_{abc}^{(2)} = -\frac{1}{2\varepsilon_0\omega_q} \frac{\partial\alpha_{ab}^*}{\partial Q_q} \frac{\partial\mu_c}{\partial Q_q} \quad (7)$$

where ε_0 is the vacuum permittivity, ω_q is the angular frequency of the q -th vibrational mode, and Q_q is the normal mode coordinate of the molecular vibration. The last two terms are the derivatives of the complex conjugate of Raman polarizability and infrared transition dipole moment components with respect to the normal coordinate of the q -th vibration mode, respectively. The “ abc ” in the equation indicates a molecular-fixed coordinate system. Experimentally, all of the surface/interfacial molecules probed by SFG can participate in this optical process.

Figure 1 also shows the energy level diagrams of the IR, Raman, and SFG processes. Clearly, an SFG process is a combination of an IR process and anti-Stokes Raman scattering. In fact, the selection rule for the vibrational modes observed in SFG is both infrared- and Raman-active modes.

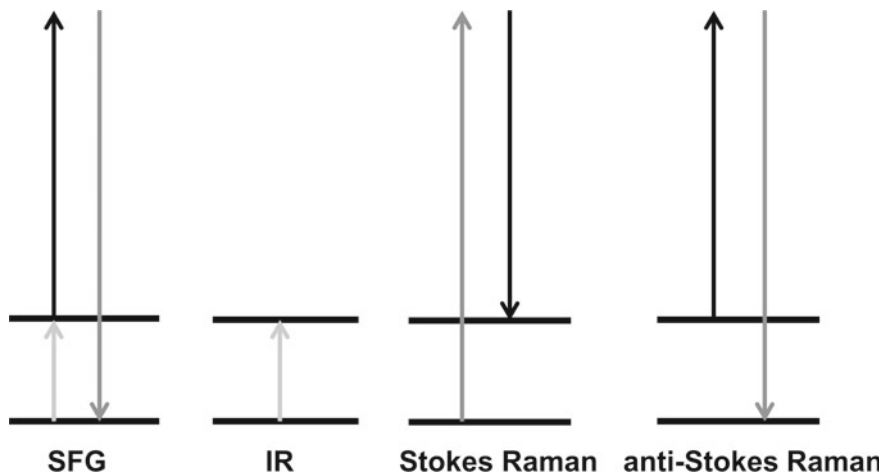


Fig. 1 The energy diagrams for SFG, IR, Stokes and anti-Stokes Raman scattering

To distinguish it from the optical process of the sum-frequency generation commonly used in nonlinear optics, this SFG spectroscopy is often referred to as infrared–visible sum-frequency generation spectroscopy or vibrational sum-frequency generation.

(C) *Component of SFG intensity and the light polarization*

Analogous with FT-IR spectroscopy, SFG can provide the molecular state at the surface/interface. In addition, the structural information can be evaluated quantitatively. Equation (8) shows the SFG output intensity in the reflection geometry. Here, $n_i(\omega_i)$ represents the refractive index of the incident medium at frequency ω_i , and ω and θ are the frequency and reflection angle of the output beam, respectively. The angle θ is deduced from the conservation of momentum of the input and output photons; $I_1(\omega_1)$ and $I_2(\omega_2)$ are the intensities of the two input beams (visible and infrared beams used in SFG) at frequencies ω_1 and ω_2 . $\chi_{eff}^{(2)}$ is the effective second-order nonlinear optical susceptibility measured for a particular polarization combination of the input and output beams in the SFG experiment.

$$I(\omega) \propto \frac{8\pi^3 \omega^2 \sec^2 \theta}{c^3 n_1(\omega_1) n_1(\omega_2) n_1(\omega)} \left| \chi_{eff}^{(2)} \right|^2 I_1(\omega_1) I_2(\omega_2) \quad (8)$$

Equation (3.8) can be used to describe SFG signal intensity generated by surface/interface molecules in SFG. Note that the actual coefficient is not important in most cases since usually only the relative SFG intensity is compared.

If the IR frequency (ω_2) is near vibrational resonances, we can write

$$\chi_{eff}^{(2)} = \chi_{NR}^{(2)} + \chi_R^{(2)} = \chi_{NR}^{(2)} e^{i\varphi} + \sum_q \frac{A_q}{\omega_2 - \omega_q + i\Gamma_q} \quad (9)$$

where A_q , ω_q , Γ_q are the peak amplitude, the resonant vibrational frequencies, and the damping constants, respectively. $\chi_{NR}^{(2)}$ and φ describes the non-resonant contributions and the phase difference between resonant and non-resonant terms, respectively. In general, Eq. (9) is used to fit all the measured spectra with A_q , ω_q , Γ_q , and $\chi_{NR}^{(2)}$ as adjustable parameters. Usually, $\chi_R^{(2)}$ is the vibrationally resonant term which has a Lorentzian line shape.

Reversing the dipole direction changes the sign (or phase) of the amplitude A_q . This indicates that the absolute spatial orientation of the molecule at the interface can be determined by SFG. In other words, it can be determined whether the functional groups are oriented toward the upper medium or the opposite direction with respect to the interface. Unfortunately, since the conventional SFG measures the square of the absolute value of $\chi_R^{(2)}$ as shown in Eq. (9), information about the absolute dipole orientations of this dipole is missing. Such absolute orientation can be measured from the phase-sensitive SFG. More information on phase-sensitive SFGs can be found in review papers [25–27].

Figure 2 shows the definition of light polarization used in SFG. SFG spectroscopy treats two incident lights and one output light. Each light can adopt a polarization parallel to the plane of incidence (p-polarization) and a polarization perpendicular to the plane of incidence (s-polarization). This combination of incident and output polarization is important for analyzing molecular orientation. As indicated before, the SFG signal consists of a second-order nonlinear susceptibility, which is composed of third-order tensor components. For example, on an isotropically oriented surface, only four out of the 27 tensor components can have independent values from the symmetry requirement. These are $\chi_{xxz} = \chi_{yyz}$, $\chi_{xzx} = \chi_{zyz}$, $\chi_{zxx} = \chi_{zyy}$, and χ_{zzz} . In the polarization combination of SSP (SFG is S-polarized, visible light is S-polarized, and infrared light is P-polarized), for example, yyz element of these four independent tensor components is observed. Similarly, in the SPS polarization combination, the yzx component will be observed, and the four components xxz , xzx , zxx , and zzz , will constitute the peaks of the spectrum in the PPP polarization combination.

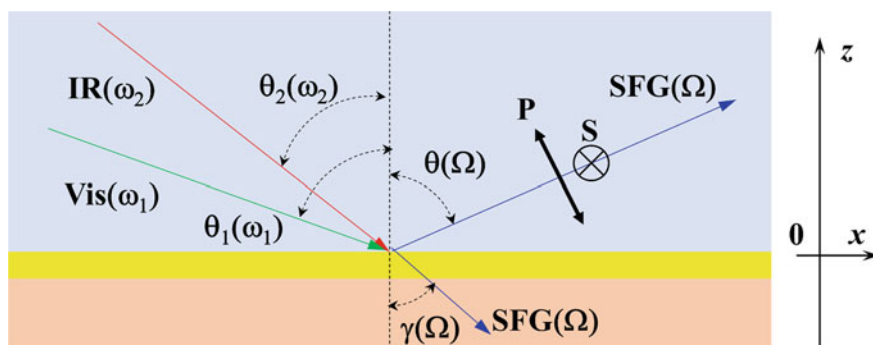


Fig. 2 Schematics of the light polarization in SFG

(D) *Determination of the molecular orientation*

Molecular orientation information of surface molecules and functional groups can be determined from SFG spectra collected with different combinations of polarizations such as SSP, PPP, and SPS [28–31]. Such orientation information can be evaluated by the intensity ratio of different vibrational modes of the functional group in the same spectrum or the intensity ratio of the same peak in SFG spectra collected with different polarization combinations.

In the case of SFG, the hyperpolarization tensor of the molecule is projected onto the lab coordinate system when the experiments are performed with laser light of a certain polarization combination. From this projection, the orientation of the molecule can be obtained, as described below.

As mentioned above, SFG probes the second-order nonlinear susceptibility $\chi^{(2)}$, which is a third-rank tensor. In SFG experiments, different combinations of polarization S or P of the input and output laser beams can probe different tensor components of the second-order nonlinear susceptibility.

$$\begin{aligned}
 \chi_{eff,SSP}^{(2)} &= L_{yy}(\Omega)L_{yy}(\omega_1)L_{zz}(\omega_2)\sin\theta_2\chi_{yyz} \\
 \chi_{eff,SPS}^{(2)} &= L_{yy}(\Omega)L_{zz}(\omega_1)L_{yy}(\omega_2)\sin\theta_1\chi_{yzy} \\
 \chi_{eff,PSS}^{(2)} &= L_{zz}(\Omega)L_{yy}(\omega_1)L_{yy}(\omega_2)\sin\theta\chi_{zyy} \\
 \chi_{eff,PPP}^{(2)} &= -L_{xx}(\Omega)L_{xx}(\omega_1)L_{zz}(\omega_2)\cos\theta\cos\theta_1\sin\theta_2\chi_{xxz} \\
 &\quad - L_{xx}(\Omega)L_{zz}(\omega_1)L_{xx}(\omega_2)\cos\theta\sin\theta_1\cos\theta_2\chi_{xzx} \\
 &\quad + L_{zz}(\Omega)L_{xx}(\omega_1)L_{xx}(\omega_2)\sin\theta\cos\theta_1\cos\theta_2\chi_{zxx} \\
 &\quad + L_{zz}(\Omega)L_{zz}(\omega_1)L_{zz}(\omega_2)\sin\theta\sin\theta_1\sin\theta_2\chi_{zzz}
 \end{aligned} \tag{10}$$

where L_{ij} denotes Fresnel factors, and θ , θ_1 , θ_2 are the angles between the surface normal and the SFG signal, input visible, and input IR beams, respectively. The second-order nonlinear susceptibility tensor $\chi^{(2)}$ in the lab-fixed (x, y, z) coordinate system is proportional to the response of the molecule as described by the molecular hyperpolarizability tensor, β_{ijk} . The nonlinear susceptibility $\chi_{ijk}^{(2)}$ is related to the molecular hyperpolarizability β_{ijk} by a coordinate transformation, which can be regarded as a projection:

$$\chi_{ijk,q}^{(2)} = N \sum_{l,m,n} \left\langle \left(\hat{i} \cdot \hat{l} \right) \left(\hat{j} \cdot \hat{m} \right) \left(\hat{k} \cdot \hat{n} \right) \right\rangle \beta_{lmn,q} \tag{11}$$

Thus, SFG measurements with a certain combination of polarized input and output beams can be related to the orientation angle of the molecule (or functional group) with respect to the laboratory coordinate system. For example, for the symmetric stretching mode of a methyl group with C_{3v} symmetry, we can obtain;

$$\begin{aligned}
\chi_{xxz,s} = \chi_{yyz,s} &= \frac{1}{2} N_s \beta_{ccc} [\cos\theta(1+r) - \cos^3\theta(1-r)] \\
\chi_{xzx,s} = \chi_{zyy,s} = \chi_{zxx,s} = \chi_{zyy,s} &= \frac{1}{2} N_s \beta_{ccc} [\cos\theta - \cos^3\theta(1-r)](1-r) \\
\chi_{zzz,s} &= N_s \beta_{ccc} [r \cos\theta + \cos^3\theta(1-r)]
\end{aligned} \tag{12}$$

Here, $r = \beta_{aac}/\beta_{ccc}$, and θ is defined as the angle between the methyl principal axis and the z -axis along the surface normal. The number density, N_s is a constant property of the surface or interface and does not change when different polarization combinations of the input and output beams are used in an SFG experiment. Therefore, important information on molecular orientation may be extracted from experimental measurements as a ratio of the signal strength measured in two polarization combinations. This approach does not require knowledge of the surface coverage, because it cancels when the signal strength ratio is taken.

(E) Purpose of the fitting of the SFG spectra and notes

By fitting the SFG spectra using Eq. (9), not only do we obtain the parameters for determining the molecular orientation, but also the obtained parameter is very useful to learn the state of the molecules at the interfaces. As described in the preceding section, $\chi_R^{(2)}$ is the vibrationally resonant term that has a Lorentzian line shape. A_q , ω_q , Γ_q are the peak amplitude, the resonant vibrational frequencies, and the damping constants, respectively. Let us consider an isotropic surface. For a certain vibrational mode, for example, the A_q obtained for SSP polarization combination corresponds to the tensor component χ_{yyz} of the nonlinear susceptibility associated with the SSP polarization. Thus, for the same vibrational mode, Γ_q and ω_q should be the same, even for different polarization combinations.

The peak positions of the vibrational modes ω_q observed in SFG are important for assignment, as in IR absorption. The peak position changes depending on the environmental conditions to which the molecule (or functional group) is exposed. For example, OH and C=O groups change their peak positions depending on hydrogen bonding strength, which is useful for studying interactions at interfaces.

Regarding the peak width, wider peak widths indicate more inhomogeneity, while narrower peak widths indicate molecules at the interface are under specific conditions. The higher the surface crystallinity, the narrower the peak width. Peak width is also influenced by environmental conditions as well as the peak position. However, the peak width is ordinarily not smaller than the resolution of the spectrometer and the line width of the lasers, so the overall resolution of the instrument should be considered in the fitting process.

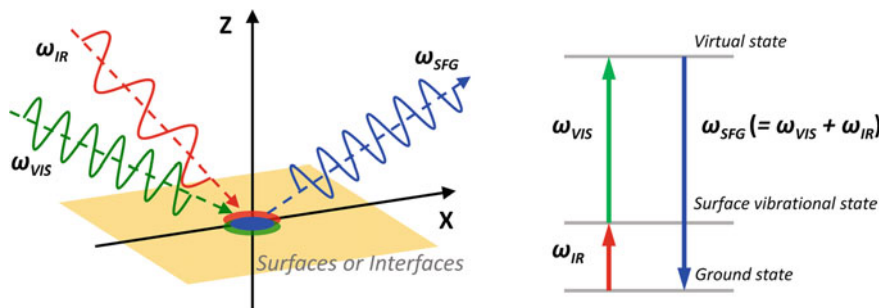


Fig. 3 Schematic of the experimental arrangement of the co-propagation geometry and the energy diagram of SFG

3 Experimental Equipment

3.1 General Description of the Experimental Equipment

Although the experimental setup for SFG is rather simple as compared with other nonlinear optical processes, its signal level is quite weak, due to the technique of acquiring only the signal coming from the sample surfaces. A schematic diagram for the SFG experimental arrangement in the co-propagation mode is depicted in Fig. 3. In general, frequency fixed visible (ω_1) beam and a frequency-tunable IR (ω_2) beam are overlapped temporally and spatially at the sample surface or interface to generate a sum-frequency ($\omega = \omega_1 + \omega_2$) beam which can be detected by the photodetectors. When the IR frequency is tuned across a vibrational transition of the surface/interfacial molecules, the SFG signal intensity is resonantly enhanced. An SFG spectrum can be acquired by plotting the SFG signal intensity as a function of the IR frequency.

Currently, SFG spectrometers are generally classified into broadband and narrow-band systems. This section describes the configuration of each equipment and its features.

3.2 SFG Spectroscopy with Narrowband Input

A scanning-type SFG spectrometer usually utilizes picosecond (ps) pulses generated from a high-energy pulse laser system to pump frequency conversion systems to generate a visible beam with a fixed wavelength and a wavelength tunable mid-IR beam.

Figure 4 depicts the schematics of the optical layout of the ps-SFG system. Generation of high-energy mid-IR beam is relatively more difficult than generating a visible or near-IR beam. For example, in a ps-SFG spectrometer, a mode-locked Nd:YAG laser beam with 1064 nm output is first frequency-doubled to 532 nm. Part of the 532 nm beam is used directly as the visible pump beam for the SFG. Other part of the 532 nm beam and a portion of the 1064 nm beam is then used for optical parametric generation (OPG) and amplification (OPA) to produce a near-IR beam, which is used in difference frequency generation (DFG) to produce the mid-IR beam. By adjusting the angle of the nonlinear optical crystal (β -BaB₂O₄) in the OPG/OPA generation and the angle of the grating for wavelength selection can sweep the mid-IR beam step by step to obtain an SFG spectrum. For the signal acquisition, a monochromator and a highly sensitive photomultiplier tube are usually used. A ps-SFG system is slow to acquire one spectrum. This is because, at each tuning step, which usually takes seconds to complete, only one frequency in the spectrum can be measured. On the other hand, ps-SFG systems usually have relatively high spectral resolution (below 5 cm⁻¹), determined by the frequency bandwidth of a ps pulse. Since the SFG signal intensity depends on the incident light intensity, the intensity of each wavelength of visible light and infrared light is measured simultaneously with an IR intensity monitor and a photodetector, respectively, and the SFG spectrum can be obtained later by dividing the SFG intensity by these values. Another disadvantage of ps-SFG system is that the sample damages due to the irradiation of highly intense laser pulses are unavoidable. To avoid the sample damages, the laser pulse intensities per unit area must be reduced, which simultaneously leads to a lower SN of the SFG spectra and a further increase in the measurement times.

Mode-locked Nd:YAG lasers provide 10–30 ps pulses at about 50 mJ/pulse with a repetition rate of 10–50 Hz. These pulses can generate the visible pump pulses used in SFG, as well as a wide range of wavelength tunable infrared pulses. Figure 5

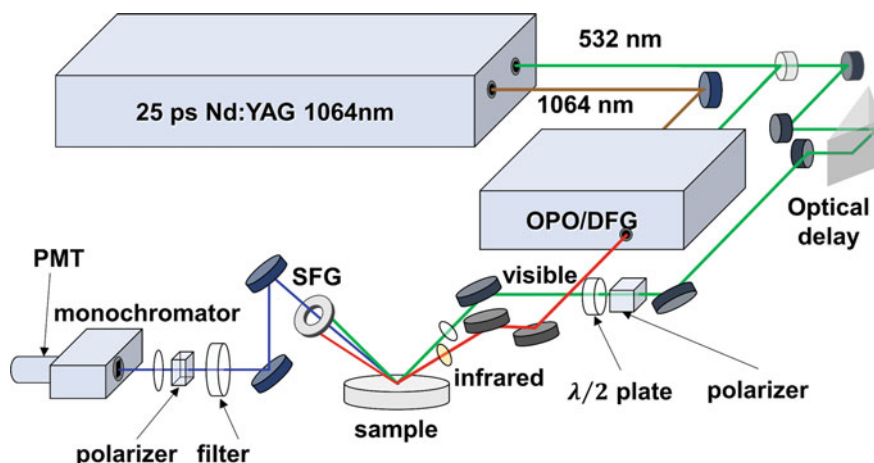


Fig. 4 Schematic of the optical setup of the ps-SFG spectrometer

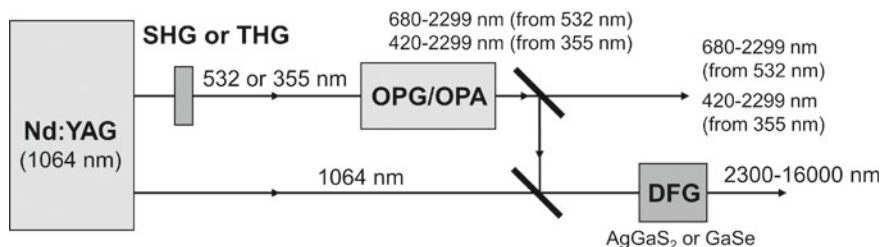


Fig. 5 Schematic of the wavelength tunable system based on an optical parametric generation/amplification (OPG/OPA) system commonly used in the ps-SFG spectrometer

illustrates the schematics of the typical wavelength tunable system. Such systems are now commercially available and have been adopted by many laboratories for SFG spectroscopic researches. Although these systems are fairly reliable and relatively easy to maintain, the disadvantage of this ps-wavelength tuning system is that the pulse repetition rate is too low and the pulse width too wide, resulting in a low signal collection rate and slow recording of a spectrum [15].

In this ps-SFG system, it is possible to use near-infrared light at 1064 nm or ultraviolet light at 355 nm instead of the visible excitation light at 532 nm for the SFG measurements. However, in these cases, mirrors, filters, polarizers, half-wave plates, and lenses used in the optical path of the visible lights as well as the grating of the spectrometer and the photomultiplier tube of the detector need to be changed to the corresponding SFG light wavelengths emitted from the sample surface. In particular, when used at longer wavelengths, a CCD detector or other detector that is compatible with longer wavelengths must be selected.

3.3 SFG Spectroscopy with a Broadband Input

A broadband SFG system usually requires a broadband high-repetition femtosecond (fs) laser source, e.g., a Ti:sapphire mode-locked laser system with an amplifier system to amplify the pulse energy. Figure 6 depicts the schematics of the optical layout of the fs-SFG system. High-energy broadband mid-IR pulses are also generated by the OPG/OPA-DFG method. Visible light pulses are usually narrowed by the bandpass filter or the monochromator. The overlapping of the narrowband visible beam and the broadband mid-IR beam simultaneously excites multiple vibrational bands at an interface. The broadband SFG spectrum is then acquired by the spectrometer equipped with a charge-coupled device (CCD) array for signal detection. A fs broadband SFG system has higher spectral collection speed, up to milliseconds. However, due to the relative wide bandwidth of the visible beam, the spectral resolution is typically lower than a ps-SFG system. However, broadband SFG with high resolution of less than 1 cm^{-1} has been recently developed [32, 33]. In recent years, the development of the heterodyne detected SFG technique for determining

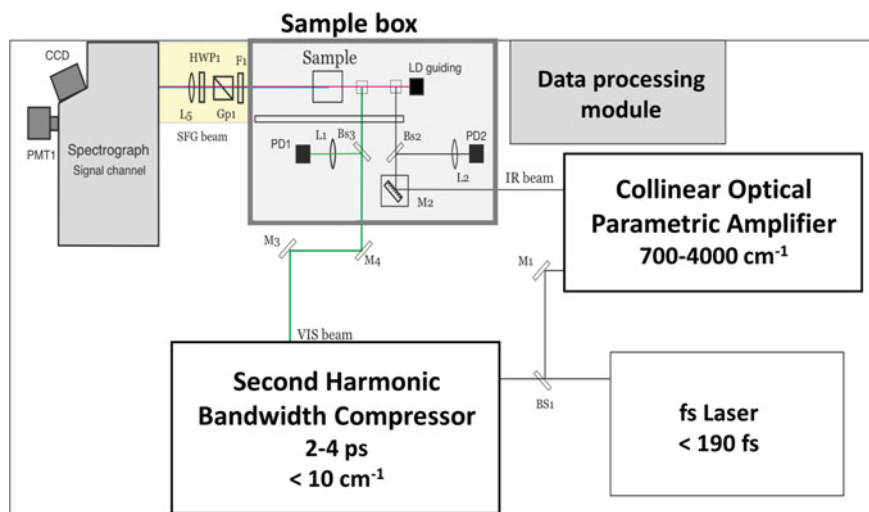


Fig. 6 Schematic of the optical setup of the fs-SFG spectrometer

the absolute molecular orientation at the interface, and in particular, the broadband SFG technique, with its high repetition rate lasers, has outstanding advantages for this method [34, 35]. Furthermore, recent improvements in laser technologies have also enabled the development of high-repetition broadband SFG systems, and the mainstream of SFG is rapidly shifting from the picosecond systems to the fs broadband SFG systems. These innovative SFG system enable to obtain hyper-spectral images at the interfaces [36–38].

3.4 Doubly-Resonant Sum-Frequency Generation Spectrometer

Doubly-resonant SFG measurements are powerful techniques to clarify the interfacial structure of the organic materials used in organic electronic and optoelectronic devices. The signal enhancement is expected only for species that have an electronic absorption at the photon energy of the SFG, as shown in Fig. 7 [39]. Therefore, doubly-resonant effect offers a kind of molecular specificity to SFG. Furthermore, an electronic excitation spectrum of the interfacial chemical species for each vibrational band can be obtained. Thus, the SFG electronic excitation profiles are valuable for studying interfacial layers that exhibit complex vibrational spectra due to the coexistence of multiple chemical species, since the vibrational bands can be classified with reference to corresponding electronic spectra. The measurement of SFG excitation profiles can be also an effective way to obtain electronic spectra of the

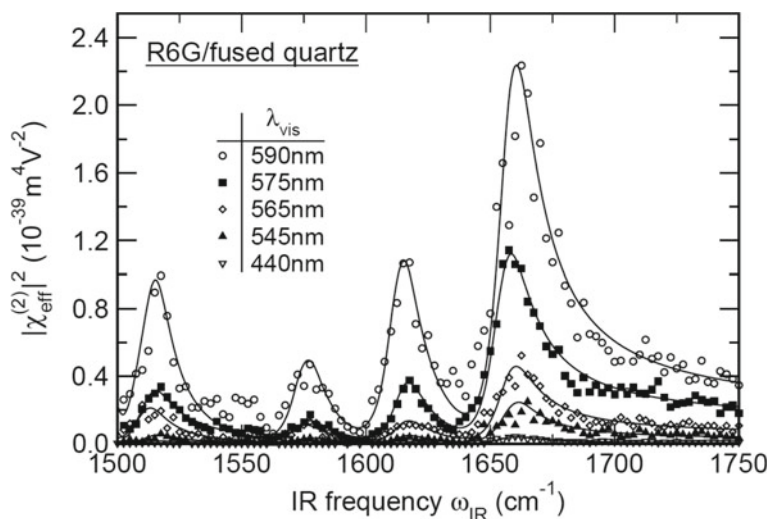


Fig. 7 Visible wavelength dependent SFG spectra of a molecular monolayer of Rhodamine 6G molecules on fused quartz in SSP polarization combination normalized against the signal from a z-cut quartz. Reprinted with permission from Ref. [39]. Copyright 2002 Elsevier, All Rights Reserved

molecules, particularly at the interface on opaque substrates where electronic absorption spectrum measurement is difficult. Additionally, it is also possible to measure the interface of the OLED materials that emit very strong photoluminescent light in visible region, since the output SFG emerges on the Anti-Stokes side of the excitation wavelength.

Detail of the experimental setup of the doubly-resonant SFG measurements is shown in the previous publications [40–42]. In addition to the frequency-tunable IR laser beam, a frequency-tunable visible laser beam was generated by the other optical parametric generators/amplifiers (OPG/OPA) pumped by a mode-locked Nd:YAG laser at 1064 nm. The visible beam, tunable from 420 to 640 nm, was generated in a LiB_3O_5 (LBO) crystal mounted in OPG/OPA pumped by the 355 nm beam. The spectral resolution of the tunable visible beam can be calibrated with the Hg lines. To eliminate the scattered visible light and the photoluminescent light from the samples, the sum-frequency output signal in the reflected direction was filtered with short-wave-pass filters, prism monochromator, and grating monochromator.

Because doubly-resonant SFG is associated with the electronic excitation of the molecules, the observed molecular vibrations are more strongly affected by the vibrations directly related to the electronic excitation, and the intensity of observed molecular vibrations is more strongly affected by the vibrations directly related to electronic excitation, such as stretching vibrations of phenyl groups, rather than those of the functional groups on the side chains, which are not directly related to the electronic excitation. Therefore, the doubly-resonant effect is very useful for SFG measurements of molecules with π -conjugated systems, especially for the investigation of

the molecular fingerprint region from 1000 to 2000 cm^{-1} . However, this wavenumber region is also strongly affected by the water vapor present in the optical path, making it difficult to measure. Therefore, the surrounding area of the optical path, including the sample stage, must be purged with N_2 gas or dry air to prevent the effect of water vapor.

3.5 Experimental Conditions for Polymeric Material Surfaces and Adhesive Interfaces

Figure 8 shows a photograph of the sample box of the SFG spectrometer. If the measurement is performed in air, the solid sample surfaces can be measured directly by setting the sample on the sample stage and adjusting the height of the sample surface to the height where the SFG light is generated.

In the practical sample measurements, if the substrate or sample is transparent, it is rather difficult to find the sample position because SFG light is hardly generated at IR wavelengths in the region where there is no SFG peak. In the case of samples with absorption in the visible light range or on metal substrates, it is necessary to adjust the laser beam intensity considering the effects of laser-induced damages to the samples. The surface of the sample should preferably be as smooth as possible, considering the loss of SFG signal, but depending on the sample, powder samples can also be measured. Note that the effect of the multiple reflections of the lights must be

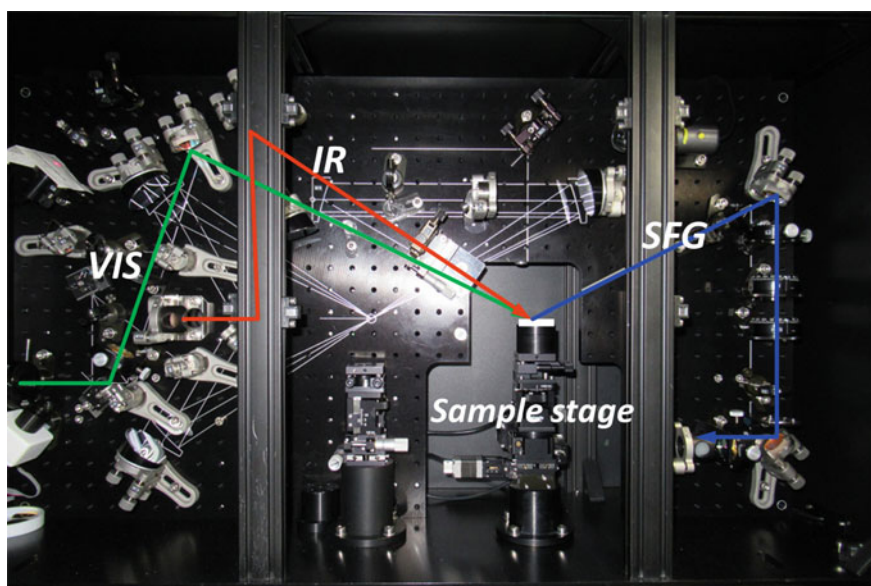


Fig. 8 Photograph of the sample box of the phase-sensitive SFG spectrometer

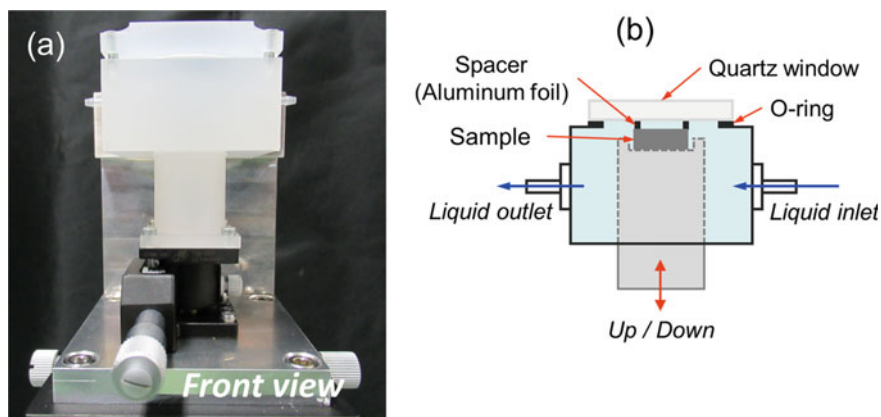


Fig. 9 **a** Photograph of the SFG liquid cell for solid/liquid interface measurement, and **b** Schematic of the SFG liquid cell

considered when using very thin substrates. Since SFG is a laser-based technique, it can easily interfere and produce interference peaks on the spectra.

To measure the interface between liquid and solid samples, it is necessary to prepare the liquid cell on the sample stage, such as shown in Fig. 9. The solid sample specimen is attached to the top of the piston unit that moves up and down and is placed in the close position to the window (e.g., transparent fused quartz, sapphire, or CaF_2).

The SFG light intensities generated from liquid and solid interfaces are often very weak because of the Fresnel coefficients at the interfaces and molecular orientation. To enhance this SFG intensity, the total internal reflection SFG technique using a prism is often used. This technique uses the total internal reflection that occurs at the interface between the prism with a high refractive index and the organic material with a lower refractive index, and is an effective technique to enhance the weak SFG signal from the interfaces. This TIR-SFG is extremely powerful at the interface between solid (refractive index ~ 1.5) and water (refractive index ~ 1.33), for example. Furthermore, by rotating the solution cell with a cylindrical prism and tuning the angle of incidence of the lights, it is possible to selectively detect SFG signals from multiple organic layer interfaces on the substrate, as illustrated in Fig. 10 [43]. However, prisms that are transparent in both the infrared and visible wavelength regions are limited to a few materials such as sapphire (refractive index, $n = 1.75$). The refractive indices of the infrared prisms made by CaF_2 or fused quartz are lower than those of general organic materials, and the laser light penetrates the sample without causing total reflection. If the film thickness of the sample in contact with the prism is too thin, the multiple reflections mentioned above may occur. If the target material is transparent polymer, it is not enough to make the thickness of the film thinner; it is necessary to place the opposite side of the polymer in contact with the prism with a

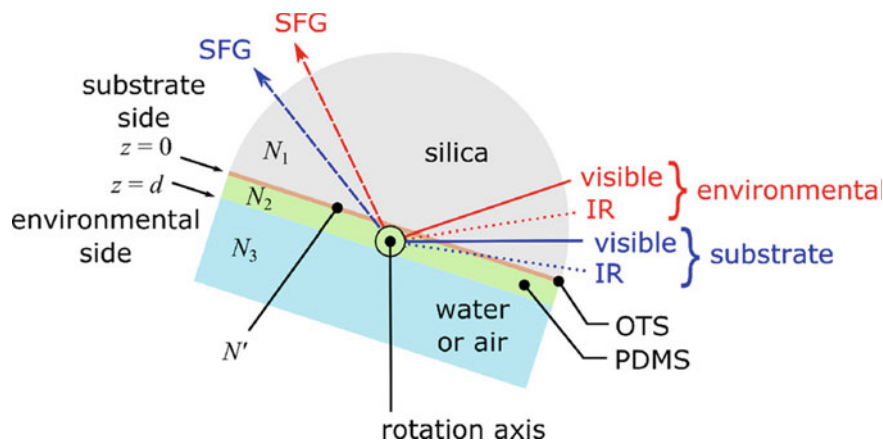


Fig. 10 Schematics of the hemicylindrical prism functionalized with OTS and then coated with PDMS pressed into a liquid cell. Two sets of beam angles are illustrated. Reprinted with permission from Ref. [43]. Copyright 2018 American Chemical Society, All Rights Reserved

rough surface or in contact with light absorbing materials. This is a very important procedure because SFG uses coherent laser lights, so it is necessary to prevent the interference fringes caused by multiple reflections to overlap in the spectra.

4 Applications of SFG Spectroscopy to Study Polymeric Materials Surfaces and Interfaces

The structure and orientation of molecules at polymer surfaces have a great impact on adhesion. Good adhesion is given by the work of adhesion at the interface between two different materials. As per the Young–Dupré equation, the work of adhesion is calculated:

$$W_{SL} = \gamma_1 + \gamma_2 - \gamma_{12} \quad (13)$$

The interfacial free energy (γ_{12}) is obtained from the surface free energy of solids 1 and 2 as follows:

$$\gamma_{12} = \gamma_1 + \gamma_2 - 2(\gamma_1 \times \gamma_2)^2 = (\sqrt{\gamma_1} - \sqrt{\gamma_2})^2 \quad (14)$$

According to Eqs. (13) and (14), γ_{12} of the interface decreases when the value of γ_2 is closer to that of γ_1 and the work of adhesion W_{SL} gets closer to γ_1 and γ_2 . Thus, the interfacial adhesion should improve when the surface free energy of the surface of solid 1 is expected to be close to that of the surface of solid 2.

In general, polymeric materials have low surface free energies, and many of them show poor adhesion properties. The surface free energies of these polymers are often governed by the orientation and segregation of the surface functional groups, and understanding the orientation of the functional groups on the polymer surfaces are important issues for adhesion.

4.1 Chemical Structure of Adherent Surfaces

4.1.1 Characterization of the Surface Modified Polymer Surfaces for Adhesion Improvement

Polymers are key materials for reducing car body weight. Reducing the car body weight allows for lower carbon dioxide emissions and reduced fuel consumption [44]. Though high adhesive properties are an essential issue for the polymers used in the automotive components, some polymer materials, such as polypropylene used for automobile bumpers, have low adhesive properties without surface treatment. Generally, surface treatments such as plasma treatment, flame treatment, deep UV/excimer laser irradiation, and chemical treatment are often used to modify the surface properties of polymers [45–54]. Adhesion improvement by the surface treatment is believed to affect the adhesion of polymers not only through the introduction of the functional groups on the polymer surfaces, but also through several other factors, including changes in surface morphology and wettability. The adhesive mechanism has been often discussed based on the studies using X-ray photoelectron spectroscopy (XPS) and Attenuated total reflection infrared spectroscopy (ATR-IR); these techniques, however, can observe the near-surface region, but not the outermost layer surface or the buried interface. In addition, it is extremely difficult to obtain information on the molecular orientation using XPS and ATR-IR. Information on molecular structure, such as the orientation and orientation distribution of functional groups at the outermost surface of polymeric materials, is extremely important for elucidating the adhesion mechanism. Therefore, it is necessary to directly observe the outermost surface both before and after surface treatments to understand the adhesion mechanisms at the surface treated polymers. In this section, we have investigated the effect of N₂ gas plasma treatment from the outermost surface to the bulk region of the polypropylene using SFG and ATR-IR measurements. Furthermore, we investigated the variations in crystallinity of the surface treated polypropylene surfaces by Raman micro-spectroscopy [55].

(A) N₂ Plasma treatment for the polypropylene resin surfaces

A commercially available 3 mm thick polypropylene board was used as the sample. Atmospheric pressure plasma treatment was performed by irradiating N₂ gas plasma at atmospheric conditions by moving the sample stage in one direction at 5 mm/s. The N₂ gas flow rate was set to 15 L/min. One reciprocation was counted as one treatment, up to 8 reciprocations in this experiment. After the N₂ plasma treatment,

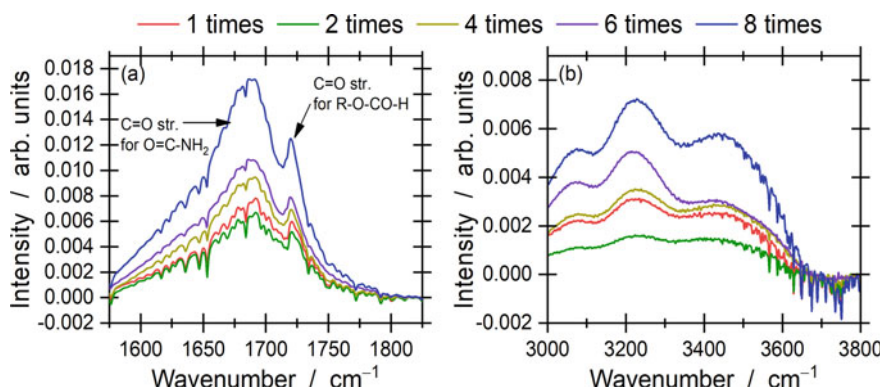


Fig. 11 The subtracted IR spectra of the pristine and N₂ plasma-treated polypropylenes in the **a** C=O and **b** O–H stretching regions collected using the Ge prism. Reprinted with permission from Ref. [55]. Copyright 2018 Elsevier, All Rights Reserved

SFG measurements were performed immediately to avoid the influence of adsorption of water molecules in the air and changes over time. The ATR-IR and confocal Raman scattering measurements were performed under ambient conditions.

Figure 11 shows the ATR-IR spectra for the N₂ plasma-treated polypropylene samples using Ge prisms. To discuss the changes in the functional groups by plasma treatments, ATR-IR spectra are subtracted from the plasma treated polypropylene to that of the untreated one. As shown in Fig. 11, the intensity of the C=O and O–H bands increased while repeating the N₂ plasma irradiation. The C=O band split into two bands at 1685 and 1720 cm⁻¹, which correspond to the amide and carbonyl groups, respectively. A simple model for the mechanism of introduction of C=O and O–H groups by plasma irradiation has been proposed in Ref. [50], in which a simple model of insertion of polar functional groups is proposed as one possibility, but the real situation at the plasma-treated surface is expected to be more complex.

Figure 12 shows the SFG spectra of the pristine and N₂ plasma treated polypropylene surfaces in the C–H stretching region. The peaks derived from the methylene (CH₂) functional groups were observed at 2838 and 2915 cm⁻¹, corresponding to the CH₂ symmetric (d⁺) and asymmetric (d⁻) stretching vibrations, respectively. The three peaks derived from the methyl (CH₃) group were observed at 2872, 2932, and 2955 cm⁻¹. The peaks at 2872 and 2955 cm⁻¹ were assigned to the symmetric (r⁺) and asymmetric (r⁻) stretching vibrational modes. The peak at 2932 cm⁻¹ corresponds to the Fermi resonance between the CH₃ symmetric stretching and bending overtone [3, 56]. As illustrated in Fig. 12a, SFG spectra were changed significantly with increasing number of surface treatments, while the SFG peak intensities after N₂ gas plasma treatment in the C–H stretching region became weaker than that of pristine sample up to the fourth treatments. This indicates that the initial stage of the N₂ gas plasma induces the disordering of the polymer chains at the surfaces. The SFG spectrum of the eight-reciprocation sample was observed to be remarkably different than that of pristine polypropylene surface. Further, additional peaks

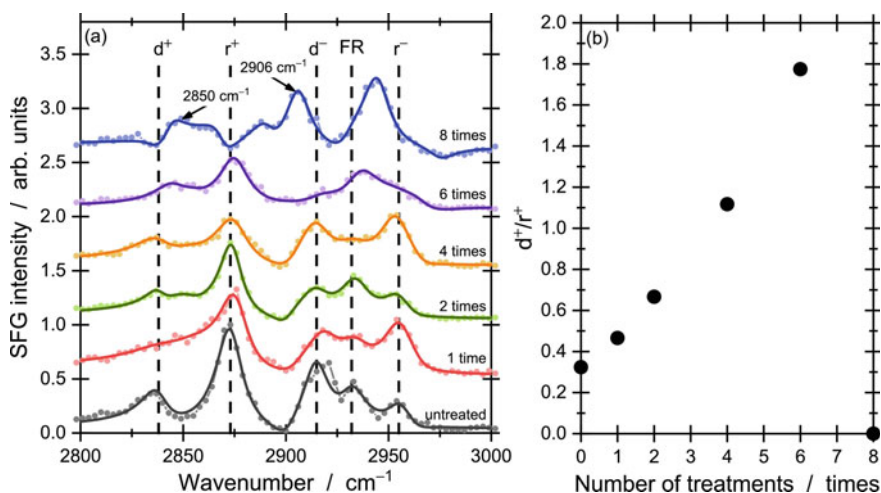


Fig. 12 **a** SFG spectra of the pristine and N₂ gas plasma-treated polypropylene surfaces in the SSP polarization combination in C-H stretching region. **b** Changes in the d⁺/r⁺ ratio of the plasma-treated polypropylene surfaces as a function of the N₂ plasma treatment cycles. Reprinted with permission from Ref. [55]. Copyright 2018 Elsevier, All Rights Reserved

appeared at 2850 and 2906 cm⁻¹. This remarkable spectral change suggests that the polymer chains at the polypropylene surfaces have been cleaved and degraded by the excessive plasma exposure.

In Fig. 12b, we show the change in the d⁺/r⁺ ratio as a function of the number of surface treatments. It is known that the d⁺/r⁺ ratio is a good indicator of the surface disorder in terms of the orientation of the long alkyl chains. On the other hand, the d⁺/r⁺ ratio is also associated with the surface free energy. As can be seen in Fig. 12b, the d⁺/r⁺ ratio increased with increasing plasma treatment cycles, i.e., the ratio of CH₂ groups increased and CH₃ decreased at the topmost surface. It is known that the surface free energy of the CH₂ groups is larger than that of the CH₃ groups [57]. Thus, this result implies that the surface free energy of polypropylene increased after conducting the N₂ gas plasma treatment. This interpretation is also consistent with previous reports, which state that the water static contact angle of plasma-treated polypropylene decreased after the plasma treatment [50].

The fact that plasma treatment improves the hydrophilicity of the polymer surfaces implies the presence of functional groups such as C=O and O-H on the surfaces. The presence of these functional groups has been previously reported by ATR-IR in Fig. 11 and XPS [58]. Depth analysis of ATR-IR experiments of the plasma treated samples in Fig. 11 reveals the introduction of both hydrophilic C=O and O-H groups in the polypropylene surface region. The intensities of these bands increase with increasing the number of the N₂ plasma treatment cycles. This indicates that the amount of the hydrophilic groups increases with increasing the cycles of N₂ gas plasma treatments. In the case of O-H bands observed for the ZnSe prism indicates

that the O–H groups are distributed at least ca. 600 nm from the topmost surface toward the bulk.

Figure 13 presents the SFG spectra of the O–H and C=O stretching regions shown in the ATR-IR in Fig. 11. In the N₂ plasma treated samples, a slight and broad O–H band was observed, which was not detected before the plasma treatment. After the eight repetitions of plasma treated samples, the O–H band was clearly observed in the SFG spectra, but interestingly, its intensity gradually decreased with time. On the other hand, the C=O stretching peak was not observed until six repetitions of the plasma exposure (Fig. 13b). The over-treated sample exhibited barely discernible C=O stretching peak, although this peak disappeared immediately during the SFG measurements. The disappearance of these C=O and O–H peaks is possibly related to the glass transition temperature. According to previous SFG reports for polystyrene, plasma exposure introduces the C=O groups on the surface [59]. For polystyrene, the glass transition temperature is known much higher than room temperature. In contrast, since the glass transition temperature of the polypropylene is below room temperature, the main chain easily rotates during the measurements and the molecular structure of the surface is easily changed. This change in molecular orientation on the surface of hydrophobic materials is called *hydrophobic recovery* [60], and by measuring the surface with SFG continuously from immediately after the surface treatments, such dynamic molecular movements can be understood.

In the case of Raman scattering, it has been reported that the intensity ratio of the peaks at 811 and 843 cm⁻¹ are related to the degree of crystallinity for polypropylene. Figure 14b shows the variations in peak intensity ratio I_{843}/I_{811} from the Raman data of the N₂ plasma treated polypropylene in Fig. 14a, and it is found that the

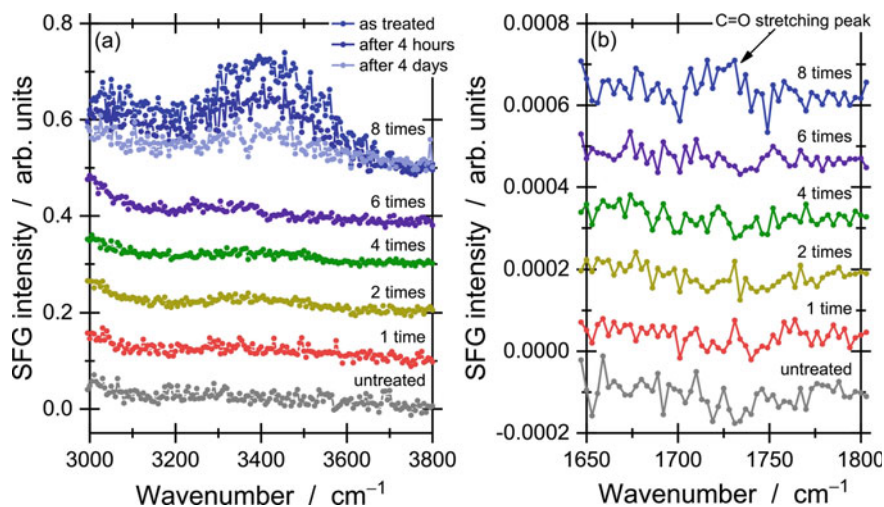
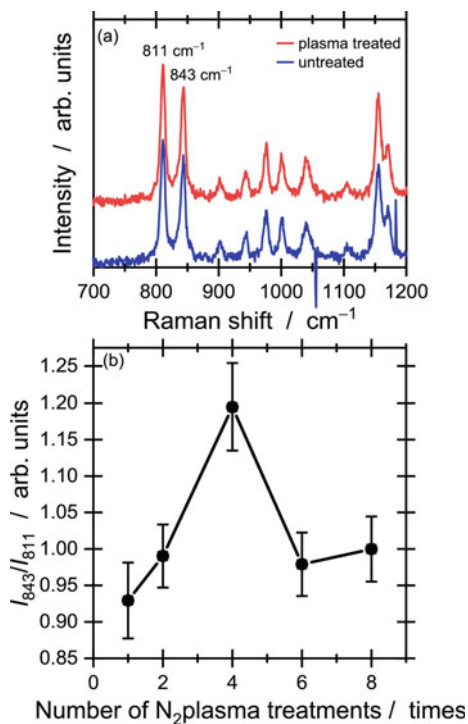


Fig. 13 The SFG spectra of the pristine and N₂ gas plasma treated polypropylene surfaces collected by SSP polarization combination. **a** O–H stretching and **b** C=O stretching regions. Reprinted with permission from Ref. [55]. Copyright 2018 Elsevier, All Rights Reserved

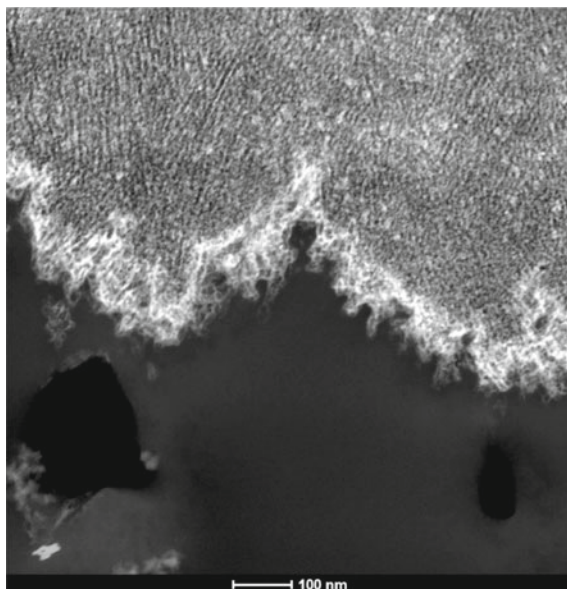
Fig. 14 **a** Raman spectra of the pristine and N₂ plasma treated polypropylene near the surface region. **b** The peak intensity ratio, I_{843}/I_{811} , is plotted as a function of the number of plasma treatments. Reprinted with permission from Ref. [55]. Copyright 2018 Elsevier, All Rights Reserved



peak intensity ratio increased with increasing treatment cycles. Since the peaks at 811 and 843 cm^{-1} are respectively related to the crystalline and amorphous phase of polypropylene, the Raman observations indicate that a thin amorphous layer is formed after plasma irradiation at the surface region.

The annular dark field (ADF) STEM image shown in Fig. 15 also reveals the existence of the amorphous layer with a thickness of ca. 50 nm formed at the 4-times N₂ plasma-treated polypropylene/adhesive interface bonded after the plasma surface treatment. This STEM image clearly indicates that the plasma treatment forms the roughness of the polypropylene surface with complicated nanometer features and the adhesive can be penetrated such small features. In polypropylene, we note that the amorphous part can be selectively stained, which enables us to see the polypropylene lamellar structure. As can be seen in the ADF-STEM image in Fig. 15, the polypropylene lamellar is formed just below the surface of polypropylene, indicating that the plasma treatment can selectively modify the surface region (ca. 50 nm thick) of the polypropylene without the damage of the bulk polypropylene. In the ADF-STEM image, the bright part indicates to the RuO₄-stained area. Therefore, it is clearly recognized that thin amorphous layer is formed at the interface even after the forming of the joint interface. The thin amorphous layer on the surface contains polar groups such as hydroxyl and carbonyl groups, and we believe that the formation of

Fig. 15 STEM-ADF image of the interfacial region between the 4-times N₂ gas plasma treated polypropylene (upper part) and the adhesive (lower part). Reprinted with permission from Ref. [55]. Copyright 2018 Elsevier, All Rights Reserved



such thin amorphous layers greatly contributes to the improvement of the adhesive properties of the poor adhesive polypropylene.

(B) *Flame treatment for the polypropylene resin surfaces*

As in the case of the plasma treatment process, flame treatment is also used to improve the adhesion strength of polypropylene. Next, we discuss how the surface structure induced by the flame treatments on the polypropylene differs from that induced by that of the plasma treatment [61]. The flame treatment of the samples was performed by a commercial gas burner and the polypropylene plates were moved at a constant speed in one direction at 200 mm/s using automatic moving stage. The distance between the polypropylene surface and the burner's nozzle was 3 cm. In each surface treatment, the samples were moved back and forth once as a one-time treatment, up to 8 times on each surface. After these surface treatments, the adhesive strengths of the polypropylene surfaces were apparently improved compared to the untreated surfaces. In the sample treated with N₂ plasma four times, the adhesive strength was improved by more than 8.0 MPa. In addition, the adhesive strengths increased up to 5.7 MPa in the case of four times flame-treated samples. These results indicate that both treatments are effective techniques for improving the adhesion properties of polypropylene surfaces.

In Fig. 16, the subtracted ATR-IR spectra of the flame-treated polypropylenes are shown. As with the plasma-treated samples, the IR band intensities of both C=O and O-H bands increased with increasing treatment cycles. The IR band intensity of the amide group, which is observed at 1680 cm⁻¹, but not the carbonyl groups, increased with repeating N₂ plasma exposure, while the intensity of the C=O band

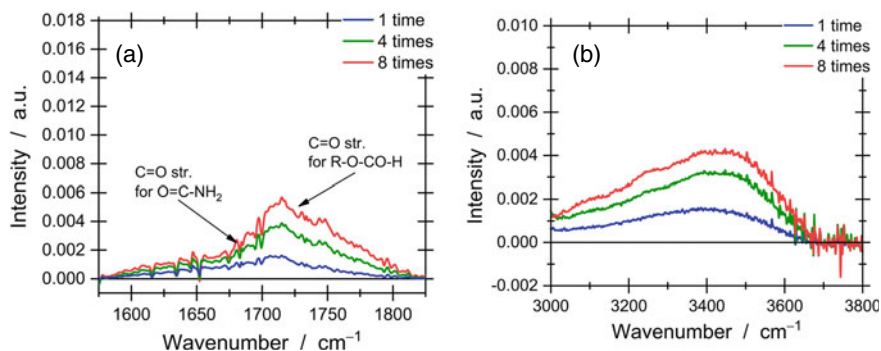


Fig. 16 Subtracted ATR-IR spectra of flame-treated polypropylenes collected using Ge prism. **a** C=O stretching region and **b** O-H stretching region. Reprinted with permission from Ref. [61]. Copyright 2018 Elsevier, All Rights Reserved

corresponding to the carbonyl group, rather than the amide group, increased with repeating flame treatment. This trend of the flame treatment was opposite to that of the N_2 gas plasma treatment case.

To examine the impact of the treatments on the bulk region of polypropylene, the depth profiles of the O-H and C=O groups were investigated using two different ATR-IR prisms, Ge and ZnSe, which have different refractive indices. The depth analyzes for the N_2 plasma-treated and flame-treated polypropylenes are shown in Fig. 17. In both surface treatments, the corresponding IR band intensities of the hydrophilic functional groups increase with increasing number of treatment cycles. These results suggest that the amount of the introduced functional groups increases with the number of treatment cycles. Although the trends of increase in the number of the hydrophilic functional groups after both treatments are almost the same, the observed IR band intensities of the introduced functional groups are quite different. The IR intensities of the O-H bands of the N_2 plasma-treated polypropylene samples are larger than those of the flame-treated samples. In addition, the IR intensities of the O-H bands of the N_2 plasma-treated samples observed with the Ge prism are larger than those observed with the ZnSe prism. This result indicates that the O-H moieties introduced by N_2 plasma irradiation are distributed unevenly near the polypropylene surface region, rather than in the bulk direction, since the IR probing depth of the O-H band region is estimated to be approximately 200 nm and 600 nm for the Ge and ZnSe prisms, respectively. On the other hand, no significant difference in the IR intensity of the C=O band is observed for both N_2 plasma- and flame-treated polypropylenes depending on the prism, indicating that the introduced carbonyl functional groups are almost uniformly distributed from the surface to the bulk region.

For the investigation of the molecular structure at the topmost surfaces of polypropylenes before and after surface treatments, SFG measurements were performed for the pristine, 4-times N_2 plasma-treated, and 4-times flame-treated polypropylene surfaces under atmospheric conditions. Figure 18 shows the SFG spectra of each sample taken with the polarization combinations of SSP and PPP

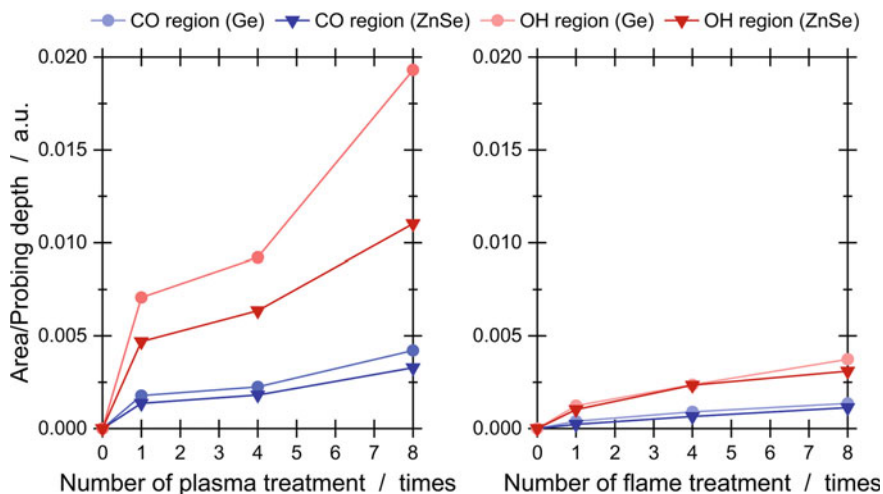
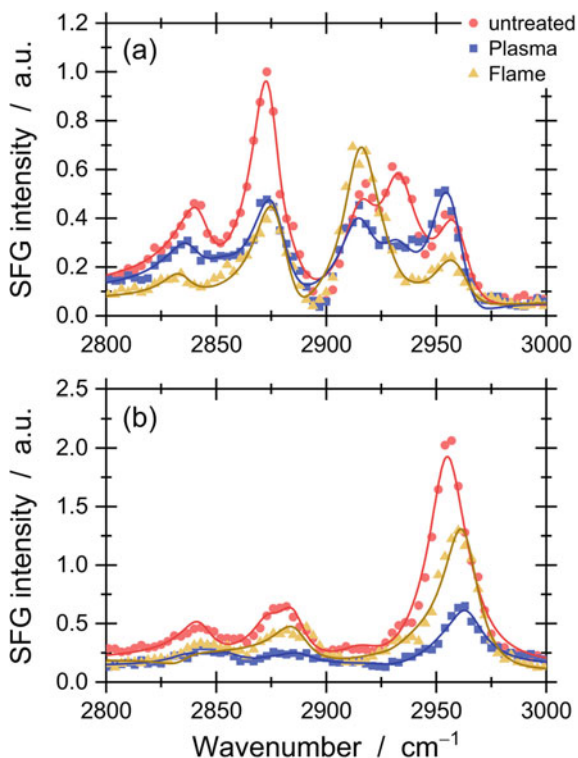


Fig. 17 Depth profile analysis of the O–H and C=O groups evaluated from ATR-IR as a function of the treatment cycles. (left) N_2 plasma treatment. (right) Flame treatment. Reprinted with permission from Ref. [61]. Copyright 2018 Elsevier, All Rights Reserved

in the C–H stretching region. The SFG spectra of the N_2 plasma-treated and flame-treated polypropylenes surfaces show a decrease in the SFG signal intensities and a shift in the peak position is observed with some peaks for each treated sample, indicating that the conformations of the treated polypropylene surfaces are changed by both the N_2 gas plasma treatment or flame treatment. To confirm the changes in the orientations of the surface functional groups before and after surface treatments, the polar tilt angles of the CH_3 group of the polypropylene are estimated. Before the surface treatments, the methyl groups on the polypropylene surfaces are inclined at about 66° from the surface normal. After the N_2 gas plasma and flame treatments, the orientations of CH_3 change to 56° and 85° from the surface normal, respectively. These results indicate that the molecular conformations of the treated polypropylene surfaces have been modified by the N_2 plasma irradiation or burning with flame, resulting in the rearrangement of the molecular orientation. For the N_2 plasma treated sample, a new broad feature is found at 2855 cm^{-1} [55] probably because decomposed species are created by excessive N_2 plasma irradiation.

Contrary to the case of the plasma-treated samples, no SFG bands derived from both C=O and O–H bands are observed for the flame-treated samples. Such a result suggests that the functional groups introduced by plasma irradiation or flame treatment are not exposed on the air side of the uppermost surfaces. Previous works have also suggested that the introduced polar functional groups are flipped toward the bulk side [58]. Because the glass transition temperature of polypropylene is lower than room temperature, the molecular orientation can be easily changed to migrate polar groups toward the bulk side, where the surface free energy becomes lower.

Fig. 18 SFG spectra in C-H stretching region of the pristine, N₂ plasma-treated and flame-treated polypropylenes acquired with the polarization combinations of **a** SSP and **b** PPP. The solid curves are the fitting curves. The SFG spectra were normalized by the peak intensities of the 2880 cm⁻¹ of the pristine polypropylenes collected by the SSP polarization combination. Reprinted with permission from Ref. [61]. Copyright 2018 Elsevier, All Rights Reserved



The question is what is formed on the polypropylene surface by these two surface treatments? Fig. 19 shows the IR spectra of polypropylene treated with plasma and flame treatment and what happens when the treated polypropylene is rinsed by water. After surface treatments of the polypropylenes, hydroxyl and C=O bands are observed in both surface treatments, but after rinsing by water, all of these bands decrease in intensity in the IR. This indicates that the molecules created by these surface treatments are relatively low molecular weights and contain large numbers of polar groups such as hydroxyl and C=O groups. Note that O–H and C=O almost disappeared after rinsing with water in the plasma treated polypropylenes, while they still remained after rinsing in the flame treated one.

The existence of such low molecular weight molecules is also indicated by the change in the contact angle before and after rinsing by water. Figure 20 illustrates the changes in static water contact angles before and after rinsing by water. The contact angle of plasma-treated polypropylene changes significantly after rinsing by water, and it shows water repellency is rather higher than that of the untreated one. Surprisingly, it is noteworthy that even when the low molecular weight molecules on the surface are almost completely removed by such rinsing, there is little difference in adhesive strength. In other words, the low molecular weight components containing

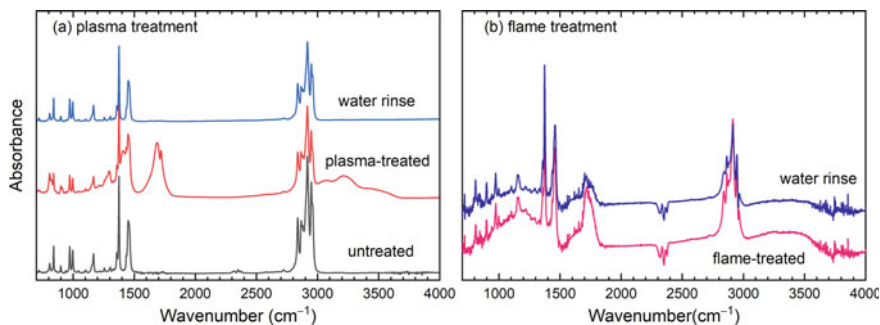


Fig. 19 ATR-IR spectra of **a** plasma-treated and **b** flame-treated polypropylenes before and the after rinsed by water

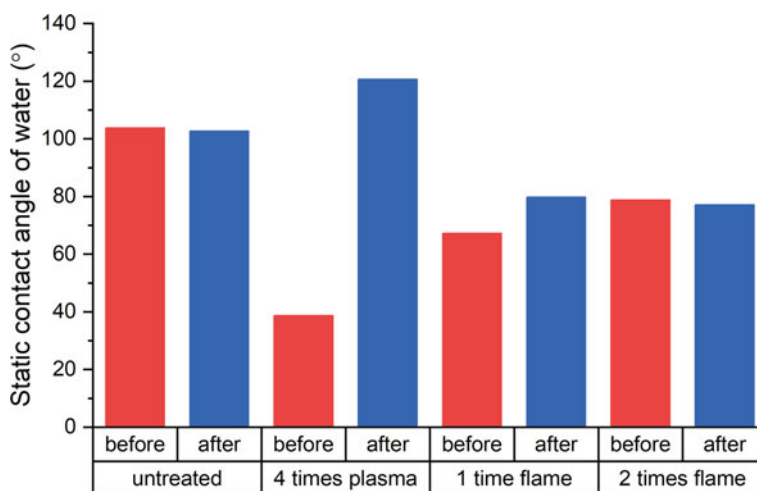


Fig. 20 Changes in the static water contact angles of the surface treated polypropylenes before and after rinsing by water

large numbers of polar groups, which are generated near the surface by the surface treatments, do not significantly affect the adhesion mechanisms.

4.1.2 Characterization of Primer Modified Polymer Surfaces

Adhesive promoters for the chemically inert materials have often been used for improvement of the poor adhesion. Such adhesion promoters are believed to connect directly to the surfaces to be bonded and thereby modify the surface properties. However, direct evidence of chemical reactions occurring at the bonding interface has not been presented for most of the material combinations used to date. This is

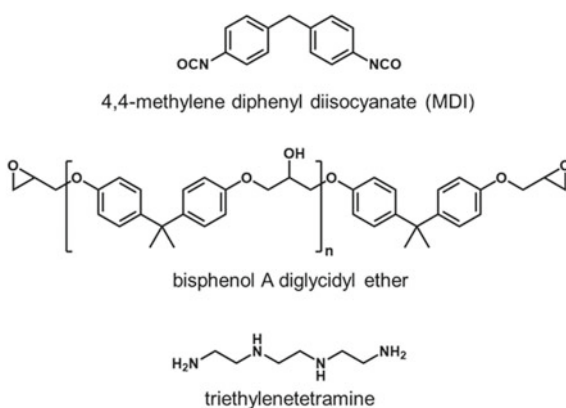
probably due to the fact that it is technically difficult to characterize the nature of chemical bonds at the buried interface between an adherent and an adhesive at the molecular level. Therefore, we have used an indirect indicator, such as the adhesion strength, to evaluate the impact of the surface pre-treatment on the process. However, adhesion strength is rarely dependent on a single factor, making it difficult to clarify the promotion of chemical bond formation only from this parameter.

Here we show the molecular reaction behavior at the interface between an epoxy polymer and a primer with isocyanate functional groups [62]. Isocyanates are well-known to react with hydroxyl groups to form urethane bonds, and this chemical reaction is popularly used in polyurethane polymerization processes. Therefore, infrared spectroscopy can be used to directly monitor the progress of the polymerization reaction in the bulk from the disappearance of isocyanate bands and the formation of C=O bands. However, since the formation of the urethane bonds at the interface between the isocyanate and the epoxy polymers has not been directly observed so far, we wished to observe this chemical reaction at the interface *in situ*.

A mixture of the precursors of the epoxy polymer, bisphenol A diglycidyl ether and triethylenetetramine, were diluted with chloroform and then spin-coated on the transparent calcium fluoride substrates coated with a 100 nm thick silica film. After spin-coating, the polymer films were cured at 80 °C for 18 h. 5 wt% butyl acetate or chloroform solutions of 4,4-methylene diphenyl diisocyanate (MDI) were prepared as a model isocyanate primer compound, since MDI is the main component of commercial isocyanate primers. The chemical structures of the precursors of the epoxy polymer and MDI are illustrated in Fig. 21.

Figure 22a, d show the SFG spectra in the C=O stretching region of the epoxy polymer when in contact with MDI butyl acetate and chloroform solutions, respectively. When urethane bonds are formed between the hydroxyl groups of the epoxy polymer and the isocyanate groups of MDI molecules, a C=O band derived from the urethane bond appears around 1730 cm^{-1} [63]. Before the contact with the MDI solution, no C=O peak is seen at the epoxy surface, as shown in the red curve in Fig. 22a. However, a C=O stretching band appeared when the epoxy polymers

Fig. 21 Chemical structures of the materials used in this study. Reprinted with permission from Ref. [62]. Copyright 2018 Royal Society of Chemistry, All Rights reserved



come into contact with the MDI solutions at room temperature. In the case of the SFG results obtained from the interface between the epoxy polymer and the MDI butyl acetate solution, we have to consider the contribution from the C=O stretching band of butyl acetate as in the case of the ATR-IR. However, the appearance of a C=O stretching peak was also observed in the SFG spectrum taken from the interface between the epoxy polymers and the chloroform solution of MDI, as shown in Fig. 22d. Therefore, we can exclude the contribution from the C=O stretching band of butyl acetate and we conclude that the SFG peak at 1730 cm^{-1} originates from the C=O stretching of urethane bonds formed at the epoxy surfaces. The SFG spectra of the hydroxyl groups of the epoxy polymer should change as they react with the isocyanates of MDI, since the urethane bonds are formed by the reaction between the isocyanate groups of the MDI molecule and the surface hydroxyl groups of the epoxy polymer. Figure 22c, f show the SFG spectra of the epoxy polymer interfaces before and after being in contact with the butyl acetate and chloroform solutions of MDI in the O–H stretching region. The hydrogen-bonded O–H bands are clearly visible in the SFG spectra of the epoxy polymer before contact with the MDI solutions, but they disappear completely after contacting the MDI solution. On the other hand, O–H bands remain in the SFG spectra of the epoxy/butyl acetate solvent interface as shown in Fig. 22c. The fact that the O–H bands completely disappear by contacting with MDI-butyl acetate solution and do not disappear only by contacting with butyl acetate solvent without MDI may support that the O–H group on the epoxy surface was spend for the reaction with MDI. Even if not, there is certainly an interaction between MDI and O–H in epoxy polymer. Note that the intensity of the O–H stretching band became weak in the SFG spectrum in contact with liquids, as shown in Fig. 22c. This is due to the Fresnel factor difference between solid/air and solid liquid interfaces. Although the SFG peak intensity does not only represent the amount of the surface functional groups, this result suggests that the hydroxyl groups on the epoxy polymer surfaces have reacted with isocyanate groups on the MDI. For comparison, in Figs. 22d, f, we also demonstrate the SFG measurements for the polypropylene/MDI chloroform solutions. Since polypropylene does not have a hydroxyl group, it can be found that no C=O stretching band is appeared at the interface, even when it contacts with the MDI solution. It can be seen that the peaks attributed to hydroxyl groups on the epoxy polymer surface may originate not only from the O–H groups on the polymer surface, but also from water molecules adsorbed on the epoxy polymer surface.

Figure 22b, e illustrate the SFG spectra in the NCO stretching region at the interfaces between the epoxy polymer and the MDI solutions. It is interesting to note that the asymmetric stretching mode of the isocyanate groups in the MDI molecule is observed at 2270 cm^{-1} for both the butyl acetate and chloroform solutions of MDI epoxy interfaces. This peak can be assigned to the unreacted isocyanates groups of MDIs. As shown in Fig. 22e, the unreacted NCO peak is also observed in the SFG spectrum of polypropylene/MDI solution interface. To remove the influence of the unreacted MDI molecules adsorbed at the epoxy polymer surfaces completely, the epoxy polymers are rinsed with acetone after being in contact with the MDI-butyl

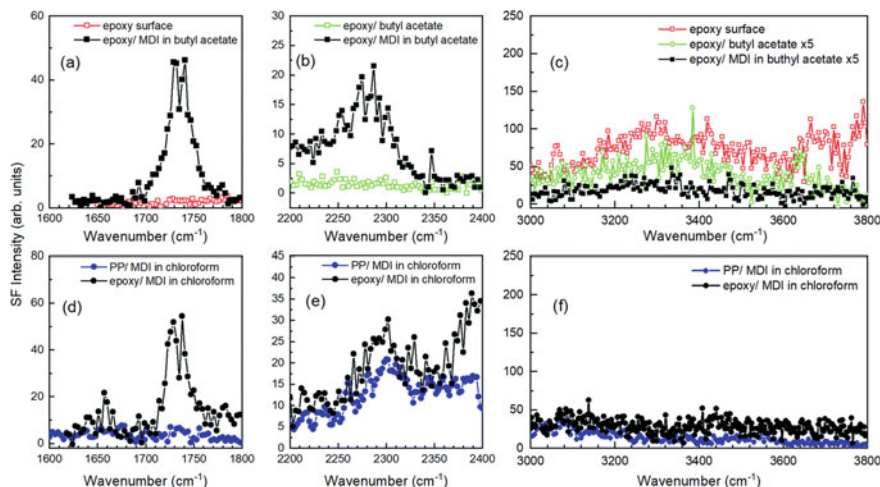


Fig. 22 **a–c** SFG spectra of the epoxy polymer surface (red open square), epoxy/butyl acetate solvent interface (green open square), and epoxy/MDI butyl acetate solution interfaces (black filled square). The SFG spectra in the O–H region **c** of the butyl acetate/epoxy interface with and without MDI were multiplied by 5 for ease of comparison with that of the air/epoxy interface. **d–f** Polypropylene/MDI chloroform solution interface (blue filled circle) and epoxy/MDI chloroform solution interface (black filled circle). Reprinted with permission from Ref. [62]. Copyright 2018 Royal Society of Chemistry, All Rights reserved

acetate solution. Furthermore, the samples are dried by heating at 80 °C to eliminate the influence of the residual butyl acetate and acetone. Even after rinsing and heating, peaks derived from both C=O and NCO stretching can be observed at the epoxy polymer surface in the air atmosphere, as shown in Fig. 23.

Based on these observations, we postulate the chemical reaction processes that can occur at the interface between the epoxy polymer and the MDI molecule, as shown in Fig. 24. Upon contact of the epoxy polymer surface with the MDI solution, the isocyanate moieties on one side of the MDI molecule react rapidly with the hydroxyl groups on the epoxy polymer surface. On the other hand, the isocyanate groups on the other side of the MDI molecule remain in the unreacted state. Since the isocyanate group reacts highly with polyols, which are components of polyurethane adhesives, the residual isocyanate function of MDI can react with the polyol groups in the adhesive. In fact, in the SFG spectra, signal of residual isocyanate completely disappears when MDI-treated epoxy surfaces are contacted with polyethylene glycol. Consequently, a chemical bridge is formed between the epoxy polymer and the adhesive by the MDI promoter. This is expected to improve the bond strength between the epoxy polymer and the polyurethane adhesive. Indeed, primers containing molecules with isocyanate groups have been used for several decades to promote adhesion between clear epoxy coatings and polyurethane adhesives.

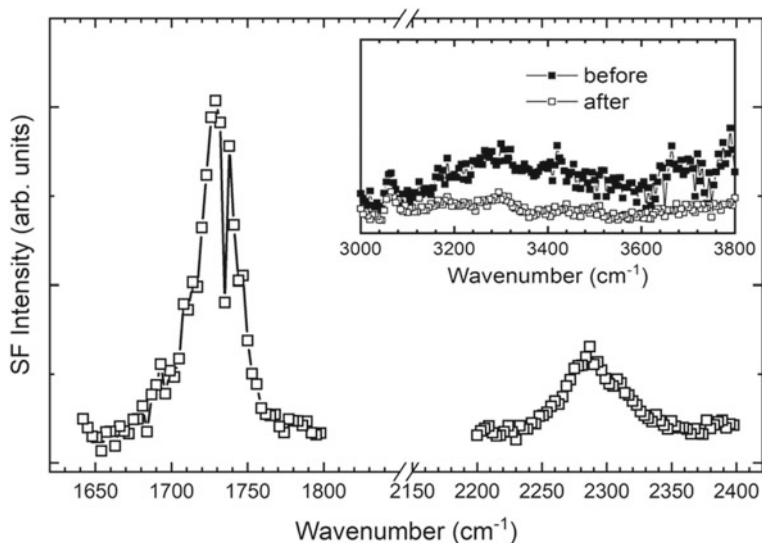


Fig. 23 SFG spectra for the C=O stretching region and NCO asymmetric stretching region of the epoxy polymer surface treated with an MDI-butyl acetate solution, after rinsing the surface with acetone and heating at 80 °C. The inset shows the SFG spectra of the epoxy polymer surface before and after treating with MDI-butyl acetate solution for the OH stretching region taken in the air atmosphere. Reprinted with permission from Ref. [62]. Copyright 2018 Royal Society of Chemistry, All Rights reserved

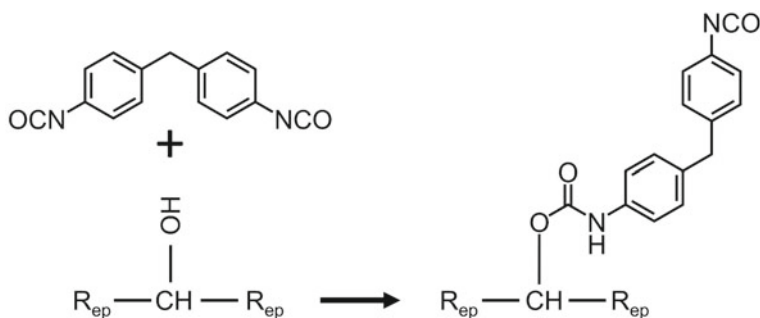


Fig. 24 Possible chemical reaction between MDI and the epoxy surface

5 Investigation of Buried Polymer/polymer Interfaces

SFG spectroscopy has been extensively applied to probe buried polymer interfaces, including those with liquids, organic solids, inorganic solids, other polymers, and metals. Dhinojwala group studied the interface between polystyrene (PS) and a comb polymer poly(vinyl N-octadecyl carbamate-co-vinyl acetate) (PVDC) using SFG spectroscopy [64].

PVDC has long alkyl side chains. The long, hydrophobic alkyl side chains segregate to the air interface and provide a nonstick surface for a good release. Therefore, the adhesion and wetting behavior is strongly influenced by the bulk side chain melting temperature. In their work, a total internal reflection (TIR) SFG geometry shown in Fig. 25 was applied based on a sapphire prism. From the SFG observation using TIR geometry, both the methyl and methylene groups from the comb polymer were ordered at the polymer/polymer interface. As shown in Fig. 26, the presence of the methylene signal at the PS/PVDC interface indicated the gauche defects on PVDC alkyl side chains at the interface. The phenyl groups from PS were also ordered at the interface, while the phenyl rings are tilted with respect to the interface normal [64]. Dhinojwala group also studied the molecular orientation of the polymer interfaces and their temperature variations of two release agents, poly(vinyl octadecylcarbamate-co-vinyl acetate) (PVNODC) and poly(octadecyl acrylate) (PA-18) [65]. On heating, an abrupt drop in SFG intensity at 43 °C for the PS/PA-18 interface coincides with the bulk transition temperatures of PA-18, also at 43 °C. The drop in SFG intensity for the PVNODC/PS interface is gradual and matches with the broad transitions observed in bulk PVNODC. These observations indicate that the disordering is correlated with the bulk structure and transition temperatures [65].

More practical adhesive/release agent interfaces are those used in pressure-sensitive adhesive (PSA) tapes [66]. Poly(ethylene-co-vinyl-n-octadecyl carbamate) (PEVODC) belongs to the general class of long alkyl side chain polymers, which are widely used as release coatings for the commercial PSA tapes. As shown in Fig. 27, there are significant differences in the peak intensities corresponding to the as-cast and annealed films. By comparing each r^+ peak intensity in the SSP and PPP modes, the net orientation of the polar tilt angles of the methyl groups was evaluated to be around 46° (non-annealed, as-cast) and 51° (annealed after casting) from the

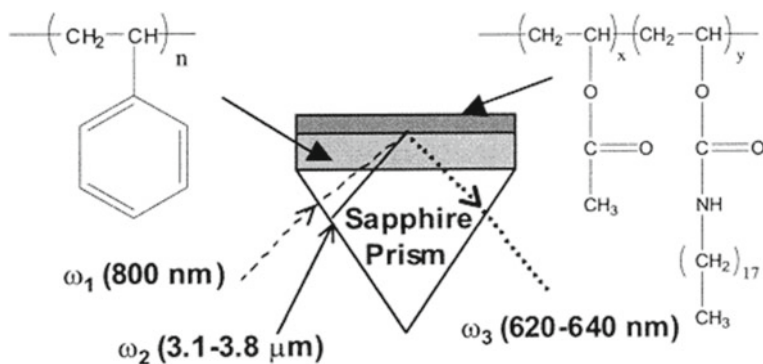


Fig. 25 Schematic illustration of the bilayer sample of the sapphire prism and experimental geometry. The bilayer consisted of a film of poly(vinyl-N-octadecyl carbamate-co-vinyl acetate) on top of a DPS or hPS film on the equilateral triangle sapphire prism. A visible beam (800 nm) and tunable IR beam (3.1–3.8 μm) were internally reflected at the Comb/dPS (or hPS) interface. Reprinted with permission from Ref. [64]. Copyright 2002 American Chemical Society, All Rights reserved

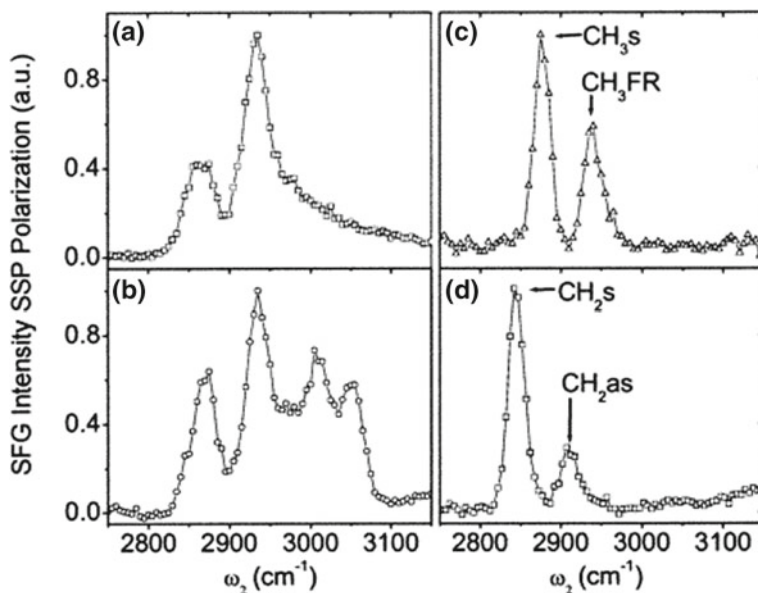


Fig. 26 SFG spectra in SSP (S-polarized SFG beam, S-polarized visible beam, P-polarized IR beam) polarization combination. **a** dPS/Comb interface of a bilayer sample at 8°. **b** hPS/Comb interface of a bilayer sample at 8°. **c** Air/Comb interface of a solitary Comb film at 42°. **d** Comb/sapphire interface of a solitary Comb film at 8°. Reprinted with permission from Ref. [64]. Copyright 2002 American Chemical Society, All Rights reserved

surface normal, respectively. Even when angle distribution is taken into account, the calculated angles are similar for both as-cast and annealed films. If comparable values for the polar tilt angle and orientation distribution of the methyl groups of the side chains are assumed, the surface density of oriented methyl groups is calculated to be 1.7 times higher in the annealed film than in the as-cast one, according to a previously reported equation. This observation clearly indicates that the highly-ordered crystalline-like domains of the octadecyl chains are formed by the annealing at the PEVODC surfaces. The peel force of the as-cast film is higher than that of the annealed one, suggesting that disordered alkyl chains between the crystalline domains can potentially increase the peel force. Therefore, the improvement in the crystallinity of the alkyl side chain suppresses the intercalation of the side chains of the adhesive at the adhesive/release agent interface and results in a reduction in the peel force. Thus, highly-ordered crystalline domain structures play important roles in reducing the peel force for the PSA tapes, which is attributed to the suppression of polymer-network entanglement.

Figure 28 presents the changes in the SSP-polarized SFG spectra of the interface between a typical acrylic adhesive and PEVODC by varying the annealing temperatures [66]. Two peaks corresponding to the methyl groups of the side chains are observed at 2880 cm^{-1} (r^+) and 2940 cm^{-1} . Note that almost no sum-frequency

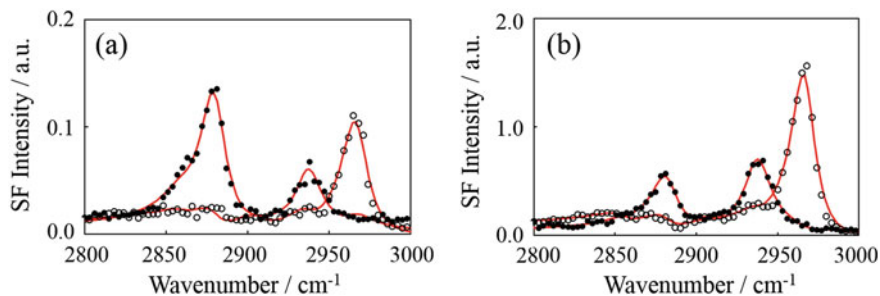


Fig. 27 SFG spectra of PEVODC films on the PET substrates. **a** as-cast film dried under ambient conditions (scaled) and **b** annealed at 100 °C. SSP (black circles) and PPP (white circles) polarization combinations. Reprinted with permission from Ref. [66]. Copyright 2018 Elsevier, All Rights reserved

signal is generated from the adhesive surface, as shown in Fig. 28. Hence, we can be confident that this peak is due to the methyl groups of the alkyl side chains of PEVODC, suggesting that the orientation of the alkyl side chains of PEVODC is maintained after contact with the adhesive. After heating the adhesive/PEVODC layer at 40 °C for 90 min, the intensity of the r^+ peak remains unchanged states, as shown in the blue curve in Fig. 28. When the films were heated at 70 °C, however, the intensity of the r^+ peak decreased drastically. In the case of the 70 °C heat-treated films, the peel force increased to 0.33 N. A curing temperature of 100 °C further decreased the r^+ peak intensity and an increase in the peel force were observed. The phase transition of the alkyl side chains occurs at 54 °C, followed by the phase transition of the main chain at 76 °C. Therefore, the intercalation of polymer chains at the adhesive/PEVODC interface is promoted by the curing process. These observations suggest that the randomization of PEVODC side chains at the interface and the intercalation of these polymer side chains by curing lead to an increase in the peel force values.

6 Probing Adhesive Interfaces

When adhesives are used in the assembling of buildings, houses, and other constructions, there are many advantages expected, such as easier assembly and weight reduction. On the other hand, it is extremely difficult to predict and evaluate the reliability of adhesion and joining. This is because adhesion between two objects occurs at a “buried interface,” and it is difficult to observe this interface directly. However, SFG spectroscopy enables to approach these interfaces by preparing the conditions that allow the light to reach the interfaces.

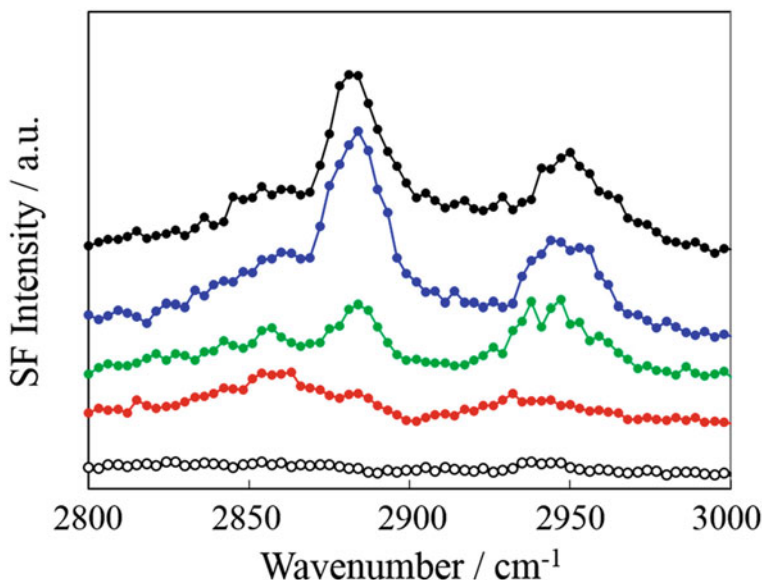


Fig. 28 SFG spectra of adhesive/PEVODC interfaces in SSP polarization combination: untreated (black) and after heated to 40 °C (blue), 70 °C (green), and 100 °C (red). The SFG spectrum of the adhesive surface is also shown for comparison (open circles). Heating time of each sample was 90 min. Reprinted with permission from Ref. [66]. Copyright 2018 Elsevier, All Rights reserved

6.1 Polyurethane Adhesives

Polyurethane compounds and sealants are widely used as encapsulants and protective barriers. Despite the utility of these polyurethanes, the basic mechanisms of adhesion are not well understood due to the difficulty of direct observation of buried interfaces. Interfacial properties such as adhesion are determined by the molecular structure of the interface. In this study, the curing behavior of polyurethane was observed in situ using SFG spectroscopy [67].

Polyurethane adhesives were prepared by mixing compounds with isocyanate groups (Millionate-NM, Tosoh) and main agents of branched aliphatic compounds having hydroxyl groups (Fig. 29), defoaming by vacuum evacuation, and stirring. This polyurethane adhesive is completely cured by heating at 120 °C for approximately 5 h after being coated on the substrates. Schematic of the heating sample stage used in the SFG measurements is shown in Fig. 30a. The temperature is monitored by the thermocouple connected to the sample stage and regulated by a digital temperature controller with proportional-integral-derivative (PID) control.

Figure 30b shows the SFG spectra of the polyurethane adhesive immediately after the preparation, which was applied to thin aluminum oxide-coated CaF₂ substrates and then heated sequentially from room temperature up to 150 °C. Around room

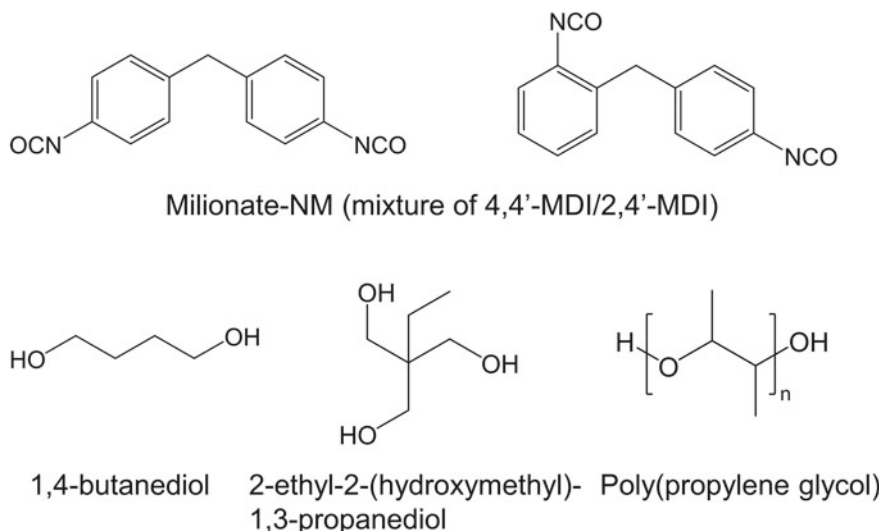


Fig. 29 Chemical structures of the compounds in polyurethane adhesive

temperature, the SFG peaks observed in the C-H stretching region gradually change with increasing temperature.

To investigate the temperature dependence of the SFG spectra, two-dimensional correlations are taken as shown in Fig. 31. Two-dimensional correlation spectroscopy, which is a well-known technique used in NMR, IR, and near-infrared spectroscopy, is a visualization method that can display the changes in a system when stimuli with certain directions (e.g., electric field, mechanical stress, temperature, or temporal changes) are applied [68–70]. By applying this two-dimensional correlation technique to the vibrational spectroscopy, it is possible to observe changes in the orientation distribution of dipole moments in a system under external stimuli. In the two-dimensional correlation spectra, there are two two-dimensional spectra that can be acquired: the synchronous and the asynchronous correlation spectra. Peaks that appear on the diagonal line in the synchronous spectra are called autocorrelation peaks, indicating that these peaks are responsive to a certain external stimulus. Peaks that appear off-diagonal are called cross-peaks and are useful for studying interactions between functional groups. If the sign of the cross-peaks of two wavenumbers (ν_1 and ν_2) is positive in synchronous correlation, it indicates that the ν_1 and ν_2 bands are oriented in the same direction to each other, i.e., they have the same reorientation in response to the external stimuli.

On the other hand, in the asynchronous correlation spectra, no autocorrelation peaks appear on the diagonal line, resulting in a two-dimensional spectrum that is asymmetric with respect to the diagonal line. The sign of the synchronous correlation represents the relative direction of the spatial reorientations, whereas the sign of the asynchronous correlation represents the temporal relationship of the reorientations, i.e., the relationship between the time before and after the reorientation changes.

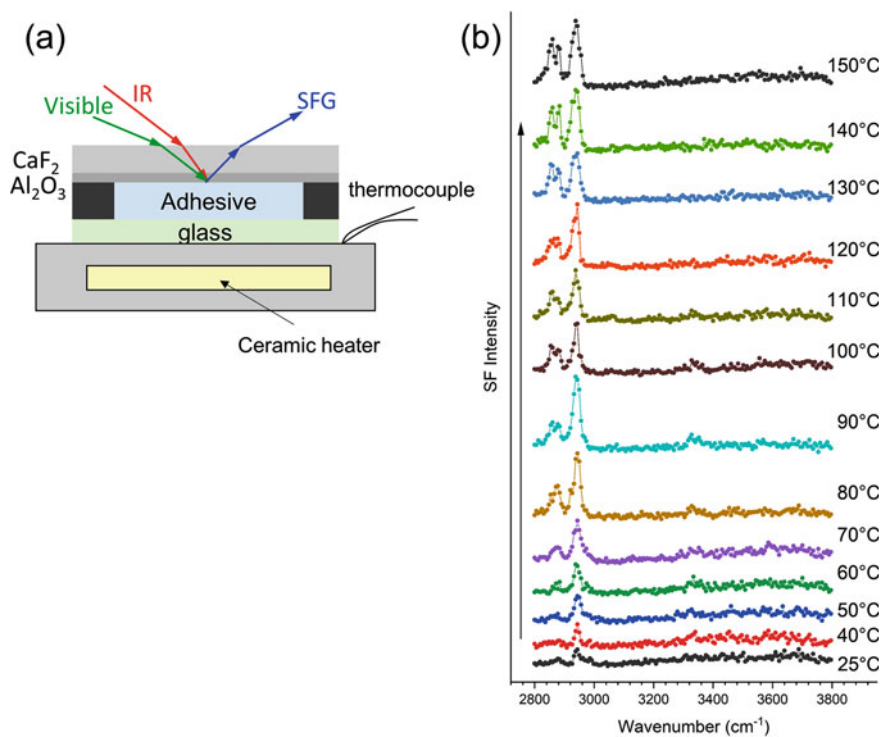


Fig. 30 **a** Schematic of the heating sample stage used in the SFG measurements. **b** Temperature dependent SFG spectra collected from aluminum oxide/polyurethane adhesive interface in SSP mode

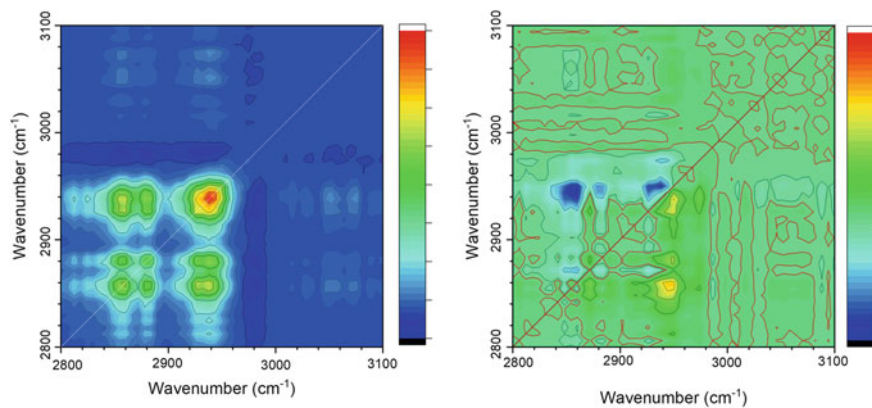


Fig. 31 (Left) Synchronous and (right) asynchronous two-dimensional correlation spectra of heat curing behavior of aluminum oxide/polyurethane adhesive interface

When the peak sign is positive, it indicates that the functional group corresponding to the wavenumber ν_1 on the horizontal axis is reoriented before the functional group corresponding to the wavenumber ν_2 on the vertical axis. In the case of a negative cross-peak in the synchronous correlation spectrum, the temporal relationship in the asynchronous correlation corresponds to the opposite of the previous relationship [68–70].

In the SFG spectra of the polyurethane adhesives in Fig. 30, the peaks at 2850, 2880, 2940, and 3320 cm^{-1} are attributed to symmetric CH_2 , symmetric CH_3 , CH_3 Fermi resonance, and NH stretching vibrations, respectively. The NH stretching derived from the urethane bond is observed immediately after application, indicating that the polymerization curing reaction is not in progress in the bulk, however, the urethane bond is already formed at the adhesive interface and the NH is already created. It is believed that adhesive strength between metal and epoxy adhesives is expressed by the interaction between the oxide film and the adhesive molecules. Functional groups such as amines and amides may act as Brønsted or Lewis bases because the oxygen and nitrogen atoms have a lone electron pair. Also, the aluminum oxide surface coated on the substrate exhibits OH groups, which can act as Brønsted acid or Lewis acid owing to the coordinatively unsaturated metals. The observation of NH groups in the SFG spectra suggests that Lewis acid–base interactions at the interface with the aluminum oxide have taken place immediately after the application of the adhesive. Such interactions may have attracted NH groups in the urethane bonds, and NH groups were observed at the interface of the polyurethane adhesive before curing. In fact, it has been reported recently that amine containing in polymers segregate at the metal–metal interfaces [71, 72]. On the other hand, the CH_2 and CH_3 of the alkyl chains are not clearly visible immediately after the application of the adhesive, and it is considered that the alkyl chains are nearly in a randomly oriented conformation.

Two-dimensional correlation spectra of the heating behavior in Fig. 31 show that the peaks of CH_2 and CH_3 have a positive sign with synchronous correlation. This indicates that immediately after the application of the adhesive, the NH groups of the urethane bond gather at the aluminum oxide interface, and CH_2 and CH_3 are in almost random orientation at room temperature. However, with the progress of the curing by heating, the SFG peaks of CH_2 and CH_3 become distinct at the interface. The cross-peaks at 2850 and 2940 cm^{-1} in the asynchronous correlation spectrum in Fig. 31 show a negative sign, indicating that the CH_3 changes occur prior to the changes in CH_2 . The signs of the cross-peaks at 2850, 2880, and 3320 cm^{-1} are both negative in the synchronous correlation spectrum and negative in the asynchronous correlations. This indicates that NH groups decrease at the interface as the curing proceeds, and that the time behavior is preceded by the changes in CH_3 and CH_2 . In general, it is known that urethane adhesives do not adhere well to the aluminum. During the curing process, the alkyl main chains are aligned and the NH groups that have been segregated at the interface due to their interaction disappear. This may be one of the reasons for the loss of adhesiveness against aluminum adherents after the curing of the polyurethane adhesives.

6.2 Silyl-Terminated Polyether Adhesives

Silyl-terminated polyester liquid polymer reacts with moisture in the air at room temperature when combined with a curing catalyst. The elastic sealants using this polymer are known as modified silicone-based sealants, and they have excellent durability, heat and cold resistances, and good economic performance. Elastic adhesives using this silyl-terminated polyester polymer also have high resistance to external stresses such as mechanical impacts and vibrations, as well as temperature changes, and are used in architectural applications.

In this study, the adhesive materials, silyl-terminated polyester (MS-polymerTM), and adhesives were provided by Cemedine Co., Ltd. SFG measurements at the interfaces during curing were performed for each of the Silyl-terminated polyester and aminosilane agent blended with the silyl-terminated polyester. The Chemical structures of the materials used in this study are shown in Fig. 32 and their compositions are summarized in Table 1 and are referred to as MS-1 and MS-3, respectively. 3-aminopropyltrimethoxysilane coupling agents are added to silyl-terminated polyester to accelerate the curing reaction, as indicated in Table 1.

As in the case of the polyurethane adhesives in the preceding section, SFG measurements at the adhesive interfaces were performed for aluminum oxide-coated CaF₂ substrates immediately after the coating, during curing, and after enough time had passed for the adhesive to become hardened.

Figure 33 shows the time evolution of the SFG spectra at the interface between MS-3 and the aluminum oxide thin layer from immediately after the application up to 22 h. Characteristic peaks at 2840 and 2940 cm⁻¹ are observed immediately after the coating of MS-3 mixed with aminosilane. The peaks are assigned to the methyl symmetric stretching vibration derived from the -OCH₃ of aminosilane and the Fermi resonance of the -OCH₃, respectively [73]. At the MS-3 interface in contact with the aluminum oxide film, these silane-derived peaks gradually decrease through time and, though it depends on the surrounding conditions, almost disappear completely after approximately 2.5–4 h. Instead of this decrease in intensities of the peaks, other new peaks appear at 2850 and 2882 cm⁻¹. These new peaks correspond to the symmetric stretching vibrations of methyl and methylene groups originating from the polyester polymer, as shown later, while the Fermi resonance at 2940 cm⁻¹ is indistinguishable because of the overlap between the methoxymethyl group origin and the

Table 1 Compositions of the silyl-terminated polyester adhesives (by weight)

		MS-1	MS-3
Polymer	Dimethoxysilyl-terminated polyester (SAT200)	100	100
Catalyst additive	Dibutyltin diacetate	2	2
	3-aminopropyltrimethoxysilane		5
	Tack-free time	3 days	6 min
	Curing condition; 23 °C, 50%RH, 7 days		

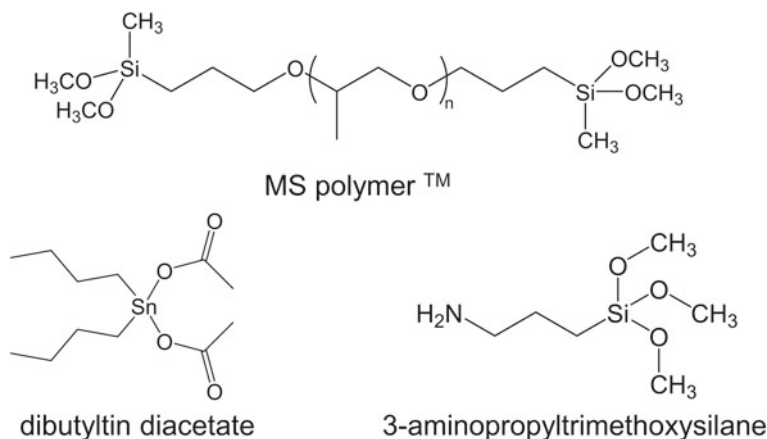


Fig. 32 Chemical structures in the silyl-terminated polyester adhesives

methyl origin. The time dependence of these SFG spectra strongly suggests that the functional groups present in the polymer main chain are not observed immediately after application, probably due to the random orientation of the polymer chains and the segregation of the silane coupling agent at the interfaces.

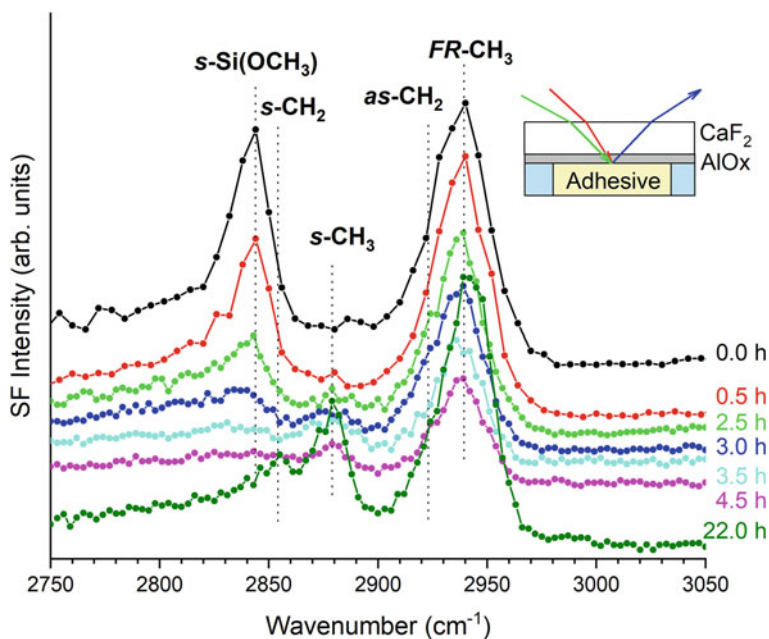


Fig. 33 SSP-polarized SFG spectra following the time evolution of the MS-3 and aluminum oxide interface after application

The $-\text{OCH}_3$ bonded to the Si atom of these aminosilanes and the $\text{SiOCH}_2\text{CH}_3$ group at the end of the MS-polymer decompose upon reaction with moisture. To observe the reaction behavior with water at the interface, SFG spectra measured from the C-H to the O-H band regions are shown in Fig. 34. Since the substrate was coated with aluminum oxide that had been cleaned by ozone treatments, broad O-H band was observed before the polymer coating, probably due to the O-H groups on the aluminum oxide and the water adsorbed on the surface. These hydrogen-bonded O-H bands are still observed immediately after adhesive application on the aluminum oxide layer, however, the water bands observed at the interface decrease in intensity as the adhesive cures. This suggests that the adsorbed water molecules present at the interface are consumed by the Si-OCH₃ decomposition reaction. The tack-free time of MS-3 is ca. 6 min on the adhesive surface. However, at the interface with aluminum oxide, the decreases of Si-OCH₃ and O-H groups are found to occur over a period of a few hours. This is probably because molecular mobilities are suppressed at the interface and there are less occasions for reaction with water than at the surface, resulting that the active silane coupling agent takes some time to react with the water molecules.

In the SFG spectrum of MS-1/ AlO_x interface shown in Fig. 35 exhibits 2850, 2882, and 2940 cm^{-1} peaks, derived from the main chain of the silyl-terminated polyester are observed. As shown in Fig. 35, the SFG spectrum of the MS-3 at the interface after completely cured is almost identical to that of MS-1 interface, which does not contain any silane coupling agents. This result suggests that the main chain of the modified silicone adhesives has almost the same structure with respect to molecular orientation at the interface after curing. However, as shown in Table 1, these adhesives

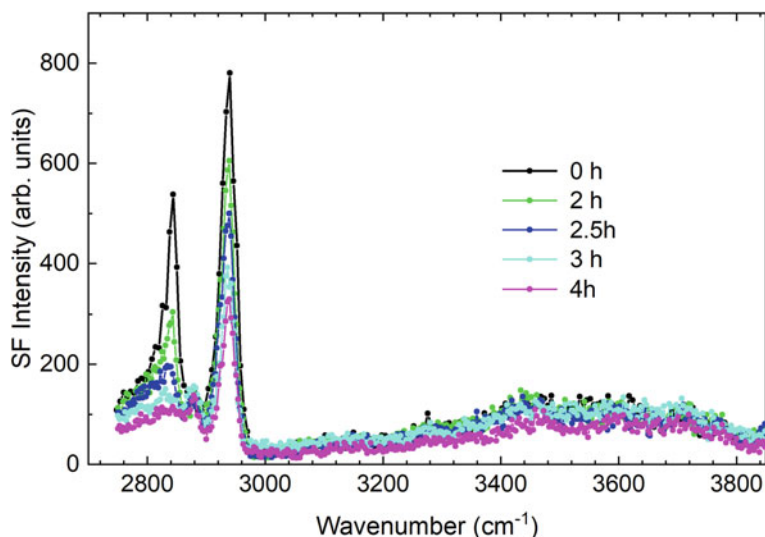


Fig. 34 SSP-polarized SFG spectra from CH to OH stretching region following the time evolution of the MS-3 and aluminum oxide interface after application

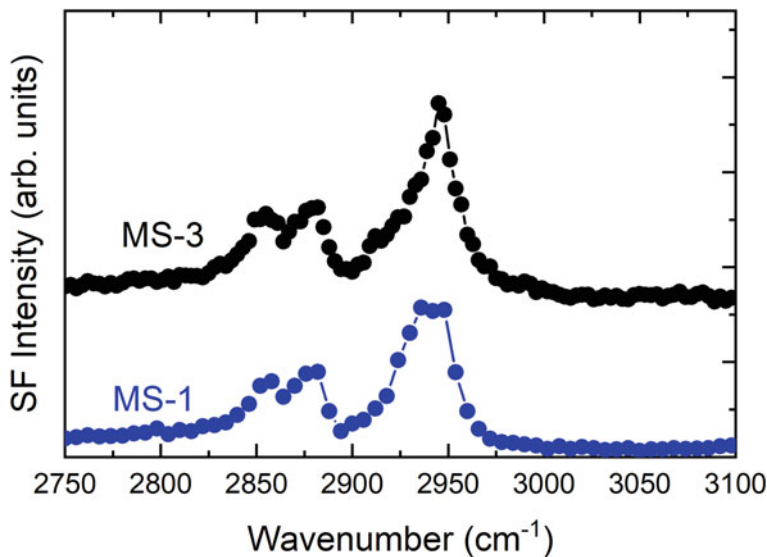


Fig. 35 SSP-polarized SFG spectra of the MS-3/ AlO_x and MS-1/ AlO_x interfaces after completely cured, respectively

differ significantly in curing time, suggesting that their curing reaction behavior in the bulk is quite different. Since the adhesion strength of MS-3 is much stronger than that of MS-1, therefore we conclude that MS-3 has different curing behavior due to the segregation of silane coupling agents at the interface, and that this different reaction behavior at the interface leads to the different adhesion strength.

7 Metal/polymer Interfaces

Polymers are frequently used in contact with metals, such as during metal coating and adhesion. Preventing delamination or adhesion failure at the interface between metal and polymer or adhesive is an extremely important issue in electronics, automobiles, and other industrial applications. The adhesion should be contributed by such molecular level physical and chemical interactions and appeared as the detectable macroscopic adhesion strength. Since SFG can be applied to any interface that light can pass through and reach, it is particularly adept in elucidating chemical interactions at heterogeneous interfaces. However, metals are opaque in both infrared and visible lights, the polymer-metal interface is usually analyzed by applying thin organic materials on to the metal, which light can pass through, and analyzing the polymer/metal interfaces through this very thin film.

X. Lu et al. studied the buried PMMA/Ag interface from the analysis of the SFG spectra using multiple reflections [74]. In this analysis, SFG signals were measured

from a series of polymer films of different thicknesses. The different thicknesses produced different interference patterns in the overall SFG spectrum (Fig. 36), which could be used to extract the SFG spectral pattern from the buried interface. Such a method requires the preparation of polymer films of different thicknesses on top of the metal surface and accurate measurement of the film thickness. By using the SFG spectra from several samples with different film thicknesses and the interference model considering multiple reflections for each film thickness, the SFG spectral pattern contributed from the PMMA/Ag buried interface can be extrapolated. This SFG spectral analysis indicates that the structure of PMMA at the PMMA/Ag interface is different from that of the PMMA surface in air. On the PMMA surfaces in air, ester methyl groups are dominant and are regularly oriented towards the surface normal direction. On the other hand, at the PMMA/Ag interface, in addition to ester methyl groups, methylene and α -methyl groups are aligned toward the surface normal direction. The presence of methylene and α -methyl groups at the interface suggests that the ester methyl groups at the PMMA/Ag interface are more tilted away from the Ag substrate with a larger tilt angle [74].

In another method, where thin polymer film is sandwiched between metal and quartz window, the polymer/metal interfacial SFG spectra are obtained in a single measurement, as shown in Fig. 37 [75, 76]. This is because the SFG signal generated from the polymer/silica (or CaF_2) interface is usually negligible compared to the signal generated at the polymer/metal interface. Consequently, it was found that the

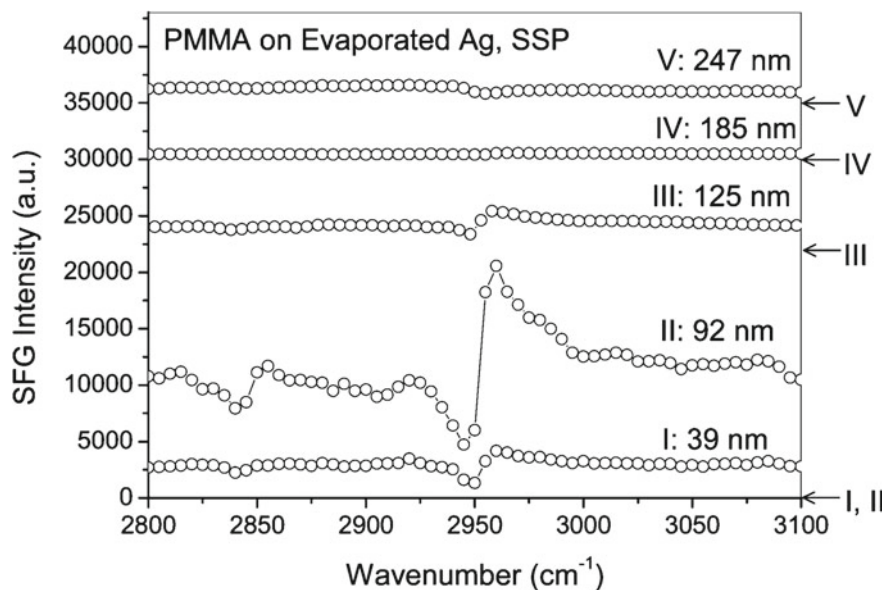


Fig. 36 The SFG spectra of PMMA films with different thicknesses on silver substrates acquired in SSP polarization combination. Reprinted with permission from Ref. [74]. Copyright 2008 American Chemical Society, All Rights Reserved

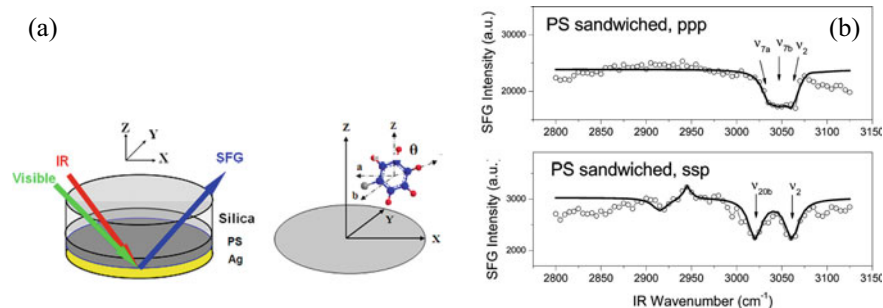


Fig. 37 **a** Schematics of the sample geometry and the relation between the surface (or interface, XYZ) and molecular (abc) coordinate systems. **b** SSP and PPP SFG spectra collected using the “sandwiched” sample geometry to probe the PS/Ag interface. Reprinted with permission from Ref. [75]. Copyright 2009 American Chemical Society, All Rights Reserved

SFG spectra measured with PPP polarization combination from thin film deposited on metal surfaces are mainly from the buried interface. In PS/silver interface using the “sandwiched” geometry, it was found that the PS phenyl rings adopted order at the interface. Molecular orientation analysis concluded that the phenyl rings at the interface tilted away from the silver surface [76].

Recently, X. Lu et al., analyzed epoxy/steel interface using sandwiched configuration [77], they concluded that the DGEBA/steel interface (Fig. 38) was dominated by the hydrophobic groups such as the CH_3 and CH_2 groups. Meanwhile, the hydrophilic groups, for example, the OH groups of DGEBA and absorbed water molecules only had very low order [77]. It should be noted that the analysis of buried interfaces of organic thin films on metals by SFG is rather more difficult and complicated than expected because of the interference effect, which requires smooth surfaces, difficulties in controlling the thickness of the polymer thin films, and the fact that the molecular orientation of both the polymer surfaces and interfaces is loose and less variable than would be expected.

By the way, if the metal is very thin, then it is possible for it to transmit both visible and infrared lights. This configuration is effective when the interaction between the metals and the polymers is to be investigated. Here describes the study of two kinds of epoxy polymers with the chemical structures shown in Fig. 39 deposited on a fused silica substrate with 2 nm Cu thin film by sputter coating, to see how the molecular orientations change at the interface due to the interaction between the polymers and the Cu. As shown in Fig. 40, the Cu sputtered thin film has a very smooth surface and is nearly unoxidized, as confirmed by AFM and Auger spectroscopy.

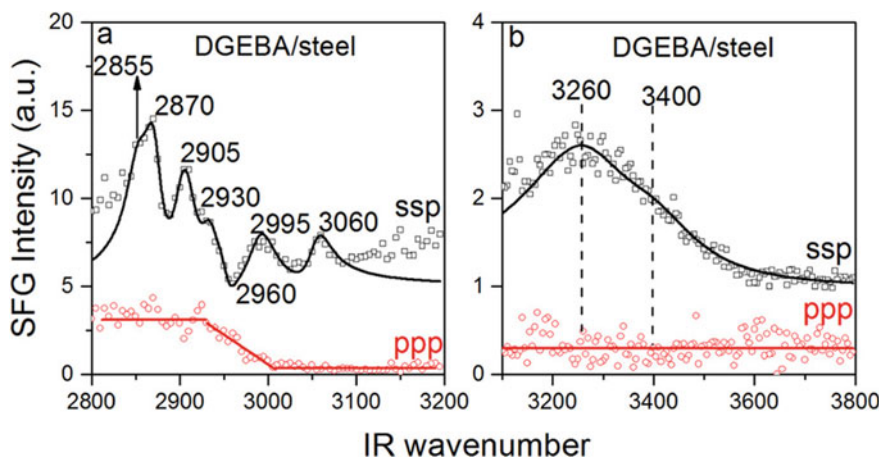


Fig. 38 SSP (black empty squares) and PPP (red empty circles) SFG spectra for the DGEBA/steel interface, with the polymer film thickness of ~ 155 nm. **a** C-H stretching region. **b** O-H stretching region. Reprinted with permission from Ref. [77]. Copyright 2022 American Chemical Society, All Rights Reserved

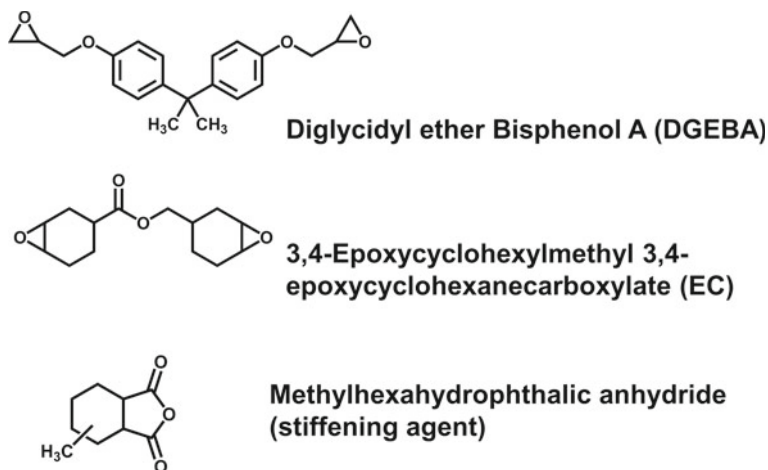
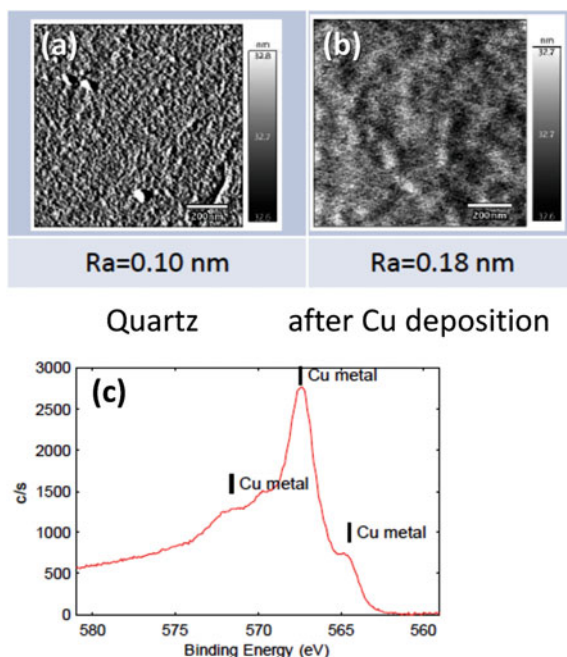


Fig. 39 Chemical structures of the epoxy polymers used in the SFG in Fig. 41

Figure 41 shows the SFG spectra of the diglycidyl ether Bisphenol A (DGEBA) based and 3,4-Epoxy cyclohexylmethyl-3,4-epoxy cyclohexanecarboxylate (EC) based epoxy polymers in C-H stretching region. For comparison, Fig. 41 also displays the SFG spectra of the fused quartz interfaces without the Cu sputter films. In the case of the SFG spectra of DGEBA, C-H modes derived from the phenyl ring are not observed, suggesting that the phenyl ring is randomly oriented at the interfaces.

Fig. 40 AFM topographic images of the **a** fused quartz and **b** 2 nm thick Cu sputtered fused quartz surfaces. Auger spectrum of the Cu sputter thin film



At the interface between fused quartz and epoxy, CH_2 stretching vibrations originating from the cyclohexane ring are observed at 2845 cm^{-1} for both polymers, but the intensities of the peaks become smaller when the Cu layers are inserted in between. Since this change is the same for both the DGEBA and the EC polymers, it is thought that the presence of Cu has significantly modified the orientation of the stiffener derived moiety. The reduction in the intensity of the symmetric stretching vibration of the CH_2 of the cyclohexane ring suggests that aliphatic rings are oriented nearly parallel to the surface at the interface with the presence of Cu.

From the analysis of the orientation angles of methyl groups at the DGEBA interfaces, the methyl groups are 62° from the surface normal at the fused silica interface without Cu, whereas this angle changes to 42° with the Cu layer in place. These results indicate that the presence of the Cu layer changes the orientation of the cyclohexane rings.

For the analysis of metal/polymer joint interfaces, the cast or spin-coated thin films on metals have been used in many cases, as we have already described. In real joints, however, molten polymeric materials to metal are not always in the same molecular state as the spin-coated thin films. Isotactic polypropylene (iPP) mixed with a small amount of maleic anhydride-grafted polypropylene (PPgMA) was found to induce a dramatic improvement in the strength of adhesion [78].

Confocal Raman spectroscopy is known to be able to characterize the local crystallinity of PP using the 808 and 840 cm^{-1} peaks assigned to helical and short chains within the crystalline phase, respectively, and the peak at 830 cm^{-1} assigned to the

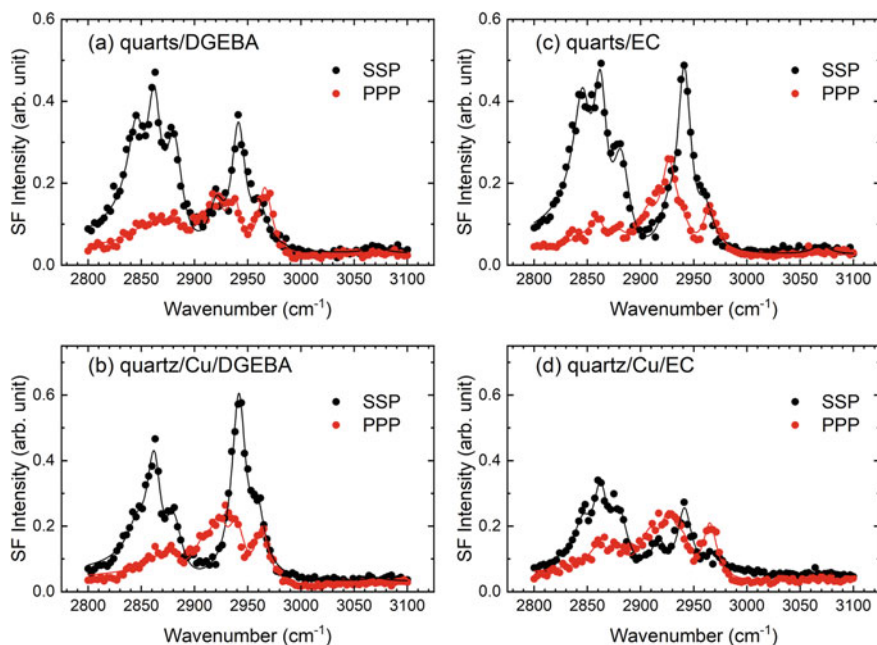


Fig. 41 SSP (black circles) and PPP (red circles) SFG spectra for the **a** quartz/DGEBA, **b** quartz/Cu/DGEBA, **c** quartz/EC, and **d** quartz/Cu/EC interfaces

nonhelical amorphous phase [79]. Figure 42 presents the spectral changes in the region near the free surface exposed to the air and plots of the amorphous fractions as a function of the distance from the surface, respectively. A less crystalline iPP/PPgMA layer is formed near the Al/PP interface based on Raman observations, the thickness of which was estimated to be ca. 3 μm . In contrast, the region below the free surface exposed to the air, in contrast, is highly crystalline, and the crystallinity is independent of the distance from the surface. The interfacial crystallinity of iPP and pure PPgMA showed a low percentage of amorphous phase regardless of the distance from the interface. This observation suggests that blending of PPgMA to iPP leads to the formation of the amorphous-rich phase near the Al/PP interface during the hot-melt bonding process.

To gain a better understanding at the interface, the SSP and PPP SFG spectra of the C-H stretching region are collected from the fractured surfaces of the Al/(iPP/PPgMA 80/20 wt%) lamination. The upper and lower panels in Fig. 43 show the SFG spectra obtained from the iPP and Al fractured surfaces, respectively.

As shown in Fig. 43a, relatively sharp peaks corresponding to the stretching bands of the segments containing the $-\text{CH}_3$ side group and the methylene groups in the main chain of iPP, were observed with high intensities from the PP surface, while the Al/iPP interface produced only a few broad peaks corresponding to the $-\text{CH}_3$ symmetric and asymmetric stretching bands with relatively low intensities compared to the SFG

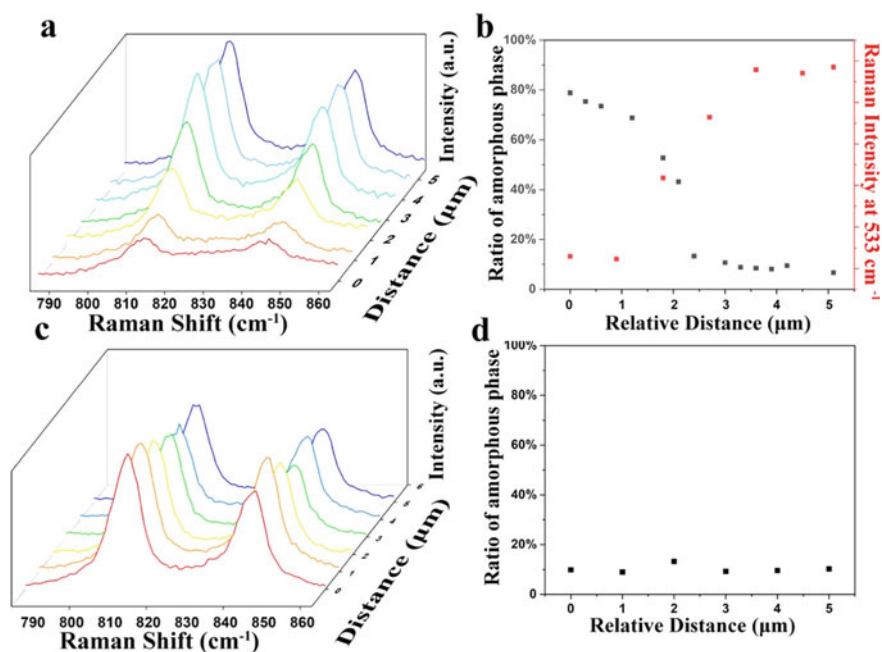


Fig. 42 a, c Cross-section Raman spectra of iPP/PPgMA 80/20 film around the interface and around the free surface face to the air, respectively. b, d Fractions of the amorphous phase around the interface and around the free surface face to the air, respectively. Reprinted with permission from Ref. [78]. Copyright 2021 American Chemical Society, All Rights Reserved

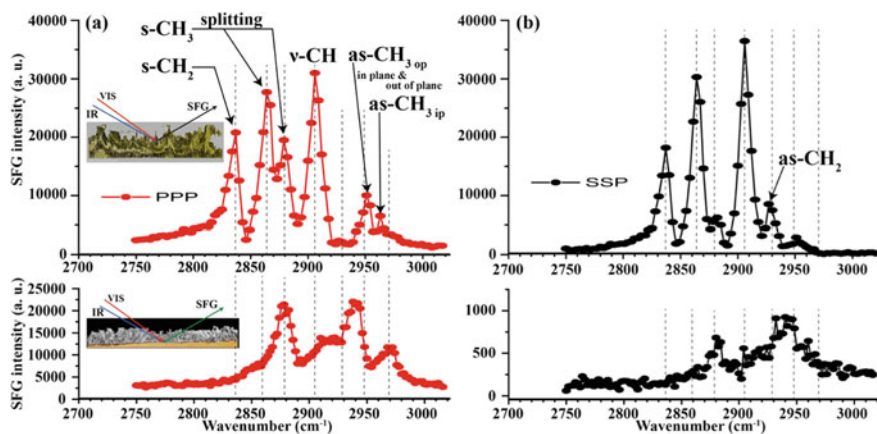


Fig. 43 SFG a ppp and b ssp spectra taken from the fracture surfaces of the PP (upper) and Al (lower) of the interface of Al(iPP/PPgMA 80/20 wt%). The IR and visible beam paths and the SFG signal generation are depicted in the insets of a. Reprinted with permission from Ref. [78]. Copyright 2021 American Chemical Society, All Rights Reserved

peaks from the iPP surface. It should be noted that the intensities of the SFG peaks did not represent the amounts of the corresponding segments at the surfaces. Instead, they represented the orientation and the orientation distribution of the functional groups at the surfaces. The asymmetric feature of the fracture surfaces observed by the TEM was associated not only with the topographic roughness but also with the orientation of the molecules at the fractured surfaces. The fracture surface of the iPP side maintained the high order of the iPP chain due to its crystalline structure which was evidenced by the strong SFG intensities. In contrast, the fact that the SFG spectra obtained from the iPP on the Al surface corresponded rather well with the previously reported spectra of iPP spin-cast films [3] indicated that the iPP/PPgMA was in a disordered and amorphous state. Thus, these SFG results suggest that the iPP/PPgMA molecules at the Al/PP interface are rather disordered and have random orientation. The Raman and SFG spectroscopies results suggested that the blending of iPP with PPgMA induces the formation of a relatively less crystalline layer in the interfacial region [78].

8 Bio-adhesive Interfaces

In nature, there are a number of bio-related adhesives used by various organisms in high-humidity and underwater environments to capture their prey, defend themselves, and build nests. Spiders often hunt in wet habitats and overcome this challenge using sticky aggregate glue droplets whose adhesion is resistant to interfacial failure under humid conditions. Dhinojwara's group investigate the mechanism of aggregate glue adhesion by using SFG spectroscopy in conjunction with infrared spectroscopy [80]. As shown in Fig. 44, by putting on the silk glue on top of the sapphire prism and controlling the humidity, they found that glycoproteins act as primary binding agents at the interface. As humidity increases, reversible changes in the interfacial structure of glycoproteins are observed, as shown in Fig. 45. Interestingly, liquid-like water at the interface bands is not observed at the interface, even though liquid-like water increases inside the bulk with increasing humidity. They conclude that the hygroscopic compounds in aggregate glue sequester interfacial water. Using hygroscopic compounds to sequester interfacial water provides a novel design principle for developing water-resistant synthetic adhesives.

A famous example of biologically related adhesion phenomena is the gecko's foot adhesion. Representative studies by Autumn et al. [81, 82] implied that van der Waals forces (vdW) dominate adhesion in geckos. Recently, the adhesive strength of gecko feet has been investigated by SFG spectroscopy by Dhinojwara et al. [83] In their experiments, gecko setae is placed in contact with a sapphire prism, and changes in the peak positions of hydroxyl groups that are not hydrogen bonded on the sapphire surface are monitored by SFG spectroscopy. In the sapphire-air interface, SFG spectrum shows a sharp peak at 3710 cm^{-1} in the OH vibration region, which can be attributed to the free OH groups on the sapphire surface [84–86]. With the gecko setae in contact, this sapphire OH peak becomes broader and shifts to lower

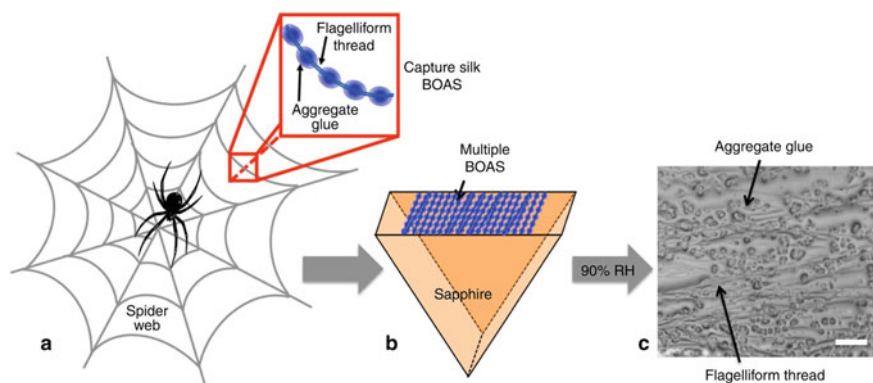


Fig. 44 Schematic illustration of the silk glue. Multiple silk beads-on-a string (BOAS) strands, comprised of aggregate glue droplets (beads) supported on an underlying flagelliform thread, are collected from 2–3 webs of *Larinioides cornutus* and deposited on a sapphire prism. The sapphire prism with BOAS strands is depicted in the optical microscope image shown in c. Scale bar is 100 μm . Reprinted with permission from Ref. [80]. Copyright 2018 Nature, All Rights Reserved

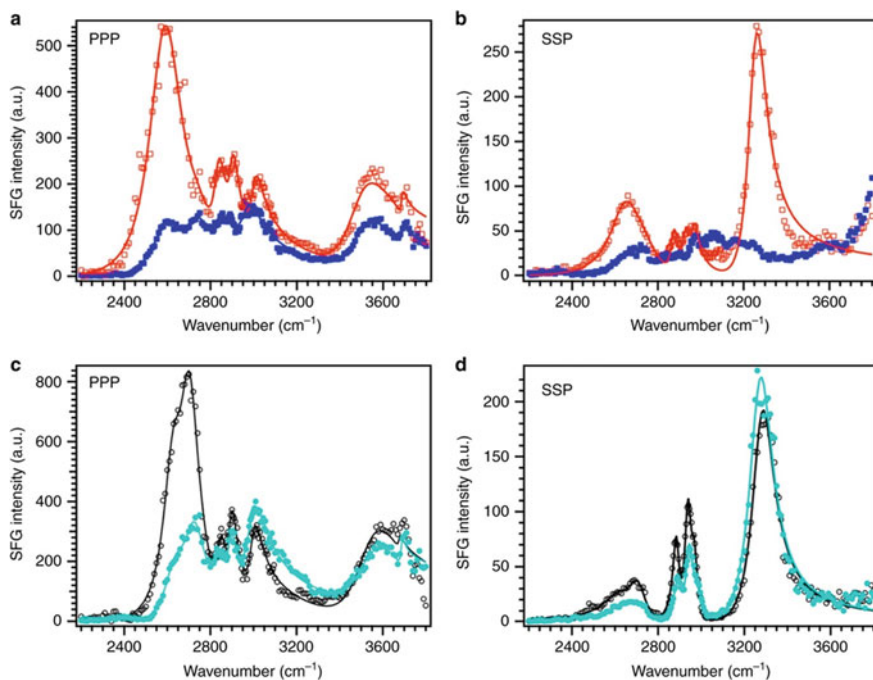


Fig. 45 SFG spectra for pristine aggregate glue/sapphire at low (red empty squares) and high (blue filled squares) humidity collected in PPP **a** and SSP **b** polarization combinations. Similar spectra are collected for washed aggregate glue/sapphire interfaces in PPP **c** and SSP **d** polarization combinations at low (black empty circles) and high (blue filled circles) humidity. Reprinted with permission from Ref. [80]. Copyright 2018 Nature, All Rights Reserved

wave numbers ($\sim 3600\text{ cm}^{-1}$). This large shift can be due to acid–base interactions between sapphire OHs and the unbound lipid groups exposed on the surface of gecko setae since the vdW interactions shift the sapphire OH peak by only $20\text{--}30\text{ cm}^{-1}$ [84–86]. When the gecko setae are again removed from contact, the SFG spectrum shows residue on the surface of the sapphire surface, confirming that a lipid footprint is left behind.

9 Molecular Conformation at the Liquid Interfaces

The adhesive is usually applied to the adherend in liquid state. In this case, adherend surfaces are likely to have different structures from those exposed to air. Thermo-responsive polymers can undergo soluble-insoluble transition when the temperature of the polymer solution reaches the lower critical solution temperature (LCST). Poly(*N*-isopropylacrylamide) (PNIPAM) exhibits a phase separation at around $32\text{ }^\circ\text{C}$. PNIPAM has hydrophilic groups as well as hydrophobic groups, thus both hydrophilic and hydrophobic interactions are an important role in the thermo-shrinking transition. When this transition occurs in solution, it is called a coil-to-globule transition and takes place over a narrow temperature range. PNIPAM has received attractive attention as an intelligent polymer in biotechnology, because of its thermal responsivity. When this polymer is grafted onto a solid substrate, the surface exhibits temperature-dependent properties, such as wettability and cell adhesion behavior [87, 88].

Figure 46 presents the SFG spectra of PNIPAM grafted on fused quartz substrate with the SSP, PPP, and SPS polarization combinations, measured in air at room temperature. The peaks at 2871 and 2975 cm^{-1} are assigned to the symmetric and the asymmetric stretching of the CH_3 of isopropyl groups, respectively [89]. The peak at 2940 cm^{-1} can be attributed from both the Fermi resonance of symmetric CH_3 and the methylene antisymmetric stretching modes [89, 90]. The shoulder at around 2850 cm^{-1} is derived from the symmetric stretching of the CH_2 group of the main chain [89, 90]. The observation of the strong CH_3 stretching peak together with the weak CH_2 peak indicates the presence of the ordered isopropyl groups tilting toward the surface normally under ambient conditions. From the quantitative analysis of the peak strengths for the CH_3 , net orientation of the polar tilt angle of the isopropyl groups is about $40 \pm 3^\circ$, with the twist angles of about $10 \pm 10^\circ$ in air atmosphere. This indicates that the side chains of the PNIPAM are nearly upright at the air/PNIPAM interface. Since the end of the isopropyl termini are hydrophobic in nature, it is reasonable to assume that the isopropyl groups are pointing toward the air side.

At the PNIPAM/ D_2O interface, as shown in Fig. 47, the SFG signal intensities derived from PNIPAM are changed depending on the water temperature, which is caused by the disordering of the polymer chain owing to the changes in the solubility of the PNIPAM. When the water temperature is increased, furthermore, red-shifts of the SFG peaks due to the dehydration of the alkyl group are observed. This result

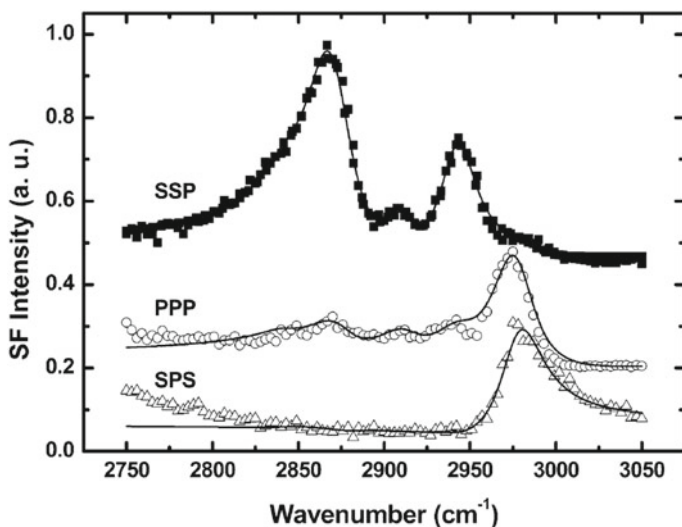


Fig. 46 SSP, PPP, and SPS SFG spectra of the grafted-PNIPAM surface in air. Reprinted with permission from Ref. [8]. Copyright 2007 American Chemical Society, All Rights Reserved

indicates that the C-H groups interact with water below LCST [91, 92]. From the quantitative analysis of the molecular orientation, restructuring of the main chain due to the dehydration at the water/PNIPAM interface is suggested [8].

The orientation of the surface functional groups when in contact with various types of liquids are important factors in determining surface properties. The conformation of the sol-gel-derived hybrid film containing decylsilyl groups ($C_{10}H_{21}Si$, C10-hybrid film) under dry (air/C10-hybrid film interface) and wet (probe liquids/C10-hybrid film interface) conditions were investigated by using SFG spectroscopy [93]. Figure 48 shows SSP-polarized SFG spectra of the hybrid films in the C-H stretching region ($2800\text{--}3000\text{ cm}^{-1}$) under both dry (in air) and wet (in contact with D_2O , DMF-d7, IPA-d8, and toluene-d8) conditions. When the hybrid film is dry, three peaks corresponding to CH_3 group were observed at 2880 , 2960 , and 2940 cm^{-1} , corresponding to the C-H symmetric stretching vibration (r^+), the C-H asymmetric stretching vibration (r^-), and the Fermi resonance (FR). Two peaks corresponding to methylene groups (CH_2) at 2850 (C-H symmetric stretching vibration (d^+)) and 2920 cm^{-1} (C-H asymmetric stretching vibration (d^-)) were also detected in the spectrum. These two peaks are indicative of the presence of gauche defects in alkyl chains because CH_2 peaks would not be detected if the alkyl chains are in the all-trans conformation. In the present case, the surface-tethered alkyl groups in the uppermost region are judged to be loosely packed, allowing for readily reorientation against their environment.

After contacting the C10-hybrid films with perdeuterated probe liquids (D_2O , DMF-d7, IPA-d8, and toluene-d8), the d^+/r^+ peak strength ratio in the SFG spectra is obviously changed, as shown in Fig. 48b. This d^+/r^+ peak strength ratio appears

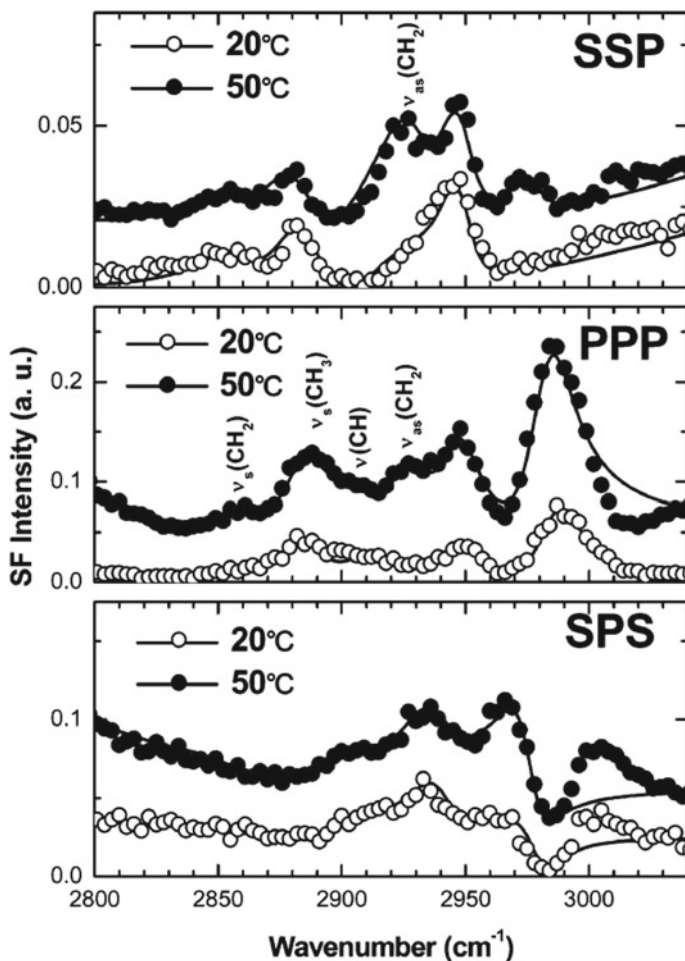


Fig. 47 SSP, PPP, and SPS SFG spectra of the $D_2O/PNIPAM$ interfaces collected at the different temperatures. Reprinted with permission from Ref. [8]. Copyright 2007 American Chemical Society, All Rights Reserved

to correlate strongly to the ratio of CH_2 to CH_3 groups at the outermost surface (but does not indicate the absolute number of CH_3 and CH_2 groups at the interfaces) and can be employed to evaluate the relative conformational order of alkyl chains because the ratio decreases with the decreasing number of gauche defects at the liquid/solid interface.

When the surface was in contact with probe liquids having high dielectric constants, such as D_2O , DMF-d7, and IPA-d8, the d^+/r^+ ratio increased from 0.61 when dry to 0.89, 1.37, and 2.09 when in contact with IPA-d8, DMF-d7, and D_2O , respectively. The greater the dielectric constant of the probe liquid, the greater the increase in the d^+/r^+ ratio observed upon wetting as shown in Fig. 48b. Such marked

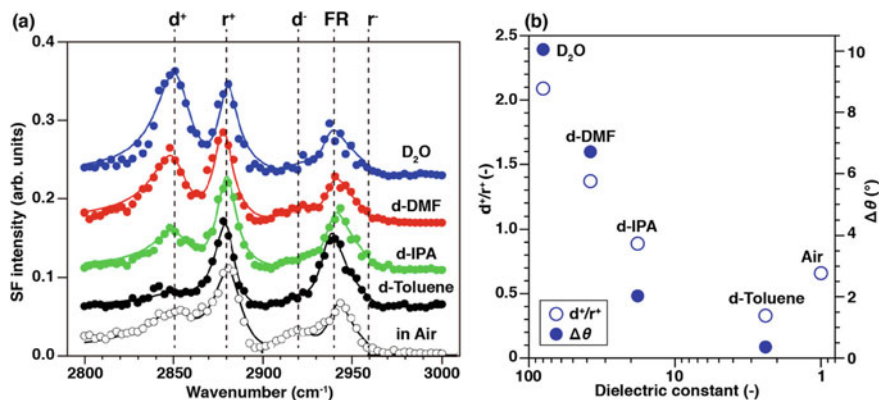


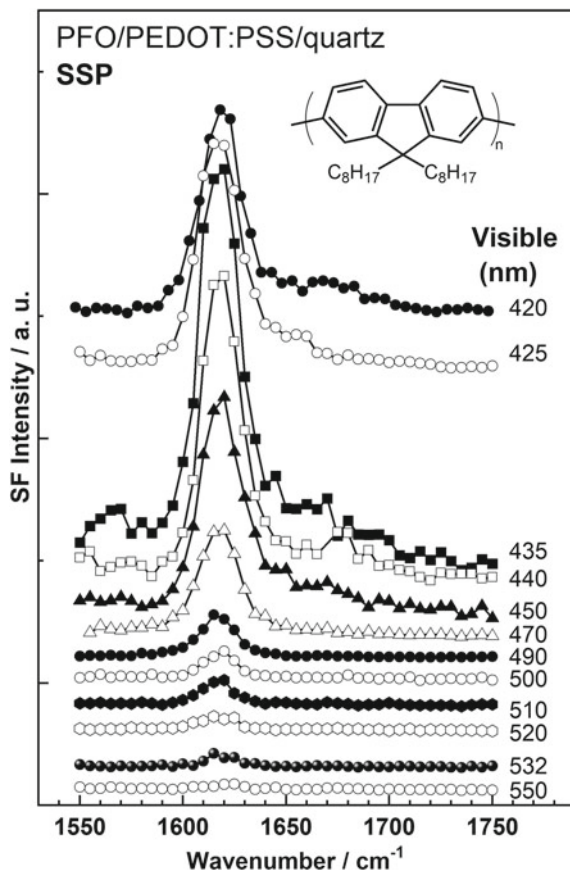
Fig. 48 **a** SSP-polarized SFG spectra of our C10-hybrid films in C-H stretching region of alkyl groups at air/and four different liquids/film interfaces. (The spectra are normalized by the peak intensity of the methyl groups and are offset upward for clarity.) **b** Changes in the d^+/r^+ ratio and contact angle hysteresis ($\Delta\theta$) as a function of the dielectric constants of four different probe liquids. Reprinted with permission from Ref. [93]. Copyright 2014 American Chemical Society, All Rights Reserved

increases in d^+/r^+ values indicate that the conformational ordering of alkyl chains at the liquid interface are collapsed when wetted with a liquid having a high dielectric constant. However, when a surface was in contact with toluene-d8, the d^+/r^+ ratio markedly decreased to 0.33, suggesting that alkyl chains assume a more extended conformation (enhanced conformational ordering) into the liquid disfavoring gauche defects. These observed changes in the d^+/r^+ ratio closely reflect the changes in contact angles as a drop of probe liquid advances and then recedes over an area of the surface (i.e., contact angle hysteresis), as shown in Fig. 48b.

10 Molecular Conformation at the Organic Device Interfaces

Polymer LEDs are one of the most promising applications given the current great interest in the development of ultrathin computer monitors and television, i.e., flat-panel displays and flexible displays. Recently, one of the conjugated polymers, the poly(9,9-dioctylfluorene) (PFO, chemical structure is depicted in the inset of Fig. 49) and fluorene-arylene copolymers have been intensively studied because of its applications in the LEDs due to their highly efficient blue photoluminescence [94]. In an organic device, the charge carriers must be injected through polymer/electrode interfaces. Since the electronic properties and energy level alignment of electrode/organic interface significantly affect the performance of the organic LEDs, it is extremely important to understand the interaction between the electrode and organic polymer materials and the electronic structures at the buried interfaces [42]. Doubly-resonant

Fig. 49 SFG spectra of PFO/PEDOT:PSS/quartz surface with various visible wavelength. Spectra are offset for clarity. Reprinted with permission from Ref. [42]. Copyright 2010 Royal Society of Chemistry, All Rights Reserved



SFG spectroscopy can be applied to study the changes in the electronic structure at the interfaces as well as the orientation of the functional groups.

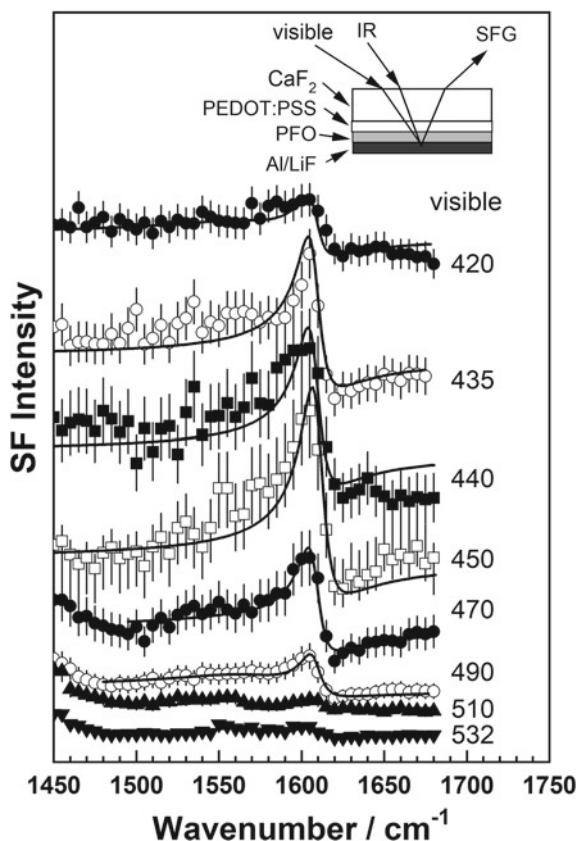
Figure 49 shows the SFG vibrational spectra from the PFO/PEDOT:PSS/quartz surface collected with various visible wavelengths in an SSP polarization combination [42]. In the SFG measurements, z-cut quartz plate is used as the reference for the SFG signal. This is because z-cut quartz is transparent to visible light, so the SFG susceptibility of the quartz is expected to be approximately constant in the visible region. As shown in Fig. 49, strong vibrational band was observed at 1610 cm^{-1} in all spectra, and the band intensity increased when the visible probe wavelength was changed from 550 to 435 nm. The vibrational band at 1610 cm^{-1} is derived from the C=C symmetric stretching of the fluorene rings located at the PFO backbone. When the visible wavelength is near 435 nm, the electronic resonance enhancement of the SFG spectra is observed which produces an SFG wavelength near 407 nm with an IR beam of 1610 cm^{-1} .

Figure 50 presents the visible wavelength dependence of the SFG spectra from the buried Al/LiF/PFO interface in SSP polarization combination [42]. In this study, the

LiF and the Al layers were directly deposited on the spin-coated PFO/PEDOT:PSS onto CaF_2 substrate, as illustrated in the inset in Fig. 50. As can be seen in Fig. 50, the vibrational band at 1610 cm^{-1} is still observed in all SFG spectra and its intensity shows remarkably visible wavelength dependence. The peak position of the band does not change between the PFO surface and the PFO interface, indicating that the PFO is not degraded by the Al deposition. It should be noted that in the case of the DR-SFG spectra of the Al/LiF/PFO interface, the SFG peak presents a different shape from that observed in the air/PFO interface. This difference is attributed to the different interference phenomena with the SFG non-resonant contribution arising from the Al substrate.

Generally, there are two types of optical processes in IR-visible SFG, as mentioned in the theoretical section. The first one is an electronic transition followed by a vibrational transition (VIS-IR SFG), and the other type begins with a vibrational transition followed by an electronic transition (IR-VIS SFG) [95]. Since the electronic relaxation times are generally quite short as compared to the vibrational relaxation times, the contribution of the VIS-IR SFG is expected to be generally negligible. If

Fig. 50 SFG spectra of buried electrode/PFO interface with various visible wavelength. Spectra are offset for clarity. Reprinted with permission from Ref. [42]. Copyright 2010 Royal Society of Chemistry, All Rights Reserved



the VIS-IR SFG occurs, increase of the non-resonant background is expected because of the ultrafast dephasing dynamics of the S1 state [96]. Therefore, only the IR-VIS SFG will be considered in the following analysis.

The curves b and c in Fig. 51 show the changes in the AI of the 1610 cm^{-1} peak extrapolated from the fitting of the DR-SFG spectra in Figs. 49 and 50 as a function of the photon energies of the output SFG light. Figure 51a also shows the optical absorption spectrum of the PFO spin-coated film. The broad optical absorption band originates from inhomogeneously broadened $\pi \rightarrow \pi^*$ transitions of the glassy PFO. As shown in Fig. 51, the SFG electronic excitation spectrum obtained from the air/PFO interface is somewhat red-shifted with respect to an optical absorption of PFO film. The SFG excitation spectrum at the Al/LiF/PFO interface is also plotted in Fig. 51c, and it is further red-shifted with respect to that of the PFO surface. It should be noted that these red-shifts are not caused by the visible variations of the Fresnel factors. We should note that the wavelength changes in the Fresnel factor F_{yyz} both the air/PFO and the CaF_2/Al interfaces do not explain the changes of the SFG electronic excitation profiles of the air/PFO and the buried interface, as shown in Fig. 51.

The red-shifts of the SFG electronic excitation spectra can be interpreted by the stress-induced surface confinement effects of the polymer backbone, as in the case of the MEH-PPV interfaces [97]. As shown in Fig. 52, K. C. Chou's group reported that the conjugation length of MEH-PPV at the solid interface is longer than that

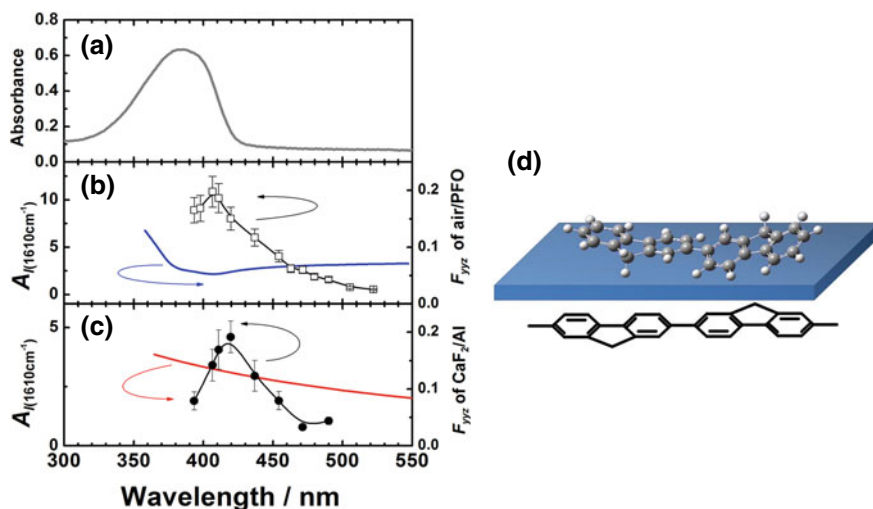


Fig. 51 a Optical absorption spectrum of the PFO. b The SFG electronic excitation profile of air/PFO interface and the Fresnel factor F_{yyz} (blue curve) at air/PFO interface, and c the SFG electronic excitation profile of Al/LiF/PFO interface and the F_{yyz} at CaF_2/Al interface (red curve). Solid black lines in a and b are guide to the eyes. d Schematics of the planar configuration at the interface. Reprinted with permission from Ref. [42]. Copyright 2010 Royal Society of Chemistry, All Rights Reserved

in the bulk, which is attributed to the stress-induced backbone flattening [97]. In general, the optical band gap of a conjugated polymer is closely correlated to the π -conjugation length. Conjugated polymer chains are composed of a series of linked segments, each of which has a different degree of π -electron delocalization. Although the extent of the conjugation is limited by the torsion of the polymer backbone, the longer the segment is, the smaller the optical band gap of the conjugated polymers due to the increasing average effective conjugation length. The restriction of the torsion angle between adjacent segments at the air/polymer and the solid/polymer interfaces induces a longer conjugation length.

It is well-recognized that the bulk solid-state films of PFO exhibit complex phase behavior. Disordered PFO forms the glassy phase where the polymer backbones do not form specific conformation with long-range order. On the other hand, PFO in the so-called β -phase is an extended conformation of PFO chains and possesses lower energy, due to the backbone planarization [98]. Single molecule spectroscopy demonstrates that the β -phase features of PFO are the results of stress-induced backbone flattening of polymer chain [99]. The optical absorption spectra of β -phase PFO exhibit the characteristic shoulder band around 430 nm in comparison with the glassy PFO. The SFG electronic excitation profiles of the PFO interfaces have a maximum

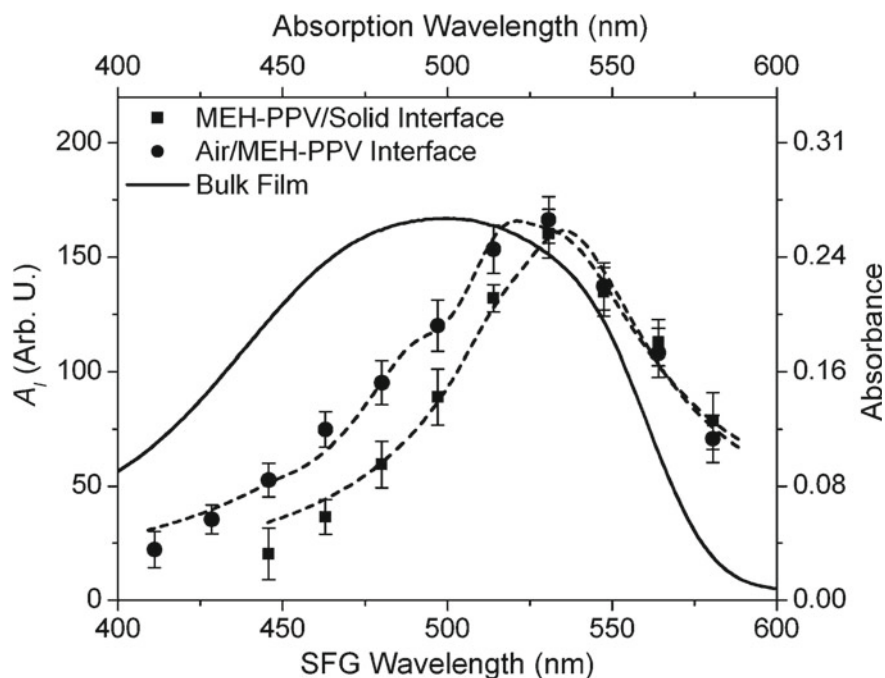


Fig. 52 Optical absorption spectrum of bulk MEH-PPV film (solid line) and the surface SFG electronic spectra of MEH-PPV at MEH-PPV/solid (■) and air/MEH-PPV interfaces (●). Reprinted with permission from Ref. [97]. Copyright 2008 American Chemical Society, All Rights Reserved

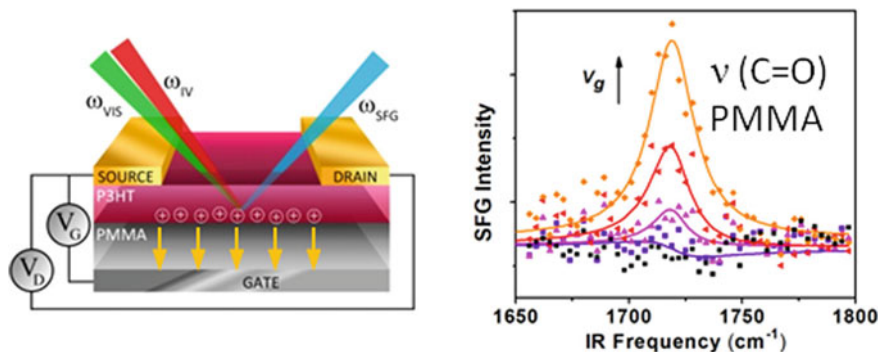


Fig. 53 Schematics of the OFET and the SFG spectra in the C=O stretching mode for the Si/SiO₂/PMMA/P3HT OFET under different gate voltages. Reprinted with permission from Ref. [102]. Copyright 2018 American Chemical Society, All Rights Reserved

of around 410–420 nm, and this peak position is close to the shoulder absorption of the β -phase PFO, rather than that of the glassy PFO. Because of the restriction of the torsion angle between adjacent segments, the conformation of the polymer backbone is limited at the polymer interfaces. As a result, the effective conjugation length at the interface is increased. The proposed planar orientation of the PFO chains at the interfaces is shown in Fig. 51d.

There is great interest on the study of the semiconductor/dielectric interface of organic field-effect transistors (OFETs), where a conducting channel is formed. SFG spectroscopy is known not only for studying the molecular orientation at the interfaces, it is also a valuable technique for obtaining the information about the charge accumulation at the interfaces. This is known as electric field-induced SFG, which utilizes phenomena in which the SFG signal intensities are modulated and increased by the electric field generated by the accumulated charges at the interface [37, 100, 101]. In SFG measurements of the OFETs that use P3HT as an organic semiconductor, Miranda's group has reported a voltage-dependent increase in the intensity of the SFG signal of the PMMA used as the insulating layer when a voltage is applied to the device, as shown in Fig. 53 [102]. SFG results revealed that in-plane electric field within the organic dielectric layer are formed by the charge injection.

11 Comprehensive Study of Adhesive Interfaces Combining SFG with Other Techniques

Elucidation of “how adhesives form their interfaces with adherends” is important for both the developer and the user of adhesives, as it helps determine the adhesive composition and surface treatment methods. Studying the interfacial phenomena will provide the information on chemical interactions, molecular orientation, and the

formation of chemical bonds and electric dipoles. Since such details on molecular scale are important to design the adhesive, it is still being studied both experimentally and theoretically. From the late 1980s to the early 1990s, many studies on the surface of exfoliated specimens by XPS have been reported [103–106]. Among them, it was confirmed that the curing agent of epoxy adhesive is protonated by the hydroxyl groups on the surface of stainless steel and aluminum, and the existence of acid–base reaction has been clarified [103, 105–107]. In addition, since an electric double layer (positive on the molecular side and negative on the metal side) is formed at the interface by protonation, the presence or absence of protonation at the interface can be indirectly detected by measuring the contact potential difference using the Kelvin probe method (KP) [104]. In addition to surface-sensitive techniques such as XPS and KP, techniques capable of characterizing buried interfaces such as SFG and scanning transmission electron microscopy (STEM)-electron energy loss (EELS) are available at the adhesive interface. By using it for analysis, it is possible to grasp the actual state of the interface, and the understanding progresses further.

This section describes analytical research on the interface between aluminum, which is a representative lightweight material used for car bodies and aircraft, and adhesives. In particular, the chemical interactions at the interface between adhesives and aluminum oxide (AlO_x) are described. Here, AlO_x was selected as the adherend because the surface of metal aluminum is covered with a naturally oxidized film, and the surface of the oxide film is in direct contact with the adhesive. Figure 54 shows the molecular structures of each component in the epoxy and urethane adhesive described in this section. Epoxy adhesive is made by mixing bisphenol A type epoxy resin (DGEBA) with triethylenetetramine (TETA) as a curing agent and adding a small amount of 2,4,6-tris(dimethylaminomethyl)phenol (TDAMP) as a curing accelerator. On the other hand, as the urethane adhesive, two kinds of diphenylmethane diisocyanate (MDI) to which polypropylene glycol (PPG), 1,4-butanediol (BG), and trimethylolpropane (TMP) were added were used. These adhesives were cured at 100 °C for 30 min. and 120 °C for 5 h, respectively.

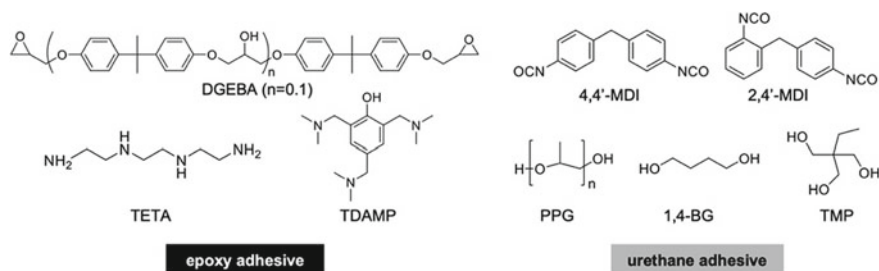


Fig. 54 Molecular structures of epoxy and urethane adhesives used in this study

11.1 Acid–Base Interaction at the Epoxy Adhesive/ AlO_x Interface

At the interface between our epoxy adhesive and AlO_x , protonation of the curing agent amine was observed. Figure 55a shows the XPS spectra in the N 1s region of the obliquely polished epoxy adhesive/Al joint. Photoemission based on N–H and N–C is observed around 400 eV. In addition, a weak component was separated around 402 eV. Since the peak at this position is attributed to a nitrogen atom that has become a cation [108], it is suggested that the amine received a proton from the hydroxyl group on the aluminum surface at the interface upon contact with the adhesive and became N^+ . Previous reports have focused on the adhesive interface, but according to STEM-EELS measurements, the aluminum hydroxide on the aluminum surface changes to aluminum oxide as the epoxy adhesive cures, and the aluminum side [109]. Even when only TETA, which was used as a curing agent, was adsorbed on aluminum foil, two photoemission peaks were separated [Fig. 55a], and their positions are 399.0 and 400.5 eV. Similar to the adhesive interface, the high binding energy side is attributed to protonated TETA. Protonation at the interface should form an electric double layer at the interface, with the TETA side being positive and the aluminum side being negative. As a result, the electric potential on the aluminum surface should decrease, but when the contact potential difference (CPD) measured by KP is compared before and after the TETA coating, the contact potential difference is indeed negative, indicating a decrease in the work function. [Fig. 55b]. The results of KP measurements are consistent with those reported by Salgin et al. [104]. If protonation at the epoxy adhesive/aluminum interface can be predicted from KP measurements, it may be possible to easily infer the interaction at the interface. However, it should be noted that protonation is not the only source of change in CPD. Amines such as TETA are known to cause *n*-type doping [110], and the formation of an interfacial dipole layer resulting from electron transfer can also change the contact potential difference. In addition, TETA itself has a permanent dipole, and orientational polarization is also possible.

Such protonation has been reported also for curing agent amines such as amidoamine [106] and diaminodiphenylmethane (DDM) [103]. Other curing agents for epoxy adhesives include aromatic amines such as 4,4'-diaminodiphenylsulfone (DDS), acid anhydrides, mercaptans, and novolac-type phenolic resins. Therefore, it is necessary to clarify the details of the chemical reaction between each curing agent and AlO_x , and carefully investigate the relationship among the interfacial phenomena, fracture modes, and durability of adhesive joints. In addition, there is still the possibility that the epoxy group of the epoxy resin reacts with the hydroxyl group on the surface [105]. Thus, full understanding of the adhesive/adherend interface is not reached.

So far, we have discussed the interfaces between clean aluminum and adhesives. In the process of assembling a car body in an actual factory environment, the aluminum surface remains covered with antirust oil, press oil, etc. [111]. The adhesive should exhibit good oil adhesion despite the presence of oil on the surface. Hong et al.

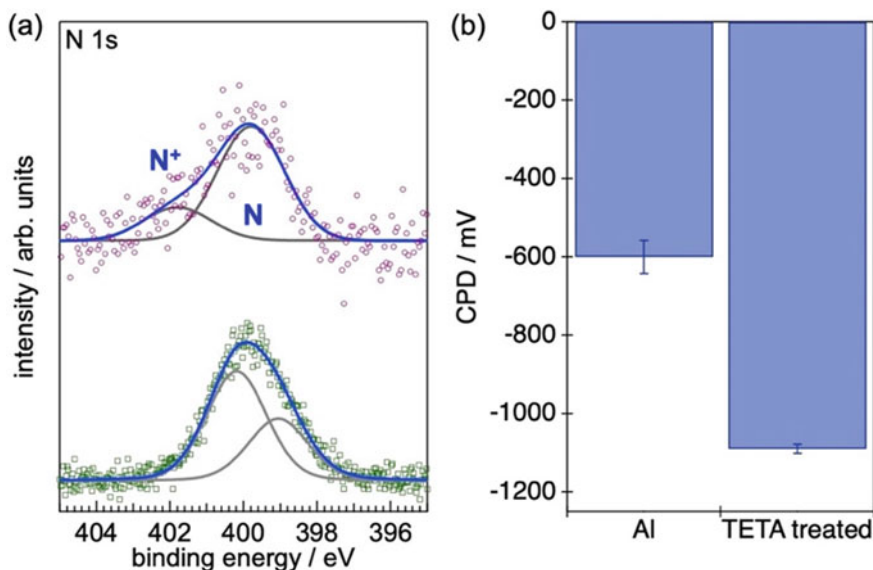


Fig. 55 a N 1s XPS spectra of epoxy/AIO_x interface (top) and TETA-treated Al sheet (bottom). b The values of CPD for a UV/ozone-cleaned Al sheet and TETA-treated Al

reported hardener amines on oiled aluminum (Al 2024-T3) as well as on clean plates [112]. This means that the amine diffuses through the oil layer and preferentially adsorbs to the aluminum surface. It has also been found that when adhering epoxy:amidoamine adhesives to oil-contaminated rigid plates, the addition of a silane coupling agent aids penetration of the curing agent and promotes protonation of the amine [113]. That is, the adhesive composition affects the acid–base reaction at the interface.

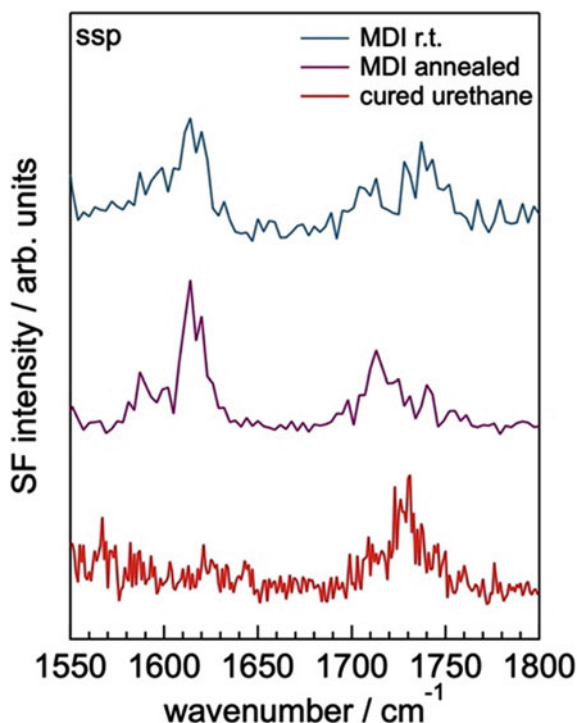
11.2 Formation of Covalent Bonds

Molecules used in adhesives contain reactive functional groups such as amino groups, epoxy groups, isocyanate groups, phosphate groups, carboxyl groups, alkoxy silanes, and so on. Upon the contact of an adhesive interface with aluminum surface, the formation of the covalent bond could be caused by the reaction of adhesives with hydroxyl groups at the adherend. That covalent bond should ensure the adhesion and thus its direct observation is desired. SFG is a powerful technique for directly observing chemical bonds between adherends. So far, research has been reported on the formation of urethane bonds at the interface between 4,4'-MDI (Fig. 54) and epoxy resin [62], and the formation of urethane bonds at the interface between primers having isocyanate groups and urethane resin [114]. We tried to observe the chemical bond formation on the MDI/AIO_x surface by SFG.

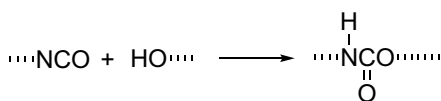
Figure 56 shows the SFG spectra taken at SSP polarization combination in the carbonyl region at the mixture of 4,4'-MDI and 2,4'-MDI/ AlO_x interface. When the isocyanate group of MDIs reacts with the hydroxyl group on the AlO_x surface, urethane bonds are formed as shown in the chemical reaction formula below.

Therefore, the formation of urethane bonds can be confirmed by detecting N–H or C=O generated by this reaction. For the MDI mixture/ AlO_x interface, multiple peaks were observed in the C=O region. The peaks observed in the range of $1700\text{--}1770\text{ cm}^{-1}$ should be derived from urethane bonds. The result suggests that the above chemical reaction is certainly progressing on the substrate surface. After heat treatment (at $120\text{ }^\circ\text{C}$ for 5 h), the peak at 1720 cm^{-1} remains, suggesting that the orientation of C=O becomes uniform due to the formation of hydrogen bonding. On the other hand, two peaks are also observed in the range of $1580\text{--}1630\text{ cm}^{-1}$. These can be attributed to the formation of urea due to the reaction between water adsorbed on the surface of the aluminum substrate or water in the atmosphere and isocyanate [115, 116]. The reaction between water and isocyanate groups is as follows.

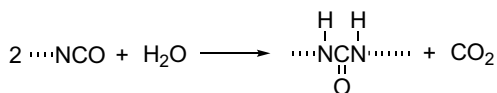
Fig. 56 SSP polarized SFG spectra of MDI/ AlO_x interfaces and cured urethane/ AlO_x interface



Scheme 1 Chemical reaction between isocyanate and hydroxyl groups



Scheme 2 Chemical reaction between urea and water



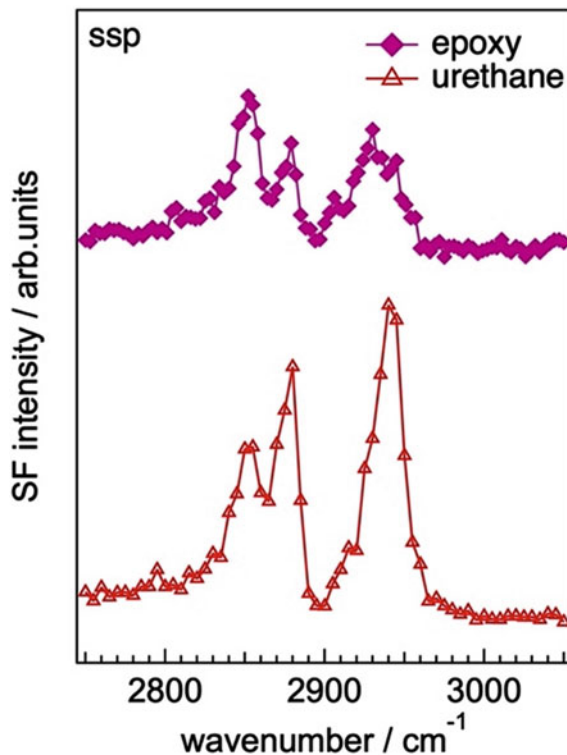
Carbonyl groups derived from urethane bonds were also observed in the SFG spectrum of the cured urethane adhesive (bottom in Fig. 56). This suggests that MDI in the urethane adhesive reacts with hydroxyl groups on the AlO_x surface. The presence of urethane bonds on the aluminum surface was also suggested by time-of-flight secondary ion mass spectrometry [116]. Direct observation of the chemical bonds, however, provides direct proof of chemical bond formation.

11.3 Ordering of Functional Group at AlO_x Interface

Various functional groups of the adhesive components orient as they interact with the substrate. Contact angle measurements for the clean AlO_x used in this study found that the surface energy of a clean AlO_x surface was about 45 mJ m^{-2} . One may expect that polar functional groups, such as amino and hydroxyl groups, preferentially orient at the interface. However, it is not always the case that only these functional groups are oriented. Figure 57 shows SFG spectra in the C-H region of cured epoxy adhesive and urethane adhesive. Distinct peaks were observed at 2850 and 2880 cm^{-1} for both adhesives. These peaks can be assigned to symmetric stretching vibrations of methylene and methyl groups, respectively. That is, hydrocarbons of DGEBA and PPG exhibit molecular order at the AlO_x interface. The ordering of hydrocarbon moieties was also observed in other adhesive systems. Thus, this observation should be a general trend at the adhesive/ AlO_x interface.

The current interpretation is that the adhesive components are constrained at the AlO_x interface through acid–base reactions and chemical bond formation. In addition to the energy stabilization associated with these phenomena, the orientation of the hydrocarbon moieties and enhancement of the molecular order maximize the energy gain via van der Waals interactions at the adherend interface. Moreover, since the ordering of alkyl chains was generally observed at the AlO_x interface even with adhesives having completely different adhesive strengths, it is difficult to assume that the presence of hydrocarbons at the interface is one of the causes of the weaker adhesion.

Fig. 57 SFG spectra of cured epoxy/ AlO_x (top) and urethane/ AlO_x interfaces taken at SSP polarization



11.4 Interaction Between Surface O–H Bonds and Adsorbates

If we can obtain physical parameters related to adhesive strength from SFG probing buried interfaces, we can obtain information on adsorption energy at the adhesive/adherend interface. Dhinojwala's group calculated the interaction enthalpy at the interface between sapphire and organic molecules using the Badger-Bauer equation, using the hydroxyl peak position on the sapphire surface as an index [117]. Basically, when an interaction including a dispersion force works, the hydroxyl group peak shifts to the lower wavenumber side. The greater the amount of shift, the stronger the interaction.

As an example, Fig. 58a shows an SFG spectrum in the O–H region for the interface between AlO_x and silicone oil. Silicone oil is used as a release agent and is a well-known source of contamination on aluminum surfaces [111]. The hydroxyl peak on the AlO_x surface is located at 3700 cm^{-1} at the air interface, but a low wavenumber shift of about 10 cm^{-1} was observed upon contact with oil. This is comparable to the amount of shift observed at the polyisobutylene/sapphire interface. Therefore, it appears that the silicone oil interface weakly interacts with the AlO_x surface via

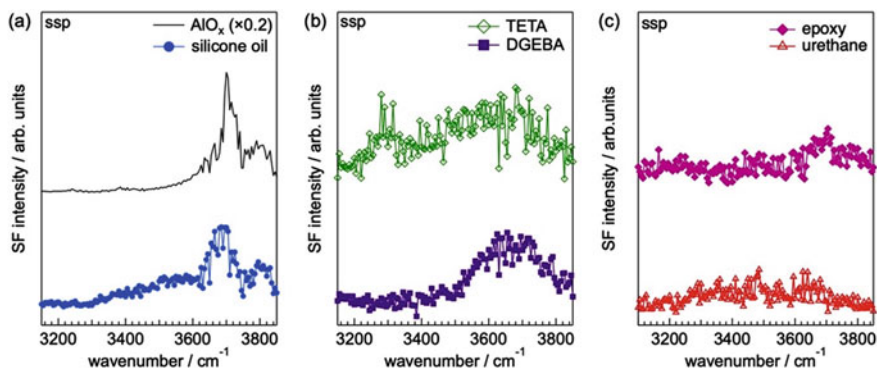


Fig. 58 SFG spectra of various adsorbates/ AlO_x interfaces. **a** silicone oil, **b** TETA, and **c** epoxy and urethane adhesives after curing. Polarization combination is ssp

dispersion forces. However, a broad peak is clearly observed below 3600 cm^{-1} . When silicon oil was spin-coated on aluminum foil and the CPD was measured by KP, a decrease of less than 0.1 eV was observed [118]. This suggests that the dipole layer was formed as a result of regular arrangement of silicon and oxygen atoms due to the constrained conformation of dimethylsiloxane at the interface. The broad tailing feature toward the low wavenumber could originate from the stronger interaction between the oil molecules having dipoles and AlO_x surface than the dispersion force. In such cases, it is not possible to simply calculate the adsorption enthalpy change from the peak shift of O–H bonds.

On the other hand, when TETA or DGEBA with polar groups such as amino and hydroxyl groups, is brought into contact with the AlO_x surface, a broad SFG with a peak below 3650 cm^{-1} is observed [Fig. 58b]. The N–H stretching vibration is observed at 3320 cm^{-1} in the TETA spectrum. When urethane and epoxy adhesives are cured, the surface hydroxyl peaks almost disappear [Fig. 58c]. Since the refractive index of the resin is larger than that of air, the Fresnel coefficient decreases, and the O–H signal on the AlO_x surface is weakened at the adhesive interface compared to the air interface. However, even if this point is taken into account, the strength of the SF signal is significantly reduced. This is considered to be the result of the consumption of hydroxyl groups on the AlO_x surface due to chemical bonding and acid–base reactions at the adhesive interface [109].

In this section, the chemical reactions, formation of covalent bonds, and orientation of functional groups at the interface between epoxy and urethane adhesives and AlO_x are analyzed using surface science techniques to clarify the adhesion. In recent years, both experimental and theoretical analyzes of adhesive interfaces have progressed, but the interface study is still necessary to obtain a deep understanding of adhesion. There are many unclear points about the relationship between the molecular scale environment at the interface and the initial adhesive strength and durability. Evaluations of chemical interaction and interfacial adhesion strength for the same specimen will provide their correlation.

12 Summary and Outlook

In this chapter, we have described the molecular behavior at the interfaces of adhesion, mainly emphasizing the analysis using SFG spectroscopy. In the analysis of adhesive interfaces, we have shown that focusing on the interfaces has the potential to reveal new phenomena that had not been observed before. However, it is most important to examine the molecular behavior at the “*interphase*” of the adhesive interfaces at the same time, and in this respect, it is essential to investigate the chemical states, crystallinity, and segregation of the molecules in the vicinity of the interfaces by means of infrared spectroscopy and Raman scattering.

It should be noted that this chapter does not specifically mention techniques such as SHG and SHG spectroscopy, phase-sensitive SFG, which is often referred to as heterodyne detected SFG, SFG scattering, and SFG imaging, but it is needless to admit that these techniques will play a large contribution to the analysis of adhesive interfaces with the advancement of laser and measuring technologies.

Acknowledgements TM thanks Professor Shoichi Yamaguchi of Saitama University for his valuable comments. TM wish to express their gratitude to Tosoh Corporation, Cemedine Co., Ltd., Fuji Electric Co., Ltd., Lion Corporation, and Resonac (formerly Showa Denko K.K.) for supplying the samples. Part of this work was supported by a Grant-in Aid for Scientific Research and New Energy and Industrial Technology Development Organization (NEDO).

References

1. J. Hunt, P. Guyot-Sionnest, Y. Shen, Chem. Phys. Lett. **133**, 189–192 (1987)
2. X. Zhu, H. Suhr, Y. Shen, Phys. Rev. B. **35**, 3047–3050 (1987)
3. D. Zhang, Y. Shen, G.A. Somorjai, Chem. Phys. Lett. **281** 394–400 (1997)
4. J. Wang, C.Y. Chen, S.M. Buck, Z. Chen, J. Phys. Chem. B **105**, 12118–12125 (2001)
5. H. Yokoyama, T. Miyamae, S. Han, T. Ishizone, K. Tanaka, A. Takahara, N. Torikai, Macromolecules **38**, 5180–5189 (2005)
6. T. Miyamae, H. Nozoye, Surf. Sci. **532–535**, 1045–1050 (2003)
7. T. Miyamae, H. Yokoyama, S. Han, T. Ishizone, e-J. Surf. Sci. Nanotech. **4**, 515–520 (2006)
8. T. Miyamae, H. Akiyama, M. Yoshida, N. Tamaoki, Macromolecules **40**, 4601–4606 (2007)
9. K.S. Gautam, A.D. Schwab, A. Dhinojwala, D. Zhang, S.M. Dougal, M.S. Yeganeh, Phys. Rev. Lett. **85**, 3854–3857 (2000)
10. T. Miyamae, H. Nozoye, Appl. Phys. Lett. **85**, 4373–4375 (2004)
11. Z. Chen, Y.R. Shen, G.A. Somorjai, Ann. Rev. Phys. Chem. **53**, 437–465 (2002)
12. J.N. Myers, X. Zhang, Y. Xiu, Y. Wei, J.M. Williamson, K.W. Lee, Z. Chen, IEEE Trans. Compon. Packag. Manuf. Technol. **5**, 1432–1440 (2015)
13. Y.R. Shen, *The Principles of Nonlinear Optics* (John Wiley & Sons, New York, 1984)
14. A. Morita, *Theory of Sum Frequency Generation Spectroscopy* (Springer, Singapore, 2018)
15. Y.R. Shen, *Fundamentals of Sum-Frequency Spectroscopy* (Cambridge University, Cambridge, 2016)
16. Y.R. Shen, Pure Appl. Chem. **73**, 1589 (2001)
17. A.G. Lambert, P.B. Davies, D.J. Neivandt, Appl. Spectrosc. Rev **40**, 103 (2005)
18. Z. Chen, Polym. Int. **56**, 577–587 (2007)
19. C.S. Tian, Y.R. Shen, Surf. Sci. Rep. **69**, 105 (2014)

20. Z. Chen, *Prog. Polym. Sci.* **35**, 1376–1402 (2010)
21. S. Roy, K.-K. Hung, U. Stege, D.K. Hore, *Appl. Spectrosc. Rev.* **49**, 233–248 (2014)
22. H.-F. Wang, L. Velarde, W. Gan, L. Fu, *Annu. Rev. Phys. Chem.* **66**, 189–216 (2015)
23. X. Lu, C. Zhang, N. Ulrich, M. Xiao, Y.-H. Ma, Z. Chen, *Anal. Chem.* **89**, 466–489 (2017)
24. C. Zhang, *Appl. Spectrosc.* **71**, 1717–1749 (2017)
25. S. Nohonyanagi, S. Yamaguchi, T. Tahara, *Chem. Rev.* **117**, 10665–10693 (2017)
26. S. Yamaguchi, T. Otsu, *Phys. Chem. Chem. Phys.* **23**, 18253–18267 (2021)
27. S. Yamaguchi, T. Takayama, Y. Goto, T. Otsu, T. Yagasaki, *J. Phys. Chem. Lett.* **13**, 9649–9653 (2022)
28. C. Hirose, N. Akamatsu, K. Domen, *J. Chem. Phys.* **96**, 997–1004 (1992)
29. C. Hirose, N. Akamatsu, K. Domen, *Appl. Spectrosc.* **46**, 1051–1072 (1992)
30. C. Hirose, H. Yamamoto, N. Akamatsu, K. Domen, *J. Phys. Chem.* **97**, 10064–10069 (1993)
31. X. Zhuang, P.B. Miranda, D. Kim, Y.R. Shen, *Phys. Rev. B* **59**, 12633–12640 (1999)
32. L. Velarde, X.-Y. Zhang, Z. Lu, A.G. Joly, Z. Wang, H.-F. Wang, *J. Chem. Phys.* **135**, 241102 (2011)
33. L. Velarde, H.-F. Wang, *Phys. Chem. Chem. Phys.* **151**, 9970 (2013)
34. S. Nihonyanagi, J.A. Mondal, S. Yamaguchi, T. Tahara, *Annu. Rev. Phys. Chem.* **64**, 579–603 (2013)
35. Y.R. Shen, *Annu. Rev. Phys. Chem.* **64**, 129–150 (2013)
36. H. Li, S. Baldelli, *J. Phys. Chem. C*, **125**, 13560–13571 (2021)
37. C. Katagiri, T. Miyamae, H. Li, F. Yang, S. Baldelli, *Phys. Chem. Chem. Phys.* **23**, 4944–4950 (2021)
38. H. Maekawa, S.K.K. Kumar, S.S. Mukherjee, N.H. Ge, *J. Phys. Chem. B* **125**, 9507–9516 (2021)
39. M.B. Raschke, M. Hayashi, S.H. Lin, Y.R. Shen, *Chem. Phys. Lett.* **359**, 367–372 (2002)
40. T. Miyamae, Y. Miyata, H. Kataura, *J. Phys. Chem. C* **113**, 15314–15319 (2009)
41. T. Miyamae, E. Ito, Y. Noguchi, H. Ishii, *J. Phys. Chem. C* **115**, 9551–9560 (2011)
42. T. Miyamae, K. Tsukagoshi, W. Mizutani, *Phys. Chem. Chem. Phys.* **12**, 14666–14669 (2010)
43. C. Cai, M.S. Azam, D.K. Hore, *J. Phys. Chem. C* **125**, 12382–12389 (2021)
44. J.J. Machado, P.M.R. Gamarra, E.A.S. Maques, L.F.M. da Silva, *Comp. Struct.* **185**, 373–380 (2018)
45. R. Snyders, O. Zabeida, C. Roberges, K.I. Shingel, M.P. Faure, L. Marinu, J.E.K. Sapielha, *Surf. Sci.* **601**, 112–122 (2007)
46. F. Awaja, M. Gilbert, G. Kelly, B. Fox, P. Pigram, *Prog. Polym. Sci.* **34**, 948–968 (2009)
47. T. Miyamae, Y. Taga, *J. Adhes.* **94**, 1155–1167 (2018)
48. D.M. Brewis, I. Mathieson, M. Wolfensberger, *Int. J. Adhes. Adhes.* **15**, 87–90 (1995)
49. Y. Ohkubo, M. Shibahara, A. Nagatani, K. Honda, K. Endo, K. Yamamura, *J. Adhes.* **96**, 776–796 (2018)
50. Q.J. Kwon, S. Tang, S.W. Myung, N. Lu, H.S. Choi, *Surf. Coat. Technol.* **192**, 1–10 (2005)
51. J. Lai, B. Sunderland, J. Xue, S. Yan, W. Zhao, M. Folkard, B.D. Michael, Y. Wang, *Appl. Surf. Sci.* **252**, 3375–3379 (2006)
52. D.F. Williams, M.L. Abel, E. Grant, J. Hrachova, J.F. Watts, *Int. J. Adhes. Adhes.* **63**, 26–33 (2015)
53. A.P. Pijpers, R.J. Meier, *J. Electron Spectrosc. Relat. Phenom.* **121**, 299–313 (2001)
54. X. Yuan, B. Zhu, X. Cai, K. Qiao, S. Zhao, J. Yu, *Appl. Surf. Sci.* **458**, 996–1005 (2018)
55. T. Sato, H. Akiyama, S. Horiuchi, T. Miyamae, *Surf. Sci.* **677**, 93–98 (2018)
56. A. Opdahal, R.A. Phillips, G.A. Somorjai, *J. Phys. Chem. B* **106**, 5212 (2002)
57. F. Schulman, W.A. Zisman, *J. Colloid Sci.* **7**, 465 (1952)
58. Y. Taru, K. Takaoka, *Kobunshi Ronbunshu* **43**, 361–367 (1986)
59. D. Zhang, S.M. Dougal, M.S. Yeganeh, *Langmuir* **16**, 4528 (2000)
60. C. Borcia, I.L. Punga, G. Borcia, *Appl. Surf. Sci.* **317**, 103–110 (2014)
61. T. Sato, S. Ise, S. Horiuchi, H. Akiyama, T. Miyamae, *Int. J. Adhes. Adhes.* **93**, 102322 (2019)
62. K. Sensui, T. Tarui, T. Miyamae, C. Sato, *Chem. Commun.* **55**, 14833–14836 (2019)

63. R.D. Adams, *Adhesive Bonding, Science, Technology and Applications* (Woodhead Pub, Cambridge, 2005)
64. G.P. Harp, K.S. Gautam, A. Dhinojwara, *J. Am. Chem. Soc.* **124**, 7908–7909 (2002)
65. G.P. Harp, H. Rangwalla, M.S. Yaganeh, A. Dhinojwara, *J. Am. Chem. Soc.* **125**, 11283–11290 (2003)
66. F. Mori, S. Kabashima, T. Kawakami, T. Yamamoto, T. Miyamae, K. Iimura, N. Tabori, *Int. J. Adhes. Adhes.* **82**, 166–172 (2018)
67. T. Miyamae, *J. Surf. Anal.* **28**, 94–101 (2022)
68. I. Noda, *Bull. Am. Phys. Soc.* **31**, 520 (1986)
69. I. Noda, *J. Am. Chem. Soc.* **111**, 8116 (1989)
70. I. Noda, *Appl. Spectrosc.* **47**, 520 (1993)
71. M. Aoki, A. Shundo, K. Okamoto, T. Ganbe, K. Tanaka, *Polym. J.* **51**, 359–363 (2019)
72. S. Yamamoto, R. Kuwahara, M. Aoki, A. Shundo, K. Tanaka, *ACS Appl. Polym. Mater.* **2**, 1474–1481 (2020)
73. C. Chen, J. Wang, C.L. Loch, D. Ahn, Z. Chen, *J. Phys. Chem. B* **107**, 10440–10445 (2003)
74. X. Lu, N. Shephard, J. Han, G. Xue, Z. Chen, *Macromolecules* **41**, 8770–877 (2008)
75. X. Lu, C.B. Kristalyn, N. Han, N. Shephard, S. Rhodes, G. Xue, Z. Chen, *Macromolecules* **42**, 9052–9057 (2009)
76. X. Lu, J.N. Myers, Z. Chen, *Langmuir* **30**, 9418–9422 (2014)
77. Z. Xu, Y. Zhang, Y. Wu, X. Lu, *Langmuir* **38**, 13261–13271 (2022)
78. Y. Liu, Y. Shigemoto, T. Hanada, T. Miyamae, K. Kawasaki, S. Horiuchi, *ACS Appl. Mater. Interf.* **13**, 11497–11506 (2021)
79. A.S. Nielsen, D.N. Batchelder, R. Pyrz, *Polymer* **43**, 2671–2676 (2002)
80. S. Singla, G. Amapuri, N. Dhopatkar, T.A. Blackledge, A. Dhinojwala, *Nat. Commun.* **9**, 1890 (2018)
81. K. Autumn, Y.A. Liang, S.T. Hseih, W. Zesch, W.P. Chan, T.W. Kenny, R. Fearing, R.J. Full, *Nature* **405**, 681–685 (2000)
82. K. Autumn, M. Sitti, Y.A. Liang, A.M. Peattie, W.R. Hansen, S. Sponberg, T.W. Kenny, R. Fearing, J.N. Israelachvili, R.J. Full, *Proc. Natl. Acad. Sci.* **99**, 12252–12256 (2002)
83. S. Single, D. Jain, C.M. Zoltowski, S. Voleti, A.Y. Stark, P.H. Niewiarowski, A. Dhinojwara, *Sci. Adv.* **7**, eabd9410 (2021)
84. A. Kurian, S. Prasad, A. Dhinojwala, *Langmuir* **26**, 17804–17807 (2010)
85. S. Singla, M.C. Wilson, A. Dhinojwala, *Phys. Chem. Chem. Phys.* **21**, 2513–2518 (2019)
86. M.C. Wilson, S. Singla, A.J. Stefin, S. Kaur, J.V. Brown, A. Dhinojwala, *J. Phys. Chem. C* **123**, 18495–18501 (2019)
87. A.E. Ivanov, J. Ekeröth, L. Nilsson, B. Mattiasson, B. Bergenståhl, I.Y. Galaev, *J. Colloid Interface Sci.* **296**, 538–544 (2006)
88. N. Yamada, T. Okano, H. Sakai, Y. Sakurai, *J. Biomed. Mater. Res.* **27**, 1243 (1993)
89. Y. Maeda, T. Nakamura, I. Ikeda, *Macromolecules* **34**, 1391–1399 (2001)
90. Y. Maeda, T. Higuchi, I. Ikeda, *Langmuir* **16**, 7503–7509 (2000)
91. Y. Maeda, T. Nakamura, I. Ikeda, *Macromolecules* **35**, 10172–10177 (2002)
92. L.A. Francis, J.M. Friedt, C. Zhou, P. Bertrand, *Anal. Chem.* **78**, 4200–4209 (2006)
93. C. Urata, B. Masheder, D.F. Cheng, D.F. Miranda, G.J. Dunderdale, T. Miyamae, A. Hozumi, *Langmuir* **30**, 4049–4055 (2014)
94. R. Mallavia, F. Montilla, I. Pastor, P. Velasquez, B. Arredondo, A.L. Alvarez, C.R. Mateo, *Macromolecules* **38**, 3185–3192 (2005)
95. M. Hayashi, S.H. Lin, M.B. Raschke, Y.R. Shen, *J. Phys. Chem. A* **106**, 2271–2282 (2002)
96. D. Wu, G. H. Deng, Y. Guo, H. F. Wang, *J. Phys. Chem. A* **113**, 6058–6063 (2009)
97. Q. Li, R. Hua, K.C. Chou, *J. Phys. Chem. B* **112**, 2315–2318 (2008)
98. M. Grell, D.D.C. Bradley, G. Ungar, J. Hill, K.S. Whitehead, *Macromolecules* **32**, 5810–5817 (1999)
99. K. Becker, J.M. Lupton, *J. Am. Chem. Soc.* **127**, 7306–7307 (2005)
100. H. Ye, J. Huang, J.R. Park, H.E. Katz, E. Katz, D.H. Gracias, *J. Phys. Chem. C* **111**, 13250–13255 (2007)

101. T.C. Anglin, D.B. O'Brien, A.M. Massari, *J. Phys. Chem. C* **114**, 17629–17637 (2010)
102. S.G. Motti, L.S. Cardoso, D.J.C. Gomes, R.M. Faria, P.B. Miranda, *J. Phys. Chem. C* **122**, 10450–10458 (2018)
103. K. Nakamae, T. Nishino, X. Airu, S. Asaoka, *Int. J. Adhes. Adhes* **15**, 15–20 (1995)
104. B. Salgin, Ö. Özkanat, J.M.C. Mol, H. Terryn, M. Rohwerder, *J. Phys. Chem. C* **117**, 4480–4487 (2013)
105. R.G. Dillingham, F.J. Boerio, *J. Adhesion* **24**, 315 (1987)
106. S.G. Hong, F.J. Boerio, *J. Adhesion* **32**, 67 (1990)
107. S.G. Hong, F.J. Boerio, *J. Adhesion* **49**, 133 (1995)
108. J.E. Baio, T. Weidner, J. Brison, D.J. Graham, L.J. Gamble, D.G. Castner, *J. Electron Spectrosc. Relat. Phenom.* **172**, 2 (2009)
109. K. Akaike, Y. Shimoi, T. Miura, H. Morita, H. Akiyama, S. Horiuchi, *Langmuir* **39**, 10625–10637 (2023)
110. I. Jo, Y. Kim, J. Moon, S. Park, J.S. Moon, W.B. Park, J.S. Lee, B.H. Hong, *Phys. Chem. Chem. Phys.* **17**, 29492 (2015)
111. F. Cavezza, M. Boehm, H. Terryn, T. Hauffman, *Metals* **10**, 730 (2020)
112. S.G. Hong, N.G. Cave, F.J. Boerio, *J. Adhesion* **36**, 265 (1992)
113. S.G. Hong, F.J. Boerio, *Surf. Interf. Anal.* **21**, 650 (1994)
114. S. Zhang, J.S. Andre, L. Hsu, A. Toolis, S.L. Esarey, B. Li, Z. Chen, *Macromolecules* **53**, 10189 (2020)
115. S. Zhang, L. Hsu, A. Toolis, B. Li, J. Zhou, T. Lin, Z. Chen, *Langmuir* **37**, 12705 (2021)
116. K. Shimizu, C. Phanopoulos, R. Loenders, M.-L. Abel, J.F. Watts, *Surf. Interf. Anal.* **42**, 1432 (2010)
117. A. Kurian, S. Prasad, A. Dhinojwala, *Langmuir* **26**, 17804 (2010)
118. K. Akaike, H. Akiyama, *J. Adhesion* **99**, 1933–1946 (2023)

Open Access This chapter is licensed under the terms of the Creative Commons Attribution 4.0 International License (<http://creativecommons.org/licenses/by/4.0/>), which permits use, sharing, adaptation, distribution and reproduction in any medium or format, as long as you give appropriate credit to the original author(s) and the source, provide a link to the Creative Commons license and indicate if changes were made.

The images or other third party material in this chapter are included in the chapter's Creative Commons license, unless indicated otherwise in a credit line to the material. If material is not included in the chapter's Creative Commons license and your intended use is not permitted by statutory regulation or exceeds the permitted use, you will need to obtain permission directly from the copyright holder.

